

AD-A114 168

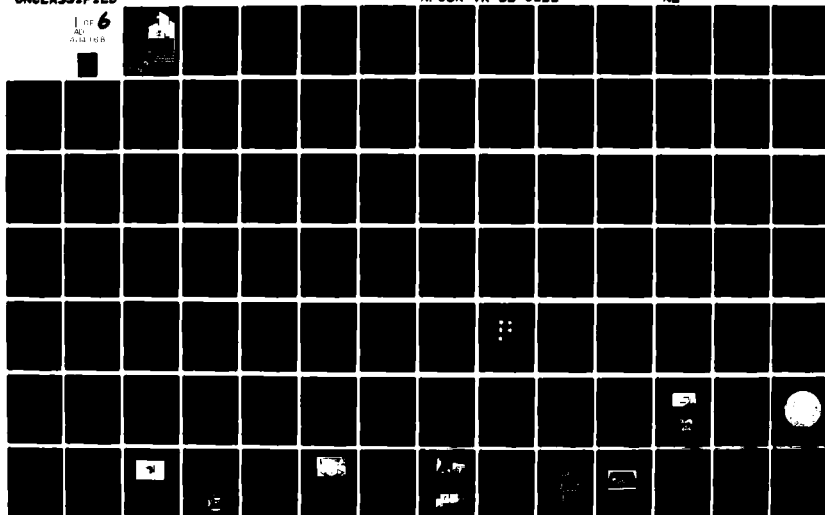
COLORADO UNIV AT BOULDER DEPT OF CIVIL ENVIRONMENTAL --ETC F/G 20/11
CONSTITUTIVE RELATIONS OF RANDOMLY ORIENTED STEEL FIBER REINFOR--ETC(U)
DEC 81 D E EGGING, H KO AFOSR-79-0065

UNCLASSIFIED

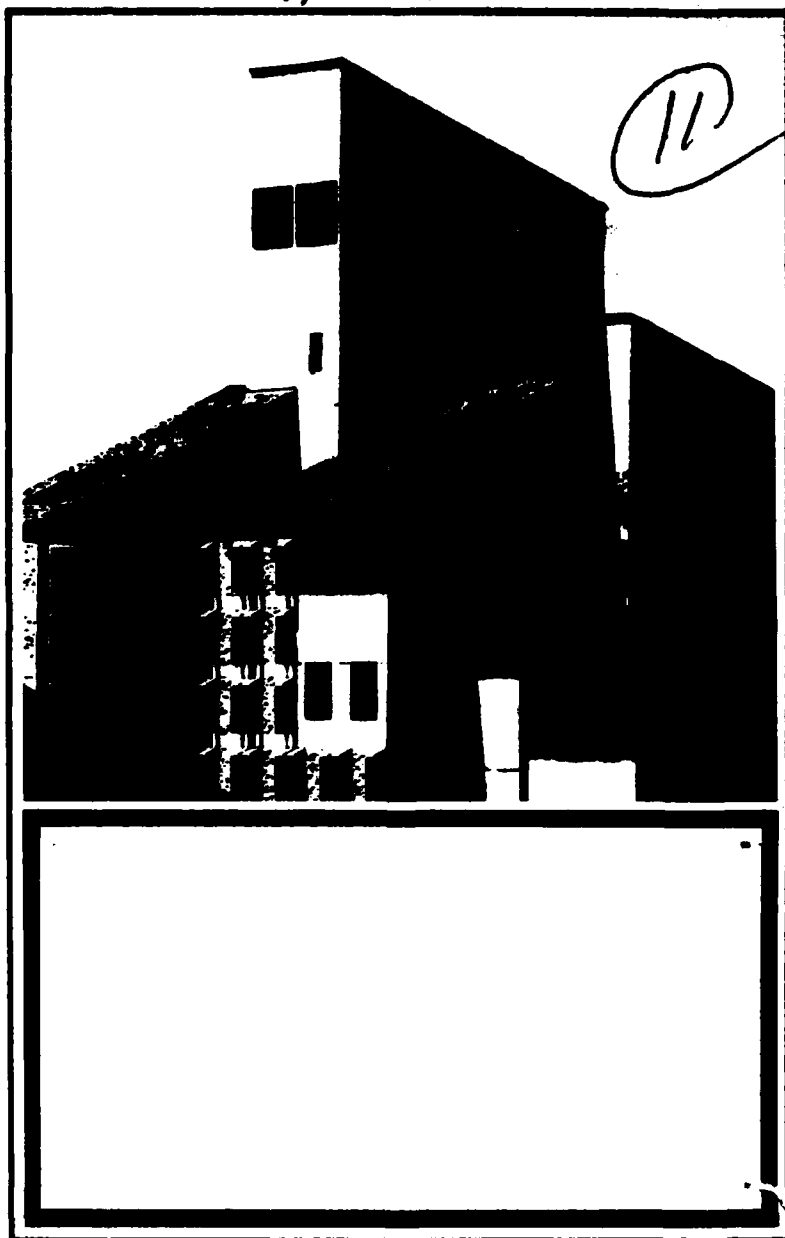
AFOSR-TR-82-0122

NL

1 OF 6
6
AD-A114 168



AD A114168



Department of Civil,
Environmental, and
Architectural Engineering

University of Colorado,
Boulder

Approved for public release;
distribution unlimited.

82 05 06 015

DTIC FILE COPY

DTIC
ELECTED
MAY 6 1982
H

11

CONSTITUTIVE RELATIONS OF RANDOMLY ORIENTED
STEEL FIBER REINFORCED CONCRETE UNDER
MULTIAXIAL COMPRESSIVE LOADINGS

by

Daniel E. Egging

and

Hon-Yim Ko

AIR FORCE OFFICE OF SCIENTIFIC RESEARCH (AFOSR)

NOTES

TRIN

SYSTEM

Dist

MAITHE

Chief, Technical Information Division

and is
10-12.

Submitted to Air Force Office of Scientific Research
under

Grant No. AFOSR-79-0065

Hon-Yim Ko and Chuan C. Feng
Principal Investigators

December, 1981

DTIC
SELECTED
MAY 6 1982
H

CONSTITUTIVE RELATIONS OF RANDOMLY ORIENTED STEEL FIBER
REINFORCED CONCRETE UNDER MULTIAXIAL COMPRESSIVE LOADINGS

by

Daniel E. Egging and Hon-Yim Ko

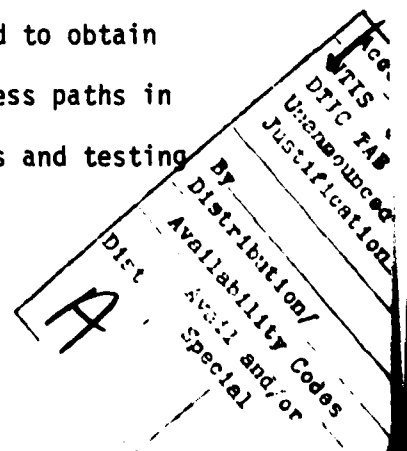
ABSTRACT

The addition of steel fibers to plain concrete has been shown to improve many of the material's engineering properties. These improvements have brought about new applications for the material, requiring the mechanical properties under multidimensional stress states. This provides the basis for the research program described herein.

A review of the state-of-the-art research on steel fiber reinforced concrete (SFRC) is given and a review of the behavior and strength of plain concrete subjected to multiaxial stresses is presented.

Two series of tests on SFRC were conducted. The first preliminary series, provides results of some basic tests on concrete randomly mixed with each of five types of commercially available steel fibers. This information allowed the determination of the optimum fiber to use in the second, final test series, where the properties of SFRC under three-dimensional compressive loadings are investigated.

A fluid-cushion, cubical testing device was used to obtain the behavior of the SFRC along various monotonic stress paths in the deviatoric plane. A description of the apparatus and testing program is presented.



The results from the final test series were used to calibrate several mathematical constitutive models including the Willam-Warnke and Lade failure criteria for strength and Gerstle's "Simple Formulation" for stress-strain behavior. The predictions from these models are compared with the experimental data, with generally favorable agreement.

The conclusions drawn from the test results are that the addition of steel fibers to plain concrete increases the toughness, ductility and stiffness of the material. The greatest improvement of the tensile strength is provided by the longer fibers, whereas the opposite is true regarding the compressive strength. The reproducibility of the experimental results is good and the SFRC proved to be nearly isotropic as observed from the multiaxial tests.

Both of the investigated failure criteria predicted the strengths of the SFRC very well, when calibrated for that material. However the Lade failure criterion proved to be less sensitive to the input data than the Willam-Warnke failure criterion. Gerstle's "Simple Formulation" predicted the stress-strain behavior of the SFRC with reasonable accuracy for the type of tests conducted but more experimental studies are needed to verify if the formulation will work for other types of tests.

CONTENTS

CHAPTER

1	INTRODUCTION AND PREVIOUS WORK	1
1.1	Introduction	1
1.2	Previous Work	4
1.2.1	Fiber Reinforced Concrete and Mortar	4
1.2.2	Plain Concrete Response to Multiaxial Stresses	15
1.3	Scope of Investigation	35
2	RESEARCH PROGRAM	38
2.1	Introduction	38
2.2	Mix Design	39
2.3	Check on Steel Fiber Reinforced Concrete Mix Proportioning	46
2.4	Casting and Curing Procedures	57
2.5	Sample Preparation	65
2.6	Multiaxial Test Apparatus	67
2.6.1	Frame	69
2.6.2	Walls	71
2.6.3	Seals	73
2.6.4	Pressure System	77
2.6.5	Deformation Measurement System	79
2.6.6	Data Acquisition and Data Reduction System ...	84
2.7	Test Procedure	87

CHAPTER

2.8	Test Program	92
3	PRELIMINARY TEST SERIES	109
3.1	Introduction	109
3.2	Stress-Strain Relations	109
3.2.1	Unconfined Compression	109
3.2.2	Multiaxial Compression	125
3.3	Strength	136
3.3.1	Unconfined Compression	136
3.3.2	Relations Between Unconfined Compressive Strength (f'_c), Indirect Tensile Strength (T), Rupture Modulus (R) and Various Fiber Properties	141
3.4	Conclusions for the Design of the Mix Used in the Final Test Series	156
4	FINAL TEST SERIES	161
4.1	Introduction	161
4.2	Unconfined Compression	162
4.3	Multiaxial Compression	166
4.3.1	Principal Stress-Strain Relations	168
4.3.1.1	Hydrostatic Compression (HC)	207
4.3.1.2	Triaxial Compression (TC) in the Octahedral Plane	208
4.3.1.3	Simple Shear (SS) in the Octahedral Plane ..	208
4.3.1.4	Triaxial Extension (TE) in the Octahedral Plane	209
4.3.2	Octahedral Stress-Strain Relations	210
4.3.2.1	Hydrostatic Compression (HC)	249
4.3.2.2	Shear Deviation	254

CHAPTER

4.3.3	Method for Determination of Elastic Material Constants	287
4.3.4	Strength	300
5	ANALYTICAL PREDICTIONS OF STRENGTH AND BEHAVIOR	308
5.1	Introduction	308
5.2	Failure Criteria	309
5.2.1	Willam-Warnke Five-Parameter Failure Criterion	313
5.2.1.1	Fitting of CU-SFRC Strength Results to the Willam-Warnke Model	322
5.2.2	Lade Three-Parameter Failure Criterion for Concrete	334
5.2.2.1	Fitting of the CU-SFRC Strength Results to the Lade Three-Parameter Model	343
5.2.3	Comparison of the Willam-Warnke and Lade Failure Criteria Using Various Input Strength Data	352
5.2.4	Normality of CU-SFRC With Respect to the Willam-Warnke Failure Criterion	375
5.3	Simple Formulation of Multiaxial Concrete Behavior	392
5.3.1	Representation of Moduli	398
5.3.2	Experimental Verification of the "Simple Formulation" with the CU-SFRC	413
6	SUMMARY, CONCLUSIONS AND RECOMMENDATIONS FOR FUTURE WORK	427
6.1	Summary	427
6.2	Conclusions	427
6.3	Recommendations for Future Work	431
	BIBLIOGRAPHY	433

APPENDIX

- A. PRINCIPAL AND OCTAHEDRAL STRESS-STRAIN CURVES
FOR INDIVIDUAL PRELIMINARY TESTS;
TABULATED PRINCIPAL STRESS-STRAIN DATA FOR
INDIVIDUAL FINAL TESTS 445

TABLES

Table

1.1	Loading Systems [Gerstle, <u>et. al.</u> (51)].....	23
2.1	Steel Fiber Sizes With Corresponding Fiber Concrete Mix Number.....	43
2.2	Preliminary Test Program. Unconfined Compression of 3x6 in. Cylinders.....	99
2.3	Preliminary Test Program. Unconfined Compression of 4 in. Cubes.....	102
2.4	Preliminary Test Program. Indirect Tension of 3x6 in. Cylinders.....	104
2.5	Preliminary Test Program. Flexural Tests of 3x3x15 in. Beams.....	105
2.6	Preliminary Test Program. Multiaxial Compression of 4 in. Cubes.....	106
2.7	Final Test Program. Unconfined Compression of 3x6 in. Cylinders.....	107
2.8	Final Test Program. Multiaxial Compression of 4 in. Cubes.....	108
3.1	Steel Fiber Sizes With Corresponding Fiber Concrete Mix Number.....	123
3.2	Summary of Average Strengths for Preliminary Tests.....	157
4.1	Summary of Average Strengths and Secant Moduli for Cylinders in Unconfined Compression.....	167
4.2	Summary of Average Compliance Values for Each of Seven Specimens.....	295
4.3	Overall Average Compliance Matrix for All Specimens Listed in TABLE 4.2.....	297
4.4	Failure Data for CU-SFRC.....	302

Table

5.1	Summary of Strengths Used for Calibrating Willam-Warnke and Lade Failure Criteria and Parameters Obtained for Parametric Study.....	353
A.1-	Principal Stress-Strain Data for the Multiaxial	
A.28	Compression Tests on 4 in. Cubes in the Final Test Series.....	470

FIGURES

Figure

1.1	Ultimate Strength as Linear Function of $p\lambda/d$. (p = volume percentage of fibers; λ/d = fiber aspect ratio).....	6
1.2	Stress-Strain Curves for Concrete Reinforced with Stirrups and Fibers Subject to Uniaxial Compression [Shah, <u>et al.</u> (117)].....	7
1.3	Effect of Volume of Fibers in Tension [Shah, <u>et al.</u> (117)].....	8
1.4	Effect of Volume of Fibers in Flexure [Shah, <u>et al.</u> (117)].....	9
1.5	Comparison of Strength Curves [Taylor, <u>et al.</u> (130)].....	16
1.6	Biaxial Strength of Concrete; Results of Experimental Investigation [Kupfer, <u>et al.</u> (74)].....	18
1.7	Five-Parameter Model - Fitting of Triaxial Test Data [Willam, <u>et al.</u> (134)].....	19
1.8	Failure Surface for Plain Concrete [Willam, <u>et al.</u> (134)].....	20
1.9	Multiaxial Test Methods [Gerstle, <u>et al.</u> (51)].....	22
1.10	Strength of Concrete Under Biaxial Loading [Gerstle, <u>et al.</u> (51)].....	24
1.11	Normalized Strength Envelopes [Gerstle, <u>et al.</u> (51)].....	25
1.12	Load Paths for Triaxial Loadings in Different Presentations [Gerstle, <u>et al.</u> (51)].....	26
1.13	Triaxial Failure Envelopes Within the Octahedral Plane $\sigma_0 = 5 \text{ ksi} = 350 \text{ kg/cm}^2$ [Gerstle, <u>et al.</u> (51)]..	27
1.14	Biaxial Strength Results Compared with Mean Values of Triaxial Results [Gerstle, <u>et al.</u> (51)].....	28

1.15	(a) Mean Volumetric Stress-Strain Curves of Triaxial Test Series with Frictionless Boundaries;	
	(b) Mean Deviatoric Stress-Strain Curves of Triaxial Test Series with Frictionless Boundaries [Gerstle, <u>et al.</u> (50)].....	31
1.16	Shear Dilatancy for Triaxial Test Series [Gerstle, <u>et al.</u> (50)].....	31
1.17	Bulk Modulus vs. Octahedral Normal Strain [Gerstle, <u>et al.</u> (50)].....	32
1.18	Shear Modulus vs. Octahedral Shear Strain [Gerstle, <u>et al.</u> (50)].....	32
1.19	Coupling Modulus vs. Octahedral Normal Stress [Gerstle, <u>et al.</u> (50)].....	33
2.1	Aggregate Gradation Curves Used and ASTM Limits.....	42
2.2	Steel Fiber Dimensions.....	44
2.3	Fiber Groups - Collated and Loose.....	45
2.4	Critical Steel Fiber Content [Moens (88)].....	48
2.5	Aggregate Mixture Gradation Curves for CU-SFRC and Moens (88).....	49
2.6	Influence of Aggregate Volume [Swamy (124)].....	51
2.7	Interaction Coefficients of Aggregate Fractions [Moens (88)].....	55
2.8	Calculating the Fiber-Aggregate Interaction Factor (C_m) for the Mixture.....	56
2.9	Typical Concrete Molds.....	62
2.10	Martin Vibrolator ® Eccentric Ball Type External Vibrator.....	62
2.11	X-Ray View of a Typical 1/2 inch Slice of a 6 x 12 inch Cylinder Vibrated Internally.....	64
2.12	Typical 4 in. Cubical Specimen After Test Preparation.....	67
2.13	Exploded View of the Test Cell.....	68
2.14	Photograph of Test Cell Frame.....	70

		xii
2.15	Dimensions of the Cell Frame.....	70
2.16	Exploded View of a Typical Wall.....	72
2.17	Front and Rear View of a Typical Assembled Wall.....	72
2.18	Detail from Assembled Test Cell.....	74
2.19	Top and Bottom Views of Polyurethane Membrane and Pad, Leather Pad and Brass Target.....	75
2.20	Leather Pad Dimensions.....	76
2.21	Hydraulic System Diagram.....	78
2.22	Pumping System and Instrumentation Panel.....	80
2.23	Set of Three Proximity - Type Displacement Transducers (Probes) Mounted on Probe Block.....	80
2.24	Typical Proximator Probe Calibration Curve.....	81
2.25	Brass Target Dimensions.....	83
2.26	Front View of Central Data Acquisition System.....	85
2.27	Hewlett-Packard Computer and Plotter.....	86
2.28	Typical Real-Time Data Output.....	88
2.29	Bolt Tightening Sequence for the Box Faces and Respective Walls.....	90
2.30	Test Cell Connected to Hydraulic and Electrical Systems.....	93
2.31	Stress Paths in (a) 3-D Stress Space; (b) Octahedral Plane... ..	95
2.32	Triaxial Load Paths with Principal Stress Orientation Given.....	96
3.1- 3.11	Unconfined Compression Stress-Strain Curves for 3x6 in. Cylinders in the Preliminary Test Series.....	111
3.12	Secant Modulus of Elasticity vs. Age for the Unconfined Compression Tests on 3x6 in. Cylinders.....	124
3.13- 3.20	Maximum Principal Stress-Strain Curves ($\sigma_1 - \epsilon_1$) for Multiaxial Compression Tests on 4-in. cubes in the Preliminary Test Series.....	126

3.21	Average Unconfined Compressive Strength of 3x6 in. Cylinders (f'_c) vs. Age for the Preliminary Test Series.....	137
3.22	Average Unconfined Compressive Strength of 4-in. Cubes (f'_c) vs. Age for the Preliminary Test Series....	139
3.23	Comparison of Average Unconfined Compressive Strength for 3x6 in. Cylinders (f'_c) and 4 in. Cubes (f'_c) vs. Age for the Final SFRC Mix Chosen.....	140
3.24	Average 50-day Unconfined Compressive Strength (f'_c) vs. Aspect Ratio (ℓ/d).....	145
3.25	Average Indirect Tensile Strength (T) vs. Aspect Ratio (ℓ/d).....	146
3.26	Average Rupture Modulus (R) vs. Aspect Ratio (ℓ/d)....	147
3.27	Average 50-day Unconfined Compressive Strength (f'_c) vs. Fiber Length.....	148
3.28	Average Indirect Tensile Strength (T) vs. Fiber Length.....	149
3.29	Average Rupture Modulus (R) vs. Fiber Length.....	150
3.30	Average 50-day Unconfined Compressive Strength (f'_c) vs. Total Fiber Cross-Sectional Area per cu.in. of Concrete.....	151
3.31	Average Indirect Tensile Strength (T) vs. Total Fiber Cross-Sectional Area per cu.in. of Concrete.....	152
3.32	Average Rupture Modulus (R) vs. Total Fiber Cross-Sectional Area per cu.in. of Concrete.....	153
3.33	Failure Modes in: (a) Indirect Tension; (b) Pure Bending.....	154
4.1	Unconfined Compression Stress-Strain Curves for 3x6 in. Cylinders.....	163
4.2	Unconfined Compression Stress-Strain Curves for 3x6 in. Cylinders.....	164
4.3	Secant Modulus of Elasticity vs. Age for the Unconfined Compression Tests on 3x6 in. Cylinders.....	165

4.4- 4.31	Principal Stress-Strain Curves for the Multiaxial Compression Tests on 4 in. Cubes in the Final Test Series.....	169
4.32- 4.40	Principal Stress-Strain Summary Results.....	197
4.41- 4.68	Octahedral Stress-Strain Curves for the Multiaxial Compression Tests on 4-in. Cubes in the Final Test Series.....	211
4.69- 4.77	Octahedral Stress-Strain Summary Results.....	239
4.78	Summary of Volumetric Behavior During Hydrostatic Compression.....	250
4.79	Tangent Bulk Modulus vs. Octahedral Normal Stress for all Results During Hydrostatic Compression.....	252
4.80	Tangent Bulk Modulus vs. Octahedral Normal Strain for all Results During Hydrostatic Compression.....	253
4.81- 4.86	Average Octahedral Shear Stress-Strain Results.....	255
4.87	Tangent Shear Modulus vs. Octahedral Shear Stress for all Results During Shear Deviation.....	263
4.88	Tangent Shear Modulus vs. Octahedral Shear Strain for all Results During Shear Deviation.....	264
4.89- 4.94	Average Tangent Shear Modulus vs. Octahedral Shear Stress.....	265
4.95- 4.100	Average Tangent Shear Modulus vs. Octahedral Shear Strain.....	271
4.101- 4.106	Average Octahedral Shear Stress-Normal Strain Results.....	279
4.107	Stress Path Along Hydrostatic Axis Used to Determine the Elastic Constants.....	294
4.108	Failure Data in τ_0 - σ_0 plane.....	303
4.109	Failure Data in Octahedral Planes.....	304
4.110	Failure Data in Rendulic Plane with Best Fit Lines Through Data.....	305

5.1	Von Mises Failure Surface.....	311
5.2	Drucker-Prager Failure Surface.....	311
5.3	τ_0 - σ_0 or Hydrostatic Section of Proposed Willam-Warnke Failure Surface.....	315
5.4	Deviatoric or Octahedral Section of Proposed Willam-Warnke Failure Surface.....	316
5.5	Willam-Warnke Failure Surface Showing One Sextant of Ellipse in Deviatoric Plane.....	318
5.6	Failure Data in τ_0 - σ_0 Plane with Willam-Warnke Prediction.....	327
5.7	Failure Data in Octahedral Planes with Willam-Warnke Predictions.....	328
5.8	Failure Data in Rendulic Plane with Willam-Warnke Prediction.....	329
5.9	Predicted Biaxial Failure Envelope Based on Willam-Warnke Failure Criterion.....	332
5.10	Translation of Principal Stress Space Along Hydrostatic Axis to Include Effect of Tensile Strength in Lade's Failure Criterion [Lade (79)].....	337
5.11	Example of Determination of Material Parameters Involved in Lade's Failure Criterion for Concrete Tested by Mills and Zimmerman [Lade (79)].....	339
5.12	Comparison of Lade Failure Criterion in Biaxial Planes with Results of Biaxial Tests Performed by Mills and Zimmerman [Lade (79)].....	340
5.13	Comparison of Lade Failure Criterion in Triaxial Planes with Results of Triaxial Compression and Extension Tests Performed by Mills and Zimmerman [Lade (79)].....	341
5.14	Comparison of Lade Failure Criterion in Octahedral Planes with Results of Tests on Concrete Performed by Mills and Zimmerman [Lade (79)].....	342
5.15	Determination of Material Parameters Involved in Lade's Failure Criterion for the CU-SFRC.....	344
5.16	Failure Data in τ_0 - σ_0 Plane with Lade Prediction.....	346

5.17	Failure Data in Octahedral Planes with Lade Predictions.....	347
5.18	Failure Data in Triaxial Plane with Lade Prediction...	348
5.19	Predicted Biaxial Failure Envelope Based on Lade Failure Criterion.....	350
5.20	Failure Data in τ_0 - σ_0 Plane with Willam-Warnke Prediction.....	358
5.21	Failure Data in Octahedral Planes with Willam-Warnke Predictions.....	359
5.22	Failure Data in Triaxial Plane with Willam-Warnke Prediction.....	360
5.23	Predicted Biaxial Failure Envelope Based on Willam-Warnke Failure Criterion.....	361
5.24	Failure Data in τ_0 - σ_0 Plane with Willam-Warnke Prediction.....	363
5.25	Failure Data in Octahedral Planes with Willam-Warnke Predictions.....	364
5.26	Failure Data in Triaxial Plane with Willam-Warnke Prediction.....	365
5.27	Failure Data in τ_0 - σ_0 Plane with Lade Prediction.....	367
5.28	Failure Data in Octahedral Planes with Lade Predictions.....	368
5.29	Failure Data in Triaxial Plane with Lade Prediction...	369
5.30	Predicted Biaxial Failure Envelope Based on Lade Failure Criterion.....	370
5.31	Failure Data in τ_0 - σ_0 Plane with Lade Prediction.....	371
5.32	Failure Data in Octahedral Planes with Lade Predictions.....	372
5.33	Failure Data in Triaxial Plane with Lade Prediction...	373
5.34	Predicted Biaxial Failure Envelope Based on Lade Failure Criterion.....	374
5.35	Failure Data in τ_0 - σ_0 Plane with Lade Prediction.....	376
5.36	Failure Data in Octahedral Planes with Lade Predictions.....	377

5.37	Failure Data in Triaxial Plane with Lade Prediction...	378
5.38	Predicted Biaxial Failure Envelope Based on Lade Failure Criterion.....	379
5.39	Stress-Strain Response Curve for an Elasto-Plastic Hardening Material [Mould (89)].....	381
5.40	Post-Failure Strain Rate Vectors of Mortar from Steel Plate Series [Andenes (8)].....	382
5.41	Post-Failure Plastic Strain Increment Vectors Superimposed Upon Failure Envelope in Invariant Plane.....	384
5.42	Post-Failure Plastic Strain Increment Vectors Superimposed Upon Failure Envelopes in Deviatoric Planes.....	385
5.43	Post-Failure Plastic Strain Increment Vectors Superimposed Upon Failure Envelope in Triaxial Plane.....	386
5.44	Exploded View for Part of Fig. 5.43.....	387
5.45	Post-Failure Plastic Strain Increment Vectors Superimposed Upon Failure Envelope in Triaxial Plane.....	388
5.46	Exploded View for Part of Fig. 5.45.....	389
5.47	γ_0 vs. $\log (1-\tau_0/\tau_{ou})$ Examples for Determining G_0	402
5.48	Initial Shear Modulus G_0 vs. Confining Pressure σ_0	403
5.49	Normalized G_T/G_0 vs. τ_0/τ_{ou} Results.....	405
5.50	ϵ_0 vs. $\log (1-\alpha \cdot \sigma_0/\sigma_{ou})$ Examples for Determining K_0 ...	408
5.51	Normalized K_T/K_0 vs. σ_0/σ_{ou} Results.....	409
5.52	Variation of Coupling Modulus H_T with Confining Pressure σ_0	412
5.53- 5.61	Principal Stress-Strain Summary Results with Predictions from the "Simple Formulation".....	415
A.1- A.12	Principal Stress-Strain Curves for the Multiaxial Compression Tests on 4 in. Cubes in the Preliminary Test Series.....	446
A.13- A.24	Octahedral Stress-Strain Curves for the Multiaxial Compression Tests on 4-in Cubes in the Preliminary Test Series.....	458

CHAPTER 1

INTRODUCTION AND PREVIOUS WORK

1.1 Introduction

The addition of fibers to cementitious materials improves many of the engineering properties of the materials by providing for a different deformation and failure mechanism from that of the plain matrix material. In steel fiber reinforced concrete, composite failure can occur in two ways, depending on the type of fibers used. For straight fibers, the composite failure generally occurs due to a bond failure at the fiber-matrix interface. The first crack in the composite occurs when the composite strain exceeds the crack strain of the matrix. On further loading, the fibers (stiffer than the plain matrix) act as crack arrestors, and a period of slow crack propagation with progressive debonding of the straight fibers follows. Near ultimate load, unstable crack propagation occurs simultaneously with the interfacial bonding reaching the ultimate bond strength between the fibers and the plain matrix, and failure by fiber pullout occurs. However, for deformed or bent fibers, the composite failure mechanism is slightly different. During the period of slow crack propagation, debonding of the deformed fibers generally does not occur because the bent ends act as anchors increasing the bond strength of the fibers in addition to the bond developed along the straight part of the fiber-matrix

interface. Therefore, rather than fiber pullout occurring when unstable crack propagation begins, the fibers break along the crack planes when the ultimate load is approached.

Let it be pointed out that the presence of any fiber type does very little when crushing of the composite occurs simply because the essential part of the matrix required to develop the bond with the fibers has been destroyed.

Regardless of the fiber type, fiber additions to concrete provide a convenient and practical means of achieving improvements in many of the material's engineering properties. Fiber reinforced concrete possesses a higher tensile strength and modulus of rupture than plain concrete as well as more impact and fatigue resistance. Although the compressive strength is not much improved, the brittle behavior that would occur in plain concrete after peak strength is not as prevalent and a ductile behavior is obtained, giving rise to an increase in toughness over that observed in plain concrete.

Such improvements in the concrete's properties by the presence of fibers brought about new applications of the material, such as pressure vessels for nuclear reactors, advanced underground protective structures, tunnel linings, overlays for bridge decks, highways and runways, and slope stabilization. These are some of the applications where concrete or concrete-type materials are subjected to multidimensional stress states. In these types of situations, the material properties of all the constituents must be accurately represented in order to take full advantage of the versatile numerical schemes developed for structural analysis for both static and dynamic loadings. It becomes necessary to

characterize the behavior of the structural elements under general three-dimensional loadings. Not only must three-dimensional tests be performed to elucidate the response of the material, but its response must also be analyzed and suitable constitutive models be derived for incorporation into the structural analysis in order that the results of the material characterization be utilized in applications.

The phenomenological formulation of the constitutive relations of steel fiber reinforced concrete has been totally lacking. This is perhaps not surprising, considering the fact that serious studies of the stress-strain behavior for plain portland cement concrete have only started in the last few years. In view of the fact that steel fiber reinforced concrete is seeing increasing usage in situations where multidimensional stress states arise, and recognizing the deficiency in characterizing this type of material, research was performed at the University of Colorado on a systematic investigation of the mechanical properties of such materials.

This report contains the results of the experimental-analytical study on the constitutive properties of one type of steel fiber reinforced concrete under three-dimensional compressive loadings. Included are the stress-strain and strength behavior of the specimens tested. The experimental data is analyzed not only to determine the suitability of various failure hypotheses, but also to formulate constitutive models on the basis of octahedral quantities and plasticity concepts.

1.2 Previous Work

This section is separated into two parts. In the first part, some of the previous work concerning the determination and characterization of the material and mechanical properties of fiber reinforced concrete materials is reviewed and some applications of the composite discussed. However, none of this work has been concerned with the constitutive properties of fiber reinforced concrete under multiaxial states of stress. Some of the strength and behavior criteria for plain concrete subjected to multiaxial loads will be used (and modified if necessary) to represent properties of the fiber concrete. Therefore in the second part of this section a synopsis is given of some of the state-of-the-art work dealing with the strength and behavior of plain concrete materials subjected to multiaxial states of stress either experimentally, analytically, or both.

1.2.1 Fiber Reinforced Concrete and Mortar

Fiber additions to concrete offer a convenient and practical means of achieving improvements in many of the engineering properties of the material such as fracture toughness, fatigue resistance, impact resistance and flexural strength (82). The idea of fiber reinforcement applications is not new. As early as 1910, Potter (5) made some attempt to apply short lengths of steel wire to increase the tensile strength of concrete. However, serious efforts to develop applications for fiber reinforced concrete started about 10-15 years ago. Application areas in which

significant field trials have taken place include bridge decks and pavements (highway and airfield), mining and tunneling, slope stabilization, refractory applications, concrete repair, industrial floors, and precast concrete products.

Studies on the strength of concrete in light of the advances made in fracture mechanics indicated that the tensile strength of concrete could be substantially increased by providing suitably arranged and closely spaced wire reinforcement (109). It was recognized in these studies that the low tensile strength of concrete is due to the initiation and propagation of tension cracks and the addition of fibers increased the tensile strength by retarding the cracking of the matrix. This was demonstrated by Romualdi and Batson (109) for the case of continuous wires arranged parallel to one another in the direction of the major principal stress. They found that the tensile strength in this type of matrix is inversely proportional to the square root of the wire spacing. Similar results were obtained by Romualdi and Mandel (110) with short lengths of wire, uniformly distributed and randomly oriented rather than having a preferred orientation. Kar and Pal (65) also investigated the effective wire spacing but considered bond deficiency of the short fibers in addition to their random orientation.

The ACI Committee-544 (4) reported on some of the mechanical and material properties of fiber reinforced concrete, its preparation and applications. Included in the mechanical properties is the concept of fiber spacings, relating it to

strength, and the effects of fibers on ultimate strength, as shown in Fig. 1.1. The material properties briefly discussed include

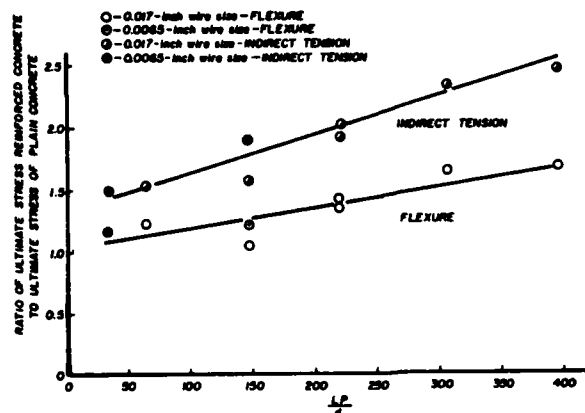


Fig. 1.1. Ultimate Strength as Linear Function of pl/d (from unpublished data by the United States Steel Corp.) (p = volume percentage of fibers; l/d = fiber aspect ratio).

static, dynamic and fatigue strength, resistance to abrasion and friction, and creep and corrosion behavior of the composite material. While examining load-deflection curves in flexure and stress-strain curves in tension and compression, Shah and Rangan (117) observed that fibers have a negligible effect on the load at which cracks initiate in the matrix (proportional limit) when compared to plain concrete and concrete with conventional types of reinforcement. The compression behavior is shown in Fig. 1.2.

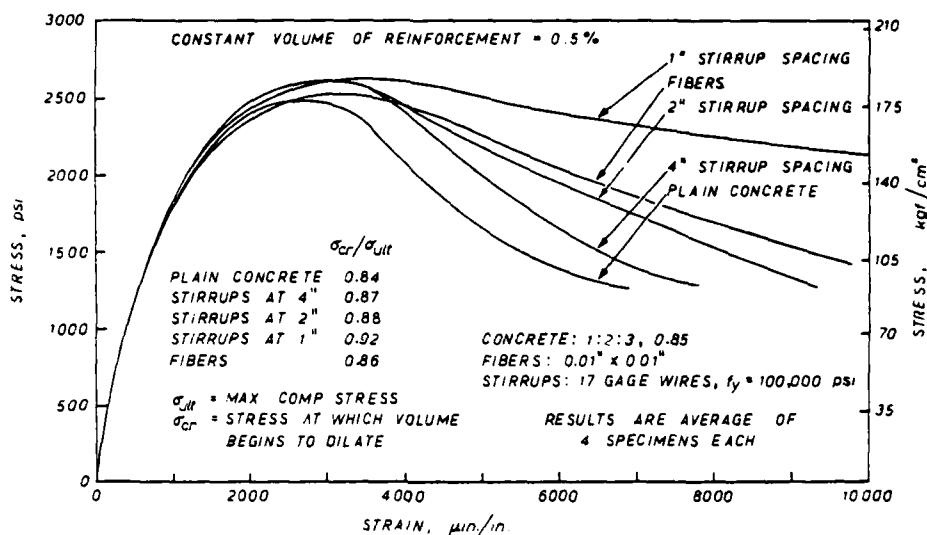


Fig. 1.2. Stress-Strain Curves for Concrete Reinforced with Stirrups and Fibers Subject to Uniaxial Compression. [Shah, et al. (117)].

However, it was observed that fibers considerably increase the resistance of concrete to crack propagation, evidenced by increased tensile and flexural strengths and considerably greater toughness and energy absorption ability. See Figs. 1.3 and 1.4. Oakley and Proctor (95) also presented tensile stress-strain curves for a number of different types of glass fiber reinforced cement composites with cement paste and cement-sand mortars as matrices. They have related composite properties to crack spacing and to fiber strength and stiffness. Chen and Carson (36) performed tests

to determine the influence of length and volume of randomly oriented steel fiber wire on the strength and ductility of mortar and concrete and suggested lengths and percentage of fiber

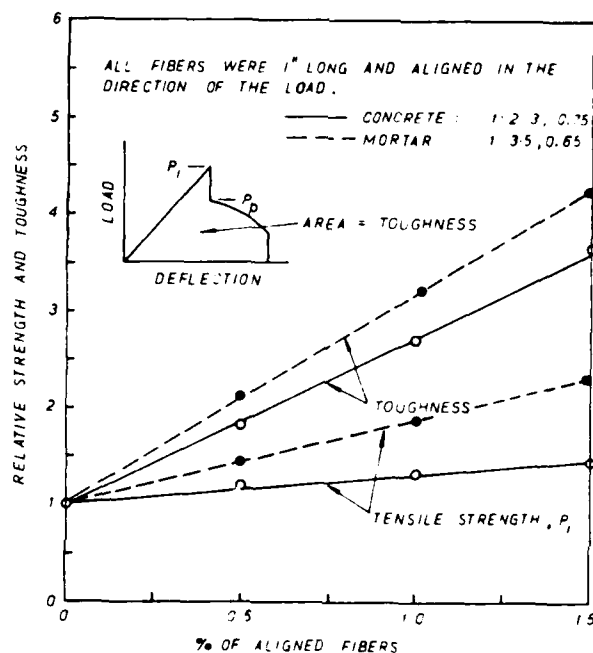


Fig. 1.3. Effect of Volume of Fibers in Tension [Shah, et al. (117)].

reinforcement for optimum compressive and tensile strength. Ali, Majumdar and Singh (2) studied the effect of fiber length and content on the composite properties of glass fiber reinforced cement reporting four to five times the bending strength, three to four times the tensile strength and fifteen to twenty times the impact strength of unreinforced cement. Shah and Naaman (116)

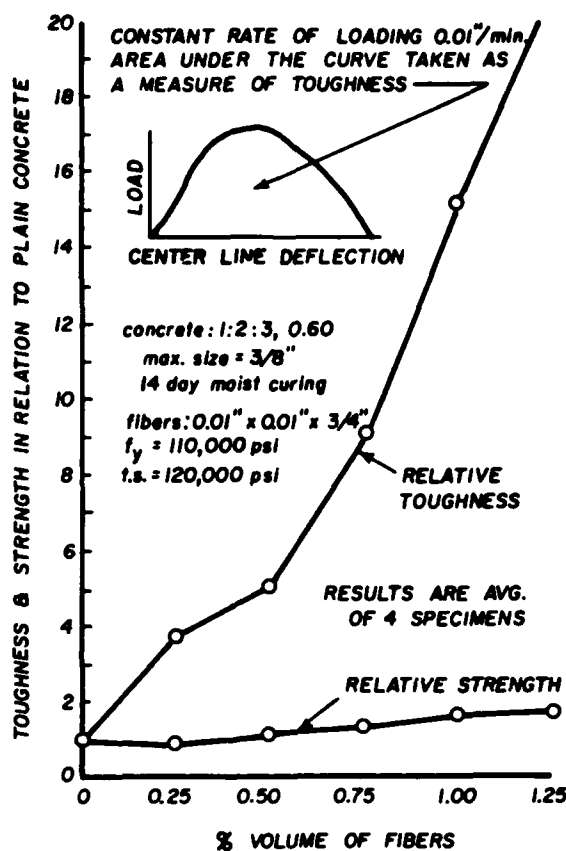


Fig. 1.4. Effect of Volume of Fibers in Flexure
[Shah, et al. (117)].

conducted similar tests on mortar reinforced with different lengths and volumes of steel and glass fibers and found that the tensile and flexural strengths were two to three times those of plain mortar while the corresponding strains or deflections were as much as ten times those of plain mortar. Swamy and Mangat (126) reported on the significant role of steel fiber reinforcement in concrete in

flexure by increasing the post-cracking properties of ductility, tensile strain capability and energy absorption capacity. Halvorsen, et al., (55) presented information regarding durability characteristics and some physical properties including strength, modulus of elasticity, corrosion and shrinkage of steel fiber reinforced concrete using regulated-set and Type I portland cements. Halvorsen (53) and Johnston (63) concluded that many of the mechanical properties of fiber reinforced mortar and concrete are governed by the product of fiber concentration (volume) and aspect ratio (pl/d). Aleszka and Beaumont (1) studied the fracture mechanisms of concrete reinforced with various lengths, diameters and volumes of steel fibers. They found that the fracture stress and work of fracture (work done in failing beams in bending) is directly proportional to fiber volume fraction and length and inversely proportional to fiber diameter.

Numerous analytical studies have been conducted based directly on experimental results or derived from existing theories, then checked by experiment. Aveston (17,19) has described such theoretical models for the behavior of brittle matrix composites. Stepanova presented a theory enabling the prediction of the mechanical properties of fiber reinforced concrete as reported by Trambovetsky (132). Her results proposed a precise definition of inter-fiber spacing, being similar to that derived by Romualdi and Mandel (110). Pakotiprapha, Pama and Lee (98) presented explicit expressions derived from the laws of mixture for predicting the mechanical properties in flexure, torsion, axial compression and

tension of random steel fiber reinforced cement mortar.

Experimental results proved to be in good agreement with the theoretically predicted values. Nair (91) theoretically determined the stress distributions and elastic properties of glass fiber reinforced cement prior to matrix cracking and also interpreted the transitional region of the stress-strain curve prior to the onset of multiple cracking. Zonsveld (137) reported on properties and testing of high and low modulus of elasticity fibers other than steel. Nielsen and Chen (93) calculated Young's modulus of fiber-filled composites using equations based on the classical theory of elasticity; the results are applicable only for the case of randomly oriented fibers in a plane. Edgington, Hannant and Williams (45) aimed at determining some of the basic engineering properties of steel fiber reinforced concrete and investigating the fiber strengthening mechanism. Swamy (123) also studied the mechanics of fiber reinforcement, the various factors influencing the effectiveness of the reinforcement and the efficiency of stress transfer through the fibers. Khrometz (68) studied the behavior of composite fiber reinforced concrete (with layers of gypsum, glass fiber and foamed plastic) and established relationships between principal strength (compressive and tensile) and strain parameters. Kurbatov and Vylegzhanin (75) studied the behavior of fiber reinforced cement-sand mortar in thin-walled structures and determined the effect of water-cement ratio on the strength of the resulting mix. Henager and Doherty (60) presented

an analytical model based on the ultimate strength approach for beams reinforced with steel bars in addition to steel fibers taking into account the bond stress, fiber stress, fiber aspect ratio and volume fraction. The theoretical ultimate moment for these beams showed good correlation with experimental values.

The workability and costs of fiber reinforced concrete as opposed to plain concrete were discussed by Kesler and Halvorsen (67). They pointed out that fiber reinforced concrete becomes a premium product for use in severe environments of wear, cavitation, impact and blast that would quickly erode or destroy plain concretes regardless of strength. Moens (88) points out that workability of steel fiber reinforced concrete is a function of fiber and aggregate content and aggregate grading and presents specific design criteria (to be discussed later) for maintaining good workability in the mix. Brown (30) provides some design formulas for steel fiber reinforced concrete; one for calculating the allowable flexural stress of the composite and the other for calculating the thickness of an overlay. Both utilize the increased flexural strength of the fiber reinforced concrete over that of plain concrete. For calculating the allowable flexural strength of fiber reinforced concrete when it is used to replace or reduce the quantity of reinforcing steel the following analysis is recommended:

$$f = \frac{\alpha \left(\text{MOR} - \frac{1.64}{s} \right)}{\gamma m} \quad (1.1)$$

where:

f = allowable flexural stress
 α = 0.85
 MOR = modulus of rupture of steel fibrous concrete
 s = probability factor equal to 20% times MOR
 γ_m = quality control factor (1.4 precast; 1.5 cast in place)

This stress should be greater than the stress computed using load factor design ($f = M/S$). When designing overlays, Brown recommended the following formula:

$$T_0 = 0.75 N \sqrt{T_0^N - C \left[\left(\frac{T_D}{T_{DB}} \right)^{T_E} \right]^N} \quad (1.2)$$

where:

T_0 = thickness of overlay
 T_D = thickness of plain concrete using MOR of fiber reinforced concrete
 T_{DB} = thickness of plain concrete using MOR of existing pavement
 T_E = thickness of existing pavement
 N = 2 for unbonded overlay
 N = 1.4 for partially bonded overlay
 N = 1.0 for bonded overlay
 C = 1.0
 C = 0.75 initial cracks (condition of existing pavement).
 C = 0.35 badly cracked

Halvorsen, et al. (54) and Herring and Kesler (61) provided information regarding the behavior of steel fiber reinforced concretes for applications in tunnel linings where combined compressive and flexural loads occur. Included is a catalog of standard mixes for tunnel liner concretes and the elastic properties of the composites employed in the investigations.

Schrader and Munch (113) reported on a situation at Libby Dam where fibrous concrete was selected for the repair work required. They described the various other repair materials and methods considered, then provided a detailed description of the fibrous concrete mix design and evaluated the results obtained.

Beam-column joints of "ductile concrete" for seismic-resistant structures are required to flex and absorb large amounts of energy during an earthquake. Because of the amount of steel used, such joints show a ductile response to loading and thus the name "ductile concrete" (25). Henager (59) describes tests performed on such ductile concrete joints designed to minimize the steel congestion common to such joints. He conducted an experimental comparison on two, full-sized, beam-column joints: one, a conventional joint using hoops in accordance with the seismic-resistant design specifications of the American Concrete Institute (ACI 318-71), and the other, a modified joint using steel fibrous concrete in the joint region in lieu of the hoops. The joints were subjected to earthquake type loadings. The results proved that the modified joint developed a higher ultimate moment capacity, greater stiffness, appeared more damage tolerant and resisted cracking better than the conventional joint. Chen and Carson (37) conducted experiments designed to determine the influence of fibers on the bearing capacity and ductility of fiber reinforced concrete materials. It was found that the bearing capacity of the reinforced material was significantly higher than that of the plain concrete. The performance of both materials could be predicted through the use of plastic limit analysis in the

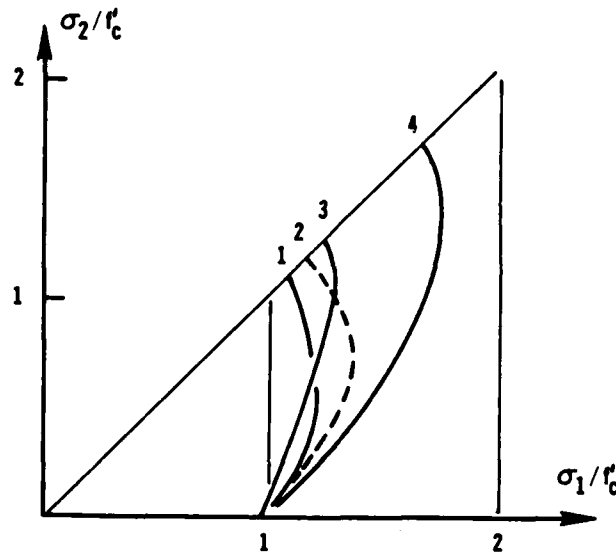
theory of plasticity but the more ductile fiber reinforced material conformed better to the theoretical predictions.

As discussed in the previous paragraphs, most of the recent research on fiber reinforced concrete and mortar focuses on the effects of varying the fiber types and content, environmental factors and placement techniques, while some attention has also been placed on the micromechanics of the fiber matrix interaction. While most of the testing has been done to determine the basic engineering properties in the uniaxial compression, tension (both direct and indirect) and flexure modes, only one piece of work by Taylor et al. (130) has been reported on the biaxial loading of fiber reinforced mortar. Even in this report, only strength properties are discussed with no regard to behavior. Their investigation revealed that fiber reinforced mortar (FRM) containing 2% fibers by volume had a higher normalized ultimate strength as shown in Fig. 1.5 compared to normal weight concrete (NWC) and lightweight concrete (LWC). The authors also noted the fiber reinforced mortar had a much higher strain capacity, toughness, post-peak strength and post-peak integrity than conventional mortar and that under suitable biaxial conditions, fiber reinforced mortar behaves as an elasto-plastic material.

1.2.2 Plain Concrete Response to Multiaxial Stresses

This section does not contain a historical review of concrete response to multiaxial stresses. A good review of that was done by Andenes (8) and Starovisky (119). Another good review describing different multiaxial test apparatuses in detail up to 1972 as well

as strength and behavior results of concrete and geologic materials tested in those apparatuses is described in four volumes of the RILEM International Symposium (107). This section does constitute a review of the state-of-the-art concerned with experimental and analytical studies of the behavior and strength of concrete under combined loads.



Line	Ref. No.	Material	Strength		Moisture condition	Loading plates
			psi	kgf/cm ²		
1	74	NWC	3000-8000	190-600	Dry	Brush
2	94	LWC	4520	316	Wet	Greased rubber
3	128	LWC	3500	245	Wet	Brush
4	130	FRM	4140	290	Wet	Brush

Fig. 1.5. Comparison of Strength Curves [Taylor, et al. (130)].

A Reinforced Concrete Model Evaluation Task Group was formed by Hegemier (58) to evaluate the capability of concrete models to describe the nonlinear response of reinforced concrete protective structures to dynamic loads (MX missile sitings in particular). Their evaluation includes a critical review of the physical and theoretical foundations of each model as well as their simulation accuracy. Dodge, et al. (42) also reviewed and assessed the analytical models available to the designer of prestressed concrete reactor vessels (PCRV's) including a discussion of some of the constitutive models and failure criteria used (such as plasticity and hyperelasticity) for representing the time-dependent and nonlinear response and strength of concrete. Included are published comparisons between experimental and predicted results, assessing the validity of these analytical models.

The majority of the literature on failure of plain concrete is devoted to monotonic, proportional loading (58). Kupfer, et al. (74) presented experimental stress-strain curves and constructed failure envelopes shown in Fig. 1.6 for three different concretes under biaxial stresses. An attempt was later made by Kupfer and Gerstle (73) to describe these deformations by means of mathematical expressions incorporating octahedral quantities to predict the strains resulting from arbitrary plane stress states. Experimental results from Launay and Gachon (83) were used by Willam and Warnke (134) to construct a triaxial failure envelope for concrete, as illustrated in Fig. 1.7. A schematic of the concrete failure surface in three-dimensional principal stress space is furnished in Fig. 1.8 [from Willam and Warnke (134)].

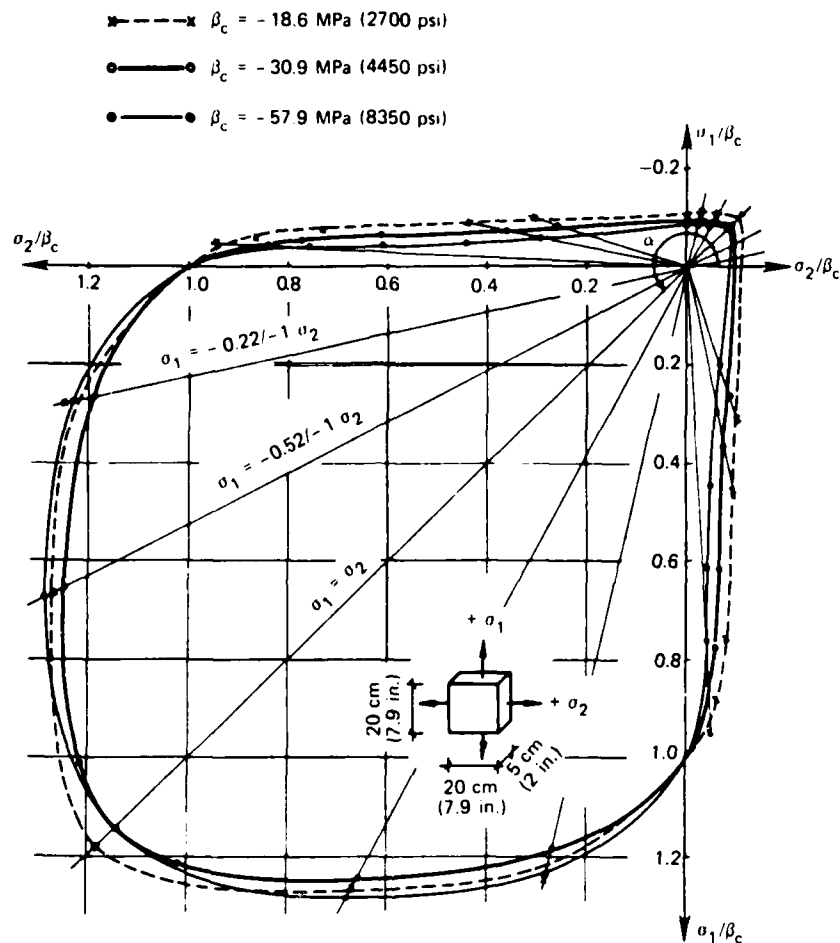


Fig. 1.6. Biaxial Strength of Concrete; Results of Experimental Investigation [Kupfer, et al. (74)].

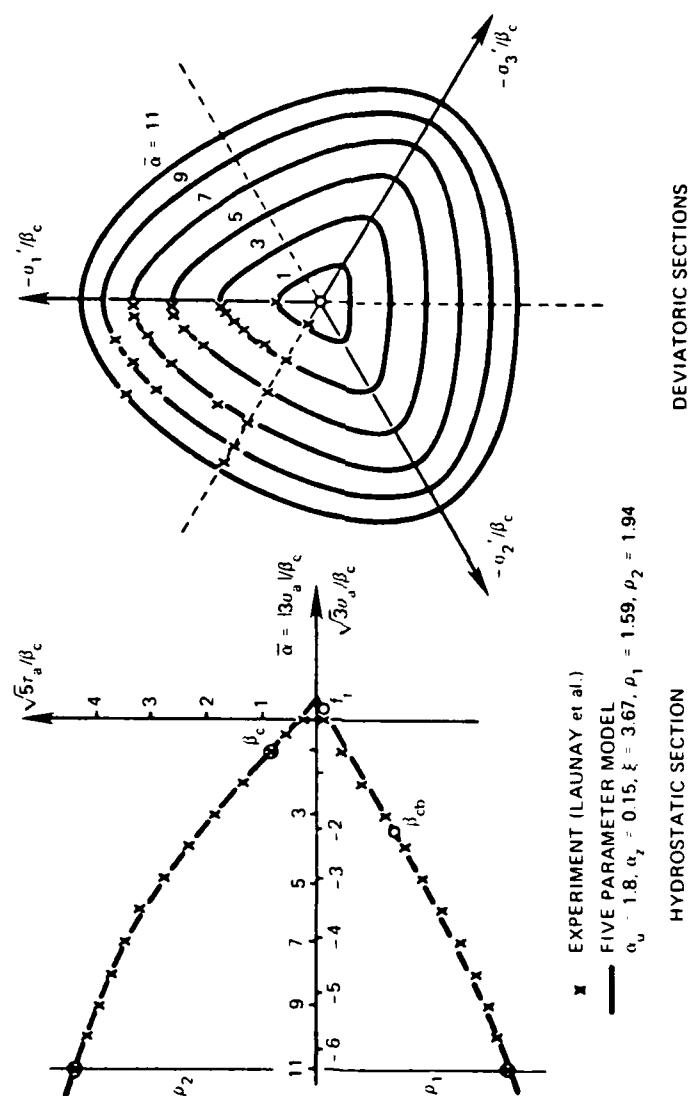


Fig. 1.7. Five-Parameter Model - Fitting of Triaxial Test Data [William, et. al. (134)].

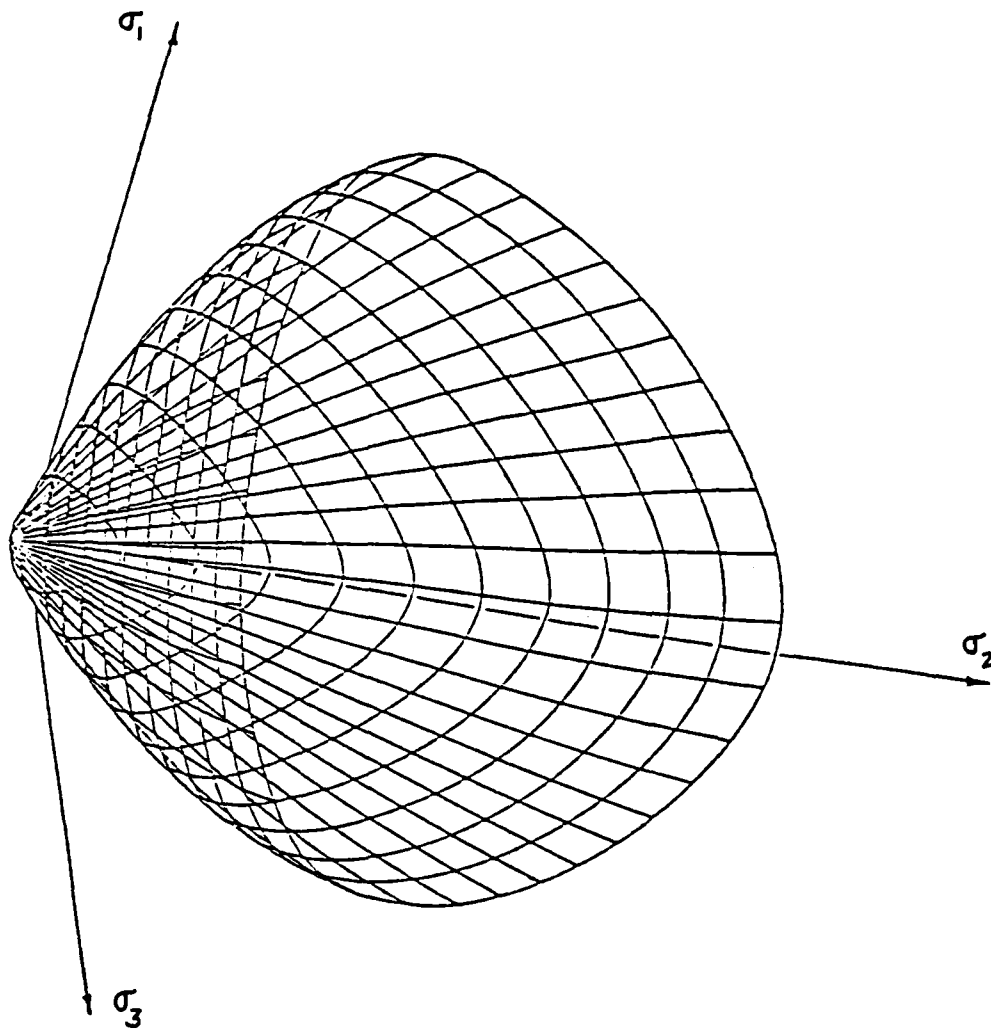


Fig. 1.8. Failure Surface for Plain Concrete
[Willam, et al. (134)].

The preceding studies, among many others, were concerned with the multiaxial behavior and strength of concrete, using a wide variety of different materials and different test methods. In order to isolate the effects of these variables, a cooperative concrete project, Gerstle, et al. (51), coordinated from the University of Colorado, was recently completed where seven institutions subjected identically cast and cured specimens (differing in size only) to a variety of biaxial and triaxial loading conditions, common to all participants. It was intended to eliminate the material variable so that systematic differences in the results could be attributed entirely to the differences in test methods. The effect of the test method is predominantly a function of the specimen boundary conditions, ranging from a specified boundary condition for perfectly flexible fluid cushion loadings, to a specified displacement boundary condition for perfectly rigid, rough platens. The various systems, among which all major variants are represented, are shown schematically in Fig. 1.9 (51). The participants included:

Bundesanstalt für Materialprüfung,
Berlin, Germany (BAM)
Ente Nazionale per l'Energia Elettrica,
Milano, Italy (ENEL)
Imperial College of Science and Industry,
London, England (ICL)
Institut für Massivbau, Technical University,
Munich, Germany (TUM)
New Mexico State University, Las Cruces,
New Mexico, U.S.A. (NMSU)
University of California at Davis,
California, U.S.A. (UCD)
University of Colorado, Boulder,
Colorado, U.S.A. (CU)

The specimen geometries and loading conditions used are described in Table 1.1 (51).

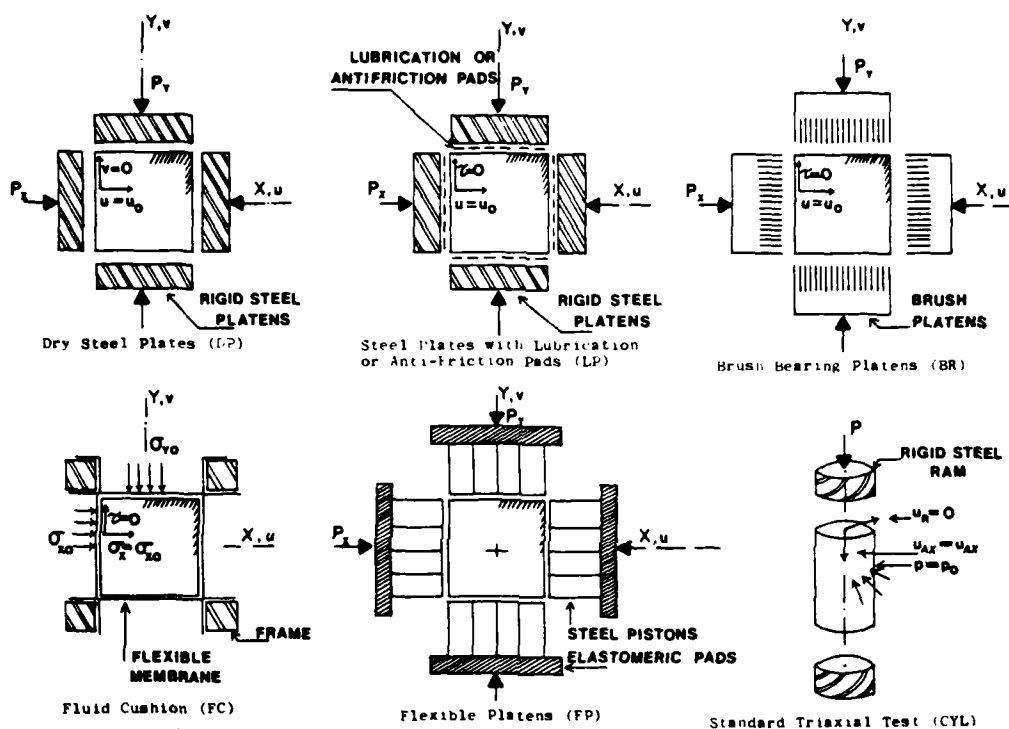


Fig. 1.9. Multiaxial Test Methods [Gerstle, et al. (51)].

Mean values of the biaxial failure data, determined by proportional loading, are shown in Fig. 1.10, and after normalization in Fig. 1.11. Variations in biaxial strengths from series to series are seen to be considerable due to the differences in load systems and/or differences in specimen sizes.

TABLE 1.1
LOADING SYSTEMS [Gerstle, et. al. (51)] .

Laboratory	Series	Ref.	Specimen Size	Description	Loading Rate
BAU	DP	1,2	10 cm cubes	Unlubricated steel platens	Stress Rate Biaxial Tests: 0.03 N/mm ² /sec Triaxial Tests: 0.075 N/mm ² /sec
	FP		" " "	Cushion type system with 16 steel platens 2.5 x 2.5 cm on elastomeric pad	
ENEL	DP	3	10 cm cubes	Unlubricated steel platens	Stress Rate Normally: 0.5 kg/cm ² /sec Series T8 and T9: 10 kg/cm ² /sec
	LP		" " "	Lubricated steel platens (four polyethylene sheets with molybdenum sulphide grease)	
ICL	CYL	4,5	16 cm x 32 cm cylinders	Axial load through steel platens, confining pressure through membrane	Stress Rate 2.0 ksi/min
	LP		10 x 10 x 4" plates	Rigid steel platens with specimen surfaces treated with 'Pebcure' curing membrane to minimize friction	
			4" x 10" cylinders	Axial load through steel platens, confining pressure through membrane	
	BR		10 cm cubes	Brush bearing platens (bristles 4x4x35 mm)	
MSU	DP	8	3" cubes	Unlubricated steel platens	Strain Rate Biaxial: 0.0002/min Triaxial: 0.0003-.0010/min
	LP			Lubricated steel platens (two 4 mil poly- ethylene sheets with axle grease)	
UCD	DP	9	2" cubes	Unlubricated aluminum platens	Stress Rate 3 to 5 ksi/min
	LP			Lubricated aluminum platens (one layer grease)	
CU	BR	10		Brush bearing platens (bristle diameter .025", length 3/16")	Stress Rate 3.0 to 4.5 ksi/min
	PC		4" cubes	Unlubricated steel platens Fluid cushion	

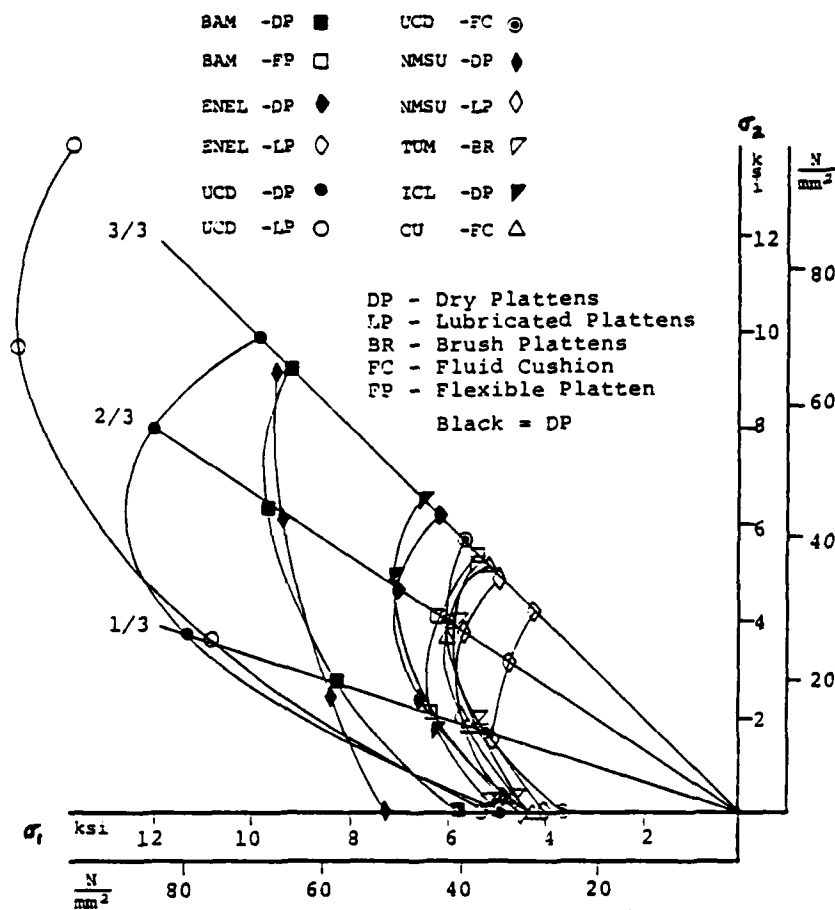


Fig. 1.10. Strength of Concrete Under Biaxial Loading
 [Gerstle, et. al. (51)].

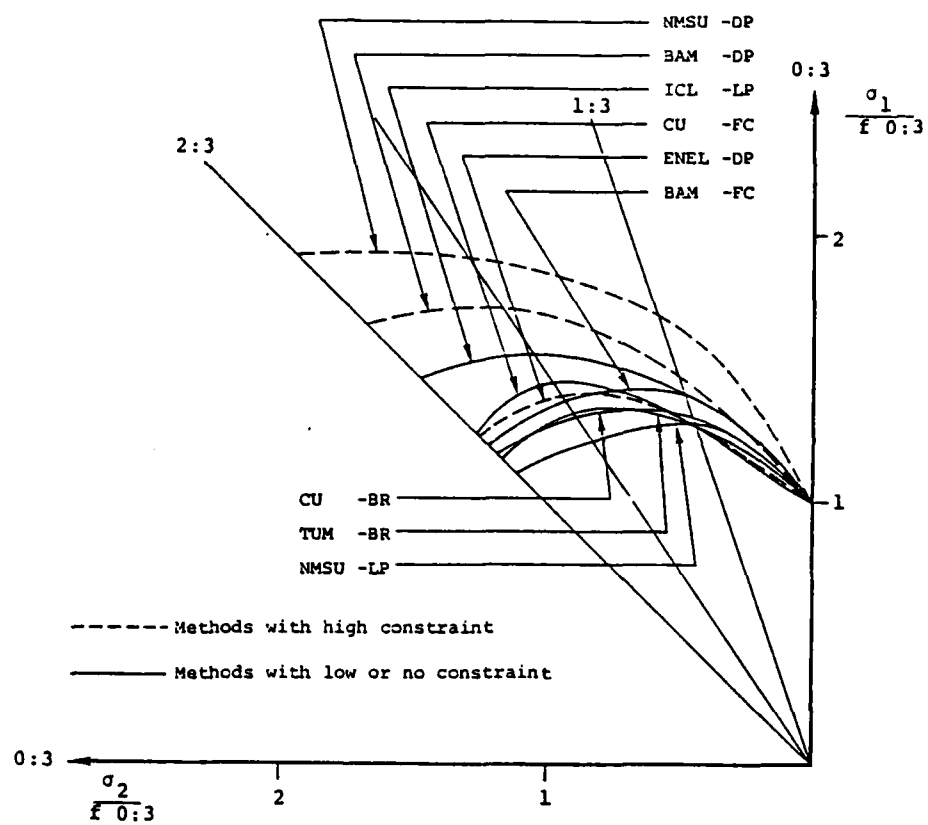
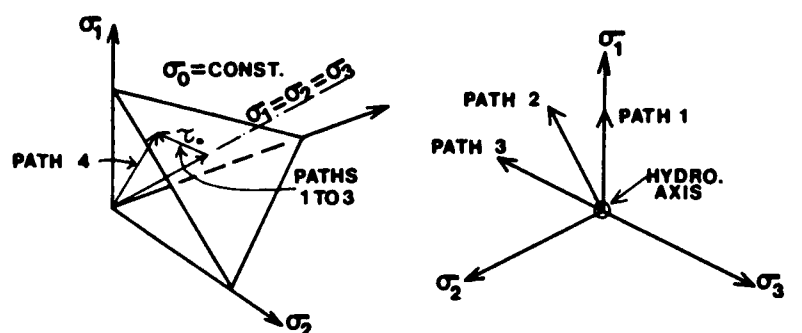


Fig. 1.11. Normalized Strength Envelopes
[Gerstle, et. al. (51)].

Mean values of the triaxial test data are shown in Fig. 1.13 for one specified octahedral plane. These tests were performed by first subjecting the specimen to a specified hydrostatic stress ($\sigma_0 = 3000$ to 8000 psi), followed by deviatoric loading along one of the three stress paths in the octahedral plane as shown in Figs. 1.12 and 1.13.



$$\sigma_0 = \frac{1}{3} (\sigma_1 + \sigma_2 + \sigma_3)$$

$$\tau_0 = \frac{1}{3} \sqrt{(\sigma_1 - \sigma_2)^2 + (\sigma_2 - \sigma_3)^2 + (\sigma_3 - \sigma_1)^2}$$

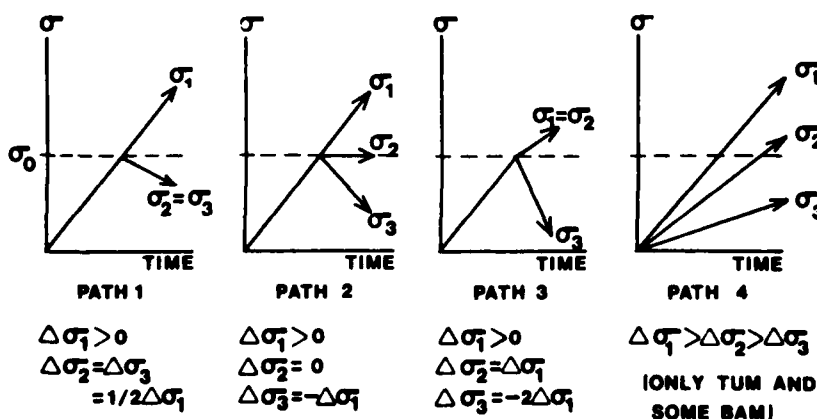


Fig. 1.12. Load Paths for Triaxial Loading in Different Presentations [Gerstle, et al. (51)].

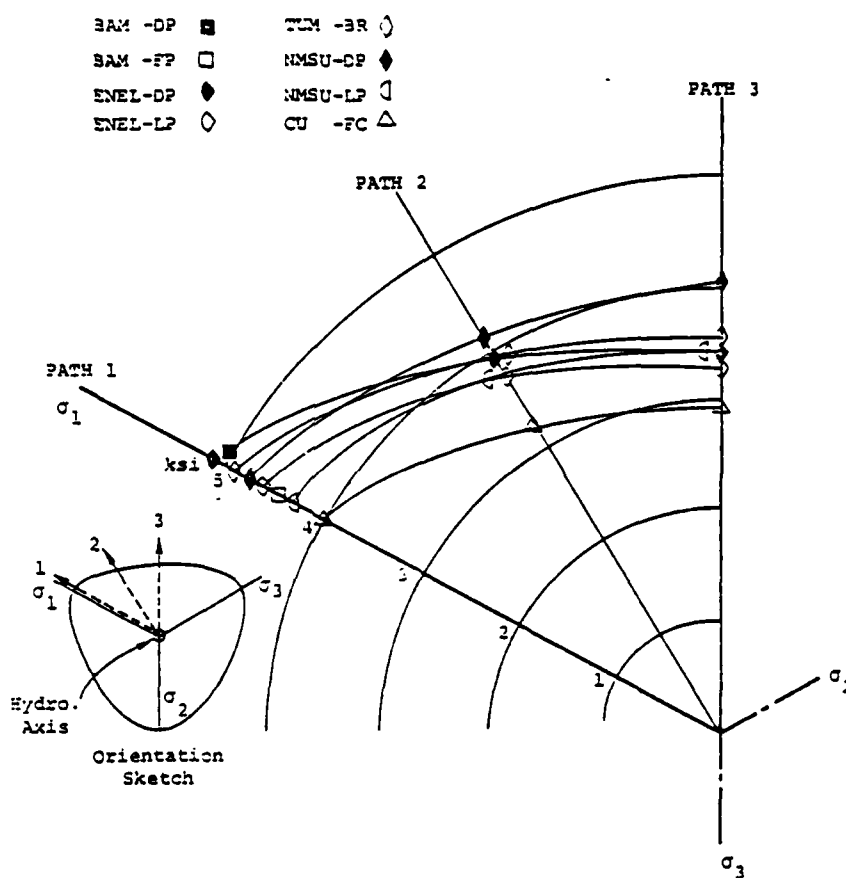


Fig. 1.13. Triaxial Failure Envelopes Within the Octahedral Plane $\sigma_0 = 5 \text{ ksi} = 350 \text{ Kg/cm}^2$ [Gerstle, et. al. (51)].

Fig. 1.14 shows the failure strength data in terms of octahedral shear and normal stresses for both the biaxial and triaxial results.

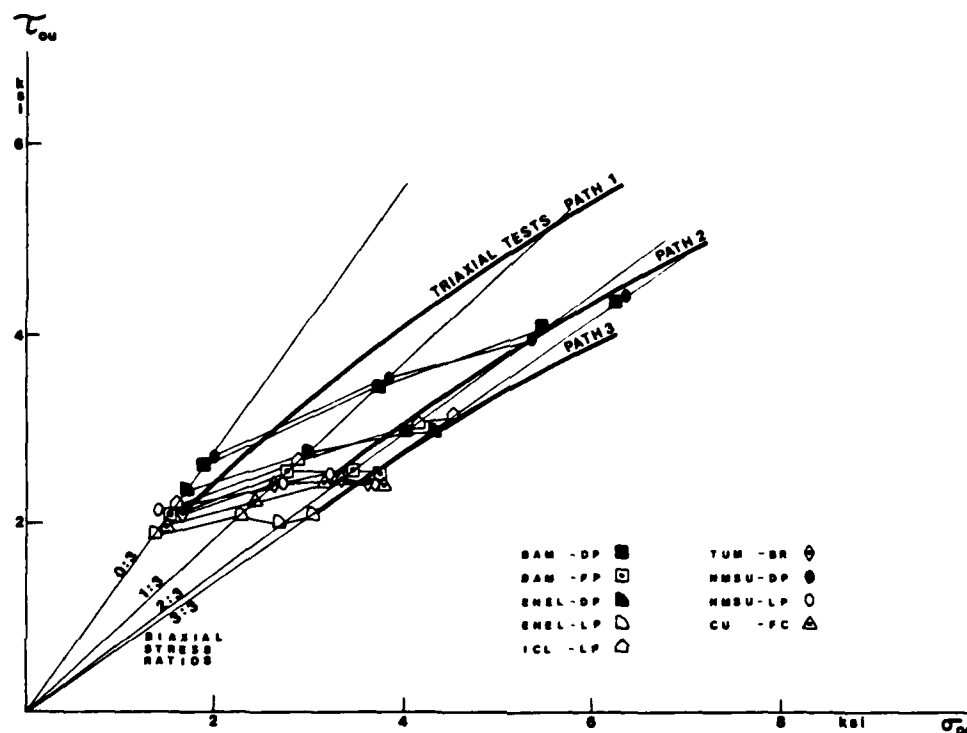


Fig. 1.14. Biaxial Strength Results Compared with Mean Values of Triaxial Results [Gerstle, et al. (51)].

The authors point out that the load systems with high constraint (ENEL-DP, BAM-DP and NMSU-DP) show higher strengths than those with low constraint (BAM-FP, NMSU-LP AND CU-FC) and that the shear strength of the material increases considerably with an increase in confining pressure.

To supplement the strength results of the Cooperative Concrete Project, stress-strain relations obtained from the same testing program are presented and discussed in a later paper by Gerstle,

et al. (50) and an attempt is made to determine generally valid constitutive laws describing the multiaxial behavior of the concrete tested. The principal stress-strain relations are transformed into octahedral space, and the material response is expressed in terms of stress- or strain-dependent bulk and shear moduli. A coupling effect relating volume change to stress deviation was observed in this study and also by Kupfer (73).

The authors propose the following relations in octahedral form for the strains resulting from the applied stresses as

$$\epsilon_0 = \frac{\sigma_0}{3K_S} + \frac{\tau_0}{H_S} \quad (1.3a)$$

$$\gamma_0 = \frac{\tau_0}{2G_S} \quad (1.3b)$$

in which σ_0 and τ_0 are the octahedral normal and shear stresses respectively, and ϵ_0 and γ_0 are the octahedral normal and shear strains respectively. These values, represented in terms of principal stresses and strains are

$$\sigma_0 = \frac{1}{3} (\sigma_1 + \sigma_2 + \sigma_3) \quad (1.4a)$$

$$\tau_0 = \frac{1}{3} \sqrt{(\sigma_1 - \sigma_2)^2 + (\sigma_2 - \sigma_3)^2 + (\sigma_3 - \sigma_1)^2} \quad (1.4b)$$

$$\epsilon_0 = \frac{1}{3} (\epsilon_1 + \epsilon_2 + \epsilon_3) \quad (1.4c)$$

$$\gamma_0 = \frac{1}{3} \sqrt{(\epsilon_1 - \epsilon_2)^2 + (\epsilon_2 - \epsilon_3)^2 + (\epsilon_3 - \epsilon_1)^2} \quad (1.4d)$$

The other terms, K_S (secant bulk modulus relating volumetric strain ϵ_0 to volumetric stress σ_0), G_S (secant shear modulus relating distortional strain γ_0 to octahedral shear stress τ_0) and H_S (coupling modulus relating the volumetric strain ϵ_0 to stress deviation τ_0) are defined as

$$K_S(\epsilon_0) = \frac{\sigma_0(\epsilon_0)}{3\epsilon_0} \quad (1.5a)$$

$$G_S(\gamma_0) = \frac{\tau_0(\gamma_0)}{2\gamma_0} \quad (1.5b)$$

$$H_S(\epsilon_0) = \frac{\tau_0(\epsilon_0)}{\epsilon_0} \quad (1.5c)$$

The mean volumetric and deviatoric stress-strain curves of the triaxial tests from this study are shown in Figs. 1.15a and 1.15b respectively. Fig. 1.16 shows the coupling effect present between octahedral shear stress and octahedral normal strain.

According to the postulation in Eqs. 1.3, the stress-strain relations require the determination of the three variable secant moduli, K , G and H , obtainable from the octahedral stress-strain curves according to Eqs. 1.5. The variations in these moduli are shown in Figs. 1.17, 1.18 and 1.19. Notice in Fig. 1.19 that the coupling modulus does not vary with volumetric strain ϵ_0 . This is because the authors assumed a straight line relation between τ_0 and ϵ_0 in Fig. 1.16. Therefore the coupling modulus H_S becomes a parameter varying only with hydrostatic pressure σ_0 .

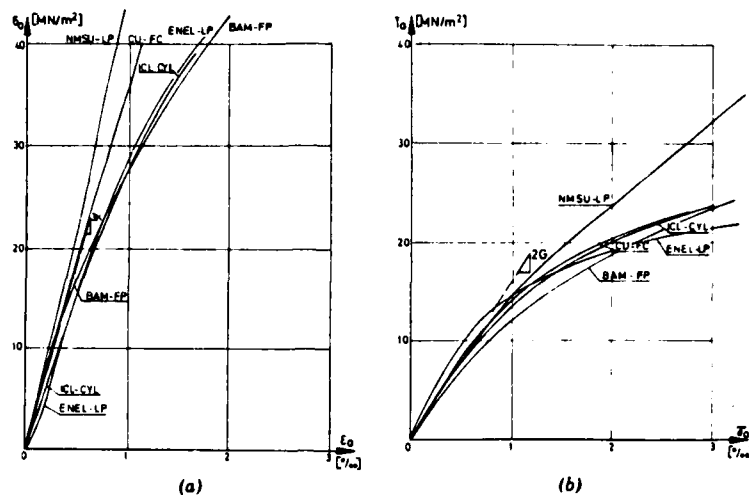


Fig. 1.15. (a) Mean Volumetric Stress-Strain Curves of Triaxial Test Series with Frictionless Boundaries; (b) Mean Deviatoric Stress-Strain Curves of Triaxial Test Series with Frictionless Boundaries [Gerstle, et al. (50)].

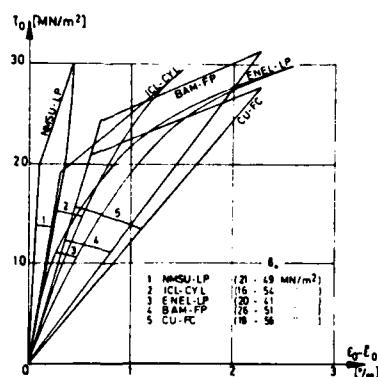


Fig. 1.16. Shear Dilatancy for Triaxial Test Series [Gerstle, et al. (50)].

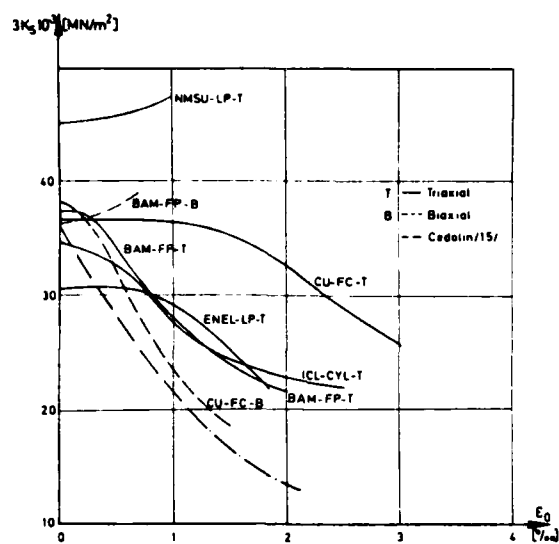


Fig. 1.17. Bulk Modulus Versus Octahedral Normal Strain [Gerstle, et al. (50)].

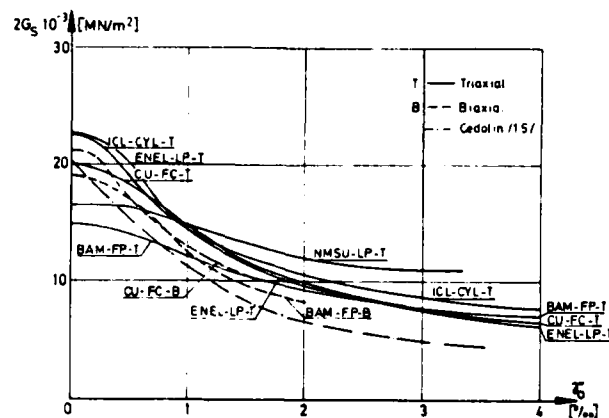


Fig. 1.18. Shear Modulus Versus Octahedral Shear Strain [Gerstle, et al. (50)].

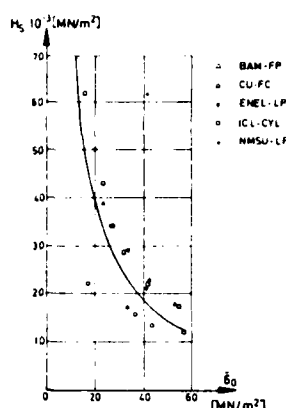


Fig. 1.19. Coupling Modulus Versus Octahedral Normal Stress [Gerstle, et al. (50)].

A soon to be published study by Gerstle is being made to develop a simple formulation for concrete behavior based on the preceding investigation by Gerstle, et al. (50) using octahedral quantities, where functional representations for the tangent bulk, shear and coupling moduli are presented. This formulation will be investigated for predicting the behavior of the steel fiber reinforced concrete currently being studied, with results reported in Chapter 5.

Following mathematical formulations for behavior of concrete type materials come the failure criteria developed by several authors based on previous test results. Two of these will be discussed in detail in Chapter 5 and therefore only a brief summary will be given here.

Chen and Chen (33, 34, 35) describe an analytical constitutive relation of concrete under general three-dimensional stress states, assuming the concrete to be a continuous, isotropic and linearly elastic-plastic strain hardening fracture material. The initial

discontinuous surface, loading surfaces, and failure surface are developed with the elastic-plastic stress-strain relationships derived from the classical theory of plasticity. These stress-strain relations are expressed explicitly in matrix form for use in an analysis routine. This formulation is independent of the third stress invariant, leaving it at a disadvantage because concrete has been shown to be strongly path dependent, i.e., a function of the third stress invariant.

Ottosen (97) defines a four-parameter failure criterion containing all three stress invariants and shown to give good agreement with experimental results for short-time monotonic loading over a wide range of stress states. This criterion satisfies the required characteristics concerning smoothness, convexity, symmetry and curved meridians.

Willam and Warnke (134) developed a mathematical model with five parameters for the triaxial failure surface of concrete type materials, assuming isotropic material behavior. The model contains all three stress invariants and is valid for stress states in the tensile and low or high compression regimes. It also satisfies the required characteristics concerning smoothness, convexity and simple identification of model parameters from standard test data. Using the derived failure surface, the authors also describe two constitutive models formulated for elastic-perfectly plastic behavior in compression and elastic-perfectly brittle behavior in tension. Argyris, Faust and Willam (12) later include an additional sixth parameter (for representing an elliptical cap) to the same

five parameter failure criterion (134) to incorporate the hardening and softening phenomena of concrete into their plasticity model.

Bazant and Tsubaki (21) describe a total strain theory (analogous to the deformation theory of metal plasticity) using algebraic relationships between the total strains and stresses rather than their increments to model the short-time nonlinear triaxial behavior of plain concrete subjected to monotonic loading. The model predicts the peak stress state (failure) with subsequent strain softening, the triaxial failure envelopes and the corresponding strains at failure.

Lade (79) describes a three-parameter failure criterion stemming from a previously developed failure criterion (77) for cohesionless soils. It is expressed in terms of the first and third stress invariants and is shown to satisfy the required characteristics of curved meridians, opening angle of the failure surface and tensile strength.

Two of the aforementioned failure criteria (134,79) will be discussed in detail in Chapter 5 and will be compared with the experimental failure results of the fiber reinforced concrete tested for this report.

1.3 Scope of Investigation

This investigation is to obtain information regarding the material properties of one type of steel fiber reinforced concrete subjected to multiaxial compressive stresses, the purpose being to formulate constitutive relations for stress analysis of structures constructed of this material.

The mix design for the experimental tests was chosen on the basis of certain governing parameters such as water-cement ratio, aggregate gradation, slump, etc. necessary for obtaining a good concrete mix compatible for use with steel fibers. Full details of this mix design are presented in Chapter 2. Since the purpose of the study is not one for investigating the effects of varying the parameters in the mix design but rather for investigating the effects of steel fiber additions to a concrete mix, the design chosen will remain constant throughout all tests conducted.

The only variable to be considered is the fiber size. In total, five different steel fiber sizes have been provided with aspect ratios ranging from 45 to 100. Chapter 2 contains the details of these.

Two sets of tests will be conducted. The first is a preliminary set of tests involving the use of all five fiber sizes. These include some basic tests on cylinders and cubes in unconfined compression, indirect tension tests on cylinders, flexural tests on small beams and some multiaxial compression tests on 4 in. cubes. The purpose of the preliminary tests is to collect data and help provide a basis for choosing one fiber size to use in the final series of triaxial experiments carried out in the 4 in. cubical testing equipment. In all the experiments, the volume ratio of fibers will remain constant for all fiber sizes such that the effects of fibers and nothing else can be studied.

Full details of the experimental program including mix design and procedures, cubical test apparatus, testing program, testing procedures and data reduction are given in Chapter 2.

Chapter 3 contains the results of the preliminary test series employing all five fiber types including stress-strain relations and conclusions for the fiber chosen for the final comprehensive test series.

Chapter 4 contains the stress-strain and strength results of the 4 in. cubical specimens tested multiaxially in the final test series, and Chapter 5 discusses the different behavior and strength criteria used for determining the constitutive relations of steel fiber reinforced concrete under multiaxial states of stress.

CHAPTER 2

RESEARCH PROGRAM

2.1 Introduction

The main purpose of the experimental work was to determine the behavior and strength of steel fiber reinforced concrete (SFRC) subjected to multiaxial compressive stresses, in order that the constitutive relations of the material could be formulated.

The test program consisted of two parts. It was necessary to find a good workable and consistent fiber concrete mix to be used in the comprehensive three-dimensional compressive tests on 4 in. cubes. Therefore the first part of the test program consisted of a preliminary test series employing five different fiber types in a predetermined plain concrete mix acceptable for use in fiber reinforced concrete. Data obtained from the tests conducted on the specimens cast from these five different fiber concrete mixes were analyzed to determine which fiber type to use in the second part of the test program, i.e., the final test series on 4 in. cubes tested in multiaxial compression in the University of Colorado's cubical testing device.

This chapter describes the different stages of the experimental program. Section 2.2 gives the details of the mix design used in the experimental work including the design of the plain concrete mix and the steel fibers employed. In Section 2.3, a check on the

workability of this design based on previous work [Moens (88)] was made. The next two sections, 2.4 and 2.5, describe the steps involved in casting and curing the control and cubical fiber concrete specimens in the laboratory and preparing these specimens for the preliminary and final series of tests after they have cured. Section 2.6 describes the multiaxial test apparatus, data acquisition and data reduction systems used in the final series of cubical tests. Finally, the test procedure followed in conducting a cubical test and the test program giving the details of the preliminary and final test series are presented in Section 2.7 and 2.8 respectively.

2.2 Mix Design

Six mixes of concrete, five with different steel fibers and one plain (for reference and control purposes) were employed in the preliminary test series whose purpose was to collect data for the selection of a suitable fiber concrete mix for the multiaxial testing of 4 in. cubical specimens.

The plain concrete mix generally used in SFRC is a high strength design with certain governing parameters. They range as follows:

- 1) low water/cement ratio = 0.40-0.50
- 2) maximum size of coarse aggregate = 3/8 in.
- 3) low fineness modulus of fine aggregate ≤ 2.70 (i.e. large percentage of fines).
- 4) coarse aggregate to fine aggregate ratio ≈ 1 .
- 5) slump of plain concrete (before addition of steel fibers) = 3-4 in.

From the above governing parameters and using TABLE 13 of the PCA Handbook (104) on the "Design and Control of Concrete Mixtures," a plain concrete mix design was chosen as follows:

water/cement ratio = 0.50

maximum size of coarse aggregate = 3/8 in.

water = 385 lb/yd³

cement = 770 lb/yd³

fine aggregate, % of total aggregate = 53%

fine aggregate (specific gravity = 2.65) = 1400 lb/yd³

coarse aggregate (specific gravity = 2.65) = 1260 lb/yd³

The above design criteria give concrete mix proportions of C1 : FA1.82 : CA1.64 : W0.5. The fine aggregate and coarse aggregate gradations are as follows:

Fine Aggregate Gradation (Nos. 100-4 sieves):

Sieve No.	Particle Size (mm)	% Passing
3/8	9.53	100
4	4.76	98
8	2.38	95
16	1.19	78
30	0.595	54
50	0.297	20
100	0.149	5
200	0.075	0

Fineness Modulus = 2.50

Coarse Aggregate Gradation (Size No. 8):

Sieve No.	% Passing
1/2	100
3/8	100
4	20
8	0

The fine and coarse aggregate gradations fall within the limits

required by ASTM C33 - Section 4.1 and TABLE 2 (7), respectively, as shown in Fig. 2.1. Specific gravity and absorption tests were conducted on the fine and coarse aggregate according to ASTM C128-73 and C127-73 specifications (7). The results are as follows:

	<u>Fine Aggregate</u>	<u>Coarse Aggregate</u>
Bulk sp. gr.	2.59	2.55
Bulk sp. gr. (SSD basis)	2.60	2.58
Apparent sp. gr.	2.62	2.62
% absorption	0.49%	0.99%

Additional water was added in the mixing process to account for the absorption of water by the aggregates.

The plain concrete mix design remained constant throughout all test series so that fiber and not concrete effect could be examined. As previously mentioned, five different fiber types were employed in the preliminary test series. Four were obtained from the Bekaert Steel Wire Corp. and one from the United States Steel Corp. Their sizes are listed in TABLE 2.1 with their respective aspect ratios (length to diameter) as well as the fiber concrete mix number corresponding to the appropriate fiber used in the preliminary (P) tests.

The Bekaert "Dramix" fibers are straight, round fibers with a patented hooked end used to increase the bond between the fiber and the concrete. The tensile strength of these fibers is approximately 170-200 ksi. They are collated into clips with a water soluble glue that readily dissolves when mixed into the wet concrete. The manufacturer claims that the glue does not hinder the concrete

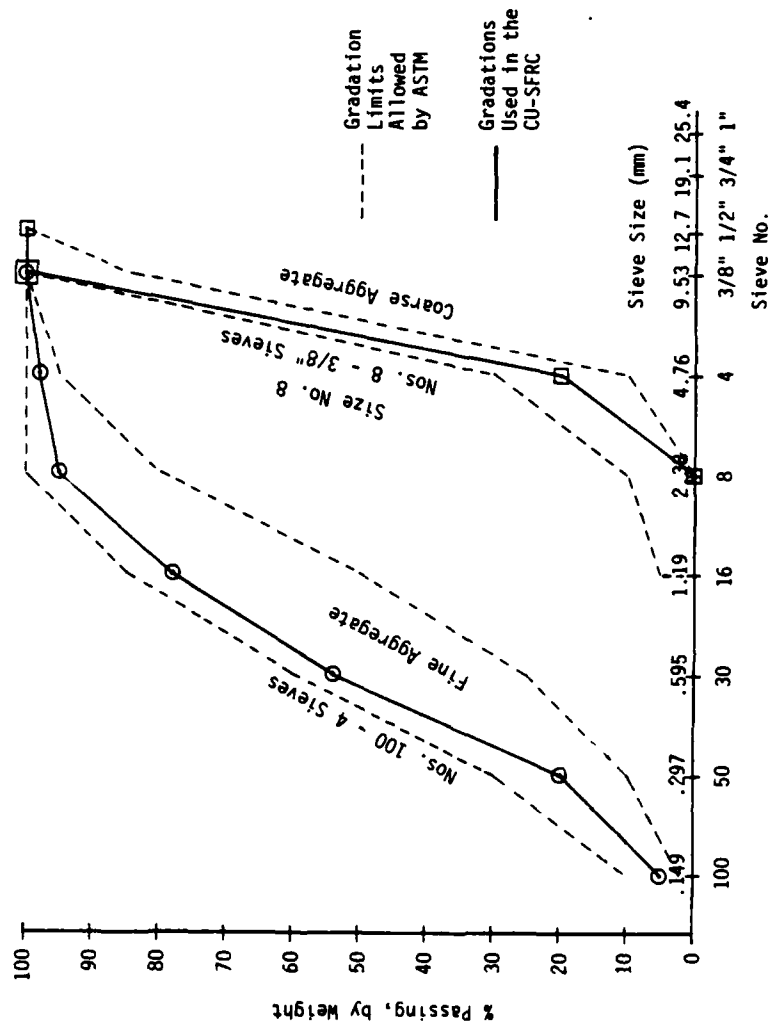


Fig. 2.1.1. Aggregate Gradation Curves Used and ASTM Limits.

TABLE 2.1

STEEL FIBER SIZES WITH CORRESPONDING FIBER CONCRETE MIX NUMBER

Manufacturer	Size Length (mm)/Dia. (mm)	Aspect Ratio (l/d)	Mix No.
	ZP 50/.50	100	P1
Bekaert	ZP 30/.50	60	P2
"Dramix"	ZP 30/.40	75	P3
Steel Fibers	ZP 40/.40	100	P4
U.S. Steel "Fibercon"	25.4 x 0.56 x 0.25 (1.00" x .022" x .010")	45 or 100	P5

strength in any way. The nomenclature before the fiber size represents the type of glue (if any) used for the collation. For example, ZP means a lightweight glue is used, beneficial for laboratory work or small jobs. ZC implies a heavyweight glue, mainly for industrial usage and large concrete mixes. ZL means no glue is used at all, i.e., the fibers are loose.

The USS "Fibercon" fibers are straight, flat fibers, loosely packaged in a random order. Their tensile strength ranges from 50-100 ksi. Figs. 2.2 and 2.3 show the relative shapes and sizes of the five fibers.

The volume ratio of fibers will remain constant for all fiber sizes. Based on field work that has been done using 80 lbs. of fibers per cubic yard of concrete (i.e., a volume ratio of fibers

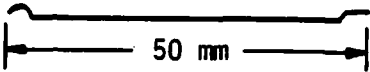
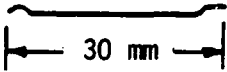
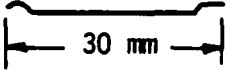
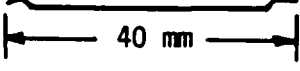
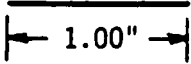
<u>Fiber</u>	<u>Length</u>	<u>Cross Section</u>
Dramix ZP 50/.50		0.50 mm ϕ
Dramix ZP 30/.50		0.50 mm ϕ
Dramix ZP 30/.40		0.40 mm ϕ
Dramix ZP 40/.40		0.40 mm ϕ
Fibercon 1.00" x 0.022" x 0.010"		0.022" x 0.010" Rectangular

Fig. 2.2. Steel Fiber Dimensions.

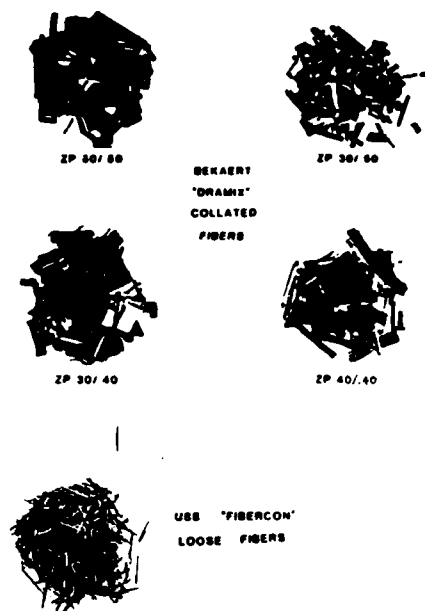


Fig. 2.3. Fiber Groups - Collated and Loose

to 0.6%), it has been found that with this volume fraction of fibers, no "balling" or clumping of the fibers occurs. This will be discussed in detail in the next section.

2.3 Check on Steel Fiber Reinforced Concrete Mix Proportioning

The constituent materials in SFRC are the same as for conventional concrete with the addition, of course, of the steel fibers to improve the material properties in comparison to those of plain concrete. The SFRC must be designed for workability since the addition of steel fibers to a concrete type material decreases the workability of the overall mix. Workability is a function of the volume percentage of fibers used in the mix. Obviously, too great a volume of fibers would result in the SFRC falling short of the building industries' expectations.

Mix design of SFRC for workability requires an understanding of the fiber characteristics and content as related to the aggregate grading and volume. Moens (88) performed tests on SFRC with this criteria in mind and gave certain guidelines in terms of design curves and charts for calculating some of the variables in SFRC mix design proportioning, especially the critical volume percentage of fibers above which the mix becomes unworkable.

The SFRC mix design chosen for the test series performed at the University of Colorado (CU-SFRC), as described in this report, was not designed from these guidelines developed by Moens (88). The following is simply a comparison to show that the mix design and fiber percentage used falls within Moens' guidelines for mix proportioning to obtain good workability.

Experimental investigations by Moens (88) were made with mortar and concrete reinforced with steel fibers of different aspect ratios to judge when the volume percentage of fibers becomes critical, resulting in unworkability of the mix. The workability was measured with a Vebe-consistometer. A Vebe-time of 12 seconds was judged an upper limit for workability. Fig. 2.4 shows the results of these experiments; the solid line is for concrete with mix proportions C1: FA1.5 : CA2.5 : W0.55:, and the dashed line is for a C1 : FA2 : W0.5 mortar. An empirical relationship

$$p_{cr} (\ell/d)^{4/3} = c \quad (2.1)$$

was found to give a good agreement between theory and the experimental results where

p_{cr} = critical volume percentage of
fibers at which the mix becomes
unworkable

ℓ/d = fiber aspect ratio

c = constant depending on the aggregate
grading and content.

From Moens' experiments, this constant c was found to be 4.65 for the concrete and 9.30 for the mortar. For either of these mixes, one can easily calculate or interpolate from the graphs the critical fiber percentage (p_{cr}). However, the SFRC mix proportions chosen for the University of Colorado tests was C1 : FA1.82 : CA1.64 : W0.5. One can see that it has a finer aggregate mixture gradation than the concrete employed by Moens, shown in Fig. 2.5, and a coarser gradation than the mortar. Therefore, the empirical critical fiber percentage curve for the CU-SFRC mix would lie between the two curves shown in Fig. 2.4. One could then postulate

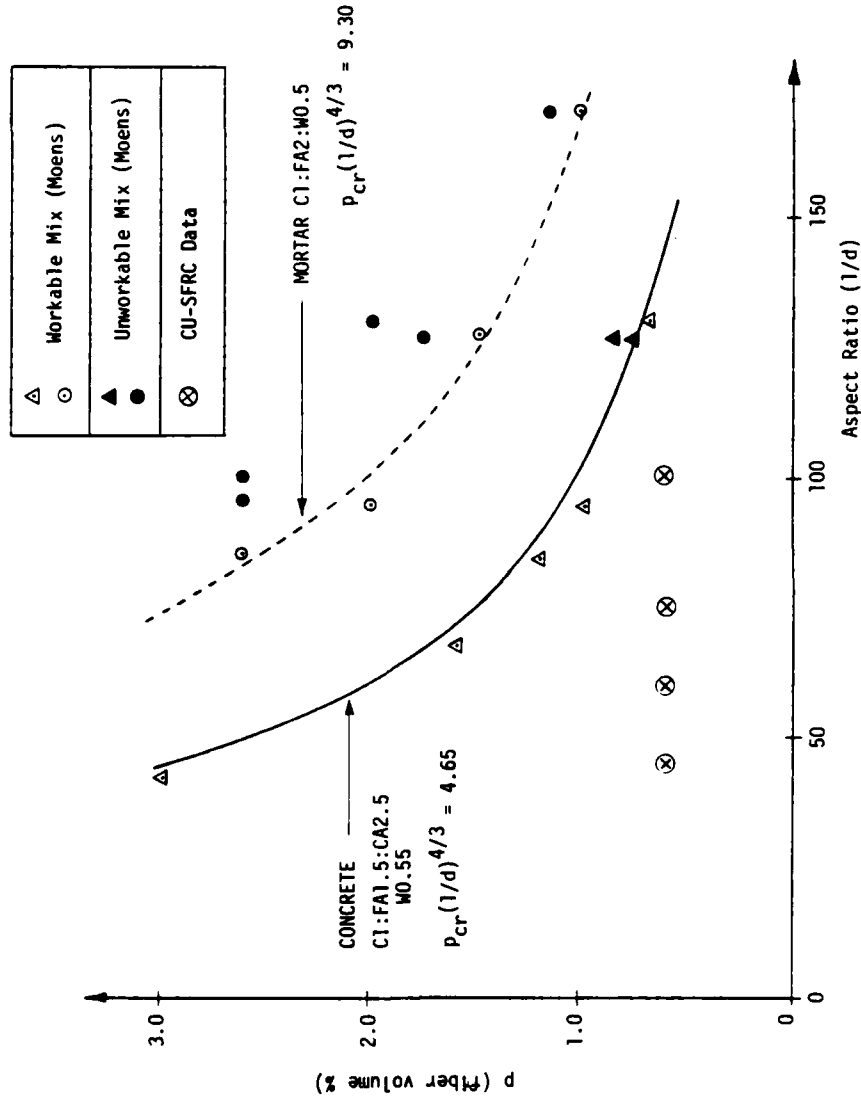


Fig. 2.4. Critical Steel Fiber Content [Moens (88)].

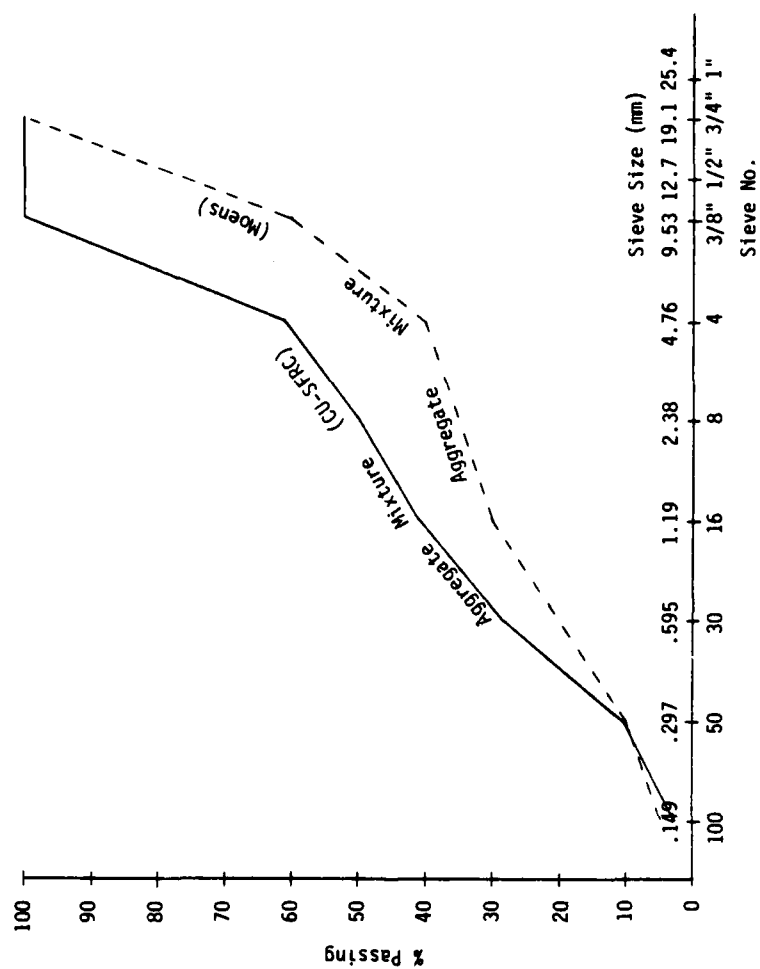


Fig. 2.5. Aggregate Mixture Gradation Curves for CU-SFRC and Moens (88).

that the two curves defined by Moens and shown in this figure would be upper and lower bounds in determining a critical fiber percentage with respect to the fiber aspect ratio, and the constant c would lie between his constants, i.e. $4.65 \leq c \leq 9.30$. Also plotted in this figure is the fiber volume percentage (p) vs. fiber aspect ratio employed in the CU-SFRC preliminary tests, with p remaining constant. Note that all these points lie below the critical curve defined for concrete, implying that good workability should be obtained for all the CU-SFRC mixes with a decrease in workability as the aspect ratio increased towards the critical curve. This indeed was found to be the case during the mixing of these concretes. It was noted that the workability did decrease for the mixes where the aspect ratio equalled 100, no so much in mixing but more so in placing and vibrating the mix into the molds, simply because these fibers were longer. However, they did not become "unworkable", but merely less workable than the mixes with fibers having lower aspect ratios.

From these results two obvious conclusions can be drawn. The concrete workability is a function of the volume percentage of fibers, and the addition of aggregates to a cement-mortar mix also reduces workability. This second conclusion can be deduced from common sense because the addition of aggregates causes the mortar volume per fiber to decrease making the fibers less free to rotate in the wet mix. Swamy (124) performed tests using a 10 mm (0.40 inch) maximum size aggregate concrete with a steel fiber aspect ratio of 100. The results plotted in Fig. 2.6 show a linear relationship between the critical fiber volume percentage (p_{cr})

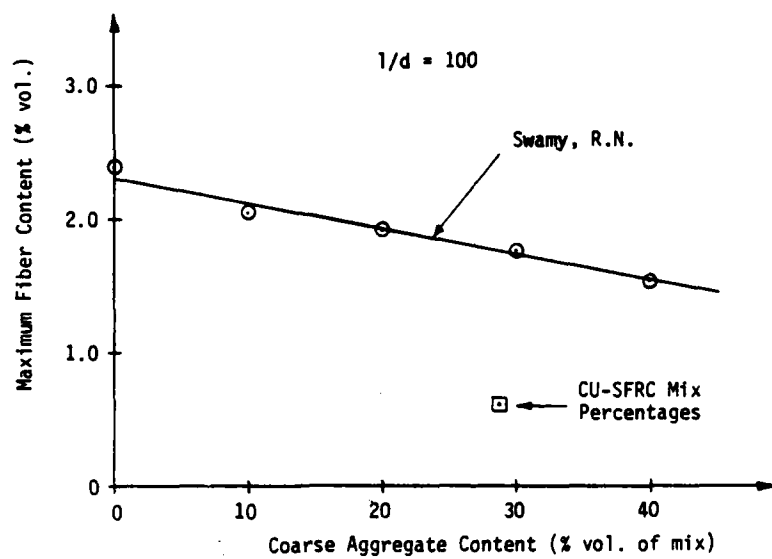


Fig. 2.6. Influence of Aggregate Volume [Swamy (124)].

and the volume of coarse aggregate. This critical fiber content was governed by "balling-up" of the fibers during mixing, and proved to decrease significantly as the volume of coarse aggregate increased. The volume percentage of the 3/8 inch maximum size coarse aggregate employed in the CU-SFRC mix was 28.6% with the corresponding fiber volume percentage of 0.6%. This point is also plotted in Fig. 2.6 showing that it lies well below the critical line determined by Swamy indicating that good workability should be obtained for this mix. This was indeed the case. Note that Swamy's critical line was determined for fibers with an aspect ratio of 100. If similar tests had been performed on SFRC mixes where the aspect ratio was less than 100, the critical lines would lie above Swamy's. This can be deduced from Fig. 2.4 because as the aspect ratio decreases, the critical fiber volume percentage governing workability increases. Therefore, the critical line obtained by Swamy shown in Fig. 2.6 could be used as an upper limit in determining the coarse aggregate volume percentage for a given fiber volume percentage, say determined from Fig. 2.4, provided the fiber aspect ratio was less than or equal to 100 and the maximum size coarse aggregate less than or equal to 10 mm. Or, the two figures could be used hand-in-hand as checks in aiding the design of the SFRC mix with respect to the fiber volume percentage, aspect ratio and coarse aggregate volume percentage.

It has been shown that for a given workability the fiber concrete and mortar employed by Moens satisfies the relation (Fig. 2.4):

$$p(\ell/d)^{4/3} \leq c \quad (2.2)$$

However, SFRC flexural strength (rupture modulus) has been shown (see Fig. 1.1) to increase linearly with respect to $p(\ell/d)$. This is also demonstrated to a certain extent in Fig. 3.26 for rupture modulus and Fig. 3.25 for tensile strength of the CU-SFRC.

Therefore, an advantage is offered by the use of $p(\ell/d)$ instead of $p(\ell/d)^{4/3}$ for estimating both strength and workability requirements. Moens showed that within a range of aspect ratio of 75 to 125, Eq. 2.2 may be substituted by

$$p(\ell/d) \leq C_m \quad (2.3)$$

where C_m is defined as the fiber-aggregate interaction factor of the concrete mix, calculated from the knowledge of the aggregate-mixture gradation curve. With a value of C_m , the critical volume percentage of fibers p_{cr} for a given aspect ratio (ℓ/d) can easily be calculated. The following shows the procedure used in calculating C_m for the CU-SFRC aggregate gradation.

Moens showed that the effect of each aggregate particle on workability may be linked to the particle size d by a fiber-aggregate interaction coefficient c_d . Then the sum of the weighted volumes of the individual particles results in the fiber-aggregate interaction factor of the mixture:

$$C_m = \sum_{i=1}^n v_i \cdot c_{d_i} \quad (2.4)$$

where

v_i = volume of aggregate i .

Particles finer than No. 100 are assumed to not interfere with the fibers in the mix, therefore particle sizes considered are limited to those retained on the No. 100 sieve. The interaction coefficient c_d is given by the logarithmic function plotted in Fig. 2.7 as a straight-dashed line.

$$c_d = 1.72 - \ln(d^{2/3}) \quad (2.5)$$

However, aggregate grading is measured by the aggregate fractions retained on a series of standard sieves. Hence, it is more convenient to use average coefficients

$$c_{ij} = 1.72 - \ln(d_i \cdot d_j)^{1/3} \quad (2.6)$$

for that aggregate portion between sizes d_i and d_j , as shown by the stepped-solid line in Fig. 2.7. Note that this figure is standard for any aggregate gradation as it represents the interaction coefficients of aggregate fractions vs. aggregate sizes.

With the average coefficients c_{ij} , the fiber-aggregate interaction factor of the mixture C_m can now be more easily calculated as:

$$C_m = \sum v_{ij} \cdot c_{ij} \quad (2.7)$$

where:

v_{ij} = volume of aggregate retained between the sieve sizes $d=d_i$ and $d=d_j$.

c_{ij} obtained from Fig 2.7.

This procedure is shown in Fig. 2.8 where C_m for the CU-SFRC is

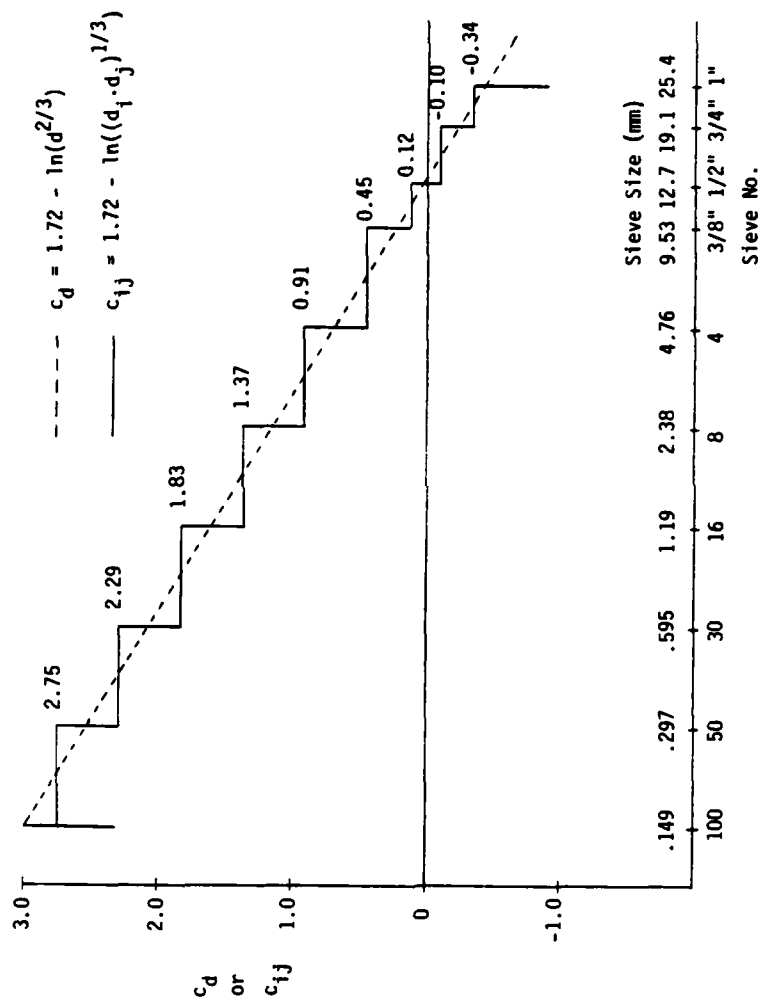


Fig. 2.7. Interaction Coefficients of Aggregate Fractions [Moens (88)].

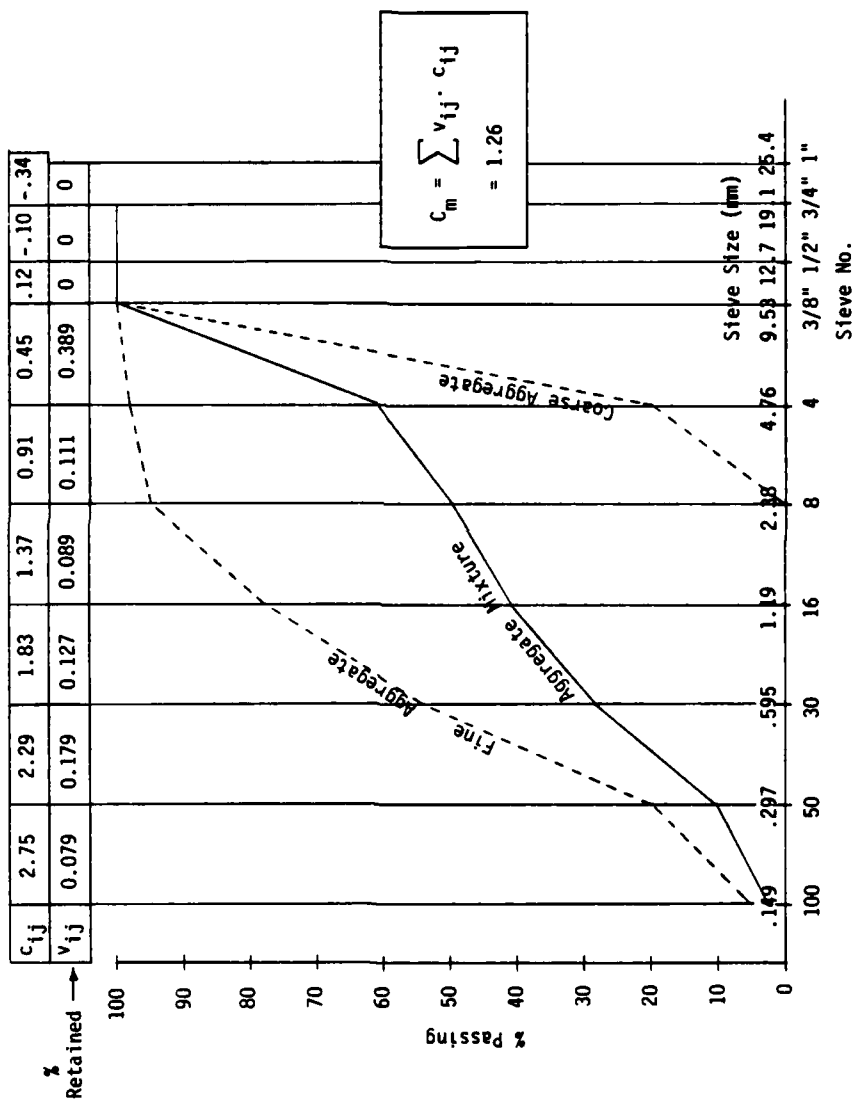


Fig. 2.8. Calculating the Fiber-Aggregate Interaction Factor (C_m) for the Mixture.

calculated as 1.26. Then from Eq. 2.3 one can find an approximate critical fiber volume percentage for a given aspect ratio i.e.:

$$p(l/d) \leq C_m = 1.26 \quad (2.8)$$

As previously mentioned, this equation is valid for aspect ratios between 75 and 125. For an aspect ratio of 100 for example,

$$\begin{aligned} p_{cr} &= \frac{C_m}{(l/d)} \times 100 = \frac{1.26}{100} \times 100 \\ &= 1.26\% \end{aligned}$$

The 1.26% of fibers by volume is equal to $1.26 \times 132 \text{ lb/yd}^3$ concrete or 166 lb. of fibers per cubic yard of concrete. If this amount were exceeded, the concrete will probably not be workable and balling may occur.

According to this criterion then, the fiber volume percentage of 0.6% (80 lb/yd³ of concrete) employed in the CU-SFRC mix should give a concrete with good workability since this 0.6% lies well below the critical percentage of 1.26% for a fiber aspect ratio of 100, the largest of all used in the CU-SFRC. As previously discussed, the fiber concrete with $p = 0.6\%$ proved to be very workable for all fiber aspect ratios.

2.4 Casting and Curing Procedures

For the preliminary test series, six concrete mixes were cast. The first, labeled P0, was a plain concrete mix used for comparison purposes. The remaining five were the SFRC mixes labeled P1, P2, P3, and P4 for the 4 Bekaert "Dramix" fibers and P5 for the USS

"Fibercon" fibers. These are listed in TABLE 2.1. The volume of each batch was 3.0 cu.ft., which is the optimal capacity of the mixer used. In all, twenty four 4-in. cubes, twenty four 3x6 in. control cylinders, and six 3x3x15 in. beams were cast for each preliminary test batch. See Fig. 2.9. After the final fiber size was decided upon from the preliminary test results, to be discussed in Chapter 3, two identical final concrete mixes (F1 and F2) were cast to obtain specimens for the multiaxial test series. In each of these were cast twenty four 4-in. cubes and twenty four 3x6 in. control cylinders. In order to reproduce identical concrete mixes for all tests, a precise standard mixing and curing procedure was established with the steps as listed below.

- 1) Prepare all the molds by cleaning and assembling. Grease them lightly to aid in the release of the specimens after curing 24 hours.

- 2) Weight all the constituents for the mix (cement, aggregates, water and fibers if used) in the proportions of C1 : FA1.82 : CA1.64 : W0.5. The aggregate gradations are given in Section 2.2. The fiber volume percentage of 0.6% comes to 80 lb. of fibers per cu. yd. of concrete. The water should be placed in surface-saturated container such that the container does not absorb any of the measured quantity of water.

- 3) "Butter" the mixer. First saturate the inside of the mixer with water. Then place 1 scoop of sand, 1/3 scoop of cement and enough water to produce a mortar. Rotate the mixer to coat the entire inner surface with the mortar. Discharge the excess. The mortar adhering to the mixer after discharging is intended to

compensate the loss of mortar from the test batch. See ASTM C192-69 (7).

4) Place all the aggregate and about 1/2 the water in the buttered mixer. Mix for 3 minutes, rest 3 minutes, then mix again for 2 minutes. The purpose of this is to produce a uniformly graded aggregate and also to allow the aggregate to absorb what water it will in the mixing process.

5) Place the cement and the remaining water into the mixer. Mix 5 minutes, rest 3 minutes, then mix again for 3 minutes.

6) Measure the slump according to the ASTM C143-74 specification (7). The desired slump of this wet mix before the addition of fibers should be about 4 in. If it is less than the desired amount, add additional water (1/2% of the total aggregate weight) to account for the water absorbed by the aggregate. (This quantity is a good starting point because, as discussed in Section 2.2, the percent absorption of the fine and coarse aggregates was 0.49% and 0.99% respectively.). Mix again as described in step 5, then measure the slump. Follow this procedure until the desired slump of 4 in. is obtained. Note here that the slump of all the mixes except P5 (discussed below), before the addition of the steel fibers was 3.5-4.0 in. Therefore, addition of the extra 1/2% of water was not required. If care is taken in weighing the constituents, buttering the mixer and surface saturating all equipment contacting the mix water, no additional water should be required in the mixing process to produce a 4 in. slump, as was the case.

7) Add steel fibers. For the plain concrete preliminary mix (P0), obviously no fibers are used so the concrete can be placed directly into the molds and vibrated. For the Bekaert "Dramix" fiber preliminary mixes (P1-P4) the fibers were added after the desired 4 in. slump on the plain concrete was achieved. Mix this combination 5 minutes, rest 3 minutes, then mix again 3 minutes. These fiber clips were simply thrown into the wet concrete mixture. Good random orientation and dispersion of these fiber types was obtained. It was noticed that the water soluble glue used to collate the "Dramix" fibers dissolved completely after about 2 minutes of mixing time. The slump was measured again for these 4 fiber mixes and ranged from 2.5-3.0 in. Regarding the USS "Fibercon" fiber preliminary mix (P5), these fibers were loose, so in order to insure good random orientation, they were sprinkled in and mixed with the dry aggregates and half of the water (step 4). Therefore, no plain concrete slump (step 6) could be recorded for this mix. Since this was the last of the six preliminary mixes, and the slump of the previous five (four before fiber additions) was 3.5-4 in., it was felt that this final mix had the same properties as the other five even though no slump prior to fiber additions could be measured. However, a slump of this USS "Fibercon" fiber mix was measured after all mixing was completed and recorded as 2.5 in.

Measuring the slump (ASTM C143-74) of a concrete mix is one way of testing the workability of the plastic concrete. This test is not very good when dealing with fibrous concrete simply because the fibers appear to cut down on the workability of the mix drastically.

Schrader and Munch (114) introduced a test (also described by Brandshaug, et al., (27) for inverted slump cone time as a new workability test for fibrous concrete. Primarily the test measures the mobility or fluidity of the mix (not apparent in the conventional slump test (ASTM C 143-74)), with the result being dependent on such parameters as aggregate size, shape and gradation, air content and admixtures, and surface friction of the fibers. They found that by using this test, a mix with a conventionally measured slump of 1/2 in. can be shown to have a fairly good workability. This test was not employed in the CU-SFRC research discussed in this report.

8) Immediately cast the specimens into the molds and vibrate externally. The vibrator used in this research was an air-powered Martin Vibrolator® eccentric ball type vibrator, model CV35 Mall, delivering up to 675 lbs. force at 10,000 vibrations per minute at 60 psi (see Fig. 2.10). It was simply held next to and/or clamped to the external surfaces of each mold. Vibrations took place for several minutes until it was felt good consolidation of the mix into the corners was achieved and until a cement-water mixture along with much of the entrapped air surfaced. The upper surfaces of the specimens were not floated or troweled for several reasons. It was found that floating or troweling was difficult due to the presence of the fibers. Floating the surface also causes the randomly oriented fibers in the upper part of the specimen to become aligned in a horizontal manner. In addition, the 4 in. cubical molds are only 4 in. high. Since such strict tolerances on the specimen sizes for the 4 in. cubical testing device are required, the specimens

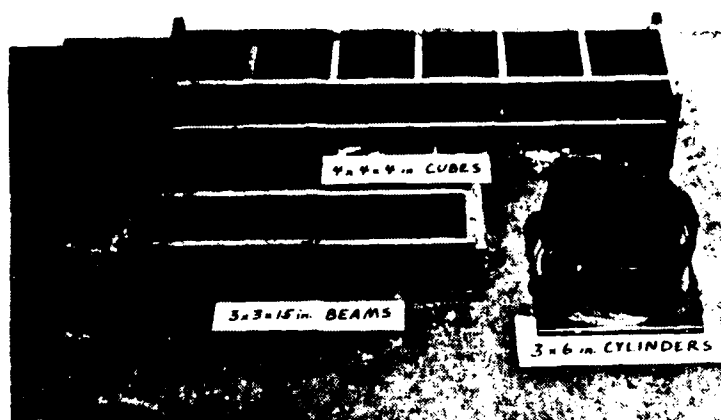


Fig. 2.9. Typical Concrete Molds.

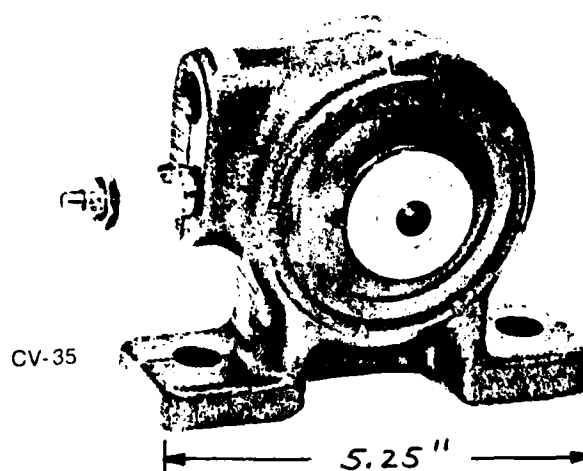


Fig. 2.10. Martin Vibrolator® Eccentric Ball Type External Vibrator.

were left with about a 1/2 inch cap that could be cut off with a diamond-bladed masonry saw after they were stripped and cured such that the 4.00 x 4.00 x 4.00 inch tolerances could be maintained.

Some sort of vibration of a fibrous concrete mix is required to ensure good compaction, because the addition of fibers causes the mix to become very stiff. Placement into the molds is made much easier with an external vibrator. Rodding or internal vibration (ASTM C192-69) should not be allowed for laboratory specimens because the rod or stinger will displace some of the fibers and destroy the random orientation. Tests were conducted on 6 x 12 inch cylinders to determine this. After they were cast, vibration was done using an internal, stinger-type vibrator. When the specimens cured, 1/2 inch slices from the center of the specimen were made with a diamond-bladed masonry saw, then X-rayed. The X-rays proved that the internal vibration did indeed displace the fibers and an area with no fibers resulted where the vibrator was inserted and removed. Fig. 2.11 shows the results of one such slice.

9) After 24 hours of dry curing, strip the specimens from the molds, carefully label each specimen with number and orientation, then place them in a 100% humidity room. After six days of wet curing, remove the specimens from the humidity room, allowing them to continue curing in air at room temperature. For example: if the specimens are cast on Monday morning, strip and place them in the fog room Tuesday morning. Remove them from the fog room the following Monday morning, 7 days later. Only after this period may the specimens be prepared for their respective tests.



Fig. 2.11. X-Ray View of a Typical 1/2 Inch Slice of a 6 x 12 inch Cylinder Vibrated Internally.

2.5 Sample Preparation

The upper surface of all the specimens was not floated or troweled after casting, therefore the extra height (except on the beams) was first cut off using a diamond-bladed masonry saw. The 3x6 in. control cylinders were tested in unconfined compression (ASTM C39-72) and indirect tension (ASTM C496-71). Therefore, after the excess was cut off, the top and bottom of the cylinders were ground to ensure that these surfaces were parallel to each other and perpendicular to the vertical axis. No additional sample preparation was required for the cylinders tested in indirect tension. The cylinders tested in unconfined compression, however, were capped with sulfur on the upper surface (ASTM C617-73) before being tested. The beams tested in flexure (ASTM C78-75) required no preparation except to sand off the excess on top of the specimens to be flush with the sides. No ASTM specification is given for preparing or testing cubes in unconfined compression. Since the cubical molds are very precise, with right angles in all corners, only the tops required grinding to obtain the 4.00 in. height after the excess was sawed off. Some of these 4 in. cubes were then tested in unconfined compression (without being capped) in the same manner as the control cylinders (ASTM C39-72).

Preparation of the 4 in. cubes for the multiaxial tests was more involved than the sample preparations described above. First the upper surface of each cube was cut off with a diamond-bladed masonry saw such that the resulting height was 4.00 in. The saw used had a fixed spindle on which the circular blade rotated at a constant velocity and an automatically fed table upon which the

specimen was mounted. The automatic feed was set slow enough so any transverse movement or vibration of the saw blade in the cutting process could be minimized.

Even though the mix was carefully vibrated when placed in the forms, there were still some air voids entrapped in the specimens. The voids on or near the surface would likely allow penetration of the flexible membranes under pressure resulting in their rupture before all substantial test data had been recorded. In order to eliminate this possibility, part of all six faces on the cubes were sandblasted to expose these voids near the surface. Sandblasting each face entirely would have damaged the right angle corners of the cubes. Since a leather pad (described in the next section) with a distorted circular hole lies between the membrane and the specimen (eliminating a rupture near the corners), the sandblasted portion was an area centered on each 4 in. face with a diameter of approximately 3.75 in. Sandblasting also exposed some of the steel fibers at the surface. To prevent these from puncturing the membrane and to ease the patching process, the exposed fibers were "clipped" at the surface of the concrete with a small pair of diagonal sidecutters. The sandblasted areas were then filled with a plastic wood filler material (Durham's Rock Hard Water Putty) and smoothed out as much as possible with a 1 in. putty knife and 5 in. broad knife. After drying 24 hours, the puttied surfaces were belt sanded. Any holes uncovered were reputtied and the surfaces finished with fine sand paper. Fig. 2.12 shows a typical 4 in. cube finished and ready to be tested. One can observe the circular puttied area on each face as previously described.

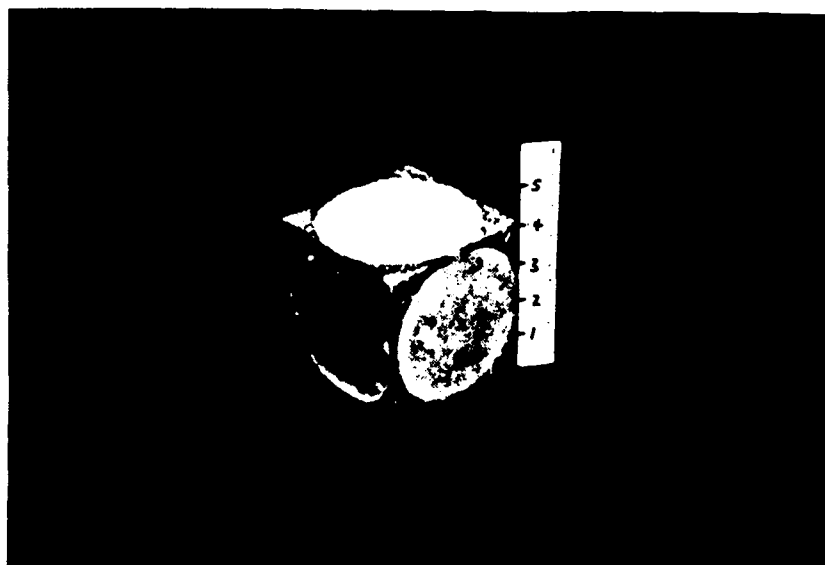


Fig. 2.12. Typical 4 in. Cubical Specimen
After Test Preparation.

2.6 Multiaxial Test Apparatus¹

A detailed description of the development of the test cell is given by Sture (120). Some slight modifications, however, were made to accommodate this study and will be discussed in detail here.

The apparatus consists of a rigid cubical space frame and six walls that function as lids, shown in an exploded view in Fig. 2.13. The openings in the frame form six similar cavities. Each of these cavities, together with the adjoining walls and a proper seal arrangement, act as a pressure vessel.

¹ This section is rewritten in part from Refs. 120, 8 and 57.

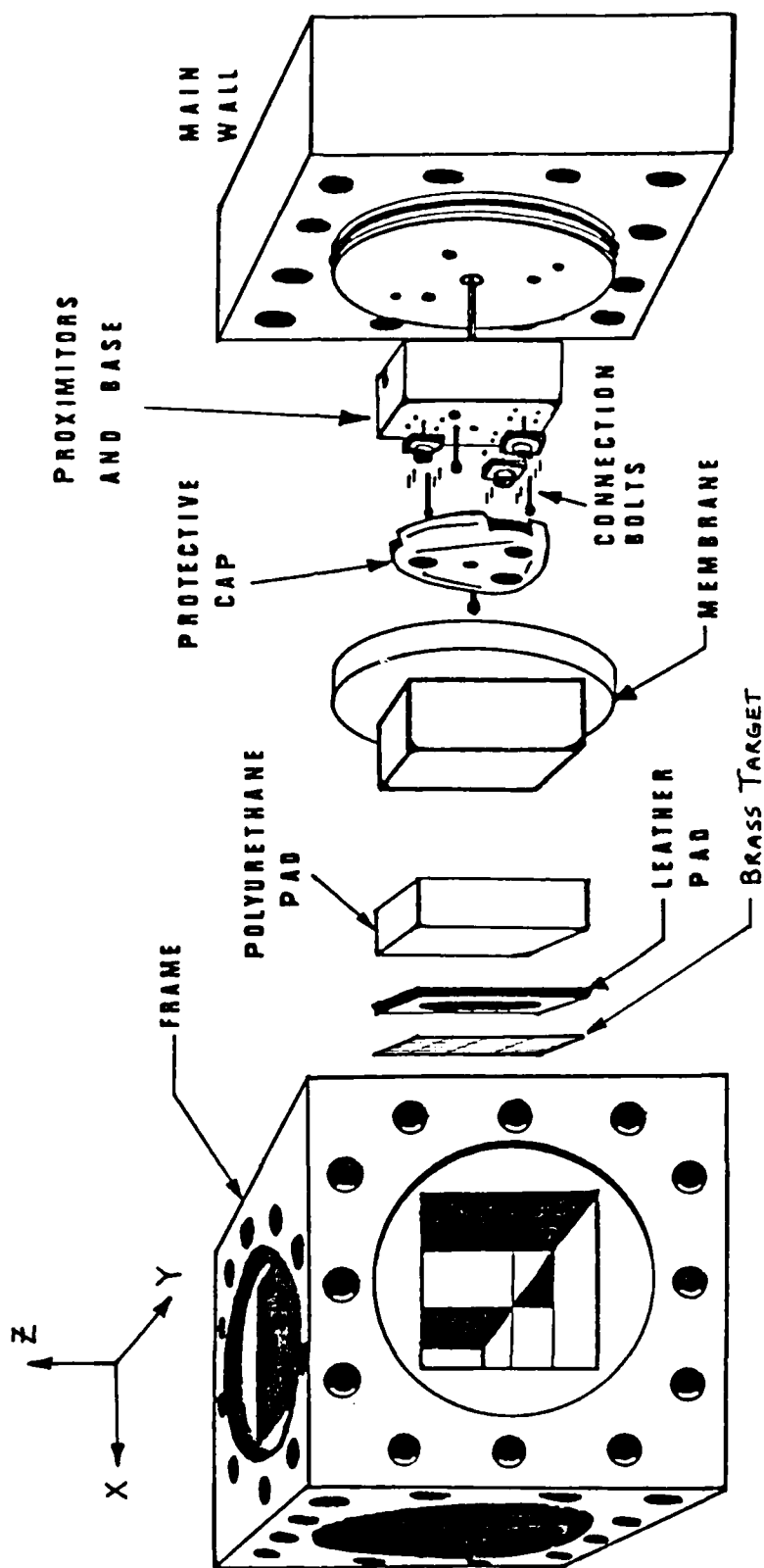


Fig. 2.13. Exploded View of the Test Cell

The 4 in. cubical specimen is placed in the center of the space frame's cubical cavity, then sealed off by the six walls which are bolted on to the frame. The load is applied via a hydraulic pressure system where urethane membranes and pressure seals located on the inner face of each wall contain the hydraulic fluid pumped into the apparatus. Each set of opposing walls is connected to an individual pumping system which regulates the stress level on that axis. Thus the stresses on each of the three axes are independently controlled such that a stress state with $\sigma_1 \neq \sigma_2 \neq \sigma_3$ can be achieved. Proximity-type transducers (probes) are used to measure the deformations in the three principal directions. All test data is monitored and plotted in real time by computer so the specimen behavior can be observed while the test is in progress.

2.6.1 Frame

The frame of the test cell, Fig. 2.14, was machined from a solid 10 in. cubical block of VASCOMAX 250 CVM 18.5% nickel maraging steel. The steel offers exceptional ductility, strength and hardness, all necessary material parameters considering the high stresses the equipment is subjected to. After machining to the dimensions given in Fig. 2.15, the block underwent heat treating to obtain the mechanical properties quoted by the manufacturer as: ultimate tensile strength, 264 ksi; yield strength at 0.2% offset, 255 ksi; elongation at ultimate, = 13%; modulus of elasticity, 26,500 ksi.

Figs 2.13 and 2.14 show the coordinate system, following the right hand rule used to describe the box frame. The test cell

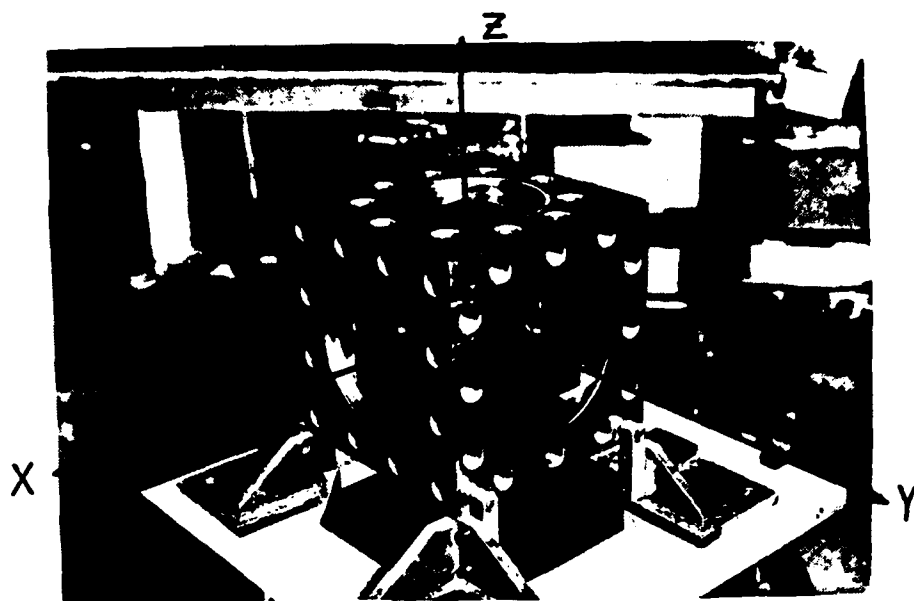
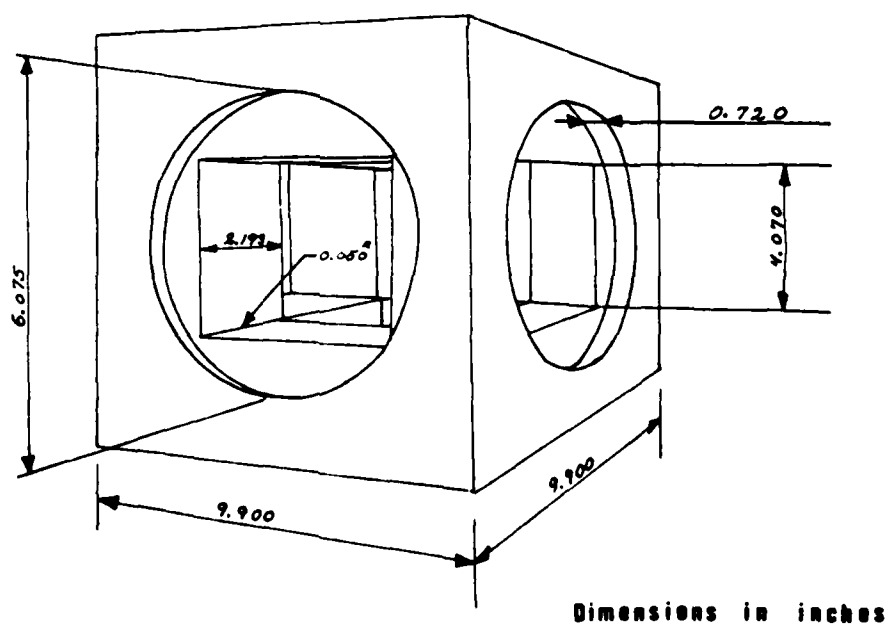


Fig. 2.14. Photograph of Test Cell Frame.



Dimensions in inches

Fig. 2.15. Dimensions of the Cell Frame.

assembly procedure discussed in Section 2.7 would be easily understood if this coordinate system is followed. In Fig. 2.13, the top of the frame is the +Z face; the left hand side is the +X face and the front side therefore becomes the +Y face. Notice the bolt hole patterns are different on adjacent faces of the frame. The +Z and -Z faces have 10 bolt holes arranged in a circular pattern. The +X and -X faces have 12 bolt holes arranged in a square pattern, with 4 on a side. The +Y and -Y faces also have 12 bolt holes arranged in a square pattern, but with 3 on a side. All bolt holes are 1.00 in diameter, NC thread and opposing faces are machined identically.

2.6.2 Walls

The walls covering the six faces on the cubical frame are built up of two components. The main frame of each wall was machined from 4 in. thick ALCLAD 7075-T6 aluminum plate and serve as the lids for the six pressure vessels and as a base for the displacement measuring probes. They contain the pressure seal devices and the hydraulic fluid inlet ports. The square top piece, bolted on the main wall, acts as a base for three probe attachments. An exploded view of a typical wall is shown in Fig. 2.16. One of the two fluid ports serves as an inlet for the hydraulic fluid, the other as an outlet to bleed entrapped air from the pressure chambers or as a pressure transducer connection port. A photograph of a typical wall is shown in Fig. 2.17.

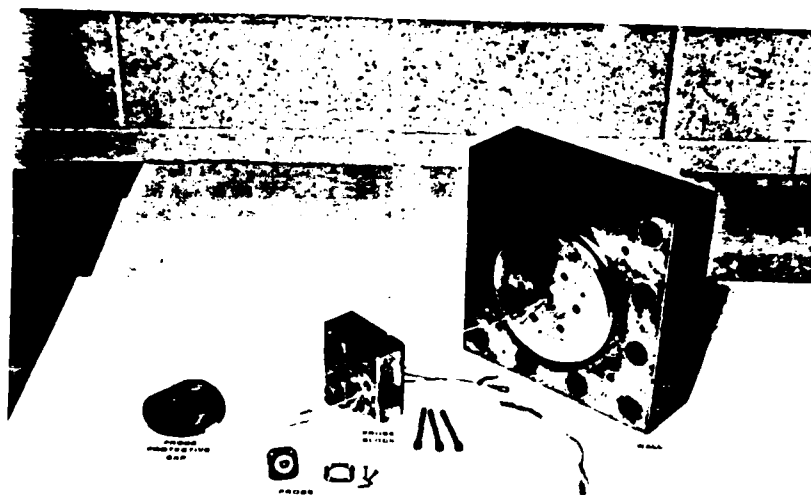


Fig. 2.16. Exploded View of a Typical Wall.

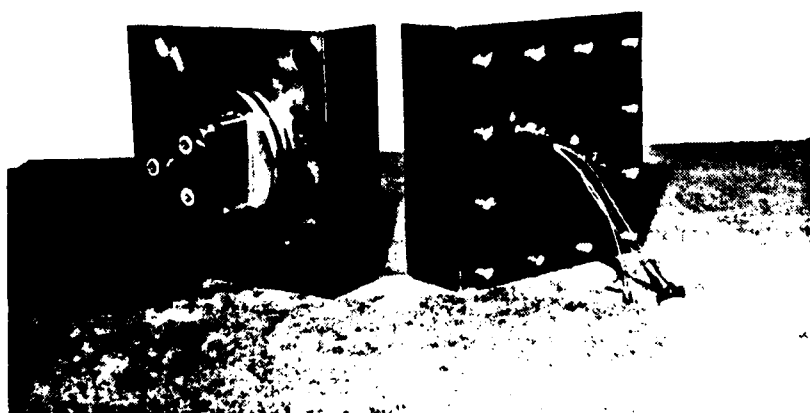


Fig. 2.17. Front and Rear View of a Typical Assembled Wall.

2.6.3 Seals

Details of the sealing system are shown in section in Fig.

2.18. Two O-ring grooves form the pressure seal between the wall and the frame. The inner groove, closest to the sample, holds the outer O-ring sleeve of the vinyl or polyurethane membrane. The outer groove houses an O-ring (Parker 2-358 durometer 70) which is compressed to a maximum when the wall is assembled to the frame. The sealing capacity of this arrangement increases with cell pressure.

A polyurethane pad with a sleeve and a leather pad rest against the sample face, and transmit the fluid pressure from the membrane to the specimen. They are flexible enough to follow minor differential distortions on the specimen surface. These two pads also help to prevent a membrane extrusion from occurring when a large deviator stress is present between two adjacent pressure vessels. Fig 2.19 shows the membrane, the polyurethane pad, the leather pad and the brass target (whose function is described in Section 2.6.5.).

The leather pads were made in-house from about 1/4 inch shoe leather to the approximate specifications given in Fig. 2.20. First the pads were cut and sanded to the 4.06 in. square dimension. They were then placed, one at a time, in a positioning fixture mounted in a turning lathe and the 3.62 in. outside diameter hole centered in the pad with a 45° bevel, was cut through. The pad was removed from the fixture and using a router with a 45° beveling bit, the three areas with a 1.55 in. outside radius (which make the circle oblique) were cut. The purpose of this hole shape in the leather pad is to

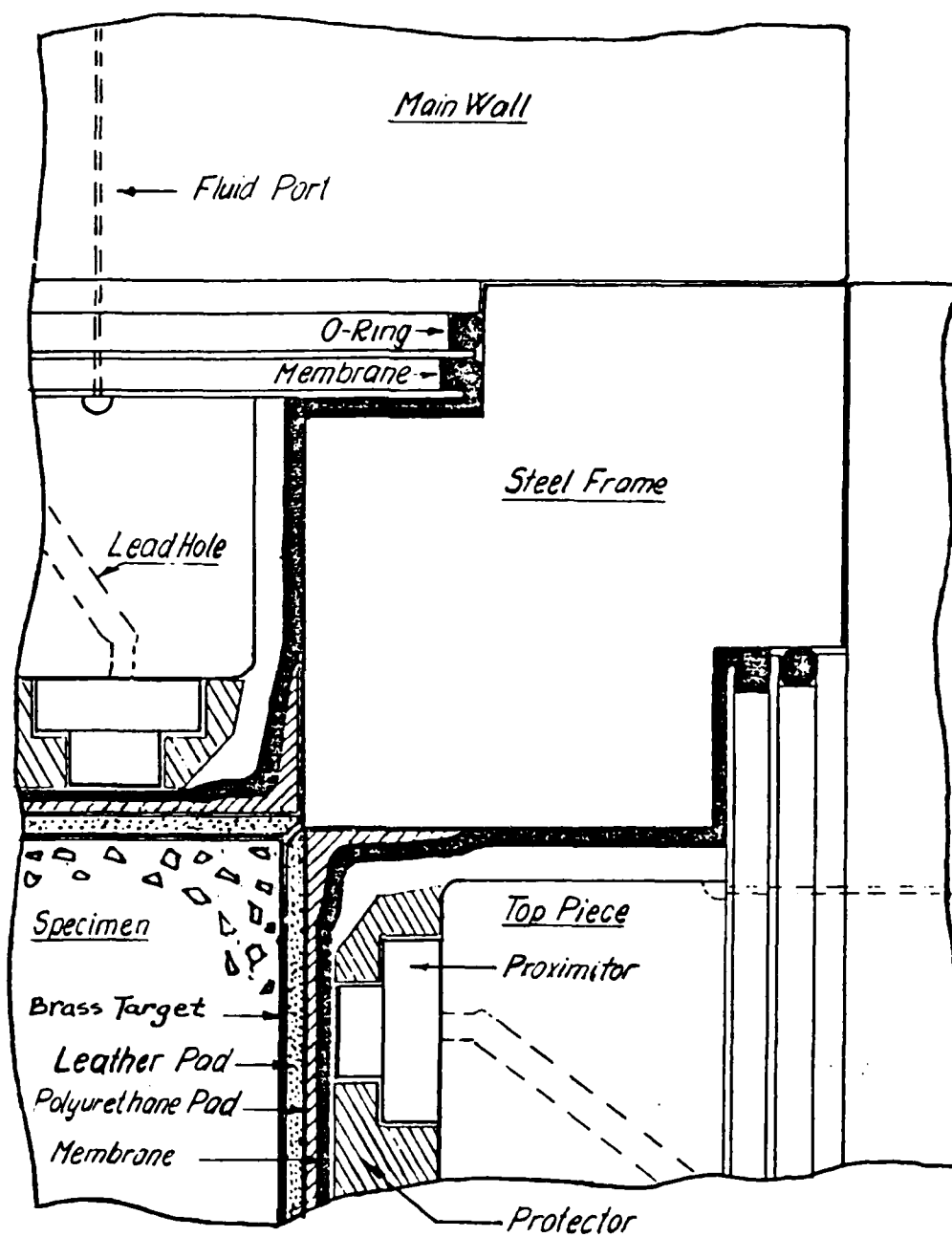


Fig. 2.18. Detail from Assembled Test Cell.

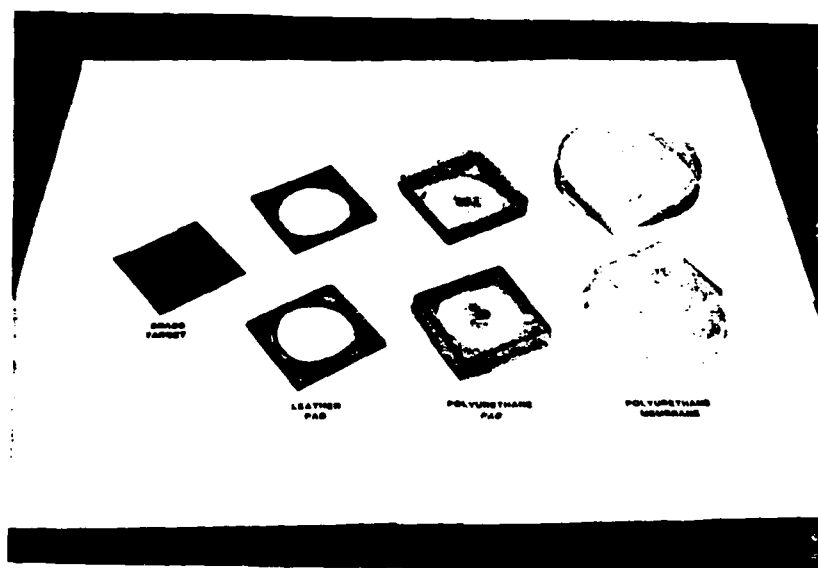


Fig. 2.19. Top and Bottom Views of Polyurethane Membrane and Pad, Leather Pad and Brass Target.

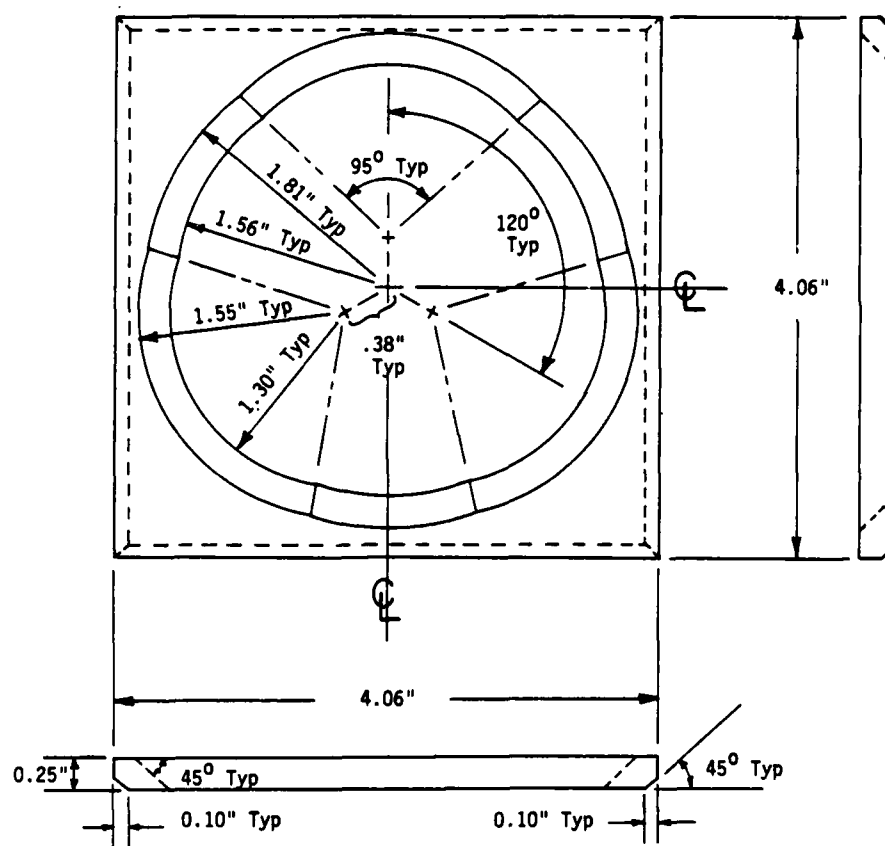


Fig. 2.20. Leather Pad Dimensions
(Dimensions given in inches).

reduce frictional interference between the proximity probes' protective cap and the membrane when the test cell is assembled. Finally the 45° bevel along the pad's edges was sanded to minimize the interference at the interfaces between leather pads of adjacent pressure vessels. After each test, these pads were checked and resanded to the 4.06 in. square dimension, and re-beveled, if necessary.

2.6.4 Pressure System

The high pressure hydraulic system shown diagrammatically in Fig. 2.21 was built around three Pressure Products Industries hand pumps; two Model OH 100-30 and one OH 102-30, all with a 0-30,000 psi operating range. By suitable valving, the three pumps could be independently operated and a $\sigma_1 \neq \sigma_2 \neq \sigma_3$ compressive stress state in the test cell could be achieved.

The pressures are monitored by Heise Bourdon tube gauges, Model CM-6" and 12", 0-30,000 psi range; one fitted to each pump and three others mounted on an instrumentation panel as shown in Fig. 2.22. Autoclave Engineers, Inc. tubings (type 304 SS, 1/4" O.D., 0.083" I.D.), fittings and valves are used to transfer the hydraulic fluid from the pumping system to the test cell. Initially, heavy duty automotive brake fluid was used as the pressurizing medium with membranes made of PVC (polyvinyl chloride). Since then, the fluid medium has changed to 100 centistokes nominal viscosity silicon oil with membranes made of polyurethane. Silicon oil was found to be more inert and had no deteriorating effect on the membrane and O-ring materials as the brake fluid did, therefore the change was

AD-A114 168

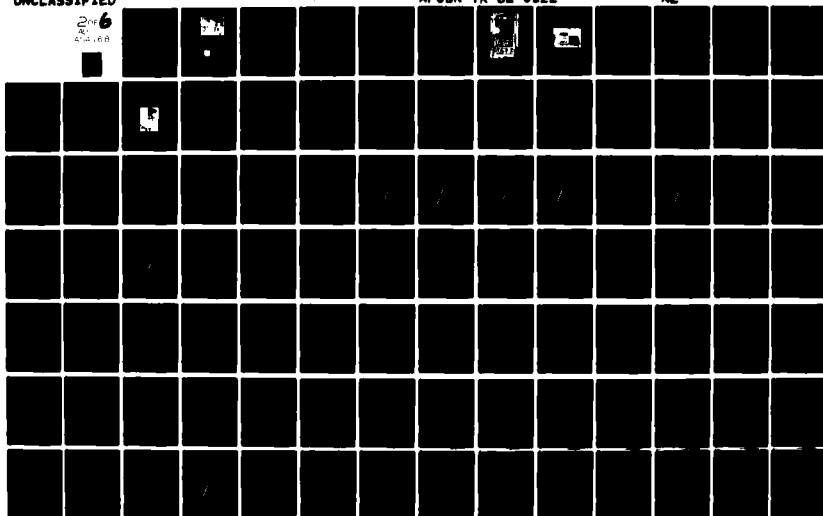
COLORADO UNIV AT BOULDER DEPT OF CIVIL ENVIRONMENTAL --ETC F/G 20/11
CONSTITUTIVE RELATIONS OF RANDOMLY ORIENTED STEEL FIBER REINFOR--ETC(U)
DEC 81 D E EGGING, H KO AFOSR-79-0065

UNCLASSIFIED

AFOSR-TR-82-0122

NL

2 of 6
AD-A114 168



made. As with the brake fluid, the silicon oil is nonelectrolytic and thus would not disturb the deformation measurement system (see next section).

2.6.5 Deformation Measurement System

Surface displacements of the specimen are measured with a Bentley-Nevada proximator probe system. The probes (Fig. 2.23) are type 308L-9229-01, have a total range of 0.250 in. and are made of fiber reinforced epoxy.

Sets of three of these proximity-type displacement transducers are mounted on each wall (Fig. 2.16). Each probe, operating on an inductive principle, measures the relative gap width between a conductive metal target on the surface of the specimen and a coil embedded in its tip, without any physical contact being made. The proximator driver, providing electrical energy to the probe, is designed to operate the probe with an 18 vdc @ 25 ma power supply. A signal proportional to the permeability of the magnetic field in front of the coil is sent back to the driver unit, which then rectifies it into a DC signal. This voltage output of the probe coil can be interpreted to represent the gap width by reference to a calibration curve previously established for that probe-driver system, test material and metal target. Each proximator probe is calibrated within a 0.050 in. to 0.250 in. range using a calibration stand filled with the same fluid used as the pressure medium. The target and probe are submerged in the fluid and voltage readings for a specified gapwidth (measured by a dial guage to the nearest 0.0001 in.) are recorded. A typical proximator probe calibration curve is shown in Fig. 2.24.

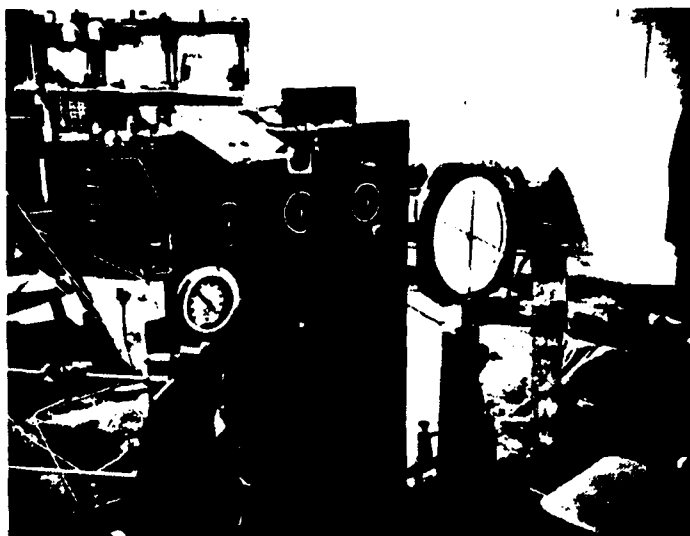


Fig. 2.22. Pumping System and Instrumentation Panel.

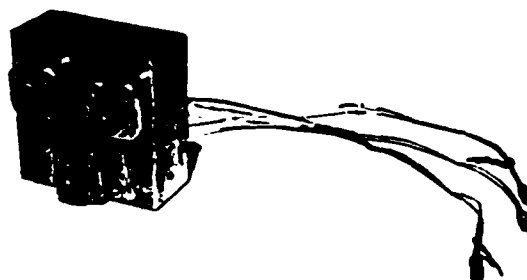


Fig. 2.23. Set of Three Proximity-Type Displacement Transducers (Probes) Mounted on Probe Block.

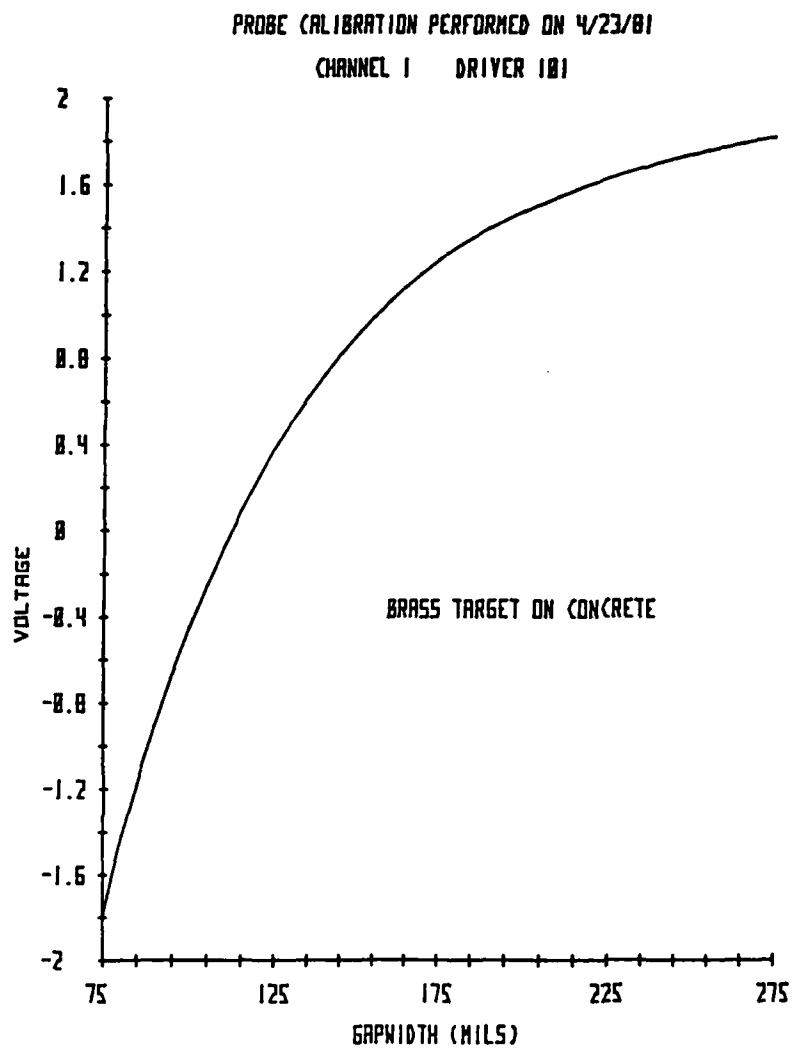


Fig. 2.24. Typical Proximator Probe Calibration Curve.

Different types of conducting targets can be used on the specimen as long as the probes are calibrated for that target. In the past, aluminum foil has been used for obtaining deformations of materials such as coal, shale, oil shale, sandstone, mortar and concrete. For this research however, much higher stresses had to be developed in the cubical testing device than ever before to fail the SFRC specimens in multiaxial compression, simply because these specimens have a much higher strength than most other materials tested in the device. Since the concrete cubes have some irregularities on or near the surfaces that may be missed in the patching process (Section 2.5) causing a pinhole failure of one or more of the flexible membranes before failure of the specimen occurs, it was decided that a thicker target material than aluminum foil would be required. Because of the ease of accessibility of brass foil in varying thicknesses, the decision to use 0.012 in. thick brass sheets as the conducting target material was made. To reduce the transverse stiffness of these sheets so they would conform to the shape of the deformed specimens surfaces, the targets were cut in a pattern shown in Fig. 2.25. The dotted circular areas shown in this figure are the regions over which the proximator probes act and therefore no slits can appear there or erroneous deformation readings may result.

Proximator probe sets are positioned so that the three probes on each wall are a mirror image of those on the opposing wall. By comparing the outputs of these probes, system deformations are measured, from which specimen deformations may be determined. By this method all rigid body translations are automatically

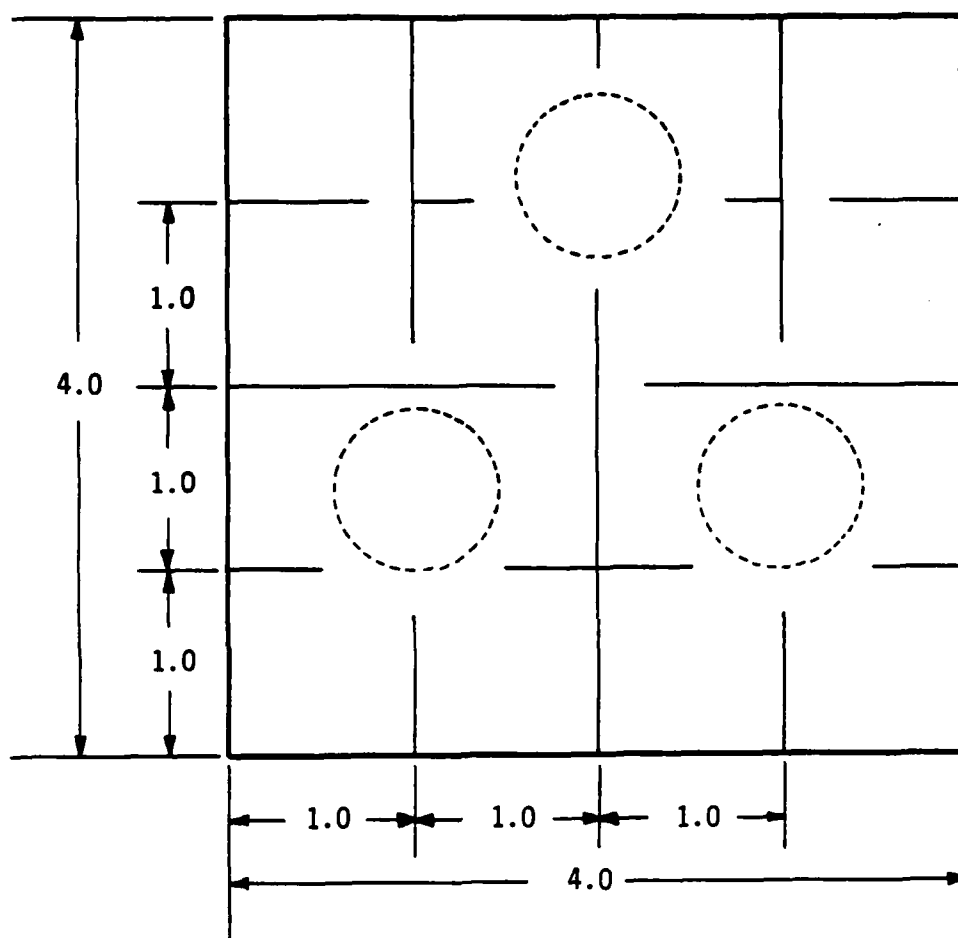


Fig. 2.25. Brass Target Dimensions
(Dimensions given in inches).

eliminated from the calculations. Each probe set also describes the orientation of the specimen surface it monitors. By examining the subsequent changes in relative inclination of adjacent sides, shear strains can be determined.

2.6.6 Data Acquisition and Data Reduction System

The data acquisition system used for collecting the deformation produced by applying loads to the cubical specimens consists of the proximator probes and the central data acquisition system which houses the proximator drivers. All data reduction is done with an HP 9830A calculator.

The electrical energy required to excite the 18 proximator probes located on the aluminum walls of the cubical cell is provided by the 18 proximator drivers located in the central data acquisition system (Fig. 2.26). This was described in the previous section. Then the multiplexer in the central data acquisition system scans through the 18 proximator channels to retrieve the return voltage signal from the proximator probes. A 19th channel is used to record the voltage from a standard probe (external to the cubical cell) in order to monitor electronic drift in the system. These voltages are then converted from analog to digital signals where they are then transmitted to the HP 9830A calculator via a BCD interface packet.

The calculator, having an 8K word memory capacity with extended memory capabilities, shown in Fig. 2.27, uses the raw digitized voltage data to calculate gapwidths between the proximator probes and the cubical specimen through appropriate calibration arrays

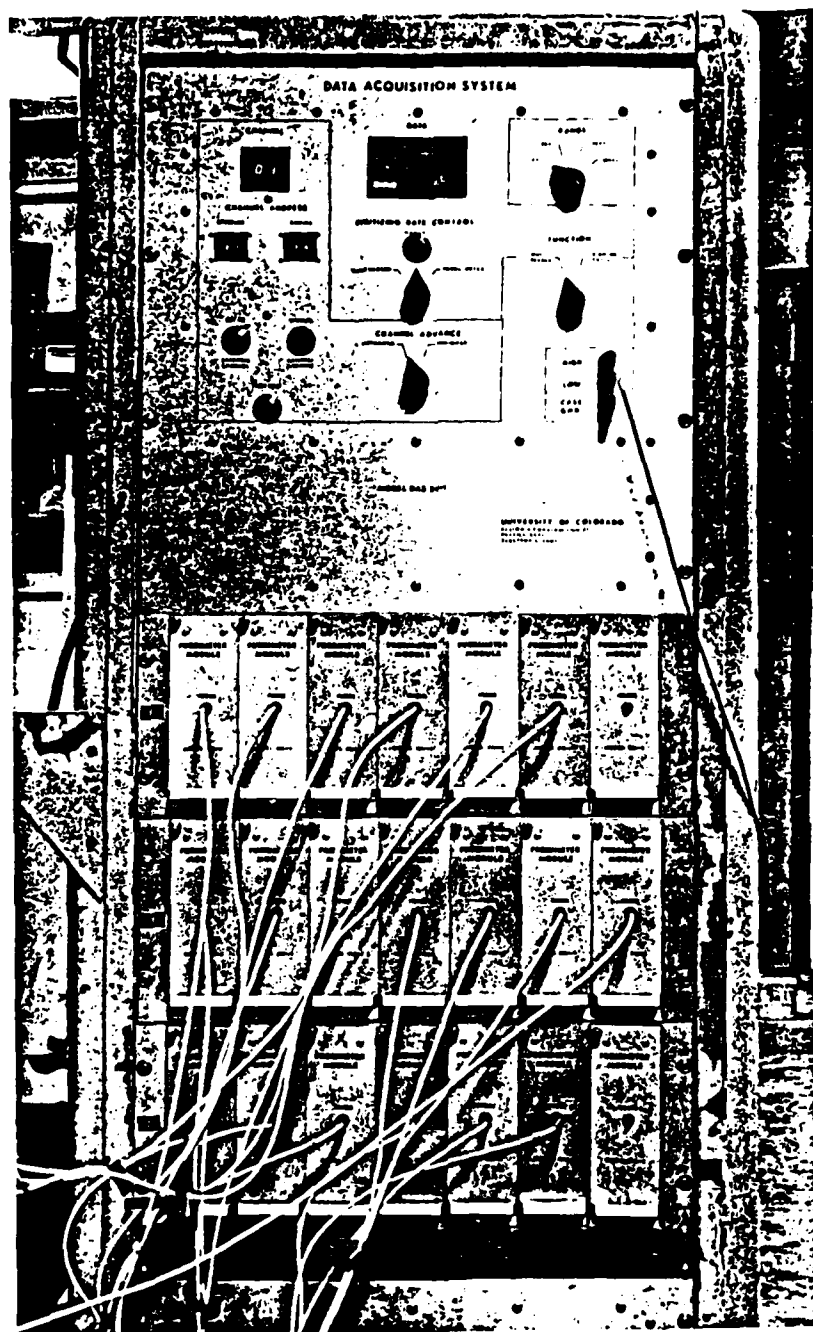


Fig. 2.26. Front View of Central Data Acquisition System.



Fig. 2.27. Hewlett-Packard Computer and Plotter.

stored in the calculator's memory. By incrementing the loads in a stepwise manner, a series of gapwidths are recorded, from which the strains are computed. Note here that the box frame and walls are not perfectly rigid. Therefore, when a load is applied to the specimen in the device, the deformations measured are for the total system and not just for the specimen. So appropriate box displacements for that given stress state must be subtracted from the total deformation measured in order to obtain specimen deformations to compute specimen strains. Following determination of the specimen strains, the information is transferred to an HP 9862A plotter unit, (Fig. 2.27), where graphical representations are produced, giving a real-time display of the stress-strain properties of the material. The entire process of collecting and reducing the data from one loading increment takes approximately 30 seconds once the specified loadings in the system are achieved. A typical printout of the real-time data for one load step is shown in Fig. 2.28. At the end of the test, the stress-strain data is stored on cassette tape for further data reduction and analysis at a later time.

2.7 Test Procedure

The coordinate system used in describing the test cell below is discussed in Section 2.6.1.

The box frame is mounted on a thick aluminum plate, about 3 in. above it. This plate is hinged about an axis parallel to the

TEST = F104 TE = 1000 F01... DATE 15 JUL 82

XXXXXXXXXXXXXXXXXXXXX LOAD STEP 12 XXXXXXXXXXXXXXXXXXXXXXXX

	PROBE VOLTAGES			PRESSURE VOLT.
+X	0.7220	0.6201	0.7626	0.0000
-X	0.4803	0.9384	0.9603	
+Y	0.5389	0.7100	0.5704	0.0000
-Y	0.8526	0.8382	0.8361	
+Z	0.5562	0.3061	0.3042	0.0000
-Z	0.7664	0.5548	0.5244	

STANDARD PROBE = 0.2006

	GAPWIDTH (MILS)			PRESSURE
+X	111.749	102.119	114.642	10000
-X	125.621	124.375	124.028	
+Y	104.431	108.118	105.731	10000
-Y	119.005	117.870	117.145	
+Z	105.076	121.037	117.046	4000
-Z	114.625	106.149	104.450	

CHANGE IN GAPWIDTH (MILS)

+X	16.094	17.102	15.825
-X	30.589	17.850	19.371
+Y	17.634	15.000	20.350
-Y	30.017	19.854	19.382
+Z	9.405	9.810	9.969
-Z	5.506	5.641	6.024

	PAIR 1	PAIR 2	PAIR 3	HYPERRGL	DO CHL
X	35.691	35.152	37.240	35.693	15.412
Y	37.711	35.937	39.740	37.736	21.010
Z	14.911	15.459	14.991	15.121	0.000

PRINCIPAL STRESSES AND STRAINS

	PRESSURE	PAIR 1	PAIR 2	PAIR 3	HYPERRGL
X	10000.00	0.00000	0.00402	0.00470	0.00411
Y	10000.00	0.00010	0.00062	0.00063	0.00041
Z	4000.00	0.00010	0.00030	0.00014	0.00010

OCT HOPE STRESS = 8000.00

OCT SHEAR STRESS = 2010.40

OCT HOPE STRAIN = 0.00250

OCT SHEAR STRAIN = 0.00130

BULK MODULUS = 7.41E+05

SHEAR MODULUS = 1.88E+06

Fig. 2.28. Typical Real-Time Data Output.

-X/-Z corner of the box frame, to an angle iron support bracket bolted to the floor.

As previously discussed, the test cell is not perfectly rigid and deformations do take place in the frame, walls, bolts, etc., when the specimen is stressed. Therefore, since the cell must be calibrated for these deformations, and in order to minimize the error that may occur in these deformations from test to test, a systematic manner of assembling the cell was established and strictly followed throughout all tests. This standard procedure also helped speed the assembly of the system. The wall mounting and bolt tightening sequences are first mentioned for the sake of being repetitious later.

The walls were mounted to the box frame and bolted down in the following sequence: -Z, +Z; -Y, +Y; -X, +X. The brass targets, leather pads and polyurethane pads were inserted first and the corresponding aluminum walls with membranes attached were mounted. Fig. 2.13 demonstrates this. Since the targets and leather pads are antisymmetric, care had to be taken to ensure that they were inserted in the manner designated by the position of the proximator probes. After opposing walls were placed, the four corner bolts for these walls were inserted and alternately tightened from wall to wall in a systematic manner such that the specimen remained centered in the frame. Once these four bolts were snugged and the walls tightly in place, the bolts were torqued to 300 ft-lbs using an indicating torque wrench. Then the remaining bolts were inserted and torqued to 300 ft-lbs in a clockwise manner, starting at the top. Fig. 2.29 shows the bolt tightening sequence followed.

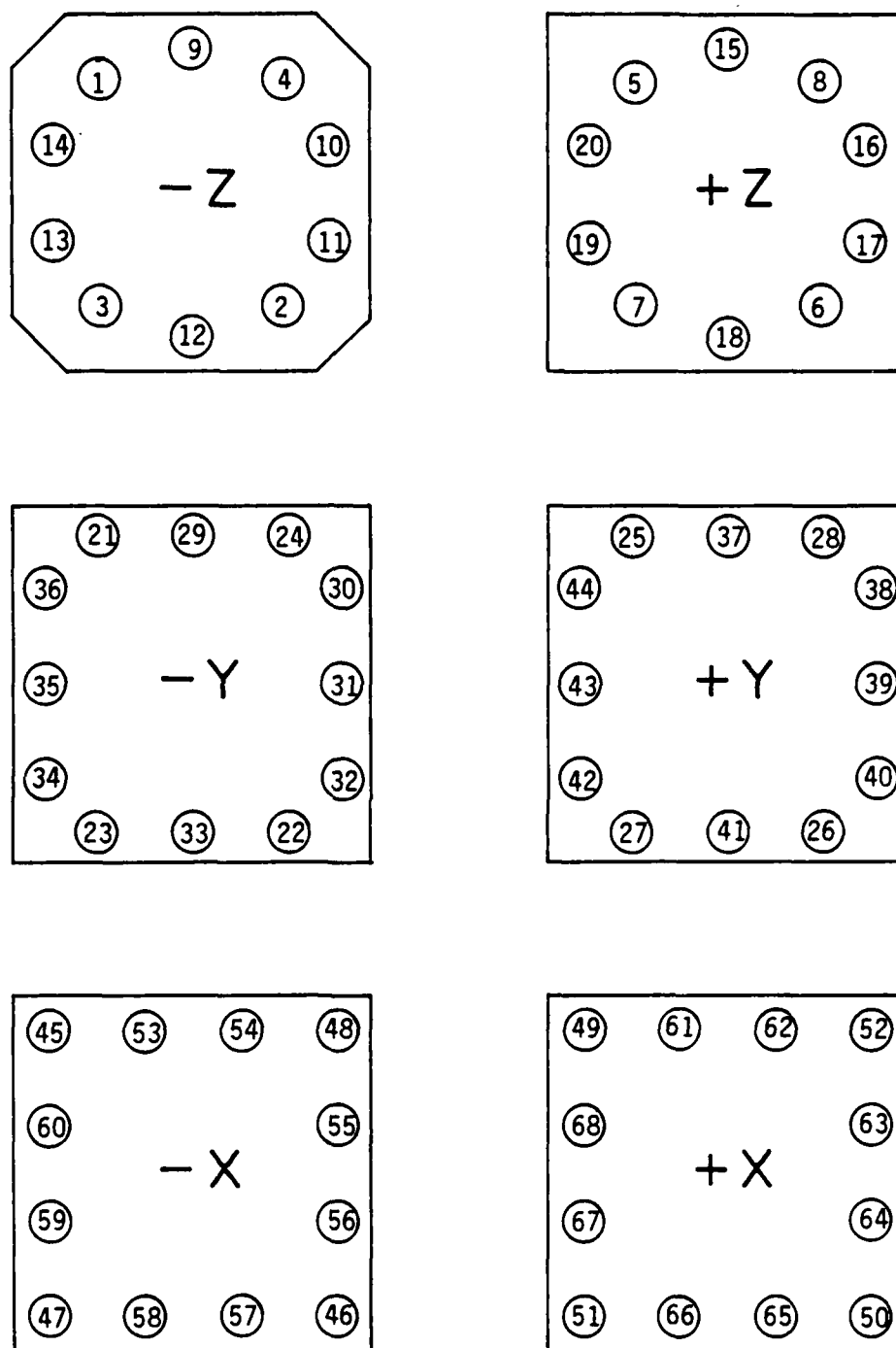


Fig. 2.29. Bolt Tightening Sequence for the Box Faces and Respective Walls.

The first step in the assembly procedure was to tip the box frame 90° such that the vertical Z-axis of the frame laid horizontally. A rectangular piece of sheet metal, 0.030-0.035 in. thick was then placed through the square opening of the frame, or the -X side. The 4 in. cubical specimen was then carefully placed into the midcavity on top of the thin plate. This centered the specimen in the now vertical X-direction. The targets and both pads were then inserted in the Z-direction and the corresponding walls with membranes mounted bolted down as described above.

The box frame with the +Z and -Z walls attached and specimen in place was then tipped back to its standard position. Then after removing the thin positioning plate, the Y-direction targets, pads, membranes and walls were positioned and affixed, followed by the components in the X-direction according to the sequences described above.

With the test cell assembled, the hydraulic tubing was hooked up and the pressure cells filled with hydraulic fluid. The entrapped air in the cells was then bled out of the system through the bleed holes. The coaxial cables from the central data acquisition system were then connected to their respective proximator probe cables. An initial manual scan through the 18 proximator channels indicated whether or not the test could be started. If necessary, as indicated by distorted proximator voltage readings, the specimen dislocation could be remedied by carefully applying pressure to one or more sides, translating the specimen any amount necessary. The data acquisition and analysis computer

program, written in BASIC, was then loaded into the HP 9830A calculator's memory, and the test conducted. The assembled test cell is shown in Fig. 2.30.

2.8 Test Program

The test program consisted of two parts:

1. The preliminary test series involving the use of all five fiber sizes, described in TABLE 2.1, in five different fiber concrete mixes labeled P1 through P5 where only the fiber size, not the concrete, changed from mix to mix and a sixth mix labeled P0, consisting only of plain concrete and used for control and reference.

The purpose of the preliminary tests was to collect data and help provide a basis for choosing one fiber size to use in the final test series, described in part 2 below, of triaxial experiments carried out in the 4 in. cubical testing equipment.

The preliminary series included tests on 3x6 in. cylinders and 4 in. cubes in unconfined compression, indirect tension tests on 3x6 in. cylinders, flexural tests on 3x3x15 in. beams and some multiaxial compression tests on 4 in. cubes. Strength data collected in this series included unconfined compressive strengths for the cylinders (f'_c) and cubes (f_c), splitting tensile strength (T) for the cylinders and flexural strength (modulus of rupture, R) for the beams. Also collected was stress-strain data for the cylinders tested in unconfined compression.

As mentioned, some tests on 4 in. cubes employing the cubical testing equipment were carried out in the preliminary series. Their

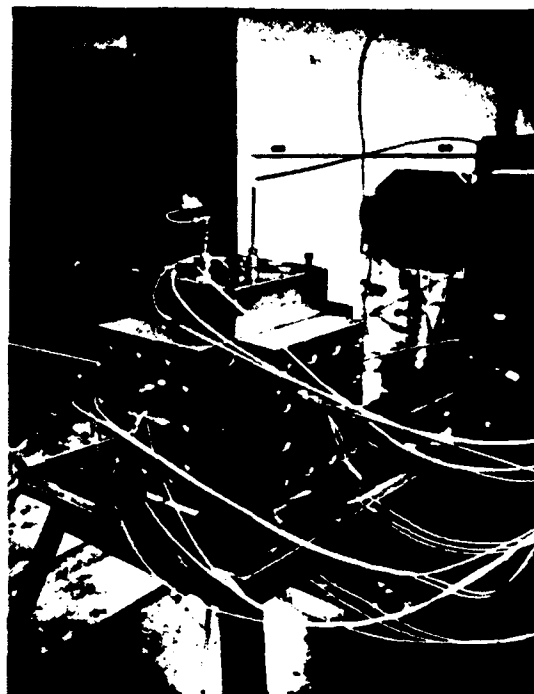


Fig. 2.30 Test Cell Connected to Hydraulic and Electrical Systems.

purpose was to obtain stress-strain information for specimens under multiaxial compression and to help debug the testing equipment in any way that arose since no material with strengths as high as the SFRC had ever been tested in the device. Since this was only the preliminary series including so many different mixes, only monotonic loading along one stress path (triaxial compression - TC) on one octahedral plane ($\sigma_0=6000$ psi) was followed for these triaxial tests. (See Figs. 2.31 and 2.32.)

The details of the preliminary test series are shown in TABLES 2.2 - 2.6 where the specimen type and test condition are given along with the specimen numbers, the age at which they were tested and the strength results (where applicable). All tests were conducted in triplicate with the exception of the 4 in. cubes tested in unconfined compression where the tests were only duplicated and the 4 in. cubes tested in multiaxial compression where only one of each test could be performed due to the time constraint imposed for testing these specimens at specified ages. Notice that the unconfined compression tests for the cylinders and cubes were conducted at varying specimen ages of 7, 14, 21 and 28 days for both plus around 50 days for the cylinders. This was done to observe the effect of specimen age on strength after the curing period of 7 days in the humidity room and the remaining time in air in order to determine if after 50 days of curing, full strength was achieved such that the cubical tests described in part 2 could be conducted without the variability of increasing strength with age coming into play.

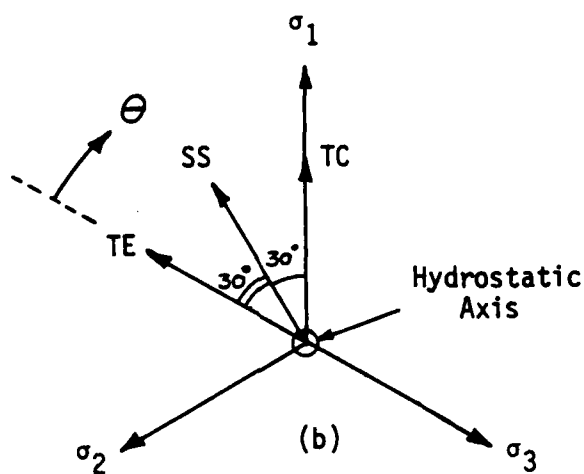
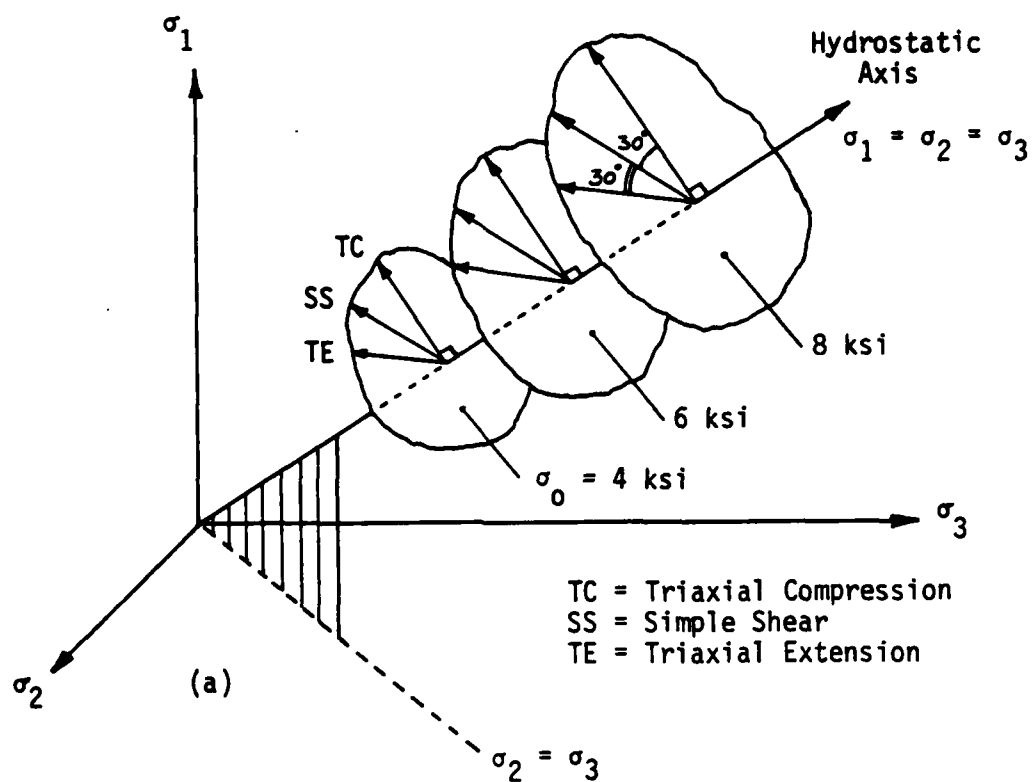


Fig. 2.31. Stress Paths in (a) 3-D Stress Space;
 (b) Octahedral Plane.
 (Compressive Stresses Positive).

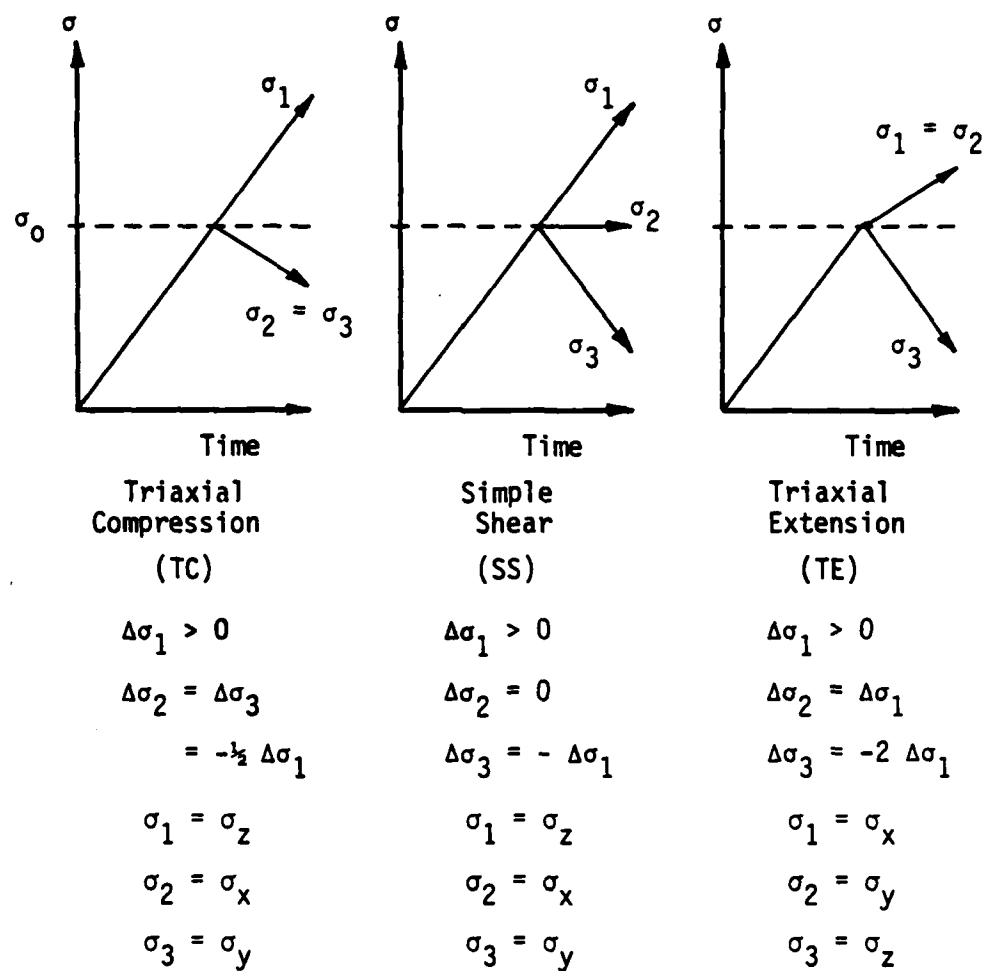


Fig. 2.32. Triaxial Load Paths With Principal Stress Orientation Given.

All stress-strain and strength results obtained in the preliminary tests described above are shown and discussed in Chapter 3. The comparison of data from the above tests using the five types of steel fibers will be examined to determine the effects of various fiber lengths and aspect ratios to help provide a basis for choosing one fiber for the final design of the SFRC to use in the comprehensive three-dimensional test series.

2. The final test series involving the use of only one SFRC mix with one fiber, chosen from the results obtained in the preliminary series. Two identical batches, labeled F1 and F2, were cast at different dates in order to obtain enough specimens for this test series. The Bekaert "Dramix" ZP 30/.40 fiber was chosen for this mix based on the preliminary test results. The reasons are discussed in Chapter 3.

In the final test series, unconfined compression tests on 3x6 in. control cylinders were conducted. Stress-strain and strength information for these control cylinders was obtained in triplicate at specimen ages near 7, 14, 21, 28 and 50 days. As in the preliminary tests, this was done to observe the effect of age on stress-strain behavior and strength after various times in the curing period and also to see if the final mixes, F1 and F2, behaved the same with respect to each other and to the preliminary mix P3 as they should. TABLE 2.7 gives the details of this part of the final test series with the stress-strain and strength results for the control cylinders shown in Chapter 4.

The main purpose of the final test series was to collect stress-strain and strength information of 4 in. cubical specimens

tested in the cubical device under triaxial loading conditions in order to determine the constitutive relations of the material for triaxial compressive stress states. These triaxial tests were conducted by loading the specimen hydrostatically to an octahedral normal stress equal to one of three selected levels ($\sigma_0 = 4, 6$ or 8 ksi), and then subsequently following a monotonic shear stress path to stay on the octahedral plane along either the triaxial compression (TC), simple shear (SS) or triaxial extension (TE) direction as shown in Figs. 2.31 and 2.32 thus inducing a change in only the octahedral shear stress (τ_0) along these paths. At least three replications were obtained for each stress path. This superposition of a pure shear stress on an initial hydrostatic state permits the investigation of the effect of a three-dimensional shear stress state on the stress-strain relations of the material. The data acquired during these tests consist of the stress-strain response in each loading direction as well as the failure data. By assuming isotropy of the material, the shape of the failure envelope for the three octahedral planes is determined from the failure data by loading along these monotonic stress paths. This data enables the testing of various hypotheses regarding concrete failure. The stress-strain information provides the basis for ascertaining the suitability of octahedral stress-strain theory and/or plasticity concepts in formulating the constitutive relations for SFRC.

TABLE 2.8 gives the details of the three-dimensional compressive tests and the stress-strain and strength results of these tests are presented in Chapter 4.

TABLE 2.2

PRELIMINARY TEST PROGRAM
 SPECIMEN TYPE: 3 x 6 in. CYLINDERS
 TEST CONDITION: UNCONFINED COMPRESSION ASTM C39-72

Designation		Casting Date mo/day/yr	Testing Date mo/day/yr	Age at Testing (days)	f' _c (psi)
Series	Specimen				
P0 plain	E1	8/27/79	9/3/79	7	4515
	H1		"	7	3874
	J1		"	7	4835
	G1		9/10/79	14	6837
	J3		"	14	7184
	K3		"	14	6553
	I3		9/17/79	21	6968
	L3		"	21	6696
	K2		"	21	7135
	F2		9/24/79	28	7282
	I2		"	28	7587
	K1		"	28	7304
	L2		10/16/79	50	7886
	E3		"	50	7325
	G2		"	50	7910
P1 Dramix 50/.50	I1	8/28/79	9/4/79	7	5491
	K1		"	7	5297
	F1		"	7	5282
	E2		9/11/79	14	7041
	F3		"	14	6423
	H2		"	14	6942
	L1		9/18/79	21	7989
	J1		"	21	7961
	G2		"	21	7597
	K3		9/25/79	28	7105
	E1		"	28	7306
	G3		"	28	8062
	H3		10/17/79	50	7786
	K2		"	50	7793
	I2		"	50	8145
P2 Dramix 30/.50	G1	8/29/79	9/5/79	7	5774
	I1		"	7	6206
	L1		"	7	6278
	K2		9/12/79	14	7902
	L2		"	14	7903
	H2		"	14	7607
	E3		9/19/79	21	7957
	J2		"	21	7686
	G3		"	21	7587
	H1		9/26/79	28	8192

TABLE 2.2 (Continued)

Designation		Casting Date mo/day/yr	Testing Date mo/day/yr	Age at Testing (days)	f' _c (psi)
Series	Specimen				
P2 Dramix 30/.50	K3	8/29/79	9/26/79	28	8588
	I2		"	28	8029
	H3		10/19/79	51	9088
	J3		"	51	9109
	G2		"	51	8972
P3 Dramix 30/.40	G1	8/30/79	9/6/79	7	6568
	J1		"	7	6221
	K1		"	7	6344
	E1		9/13/79	14	7929
	L1		"	14	7659
	F3		"	14	7832
	K3		9/20/79	21	7103
	I1		"	21	8310
	H3		"	21	7342
	K2		9/27/79	28	8058
	H2		"	28	8642
	G2		"	28	8729
	E2		10/19/79	50	8945
	L3		"	50	8927
	H1		"	50	9426
P4 Dramix 40/.40	K1	8/31/79	9/7/79	7	5588
	H1		"	7	5716
	I1		"	7	5341
	J1		9/14/79	14	8526
	G2		"	14	8312
	F2		"	14	8282
	L1		9/21/79	21	6786
	G3		"	21	6618
	J2		9/22/79	22	8758
	E1		9/28/79	28	8836
	H2		"	28	8961
	G1		"	28	9046
	F1		10/21/79	51	9043
	I2		"	51	8874
	E2		"	51	8473
P5 Fiber- con	E1	9/1/79	9/8/79	7	6208
	F1		"	7	6121
	G1		"	7	6035
	E3		9/15/79	14	9075
	J3		"	14	8648
	L2		"	14	9013

TABLE 2.2 (Continued)

Designation		Casting Date mo/day/yr	Testing Date mo/day/yr	Age at Testing (days)	f' c (psi)
Series	Specimen				
P5 Fiber- con	H2	9/1/79	9/22/79	21	8142
	G2		"	21	8090
	I1		"	21	7728
	I3		9/29/79	28	9487
	L3		"	28	9927
	K1		"	28	10,109
	F3		10/21/79	50	9766
	E2		"	50	9527
	J1		"	50	8583

TABLE 2.3

PRELIMINARY TEST PROGRAM
 SPECIMEN TYPE: 4 in. CUBES
 TEST CONDITION: UNCONFINED COMPRESSION

Designation		Casting Date mo/day/yr	Testing Date mo/day/yr	Age at Testing (days)	f _c (psi)
Series	Specimen				
P0 plain	D1	8/27/79	9/3/79	7	5856
	B1		"	7	5469
	A1		9/10/79	14	6231
	B2		"	14	7078
	B3		9/17/79	21	6938
	A2		"	21	7234
	B6		9/24/79	28	7555
	--		--	--	--
P1 Dramix 50/.50	B4	8/28/79	9/4/79	7	6488
	D1		"	7	6675
	B1		9/11/79	14	7244
	D3		"	14	8031
	B6		9/18/79	21	7294
	A6		"	21	8200
	C4		9/25/79	28	7988
	B3		"	28	8309
P2 Dramix 30/.50	C2	8/29/79	9/5/79	7	4656
	A6		"	7	4894
	C5		9/12/79	14	7563
	B4		"	14	7828
	B2		9/19/79	21	7834
	A5		"	21	7968
	A2		9/26/79	28	6956
	B6		"	28	7063
P3 Dramix 30/.40	C1	8/30/79	9/6/79	7	6538
	D1		"	7	6188
	A1		9/13/79	14	7613
	B1		"	14	7656
	A3		9/20/79	21	6469
	B2		"	21	7894
	B4		9/27/79	28	7722
	A5		"	28	8969
P4 Dramix 40/.40	D1	8/31/79	9/7/79	7	6513
	A1		"	7	6344
	A2		9/14/79	14	7766
	B1		"	14	8669
	A6		9/21/79	21	8422
	B5		"	21	8363
	B3		9/28/79	28	6722
	A4		"	28	5844

TABLE 2.3 (Continued)

Designation		Casting Date mo/day/yr	Testing Date mo/day/yr	Age at Testing (days)	f_c (psi)
Series	Specimen				
P5 Fiber- con	C1	9/1/79	9/8/79	7	7144
	A1		"	7	7194
	B4		9/15/79	14	8194
	A6		"	14	9156
	B1		9/22/79	21	9234
	A5		"	21	9466
	A4		9/29/79	28	6000
	B2		"	28	865C

TABLE 2.4

PRELIMINARY TEST PROGRAM
 SPECIMEN TYPE: 3 x 6 in. CYLINDERS
 TEST CONDITION: INDIRECT TENSION ASTM C496-71

Designation		Casting Date mo/day/yr	Testing Date mo/day/yr	Age at Testing (days)	T (psi)
Series	Specimen				
P0 plain	J2 E2 L1	8/27/79	9/24/79	28	665 661 644
P1 Dramix 50/.50	H1 L3 I3	8/28/79	9/25/79	28	1045 1060 1372
P2 Dramix 30/.50	E2 L3 I3	8/29/79	9/26/79	28	1075 958 1024
P3 Dramix 30/.40	F2 J2 E3	8/30/79	9/27/79	28	1001 942 916
P4 Dramix 40/.40	K2 I3 H3	8/31/79	9/28/79	28	1071 1045 1100
P5 Fiber- con	H3 F2 J2	9/1/79	9/29/79	28	765 666 801

TABLE 2.5

PRELIMINARY TEST PROGRAM
 SPECIMEN TYPE: 3 x 3 x 15 in. BEAMS
 TEST CONDITION: FLEXURE (THIRD-POINT LOADING) ASTM C78-75

Designation		Casting Date mo/day/yr	Testing Date mo/day/yr	Age at Testing (days)	R (psi)
Series	Specimen				
P0 plain	P R O	8/27/79	9/27/79	31	610 749 578
P1 Dramix 50/.50	R P M	8/28/79	9/27/79	30	702 878 846
P2 Dramix 30/.50	N R O	8/29/79	9/27/79	29	709 668 641
P3 Dramix 30/.40	M O -	8/30/79	9/27/79	28	857 853 -
P4 Dramix 40/.40	O M R	8/31/79	9/28/79	28	877 1453 1197
P5 Fiber- con	R Q O	9/1/79	9/29/79	28	819 942 788

TABLE 2.6

PRELIMINARY TEST PROGRAM
 SPECIMEN TYPE: 4 in. CUBES
 TEST CONDITION: MULTIAXIAL COMPRESSION

Designation		Casting Date mo/day/yr	Testing Date mo/day/yr	Age at Testing (days)	Stress Path Fig. 2.31	Hydrostatic Stress Level σ_o (psi)
Series	Specimen					
P1 Dramix 50/.50	C5	8/28/79	9/11/79	14	TC	6000
	C6		9/18/79	21		
	D4		9/25/79	28		
P2 Dramix 30/.50	C1	8/29/79	9/12/79	14	TC	6000
	D6		9/19/79	21		
	D3		9/26/79	28		
P3 Dramix 30/.40	D4	8/30/79	9/13/79	14	TC	6000
	--		--	--		
	C2		9/27/79	28		
P4 Dramix 40/.40	--	8/31/79	--	--	TC	6000
	D5		9/21/79	21		
	D4		9/29/79	29		
P5 Fiber- con	D1	9/1/79	9/17/79	16	TC	6000
	--		--	--		
	C2		9/30/79	29		

TABLE 2.7

FINAL TEST PROGRAM
 SPECIMEN TYPE: 3 x 6 in. CYLINDERS
 TEST CONDITION: UNCONFINED COMPRESSION ASTM C39-72

Designation		Casting Date mo/day/yr	Testing Date mo/day/yr	Age at Testing (days)	f' _c (psi)
Series	Specimen				
F1 Dramix 30/.40	H3	10/15/79	10/22/79	7	7302
	I3		"	7	6973
	K3		"	7	7109
	L2		10/29/79	14	8837
	J1		"	14	8487
	E2		"	14	8752
	G1		11/5/79	21	9098
	J2		"	21	9071
	F2		"	21	9454
	H1		11/12/79	28	10,222
	E3		"	28	9846
	K1		"	28	9440
	G2		12/6/79	52	9968
	J3		"	52	9145
	E1		"	52	8803
F2 Dramix 30/.40	L1	11/30/79	12/7/79	7	7289
	H2		"	7	6854
	I3		"	7	6973
	E2		12/16/79	16	8762
	G1		"	16	8155
	J1		"	16	9201
	G3		12/22/79	22	8715
	H3		"	22	8516
	F3		"	22	8538
	J2		12/28/79	28	9051
	K3		"	28	9034
	L3		"	28	8804
	I1		1/21/80	52	9130
	F2		"	52	8473
	K2		"	52	9503

TABLE 2.8

FINAL TEST PROGRAM
 SPECIMEN TYPE: 4 in. CUBES
 TEST CONDITION: MULTIAXIAL COMPRESSION

Designation		Casting Date mo/day/yr	Testing Date mo/day/yr	Age at Testing (days)	Stress Path Fig. 2.31	Hydrostatic Stress Level σ_0 (psi)
Series	Specimen					
F1	D6	10/15/79	1/17/80	94	TC	8000
	D3		1/17/80	94	TC	8000
	D5		1/31/80	108	TC	8000
	A1		2/1/80	109	TC	4000
	B1		2/7/80	115	TE	4000
	A6		2/28/80	136	SS	4000
	C5		3/5/80	142	TE	6000
	C2		3/6/80	143	SS	6000
	D2		3/11/80	148	TC	6000
	C4		3/13/80	150	TE	8000
	C1		3/17/80	154	SS	8000
	D1		3/21/80	158	SS	8000
	B4		3/24/80	161	TC	6000
	A5		4/4/80	172	SS	6000
	C3		4/8/80	176	SS	8000
	A2		4/9/80	177	TE	8000
	B3		4/10/80	178	TC	6000
	B2		4/14/80	182	SS	8000
F2	B5	11/30/79	5/6/80	158	TE	8000
	C5		5/7/80	159	TE	6000
	D3		5/9/80	161	SS	6000
	D4		5/21/80	173	TE	6000
	B6		5/23/80	175	TC	4000
	B3		5/27/80	179	SS	4000
	C1		6/3/80	186	TE	4000
	C3		6/4/80	187	SS	4000
	B2		6/6/80	189	TC	4000
	C2		6/9/80	192	TE	4000

CHAPTER 3

PRELIMINARY TEST SERIES

3.1 Introduction

In this chapter, the results of the preliminary test series, described in Section 2.8, on one plain and five different SFRC mixes are presented. Data obtained from these tests is examined to help provide a basis for choosing one fiber size to be used in the final test series of multiaxial compression tests. In Section 3.2, the stress-strain behavior obtained for tests in the unconfined compression and multiaxial compression modes is discussed. In Section 3.3, strength results are presented for specimens tested in unconfined compression, indirect tension and pure bending, and relationships between these strength values and various fiber properties are discussed. Finally, in Section 3.4, based on all the preliminary tests conducted, conclusions are made for which fiber to use in the final series of multiaxial compression tests. In this and subsequent discussions, compressive stresses and strains are assumed to be positive.

3.2 Stress-Strain Relations

3.2.1 Unconfined Compression

The tests for compressive strength of the 3x6 in. cylindrical

specimens were performed according to ASTM C39-72 specification. The load rate was maintained at 15 kips/min. and axial strains were measured by an extensometer mounted around the specimen. The machine used in applying the load was not a "stiff" testing machine; therefore, no post-peak behavior could be recorded.

The stress-strain curves for these preliminary tests are plotted in different envelope combinations as shown in Figs. 3.1-3.11. In the preliminary tests, two variables entered into the results. One was the mix number (employing different fibers with various aspect ratios as listed in TABLE 2.1) and the second was specimen age. Mix number P0 was the plain concrete mix used for comparison purposes. Figs. 3.1-3.6 show the stress-strain envelopes for constant mix numbers, with specimen age as the variable. Note the rapid increase in strength, stiffness and failure strain between the 7 and 14 day tests, then the much slower increase in strength and stiffness for specimen ages beyond 14 days. This is due to the curing procedure described in Section 2.4, i.e., 7 days wet curing (including the casting day) followed by air curing at room temperature until tested. In other words, the curing procedure forced these parameters to level off sooner than had they been wet cured the entire period. Note also the good reproducibility of identically aged specimens' stress-strain results.

Figs. 3.7-3.11 show the stress-strain envelopes for constant specimen age, with preliminary mix numbers as the variable. Even though the primary function of the fibers is to increase tensile strength, toughness, impact resistance, etc. and not compressive

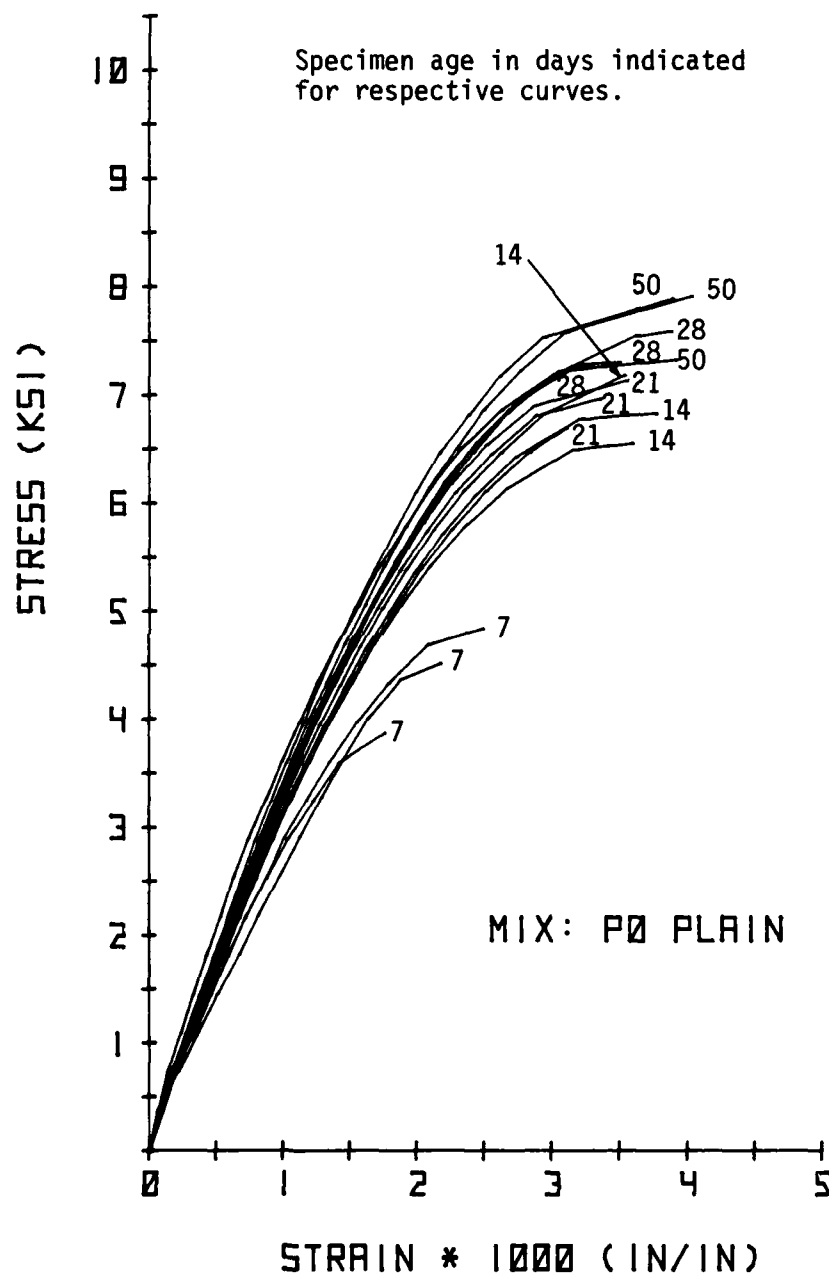


Fig. 3.1. Unconfined Compression Stress-Strain Curves for 3x6 in. Cylinders.

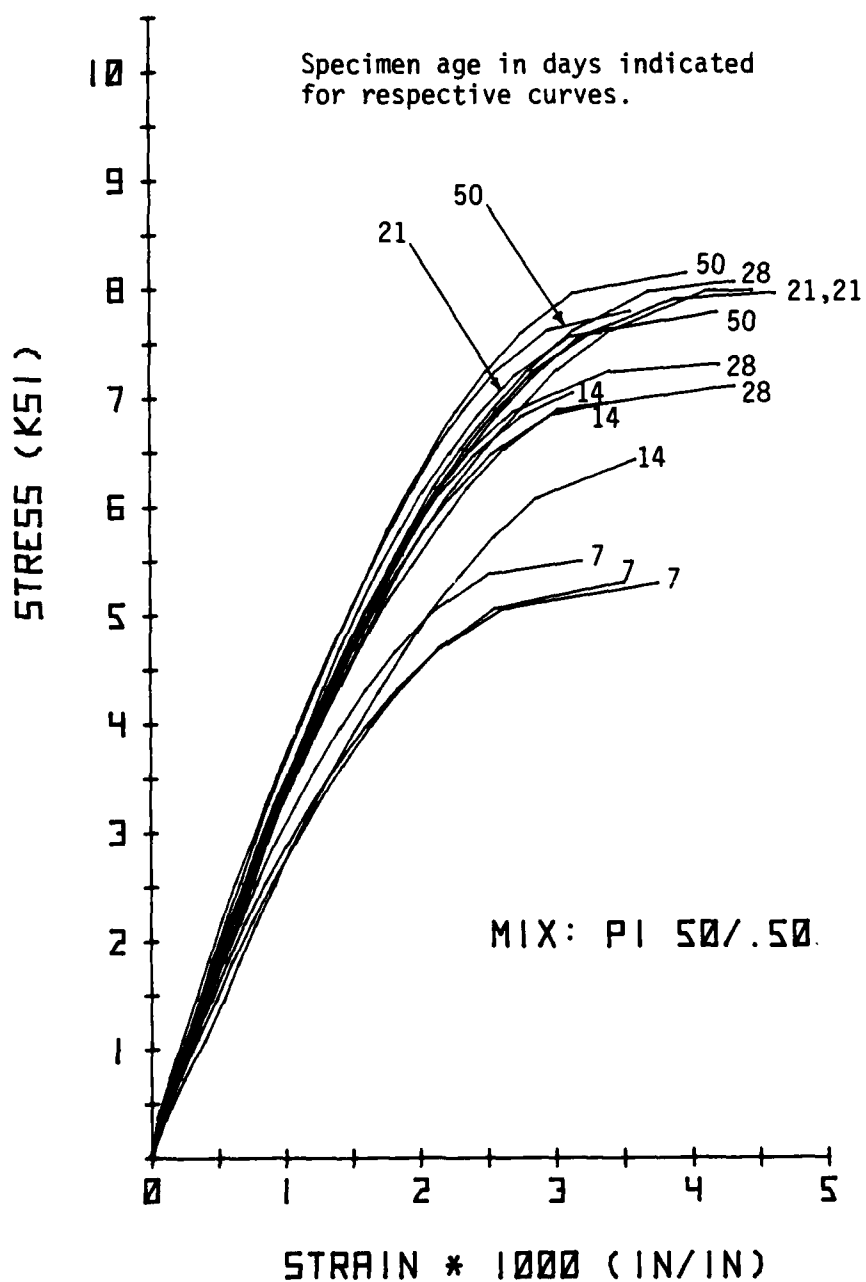
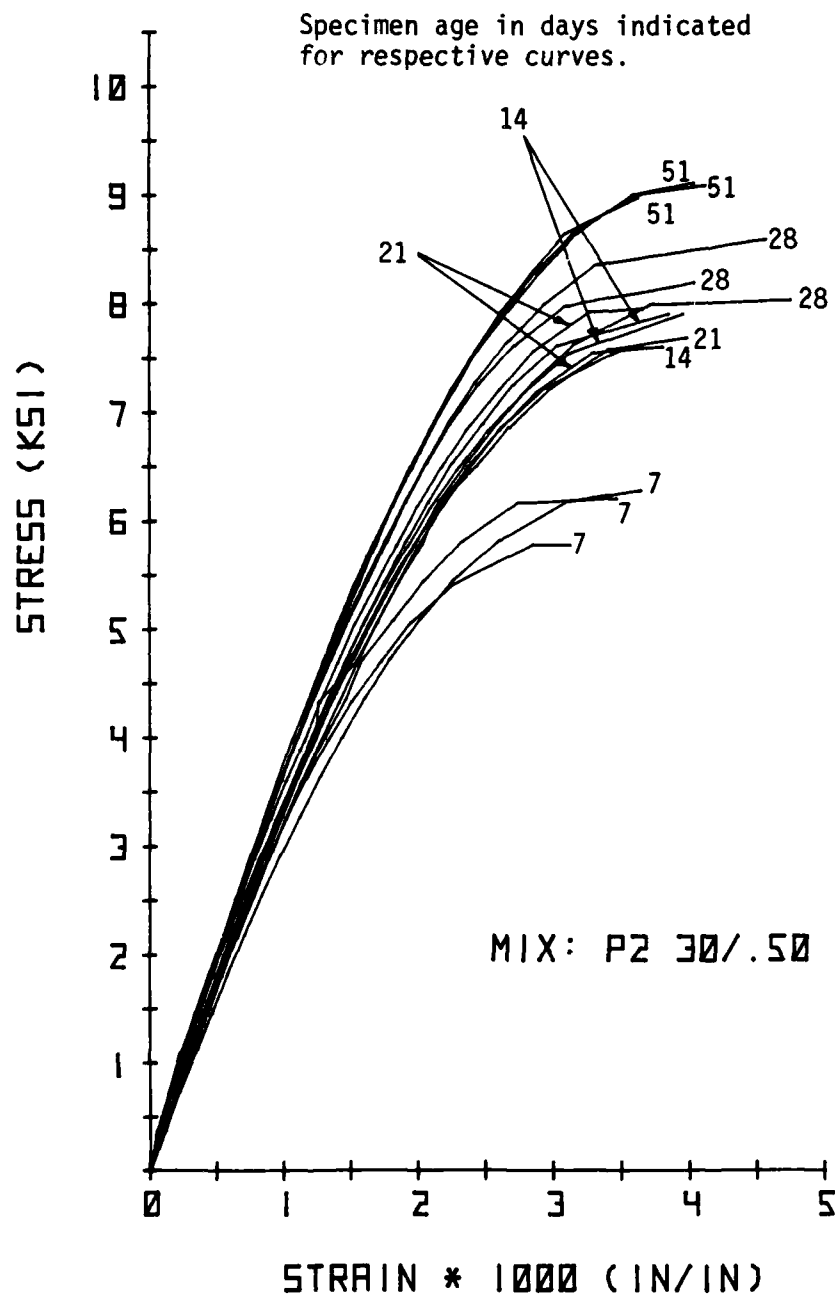


Fig. 3.2. Unconfined Compression Stress-Strain Curves for 3x6 in. Cylinders.



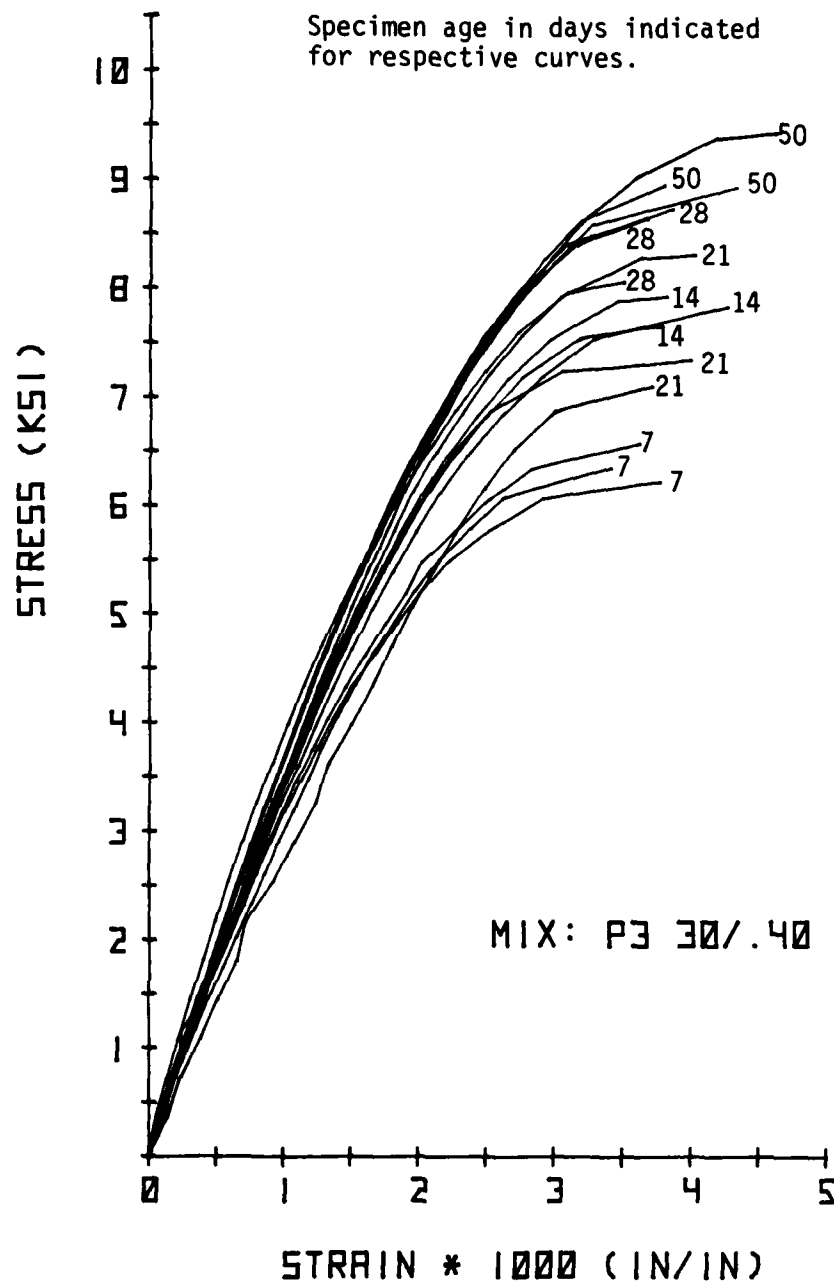


Fig. 3.4. Unconfined Compression Stress-Strain Curves for 3x6 in. Cylinders.

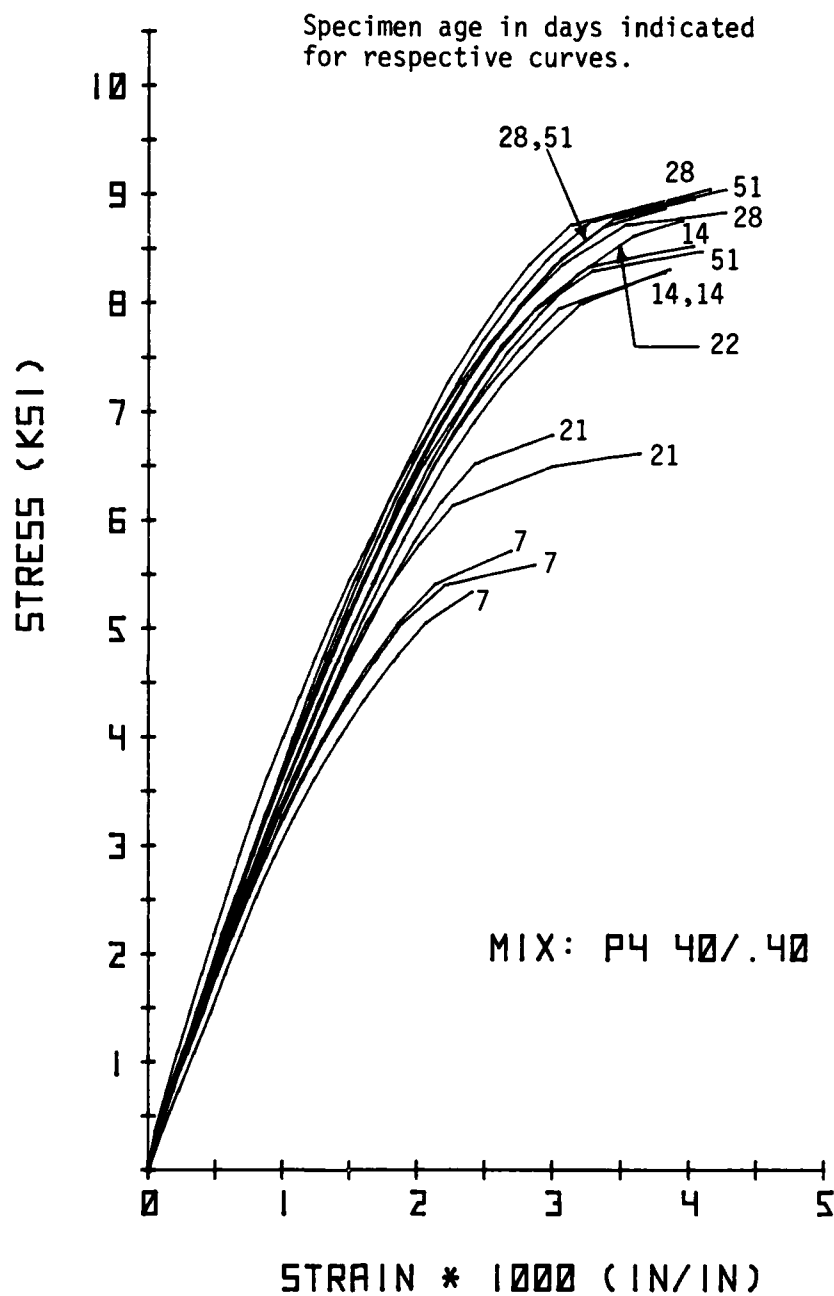


Fig. 3.5. Unconfined Compression Stress-Strain Curves for 3x6 in. Cylinders.

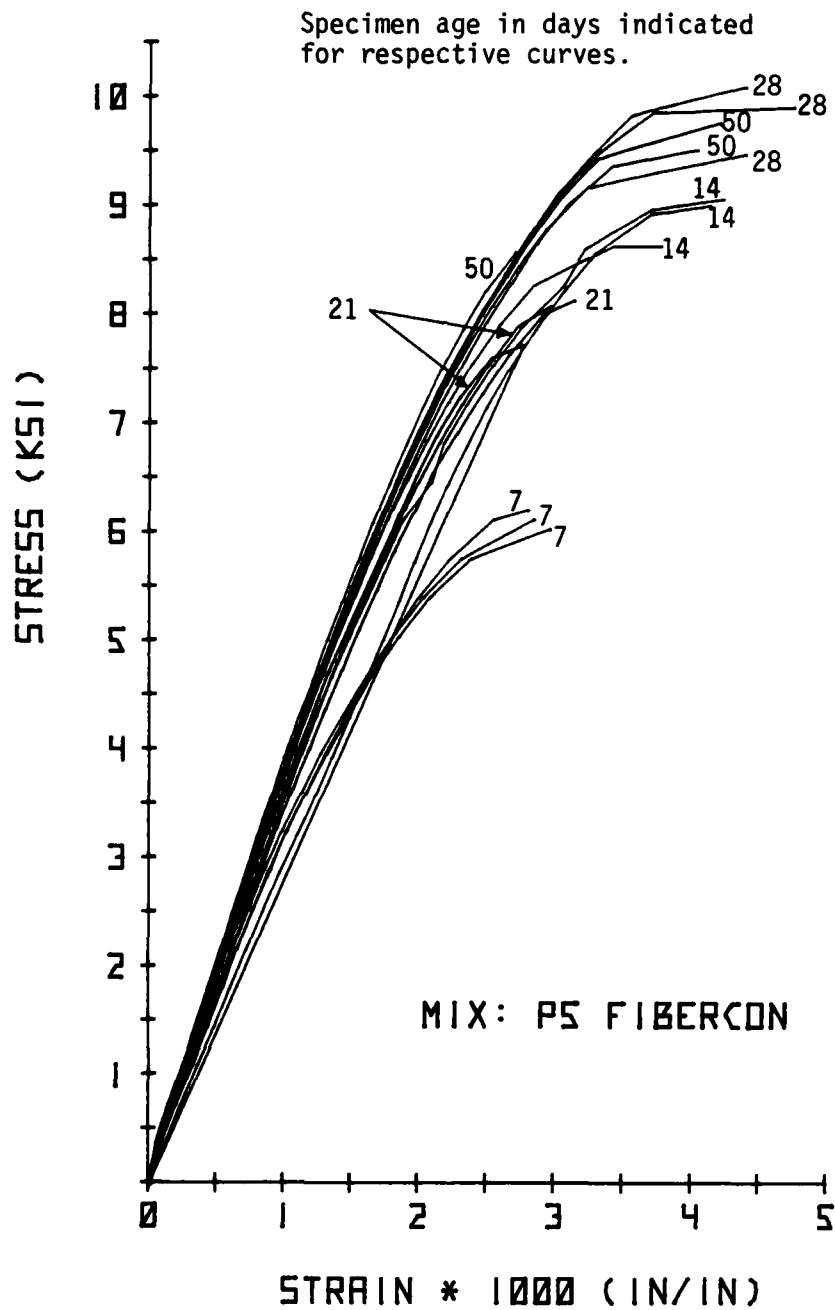


Fig. 3.6. Unconfined Compression Stress-Strain Curves for 3x6 in. Cylinders.

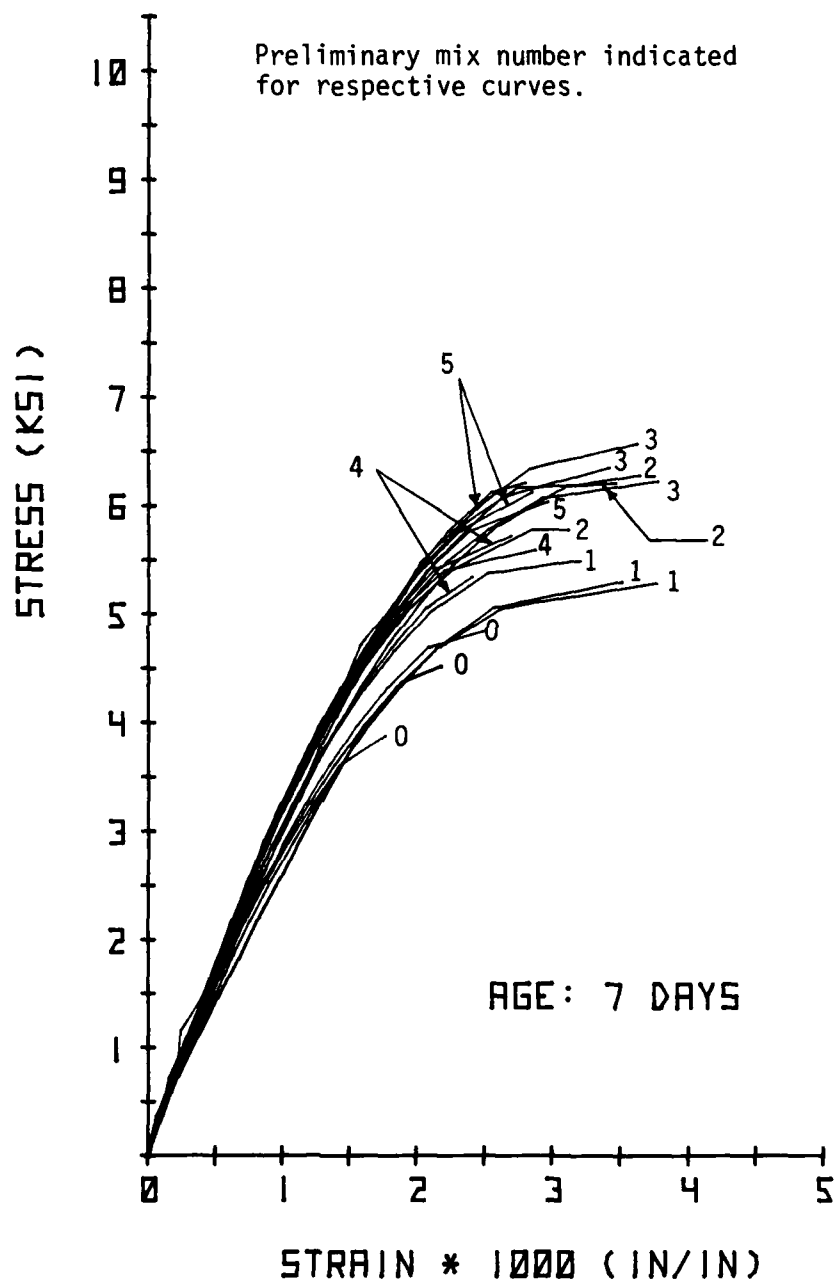


Fig. 3.7. Unconfined Compression Stress-Strain Curves for 3x6 in. Cylinders.

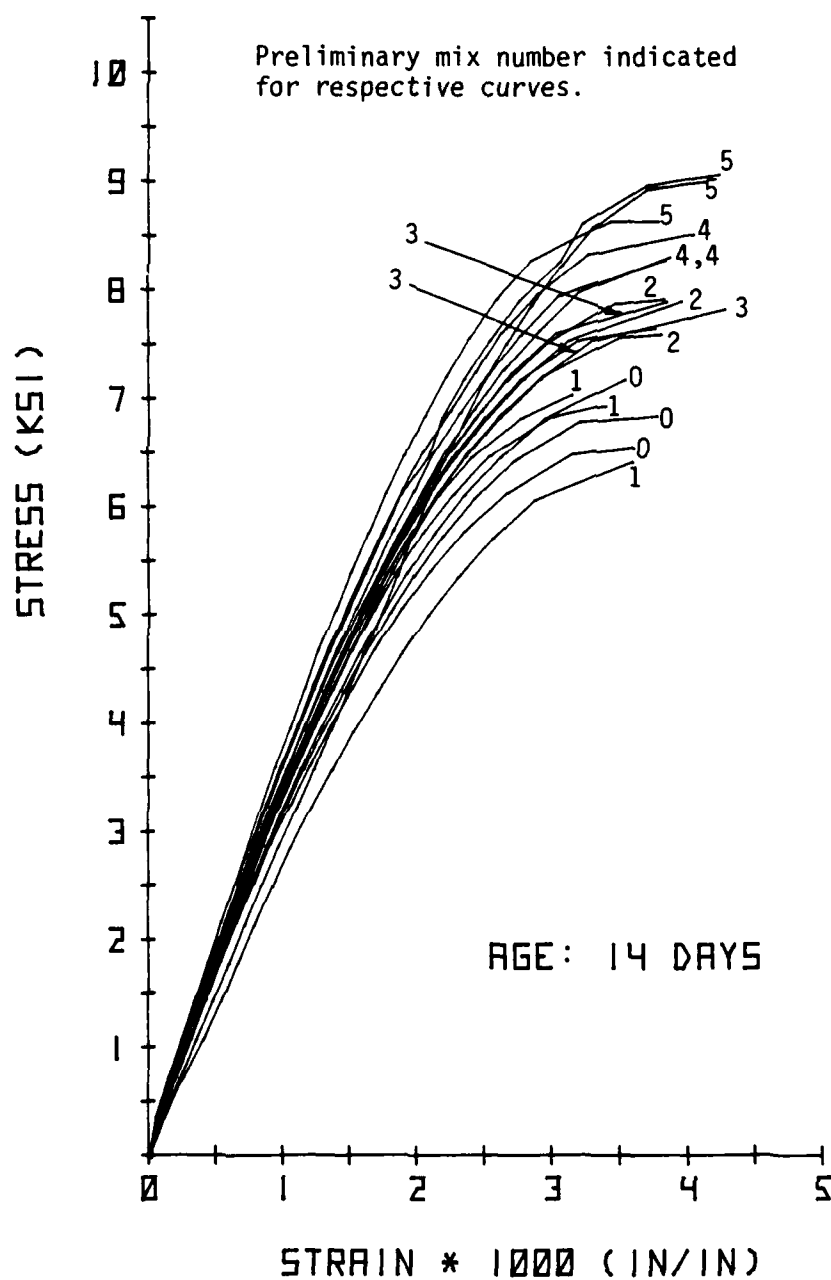


Fig. 3.8. Unconfined Compression Stress-Strain Curves for 3x6 in. Cylinders.

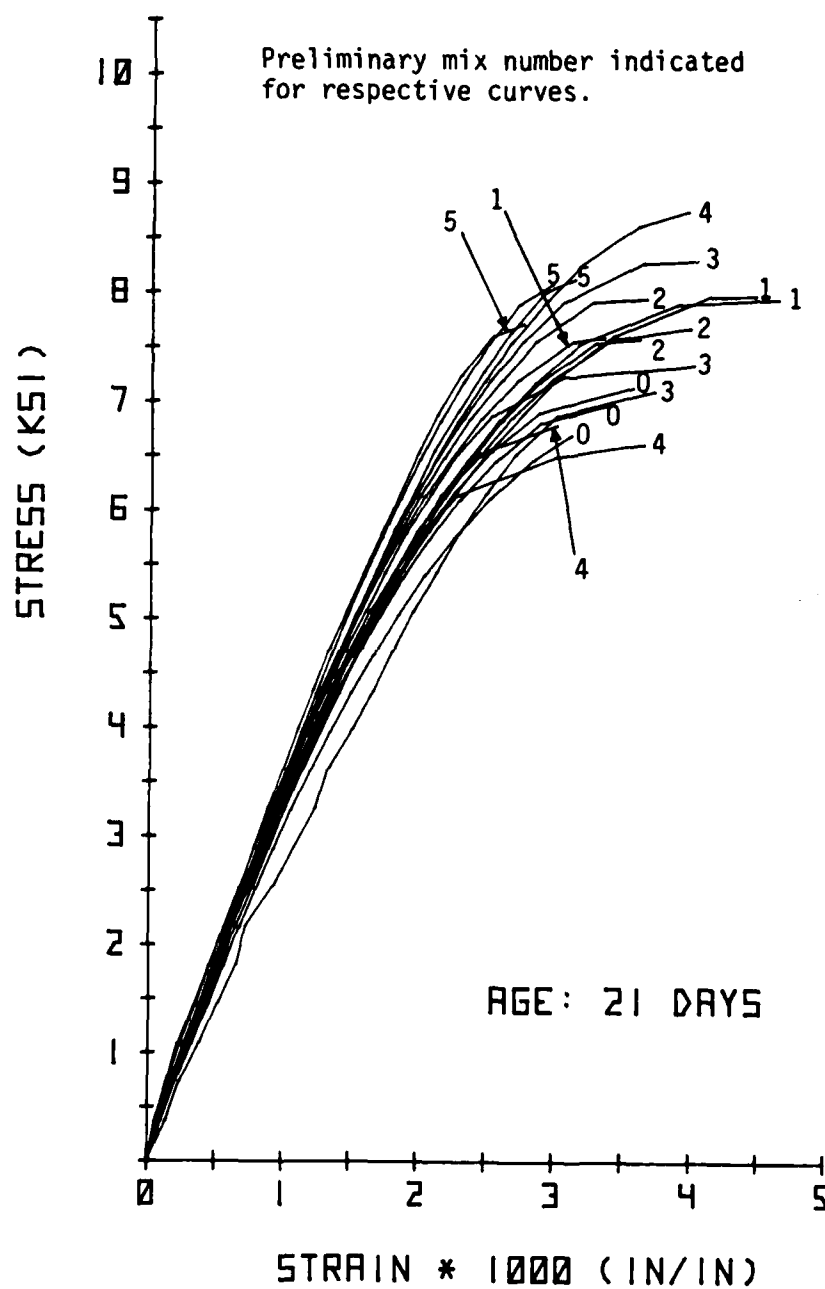


Fig. 3.9. Unconfined Compression Stress-Strain Curves for 3x6 in. Cylinders.

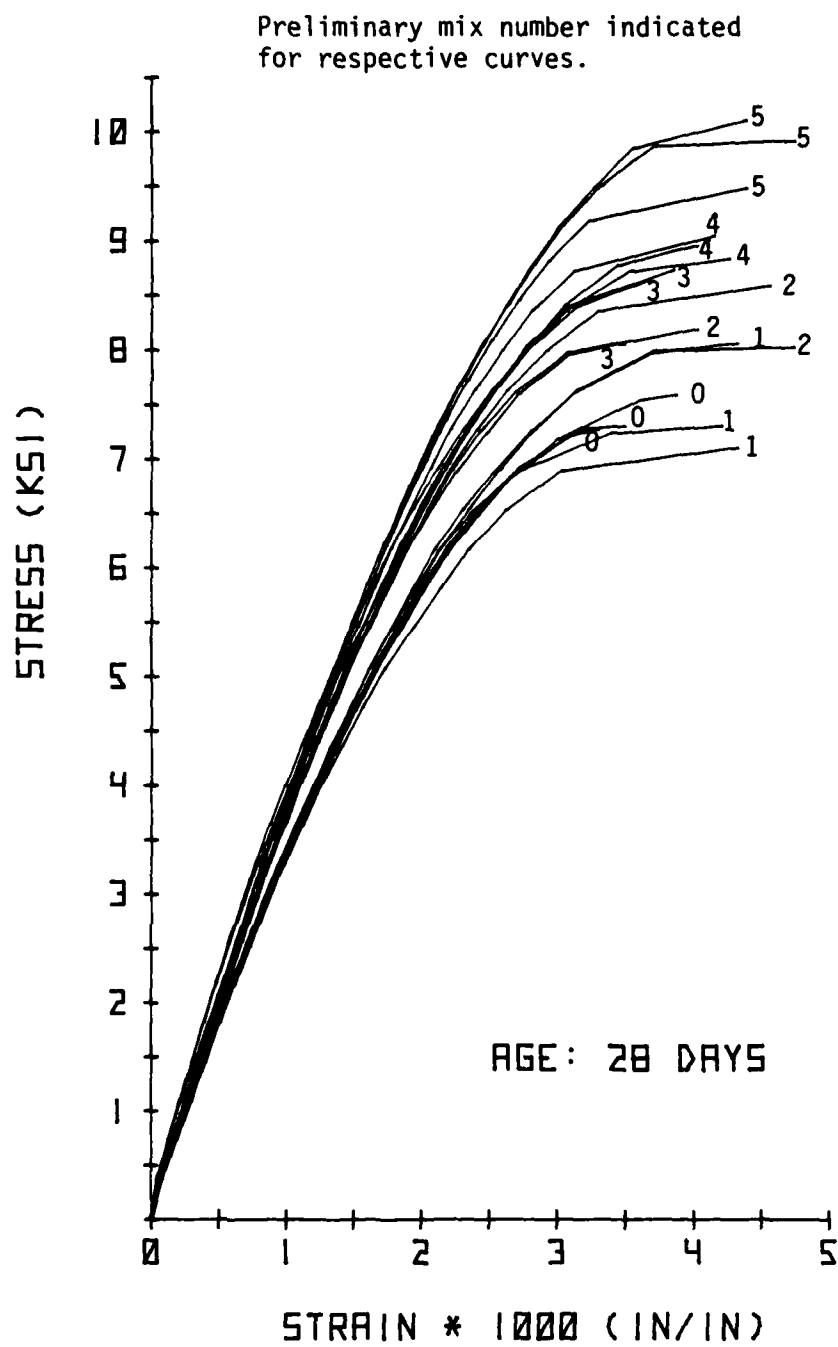


Fig. 3.10. Unconfined Compression Stress-Strain Curves for 3x6 in. Cylinders.

Preliminary mix number indicated
for respective curves.



Fig. 3.11. Unconfined Compression Stress-Strain Curves for 3x6 in. Cylinders.

strength, the presence of the fibers do improve the compressive strength and stiffness of concrete when compared to the plain concrete mix (P0), as demonstrated in these figures. There does appear to be one exception however. The mix employing the ZP 50/.50 fiber (P1) has about the same properties in unconfined compression as the plain concrete mix (P0). This fiber has a length of 50 mm (1.97 in.) which is only one inch less than the diameter of the cylindrical specimens tested. Therefore, this size effect could be the cause of the similar results between these two mixes. Also, as shown in TABLE 3.1, the P1 mix has only 10 fibers per cu. in. of concrete with an aspect ratio of 100. The smaller the number of fibers per unit volume of concrete, the less likely will stress redistribution through the fibers take place, thus causing the strength and the stiffness of this mix to be closer to those for plain concrete than are the other fiber concrete mixes.

From these same figures, one can see that the mix employing the straight "Fibercon" fiber (P5), show higher stiffness and usually higher compressive strength than the other mixes. Again, from TABLE 3.1, one notes there are over 27 fibers per cu. in. of concrete for this mix, possibly allowing more stress redistribution through the fibers to take place, thus indicating higher strength and stiffness. The stress-strain results of the other mixes (P2-P4) are seen to usually make up the center of the envelopes.

Fig. 3.12 shows the average secant moduli of the cylindrical specimens measured from their unconfined compression stress-strain curves according to ASTM C469-65 specifications. Note the increase

TABLE 3.1
STEEL FIBER SIZES WITH CORRESPONDING FIBER CONCRETE MIX NUMBER

Manufacturer	Size Length (mm)/Dia. (mm)	Aspect Ratio (l/d)	Mix No.	No. of Fibers per cu. in. Concrete
Bekaert "Dramix"	ZP 50/.50	100	P1	10.0
	ZP 30/.50	60	P2	16.7
	ZP 30/.40	75	P3	26.1
	ZP 40/.40	100	P4	19.6
U.S. Steel "Fibercon"	25.4 x 0.56 x 0.25 (1.00" x .022" x .010")	45 or 100	P5	27.3

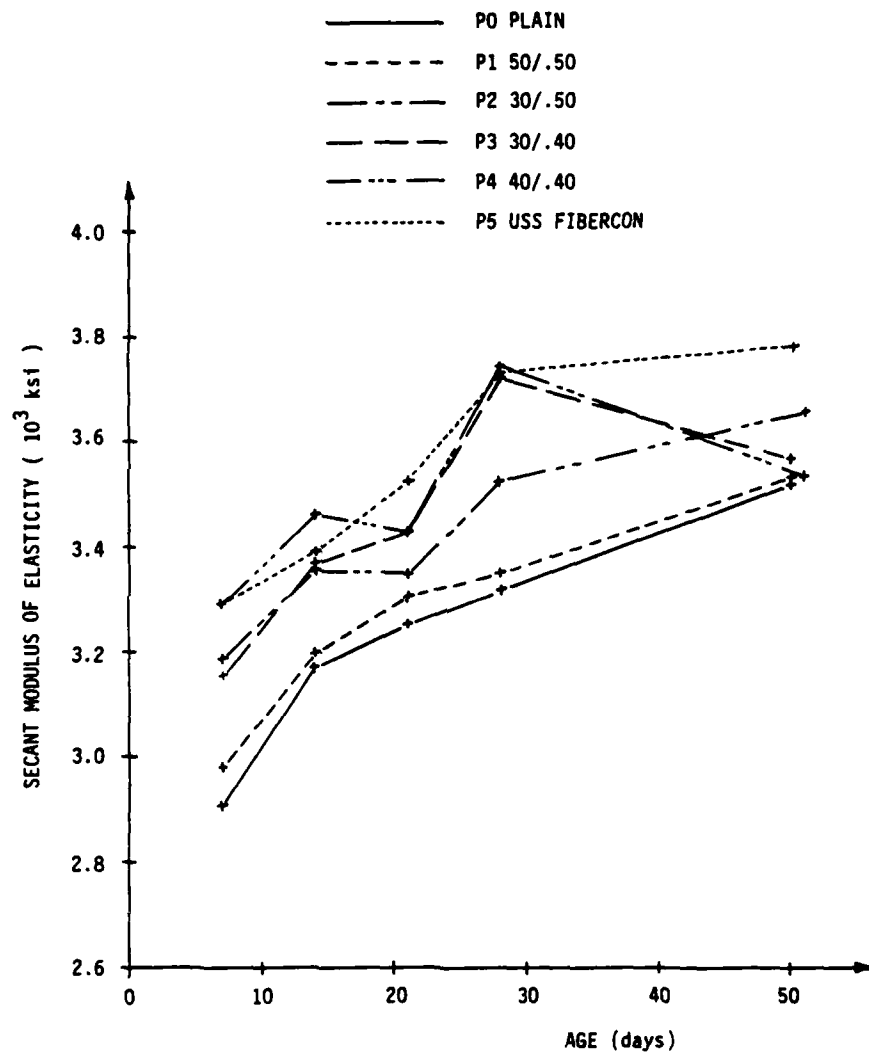


Fig. 3.12. Secant Modulus of Elasticity vs. Age for the Unconfined Compression Tests on 3x6 in. Cylinders.

in stiffness with specimen age (as should be expected), how this envelope's limits are set by the P0 plain mix and primarily by the P5 "Fibercon" mix, and the similarity between the P0 mix and the mix employing the ZP 50/.50 fiber (P1), all as previously discussed. There appears to be a large amount of scatter present in this figure, but notice how the scale is greatly expanded. If one were to use a secant modulus E of 3520 ksi set by the P0 plain mix at 50 days as a point of reference, then the most extreme change in E is only 7.1% greater at 3770 ksi.

3.2.2 Multiaxial Compression

In this section, stress-strain curves for all cubical tests conducted in the preliminary test series (TABLE 2.6) are presented. The cubical device used for testing these specimens and the stress path employed in these tests are described in Sections 2.6 and 2.8 respectively.

Figs. 3.13-3.20 show the summaries of the maximum principal stress-strain curves (σ_1 - ϵ_1) obtained from these tests. The data is presented this way because the purpose of the preliminary tests was to provide information that could be inspected visually to aid in choosing the one fiber for the final test series. Since the unconfined compression data discussed in the previous section is shown in the same form, it was felt sufficient for discussion purposes to present only the maximum principal stress-strain results for the multiaxial compression tests. (The complete principal and octahedral stress-strain curves for these preliminary tests on 4 in. cubes in multiaxial compression are presented in Appendix A).

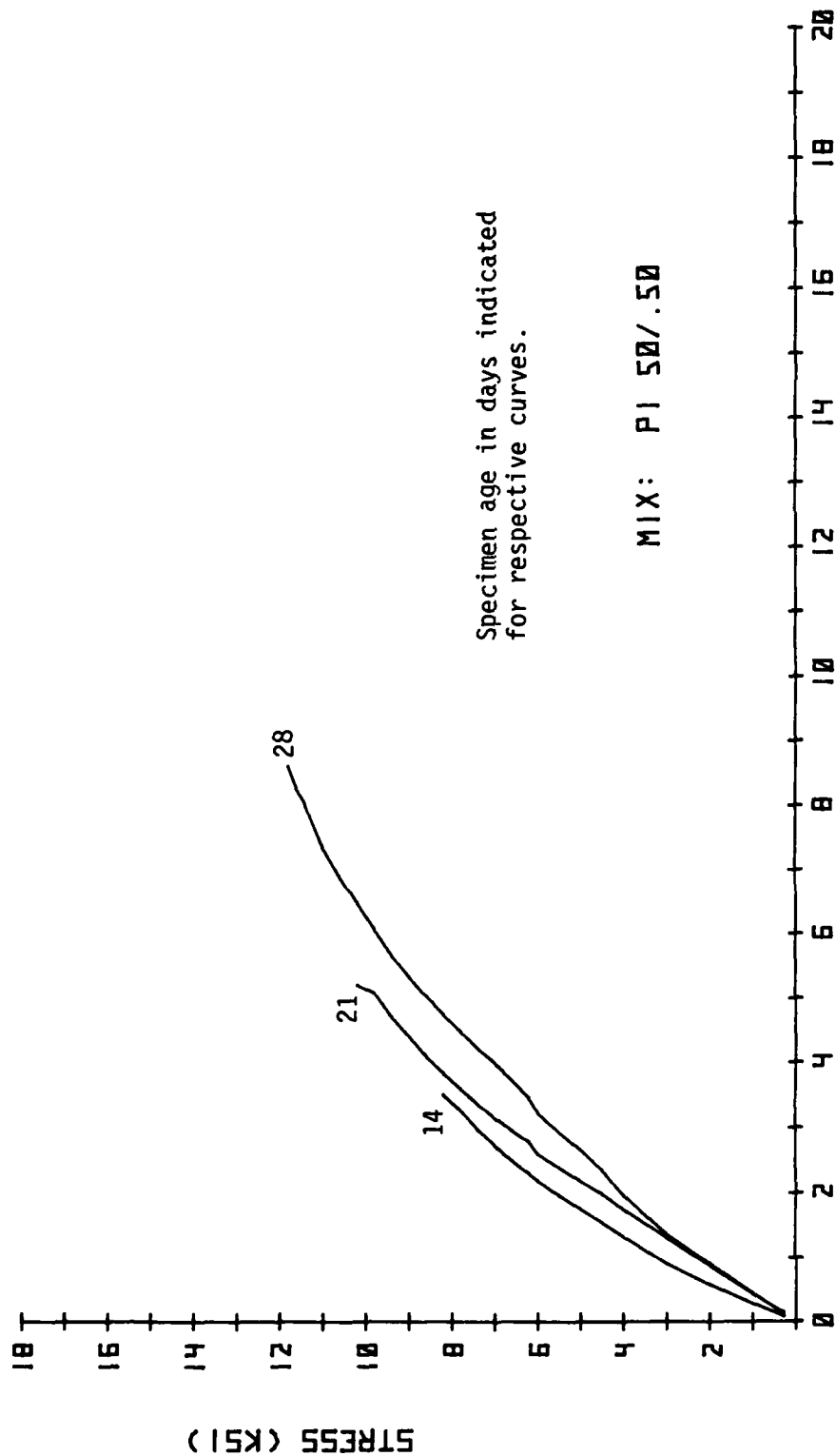


Fig. 3.13. Maximum Principal Stress-Strain Curves ($\sigma_1 - \epsilon_1$) for Multiaxial Compression Tests on 4 in. Cubes.

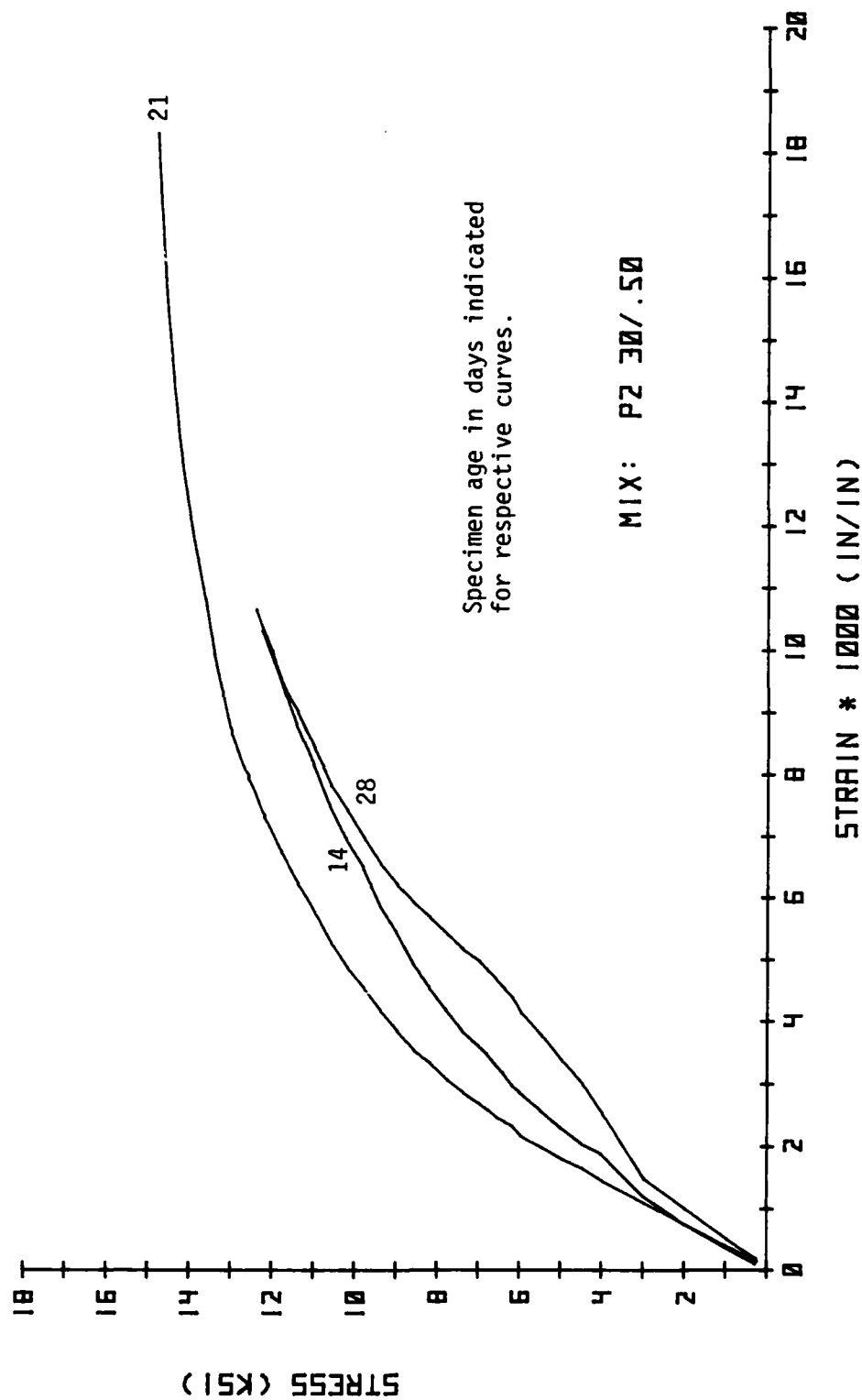


Fig. 3.14. Maximum Principal Stress-Strain Curves ($\sigma_1 - \epsilon_1$) for Multiaxial Compression Tests on 4 in. Cubes.

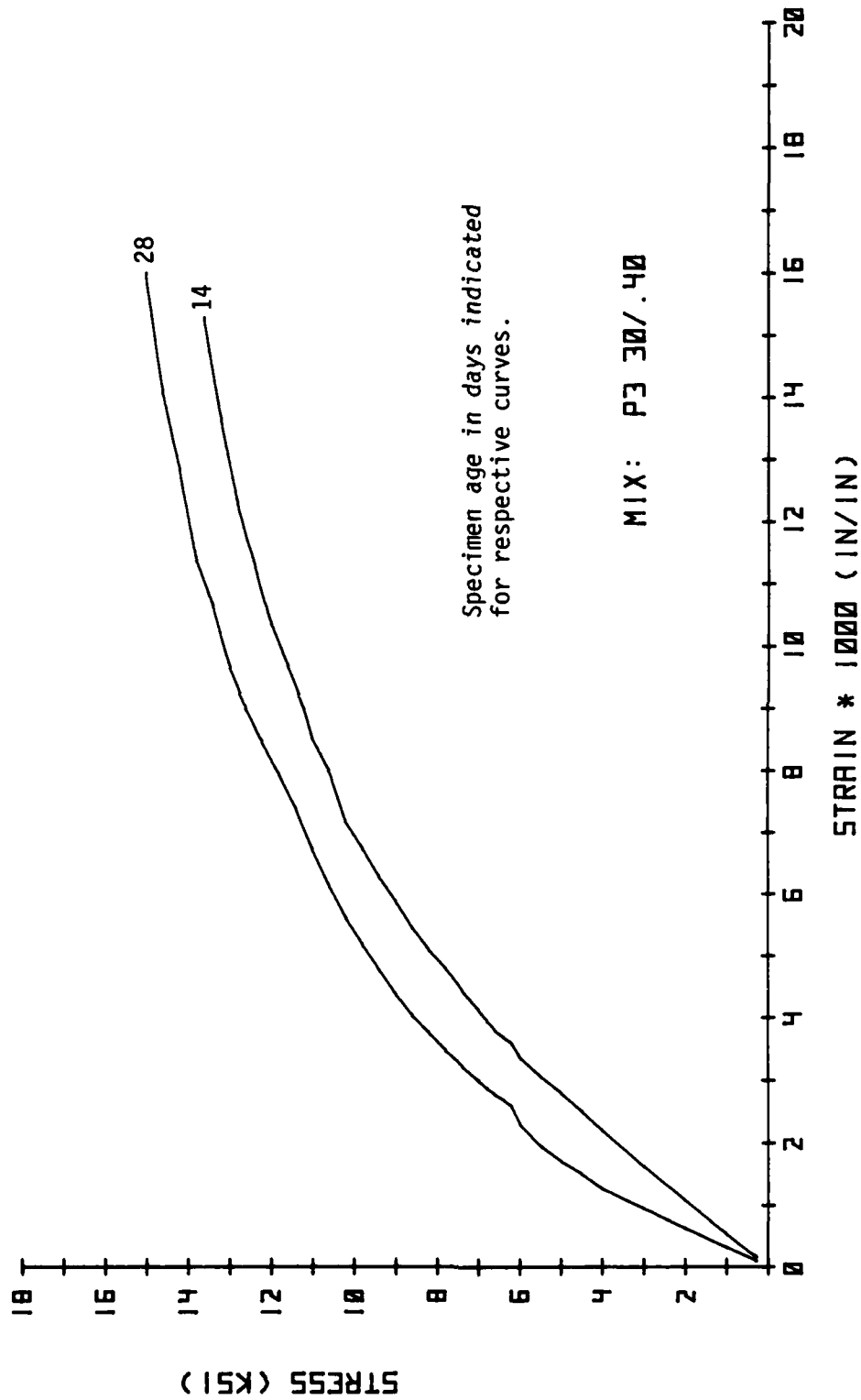


Fig. 3.15. Maximum Principal Stress-Strain Curves ($\sigma_1 - \epsilon_1$) for Multiaxial Compression Tests on 4 in. Cubes.

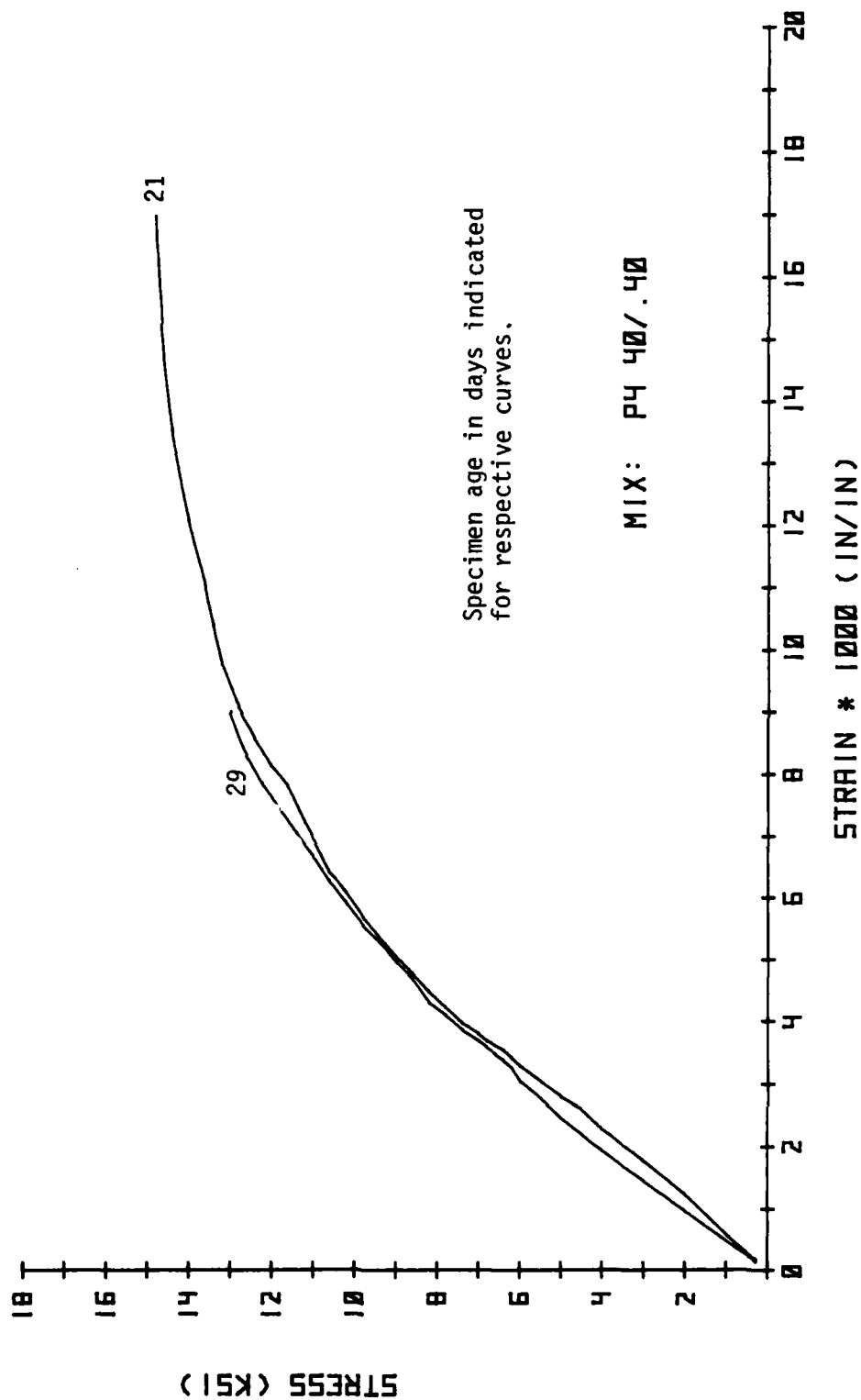


Fig. 3.16. Maximum Principal Stress-Strain Curves (σ_1 - ϵ_1) for Multiaxial Compression Tests on 4 in. Cubes.

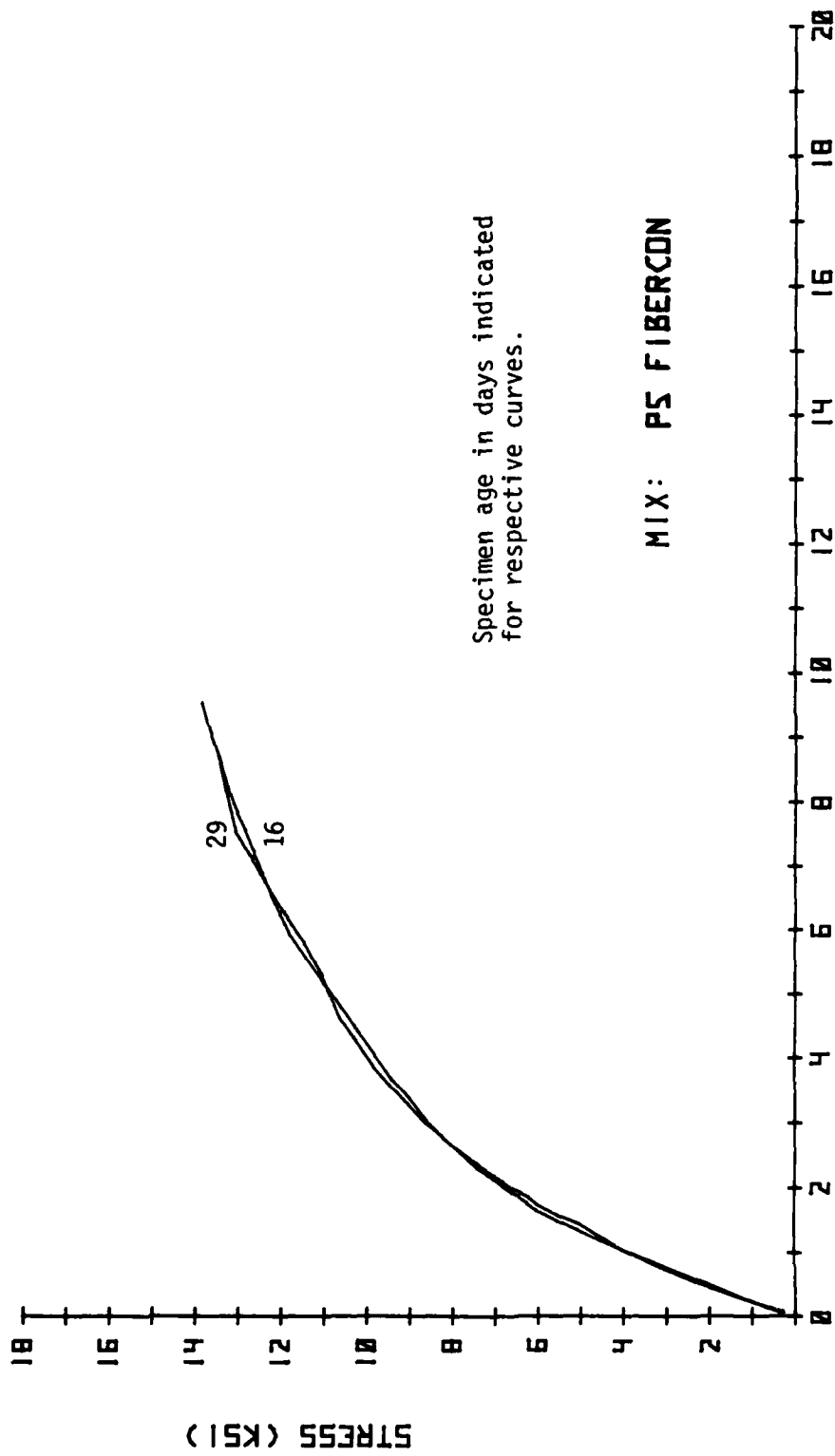


Fig. 3.17. Maximum Principal Stress-Strain Curves ($\sigma_1 - \epsilon_1$) for Multiaxial Compression Tests on 4 in. Cubes.

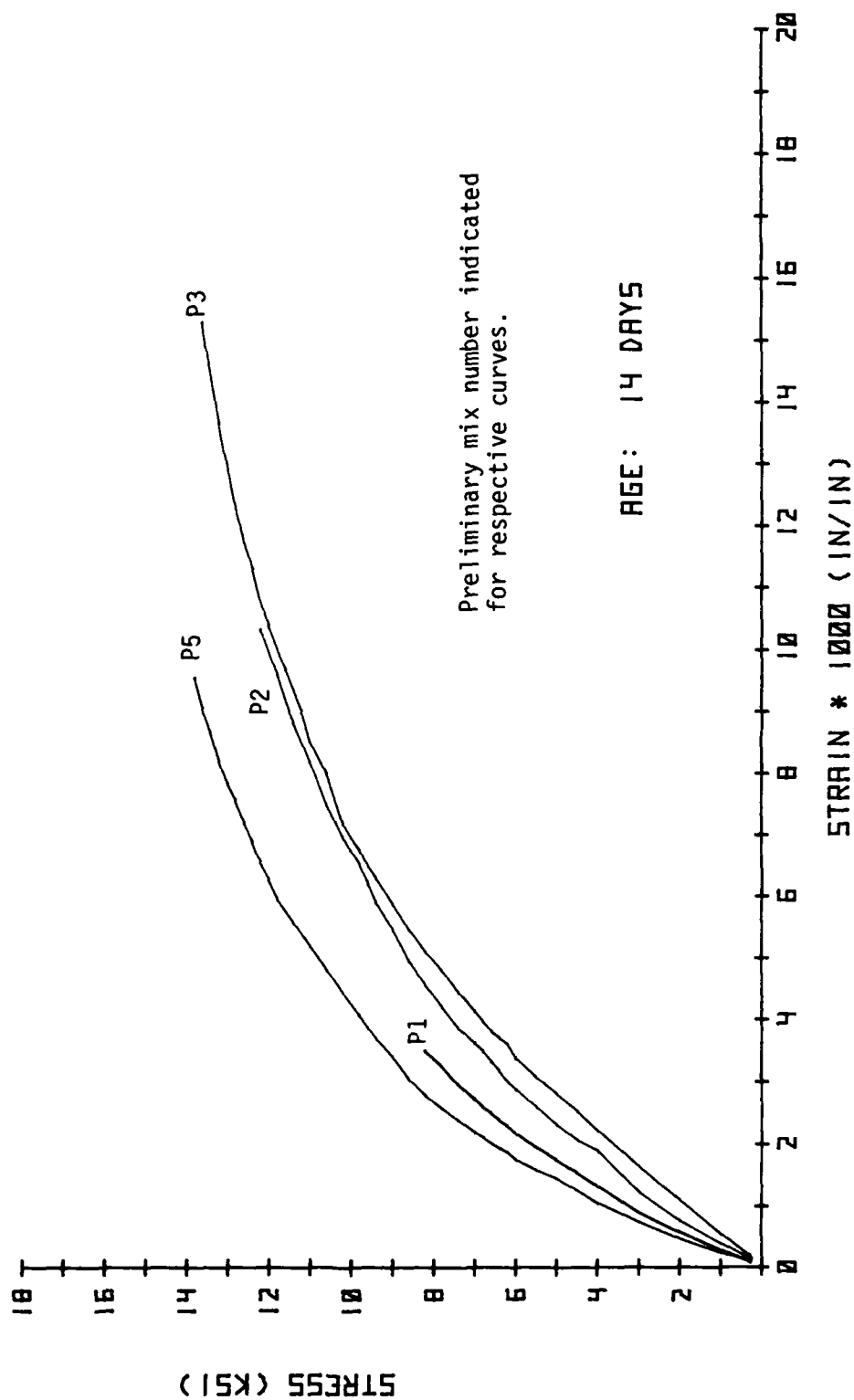


Fig. 3.18. Maximum Principal Stress-Strain Curves ($\sigma_1 - \epsilon_1$) for Multiaxial Compression Tests on 4 in. Cubes.

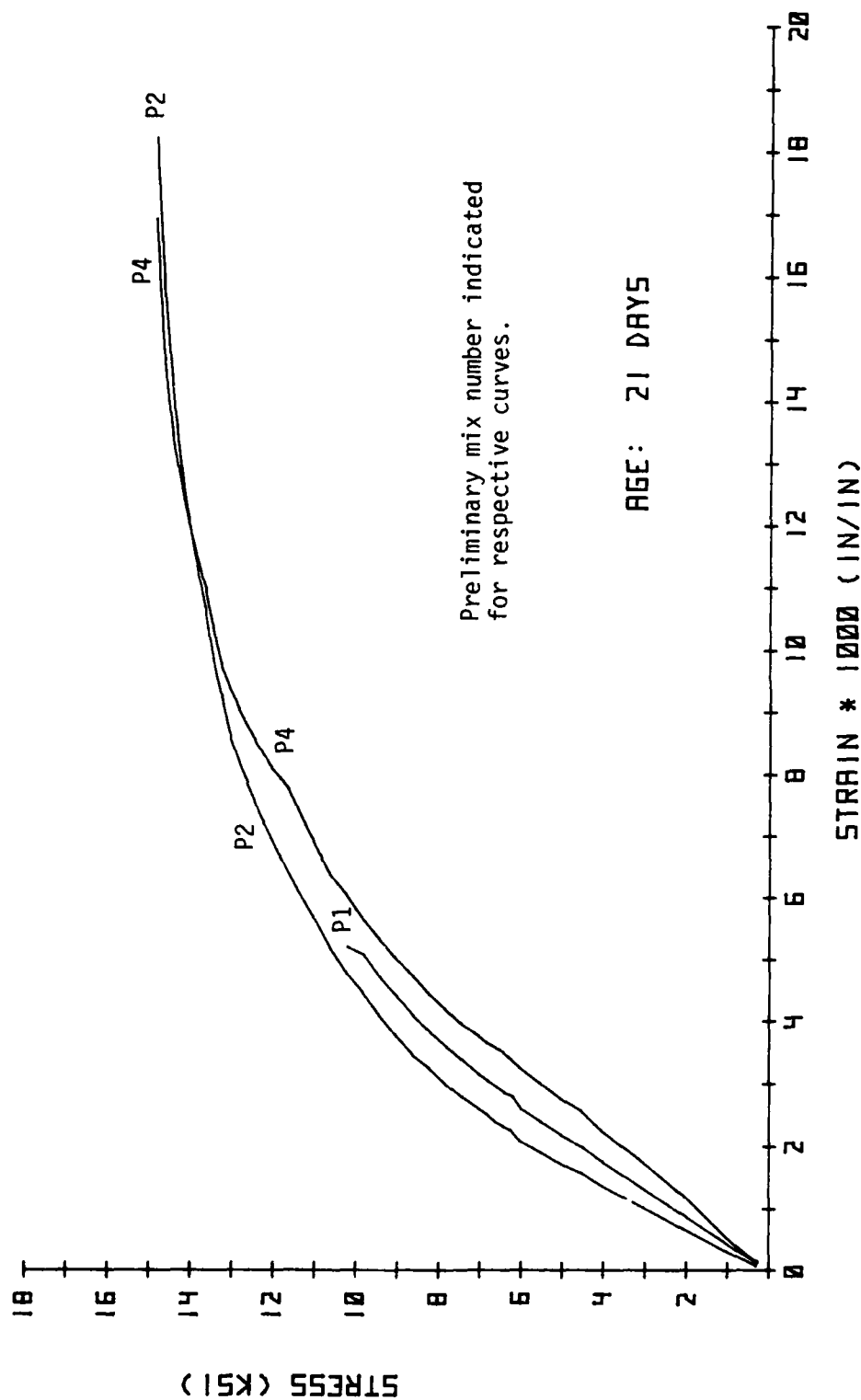


Fig. 3.19. Maximum Principal Stress-Strain Curves ($\sigma_1 - \epsilon_1$) for Multiaxial Compression Tests on 4 in. Cubes.

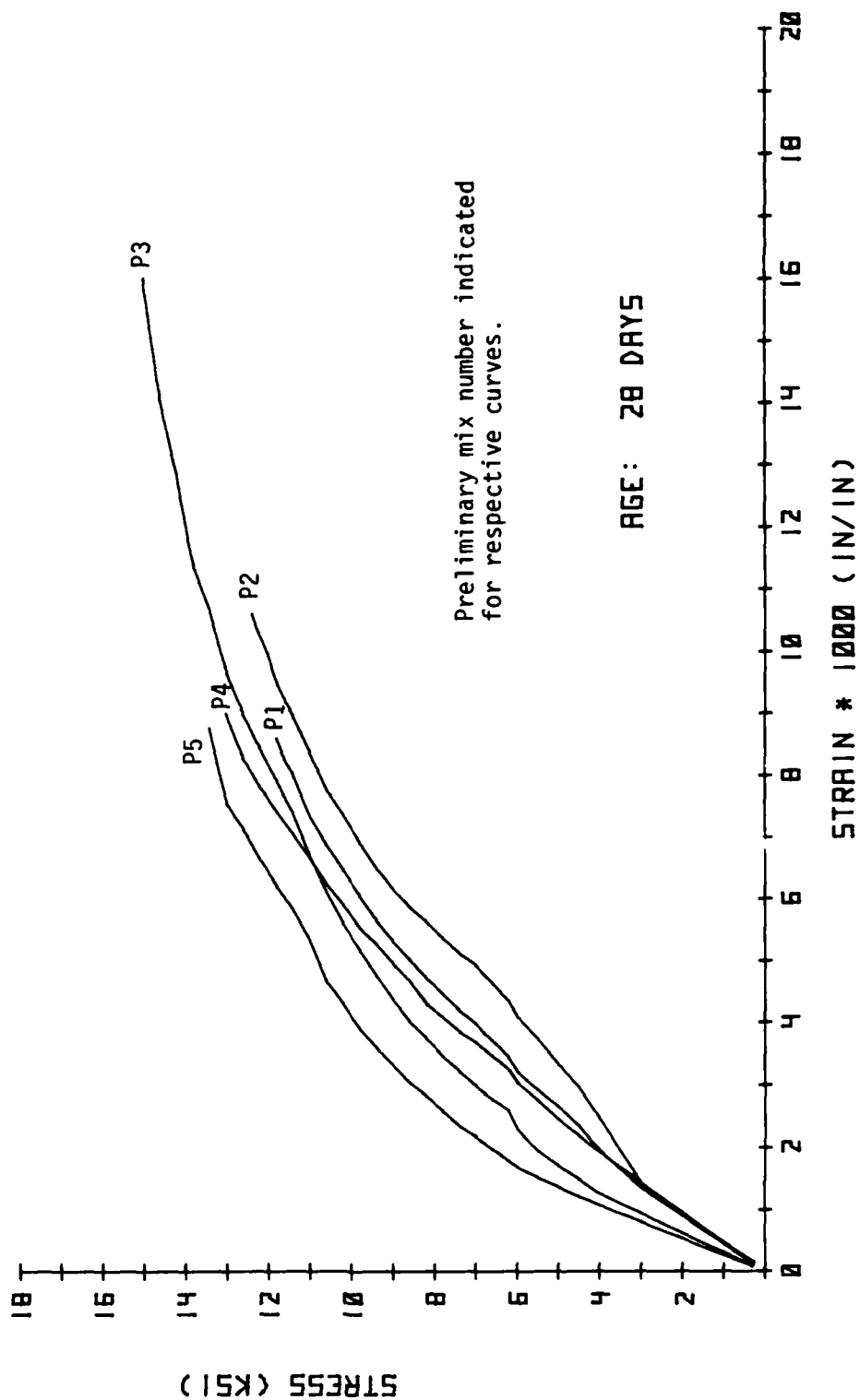


Fig. 3.20. Maximum Principal Stress-Strain Curves ($\sigma_1 - \epsilon_1$) for Multiaxial Compression Tests on 4 in. Cubes.

As in the unconfined compression tests, the mix number and specimen age were the two variables involved. No cubical tests on the plain concrete (P0) were conducted.

Figs. 3.13-3.17 show the maximum principal stress-strain envelopes for each mix, with specimen age as the variable. In Figs. 3.18-3.20 the stress-strain envelopes are plotted for constant specimen age, with mix numbers as the variable. Note here that in all these figures, each curve represents stress-strain results for single tests only. This was because of the time constraint involved in trying to test these specimens at specified ages, since the six mixes (including the P0 plain mix) were all cast in the same week, each on separate days.

In the first set of these figures (Figs. 3.13-3.17), one would expect as in the unconfined compression tests to see an increase in stiffness with specimen age before leveling off. Fig. 3.15 for the P3 30/.40 mix shows this whereas the P1 50/.50 mix data in Fig. 3.13 shows just the opposite. The P4 40/.40 and P5 "Fibercon" mixes shown in Figs. 3.16 and 3.17 respectively show nearly identical behavior in the major principal stress direction, indicating the age at which these tests were conducted had no influence.

A large difference in stiffnesses is seen in the second set of figures (Figs. 3.18-3.20) where the specimen age is constant. One can only say the P5 "Fibercon" mix was stiffer than the others at 14 and 28 days as it nearly was in the unconfined compression tests on cylinders (see Fig. 3.12), and the P1 50/.50 mix did not have the

lowest SFRC stiffness as it showed in the unconfined compression mode.

With only single stress-strain results for each type of test, it becomes very difficult if not impossible to draw any statistical conclusions regarding stiffness, strength, etc. increasing with age or how these values might change with mix number for the multiaxial compression tests. After all, since the material is concrete, and even identically tested concrete specimens normally show some scatter, one cannot call these stress-strain curves representative of how other identically tested specimens would behave. Also note that some of the curves extend to higher stress-strain values than others. Only the 21 day - P2 30/.50 specimen shown in Figs. 3.14 and 3.19 was taken to failure (dilation). In all the other tests, either the testing equipment broke down, a specimen's edge chipped off causing a membrane to extrude and burst from the major principal stress direction (σ_1) to the minor direction (σ_3), or a pinhole in a membrane caused failure on the surface of the specimen to occur. Therefore, the peak value indicated by all but one of these curves does not imply specimen failure but rather termination of the test by one of these other means. As mentioned in Section 2.8, one purpose of these cubical tests in the preliminary series was to debug the testing procedure. Most of these bugs, including the ones in the testing equipment, sample preparation, brass target and leather pad design were worked out before the final test series began.

3.3 Strength

3.3.1 Unconfined Compression

In this section, the unconfined compressive strengths of 3x6 in. cylinders tested as defined in Section 3.2.1 and 4 in. cubes are reported. These tests were conducted at various specimen ages to observe the effect of age on strength (after following the curing period previously described) in order to determine if after 50 days of curing, full strength could be achieved so that the final multiaxial compression tests on 4 in. cubes could be conducted without increasing concrete strength with age becoming an additional unwanted variable.

Fig. 3.21 shows the average unconfined compressive strengths (f'_c) plotted versus age for all the 3x6 in. cylinders tested in the preliminary series. Notice how the strengths do indeed level off at 50 days with only some slight increases in a few of the mixes. Also note that the largest increase in f'_c at 50 days of the SFRC over plain concrete (P0) is about 21% for the straight fiber mix (P5 "Fibercon") and about 18% for the P3 30/.40 deformed fiber mix. The increase in f'_c for the P1 50/.50 deformed fiber mix over plain concrete (P0) is only about 3% indicating that the shorter fibers appear to add to the compressive strength somewhat more than the long fibers.

Some of the mixes show a drop in average unconfined compressive strength with increasing age, which is especially noticeable between 14 and 21 days. All that can be concluded from this is that the curing procedure may have caused this or that the decrease in

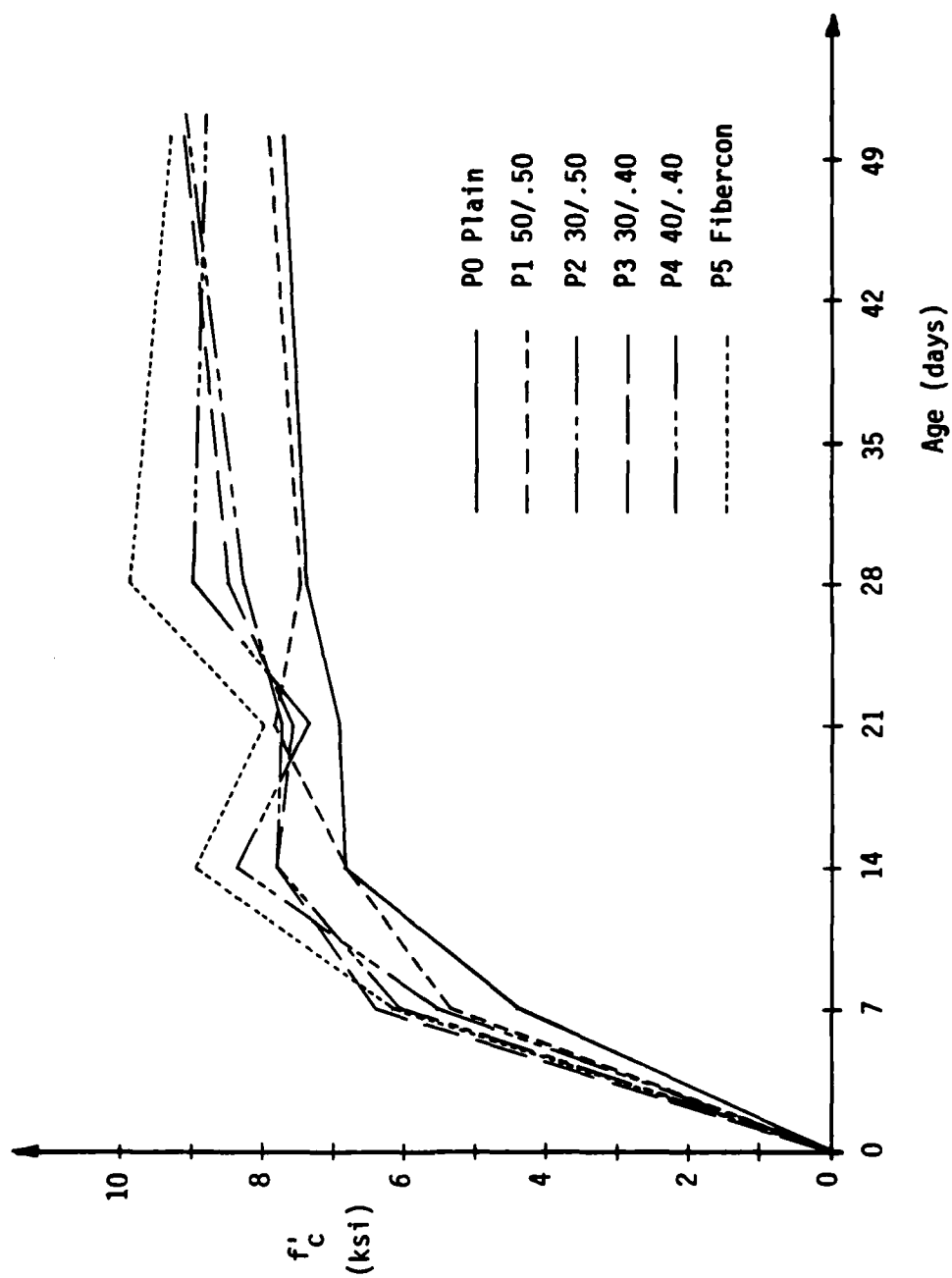


Fig. 3.21. Average Unconfined Compressive Strength of 3x6 in. Cylinders (f'_c) vs. Age for the Preliminary Test Series.

strength is due to scatter inherent in concrete behavior since the values plotted are average values of strength, each for at least three randomly chosen specimens. TABLE 2.8 shows that all the cubical tests in the final test series were conducted at ages well beyond 50 days; therefore the probability of strength increasing with age after 50 days could comfortably be neglected.

Fig. 3.22 shows the average unconfined compressive strengths (f_c), each for two randomly chosen specimens, plotted versus age for all the 4 in. cubes tested in the preliminary series. Tests on these cubes were conducted only up to 28 days of age. Once again it can be seen that the strengths do begin to level off after 14 days. However, as in the tests on cylinders, a drop in strengths is present between 21 and 28 days, even with some dropping below the strength of plain concrete. The cause may be the same as those described in the previous paragraph or that the size of the 4 in. cubical specimens may affect the strengths reported.

Fig. 3.23 shows the comparisons of average strengths versus age in unconfined compression of cylinders (f'_c) and cubes (f_c) for the one SFRC mix that was eventually chosen to be used in the final test series employing the Bekaert ZP 30/.40 deformed fiber. The "P3" indicates the mix tested in the preliminary series and "F1" and "F2" represent the two identical mixes cast a later date for the final test series. The purposes of this figure are to demonstrate the differences between identical mixes, cast at different times and to see if the results of some basic tests on the same mix were reproducible. Notice the similarity between the cylinders and cubes

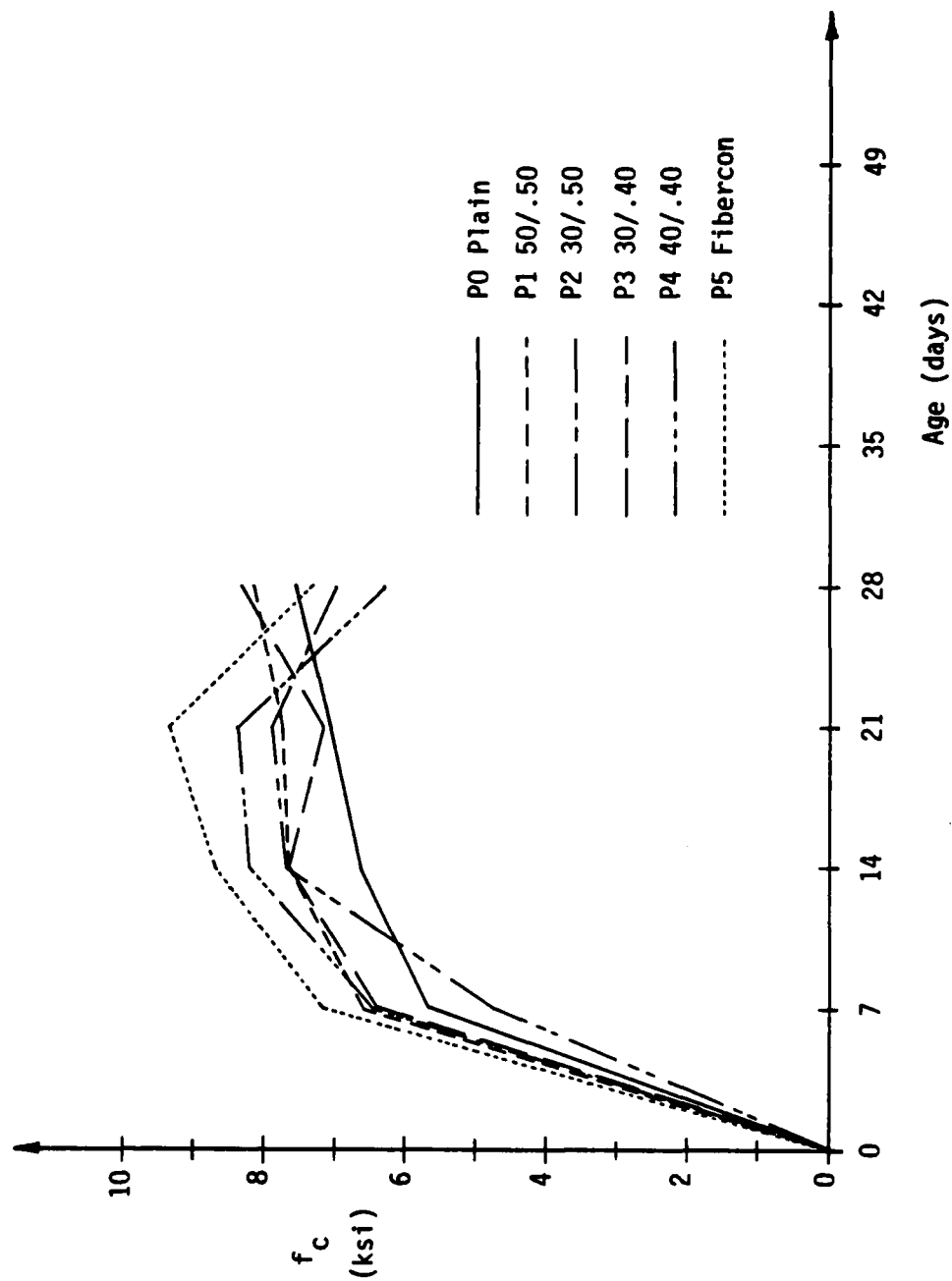


Fig. 3.22. Average Unconfined Compressive Strength of 4 in. Cubes (f_c) vs. Age for the Preliminary Test Series.

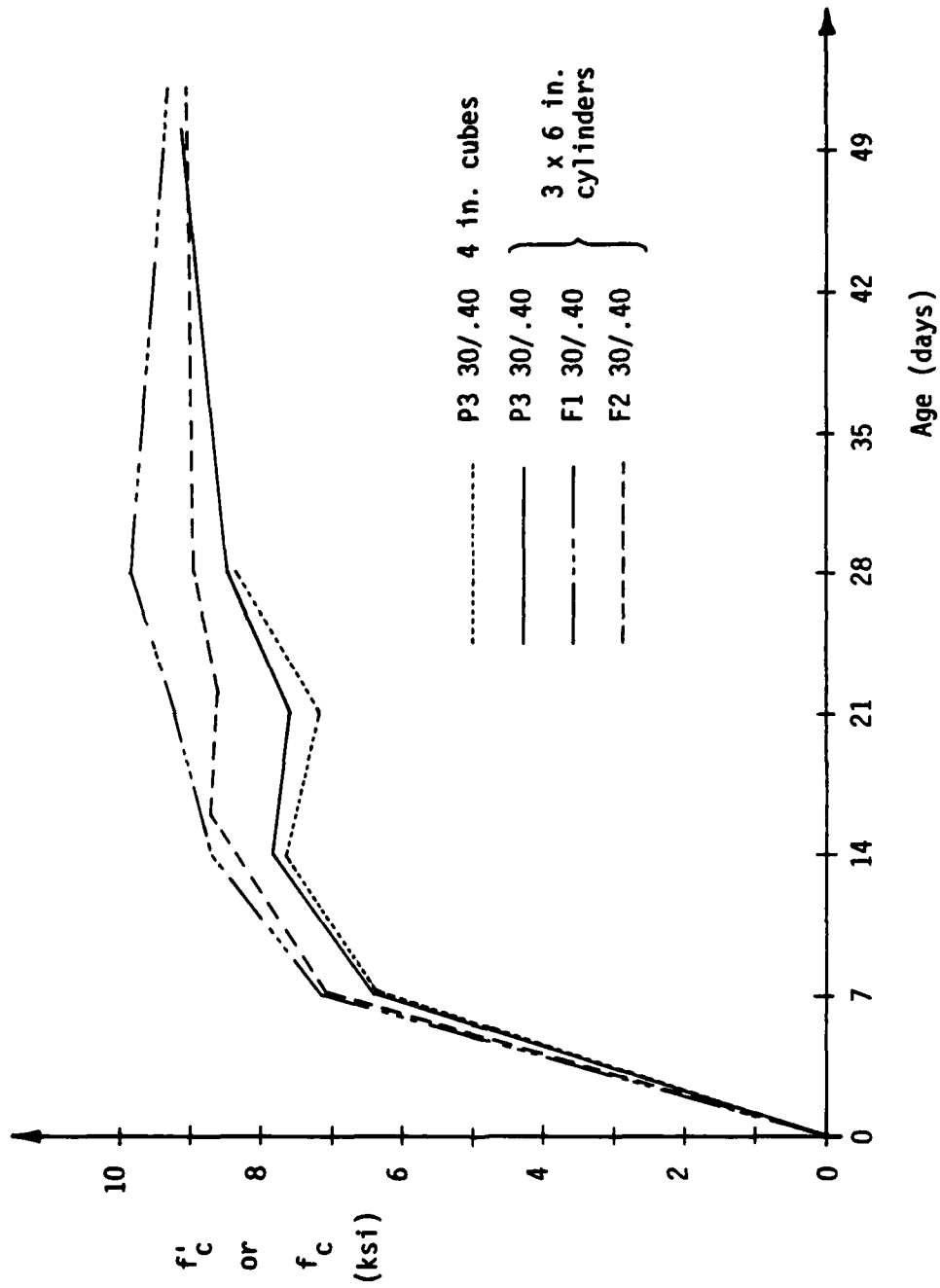


Fig. 3.23. Comparison of Average Unconfined Compressive Strength for 3x6 in. Cyls. (f'_c) and 4 in. Cubes (f_c) vs. Age for the Final SFRC Mix Chosen.

tested in the preliminary series (P3). Also note the small variations in strength results at 50 days, even though a greater scatter is present at 28 days. The value of the unconfined cylinder compressive strength (f'_c) used for reference in the final test series was 9200 psi (based on 50-52 day F1 and F2 test results).

3.3.2 Relations Between Unconfined Compressive Strength (f'_c), Indirect Tensile Strength (T), Rupture Modulus (R) and Various Fiber Properties.

As previously mentioned, 80 lbs of fibers per cubic yard of concrete were incorporated into the concrete mix for all fiber types and sizes. This is equivalent to a volume percentage of fibers equal to 0.6%. A simple calculation can be made to find the number of fibers per unit volume of concrete:

$$\frac{\text{no. of fibers}}{\text{unit vol. concrete}} = \frac{\text{vol. \% of fibers}}{\text{vol. per fiber}} \quad (3.1)$$

In TABLE 3.1, the steel fiber sizes used in the preliminary test series are listed. The Bekaert "Dramix" deformed fibers have a circular cross section and the USS "Fibercon" straight fibers have a flat cross section (See Fig. 2.2). Therefore the volume per fiber can easily be calculated as:

$$(\text{vol./fiber})_{\text{circular}} = \frac{\pi d^2}{4} \ell ; \text{Bekaert} \quad (3.2)$$

$$(\text{vol./fiber})_{\text{flat}} = w t \ell ; \text{USS}$$

where d = diameter

λ = length

w = width

t = thickness .

For example, for the "Dramix" ZP 50/.50 fibers,

$$\begin{aligned}\text{vol./fiber} &= \frac{\pi}{4} (0.50 \text{ mm})^2 (50 \text{ mm}) \\ &= 9.817 \text{ mm}^3 \\ &= 6 \times 10^{-4} \text{ in.}^3\end{aligned}$$

Therefore from Eq. 3.1:

$$\frac{\text{no. of fibers}}{\text{in.}^3 \text{ concrete}} = \frac{0.6\%}{6 \times 10^{-4} \text{ in.}^3} = \frac{10 \text{ fibers}}{\text{in.}^3 \text{ concrete}} .$$

In TABLE 3.1, the number of fibers per cu. in. of concrete calculated for all fibers used is also given.

In the preliminary series, various tests were performed to determine the effect of the fiber aspect ratio (λ/d) and fiber length (λ) on the following strength properties of the mixes:

- 1) unconfined compressive strength (f'_c) of 3x6 in. cylindrical specimens tested in accordance with ASTM C39-72 specifications. Results are shown in Figs. 3.24 and 3.27.
- 2) indirect tensile strength (T) of 3x6 in. cylindrical specimens tested in accordance with

ASTM C496-71 specifications. Results are shown in Figs. 3.25 and 3.28.

- 3) modulus of rupture (R) (flexural strength) of 3x3x15 in. simple beams with third-point loading tested in accordance with ASTM C78-75 specifications. Results are shown in Figs. 3.26 and 3.29.

One could argue as to whether aspect ratio or length is more appropriate to use in representing these various strengths. Note that if the diameters of all the fibers were equal, these two factors would be identical. However, the diameter of fibers used varied from 0.40 mm to 0.50 mm for the "Dramix" fibers. It is sometimes easier to explain the strength results in terms of the fiber length alone, or both length and aspect ratio, rather than aspect ratio alone. In most literature on this subject, only aspect ratio is considered.

The data shown in Figs. 3.24 and 3.27 demonstrates a decrease in the unconfined compressive strength with respect to the fiber aspect ratio and length. The volume percentage of fibers is constant throughout. In an unconfined compression test performed on concrete, the actual failure mode is due to shear. In plain concrete, these fracture or shear planes are well defined and actual separation along these shear planes occurs at failure. However, in the SFRC tested, these shear planes are much less defined due to the fact that at failure, shearing takes place across the fibers as well as the concrete causing a stress redistribution at concrete failure to occur through the fibers. Therefore the cross-sectional area of

the fibers through the shear planes is important. If one were to imagine a hypothetical case in which one "smooth" shear plane developed at failure and that all the fibers were oriented perpendicular to this plane, then a correlation can be seen between the unconfined compressive strength and the total fiber cross-sectional area of all the fibers per square inch of concrete area. That is, assume all the fibers per unit volume of concrete (TABLE 3.1) are aligned perpendicular to the shear plane that occurs in unconfined compression. Then one can easily calculate, knowing the fiber cross-section, the cross-sectional area of all the fibers per square inch of concrete through the shear plane. In Fig. 3.30, it is seen that the compressive strength increases with increasing total fiber cross-sectional area simply because there is more fiber area across the shear plane when failure takes place. Note also the inverse relationship between fiber length vs. compressive strength and fiber area vs. compressive strength as shown in Figs. 3.27 and 3.30 respectively. For a constant volume percentage of fibers, the total fiber cross-sectional area per unit volume of concrete must decrease as the length increases, thereby explaining the phenomenon of decreasing compressive strength with increasing fiber length. That is, the compressive strength decreases due to the decreased fiber area (for increasing fiber lengths) across the shear plane, regardless of the direction of the shear plane.

The same argument of increasing strength with regard to the total fiber cross-sectional area does not seem to apply to the indirect tensile strength (T) (split cylinder strength) nor the

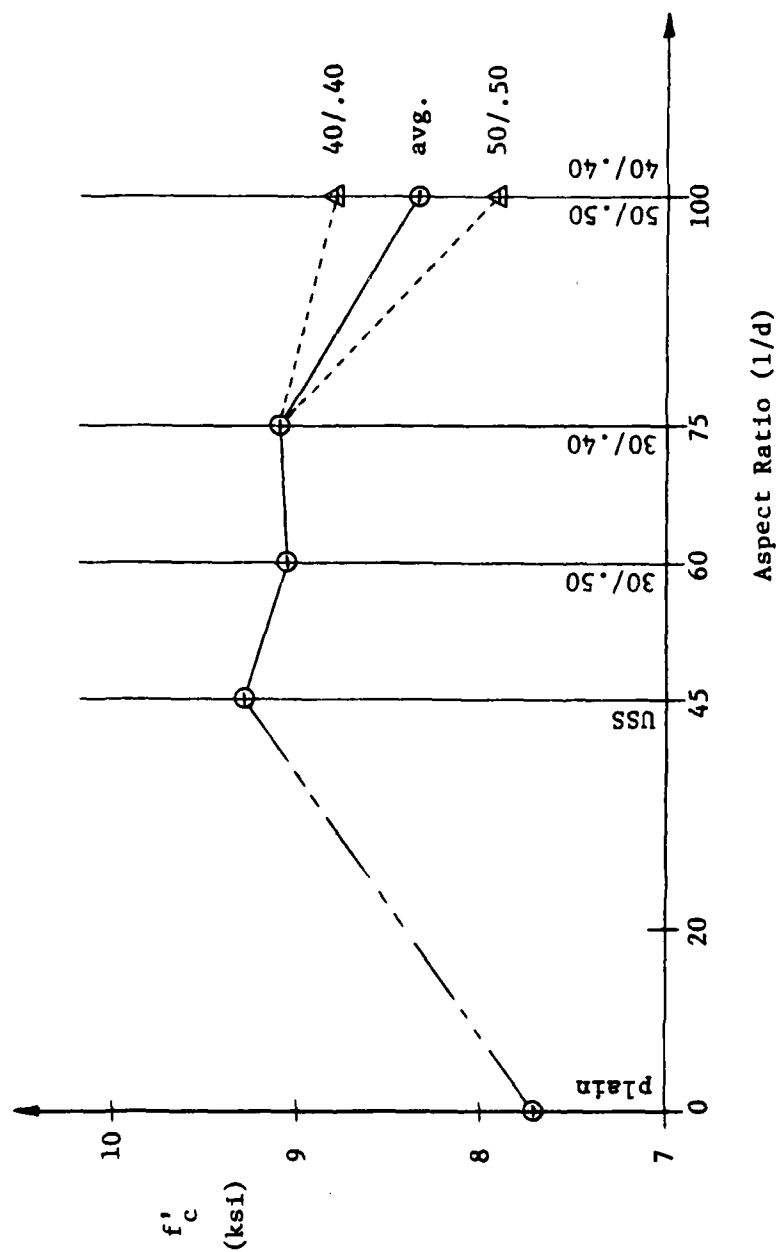


Fig. 3.24. Average 50 day Unconfined Compressive Strength (f'_c) vs. Aspect Ratio (l/d).

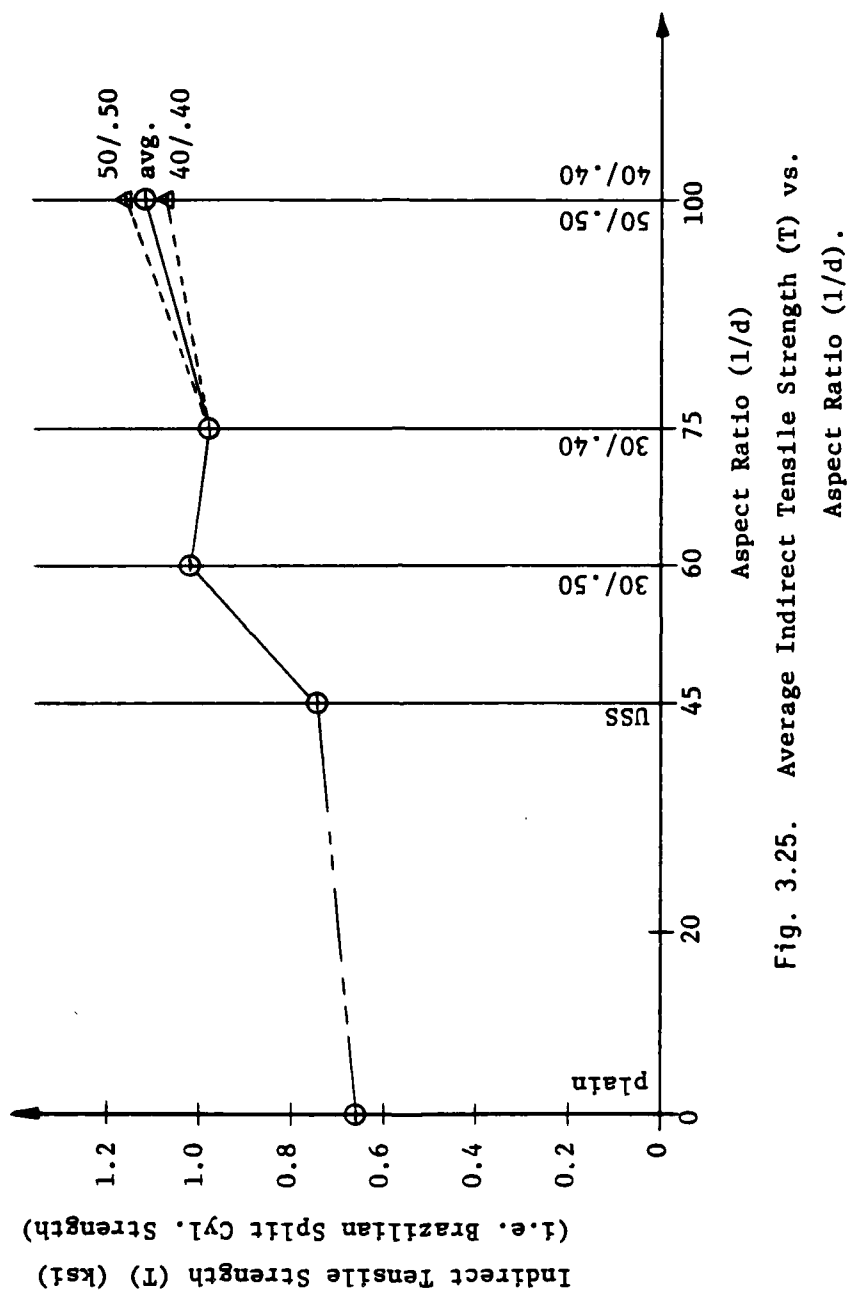


Fig. 3.25. Average Indirect Tensile Strength (T) vs. Aspect Ratio (l/d).

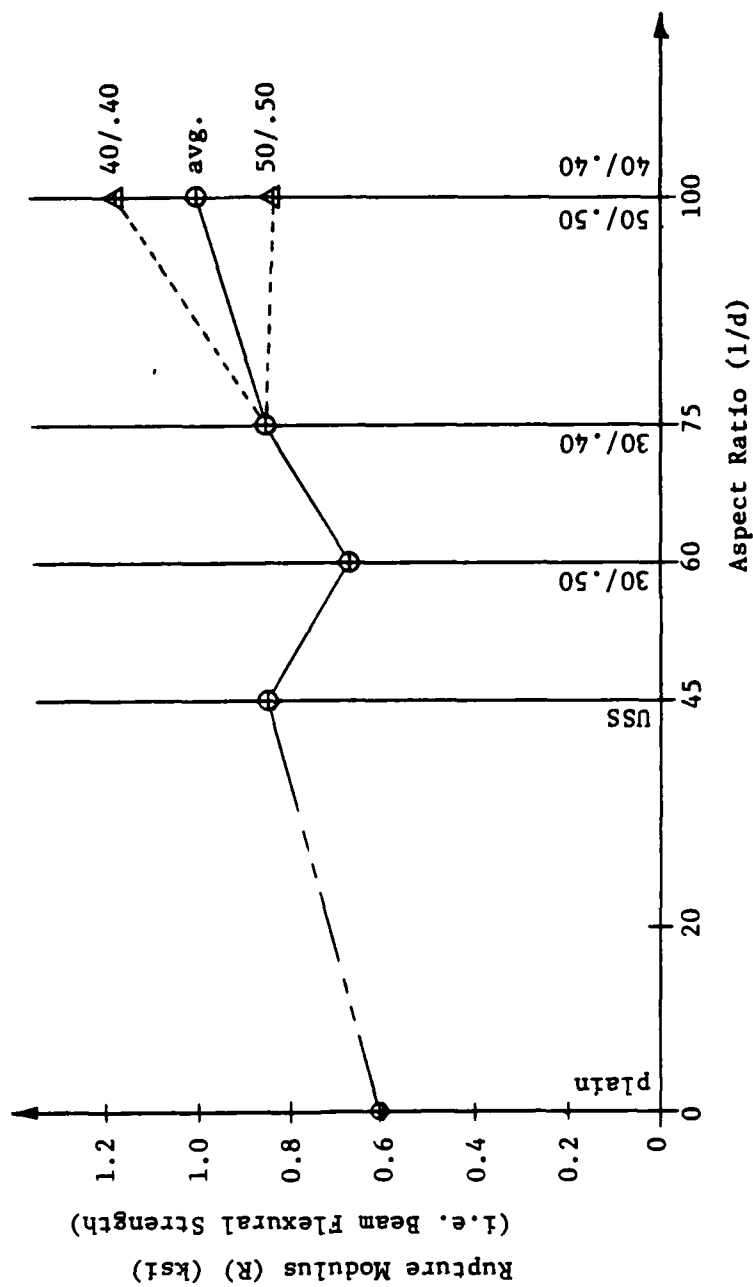


Fig. 3.26. Average Rupture Modulus (R) vs. Aspect Ratio (1/d).

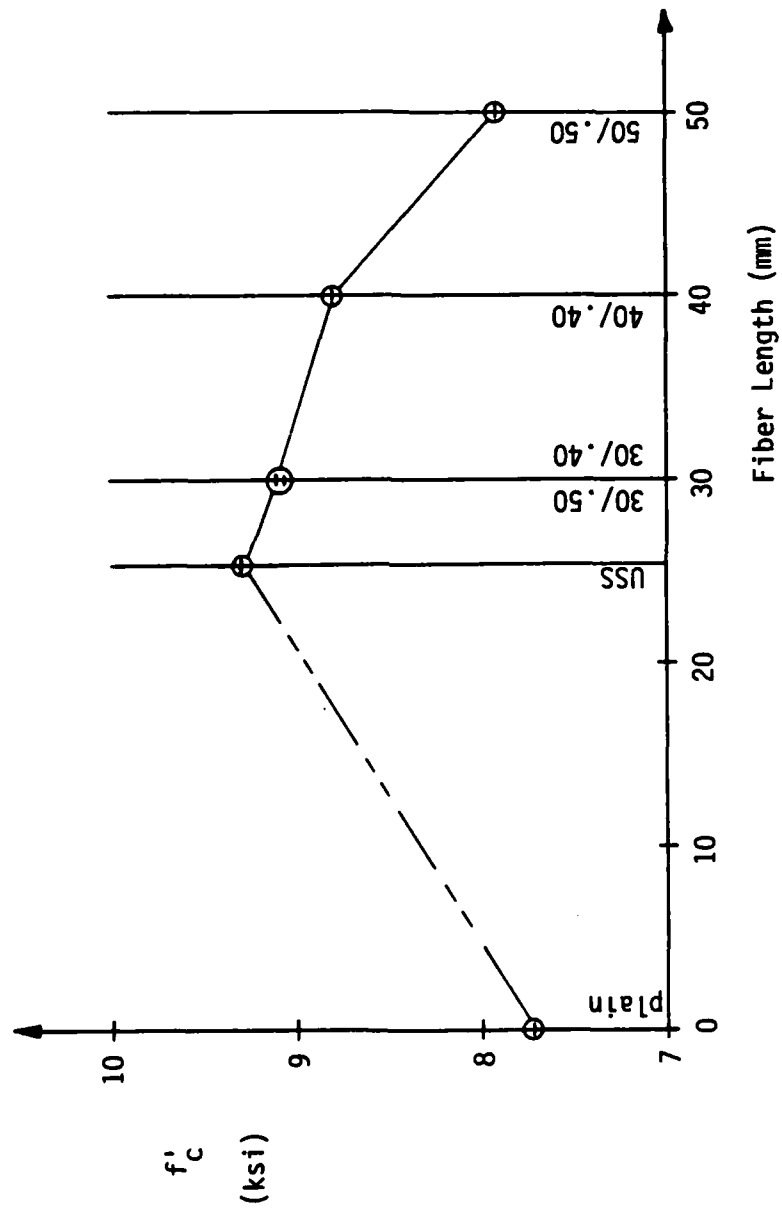


Fig. 3.27. Average 50 day Unconfined Compressive Strength (f'_c) vs. Fiber Length.

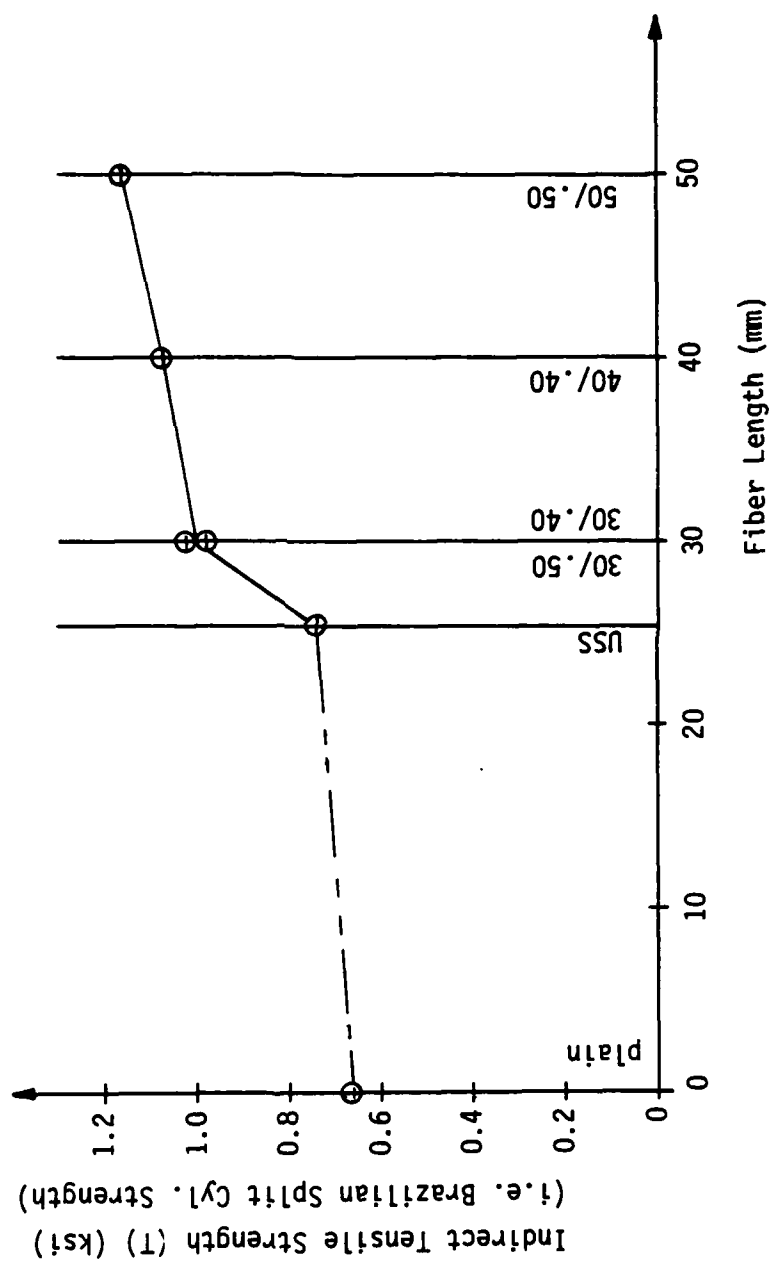


Fig. 3.28. Average Indirect Tensile Strength (T) vs. Fiber Length.

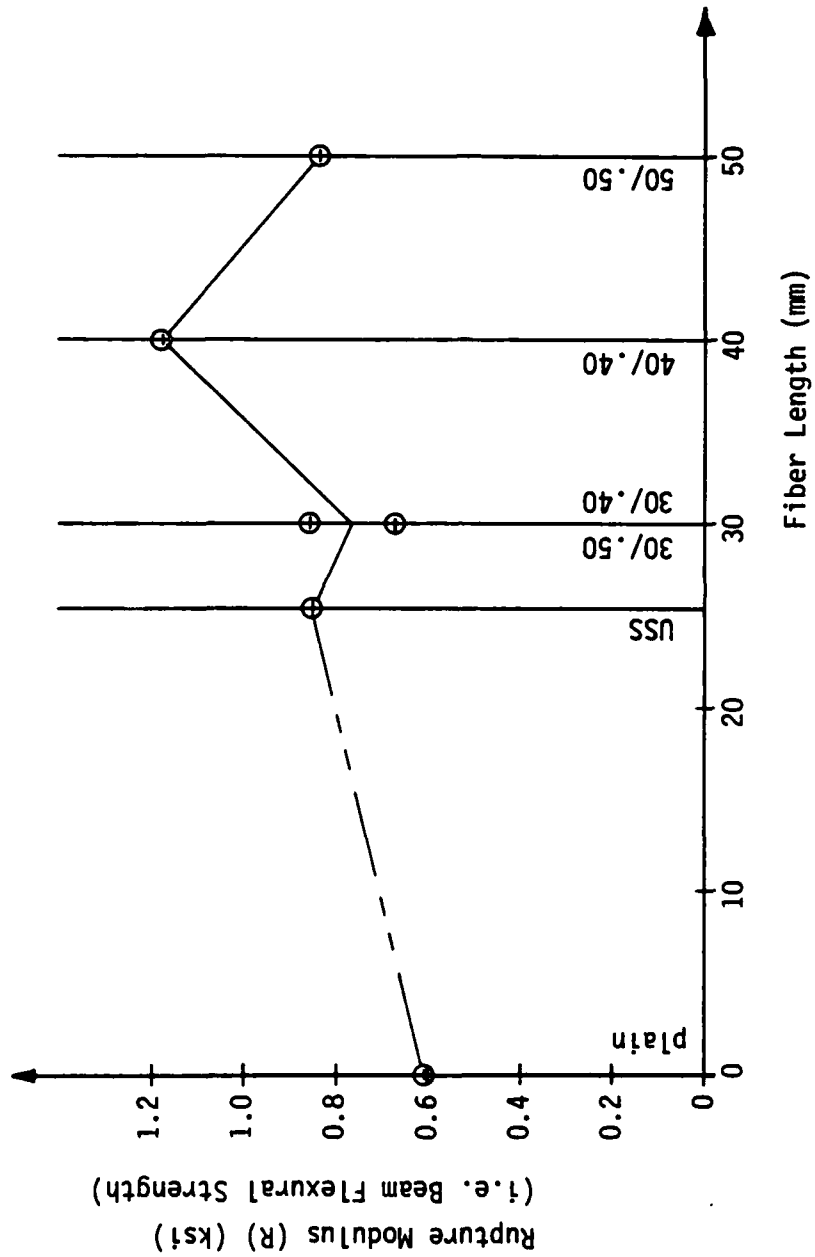


Fig. 3.29. Average Rupture Modulus (R) vs. Fiber Length.

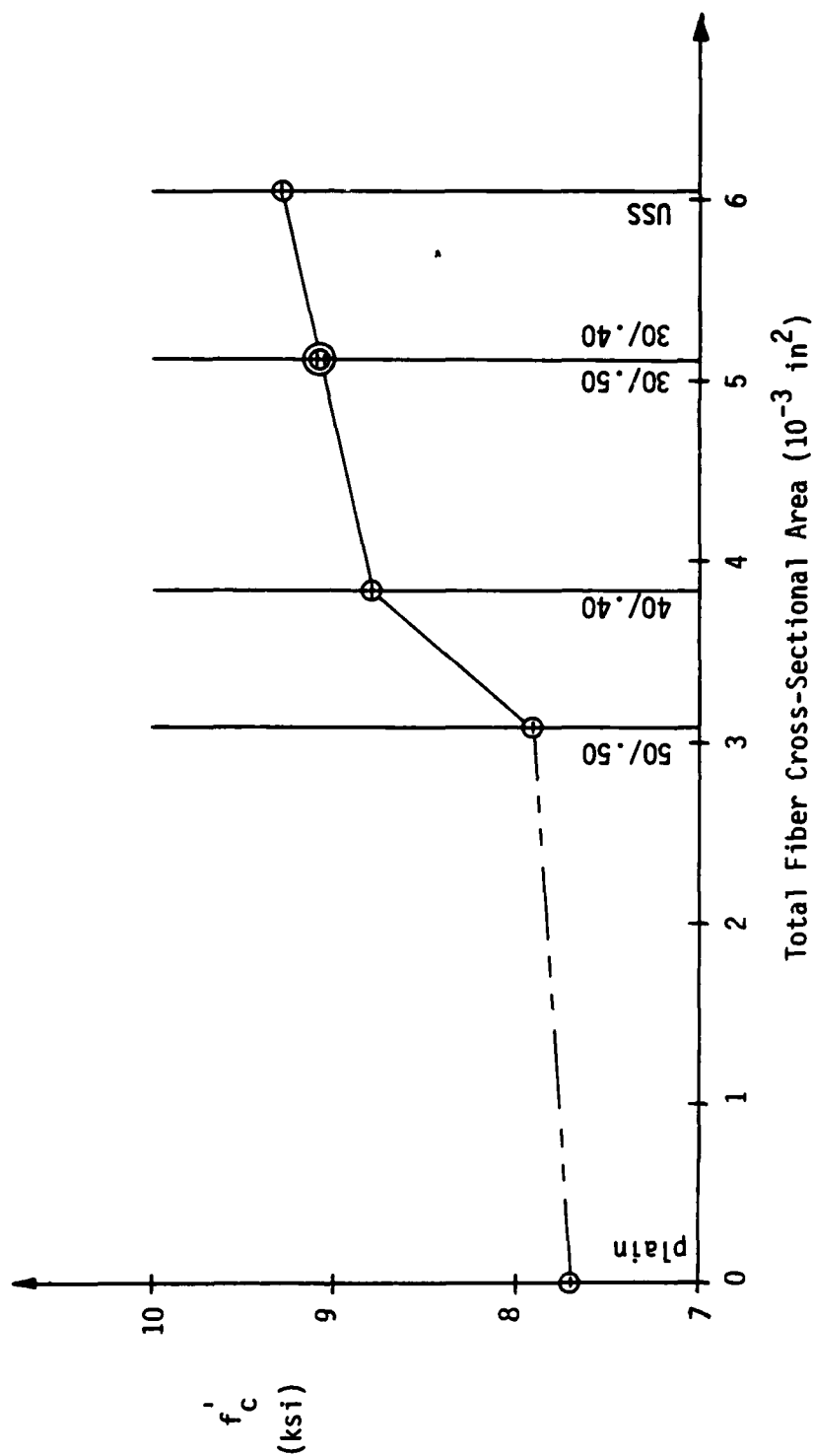


Fig. 3.30. Average 50 day Unconfined Compressive Strength (f'_c) vs. Total Fiber Cross-Sectional Area per cu.in. of Concrete.

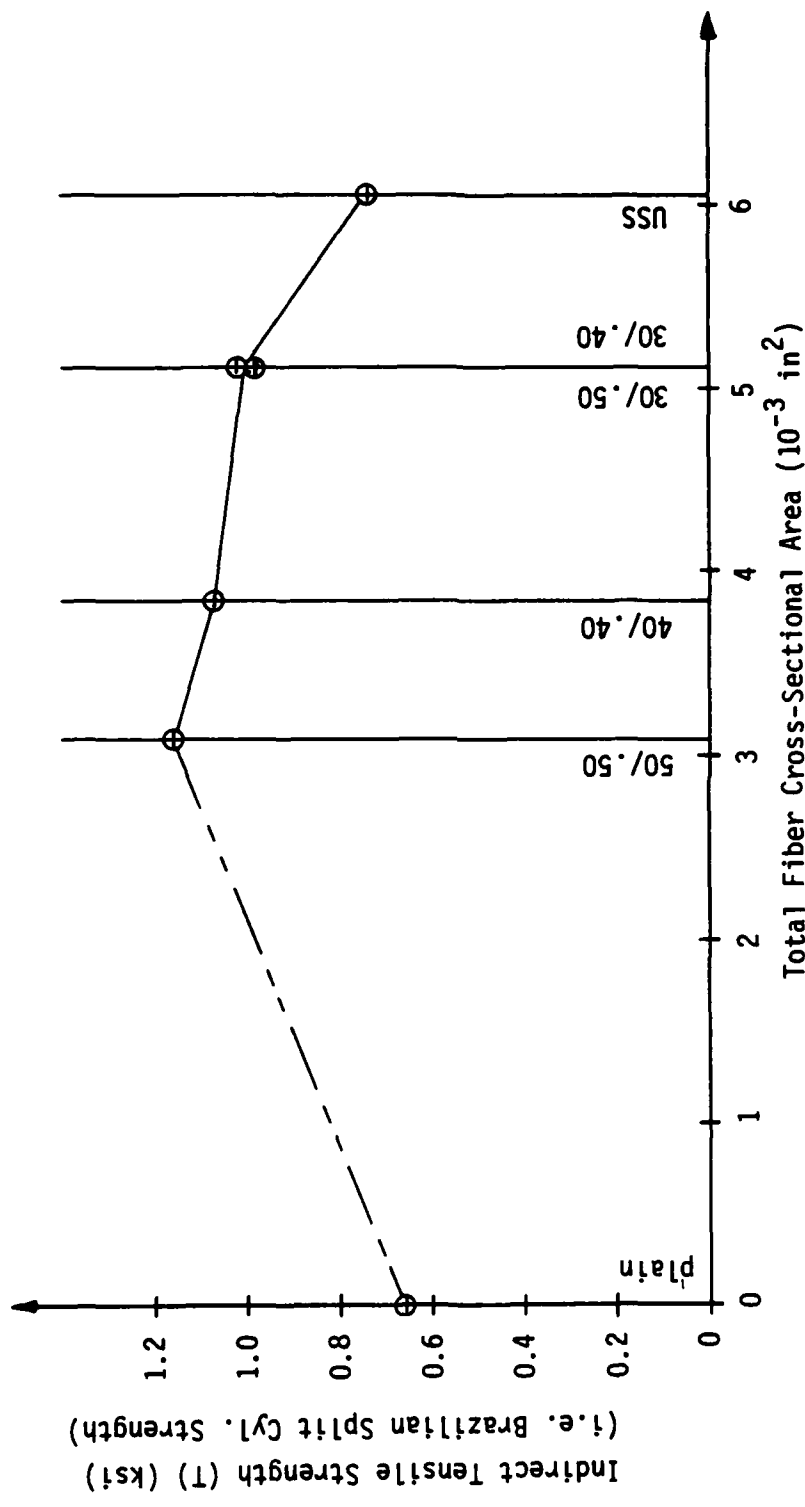


Fig. 3.31. Average Indirect Tensile Strength (T) vs. Total Fiber Cross-Sectional Area per cu.in. of Concrete.

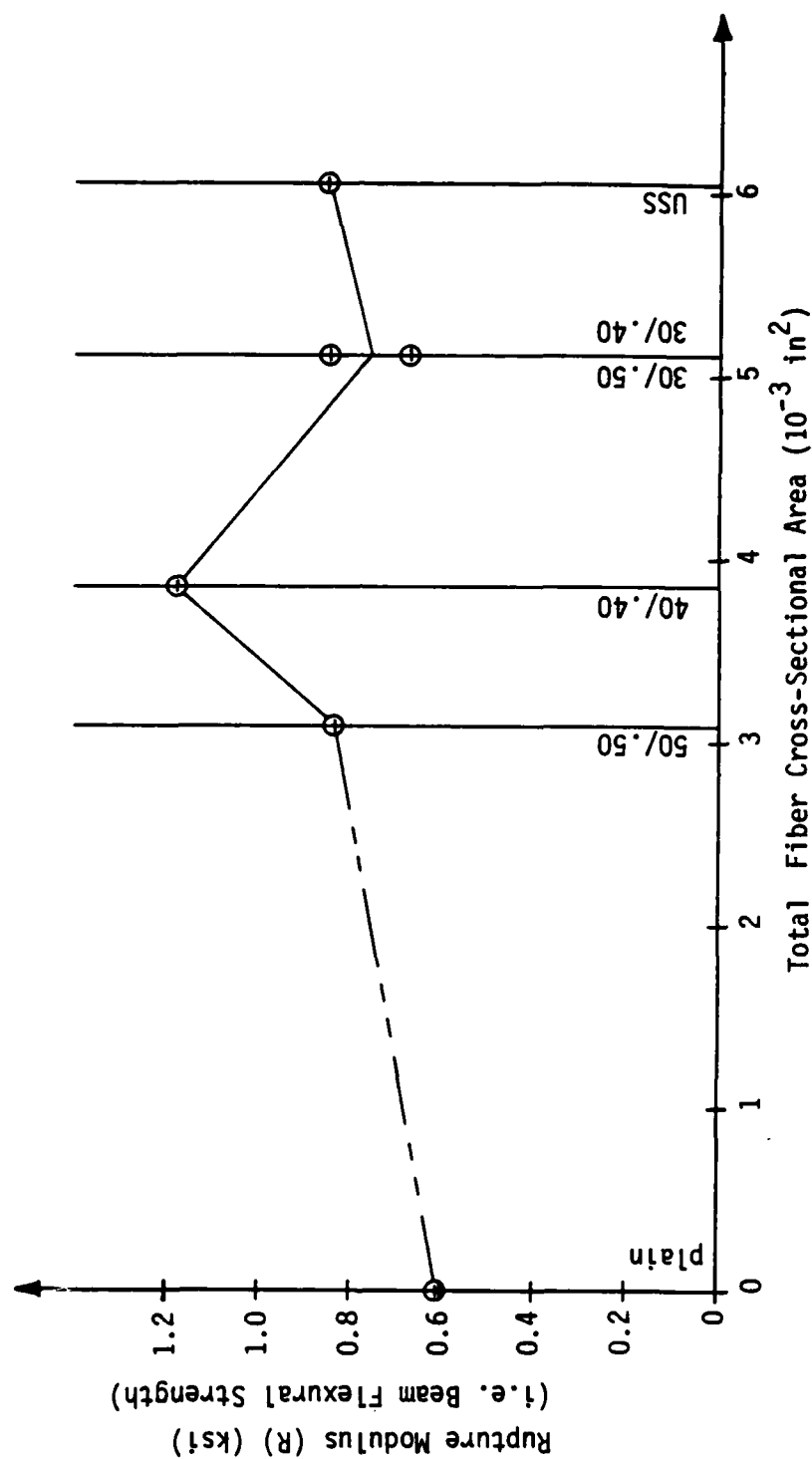


Fig. 3.32. Average Rupture Modulus (R) vs. Total Fiber Cross-Sectional Area per cu.in. of Concrete.

rupture modulus (R) (pure bending strength) as shown in Figs. 3.31 and 3.32. A better explanation for the increase in these strengths would be with regard to the fiber aspect ratio and/or fiber length as shown in Figs. 3.25 and 3.28 for the indirect tension tests and Figs. 3.26 and 3.29 for the pure bending tests. In both types of tests, the SFRC specimens fracture along a straight line with a tensile type failure, as shown in Fig. 3.33, rather than a shear failure, as occurs in unconfined compression.

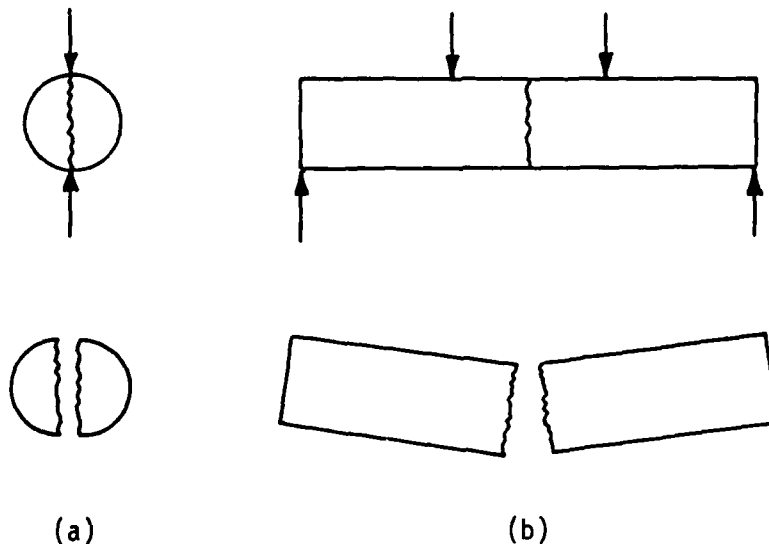


Fig. 3.33. Failure Modes in: (a) Indirect Tension;
(b) Pure Bending.

The reason for the increase in these strengths (especially the indirect tensile strength) with respect to increasing fiber length and/or aspect ratio is that for longer fibers, there is more bond or

"development" length between the fibers and the mortar in the concrete. The fibers can either pull out or actually break in tension. During the tests, one could actually hear the popping of the fibers failing in tension. But regardless of that, an increase of bond length implies an increase in the tensile strength of the composite because in tension, the steel must be developed to be effective. Therefore long fibers carry a larger portion of the load in tension than shorter fibers would. This can be seen in Fig. 3.28. Note also the indirect tensile strength of the SFRC is much less for the "Fibercon" composite than reported for the others. These fibers are straight so pull out is much easier, whereas the "Dramix" fibers employ bent ends which act as anchors, increasing the development length. It seems obvious that the deformed ends of these fibers should contribute significantly to the increase in the bond between fiber and matrix. It should be pointed out that the "Dramix" fibers did not always break in tension. They too pulled out on occasion, especially at failure when the concrete itself began to breakdown or be crushed. Some concrete crushing does occur in the indirect tension tests. This is one drawback of this type of test, since direct tensile strength is not measured. Thus, the name of "indirect tension" is given to it. It should also be pointed out that the USS "Fibercon" fibers were used in the same volume percentage as for the Bekaert "Dramix" fibers, so that the results could be used to compare deformed to straight fibers for the few simple tests performed. Normally in practice, a higher volume percentage is recommended for the "Fibercon" fibers (1.05% or 140 lb/yd³

as compared to 0.6% or 80 lb/yd³ recommended and used for the "Dramix" deformed fibers) but this additional variable was not considered in the analysis of results; therefore the volume percentage was kept constant for all fibers.

TABLE 3.2 summarizes from TABLES 2.2, 2.4 and 2.5 the average strengths for three of the tests in the preliminary series with percentage increases in plain concrete strengths for the same type of tests also given. For a constant volume percentage of all the fibers, one can see, as in the appropriate figures, an inverse relationship between fiber length and aspect ratio with compressive strength and a direct relationship between fiber length and aspect ratio with tensile strength. The number of fibers per cu. in. of concrete (TABLE 3.1) and fiber development length seem to be the important parameters governing the compressive and tensile strengths, respectively. The deformed ends on the "Dramix" fibers add more to the fiber development length for tensile behavior than does the fiber without the deformed ends ("Fibercon").

3.4 Conclusions for the Design of the Mix Used in the Final Test Series

- 1) All the fibers performed well during mixing. The glue on the collated "Dramix" fibers dissolved completely after about two minutes of mixing and random orientation of the fibers could visually be seen. The mixing of the straight, loose "Fibercon" fibers with the dry aggregate prior to adding cement and water was necessary to achieve good random orientation of these fibers in the mix. The

TABLE 3.2

SUMMARY OF AVERAGE STRENGTHS FOR PRELIMINARY TESTS *

* STRENGTH VALUES GIVEN IN PSI WITH PERCENTAGE INCREASES OVER PLAIN CONCRETE STRENGTHS INDICATED IN PARENTHESES.

Test Mix No.	Unconfined Compressive Strength of Cylinders [50 day f'_c]	Indirect Tensile Strength of Cylinders [28 day T]	Flexural Strength of Beams [~ 28 day R]
P0 Plain	7707	657	646
P1 Dramix 50/.50	7908 (2.6%)	1159 (76.5%)	809 (25.2%)
P2 Dramix 30/.50	9056 (17.5%)	1019 (55.2%)	673 (4.2%)
P3 Dramix 30/.40	9099 (18.1%)	953 (45.1%)	855 (32.4%)
P4 Dramix 40/.40	8797 (14.1%)	1072 (63.2%)	1176 (82.1%)
P5 Fibercon	9292 (20.6%)	744 (13.3%)	850 (31.6%)

workability and casting of the SFRC mixes was much better for mixes employing short fibers probably due to the size effect between fiber lengths and specimen sizes. As a result, the reproducibility of test results were better for the mixes with shorter fibers.

- 2) Unconfined compressive strengths were found to level off at 50 days of age, indicating that the cubical tests in the final series could be conducted after this time without increasing concrete strength with age becoming an additional variable.
- 3) The deformed ZP 50/.50 fiber in the P1 mix only gave slight improvements over plain concrete strength and stiffness, but large improvements in tensile strength. Conversely, the straight "Fibercon" fiber in the P5 mix improved compressive strength and stiffness significantly but offered little to tensile strength. In general, the deformed fibers are superior to the straight fibers in load carrying capacity in tension, for the same volume percentage. One should not consider only fiber aspect ratio in analyzing results but also examine the effects of the number of fibers per cu. in. of concrete and especially fiber length on strengths.
- 4) Since the purpose of the preliminary tests was to study the effects of fiber aspect ratio and/or fiber length on different material properties and to choose

one fiber based on these tests, the "Fibercon" fiber was not to be considered for use in the final test series because it was straight and only one aspect ratio of this fiber type was available for this research.

- 5) Mix number P3 employing the ZP 30/.40 deformed fiber produced results intermediate with all the other mixes tested in the preliminary series. The consistency of this mix was good and reproducibility of test results were very good. Above all, workability was a very important consideration in choosing a SFRC mix primarily for the ease with which the test specimens could be prepared. It was intended from the start to use one of the deformed fibers rather than the straight fiber so the effect of aspect ratio for all the same type of fibers could be investigated. The ZP 30/.40 fiber, having the greatest quantity per cu. in. of concrete of all the deformed fibers, was one of the two shortest deformed fibers used. Therefore the size effect between specimen size and fiber length would be less likely seen.

From the above criteria, the ZP 30/.40 fiber was selected for the final three-dimensional test series. Material properties obtained for this mix in the preliminary test series are summarized as follows with percent improvements over plain concrete shown in parentheses:

- a) 50 day Secant Modulus of Elasticity in Unconfined Compression (E) = 3570 ksi (1.4%)

b) 50 day Unconfined Compressive Strength (f'_c) = 9099 psi
(18.1%)

c) 28 day Indirect Tensile Strength (T) = 953 psi (45.1%)

d) 28 day Flexural Strength (R) = 855 psi (32.4%)

Using the ZP 30/.40 deformed fiber, two mixes identical to P3 were cast for the final test series according to the procedures outlined in Chapter 2. Each casting produced twenty four 4-in. cubical test specimens and a number of 3x6 in. cylindrical control specimens.

CHAPTER 4

FINAL TEST SERIES

4.1 Introduction

Recall from Chapter 3 the decision to use the Bekaert "Dramix" ZP 30/.40 steel fiber for the final series of tests. This chapter presents the stress-strain and strength results of the CU-SFRC, employing only that fiber, for the tests conducted on 3 x 6 in. control cylinders tested in unconfined compression and for the extensive tests on 4 in. cubes tested in multiaxial compression. No constitutive relations regarding stress-strain or strength behavior are discussed. They are in Chapter 5.

The two identical mixes in the final test series are labeled F1 and F2 and were cast and cured identically to each other and to the P3 mix from the preliminary test series. The casting and curing procedures, sample preparation, test procedure, etc., are discussed in detail in Chapter 2.

TABLE 2.7 gives the details of the 3 x 6 in. cylinder test program for this series of tests. Section 4.2 presents the results of these simple tests, with comparisons made to the same tests conducted on mixes in the preliminary series.

TABLE 2.8 gives the 4 in. cube test program details for the multiaxial compression tests. Section 4.3.1 and 4.3.2 present the

stress-strain results in principal and octahedral form for these tests. Stress-strain summary curves are also presented as well as average results, and discussion of the observed stress-strain behavior is given. In Section 4.3.3, the results of some specialized tests to determine the elastic material constants along with the theory behind those tests are presented. Finally, the failure strengths of the SFRC specimens with discussions for the observed strengths are given in Section 4.3.4.

4.2 Unconfined Compression

The tests for compressive strength of the 3 x 6 in. cylindrical control specimens in this, the final test series, were performed identically to those in the preliminary series. The procedure has been described fully in Section 3.2.1.

The stress-strain envelopes for these tests on identical mixes (F1 and F2) are shown in Figs. 4.1 and 4.2 respectively. All the tests were done in triplicate and in these figures, specimen age is the variable. Note the good reproducibility of the stress-strain results for identically aged specimens. Figs 3.23 and 4.3 show the average unconfined compressive strength (f'_c) and the average secant modulus E (ASTM C469-65), respectively, for cylindrical specimens from mixes F1 and F2. Note in all the aforementioned figures, as in identical tests for the preliminary series, that due to the curing procedure described in Section 2.4 there is a rapid increase in strength and stiffness between the 7 and 14 (or 16) day tests, then a much slower increase in strength and stiffness for specimen ages

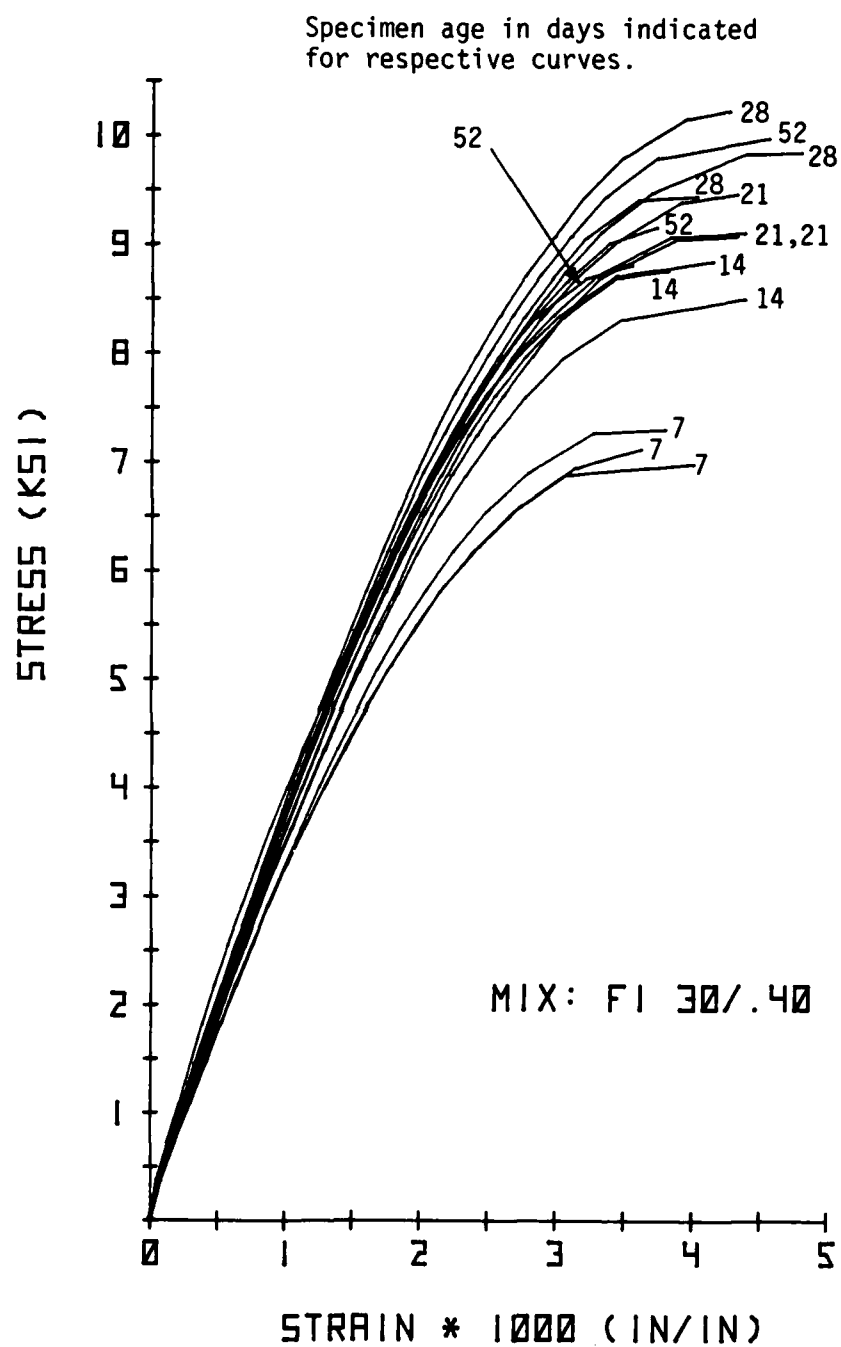


Fig. 4.1. Unconfined Compression Stress-Strain Curves for 3x6 in. Cylinders.

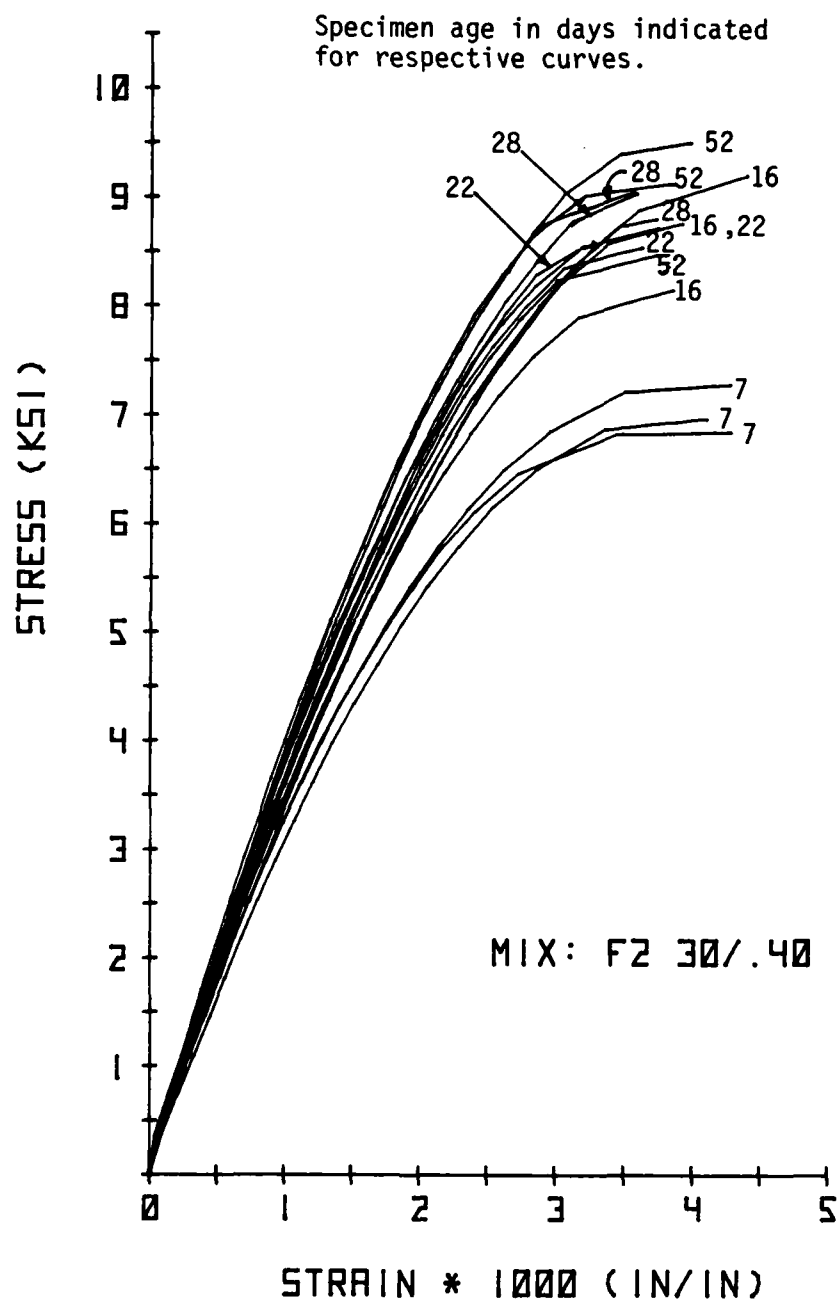


Fig. 4.2. Unconfined Compression Stress-Strain Curves for 3x6 in. Cylinders.

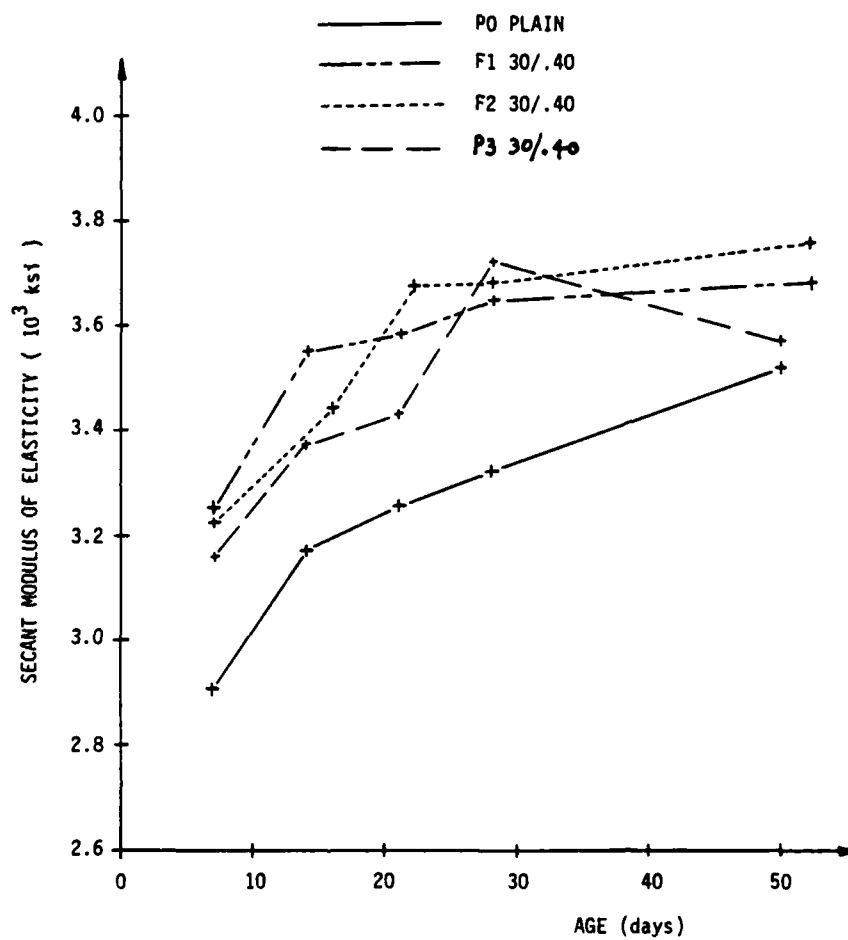


Fig. 4.3. Secant Modulus of Elasticity vs. Age for the Unconfined Compression Tests on 3x6 in. Cylinders.

beyond 14 days where gradual leveling off begins. One can see from Fig. 3.23 that for identical mixes (P3, F1 and F2) that were cast at different times, some scatter in compressive strength for the same age is present. However, note the small variations in strength results at or near 50 days. Good reproducibility is observed in the stiffness values shown in Fig. 4.3 for the F1 and F2 mixes. Notice also the increased fiber reinforced concrete stiffness over that of plain concrete for all ages.

Tabulated values of f'_c and E for the plain concrete mix (P0) and the three identical fiber concrete mixes (P3, F1 and F2) are given in TABLE 4.1, with percent improvements over the plain concrete properties shown in parentheses.

4.3 Multiaxial Compression

In the following subsections, the results of all the multiaxial compression tests on 4 in. cubes tested in the final series are presented. Section 2.8 - Part 2 gives the details of the procedure for these tests with TABLE 2.8 listing the type of tests conducted on each specimen. To repeat again, these monotonic tests were conducted by loading the specimens hydrostatically to one of three specified levels of hydrostatic stress ($\sigma_0 = 4, 6$ or 8 ksi) subsequently followed by shear deviation at that constant hydrostatic stress along one of the three prescribed stress paths shown in Figs. 2.31 and 2.32. Stress-strain and strength data was collected for the tests and is presented below. Compressive stresses and strains are assumed to be positive and the applied stresses and measured strains in the three loading directions are

TABLE 4.1
SUMMARY OF AVERAGE STRENGTHS AND SECANT MODULI
FOR CYLINDERS IN UNCONFINED COMPRESSION *

* PERCENT INCREASES OVER PLAIN CONCRETE
VALUES INDICATED IN PARENTHESES.

Result Mix No.	Unconfined Compressive Strength of Cylinders (psi) 50-52 day f'_c	Secant Modulus of Elasticity of Cylinders (ksi) 50-52 day E
P0 Plain	7707	3520
P3 Dramix 30/.40	9099 (18.1%)	3570 (1.4%)
F1 Dramix 30/.40	9305 (20.7%)	3682 (4.6%)
F2 Dramix 30/.40	9035 (17.2%)	3757 (6.7%)

regarded as the principal stresses and strains. Tabulated principal and octahedral stress-strain data for all tests in the final series is given in Appendix A.

4.3.1 Principal Stress-Strain Relations

The principal stress-strain curves obtained for these tests are plotted individually in Figs. 4.4 - 4.31. Figs. 4.32 - 4.40 show the same results plotted together for identical tests on different specimens in order to examine the scatter present from one specimen to the next. In all these figures, the results are plotted as the major principal stress (σ_1) normalized with respect to the hydrostatic stress at the respective octahedral plane for that test (σ_{om}) versus all principal strains and volumetric strain ($\epsilon_v = \epsilon_1 + \epsilon_2 + \epsilon_3 = \epsilon_x + \epsilon_y + \epsilon_z$). In other words, σ_{om} is the maximum value of hydrostatic stress employed in the test. All curves are labeled with an x, y, z or v respectively for the normalized major principal stress (σ_1/σ_{om}) vs. principal strain ($\epsilon_1, \epsilon_2, \epsilon_3$ or $\epsilon_x, \epsilon_y, \epsilon_z$) results. It seems obvious which strain (ϵ_x, ϵ_y or ϵ_z) corresponds to the principal strains (ϵ_1, ϵ_2 or ϵ_3) but to prevent any confusion, refer to Fig. 2.32 where the relationships between principal directions (1, 2 or 3) and the cubical specimens' reference directions (x, y or z) are given. Information regarding the specimen number, loading condition (TC, SS or TE) and the value of σ_{om} (4, 6 or 8 ksi) for the test are also given in each figure.

Three different strain scales were used for presenting the results for no other reason than to be able to "see" the

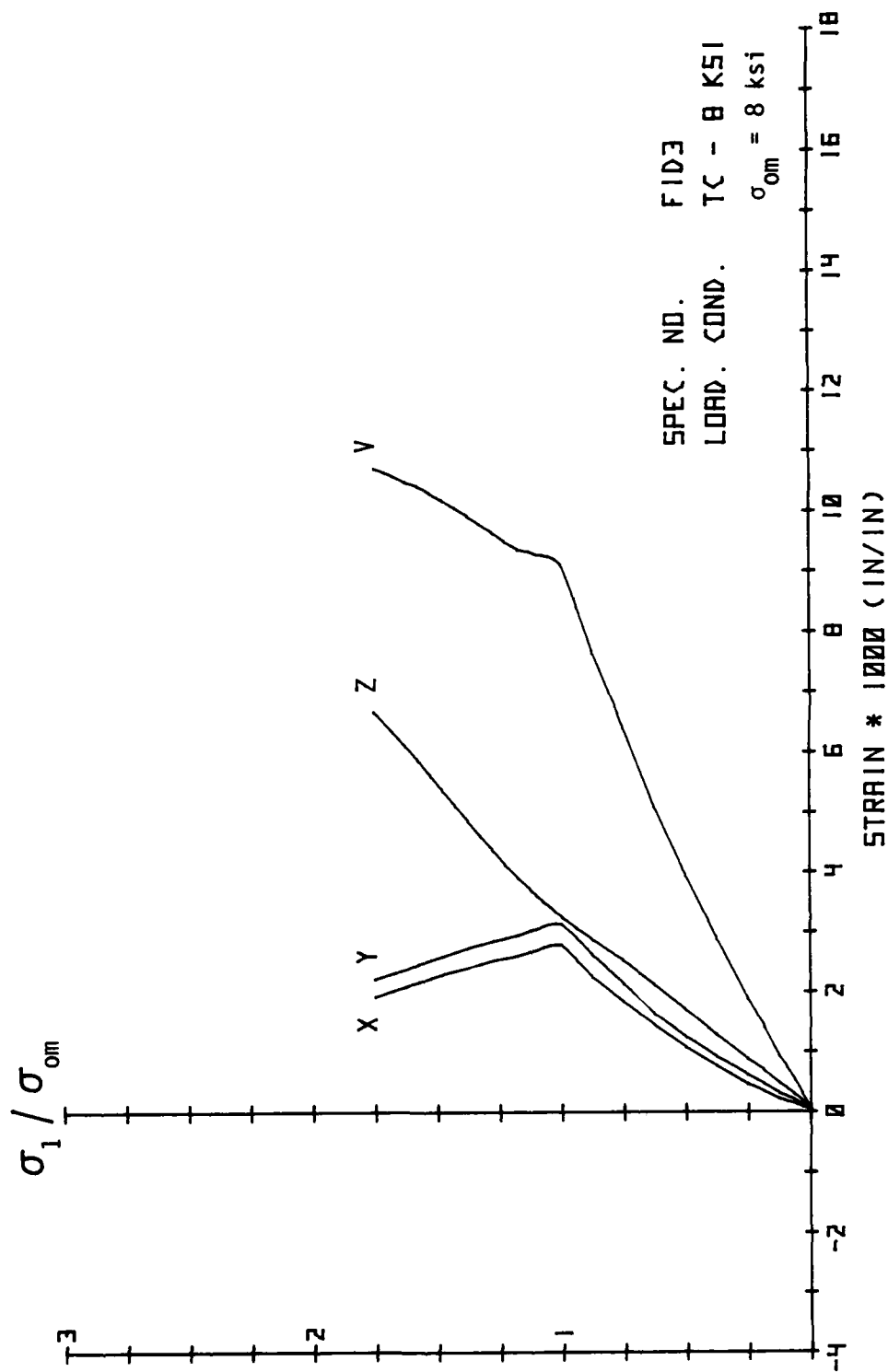


Fig. 4.4. Principal Stress-Strain Results.

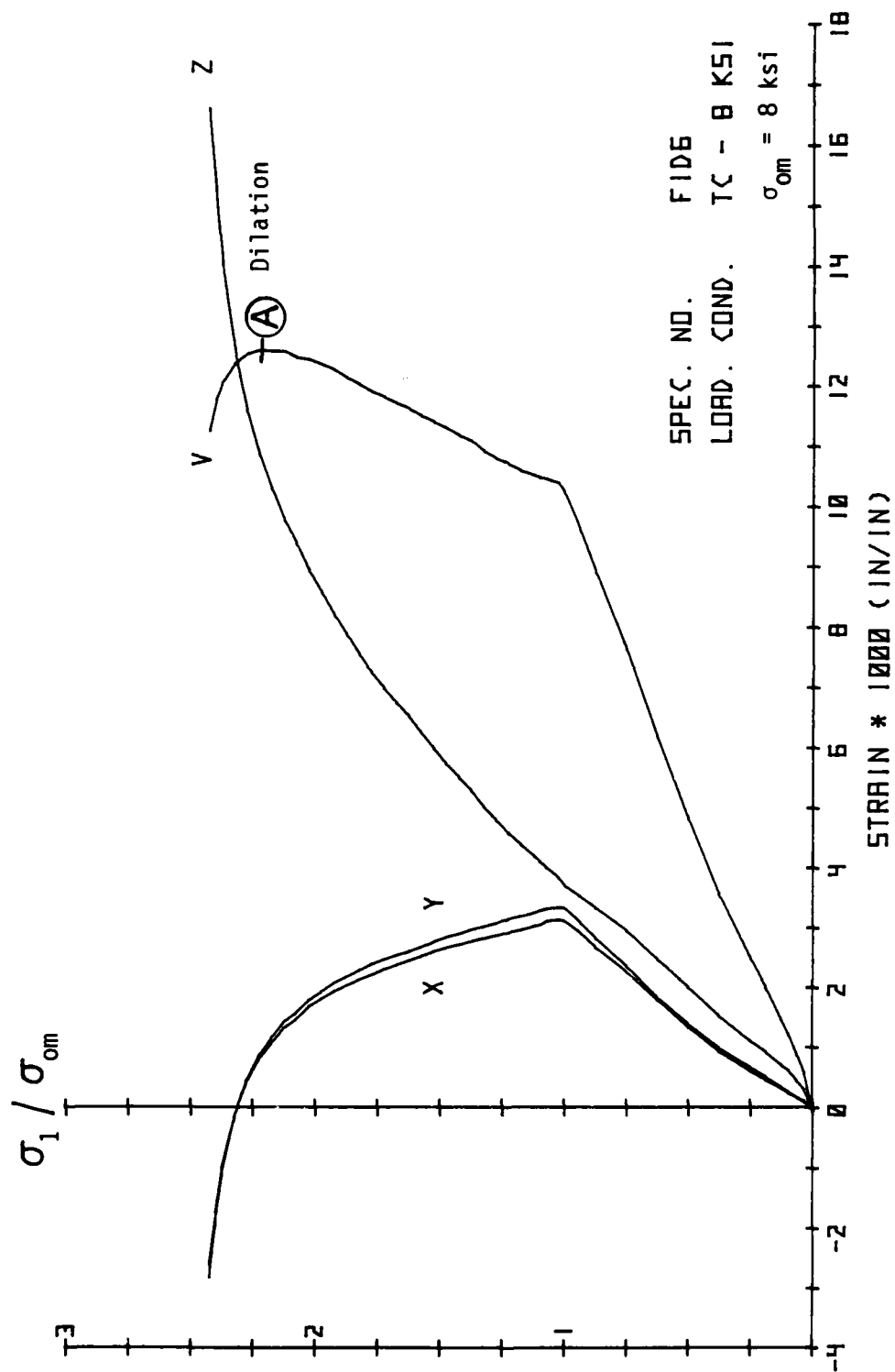


Fig. 4.5. Principal Stress-Strain Results.

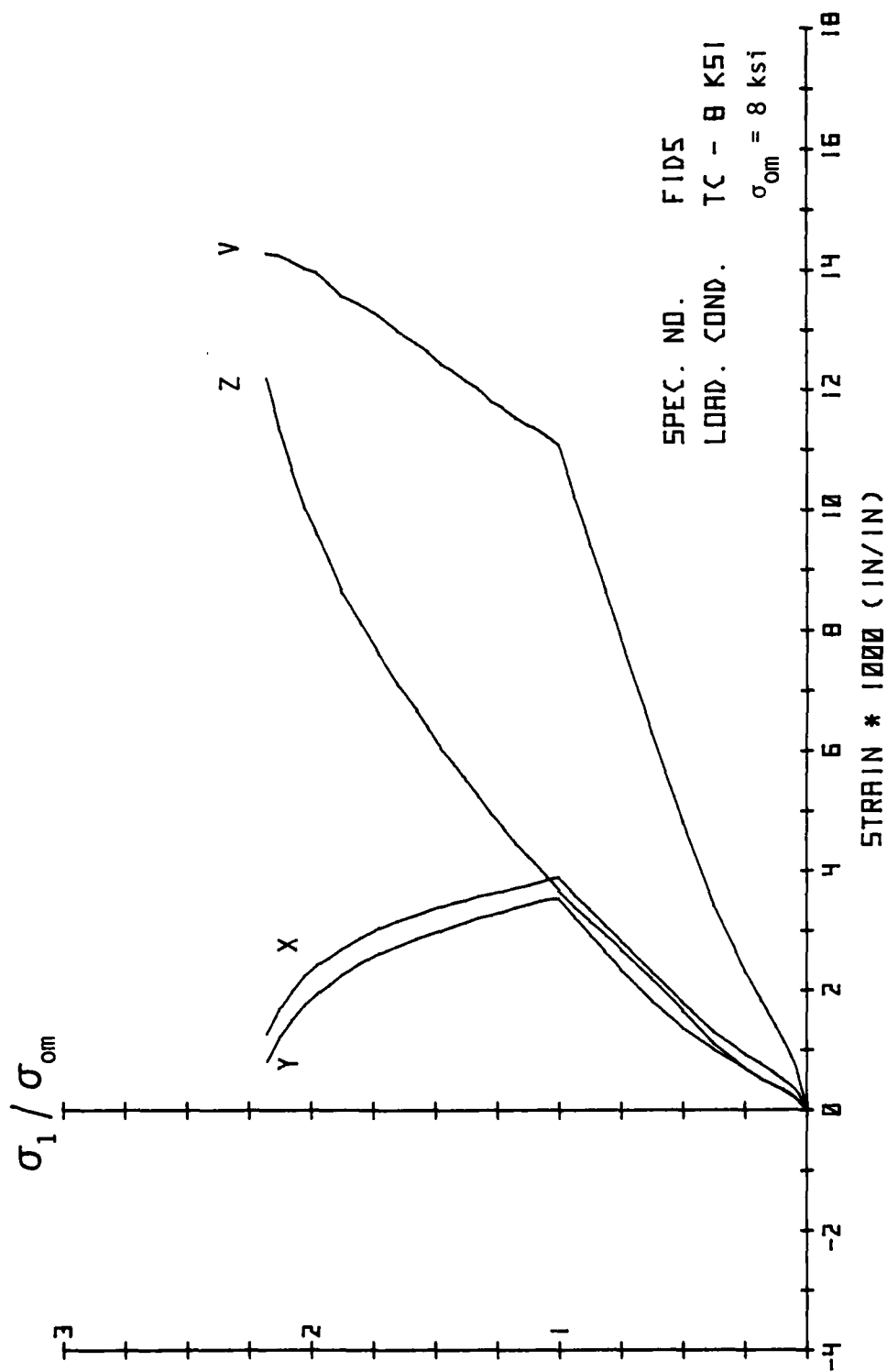


Fig. 4.6. Principal Stress-Strain Results.

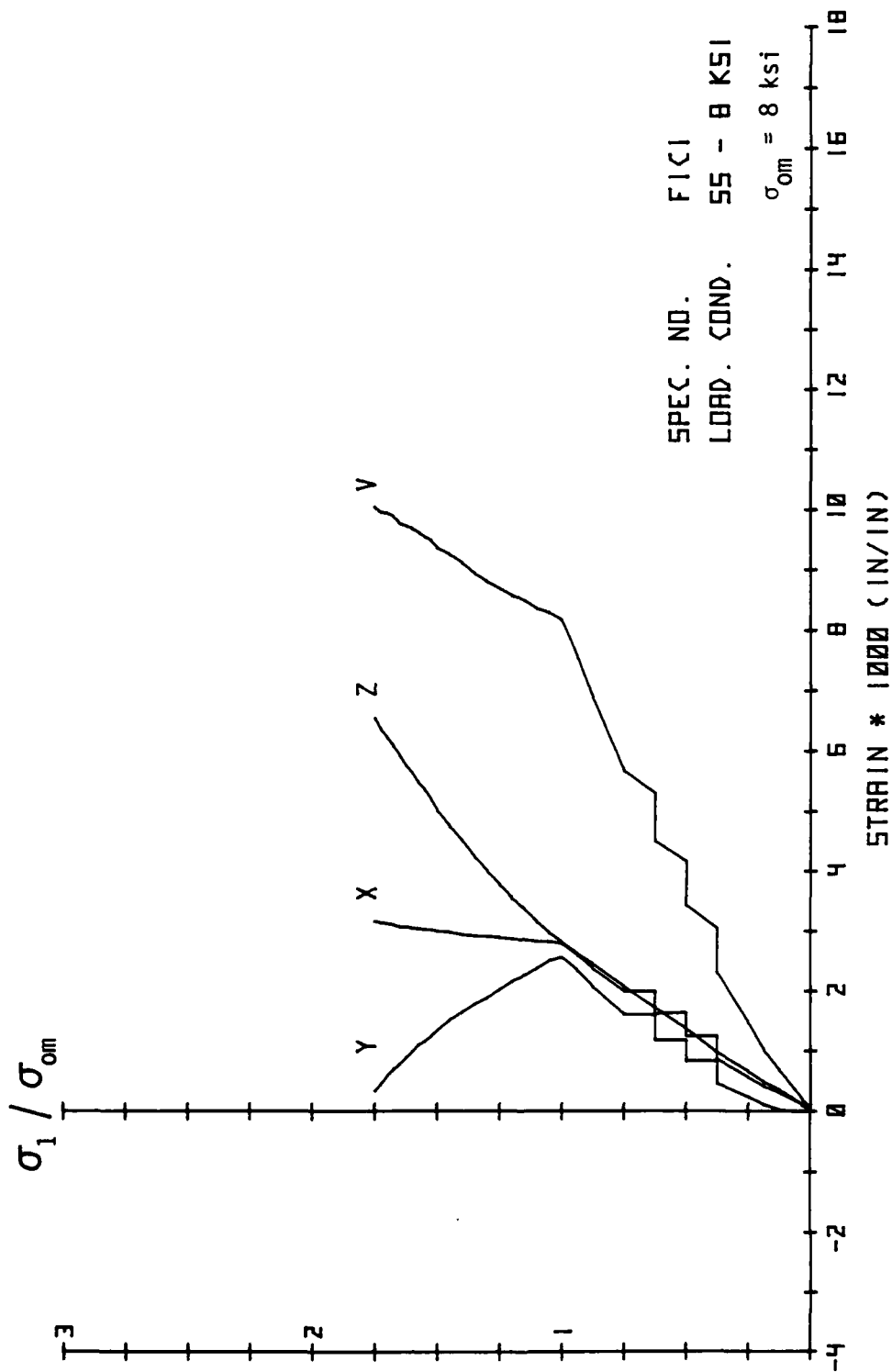


Fig. 4.7. Principal Stress-Strain Results.

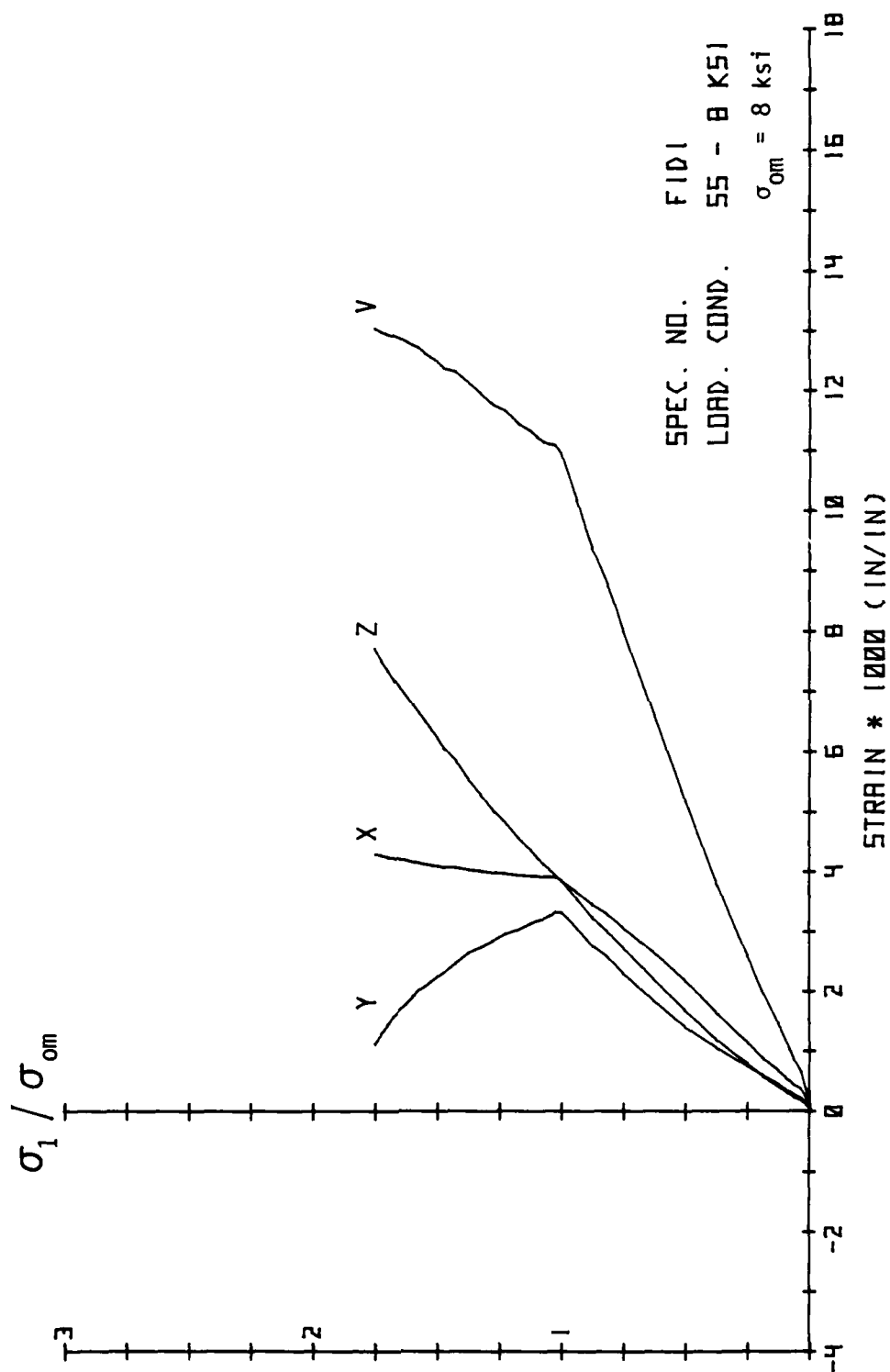


Fig. 4.8. Principal Stress-Strain Results.

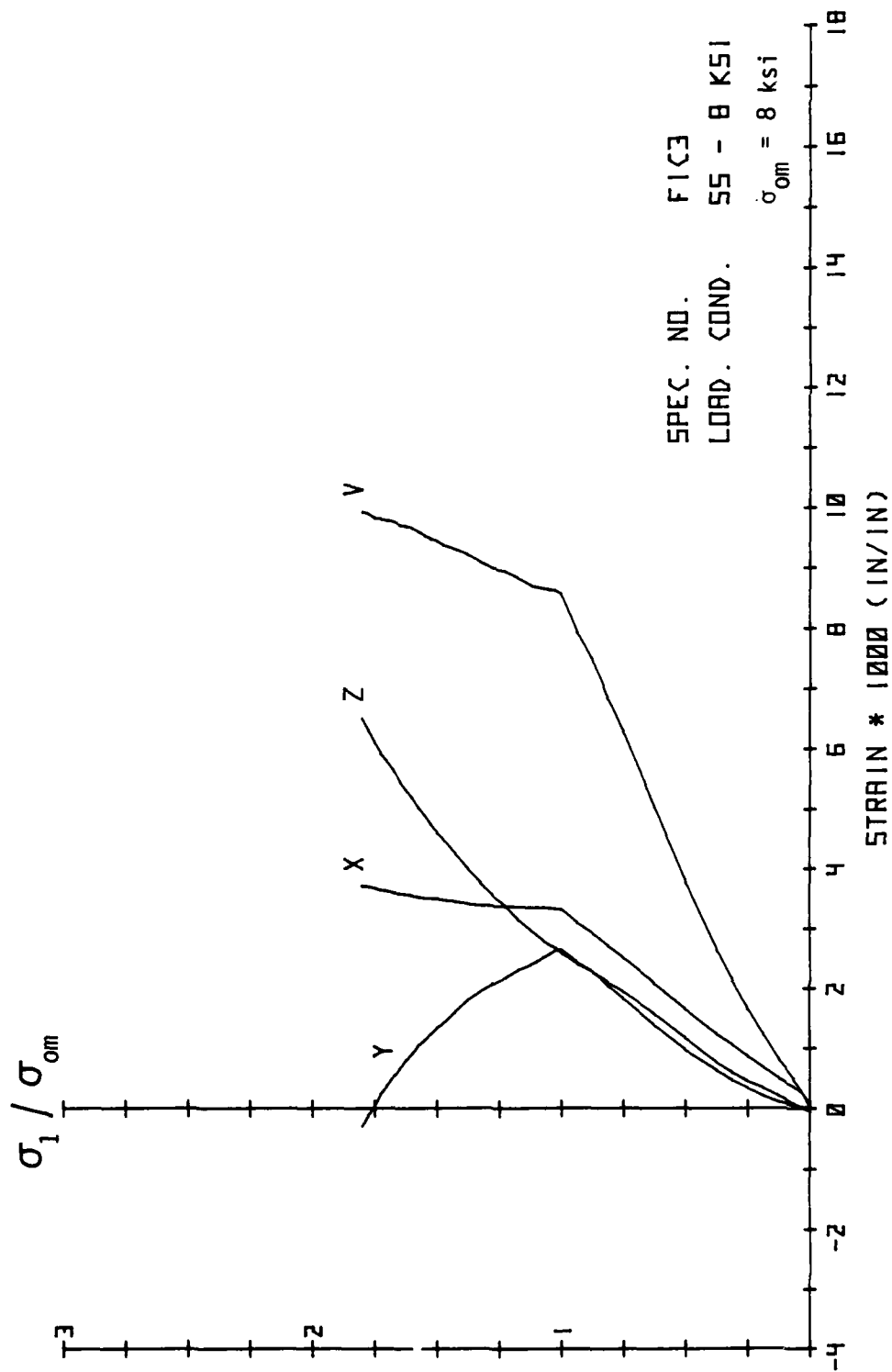


Fig. 4.9. Principal Stress-Strain Results.

AD-A114 168

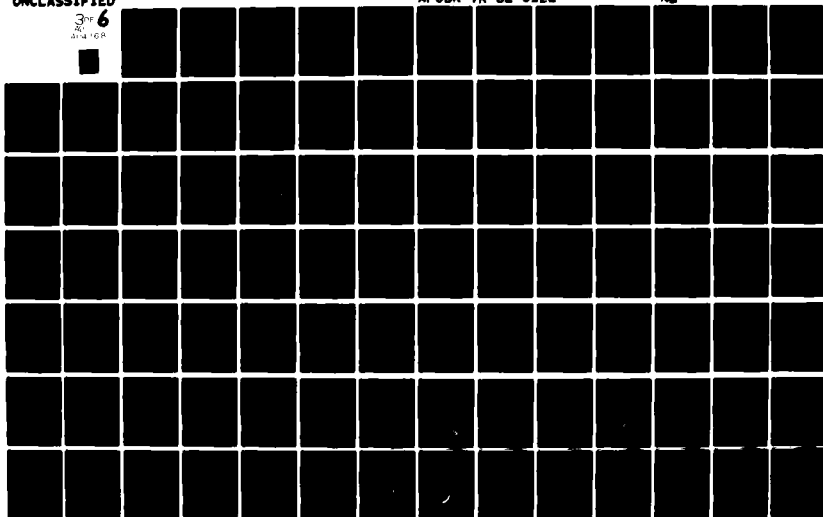
COLORADO UNIV AT BOULDER DEPT OF CIVIL ENVIRONMENTAL --ETC F/6 20/11
CONSTITUTIVE RELATIONS OF RANDOMLY ORIENTED STEEL FIBER REINFOR--ETC(U)
DEC 81 D E EGGING, H KO AFOSR-79-0065

UNCLASSIFIED

AFOSR-TR-82-0122

NL

3-6
24 FOR



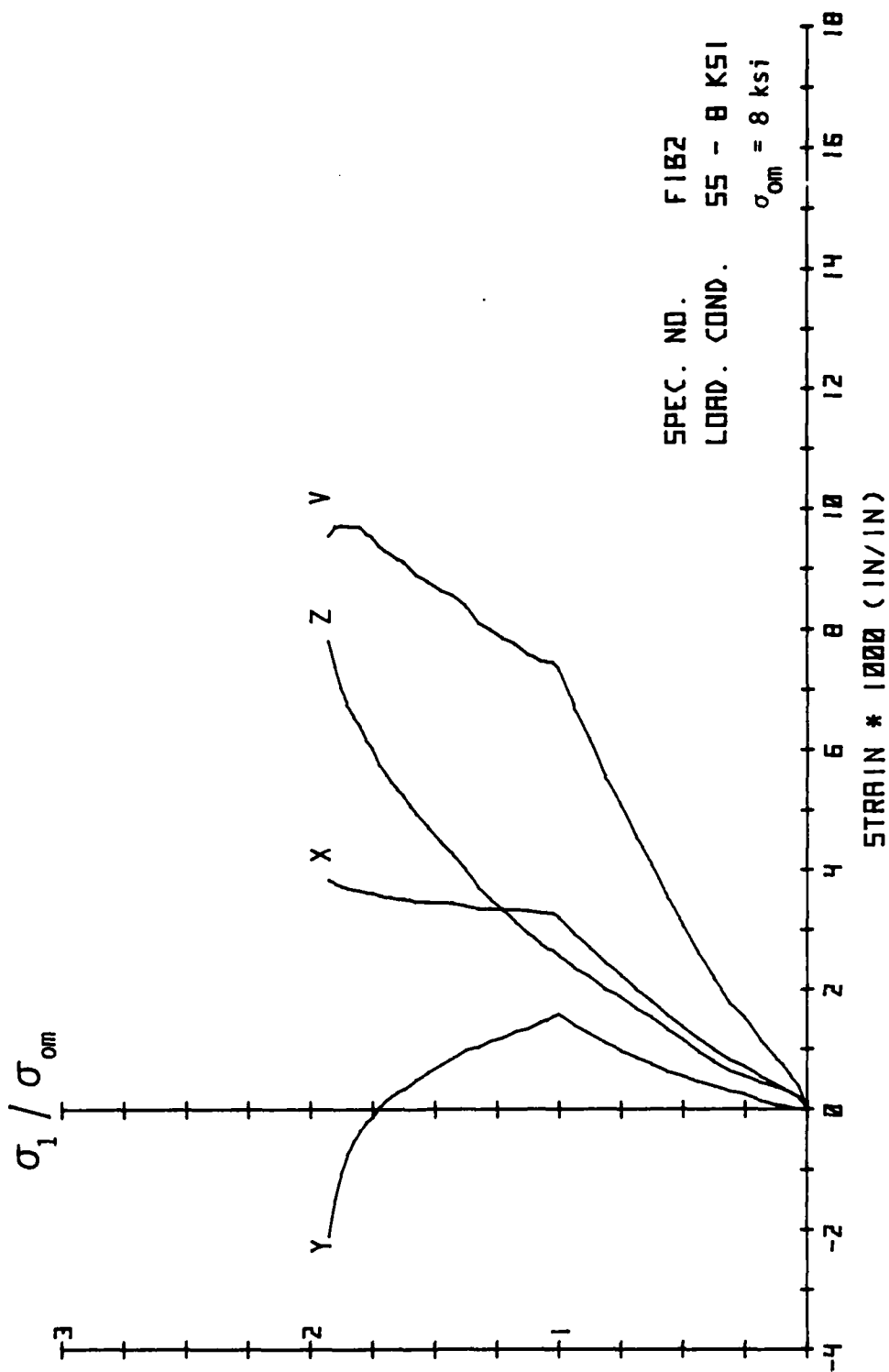


Fig. 4.10. Principal Stress-Strain Results.

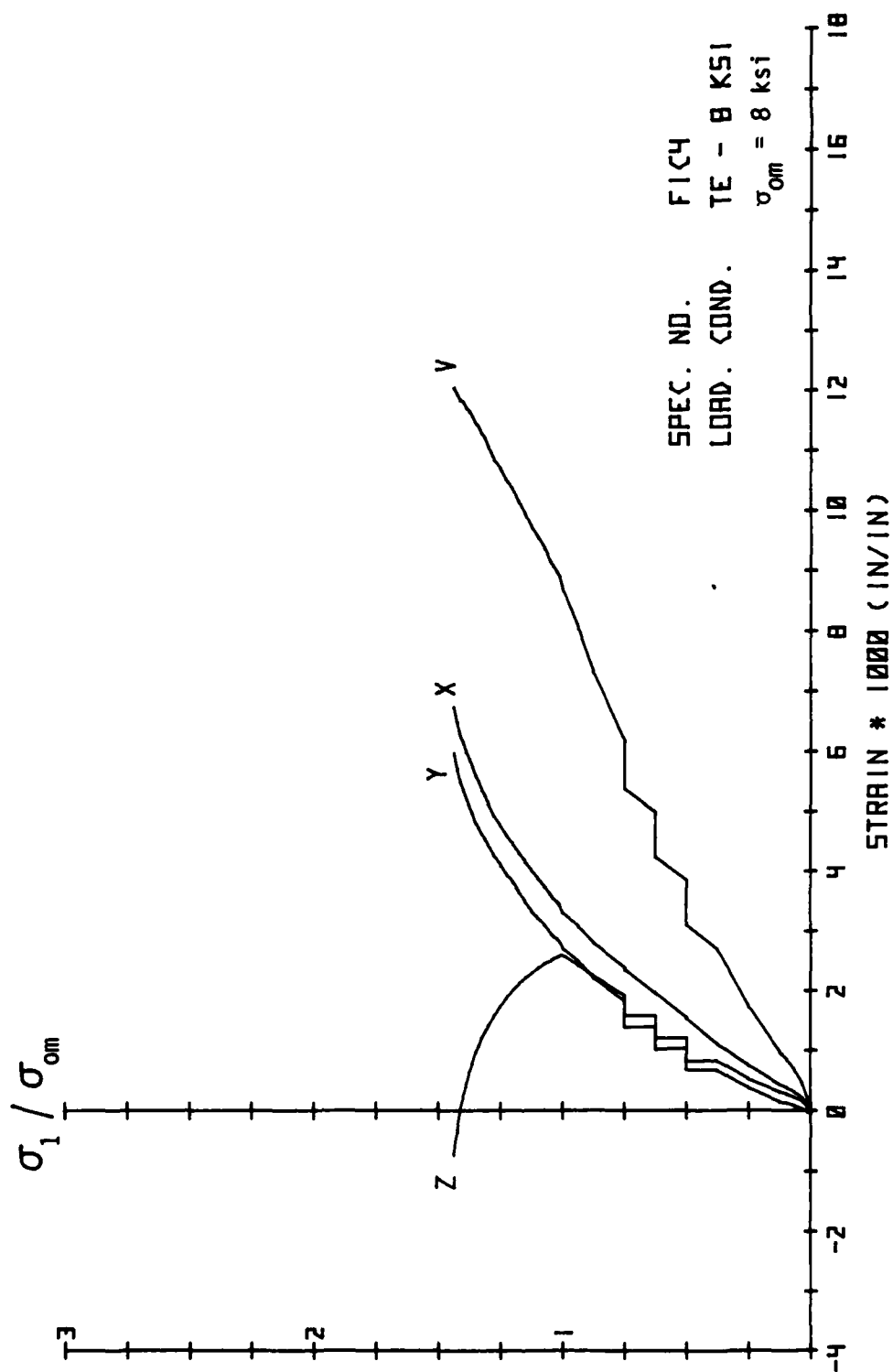


Fig. 4.11. Principal Stress-Strain Results.

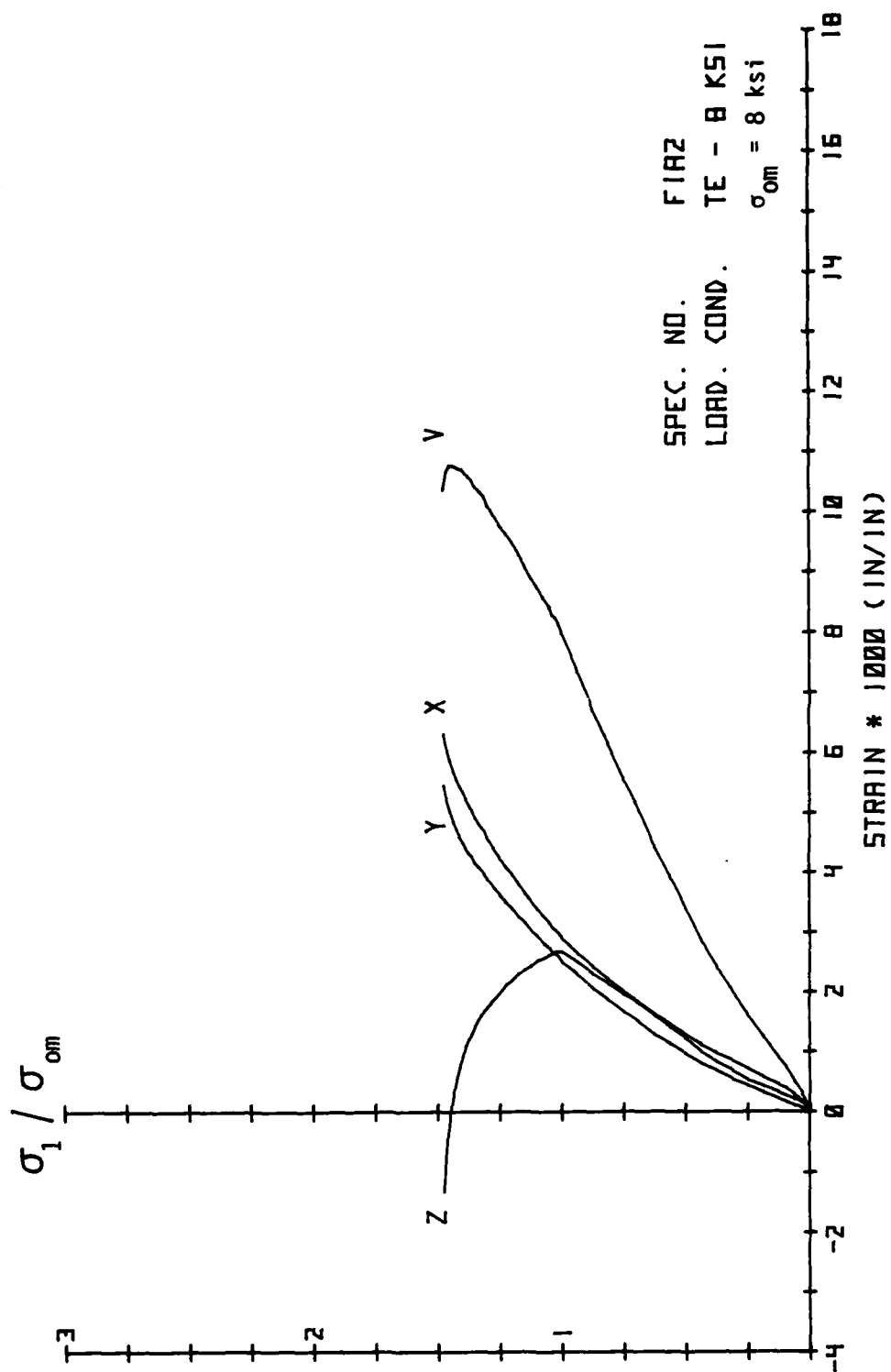


Fig. 4.12. Principal Stress-Strain Results.

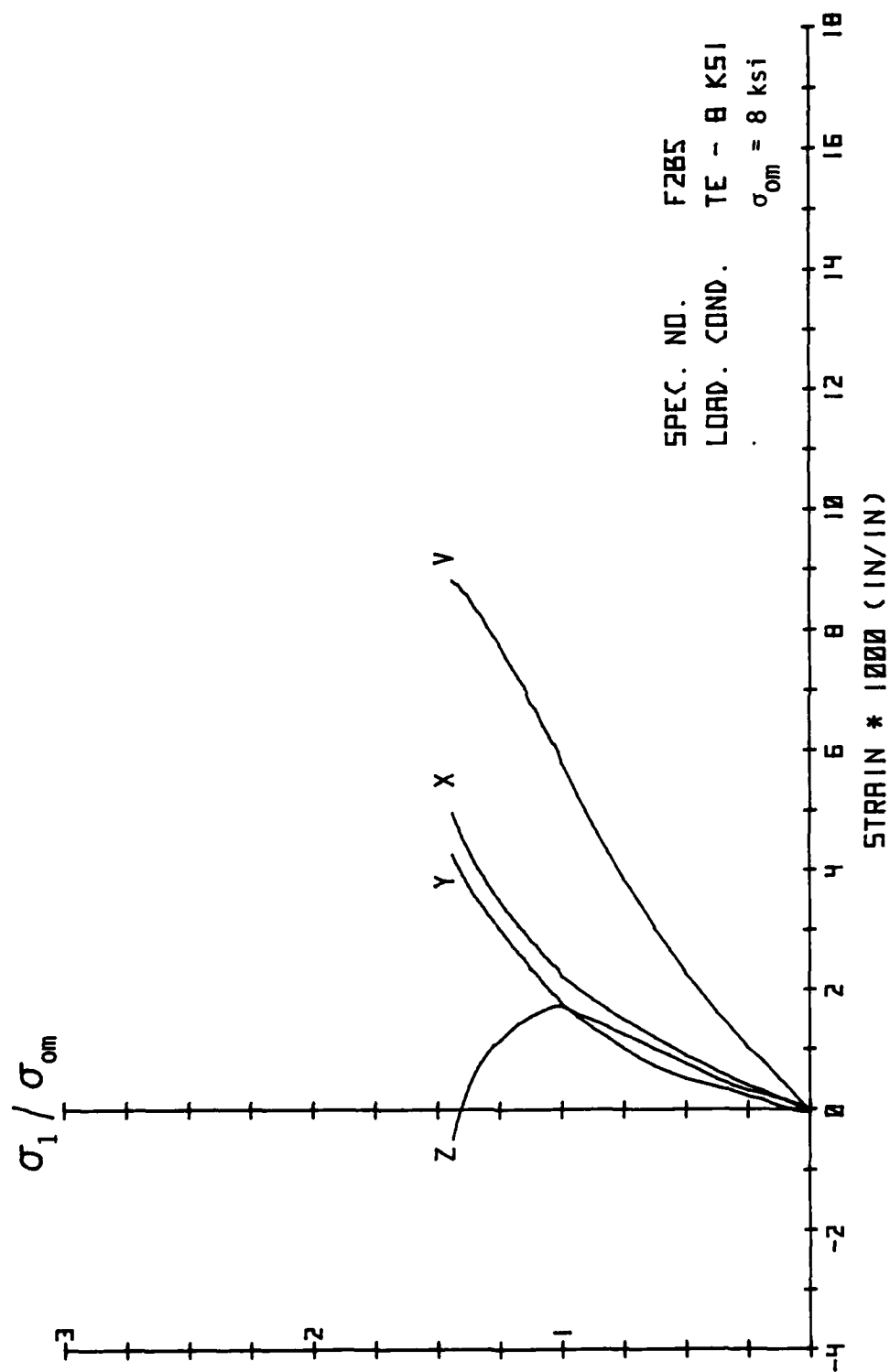


Fig. 4.13. Principal Stress-Strain Results.

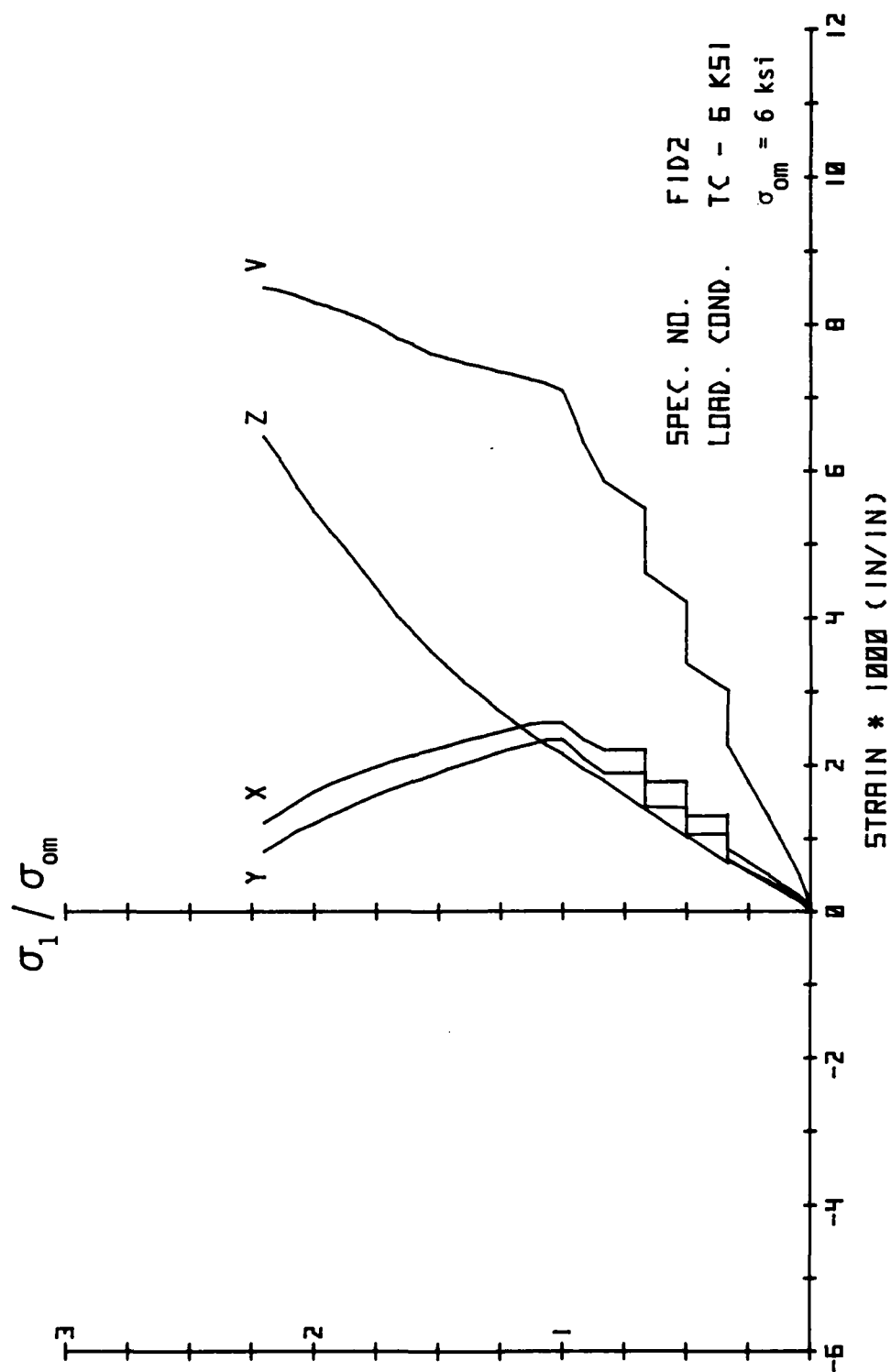


Fig. 4.14. Principal Stress-Strain Results.

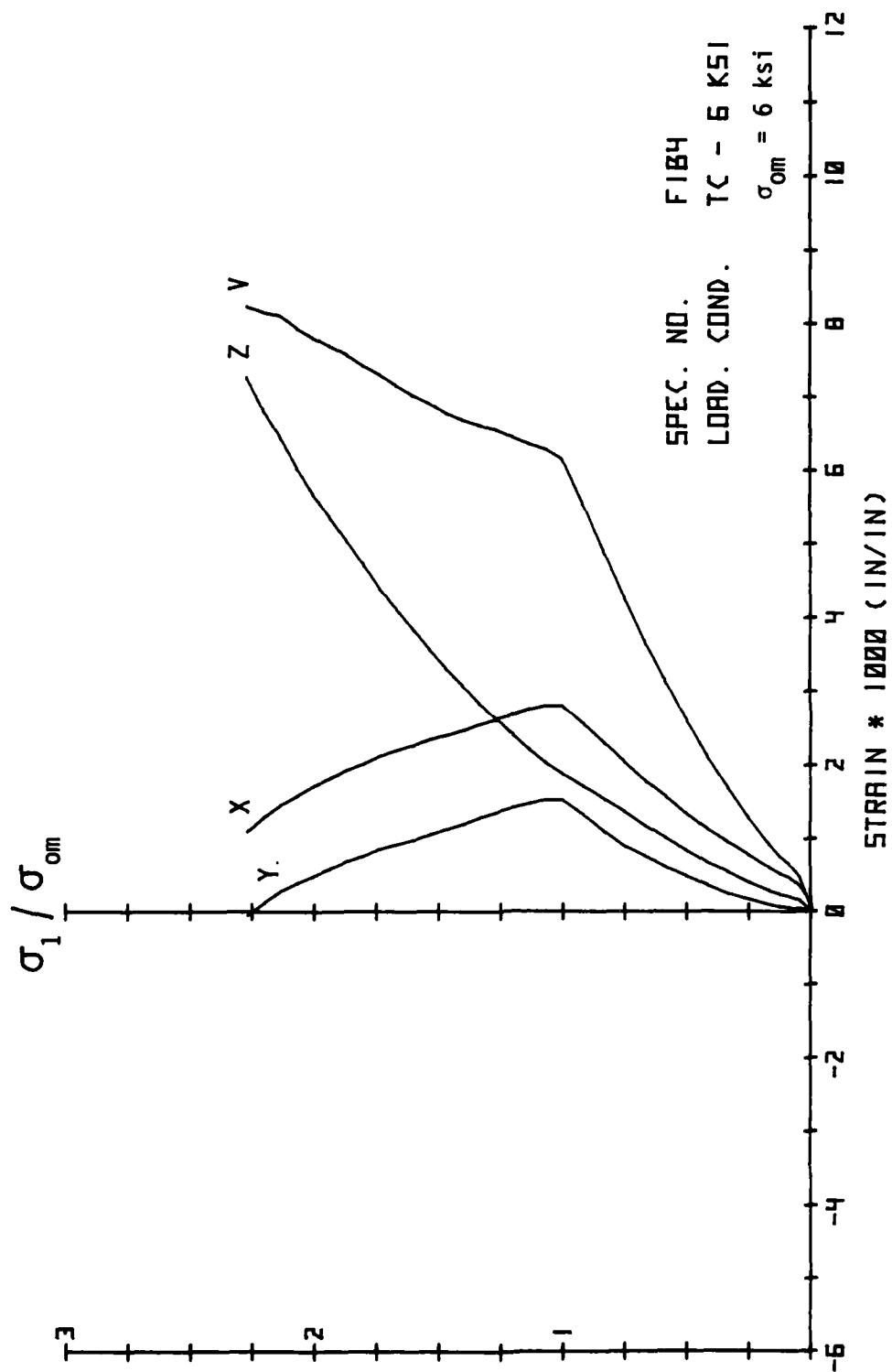


Fig. 4.15. Principal Stress-Strain Results.

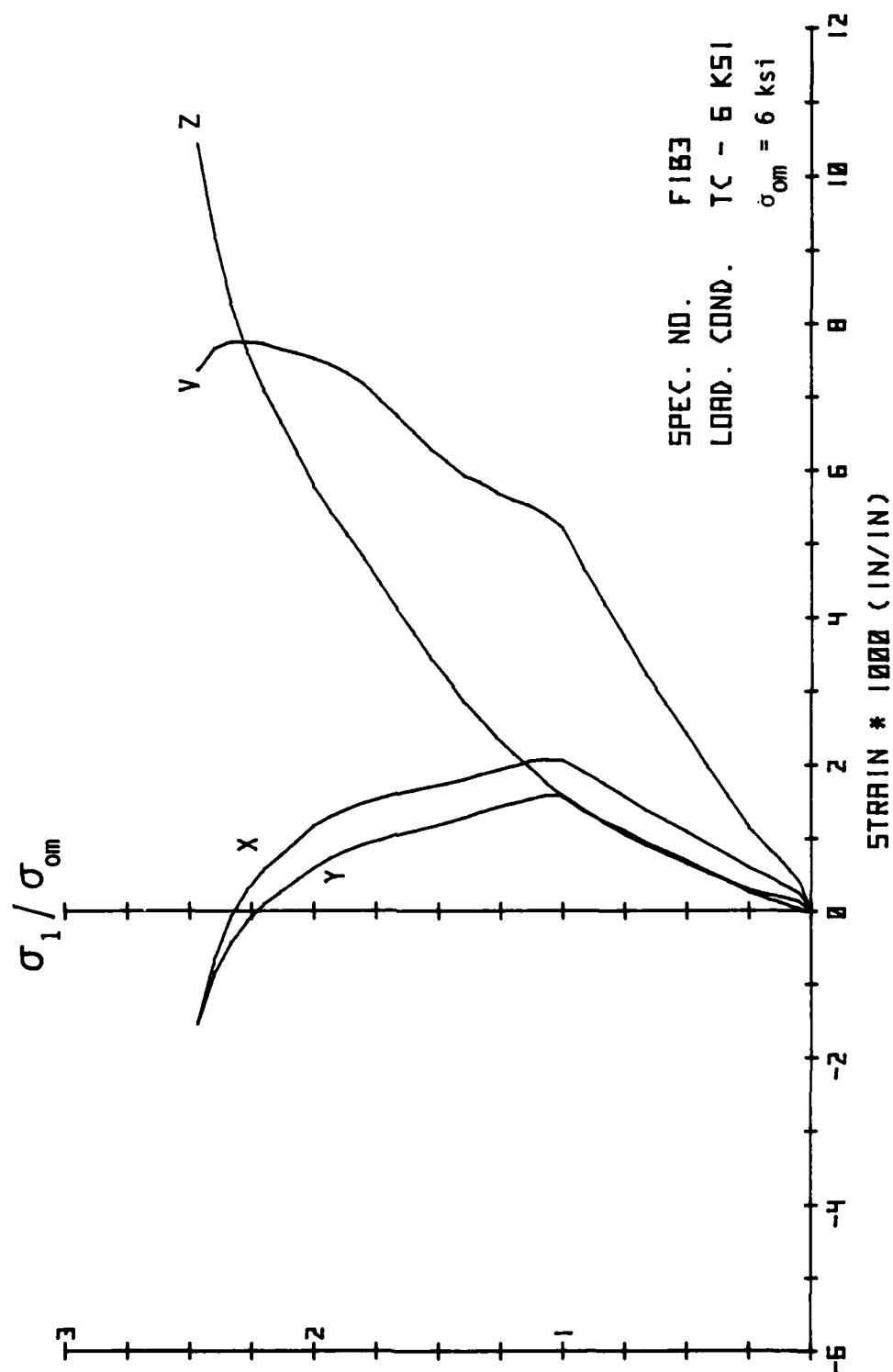


Fig. 4.16. Principal Stress-Strain Results.

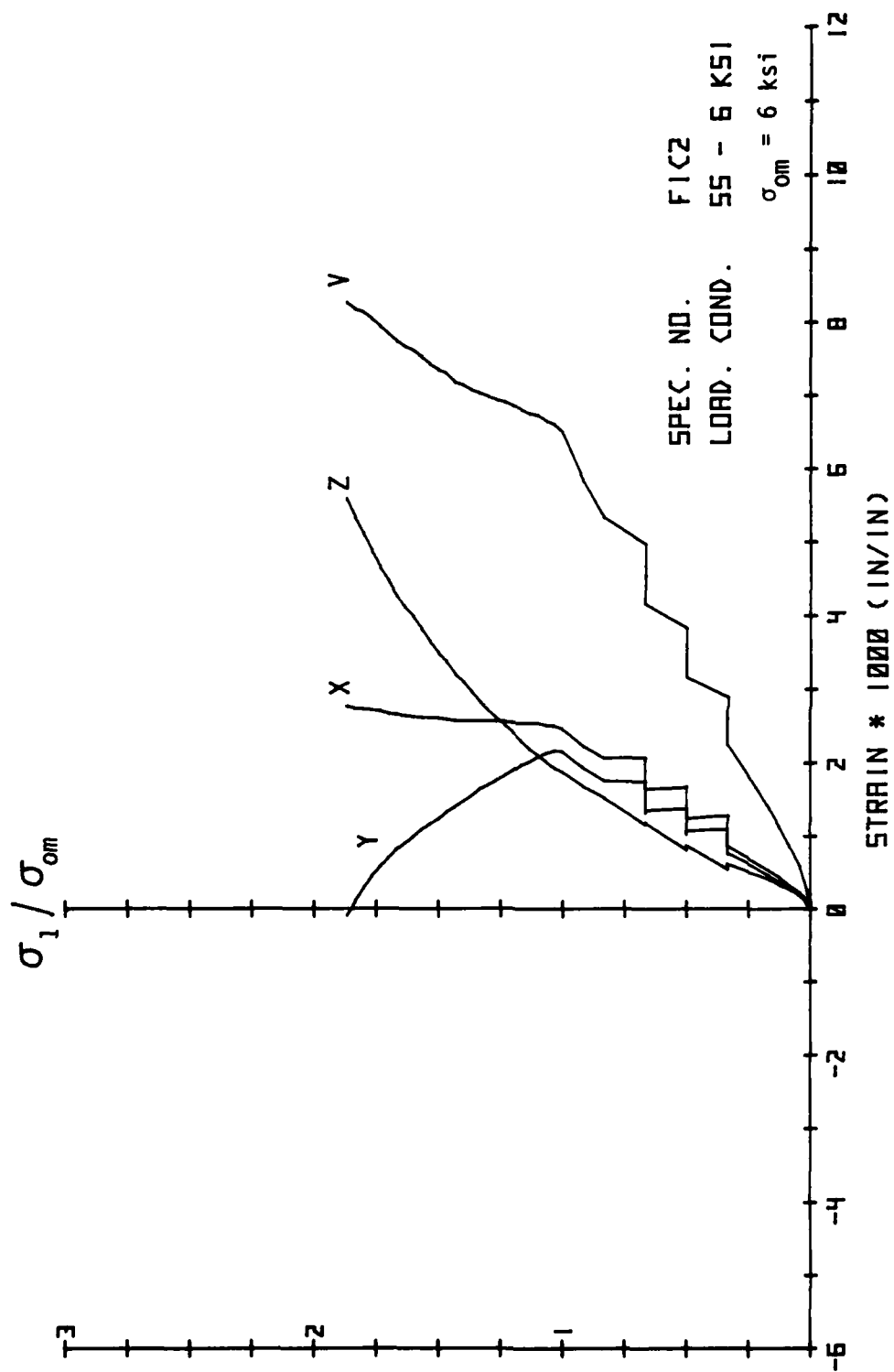


Fig. 4.17. Principal Stress-Strain Results.

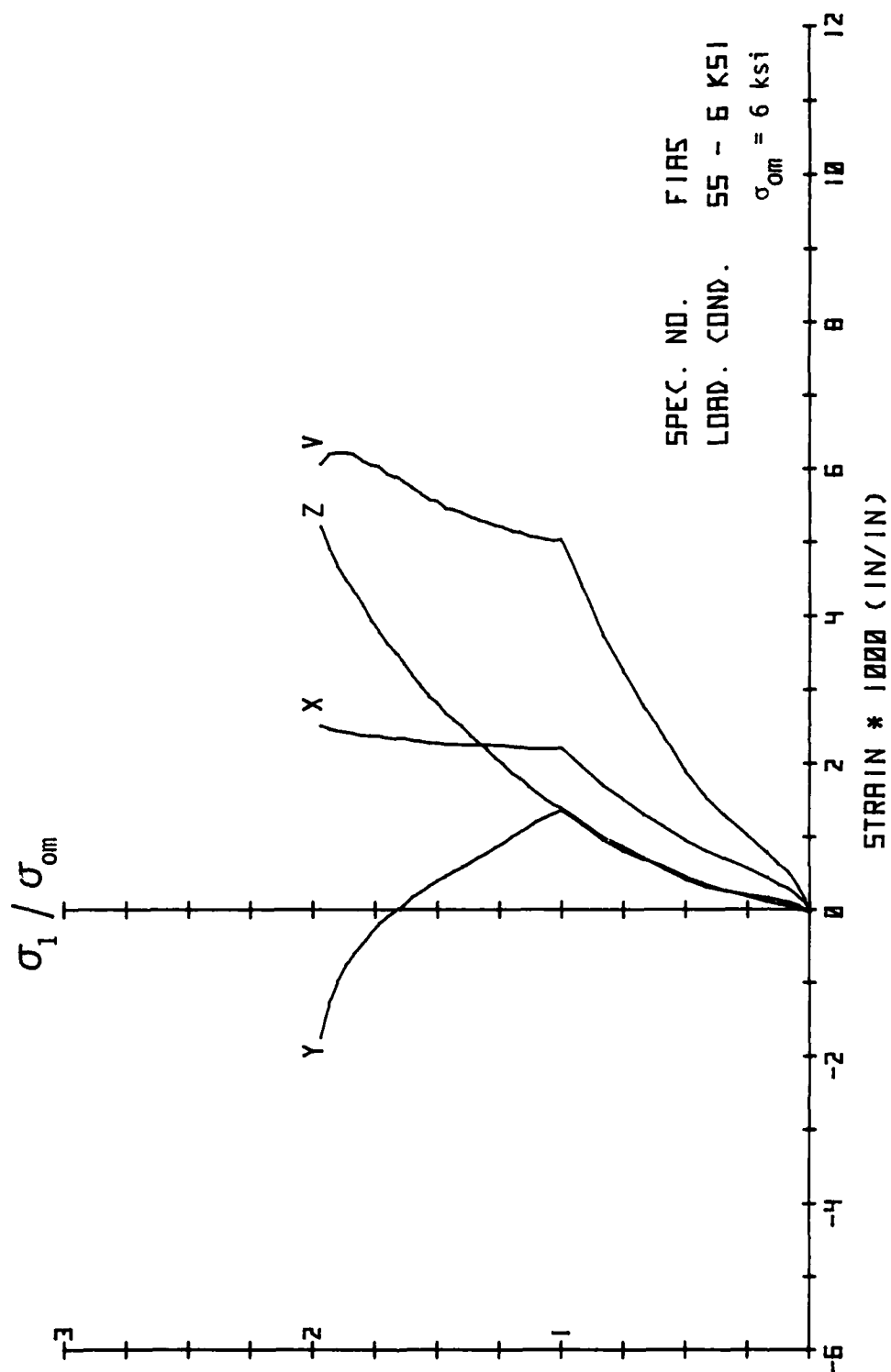


Fig. 4.18. Principal Stress-Strain Results.

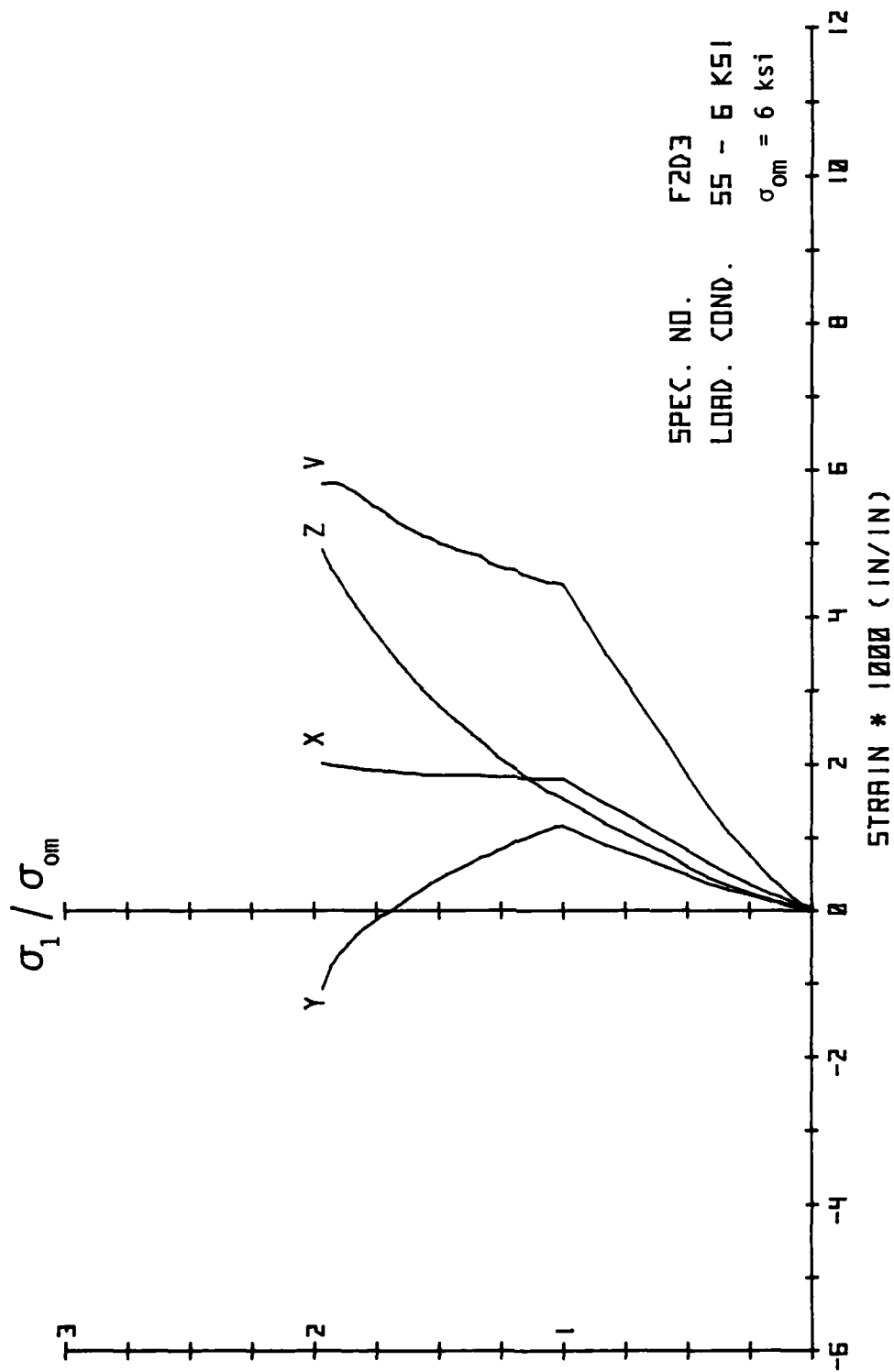


Fig. 4.19. Principal Stress-Strain Results.

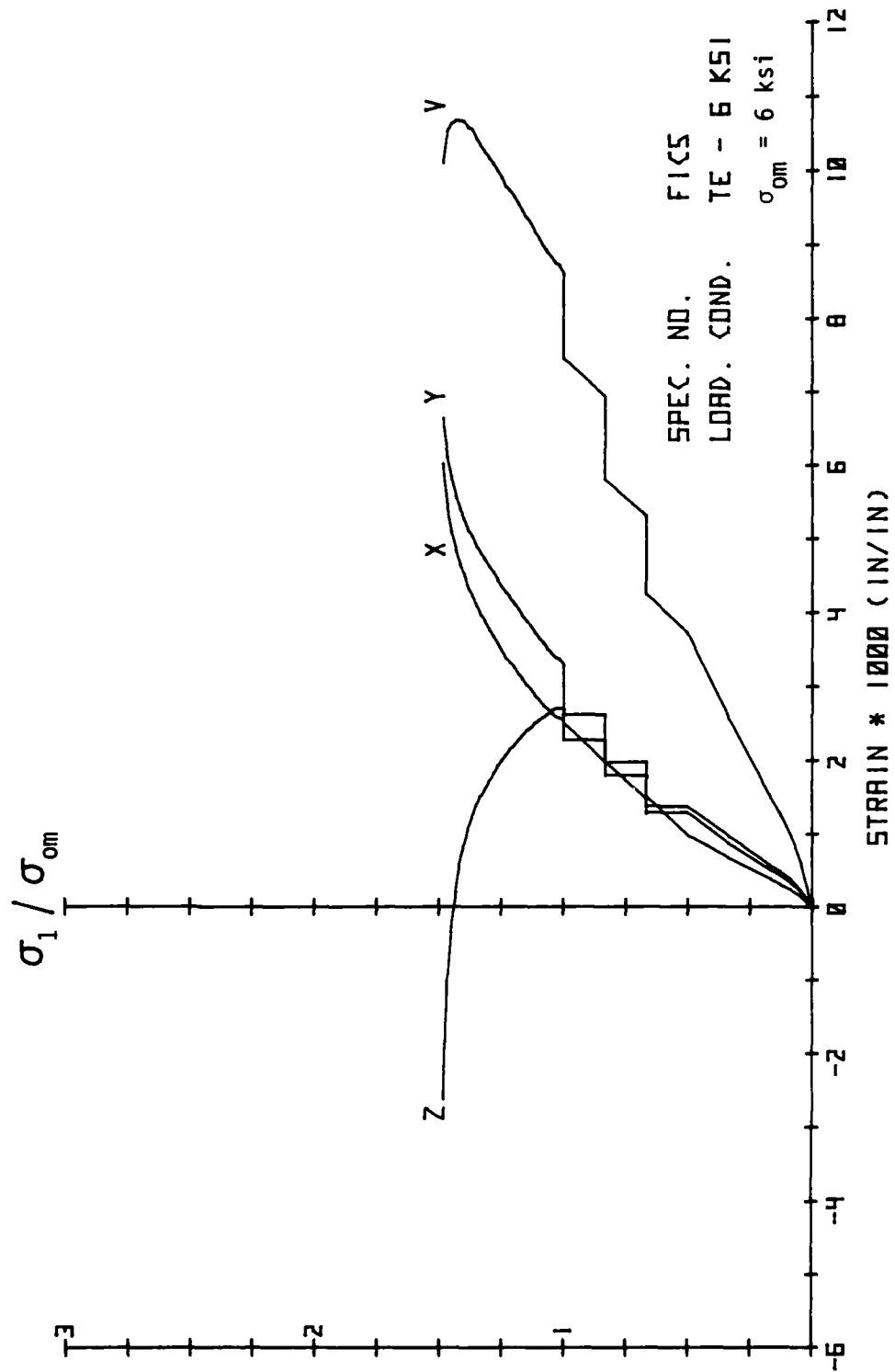


Fig. 4.20. Principal Stress-Strain Results.

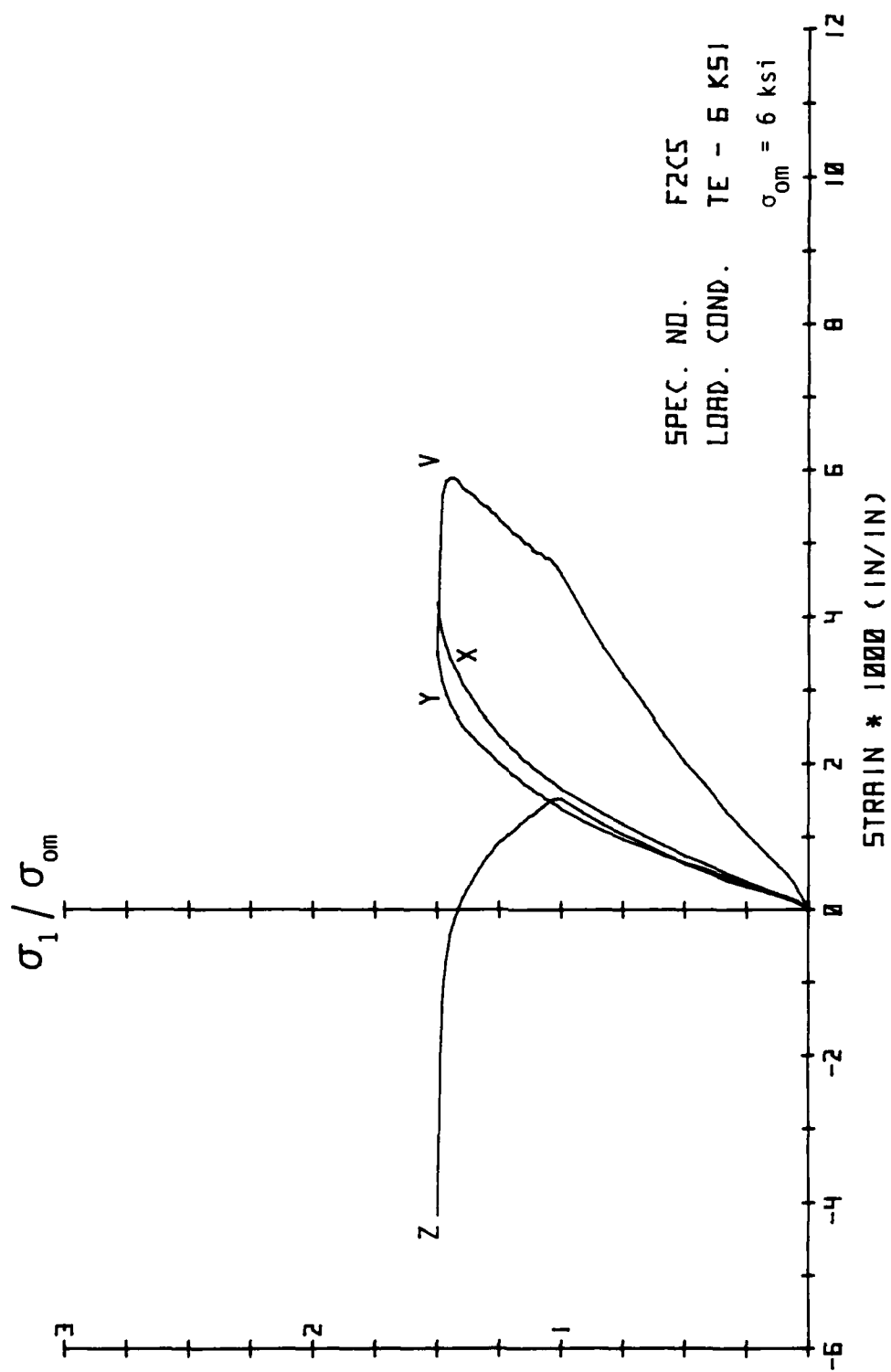


Fig. 4.21. Principal Stress-Strain Results.

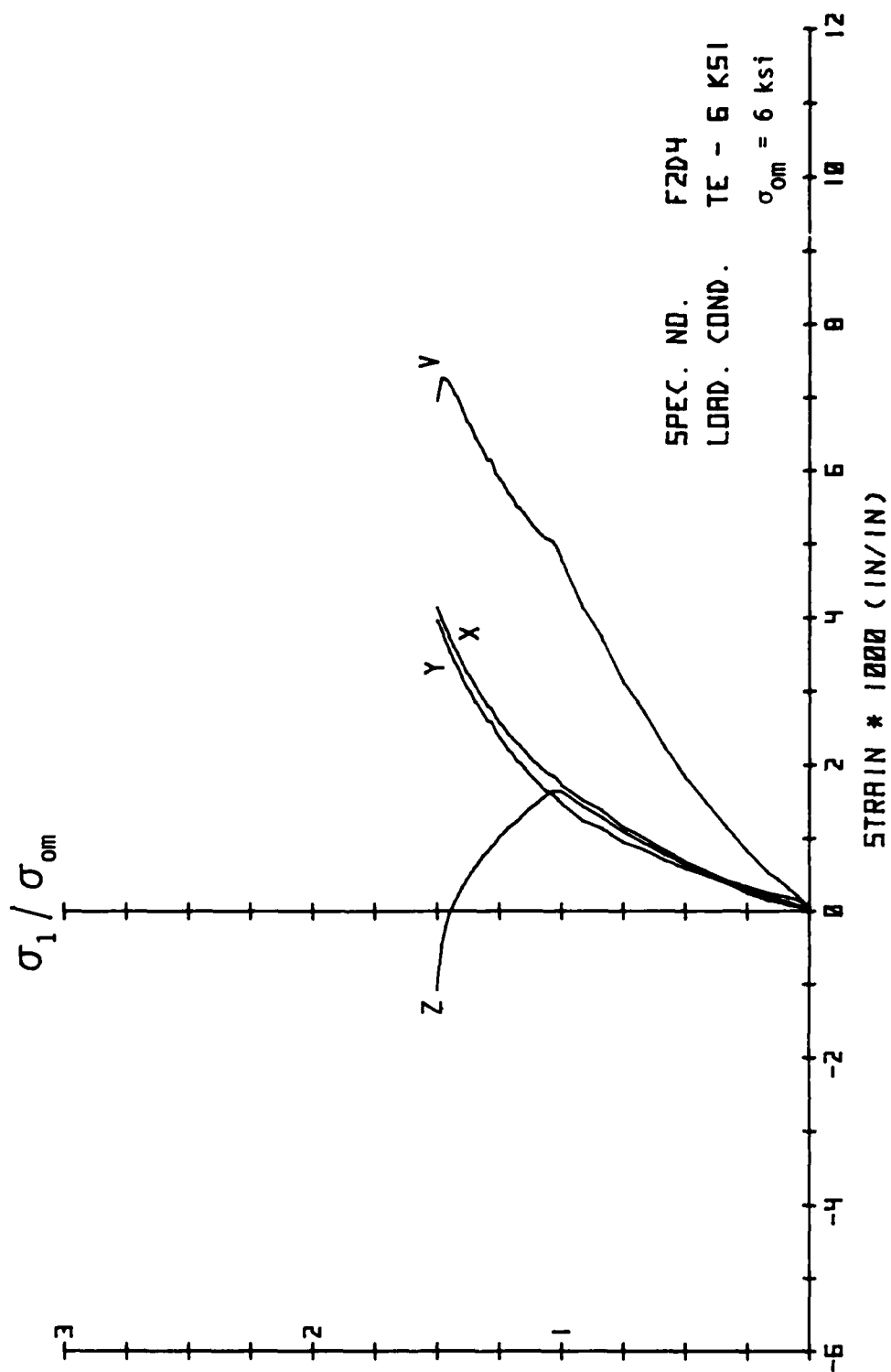


Fig. 4.22. Principal Stress-Strain Results.

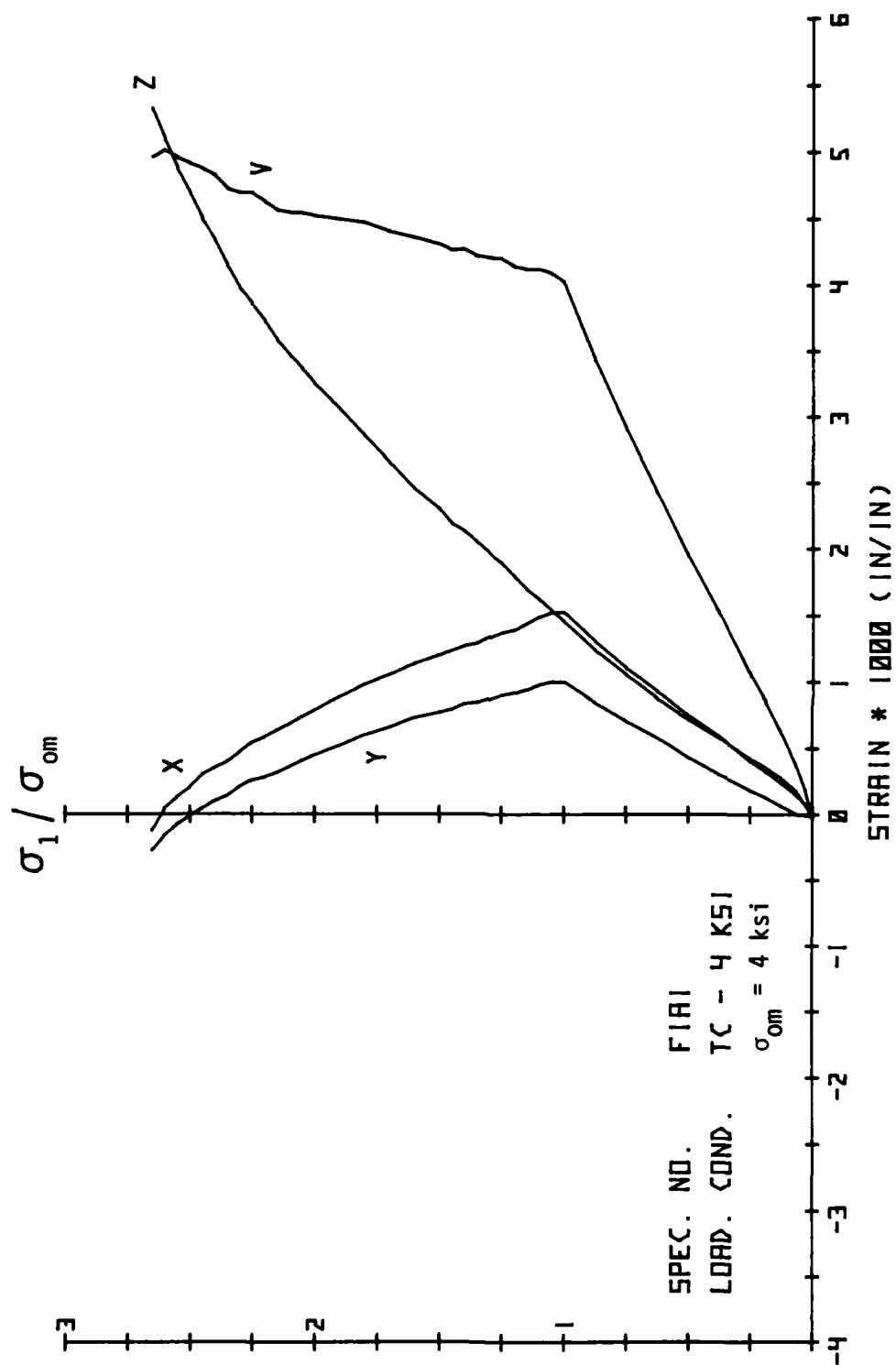


Fig. 4.23. Principal Stress-Strain Results.

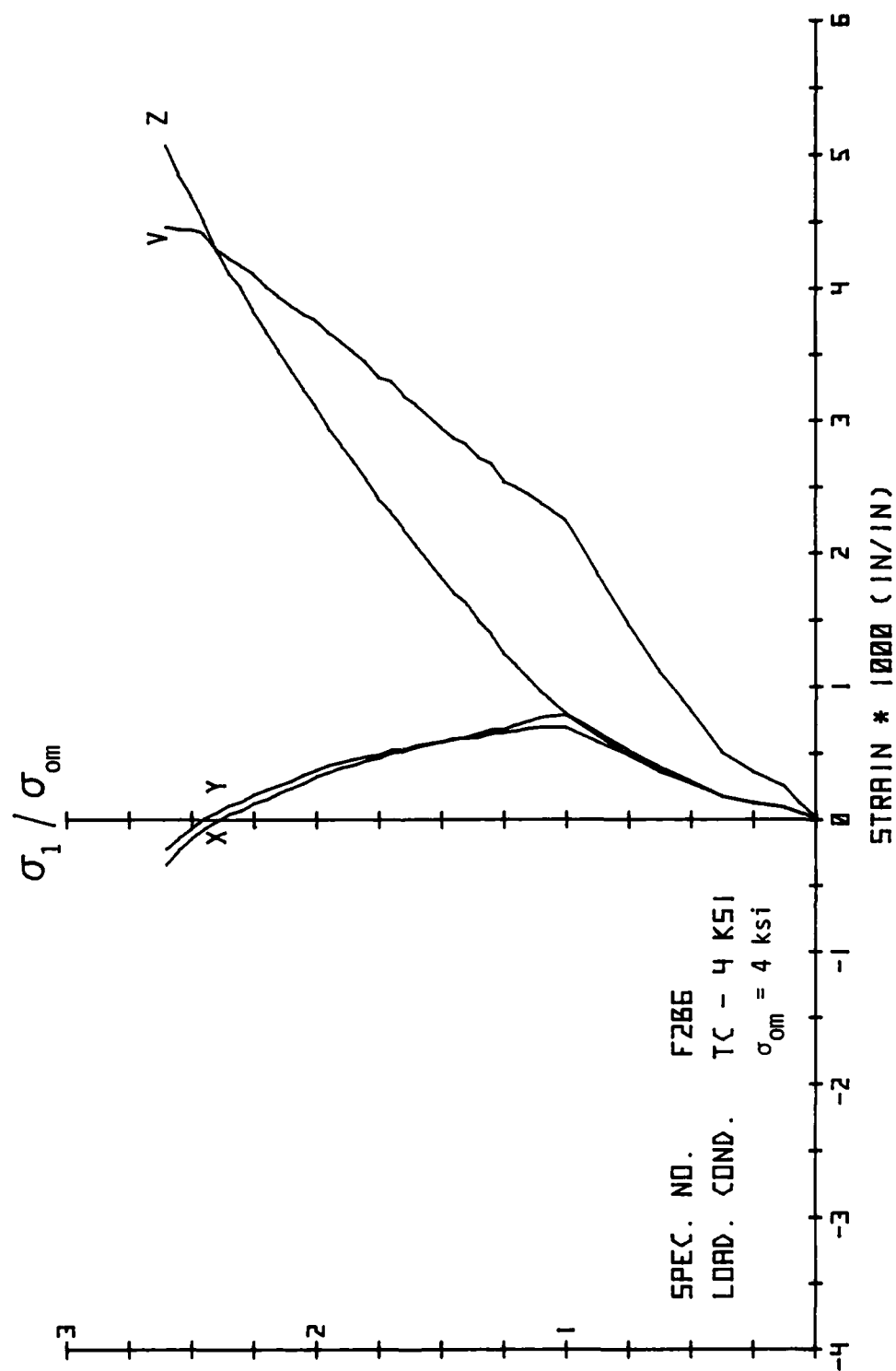


Fig. 4.24. Principal Stress-Strain Results.

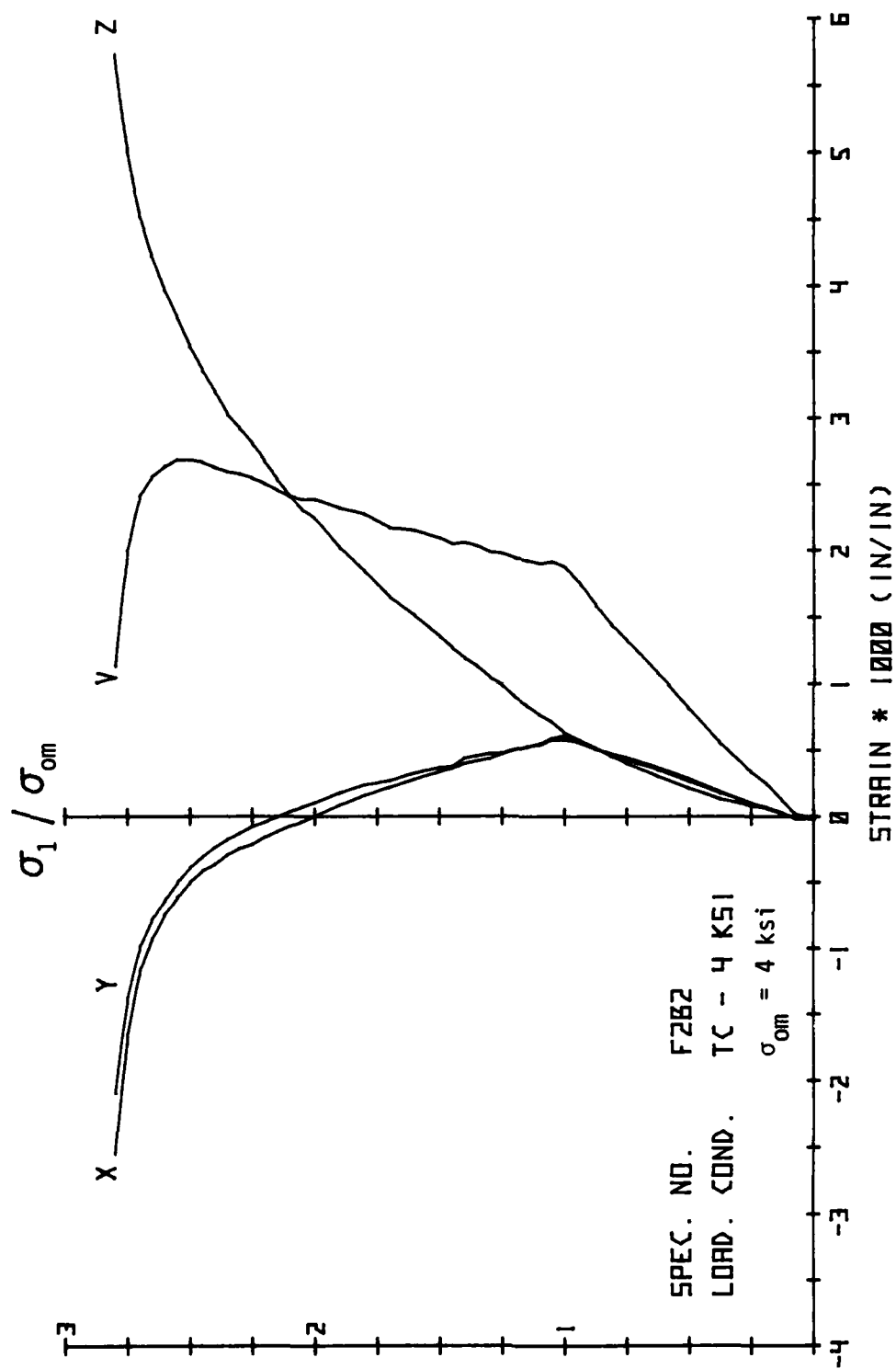


Fig. 4.25. Principal Stress-Strain Results.

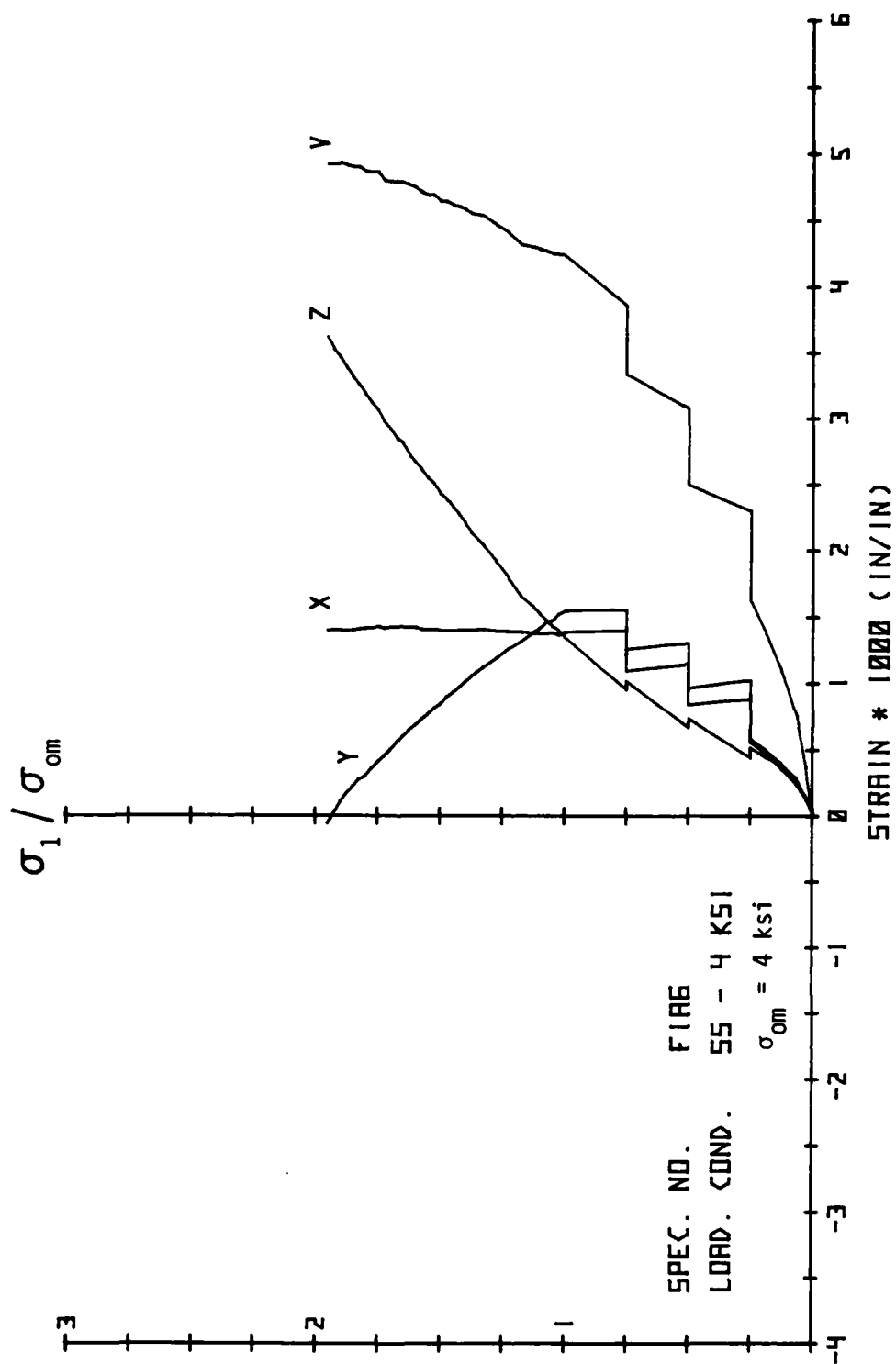


Fig. 4.26. Principal Stress-Strain Results.

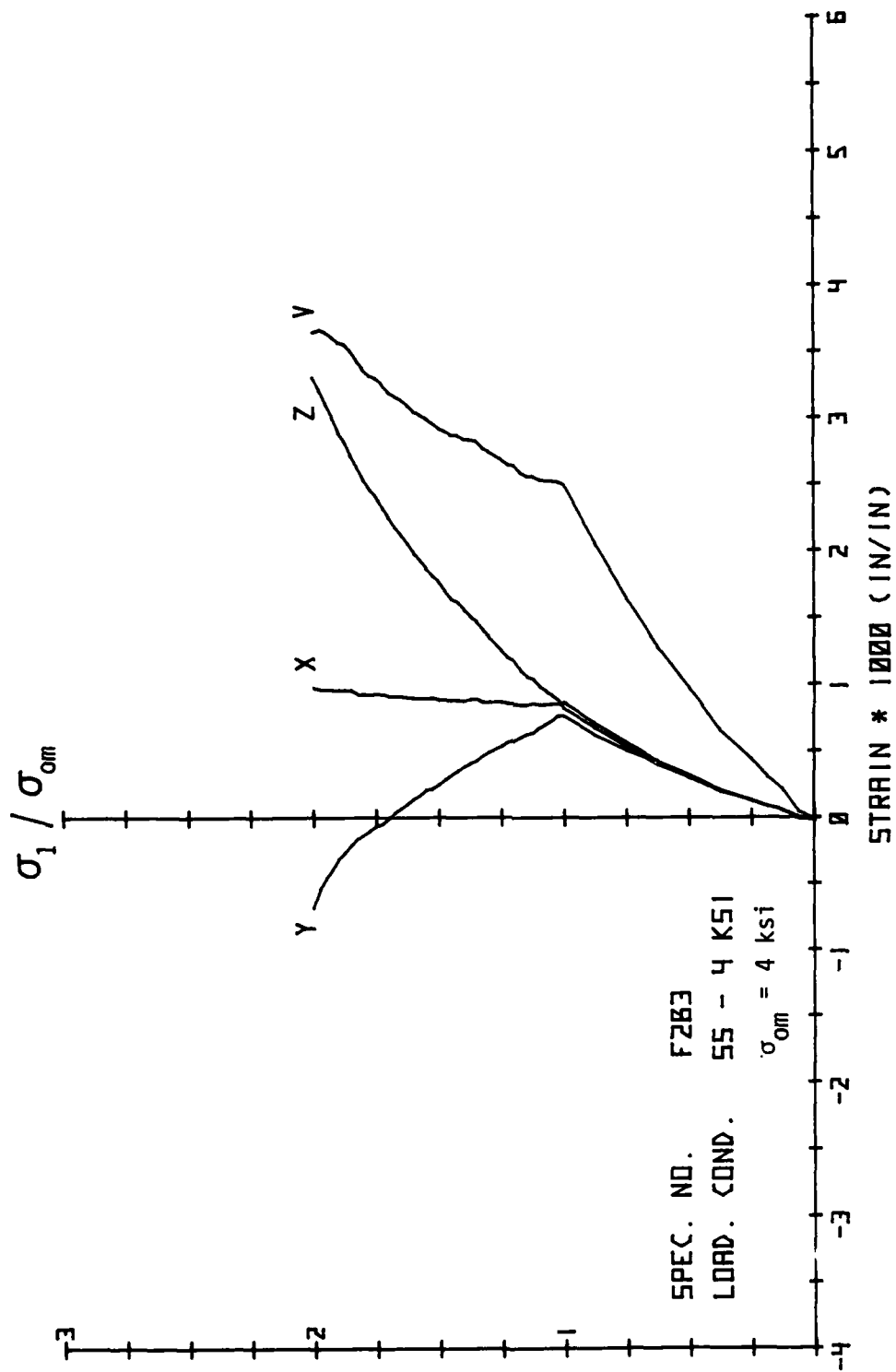


Fig. 4.27. Principal Stress-Strain Results.

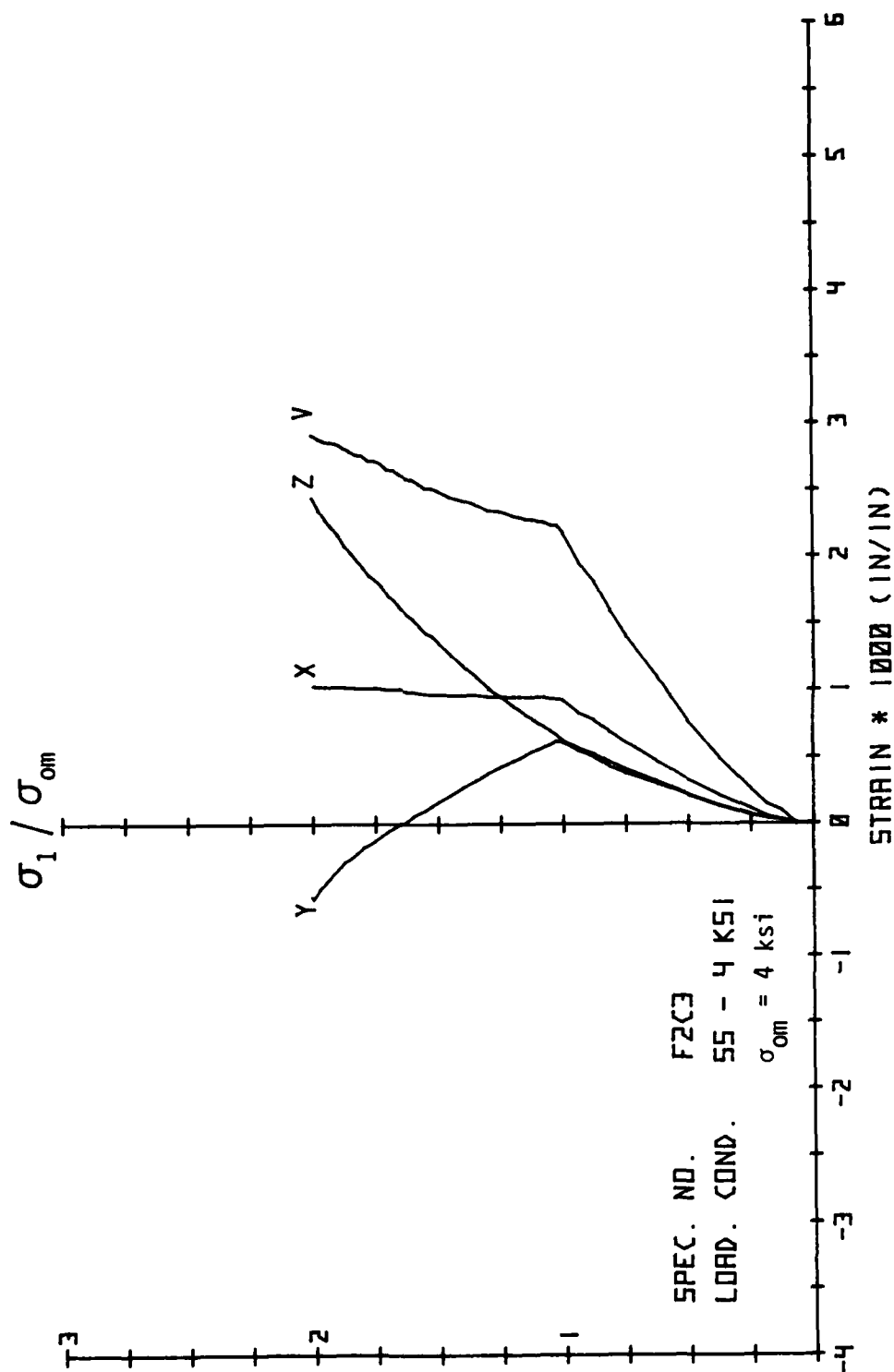


Fig. 4.28. Principal Stress-Strain Results.

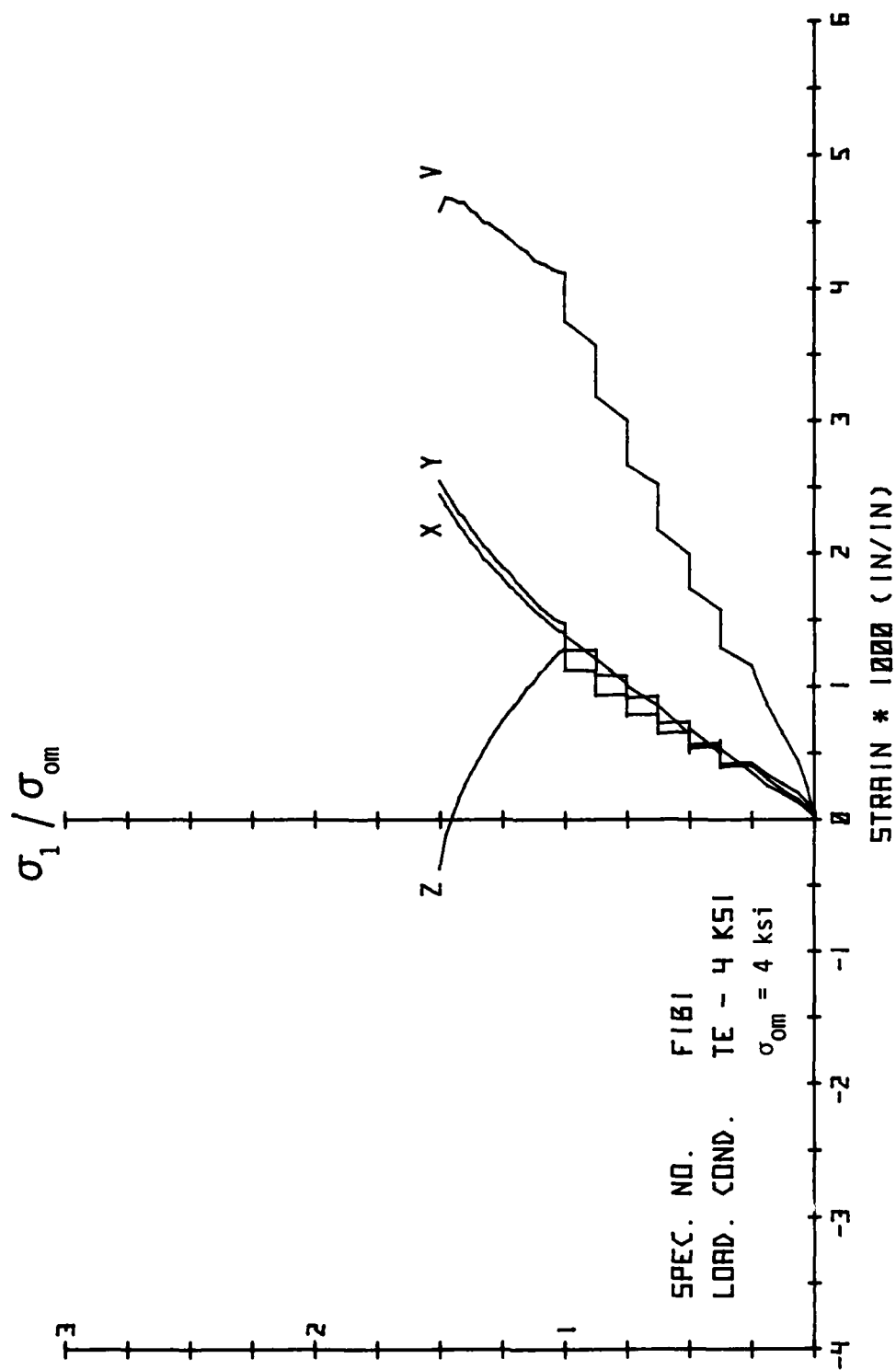


Fig. 4.29. Principal Stress-Strain Results.

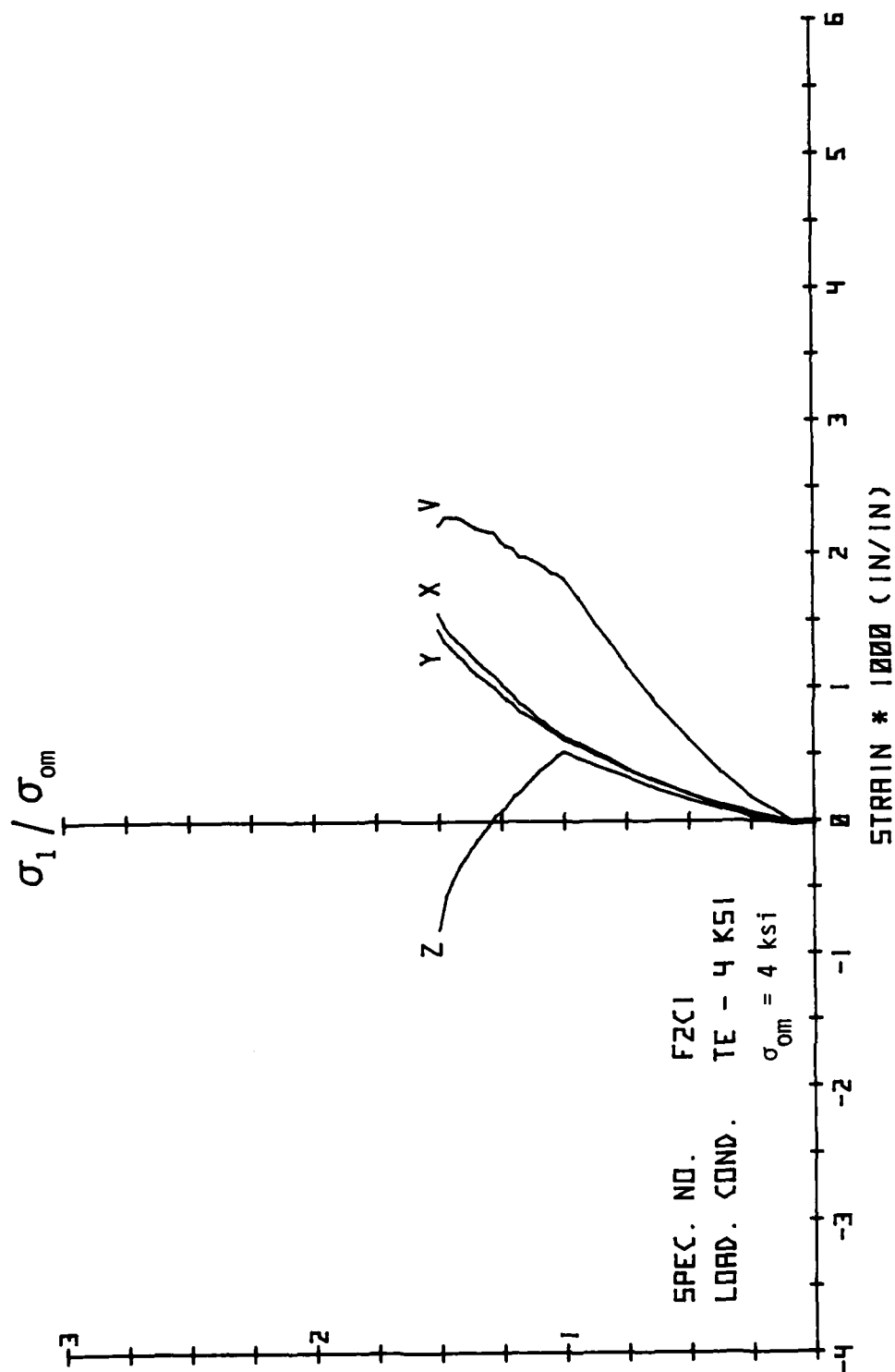


Fig. 4.30. Principal Stress-Strain Results.

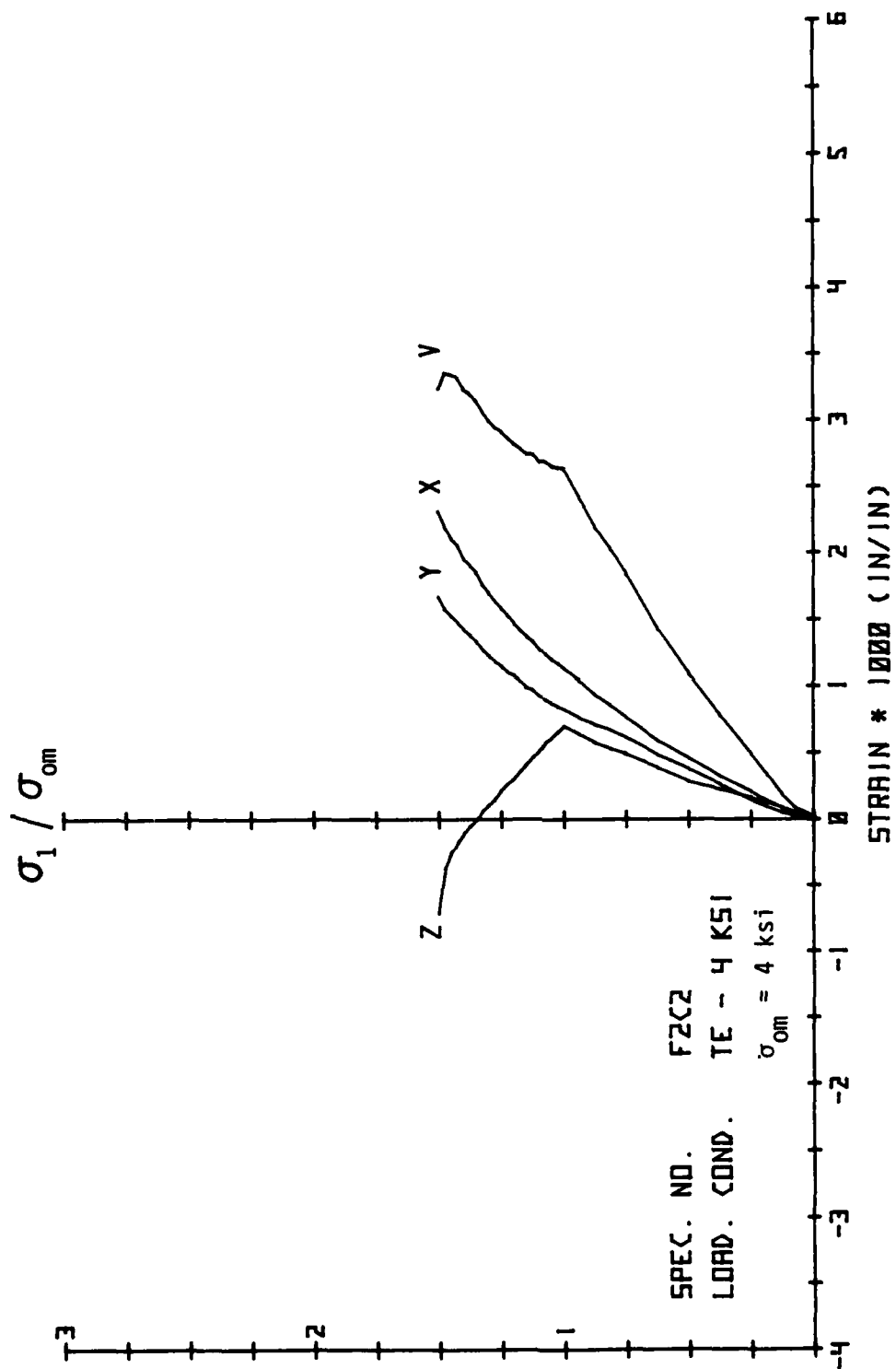


Fig. 4.31. Principal Stress-Strain Results.

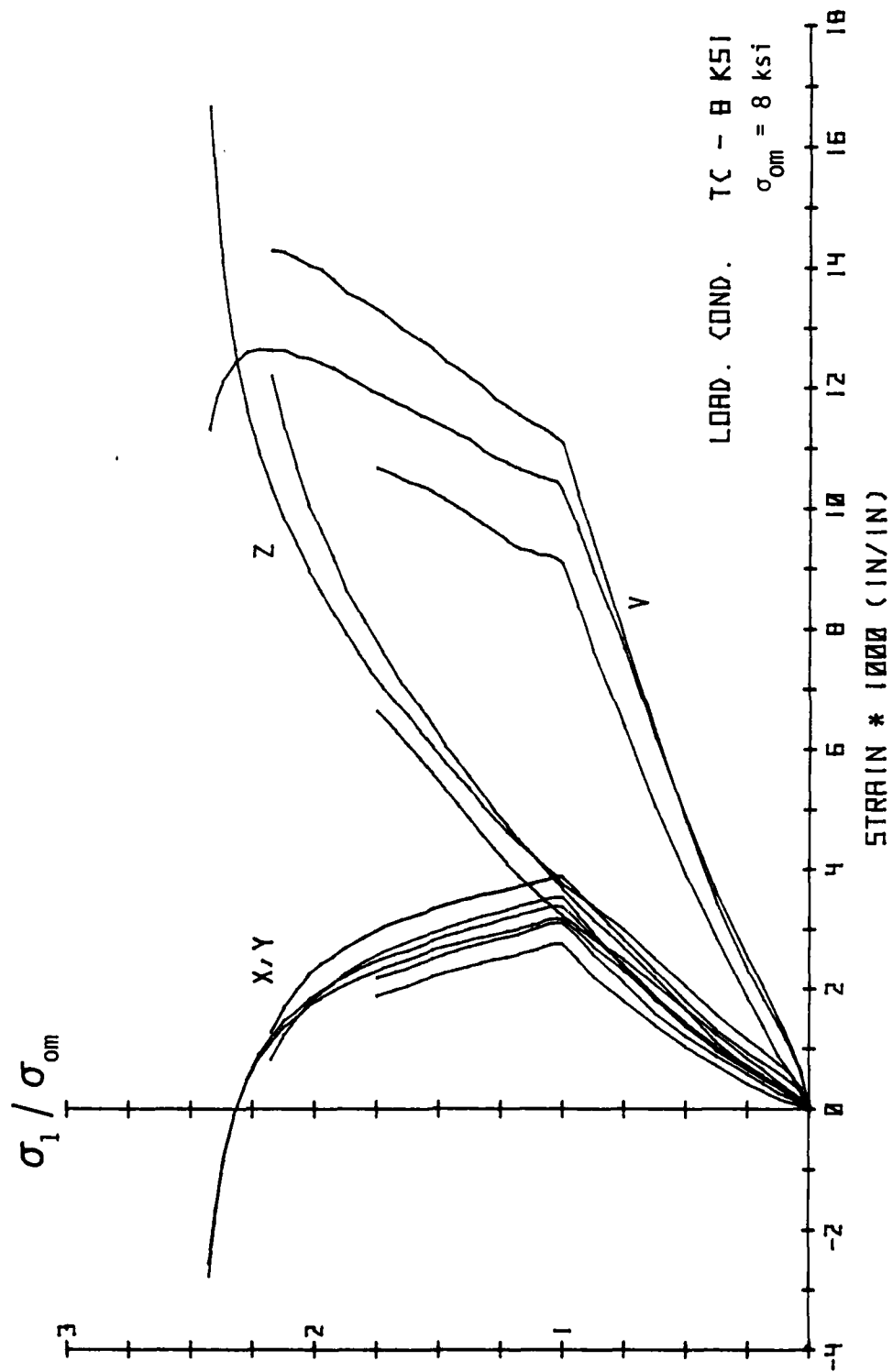


Fig. 4.32. Principal Stress-Strain Summary Results.

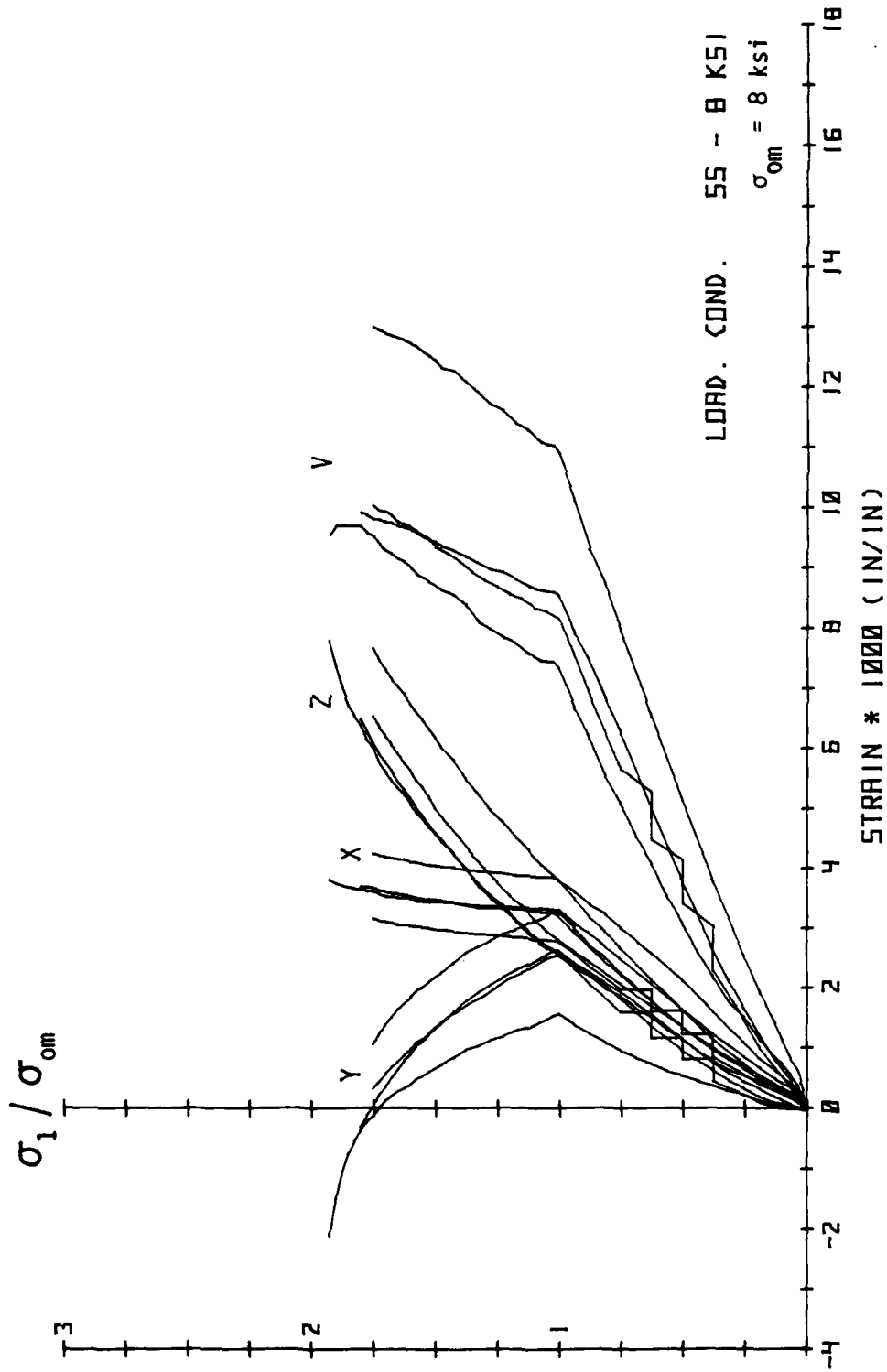


Fig. 4.33. Principal Stress-Strain Summary Results.

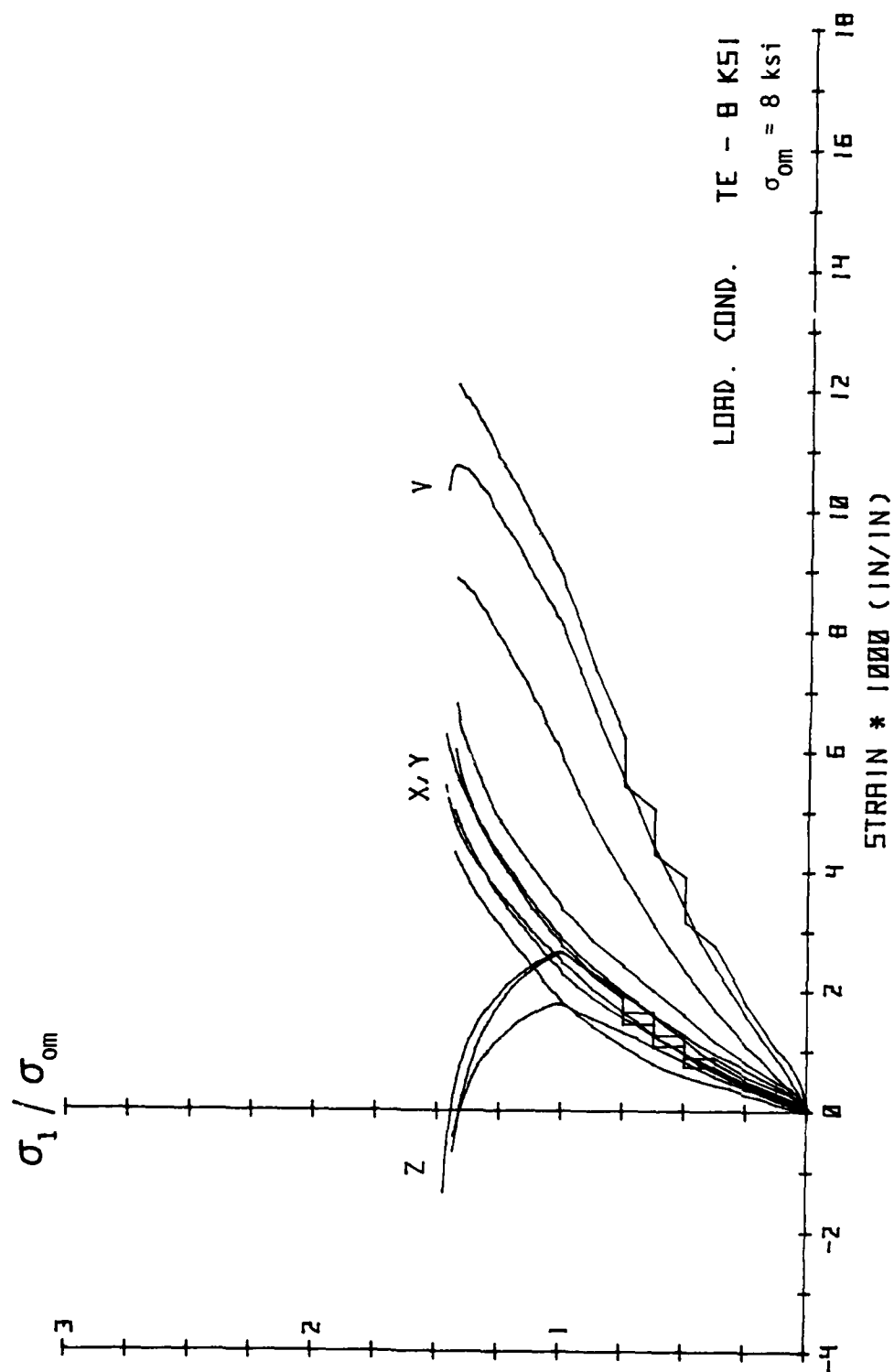


Fig. 4.34. Principal Stress-Strain Summary Results.

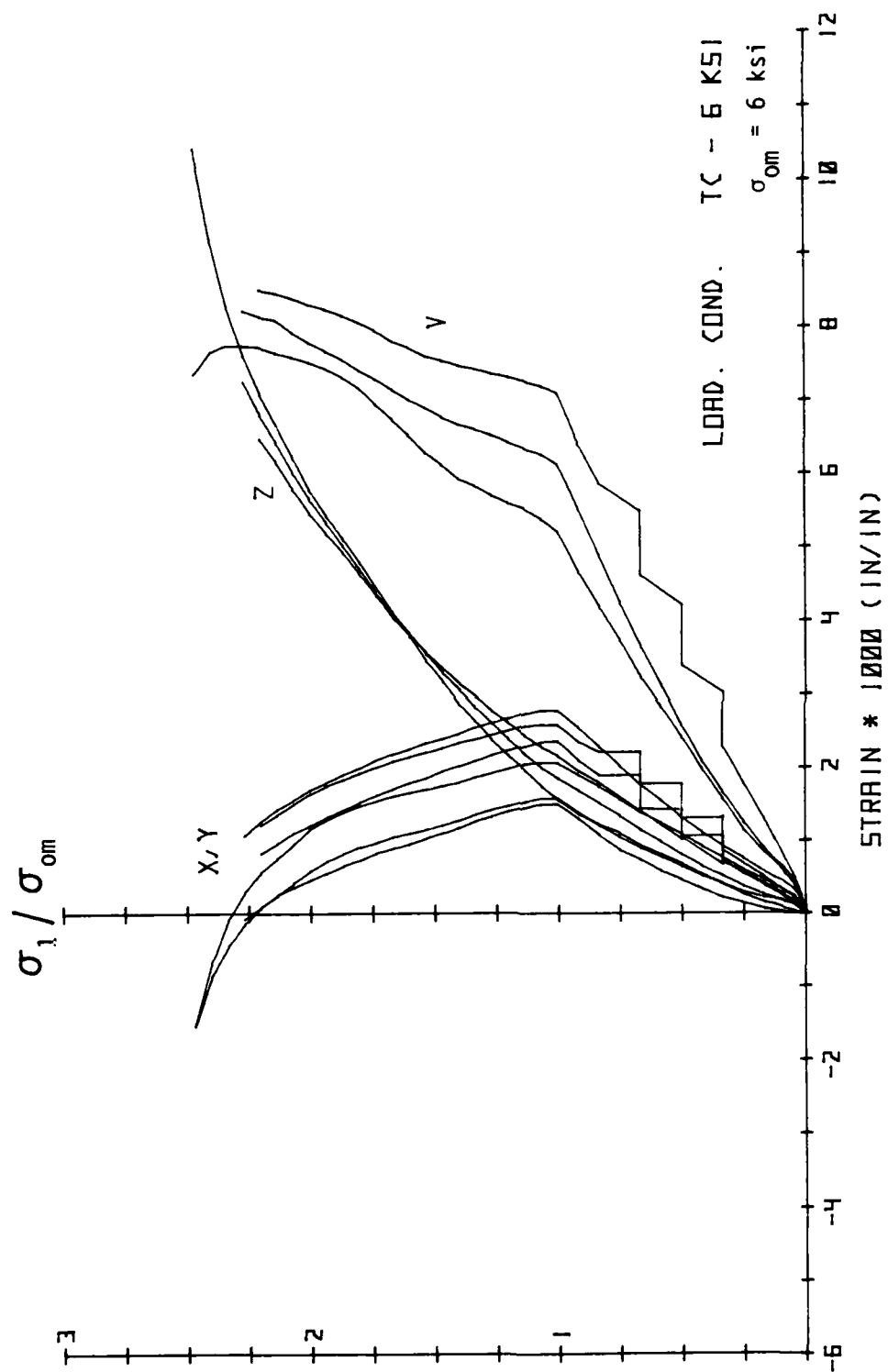


Fig. 4.35. Principal Stress-Strain Summary Results.

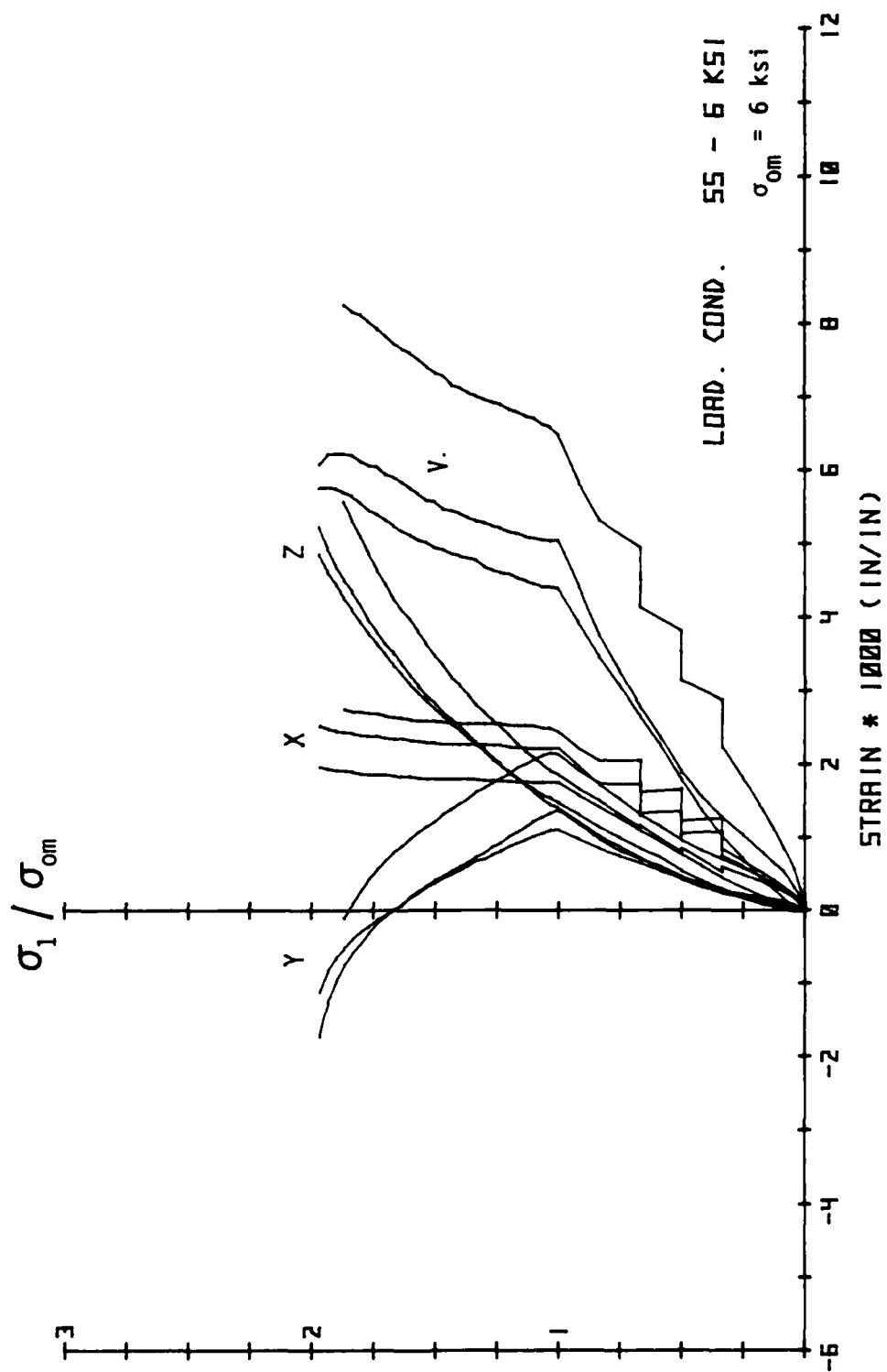


Fig. 4.36. Principal Stress-Strain Summary Results.

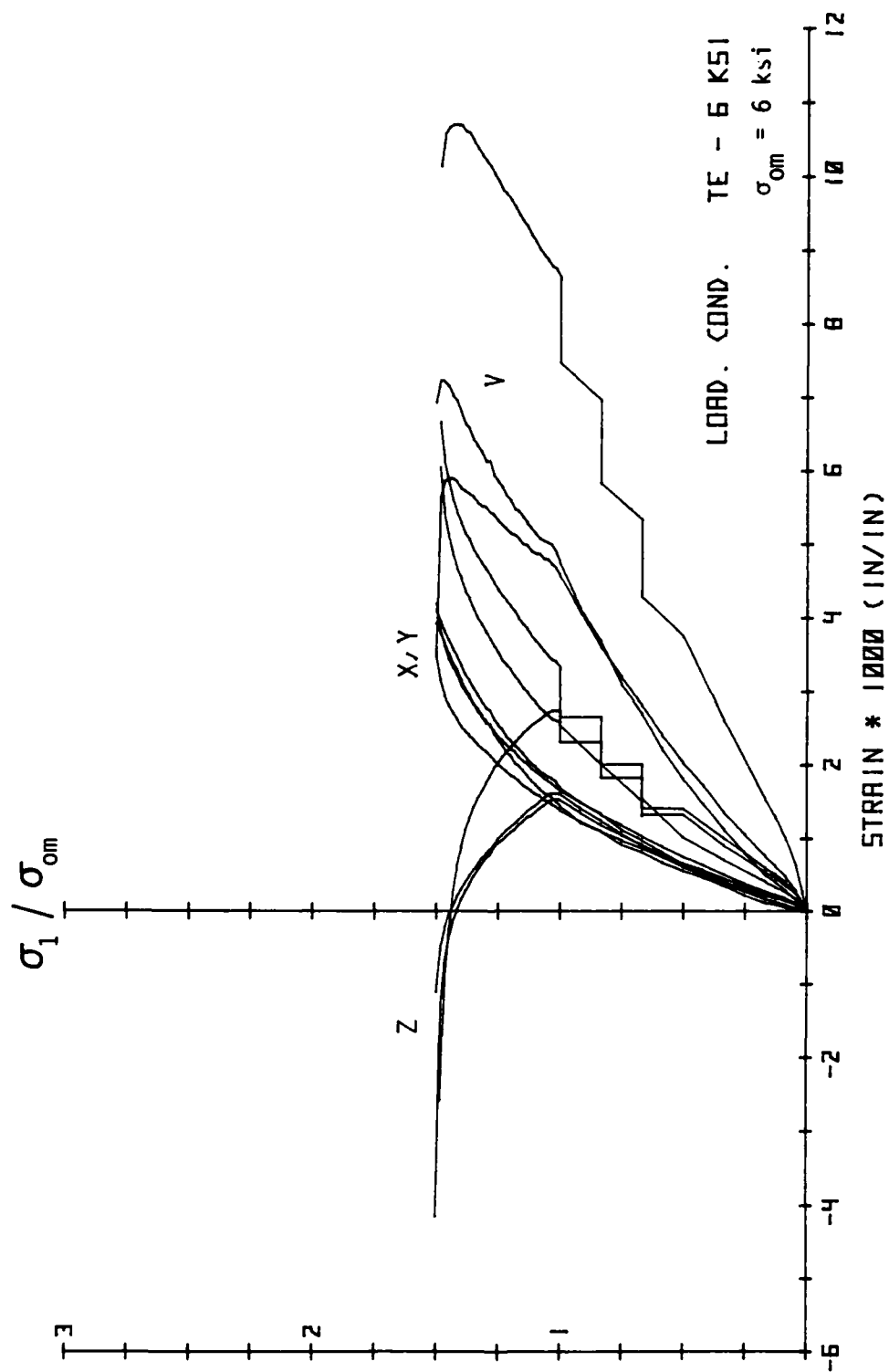


Fig. 4.37. Principal Stress-Strain Summary Results.

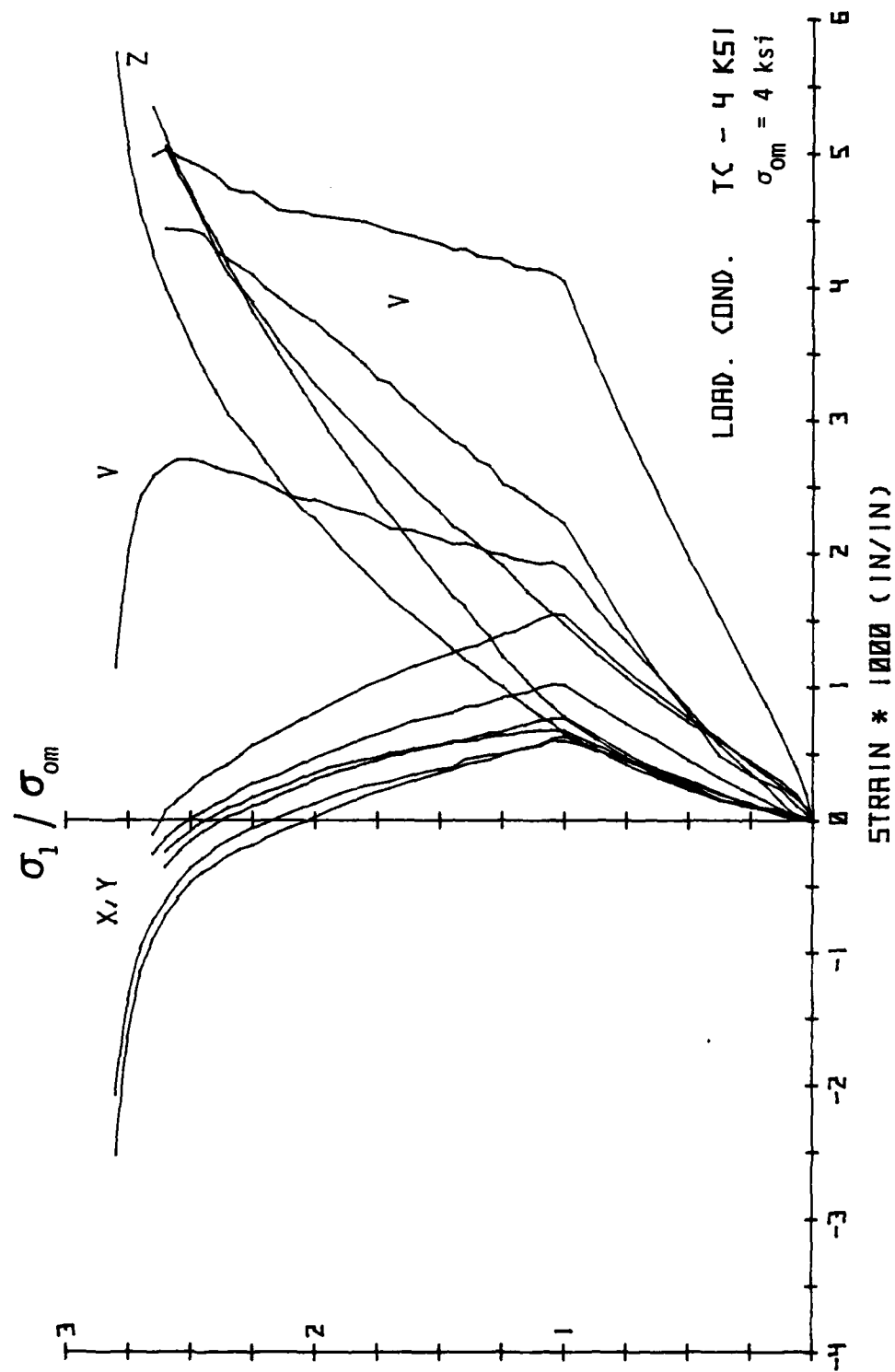


Fig. 4.38. Principal Stress-Strain Summary Results.

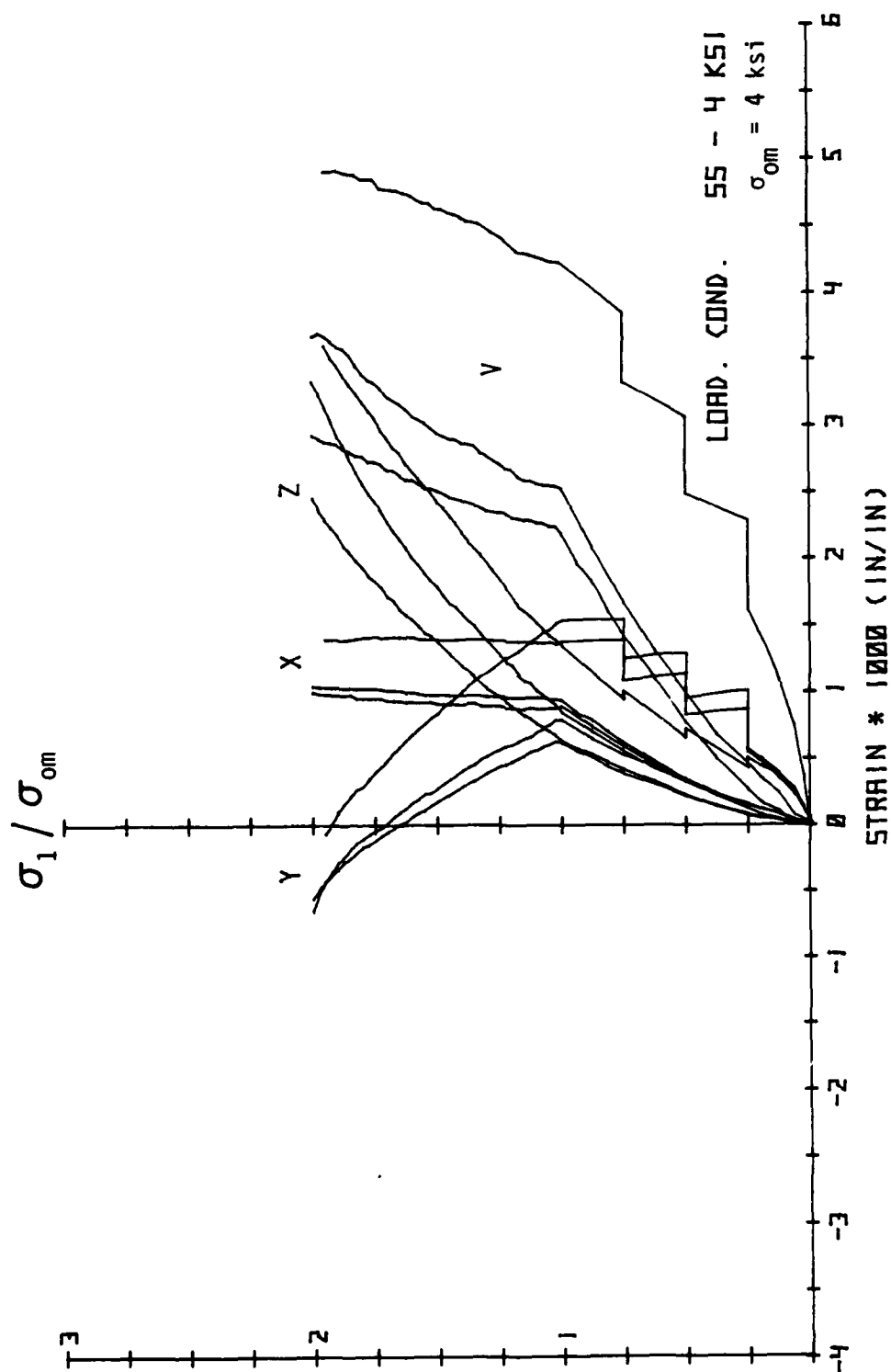


Fig. 4.39. Principal Stress-Strain Summary Results.

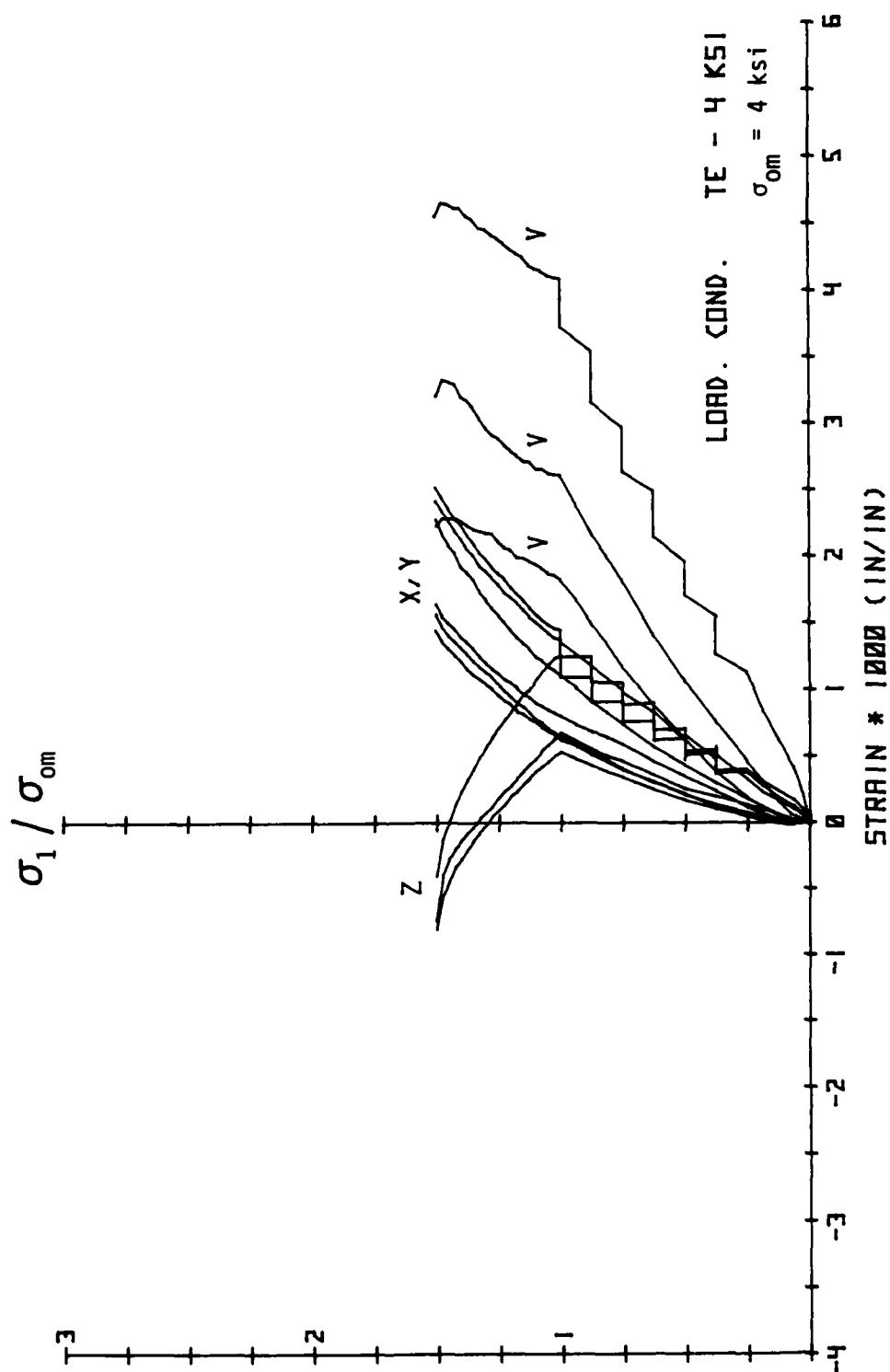


Fig. 4.40. Principal Stress-Strain Summary Results.

stress-strain curves. All tests conducted on the same octahedral plane ($\sigma_0 = 4, 6$ or 8 ksi) employ the same strain scale.

One can see that the hydrostatic portion of the tests occurs in the $0 \leq \sigma_1/\sigma_{0m} \leq 1$ range and the deviatoric part occurs at values of $\sigma_1/\sigma_{0m} > 1$. Notice that in some of the individual and grouped curves there are "kinks" or "steps" in the hydrostatic compression part of the stress-strain curves. In these seven tests, a stepped-loading path along the hydrostatic axis was followed as a method for determining the elastic material constants of the material. The procedure and results of this are presented in Section 4.3.3.

For the same type of test (identical stress path and octahedral plane), the normalized maximum principal stress (σ_1/σ_{0m}) is higher in some cases than in others. All tests followed a monotonic stress path until specimen failure or equipment breakdown occurred, or until the test got to the point where tensile stresses would have to be applied in order to continue; which was not possible at the time of this research. The cubical device is, at this time, a stress-controlled, fluid cushion apparatus. In all cases of "equipment breakdown", the cause was one or more of the flexible membranes rupturing (thus ending the test) when a corner or edge of the specimen chipped off due to the large deviator stress present between major and minor principal directions. Even though specimen failure data could not be recorded for these tests, valuable stress-strain data was obtained.

Some of the tests were taken to and beyond the point of volume dilation as indicated by the stress-volumetric strain curve.

"Equipment breakdown" is the reason the others were not. The stress-volumetric strain behavior plays an important role in the determination of the failure stress. This discussion is presented in Section 4.3.4.

For discussion purposes, the principal stress-strain behavior can be separated into two parts: the hydrostatic compression part ($\sigma_1 = \sigma_2 = \sigma_3$) and the deviatoric part. In this series of tests, three different deviatoric stress paths were followed: triaxial compression (TC), simple shear (SS) and triaxial extension (TE). See Fig. 2.31. The behavior corresponding to the different parts of the different stress paths is described separately below.

4.3.1.1 Hydrostatic Compression (HC)

The material demonstrates fairly good isotropy as seen in the hydrostatic portion of the principal stress-strain curves. Just by examining the curves, no claims can be made as to which direction provides stiffer response during HC. Some specimens exhibit stiffer behavior than others under HC. This scatter is apparent in the summary curves (Figs. 4.32 - 4.40). However, one can see that the shape of the deviatoric part of the curves is nearly identical for similar tests. One can therefore say that the HC part of these tests constitutes most of the scatter present in the results from one test to the next. In other words, if the HC response from test to test was identical, then the scatter in the complete stress-strain response from test to test would be minimal. No reason, other than random material behavior, can be given to explain this scatter that appears during HC.

4.3.1.2 Triaxial Compression (TC) in the Octahedral Plane

In the TC stress path, σ_1 is increased with σ_2 and σ_3 decreasing in such a way to keep σ_0 constant. Since σ_2 and σ_3 are equal, ϵ_2 and ϵ_3 should also be equal for isotropic or transversely isotropic behavior. One can see the good agreement between these strains (ϵ_x and ϵ_y in this case) from the individual results. The ϵ_x curve is simply a translation of the ϵ_y curve if both are judged from the end of the HC stress-strain curve. During TC, the volumetric behavior is compressive and nearly linear just prior to dilation, then becomes expansive. This phenomenon occurring under shear distortion at constant confining pressure is nothing new to observed concrete behavior. Gerstle, et. al. (50) observed similar behavior to occur in plain concrete, with some of their results shown in Fig. 1.16. One interesting thing is that for all the TC tests, regardless of the amount of confining pressure, the intermediate and minor principal strains (ϵ_x and ϵ_y) were about zero when volume dilation occurred, or all strain in the specimen was compressive and in one direction. The deviatoric behavior is stiffer for low confining pressures (σ_{0m}) than it is for high.

4.3.1.3 Simple Shear (SS) in the Octahedral Plane

For the SS stress path, σ_1 and σ_3 are increased and decreased respectively by the same amount while σ_2 is held constant, thus keeping σ_0 constant also. As in the TC tests, the volumetric behavior is compressive and nearly linear with increasing shear distortion until dilation of the specimen takes place. Also note that the change in intermediate principal strain ($\Delta\epsilon_x$ in this

case) is nearly zero throughout all the SS tests except for high values of confining pressure and shear stress, when this strain becomes slightly compressive. This indicates that plane strain conditions are almost satisfied by the SS stress state with true plane strain conditions lying somewhere between the SS and TC stress paths, very close to the SS.

4.3.1.4 Triaxial Extension (TE) in the Octahedral Plane

In the TE stress path, σ_1 and σ_2 are increased equally while σ_3 is decreased to maintain σ_0 at a constant level. Since σ_1 and σ_2 are equal, ϵ_1 and ϵ_2 should also be equal for isotropic material behavior. As in the TC results for ϵ_2 and ϵ_3 , one can see good agreement between ϵ_1 and ϵ_2 (ϵ_x and ϵ_y in this case) for the TE tests from the individual results, the difference stemming from the HC portion. As in the other tests, the volumetric behavior is compressive and nearly linear up to the point of dilation. But immediately after dilation of the specimen, rapid expansion in the volumetric behavior takes place, as if the specimen were splitting in half and coming apart. However, careful examination of the specimens subjected to the TE stress path revealed nothing significant regarding specimen deformation. The reason could be attributed to the fibers "holding" everything together. These deformations were indeed measurable and very significant but just too small to detect visually. Also note that analogous to the TC tests, the minor principal strain (ϵ_z) was practically zero when volume dilation occurred, or all strain in the specimen was

compressive but in two directions, even though a three-dimensional stress state was present.

4.3.2 Octahedral Stress-Strain Relations

The octahedral normal and shear stresses σ_0 and τ_0 , and the octahedral normal and shear strains ϵ_0 and γ_0 are represented in terms of principal stresses and strains by the following relations:

$$\sigma_0 = \frac{1}{3} (\sigma_1 + \sigma_2 + \sigma_3) \quad (4.1a)$$

$$\tau_0 = \frac{1}{3} \sqrt{(\sigma_1 - \sigma_2)^2 + (\sigma_2 - \sigma_3)^2 + (\sigma_3 - \sigma_1)^2} \quad (4.1b)$$

$$\epsilon_0 = \frac{1}{3} (\epsilon_1 + \epsilon_2 + \epsilon_3) \quad (4.1c)$$

$$\gamma_0 = \frac{1}{3} \sqrt{(\epsilon_1 - \epsilon_2)^2 + (\epsilon_2 - \epsilon_3)^2 + (\epsilon_3 - \epsilon_1)^2} \quad (4.1d)$$

The octahedral stress-strain curves obtained from the tests in the final series are plotted individually in Figs. 4.41 - 4.68. The same results are shown in summary form for identical tests on different specimens in Figs. 4.69 - 4.77. All possible combinations of octahedral stresses and strains are shown: two for the hydrostatic compression (HC) part of the test, σ_0 - ϵ_0 and σ_0 - γ_0 ; and two for the deviatoric part, τ_0 - γ_0 and τ_0 - ϵ_0 . The slope of the σ_0 - ϵ_0 curve is three times the bulk modulus K and the slope of the τ_0 - γ_0 curve is two times the shear modulus G . All octahedral stress-strain results for each specimen are presented on the same graph for convenience. To prevent any

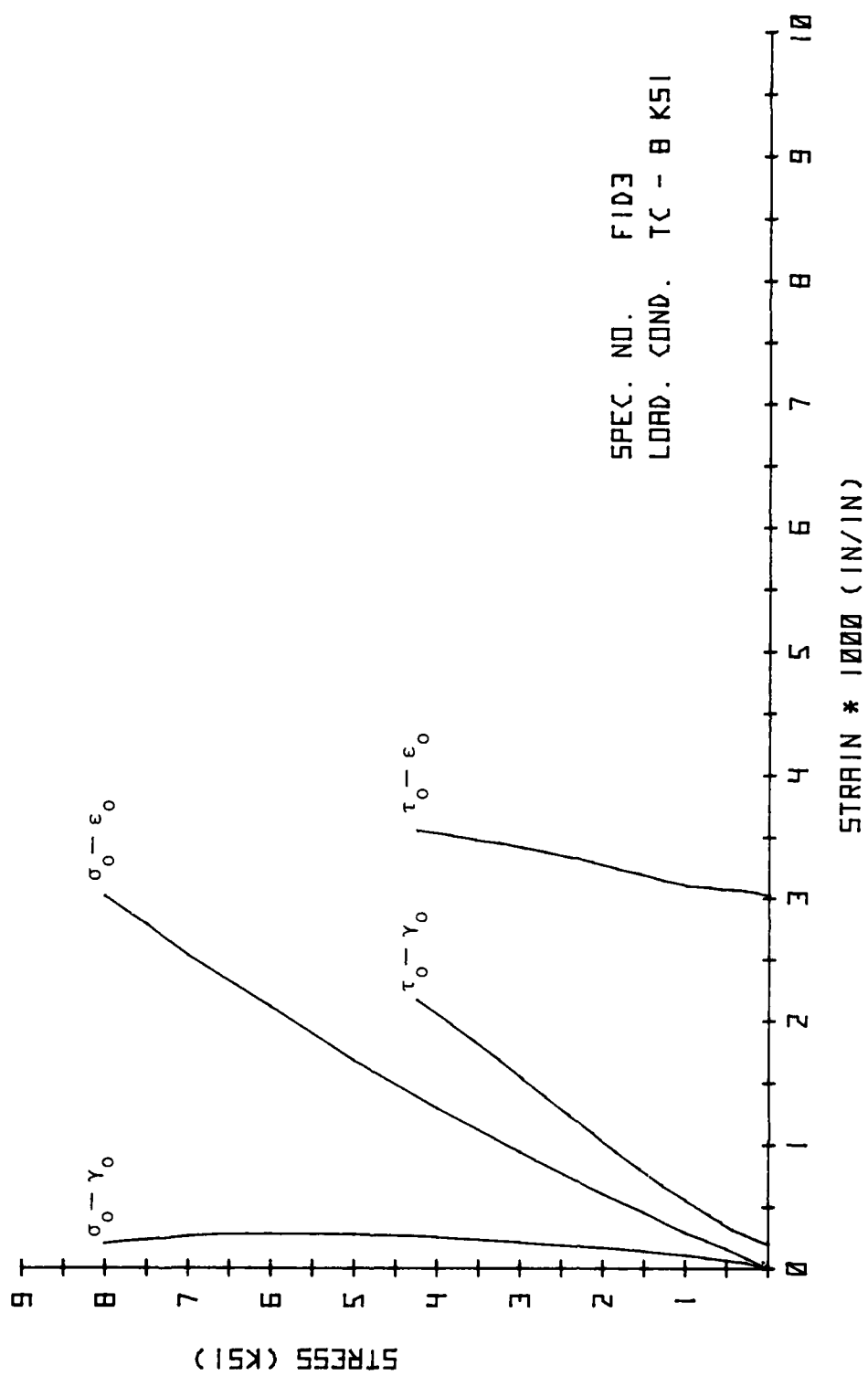


Fig. 4.41. Octahedral Stress-Strain Results.

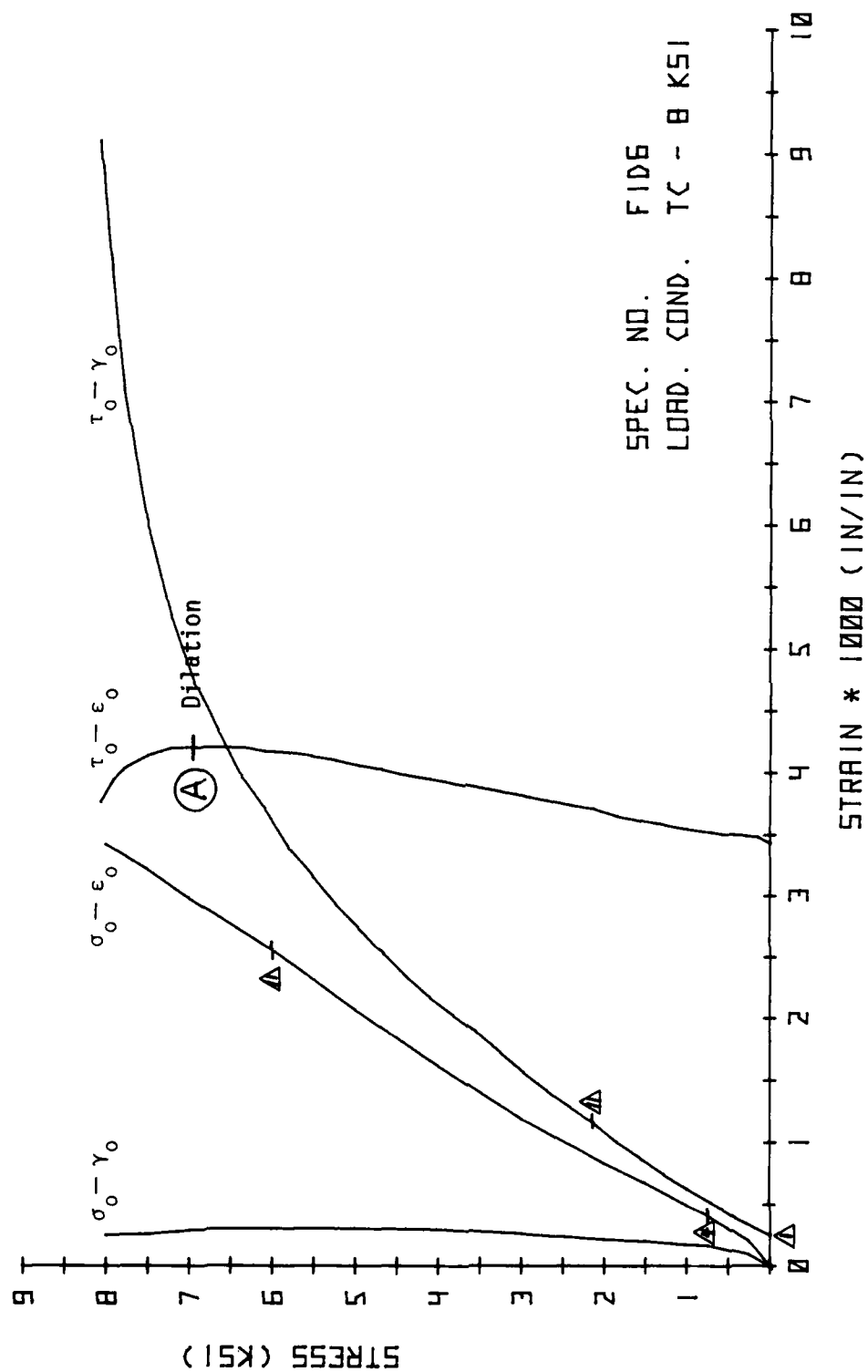


Fig. 4.42. Octahedral Stress-Strain Results.

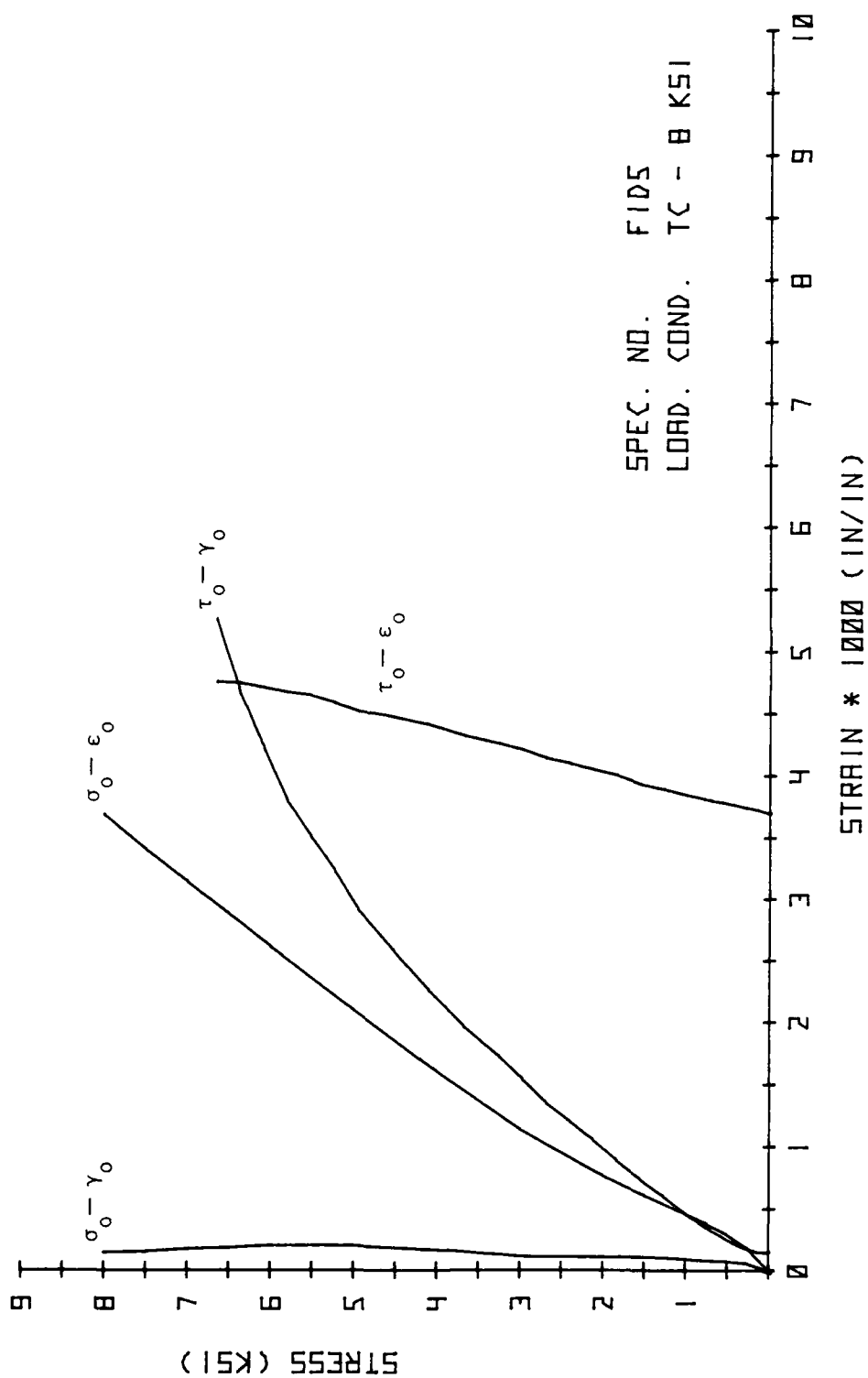


Fig. 4.43. Octahedral Stress-Strain Results.

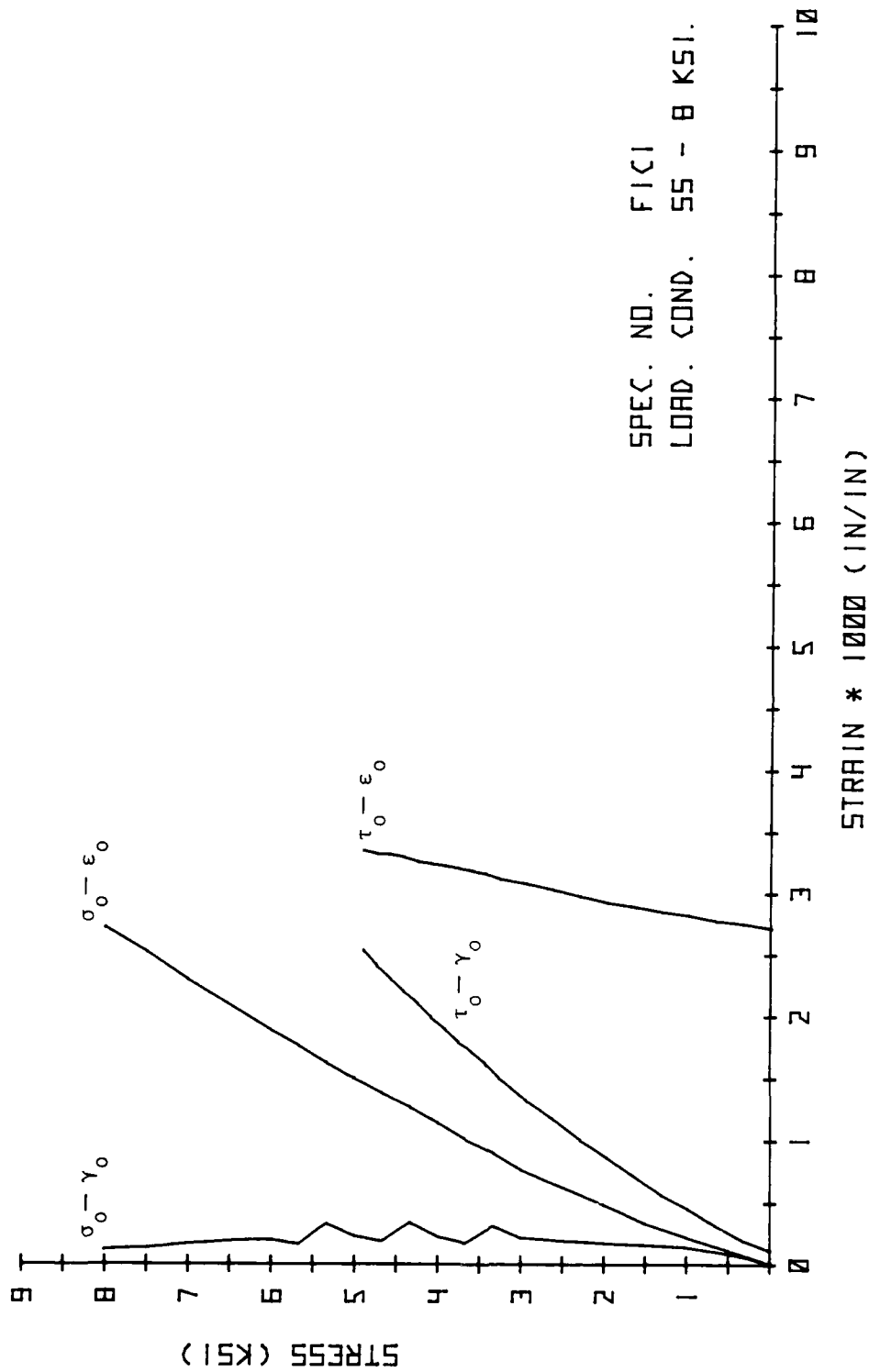


Fig. 4.44. Octahedral Stress-Strain Results.

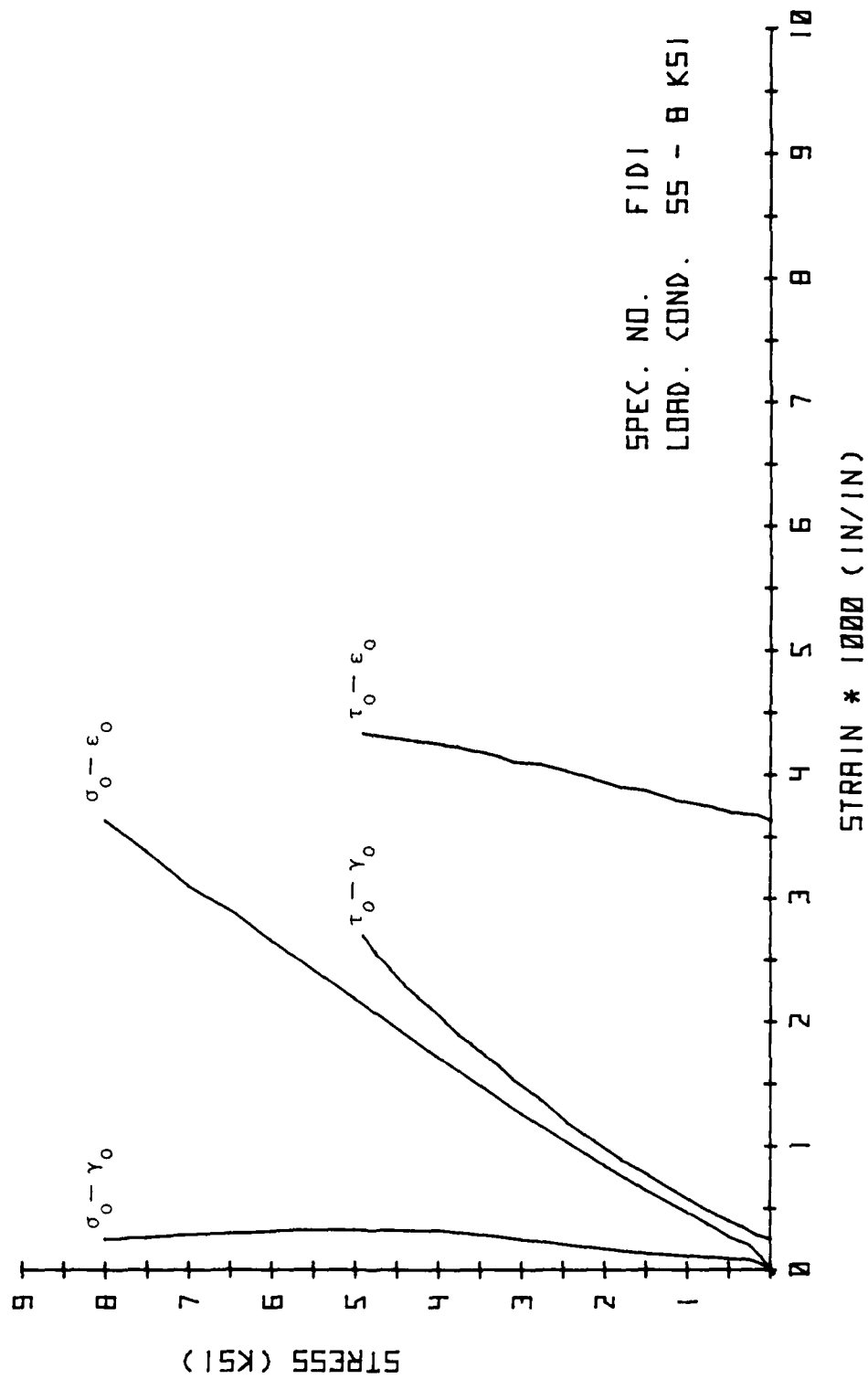


Fig. 4.45. Octahedral Stress-Strain Results.

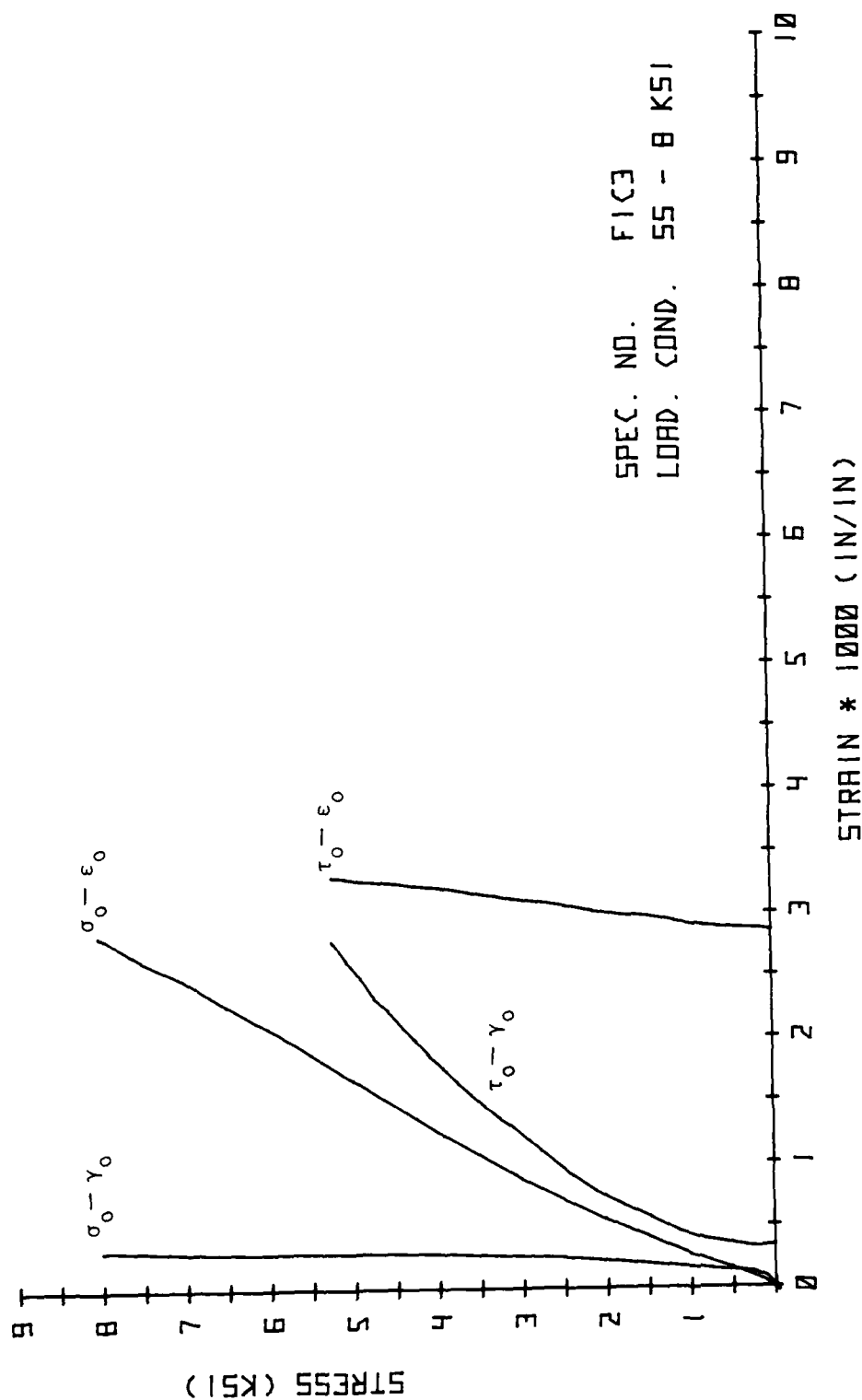


Fig. 4.46. Octahedral Stress-Strain Results.

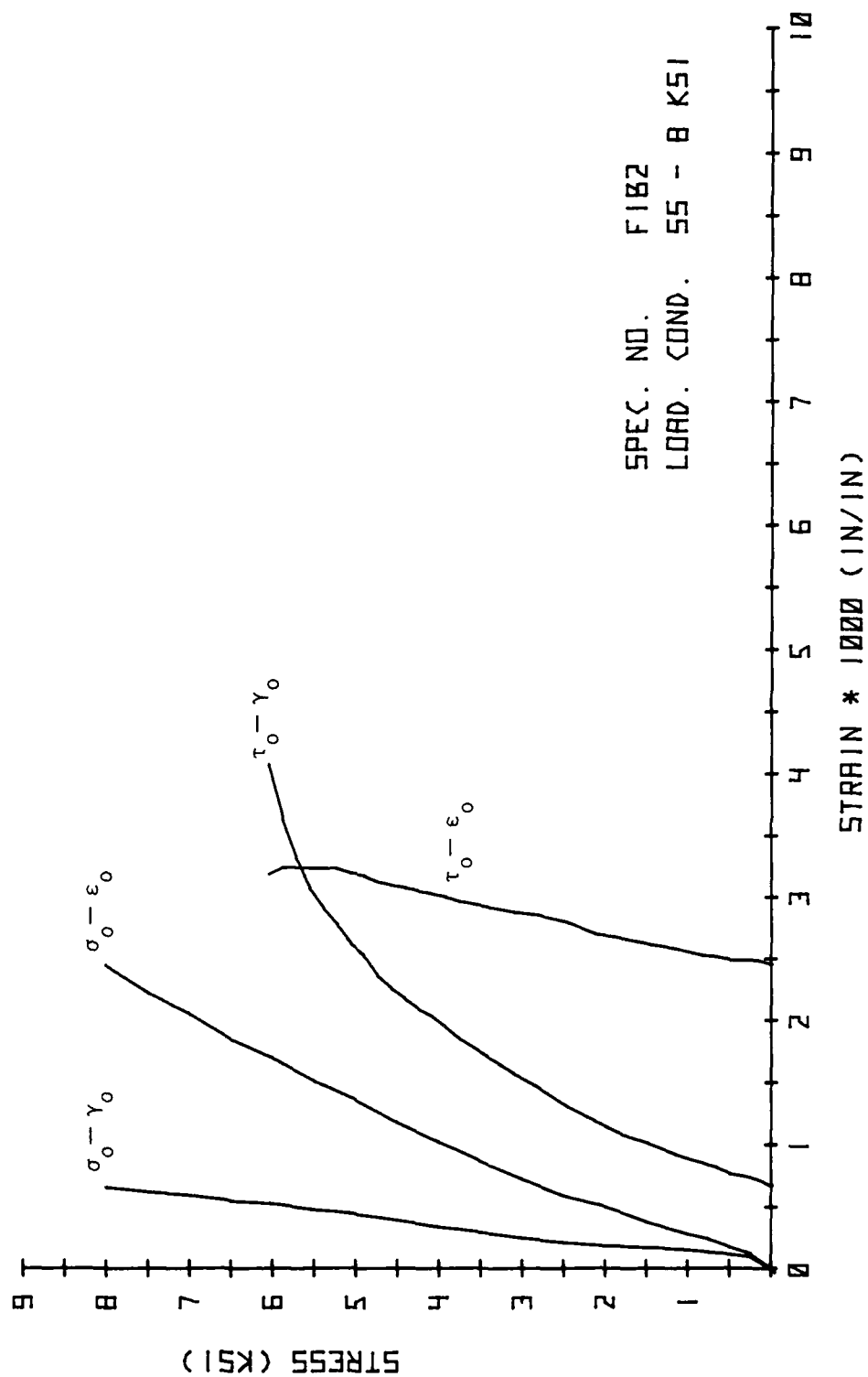


Fig. 4.47. Octahedral Stress-Strain Results.

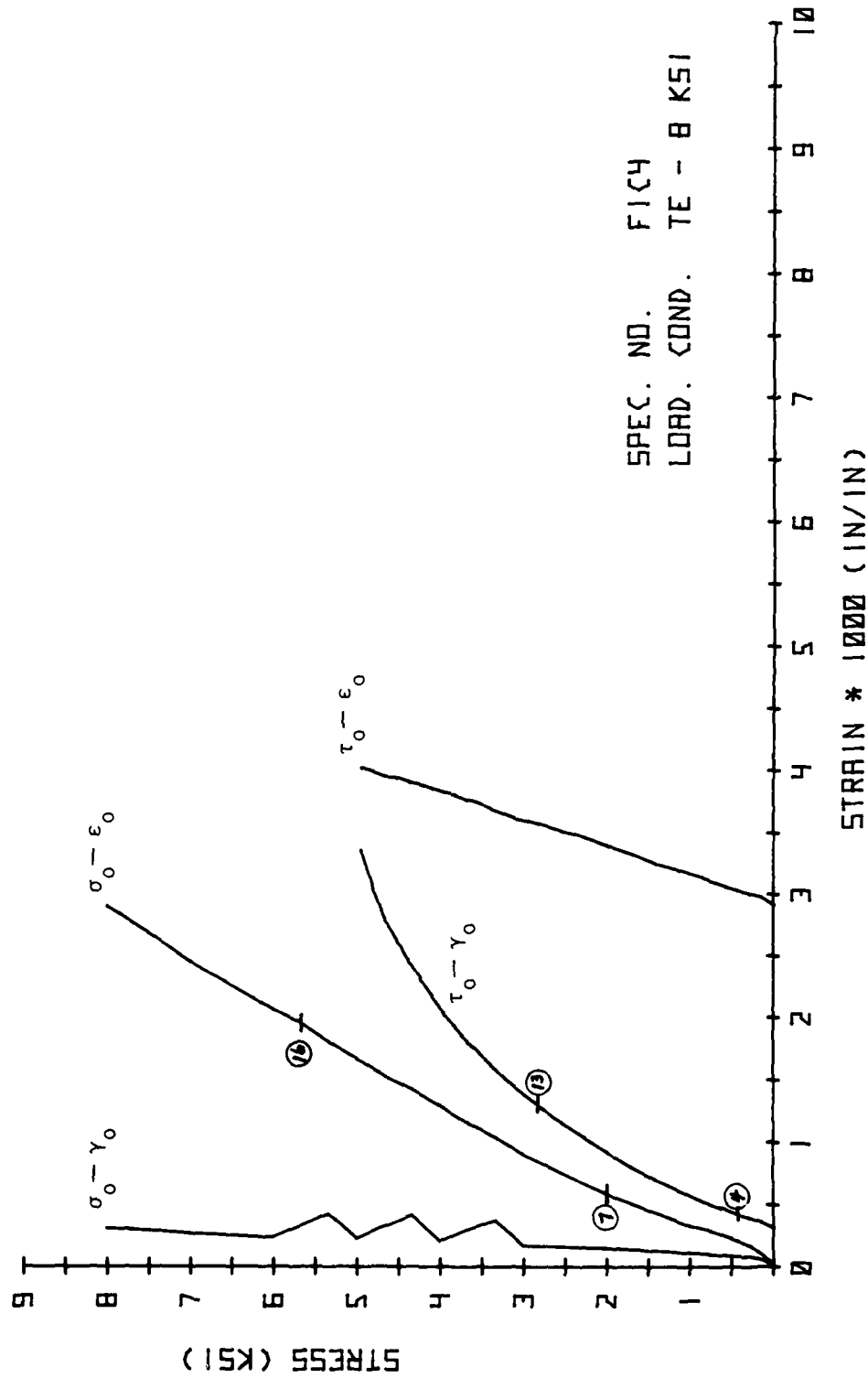


Fig. 4.48. Octahedral Stress-Strain Results.

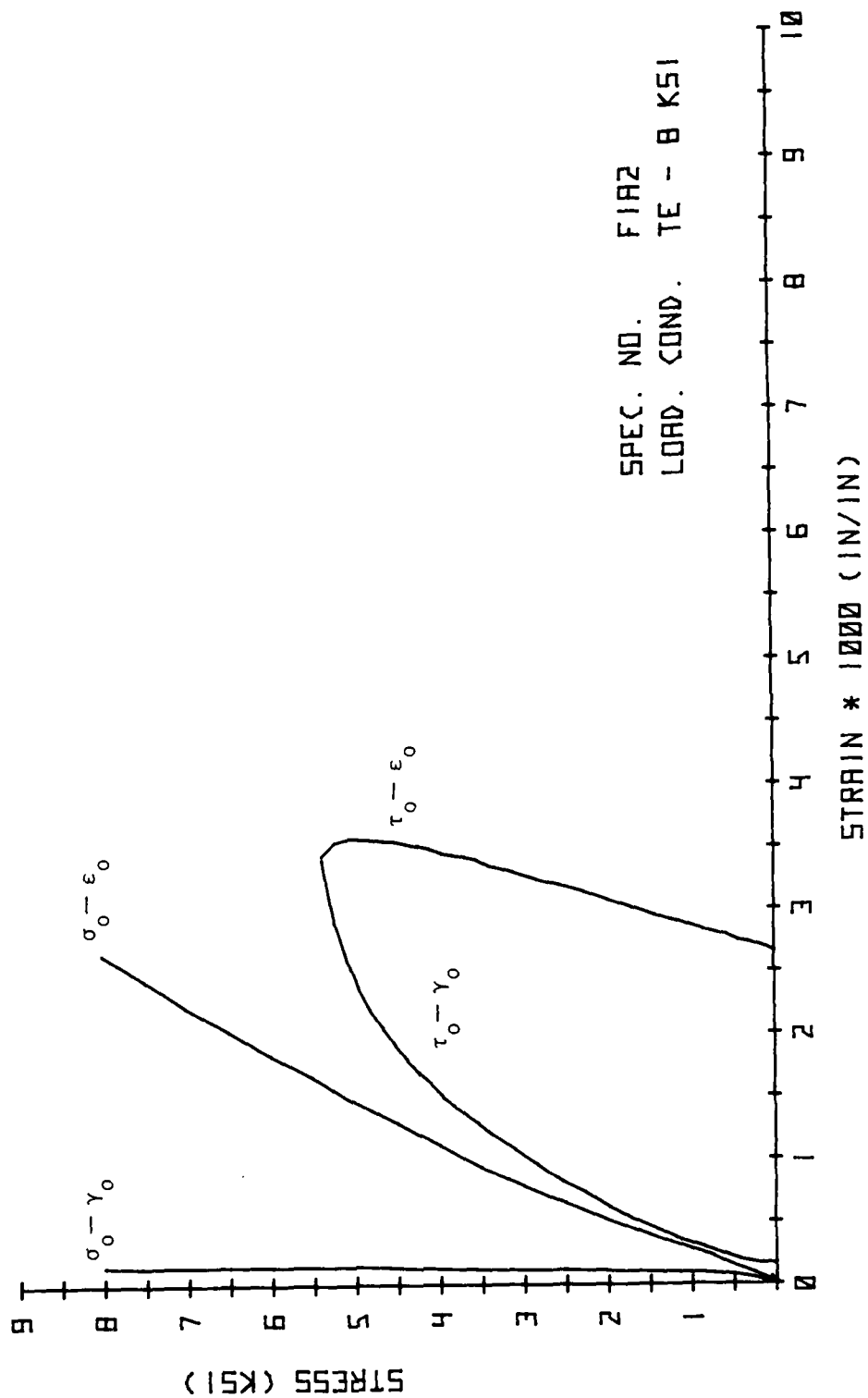


Fig. 4.49. Octahedral Stress-Strain Results.

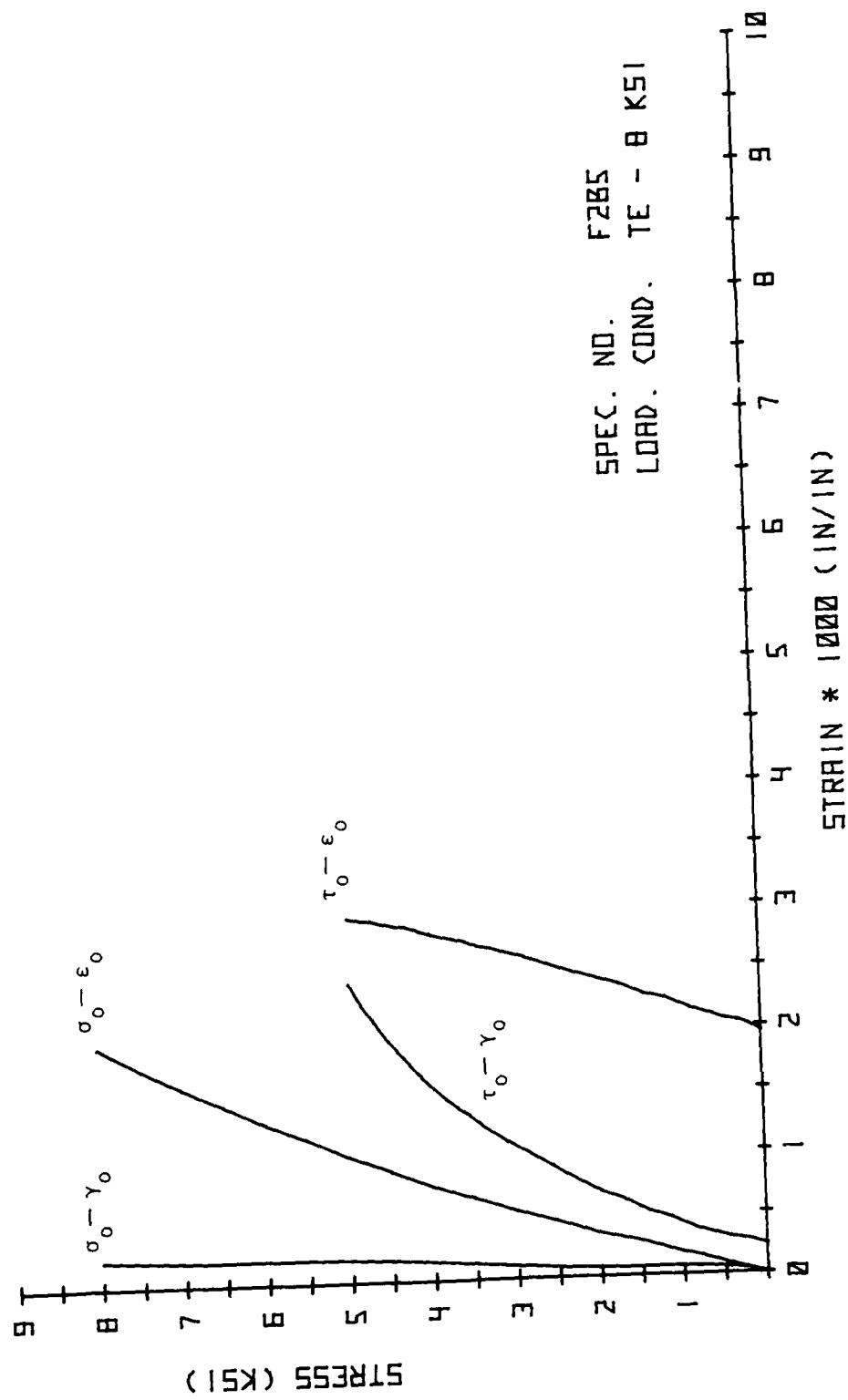


Fig. 4.50. Octahedral Stress-Strain Results.

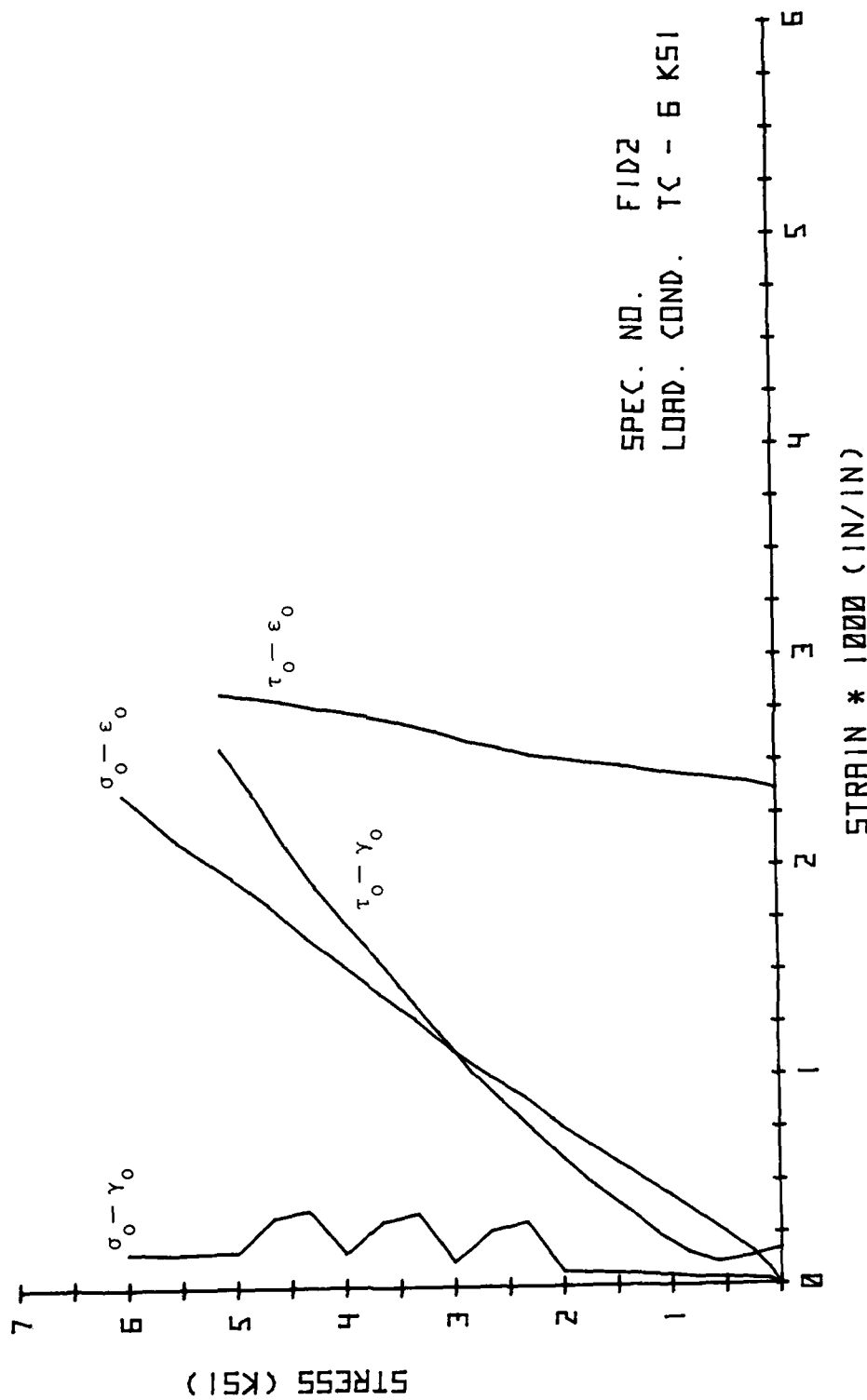


Fig. 4.51. Octahedral Stress-Strain Results.

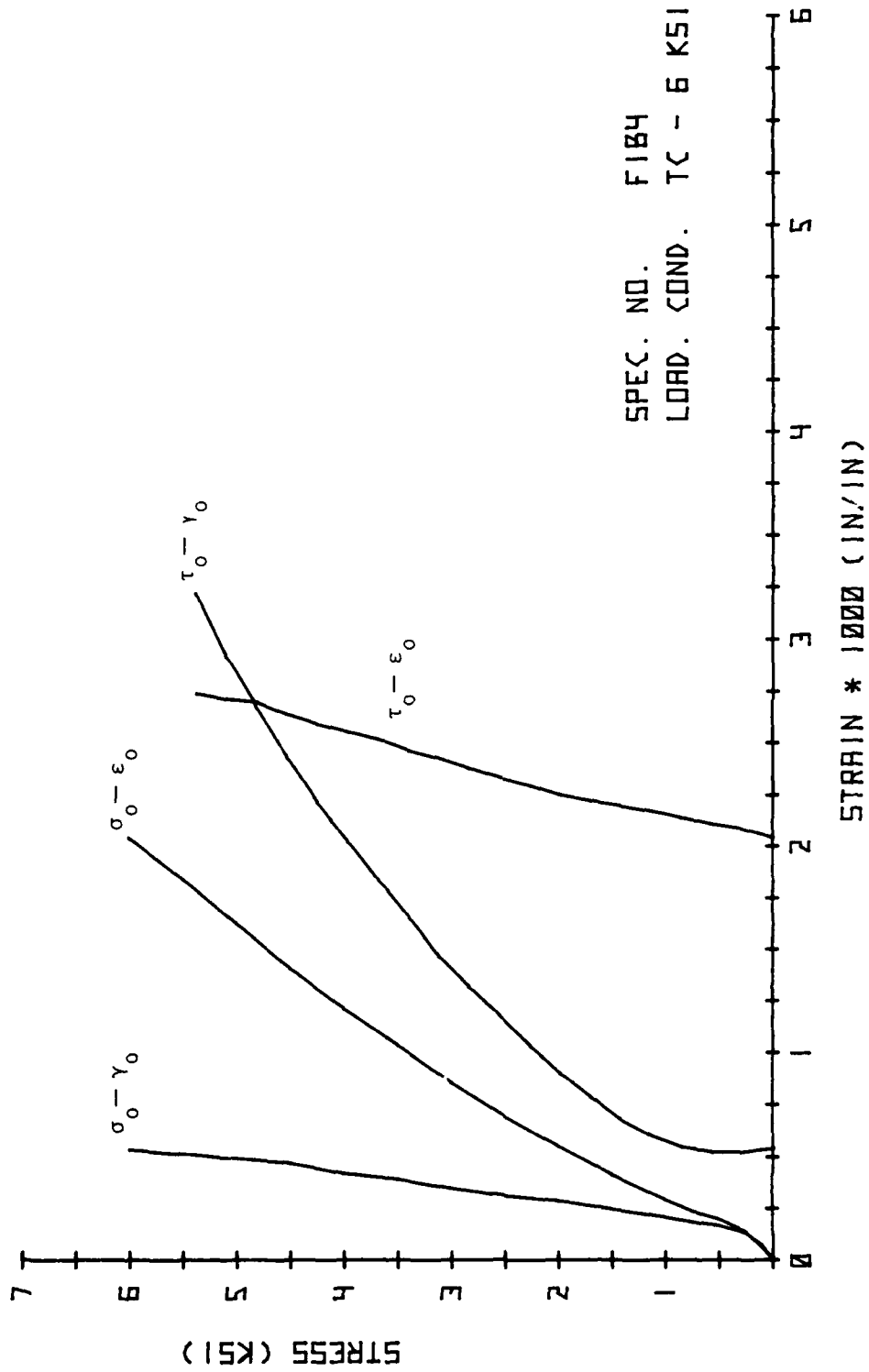


Fig. 4.52. Octahedral Stress-Strain Results.

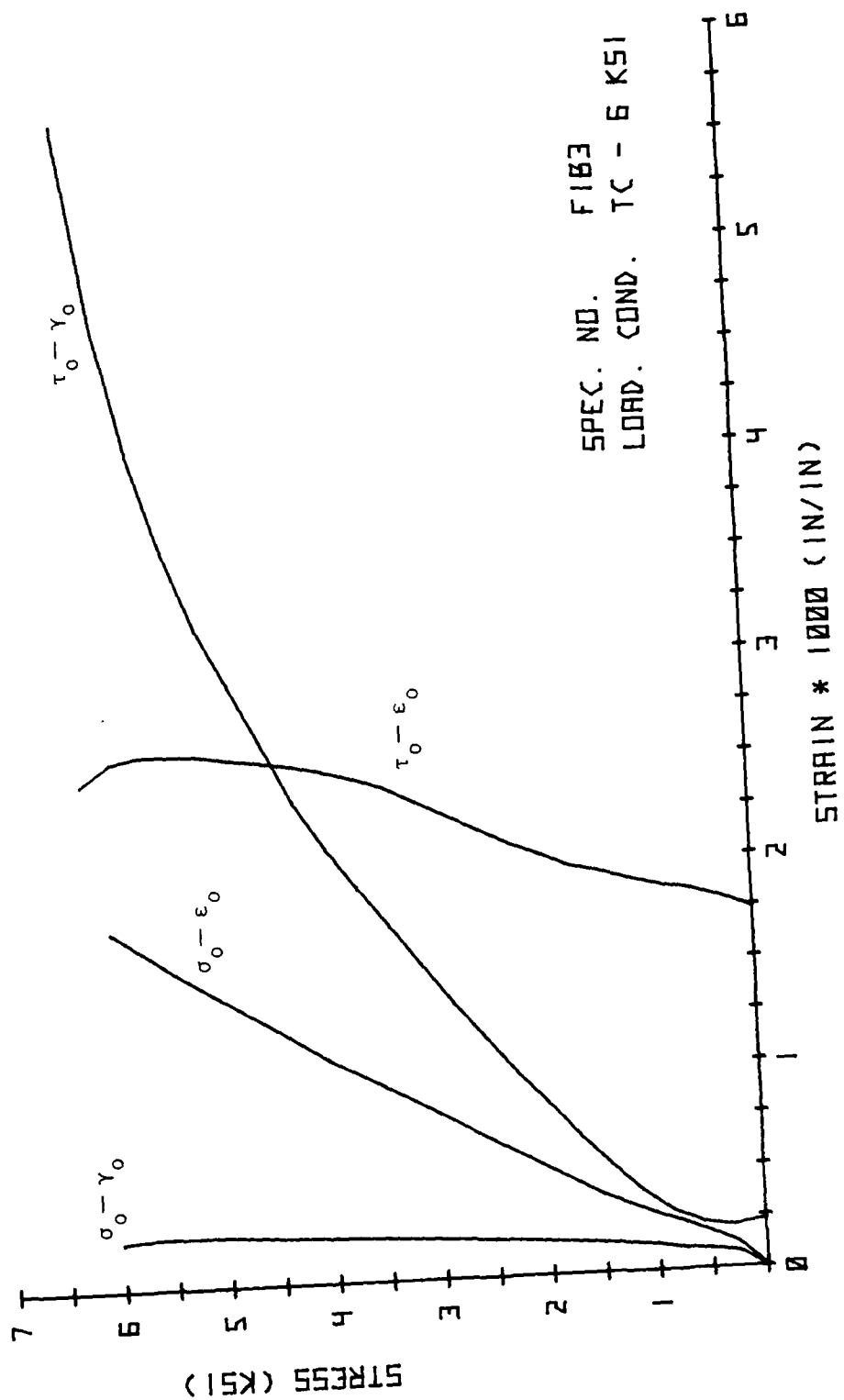


Fig. 4.53. Octahedral Stress-Strain Results.

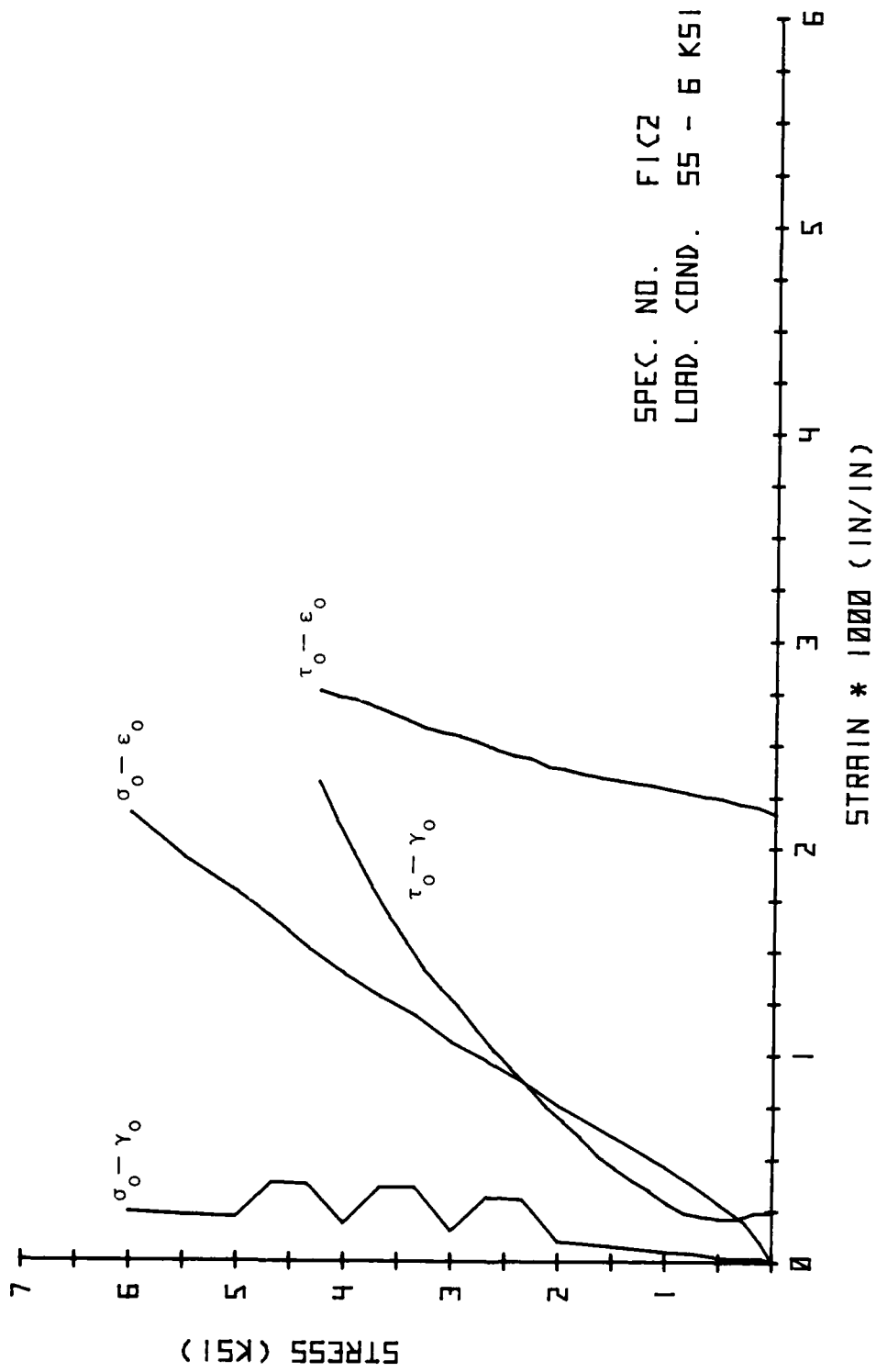


Fig. 4.54. Octahedral Stress-Strain Results.

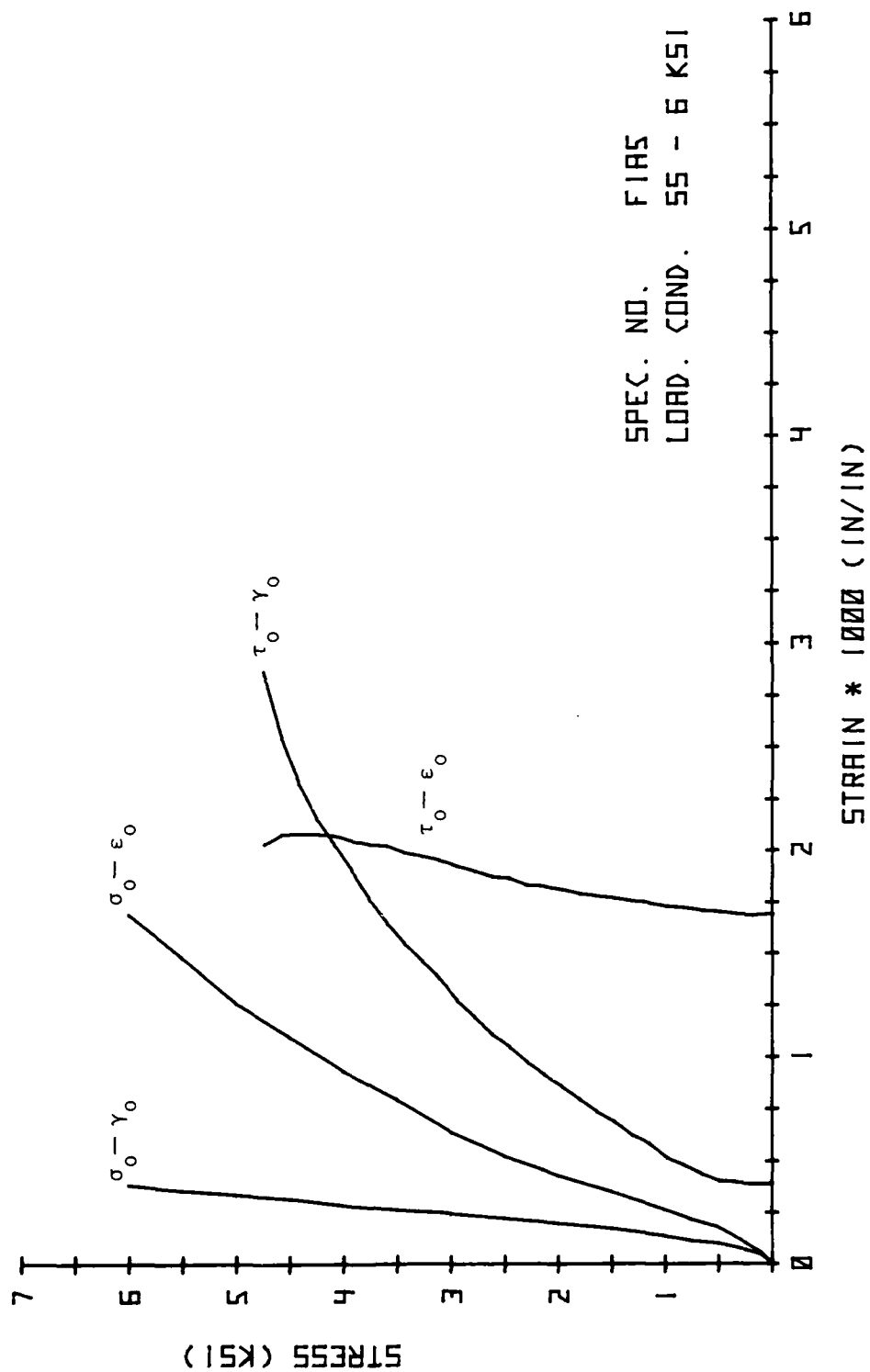


Fig. 4.55. Octahedral Stress-Strain Results.

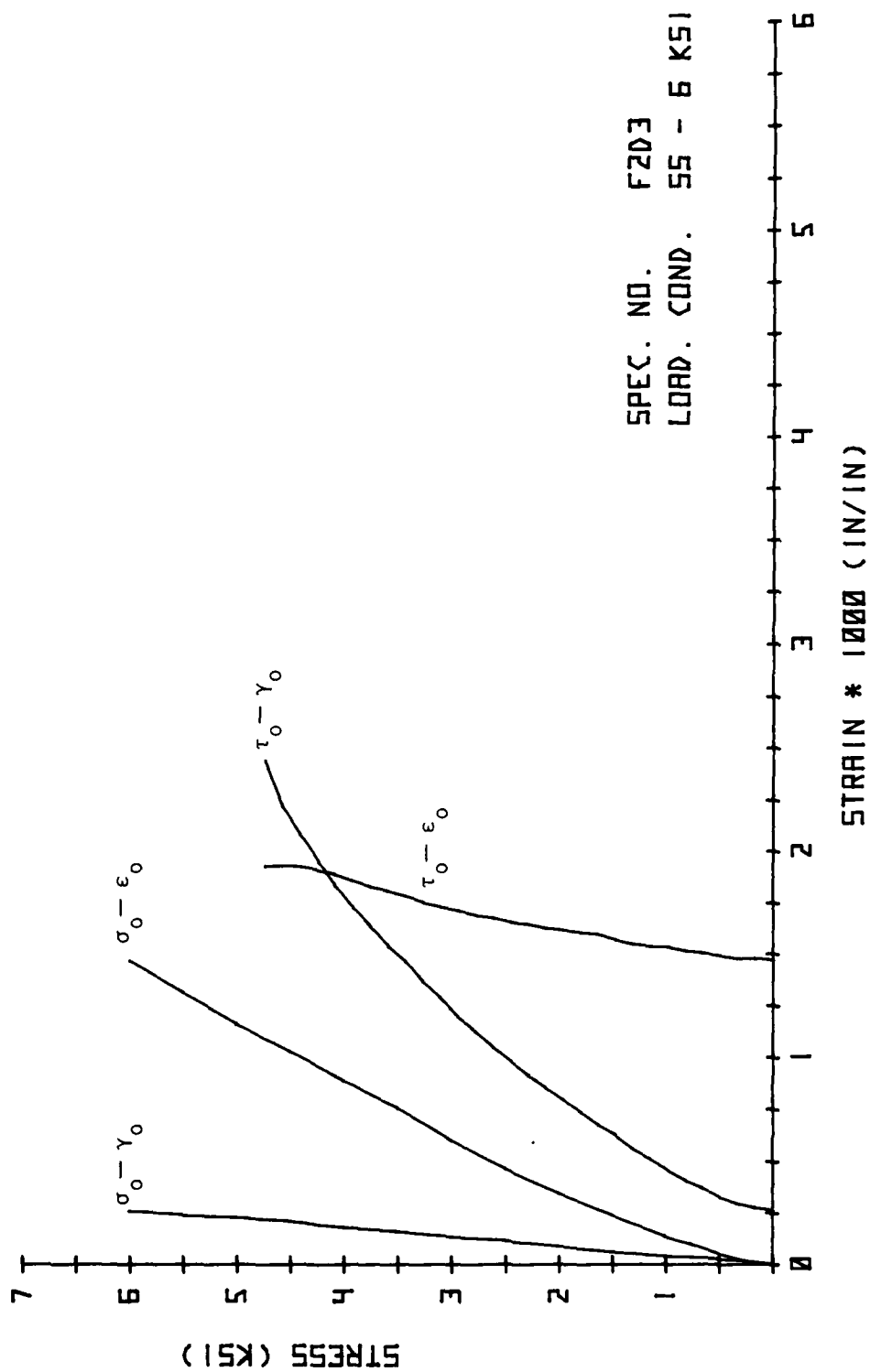


Fig. 4.56. Octahedral Stress-Strain Results.

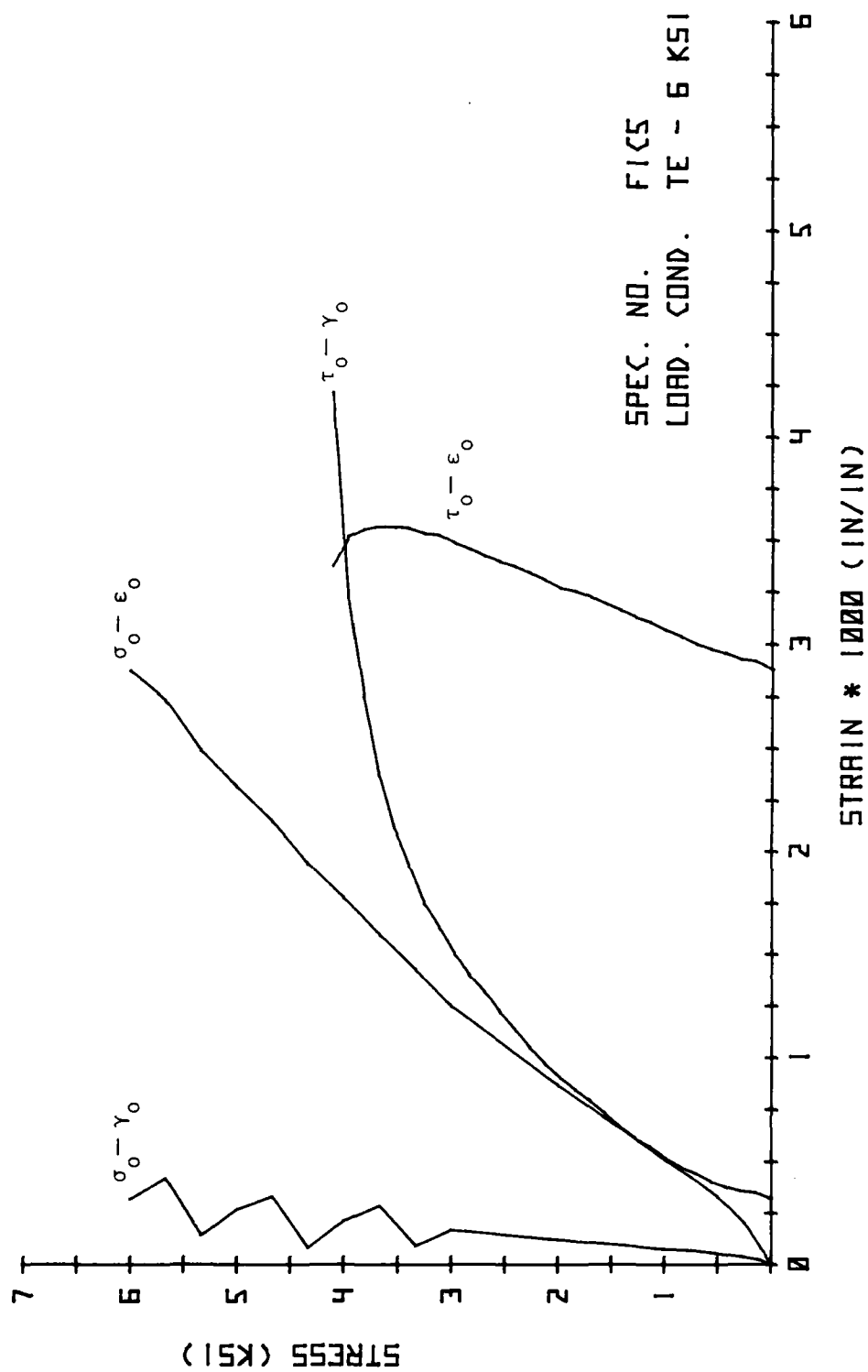


Fig. 4.57. Octahedral Stress-Strain Results.

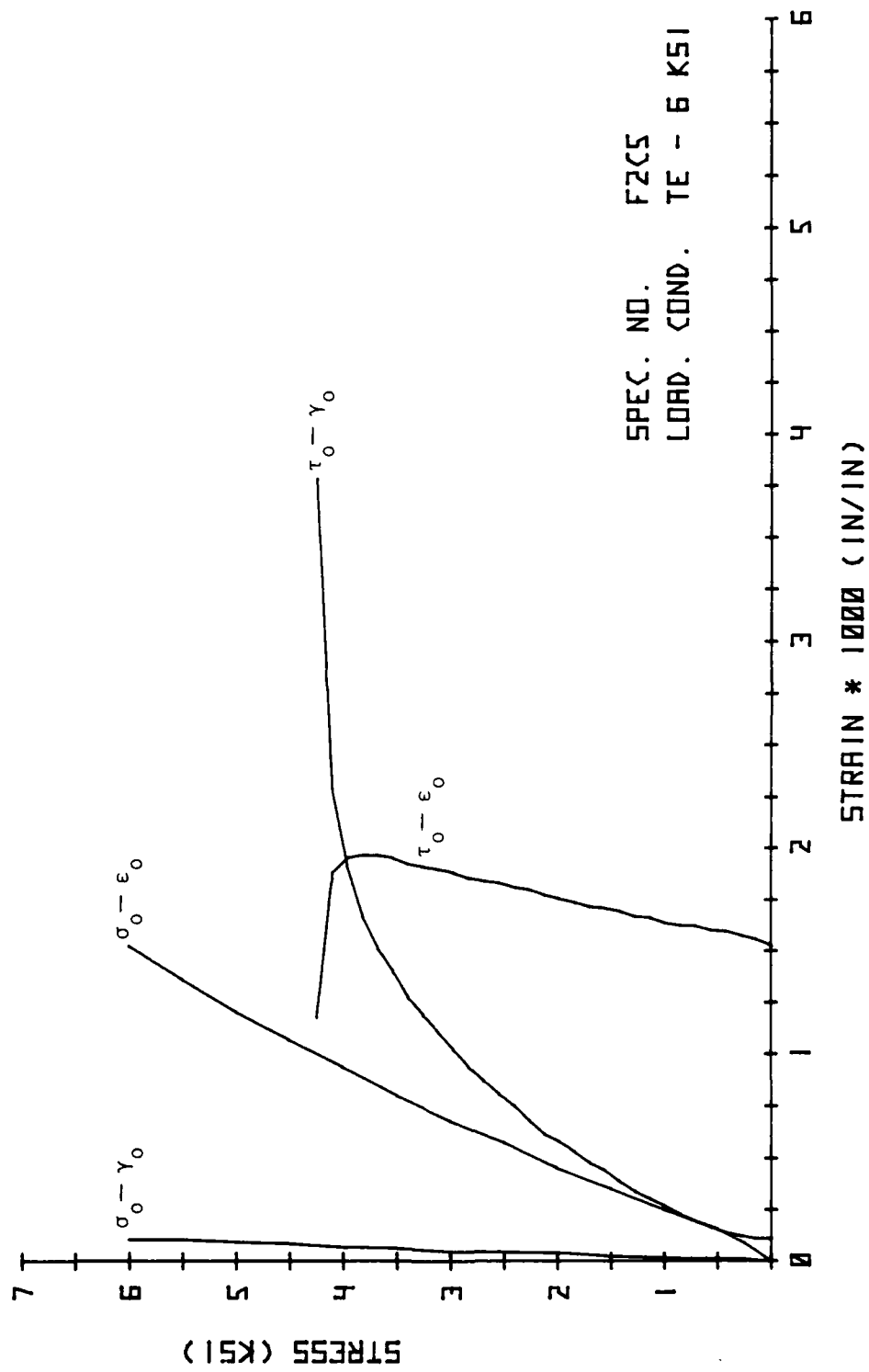


Fig. 4.58. Octahedral Stress-Strain Results.

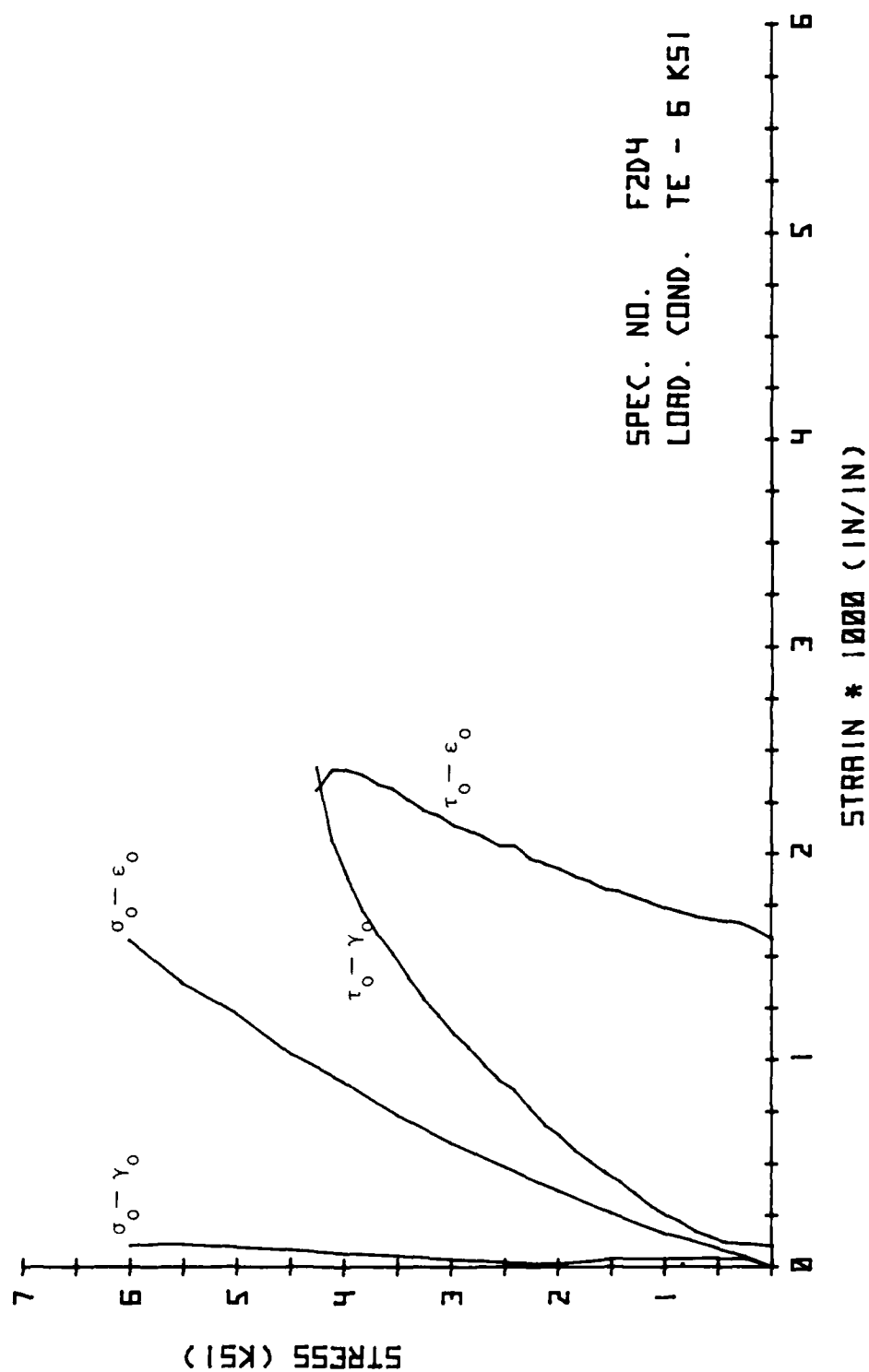


Fig. 4.59. Octahedral Stress-Strain Results.

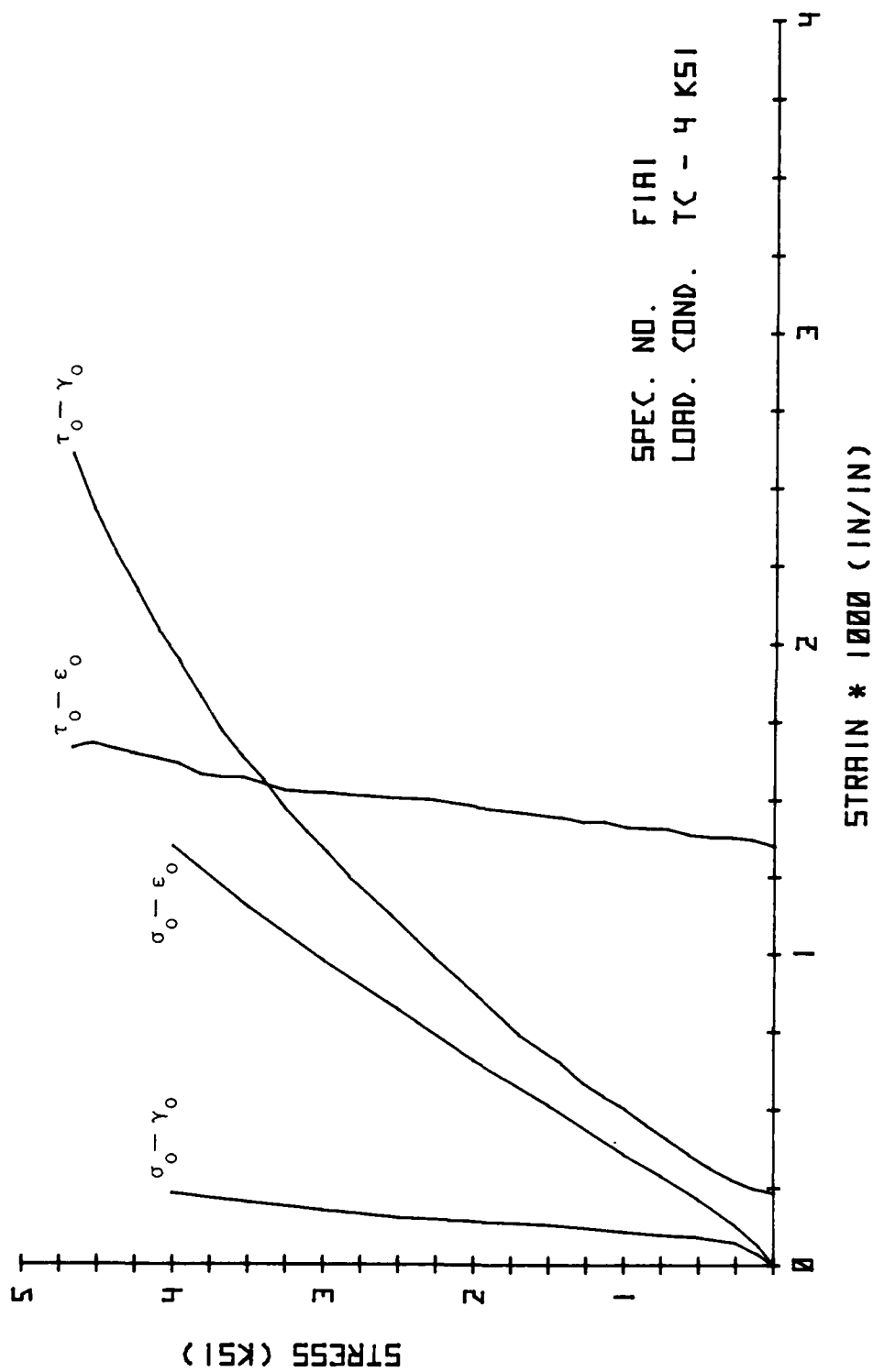


Fig. 4.60. Octahedral Stress-Strain Results.

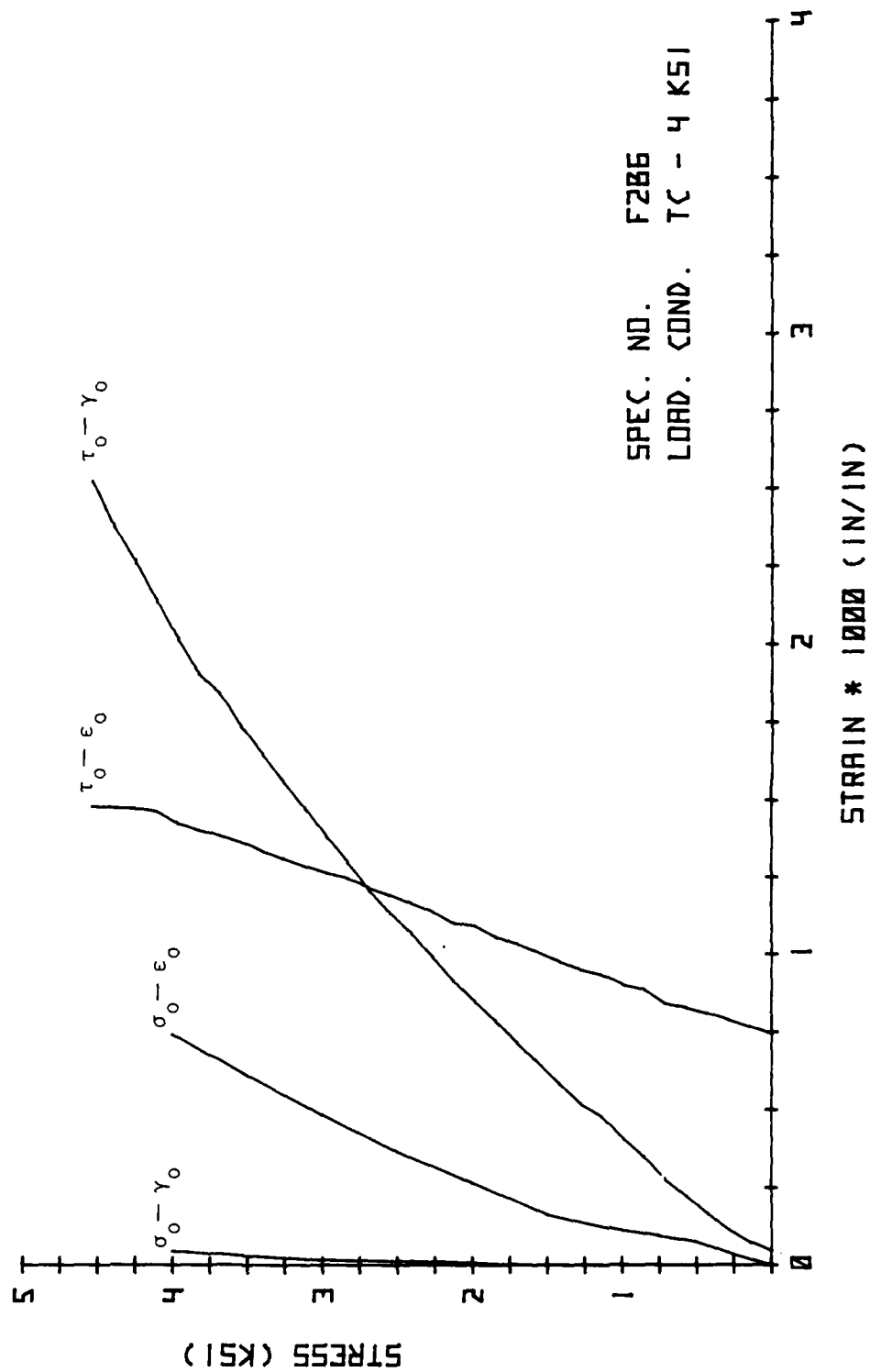


Fig. 4.61. Octahedral Stress-Strain Results.

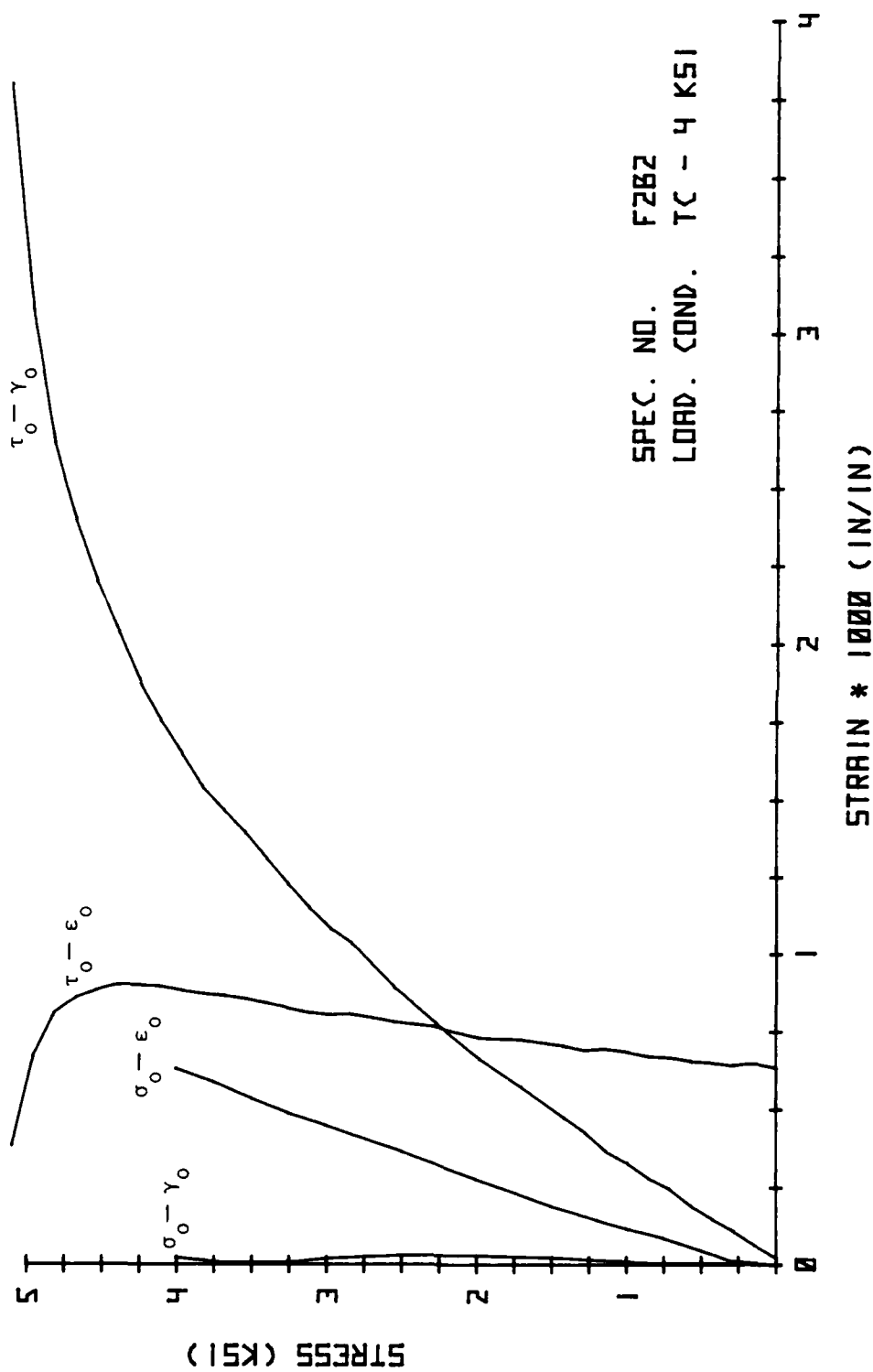


Fig. 4.62. Octahedral Stress-Strain Results.

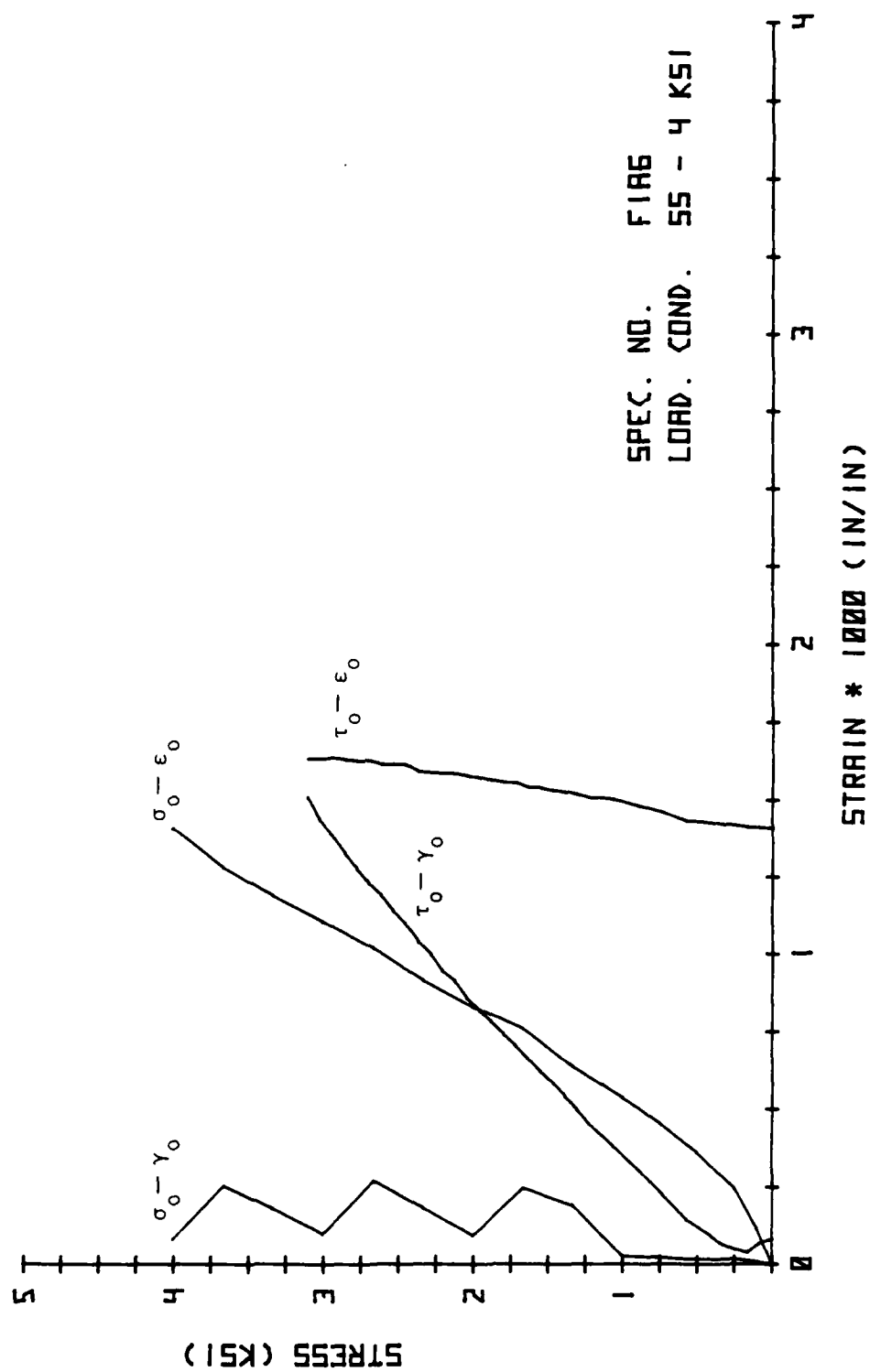


Fig. 4.63. Octahedral Stress-Strain Results.

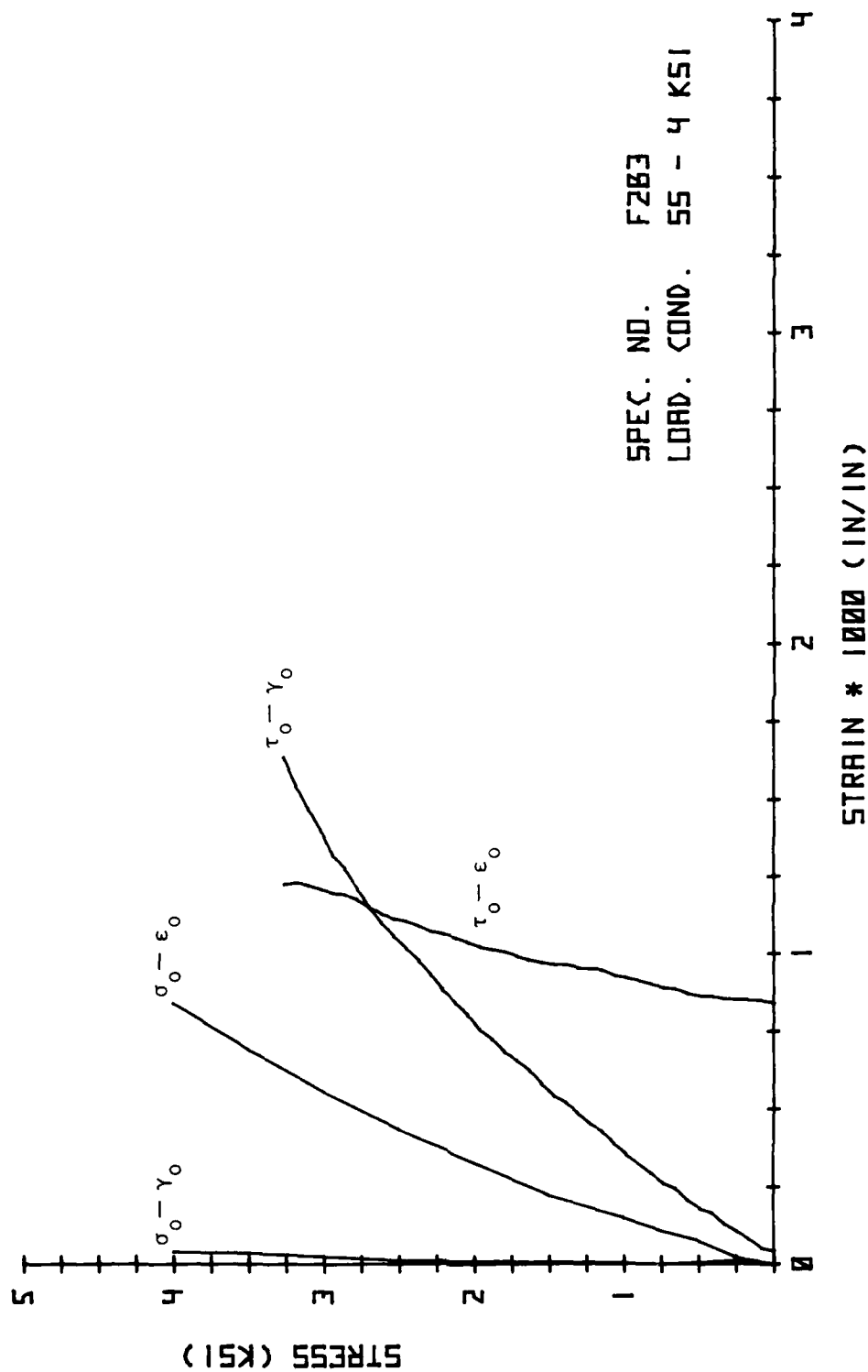


Fig. 4.64. Octahedral Stress-Strain Results.

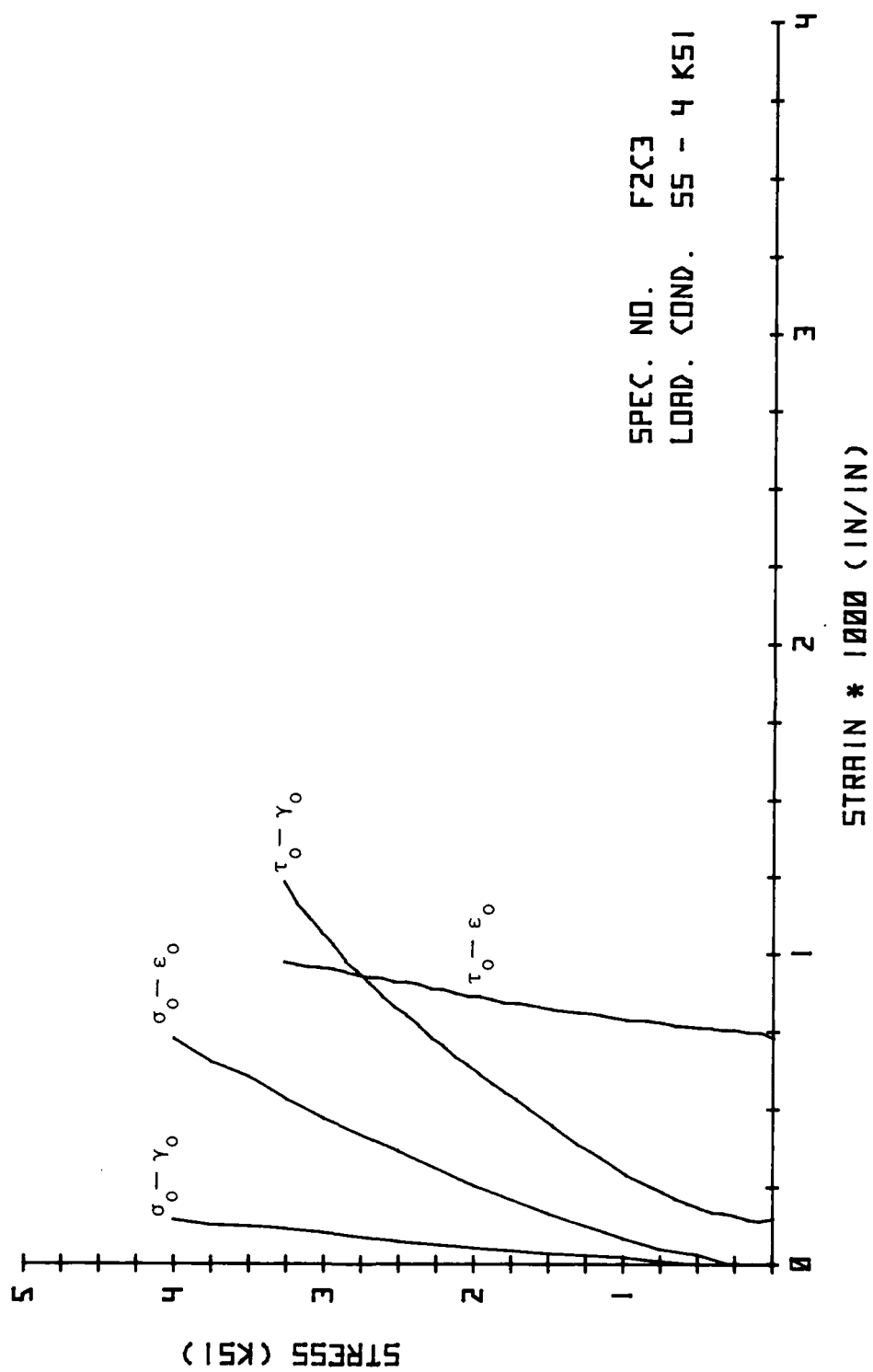


Fig. 4.65. Octahedral Stress-Strain Results.

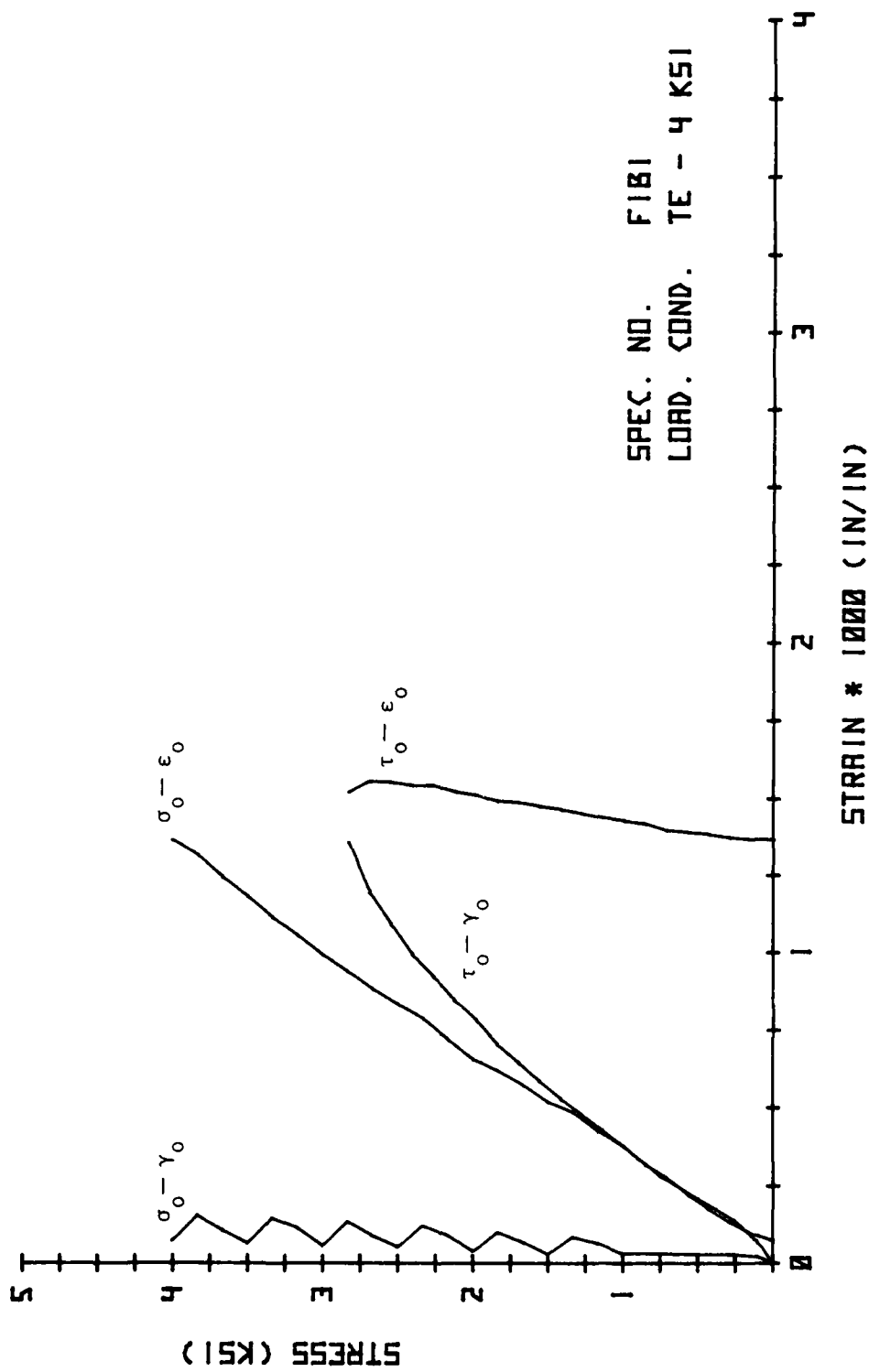


Fig. 4.66. Octahedral Stress-Strain Results.

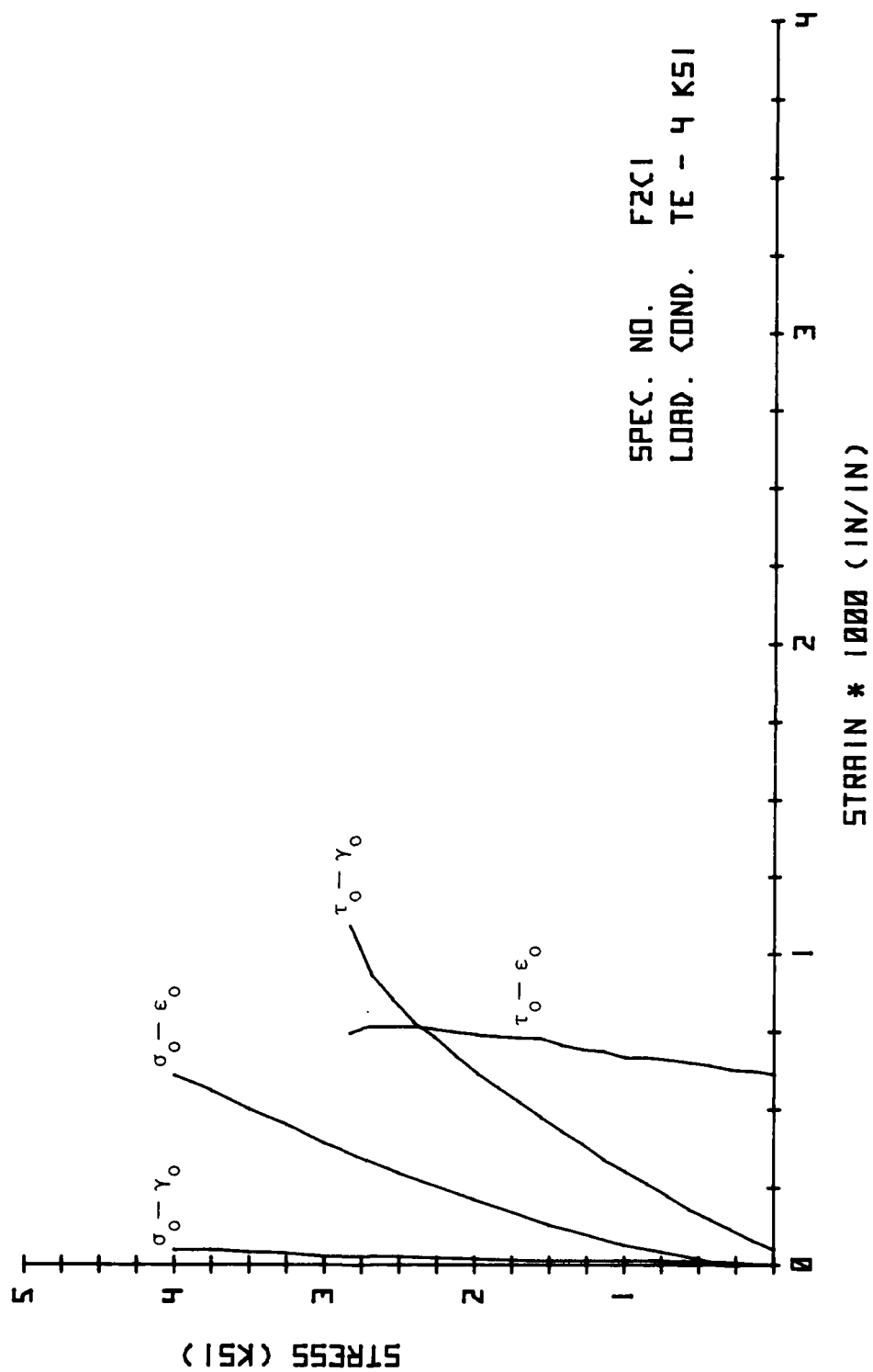


Fig. 4.67. Octahedral Stress-Strain Results.

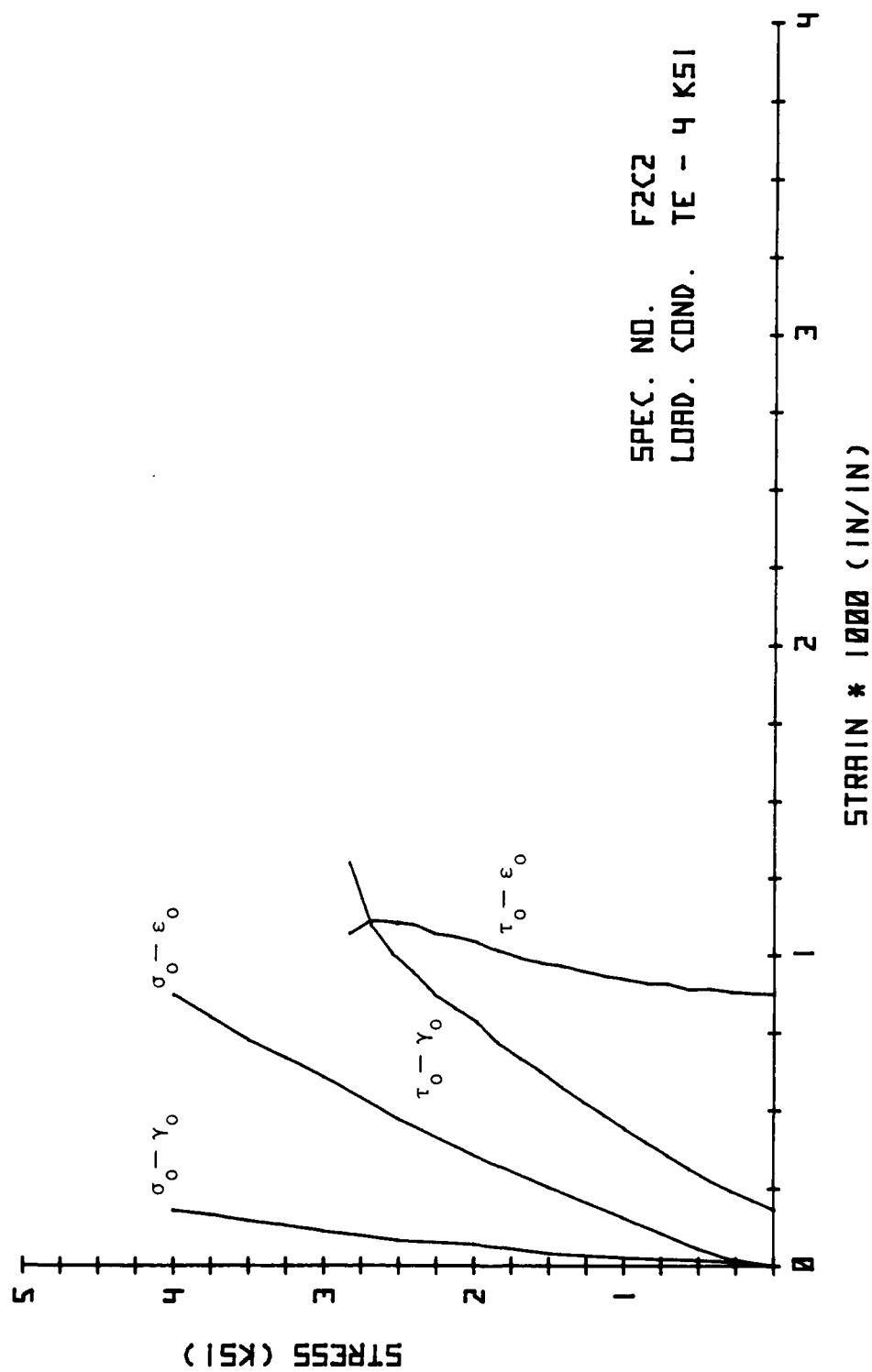


Fig. 4.68. Octahedral Stress-Strain Results.

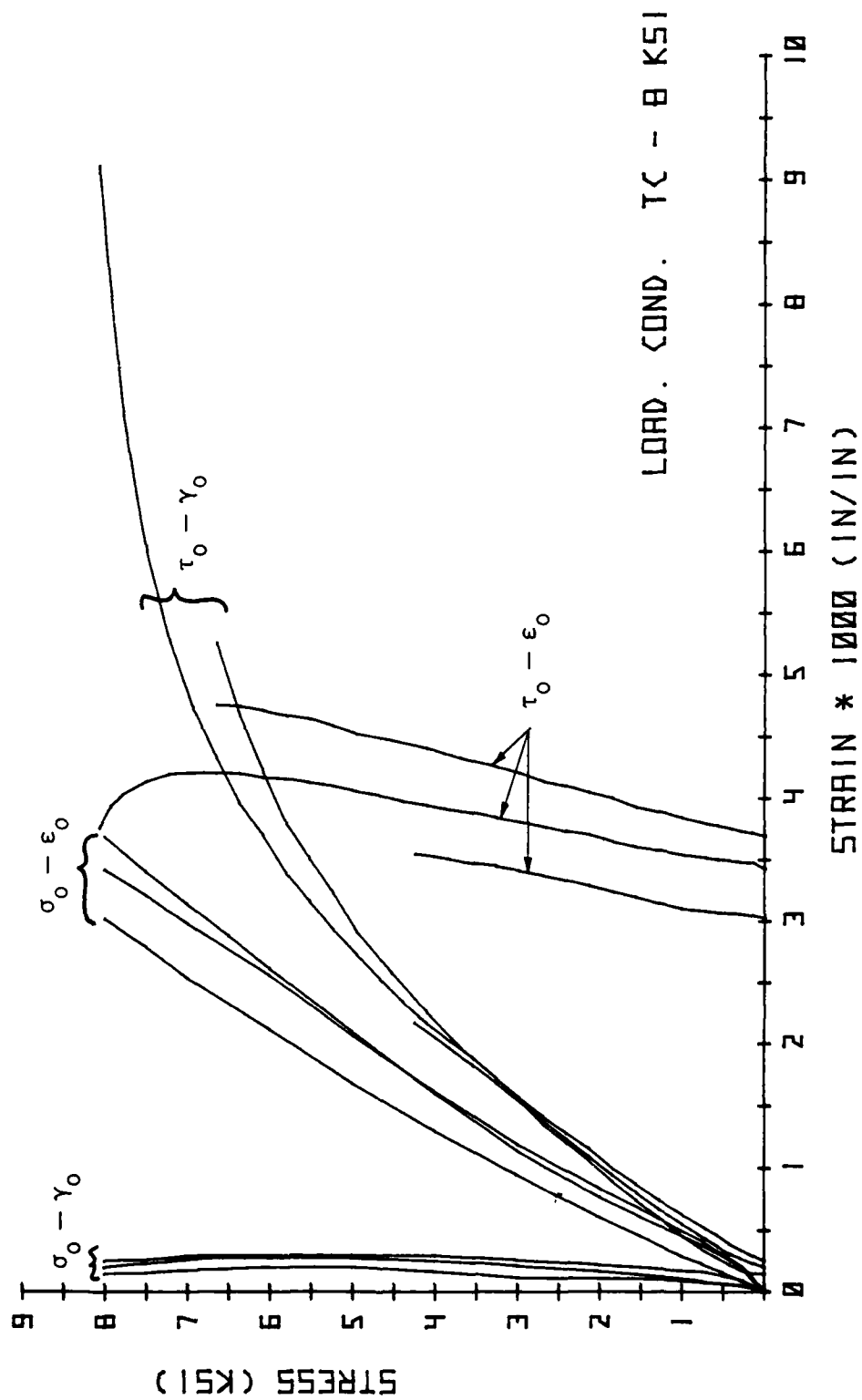


Fig. 4.69. Octahedral Stress-Strain Summary Results.

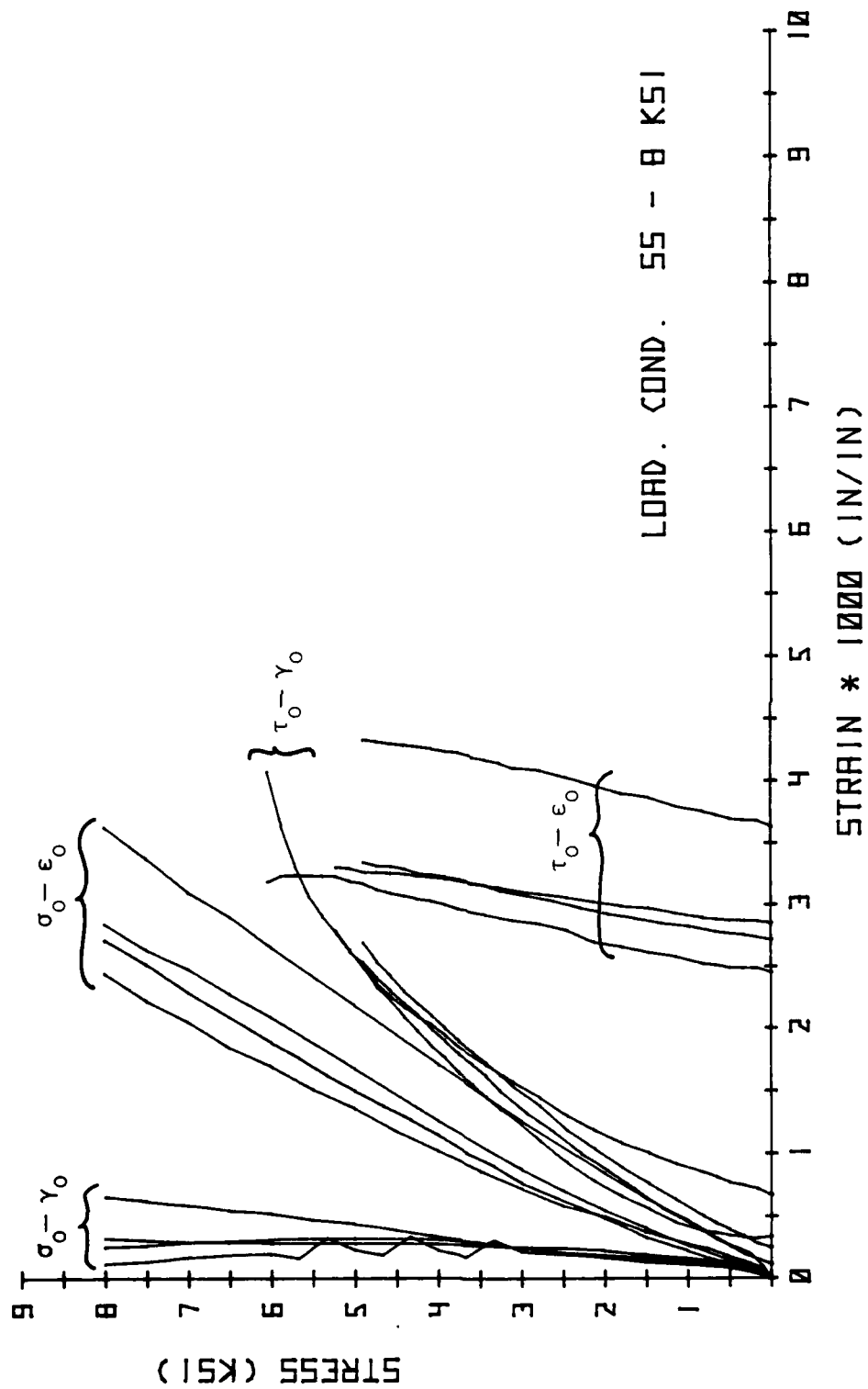


Fig. 4.70. Octahedral Stress-Strain Summary Results.

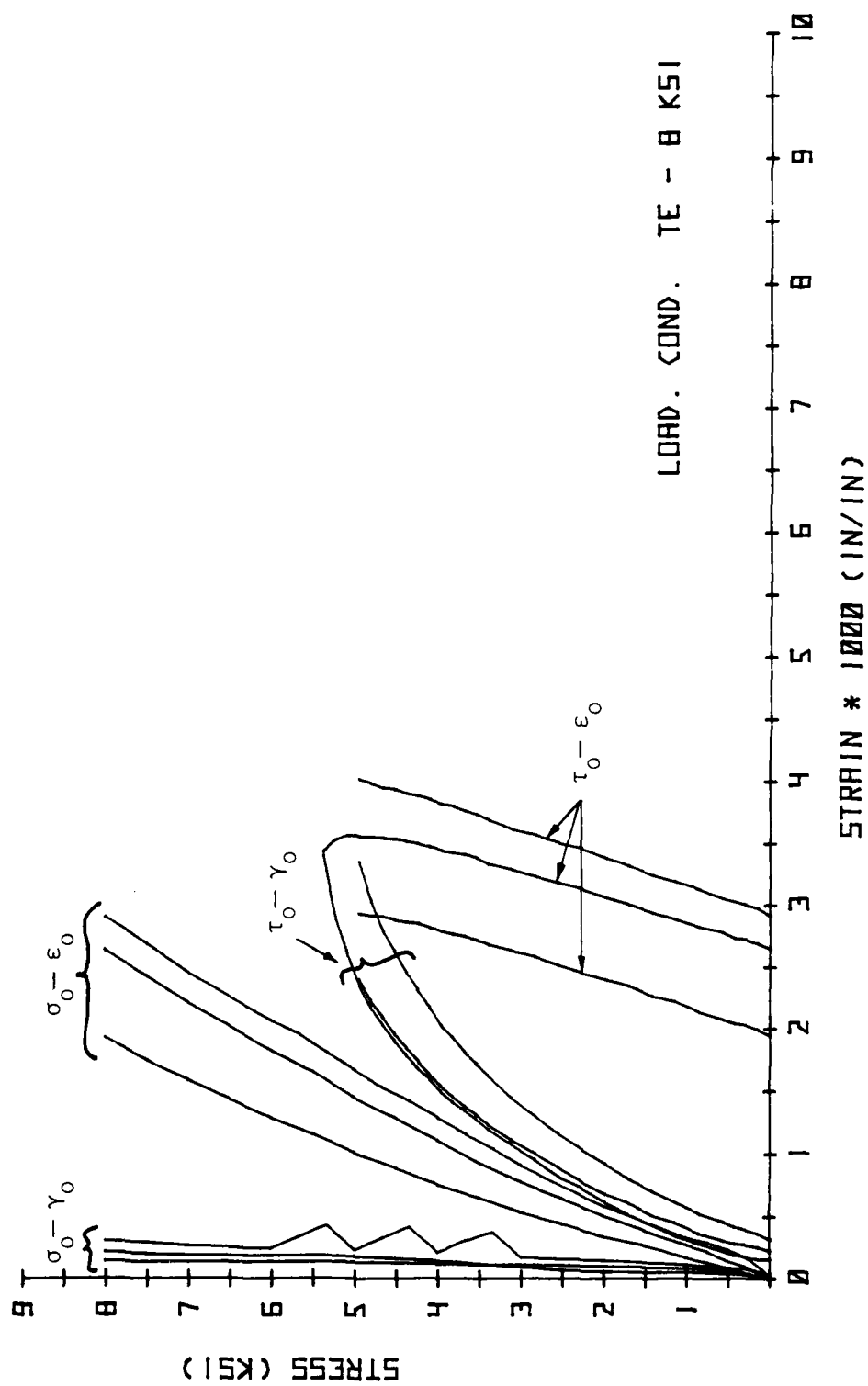


Fig. 4.71. Octahedral Stress-Strain Summary Results.

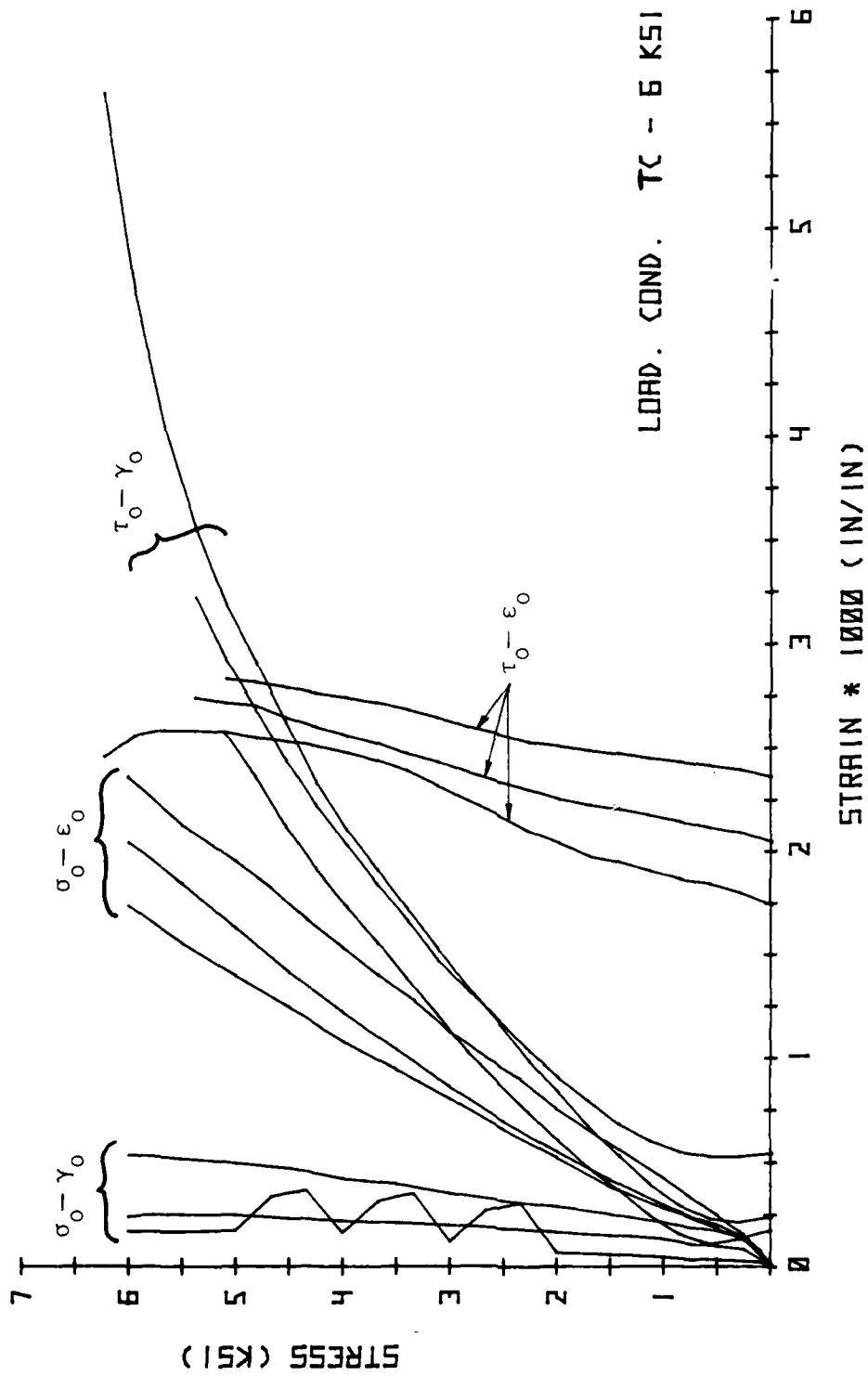


Fig. 4.72. Octahedral Stress-Strain Summary Results.

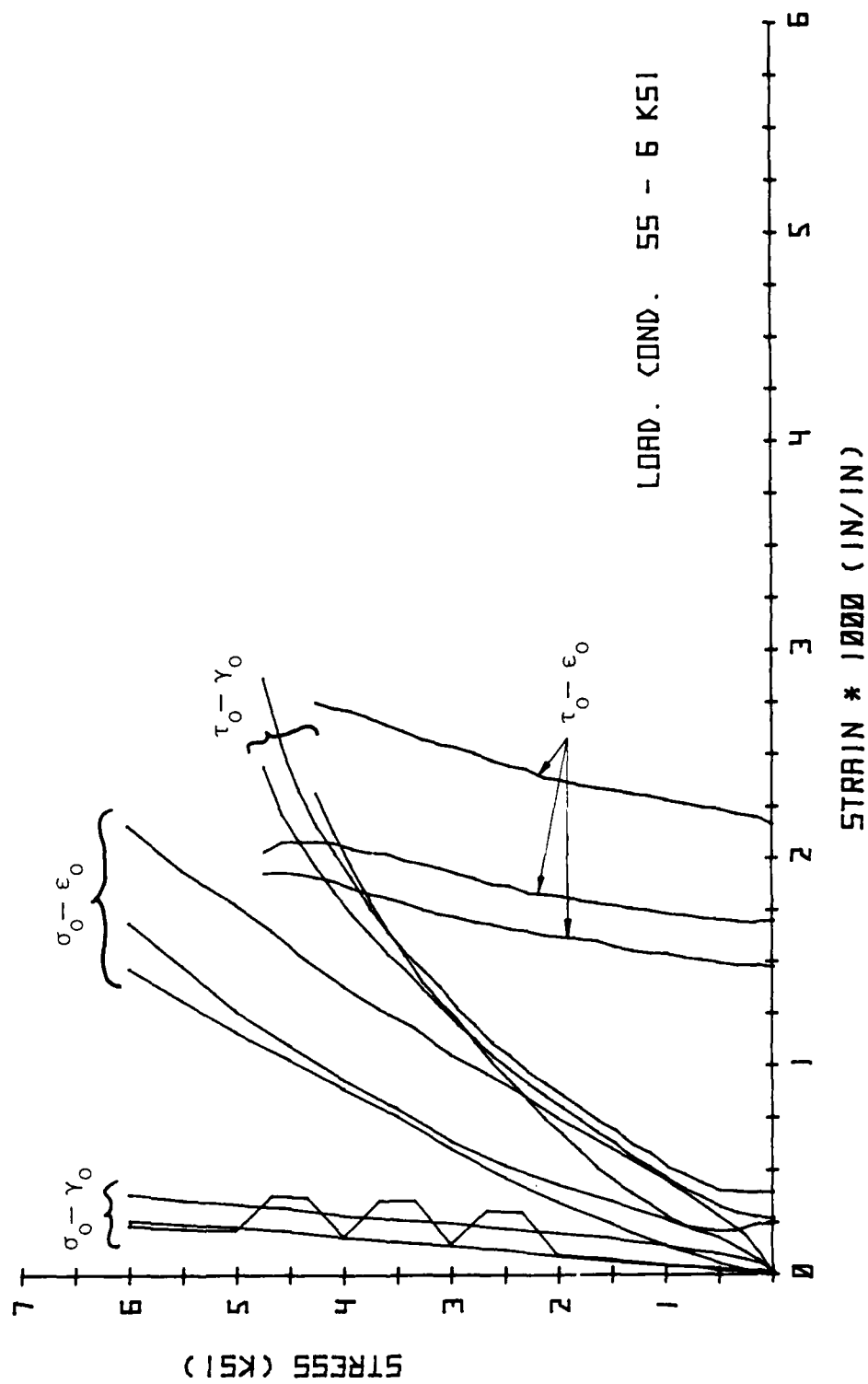


Fig. 4.73. Octahedral Stress-Strain Summary Results.

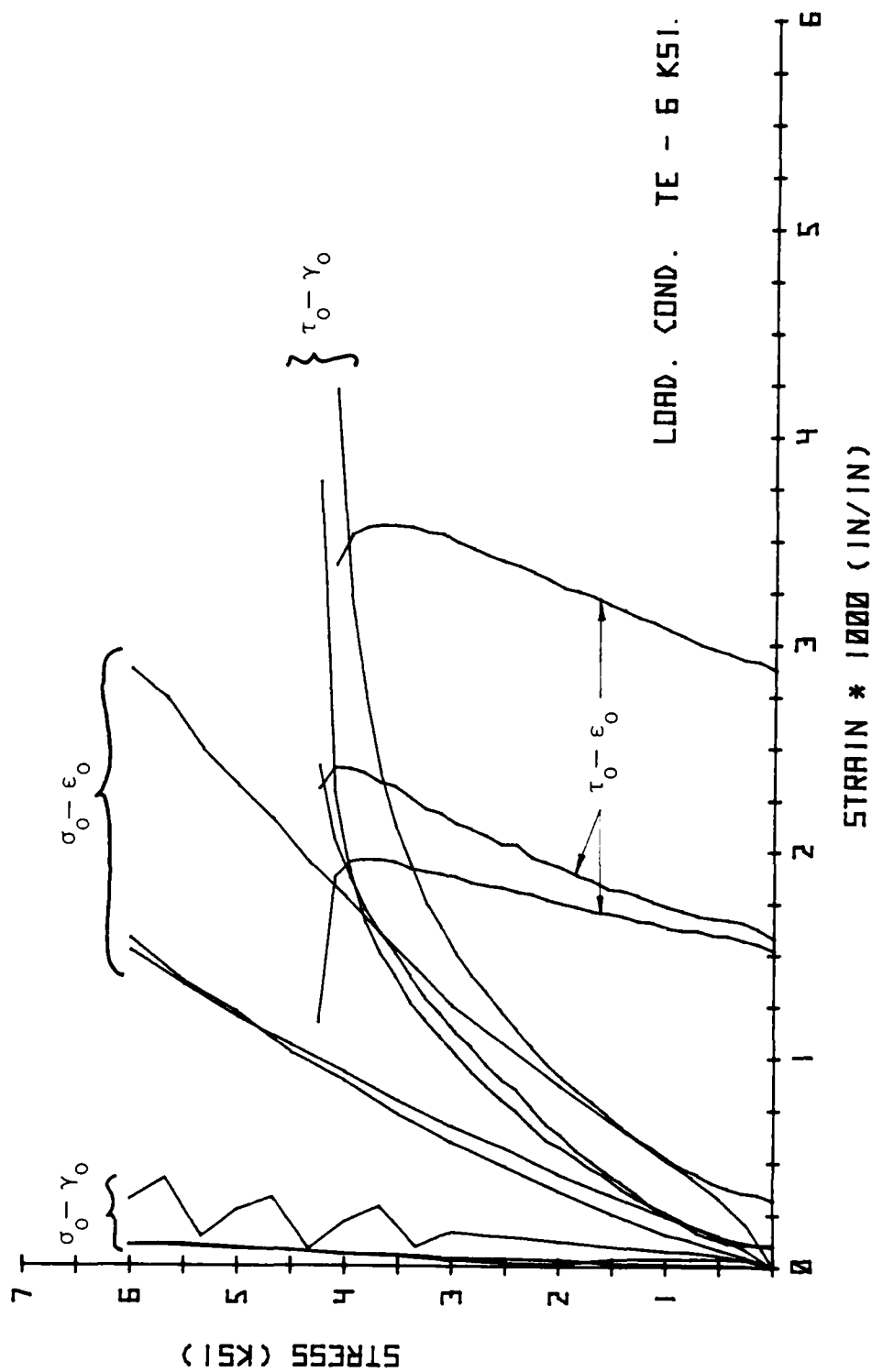


Fig. 4.74. Octahedral Stress-Strain Summary Results.

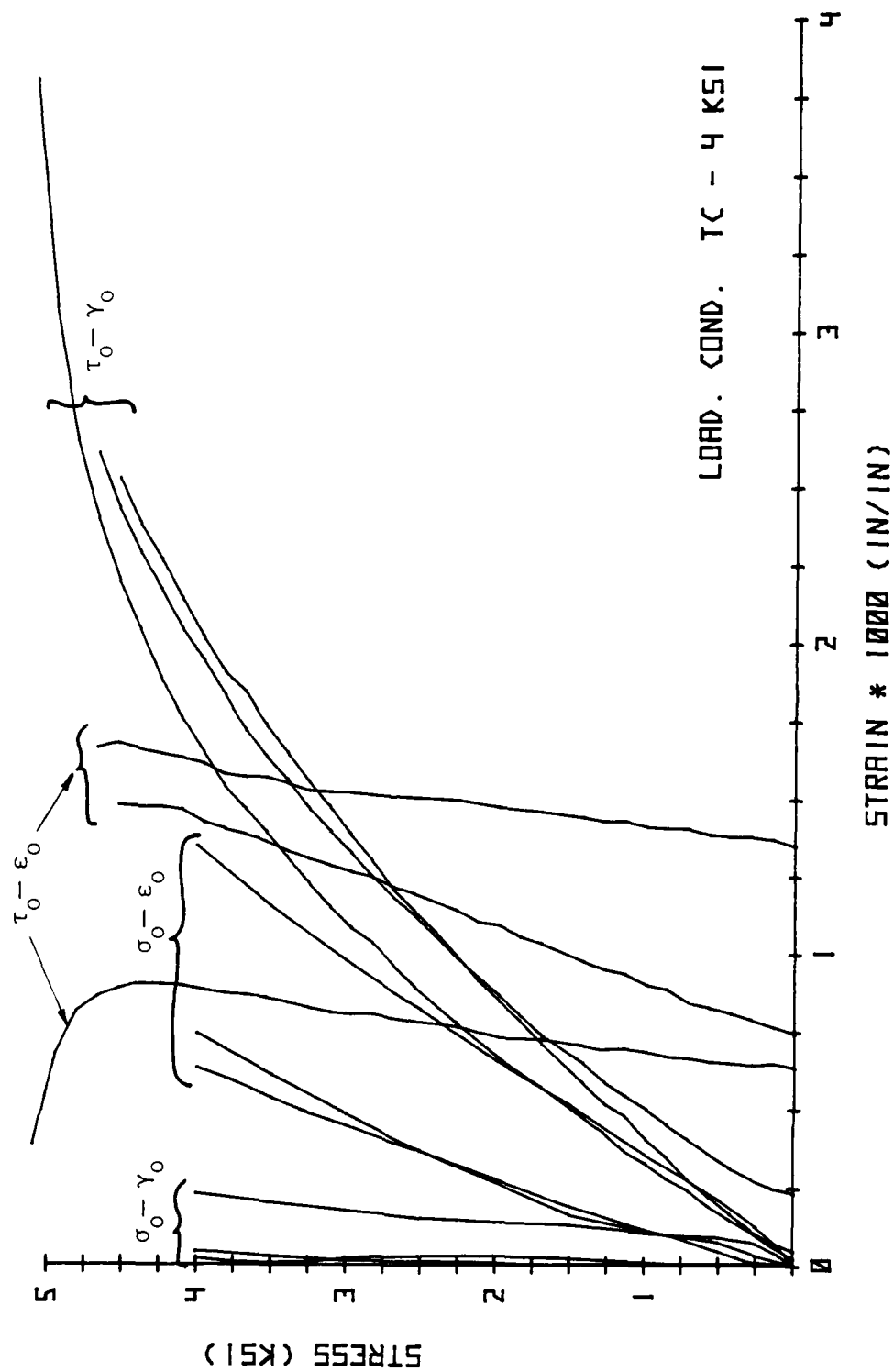
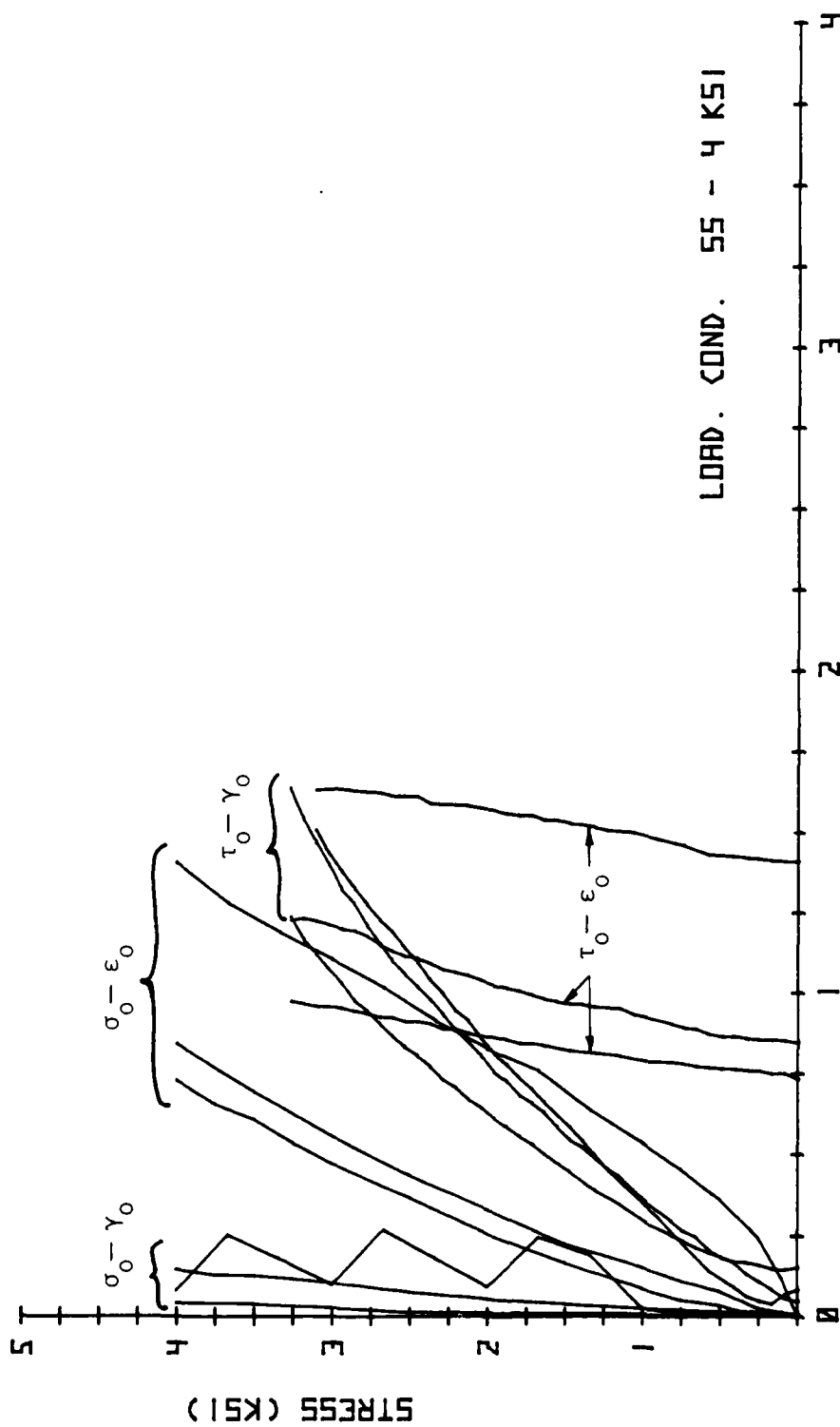


Fig. 4.75. Octahedral Stress-Strain Summary Results.



STRAIN * 1000 (IN/IN)

LOAD. COND. 55 - 4 KSI

Fig. 4.76. Octahedral Stress-Strain Summary Results.

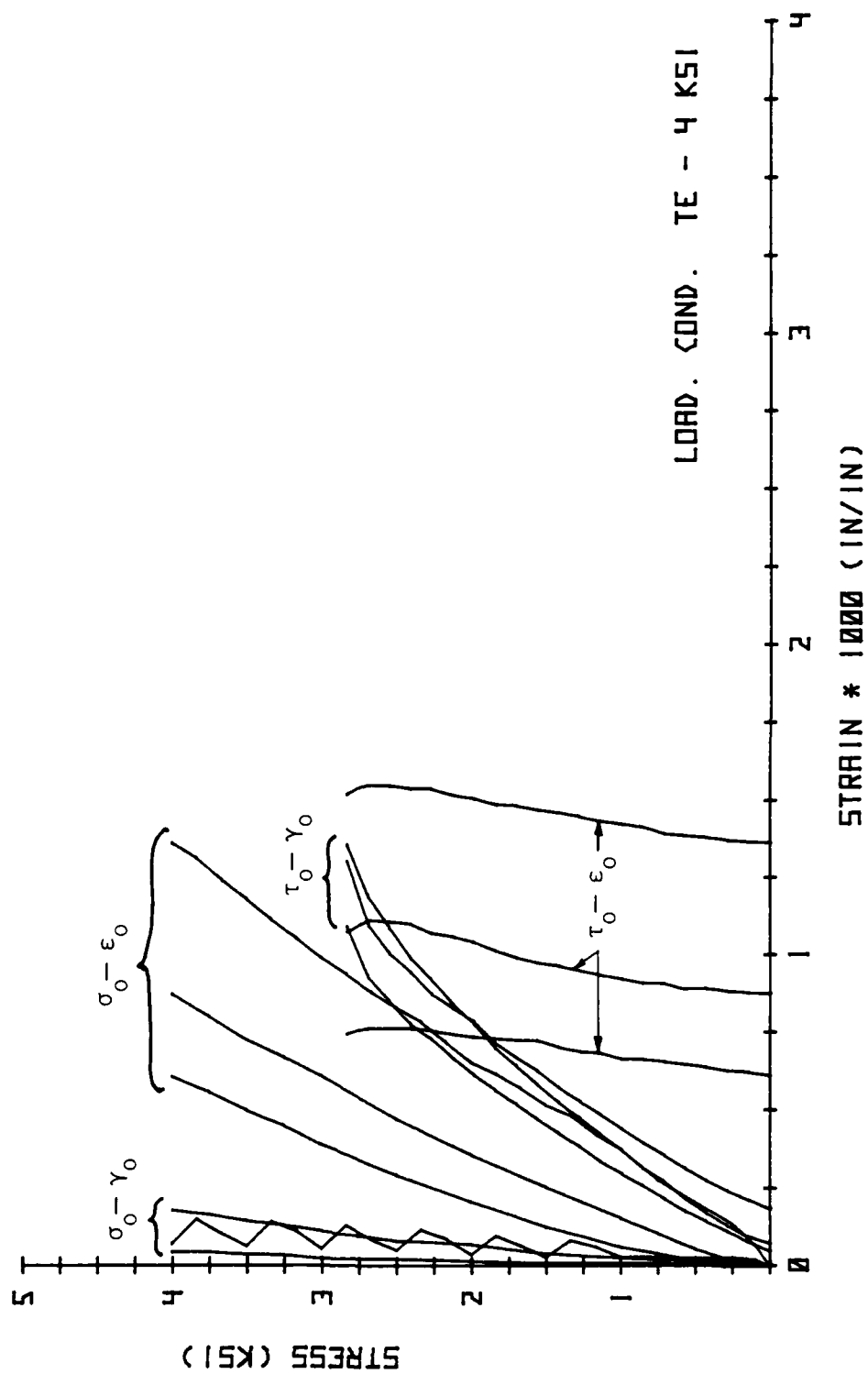


Fig. 4.77. Octahedral Stress-Strain Summary Results.

confusion, an explanation of this presentation follows. During HC, the only stress involved is the hydrostatic stress, or the octahedral normal stress σ_0 ; the octahedral shear stress τ_0 is zero. Obviously, octahedral normal strain ϵ_0 (one third of the volumetric strain) is developed during HC, and if the material is not isotropic, shear distortion will occur even for HC. In other words, there is a coupling between octahedral shear strain γ_0 and hydrostatic stress σ_0 . Therefore, two stress-strain curves result for HC: σ_0 - ϵ_0 and σ_0 - γ_0 . Once HC is completed, monotonic deviation from the hydrostatic axis occurs along an octahedral plane, i.e., at constant σ_0 . The only stress that changes is τ_0 . This time, shear distortion γ_0 obviously occurs in the presence of shear stress τ_0 . Analogous to HC, a coupling occurs between volumetric behavior ϵ_0 and shear deviation τ_0 . Therefore, two stress-strain curves result for shear deviation at constant σ_0 : τ_0 - γ_0 and τ_0 - ϵ_0 . The τ_0 - γ_0 curve starts at zero stress but at the strain γ_0 where HC ended, i.e., the strain where the σ_0 - γ_0 curve ended. Likewise, the τ_0 - ϵ_0 curve does not start at the origin either. It starts at zero stress as well but at the strain ϵ_0 where HC ended, i.e., the final strain of the σ_0 - ϵ_0 curve for pure HC. In reality, for the stress paths employed here, the σ_0 - ϵ_0 and σ_0 - γ_0 curves continue past HC but become horizontal when the HC part of the test is completed, i.e., when σ_0 is constant. Therefore, these curves are shown for HC only.

As in the principal stress-strain curves, three different strain scales were used for presenting the results. However, all tests conducted on the same octahedral plane have the same strain scale. The specimen number and/or loading condition (TC, SS or TE) and value of σ_{om} (4, 6 or 8 ksi) are given in each figure.

Notice that during HC, "kinks" appear in some of the σ_0 - γ_0 curves. As described in Section 4.3.1, these tests employed a stepped-loading path along the hydrostatic axis. Since small cyclic shear stresses are induced (well within the elastic range), changes in shear strains γ_0 will result. Section 4.3.3 gives full details of this stepped-loading procedure.

For discussion purposes, the octahedral stress-strain behavior is separated into two parts: hydrostatic and deviatoric. The behavior corresponding to these two different parts is described below.

4.3.2.1 Hydrostatic Compression (HC)

σ_0 - ϵ_0

Fig. 4.78 summarizes the volumetric behavior during HC of all the tests conducted. The results are shown as the solid lines. The dashed line is the overall calculated average for the σ_0 - ϵ_0 response. The initial bulk modulus (K_0) of this average response is 1433 ksi (neglecting the flatter portion of the curve between 0 and 500 psi). This initial flatter portion is the behavior of the test apparatus (bolt slip, seating of the sealing system, etc.) measured during the first few small load steps, and is not material behavior.

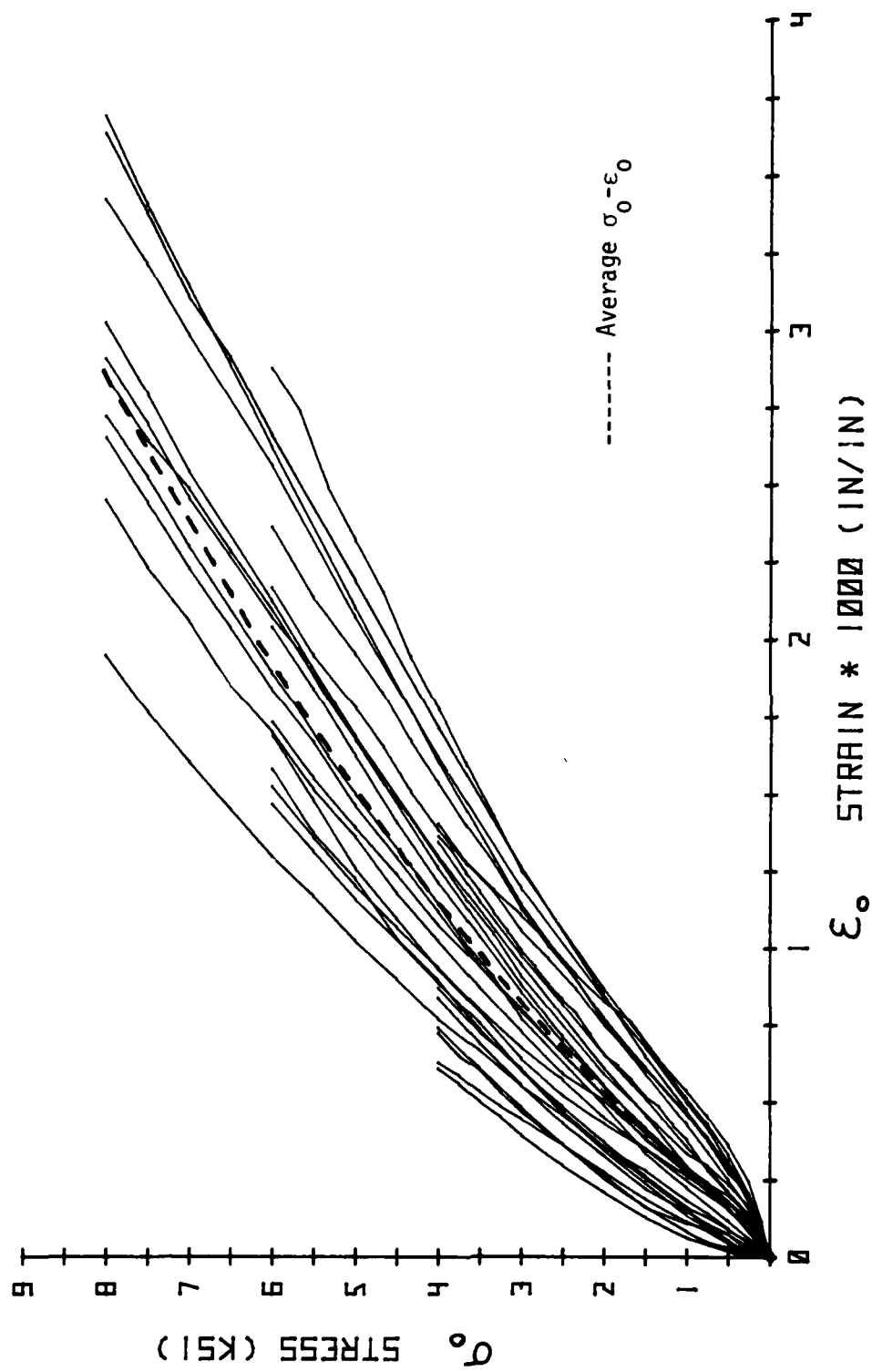


Fig. 4.78. Summary of Volumetric Behavior During HC.

Some specimens exhibit a much stiffer volumetric behavior than others during HC; however, the response of all the specimens is only slightly nonlinear, with the final slope being about one-half the initial slope. Figs 4.79 and 4.80 show the variation in the tangent bulk modulus (K_T) for increasing σ_0 and ϵ_0 respectively. The scatter present in Fig. 4.78 shows up again in these two figures, especially Fig. 4.79. Notice however, on the whole, the nearly linearly decreasing relationship between K_T and σ_0 , whereas a more nonlinear relationship between K_T and ϵ_0 exists. Notice also in Fig. 4.80, the initial rapid decrease in K_T for increasing ϵ_0 , then the much slower decrease, eventually becoming constant (but greater than zero) for larger values of ϵ_0 . In both figures, the dashed line represents the average response.

The scatter seen in the volumetric response (σ_0 - ϵ_0) during HC, shown in Fig. 4.78, contributes to the differences in starting points of the τ_0 - ϵ_0 curves presented in Figs. 4.69-4.77, thereby making this coupling behavior appear to have more variation than it actually does. This will be discussed further in a later section.

σ_0 - γ_0

If shear strains (γ_0) are developed during HC, the material is not completely isotropic. The σ_0 - γ_0 curves shown in Figs. 4.41-4.77 demonstrate the degree of anisotropy in the SFRC. Notice that in some of the σ_0 - γ_0 curves, an initial flatter portion exists for the first few load steps between, say, 0 and 500 psi, then the curves become very steep with very large slopes. Again, as previously discussed, this is apparatus and not material behavior.

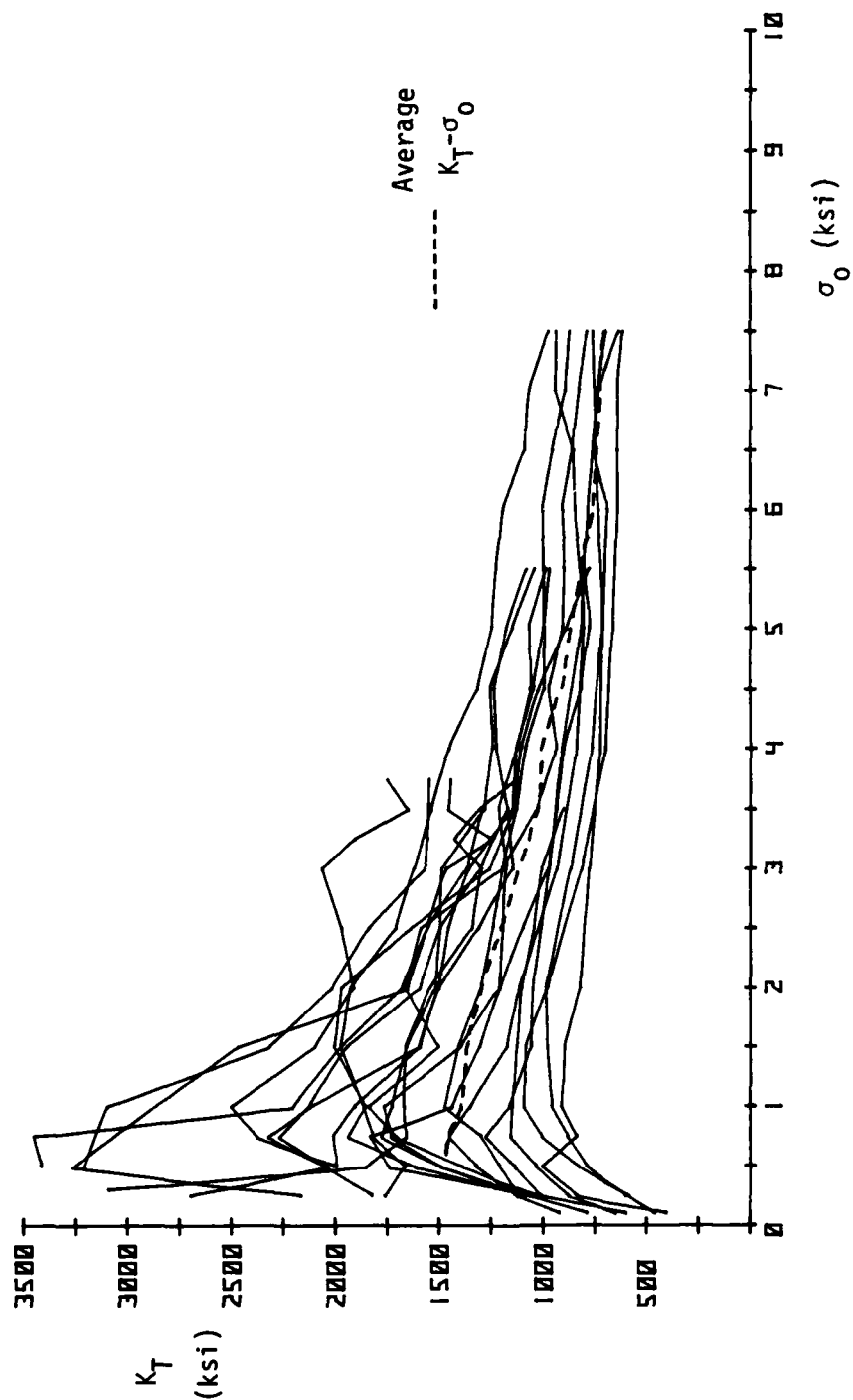


Fig. 4.79. Tangent Bulk Modulus vs. Octahedral Normal Stress for all Results During HC.

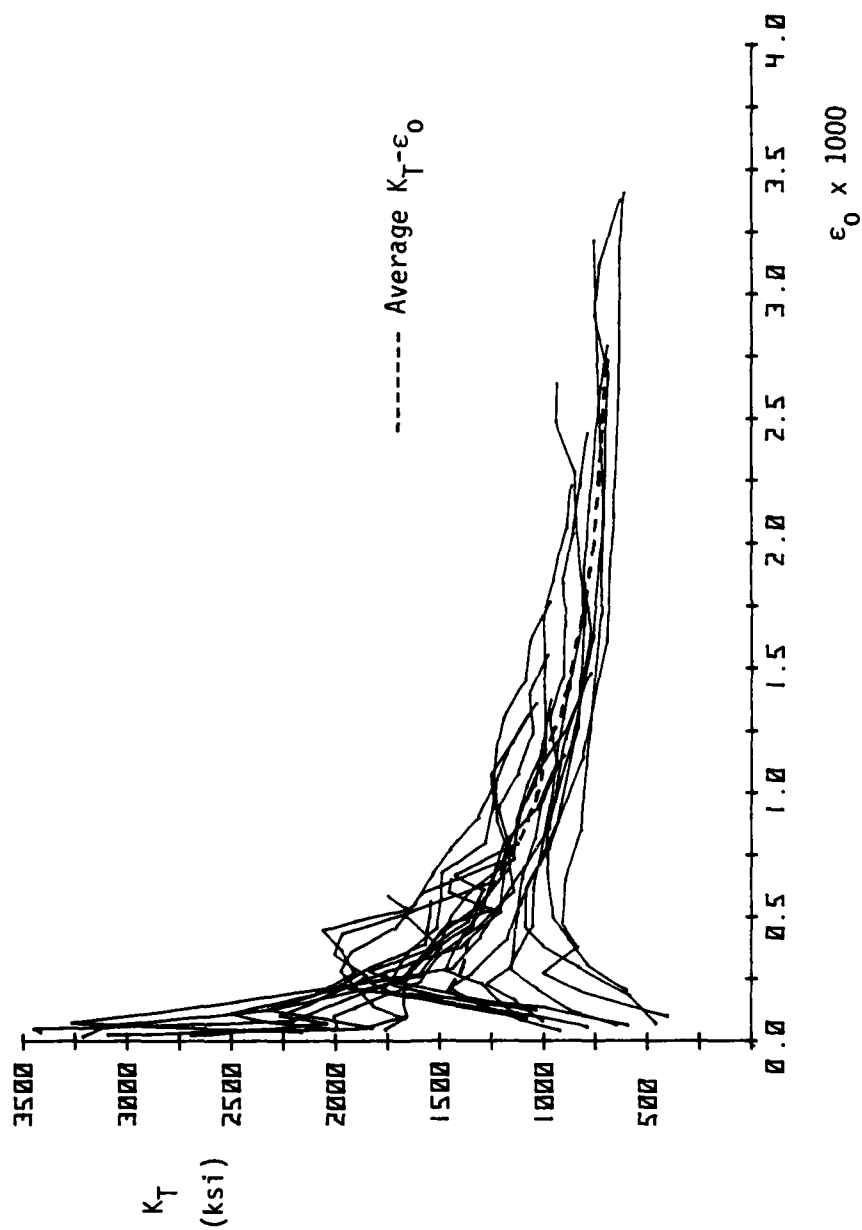


Fig. 4.80. Tangent Bulk Modulus vs. Octahedral Normal Strain for all Results During HC.

The coupling between σ_0 and γ_0 is very slight, and the shear strains (γ_0) developed during HC are about an order of magnitude less than the normal strains (ϵ_0) when examining the behavior of each test separately. Therefore, one could safely assume isotropy exists for this material and neglect the coupling between σ_0 and γ_0 as is done when dealing with and defining failure criteria for concrete materials. Therefore no average results of the σ_0 - γ_0 behavior are presented.

Analogous to the σ_0 - ϵ_0 case, the scatter seen in the σ_0 - γ_0 behavior, shown in the summary curves (Figs. 4.69-4.77), is the reason for the differences in starting points of the τ_0 - γ_0 summary curves shown in the same figures, compounding the scatter that appears in the τ_0 - γ_0 results.

4.3.2.2 Shear Deviation

τ_0 - γ_0

Individual and summary results are shown in Figs. 4.41-4.77. From these, average τ_0 - γ_0 behavior was calculated and the results are presented in:

- 1) Figs. 4.81-4.83 for different stress paths (TC,SS,TE); same confining pressure (σ_0).
- 2) Figs. 4.84-4.86 for the same stress path; different confining pressures ($\sigma_0 = 8, 6, 4$ ksi).

Only the average results are shown in these different comparative forms (in contrast to presenting all results) for neatness and to avoid confusion if all results were shown. As previously mentioned, the initial difference in starting points, i.e. $\gamma_0 \neq 0$, is due to the small shear strains developed during HC and shown in the

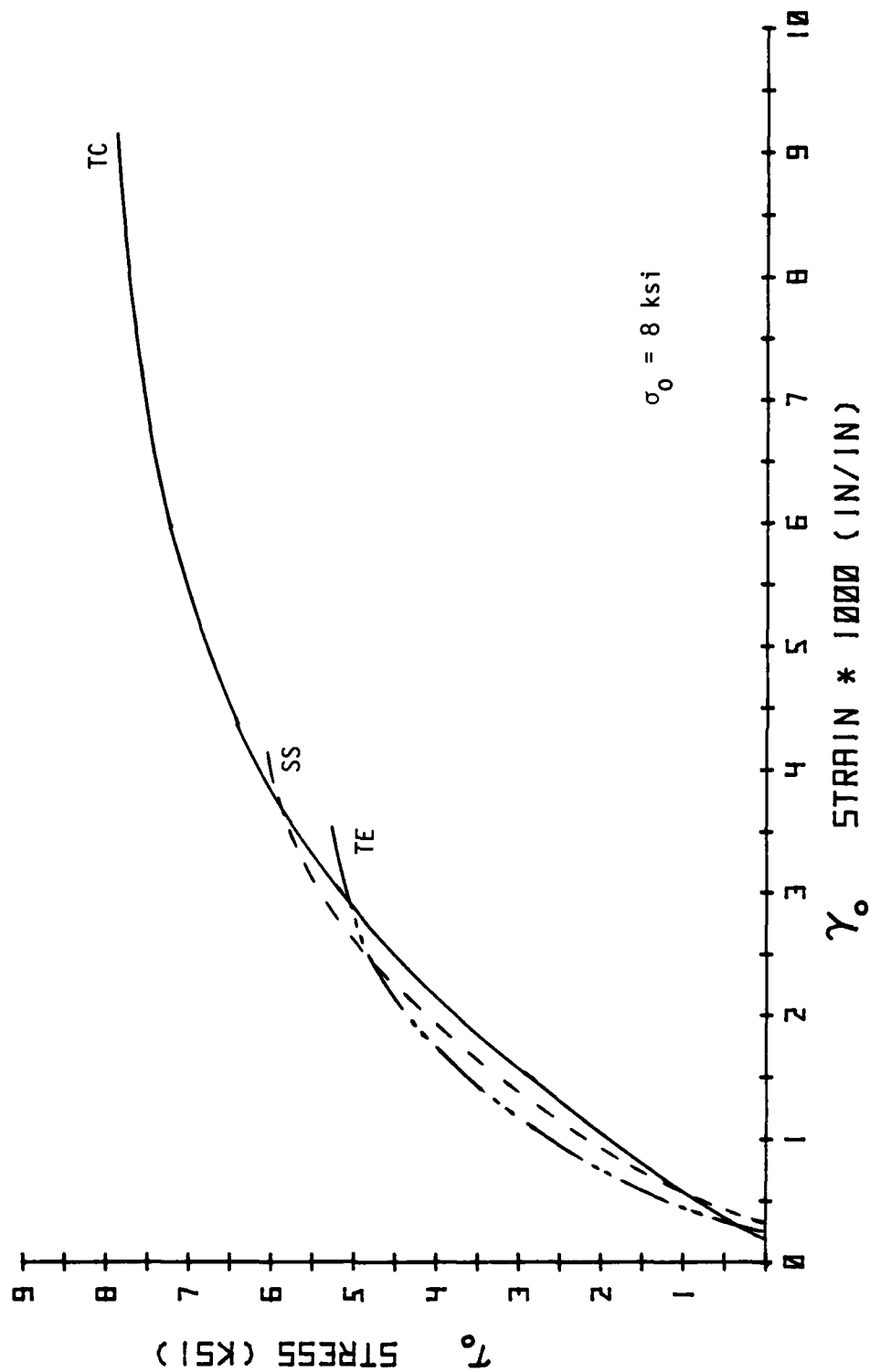


Fig. 4.81. Average Octahedral Shear Stress-Strain Results.

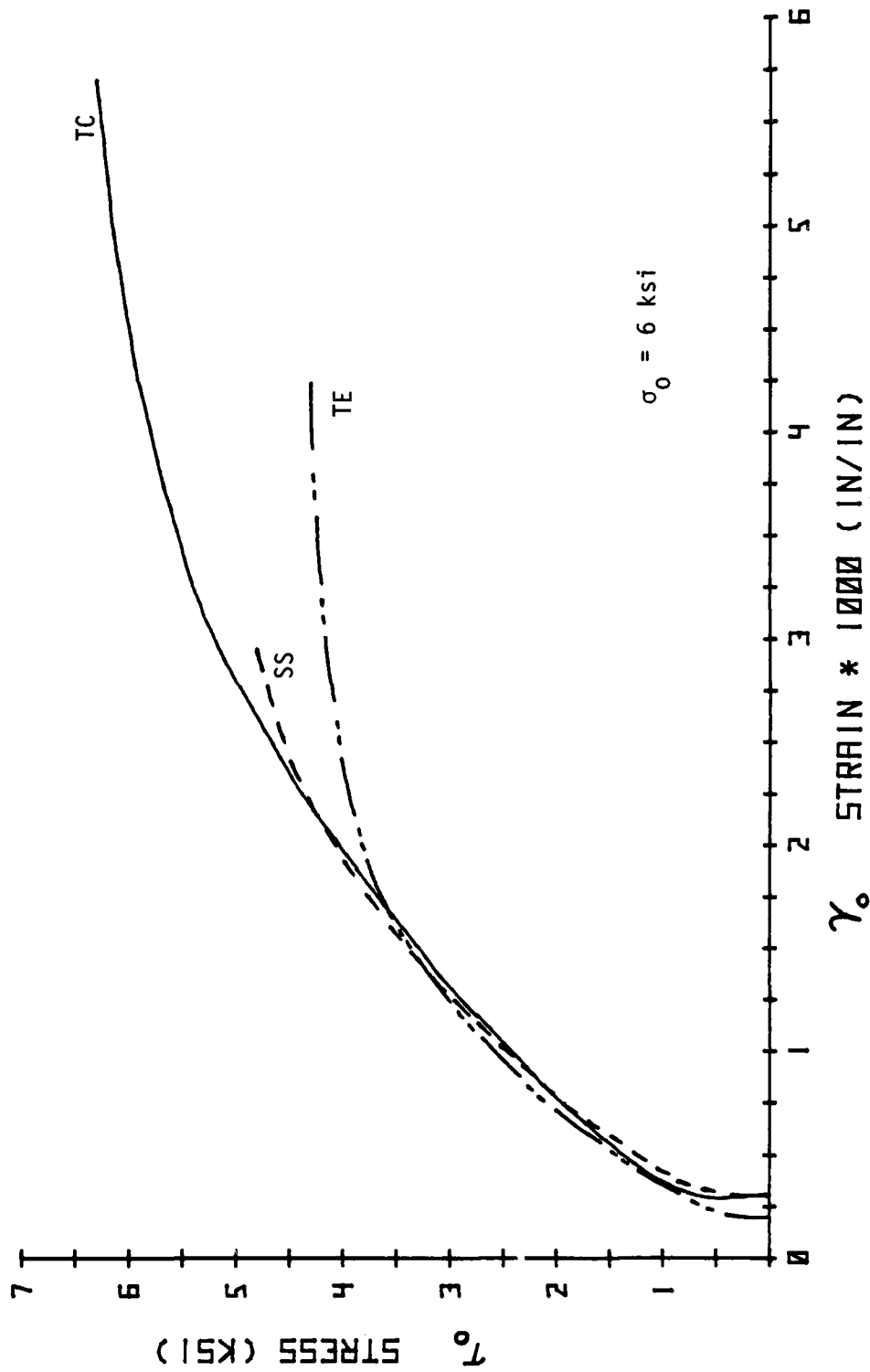


Fig. 4.82. Average Octahedral Shear Stress-Strain Results.

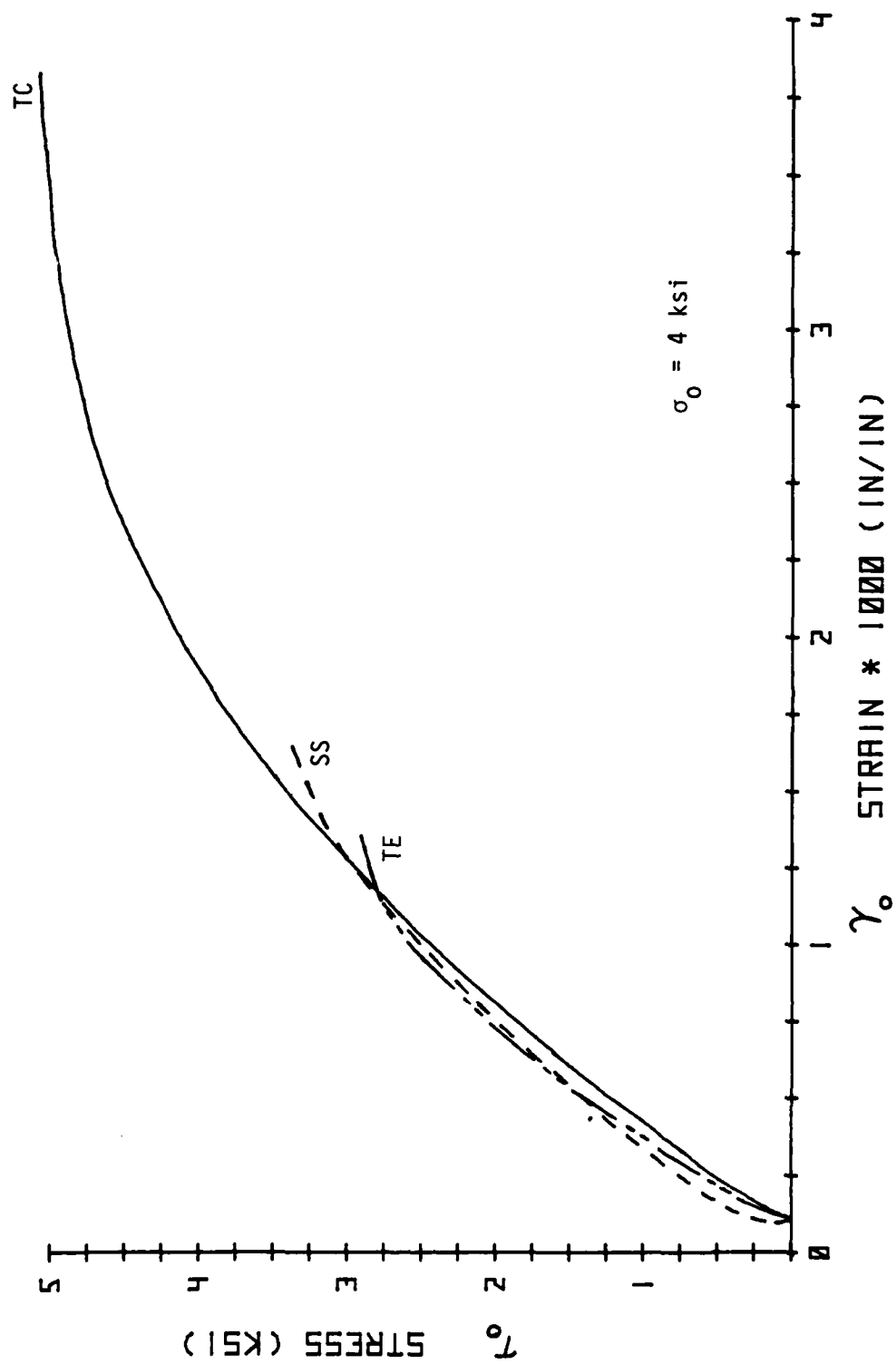


Fig. 4.83. Average Octahedral Shear Stress-Strain Results.

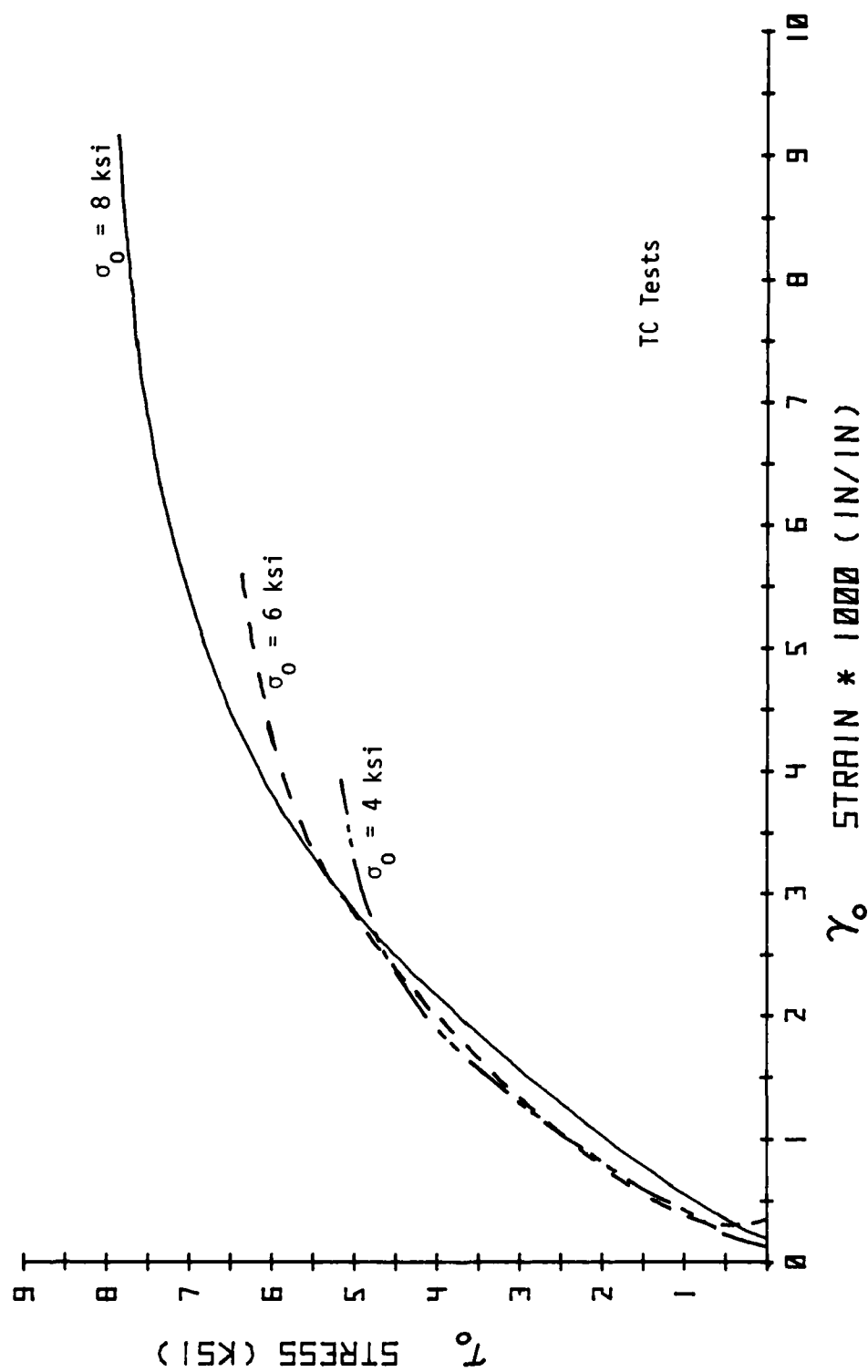


Fig. 4.84. Average Octahedral Shear Stress-Strain Results.

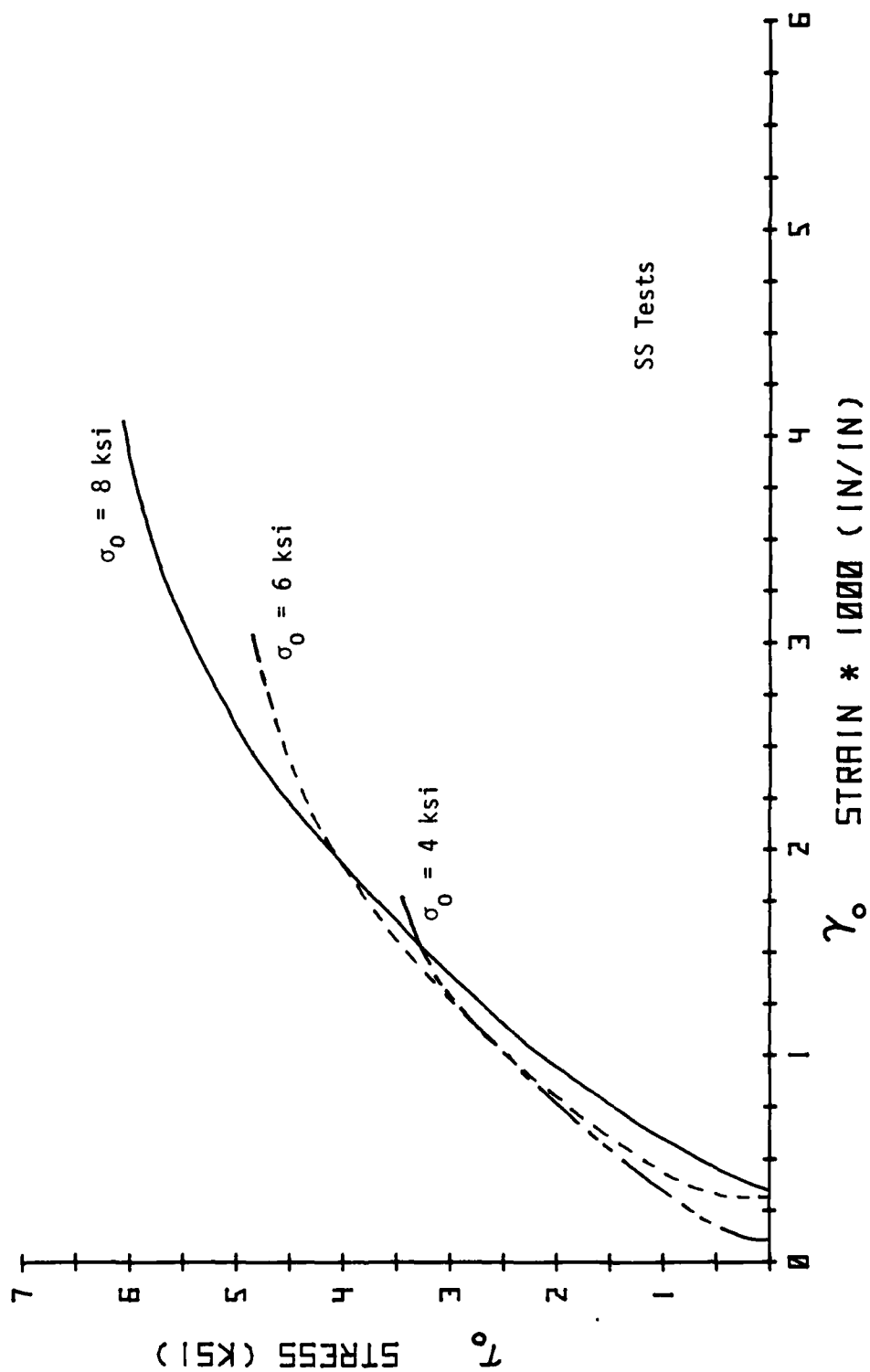


Fig. 4.85. Average Octahedral Shear Stress-Strain Results.

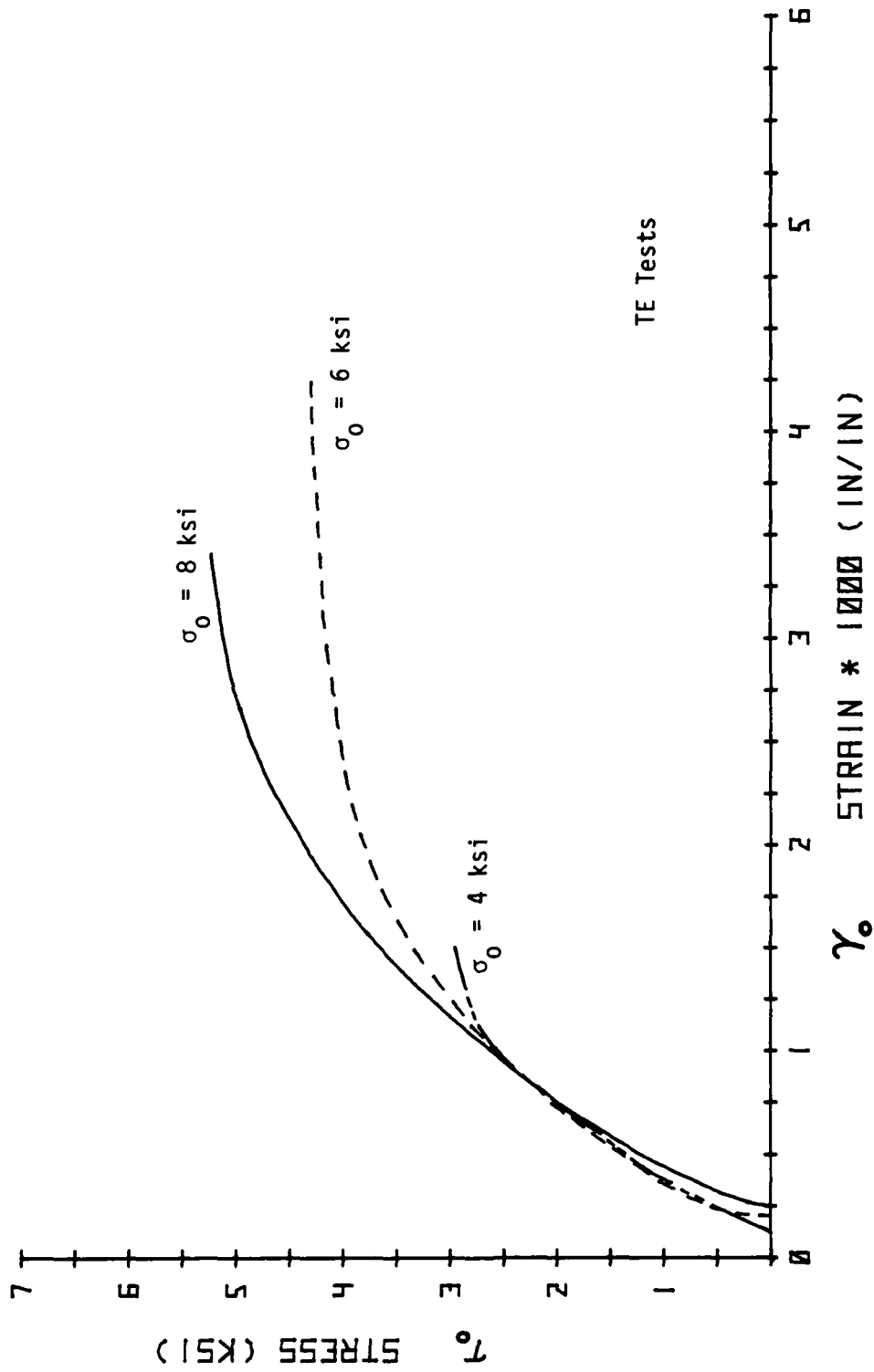


Fig. 4.86. Average Octahedral Shear Stress-Strain Results.

σ_0 - γ_0 results. If these average τ_0 - γ_0 curves were shifted to a common origin, slightly less scatter would appear. However, the offset of these curves is only slight, therefore it was felt unnecessary to force them to a common origin.

In the two lowest confining pressure tests ($\sigma_0 = 6$ and 4 ksi) the initial average τ_0 - γ_0 response shown in Figs. 4.82 and 4.83, regardless of the stress path, is nearly identical. On the other hand, in the tests employing the highest confining pressure ($\sigma_0 = 8$ ksi), shown in Fig. 4.81, the τ_0 - γ_0 response for the TE stress path exhibits the stiffest initial behavior, followed by the SS path, then the TC path where softer initial behavior appears. Notice in these three figures, that in all the tests regardless of the confining pressure (σ_0), the TE shear behavior is the most elastic-perfectly plastic, followed by the SS tests and finally the TC where the most nonlinearity and much more ductility exists. In other words, these results demonstrate that the octahedral shear stress-octahedral shear strain behavior and shear strength are strongly stress path dependent.

Figs. 4.84-4.86 show the comparison of the average τ_0 - γ_0 results for the tests employing the same stress path but at different confining pressures. The shape of these curves in the initial stages is also very similar. Obviously, tests along the same stress path but at higher confining pressures exhibit more ductility in comparison to tests where σ_0 is lower. That is to say, the shear stress-shear strain behavior and shear strength are also strongly dependent on the confining pressure (σ_0). After

all, the failure envelope for any concrete does not have the Von-Mises cylindrical shape.

Figs. 4.87-4.88 show the variation in the tangent shear modulus (G_T) for increasing τ_0 and γ_0 respectively. A large amount of scatter is present in both these figures because of the stress path and confining pressure dependency on the shear behavior, as discussed above. Therefore, for discussion purposes, average G_T - τ_0 results are presented in:

- 1) Figs. 4.89-4.91 for different stress paths (TC, SS, TE); same confining pressure.
- 2) Figs. 4.92-4.94 for the same stress path; different confining pressures ($\sigma_0 = 8, 6, 4$ ksi).

Average G_T - γ_0 results are shown in:

- 1) Figs. 4.95-4.97 for different stress paths; same confining pressure.
- 2) Figs. 4.98-4.100 for the same stress path; different confining pressures.

Obviously, the shape of the G_T - τ_0 and G_T - γ_0 curves is dictated by the τ_0 - γ_0 behavior.

As previously discussed regarding the τ_0 - γ_0 behavior, the shape of the G_T - τ_0 and G_T - γ_0 curves in the initial stages of the comparisons with the two lowest confining pressures, regardless of the stress path, is very similar (Figs. 4.90, 4.91; 4.96, 4.97). The comparison of results for the highest confining pressure, Figs. 4.89 and 4.95 for G_T - τ_0 and G_T - γ_0 respectively, show the stiffest to softest initial behavior occurring in the order of TE, SS and TC. Notice again that in all the comparisons, regardless of confining pressure, the G_T - τ_0 and G_T - γ_0 curves for the TC

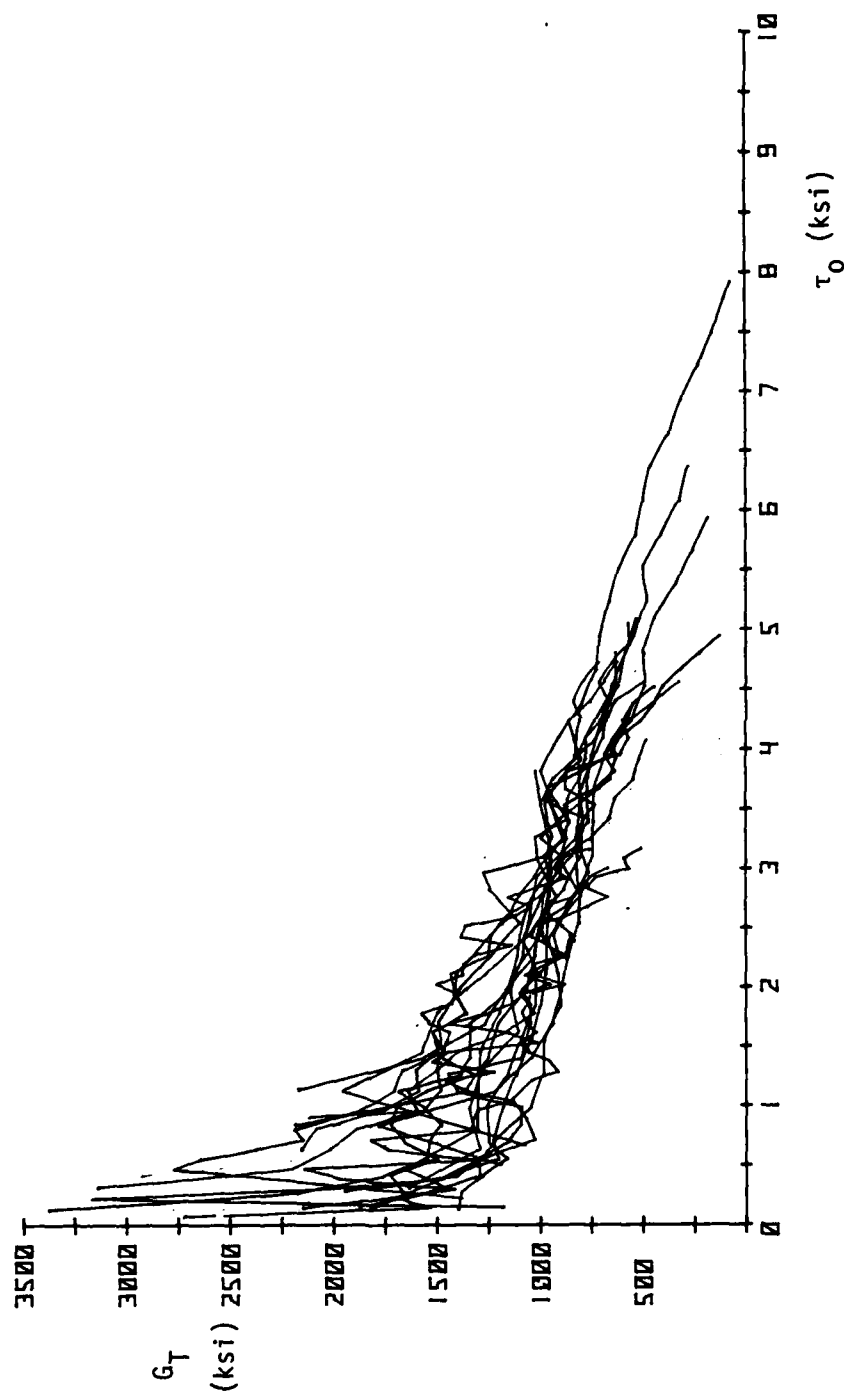


Fig. 4.87. Tangent Shear Modulus vs. Octahedral Shear Stress for all Results During Shear Deviation.

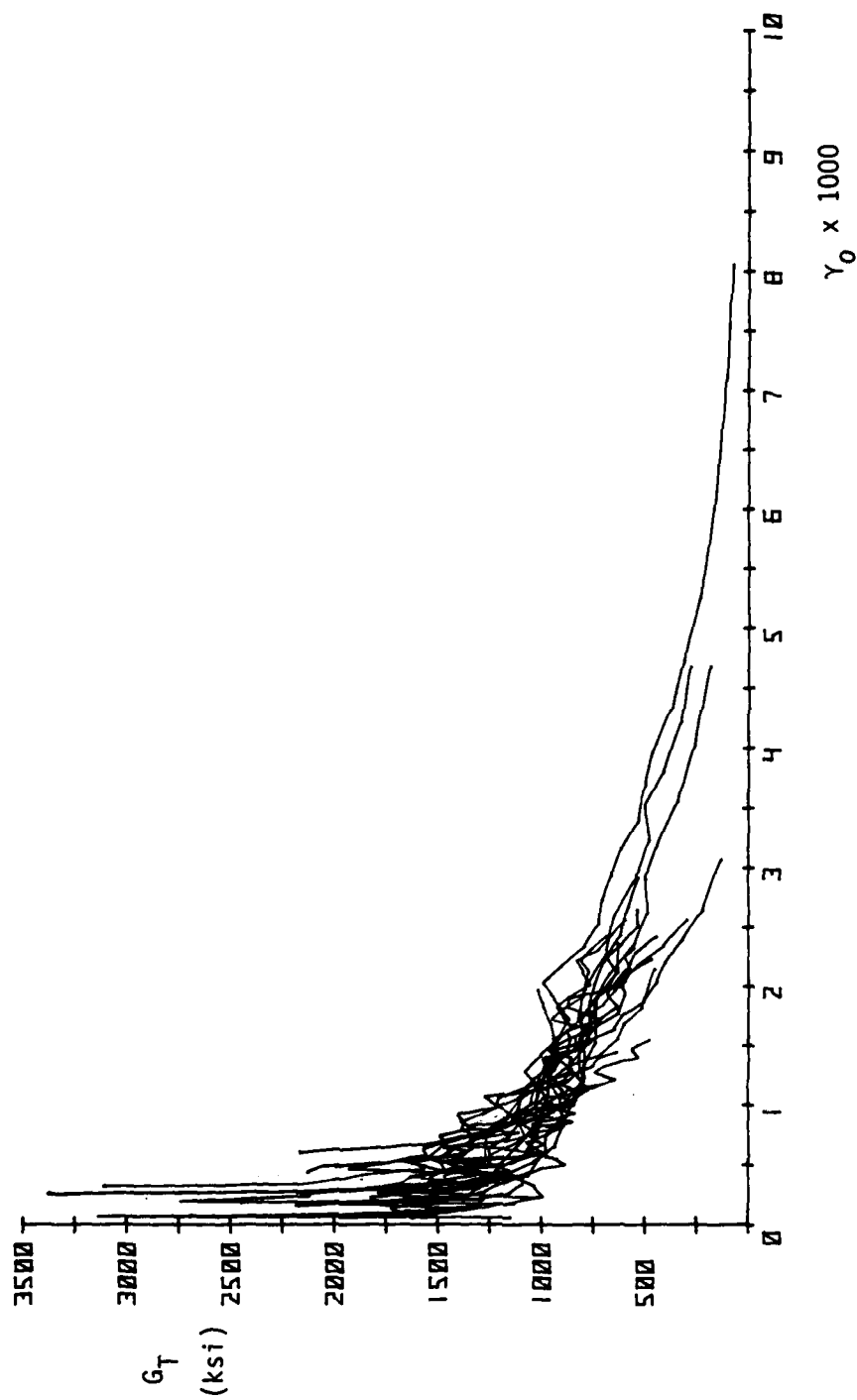


Fig. 4.88. Tangent Shear Modulus vs. Octahedral Shear Strain for all Results During Shear Deviation.

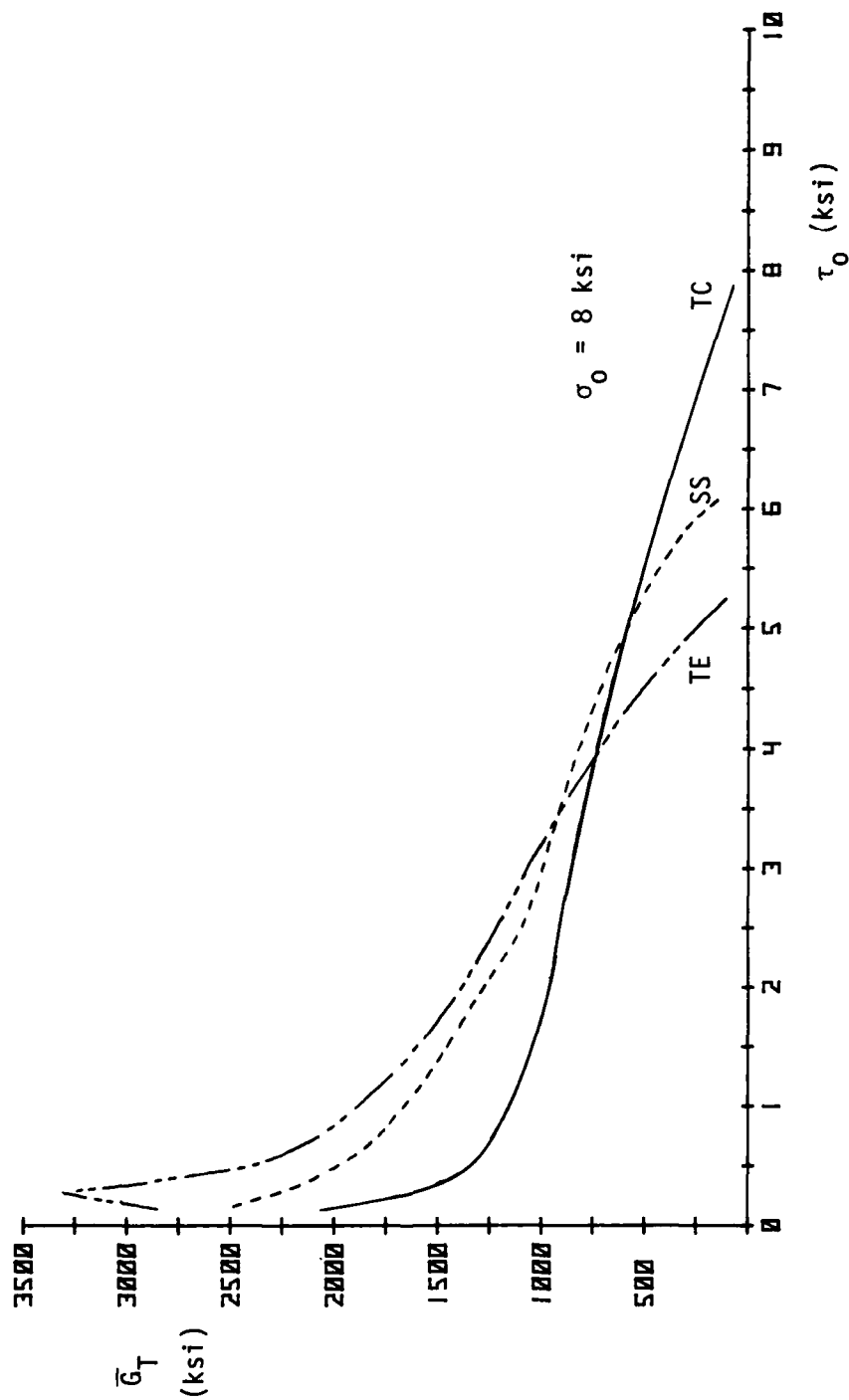


Fig. 4.89. Average Tangent Shear Modulus vs. Octahedral Shear Stress.

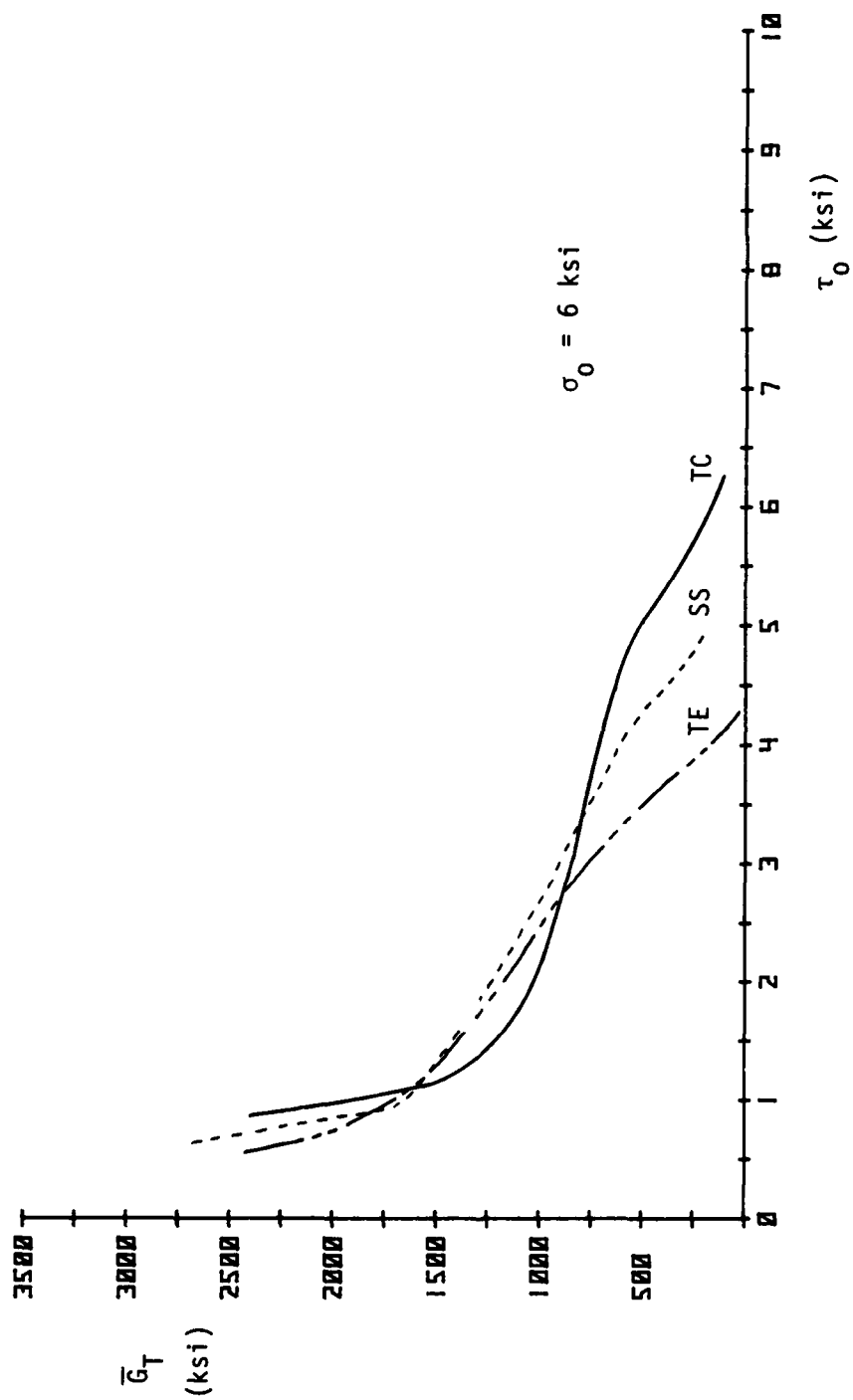


Fig. 4.90. Average Tangent Shear Modulus vs. Octahedral Shear Stress.

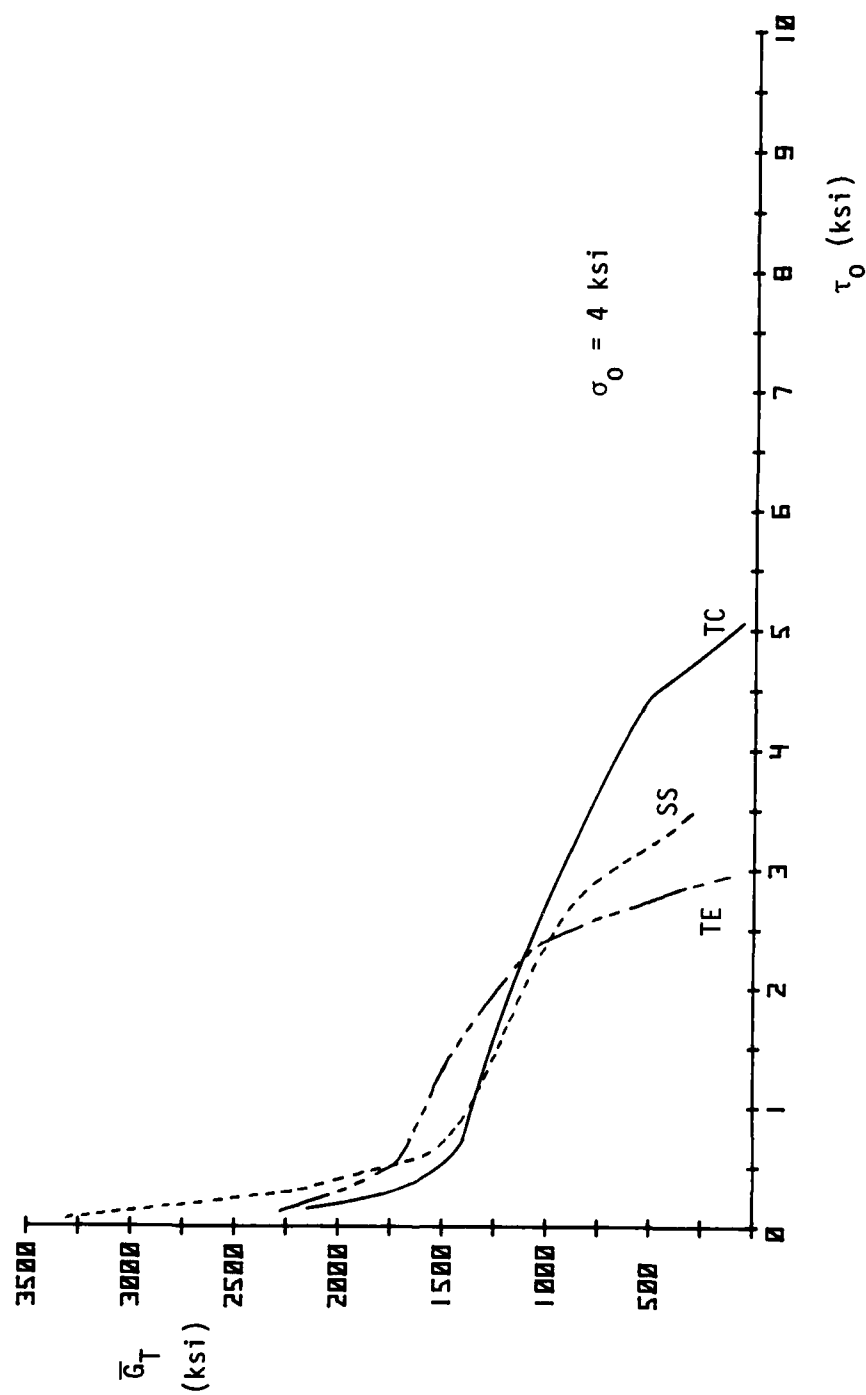


Fig. 4.91. Average Tangent Shear Modulus vs. Octahedral Shear Stress.

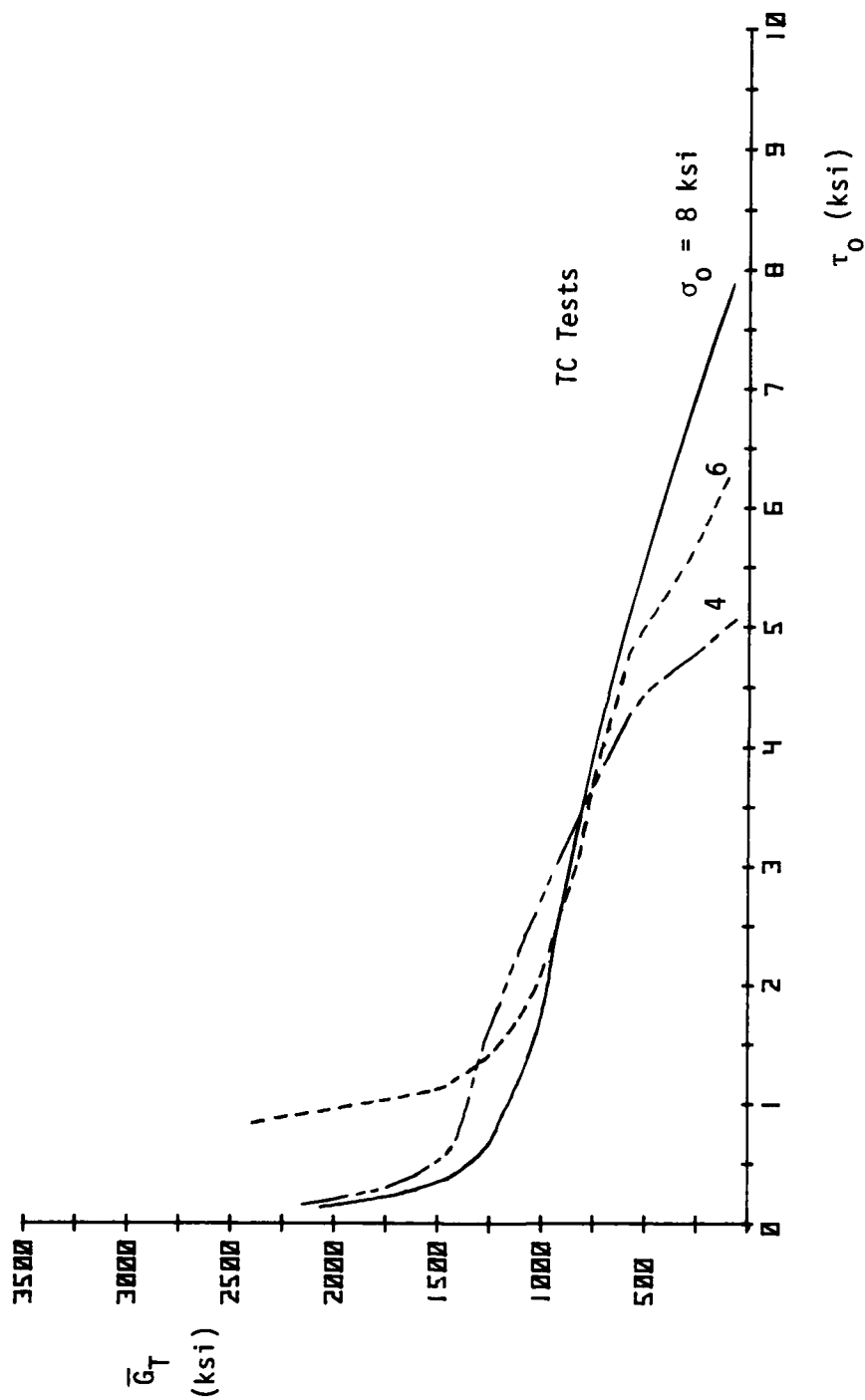


Fig. 4.92. Average Tangent Shear Modulus vs. Octahedral Shear Stress.

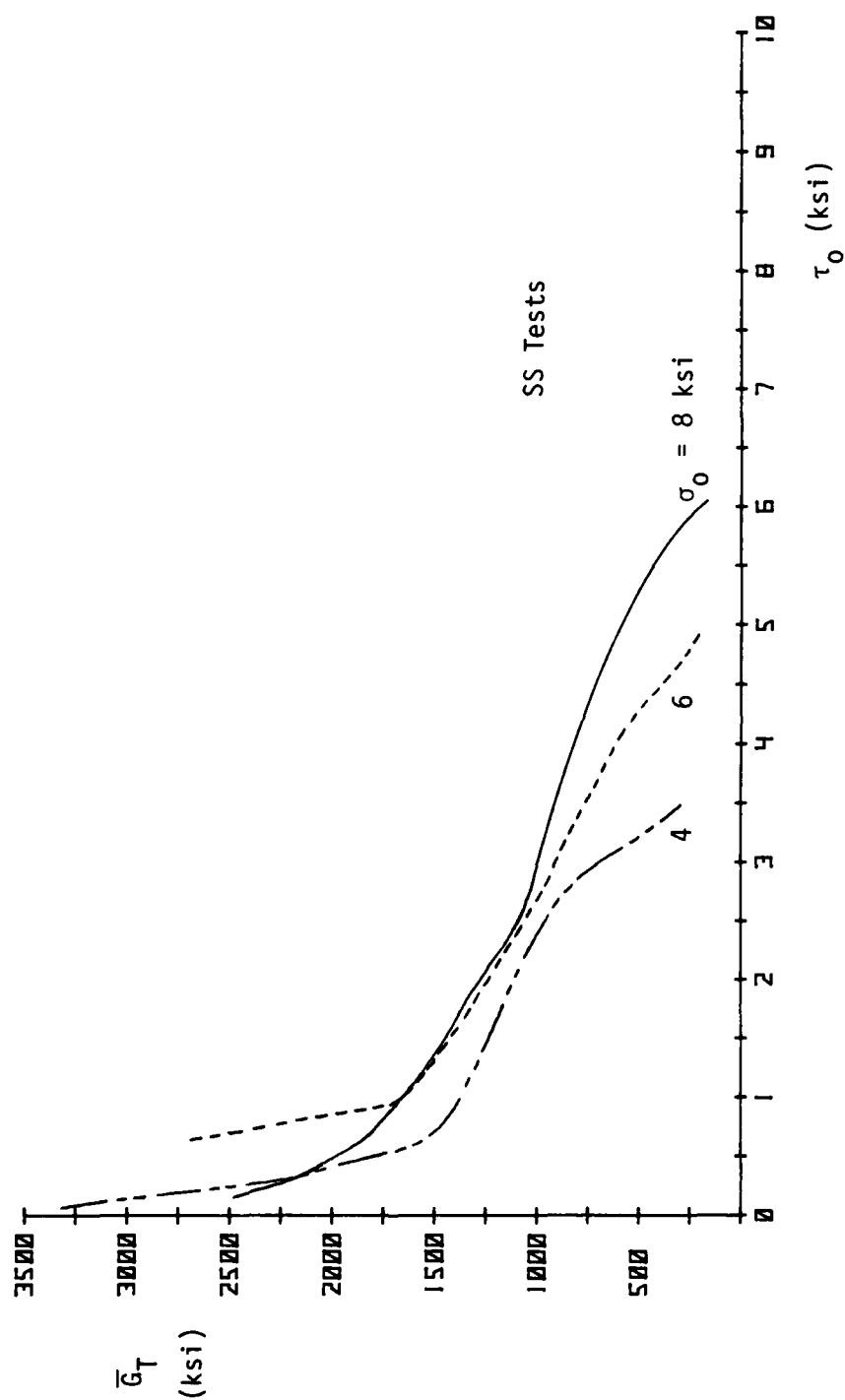


Fig. 4.93. Average Tangent Shear Modulus vs. Octahedral Shear Stress.

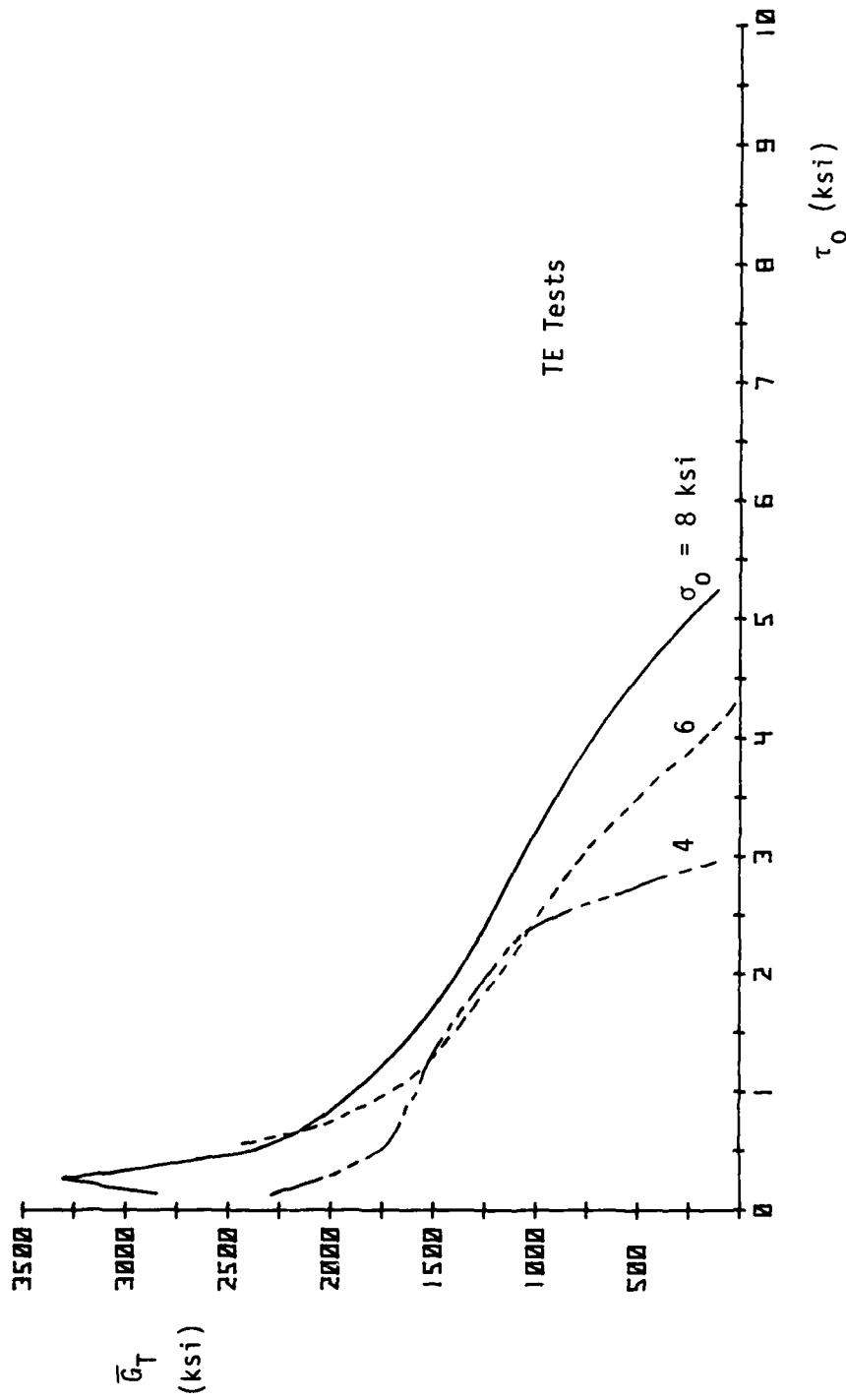


Fig. 4.94. Average Tangent Shear Modulus vs. Octahedral Shear Stress.

AD-A114 166

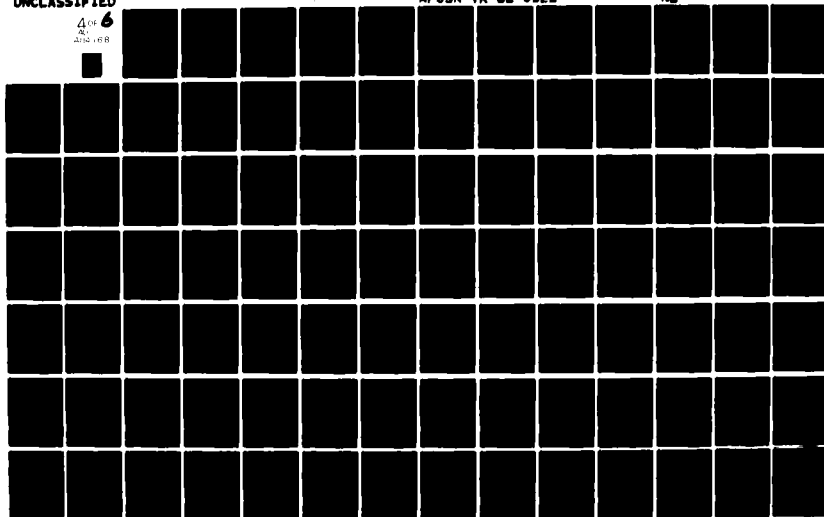
COLORADO UNIV AT BOULDER DEPT OF CIVIL ENVIRONMENTAL --ETC F/8 20/11
CONSTITUTIVE RELATIONS OF RANDOMLY ORIENTED STEEL FIBER REINFOR--ETC(U)
DEC 81 D E EGGING, H KO AFOSR-79-0065

UNCLASSIFIED

AFOSR-TR-82-0122

ML

4 of 6
AL
APR 1988



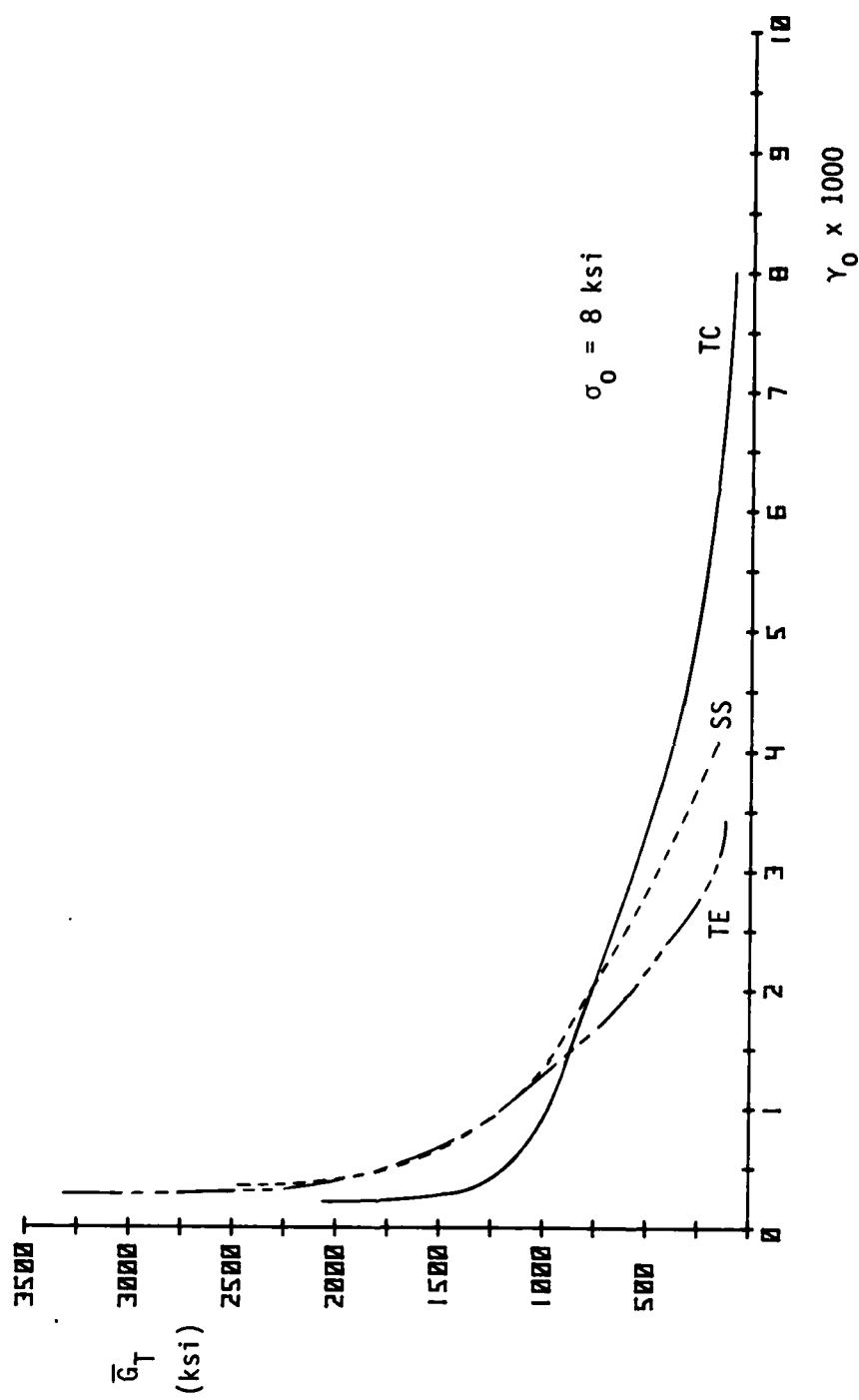


Fig. 4.95. Average Tangent Shear Modulus vs. Octahedral Shear Strain.

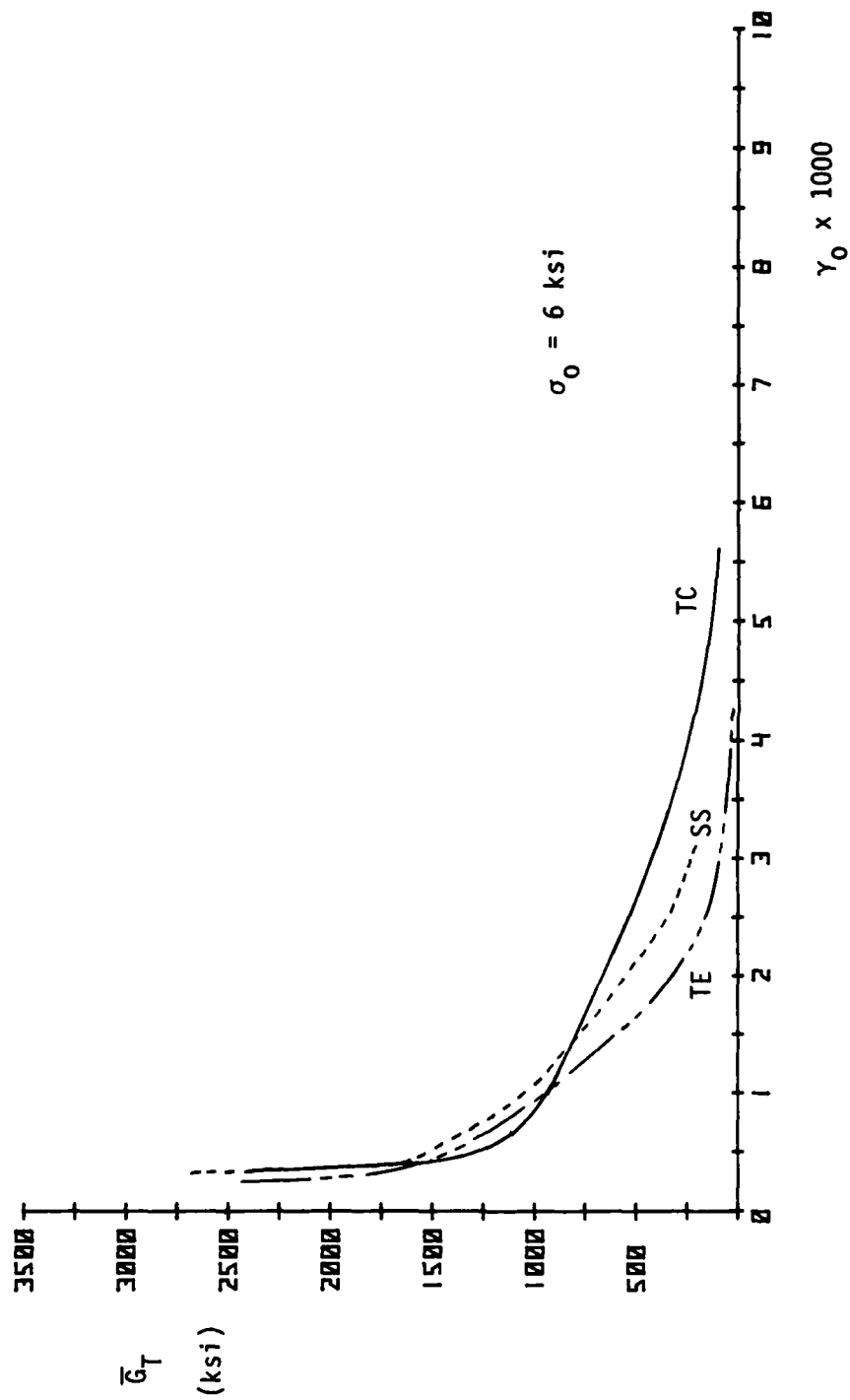


Fig. 4.96. Average Tangent Shear Modulus vs. Octahedral Shear Strain.

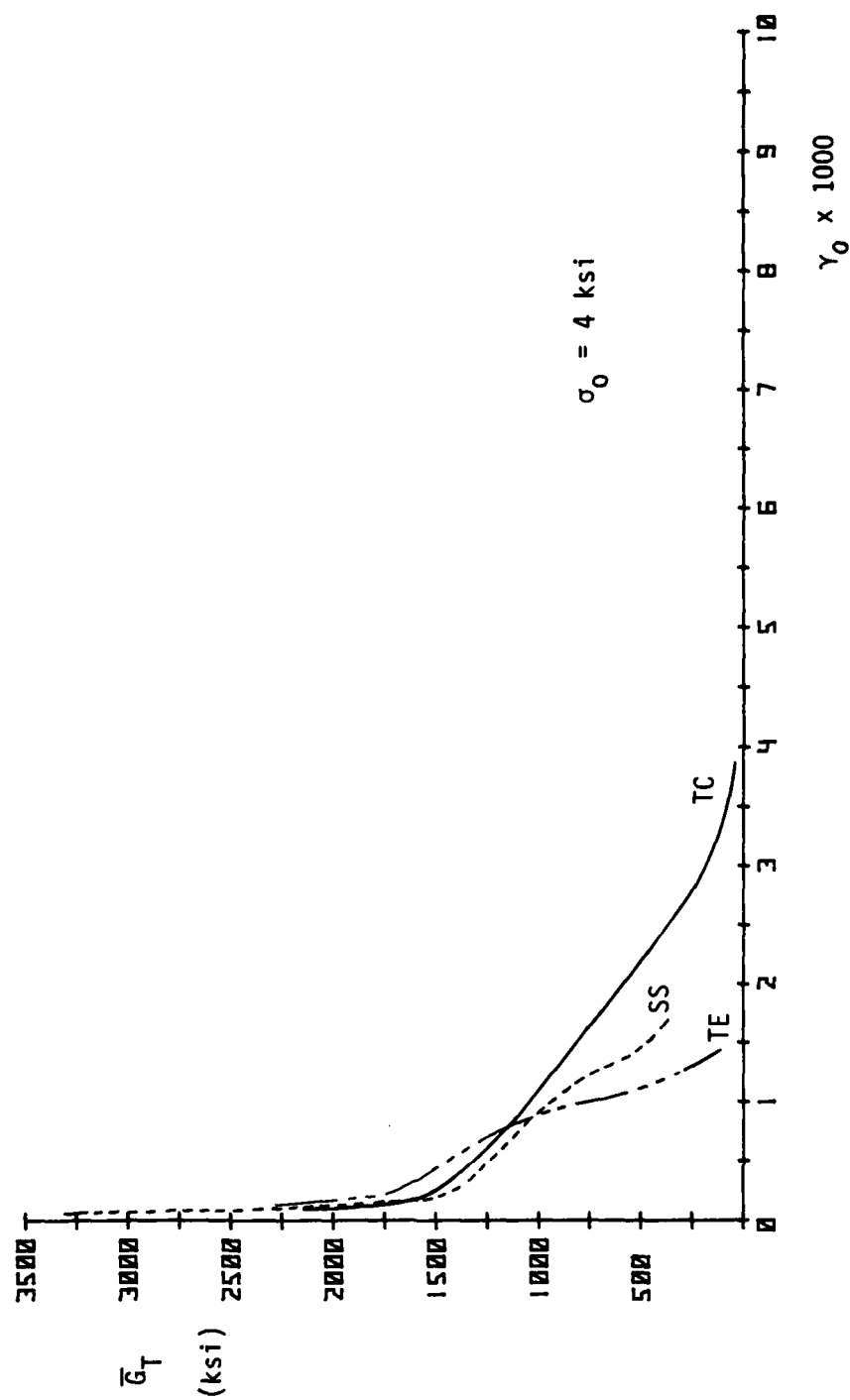


Fig. 4.97. Average Tangent Shear Modulus vs. Octahedral Shear Strain.

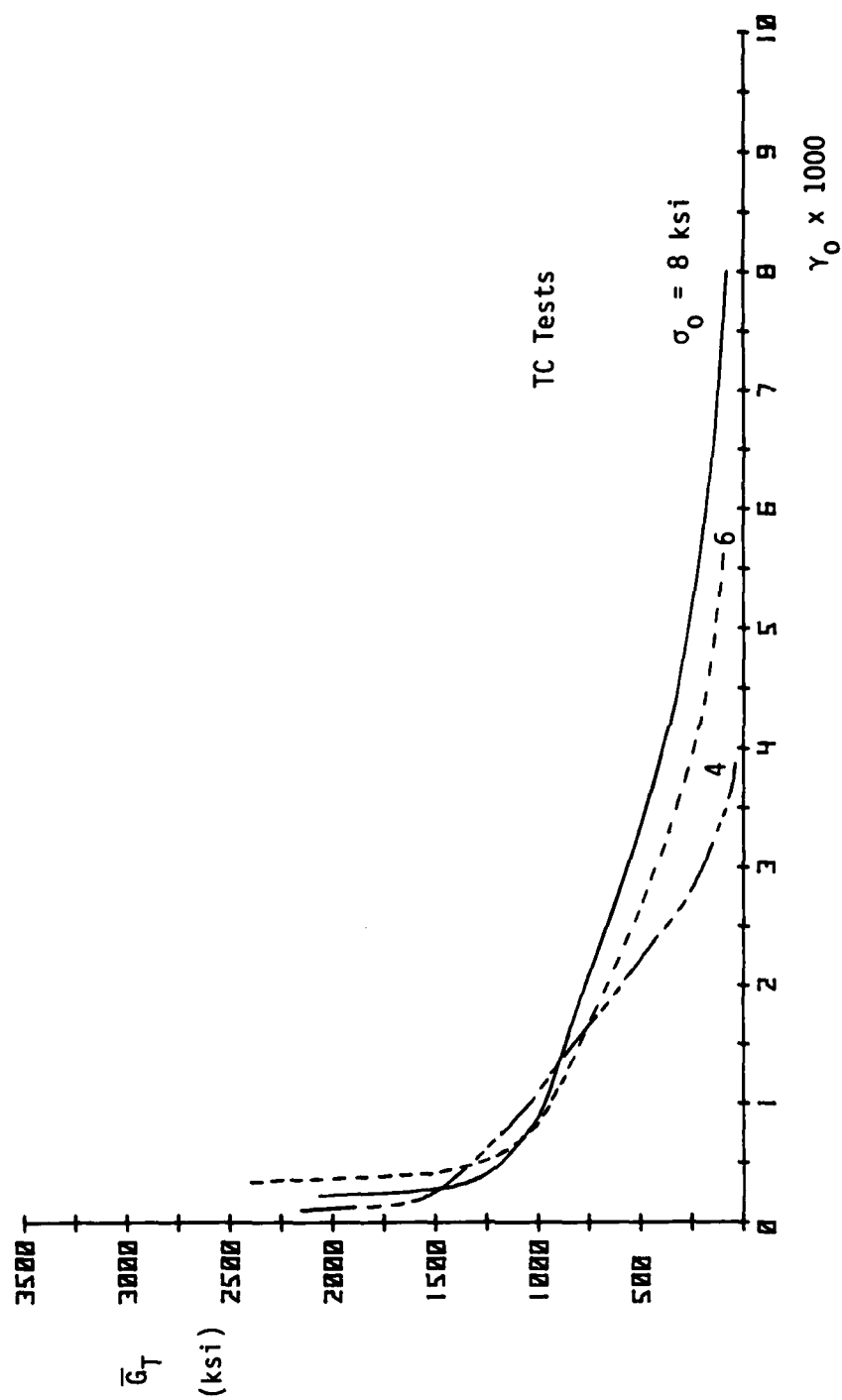


Fig. 4.98. Average Tangent Shear Modulus vs. Octahedral Shear Strain.

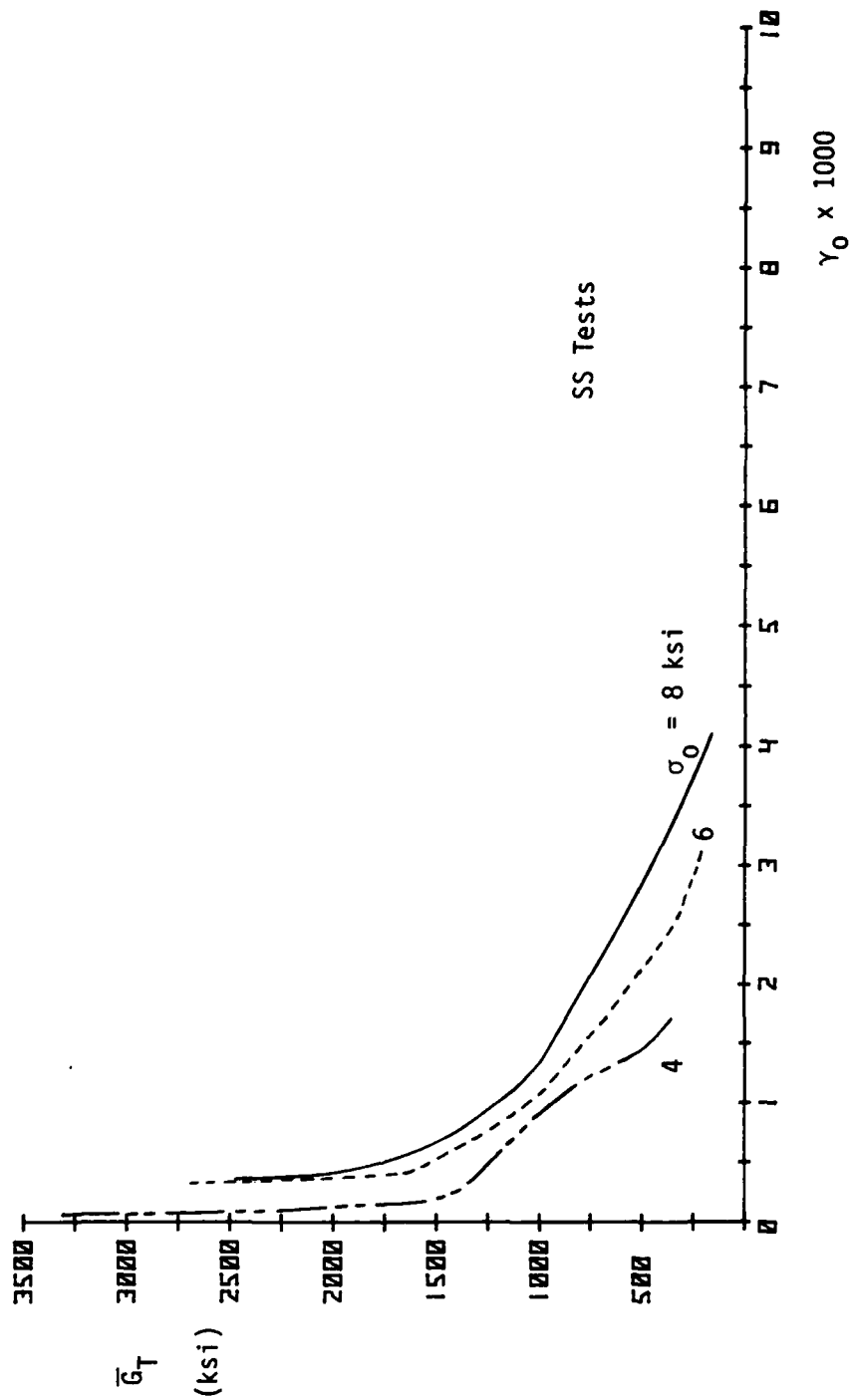


Fig. 4.99. Average Tangent Shear Modulus vs. Octahedral Shear Strain.

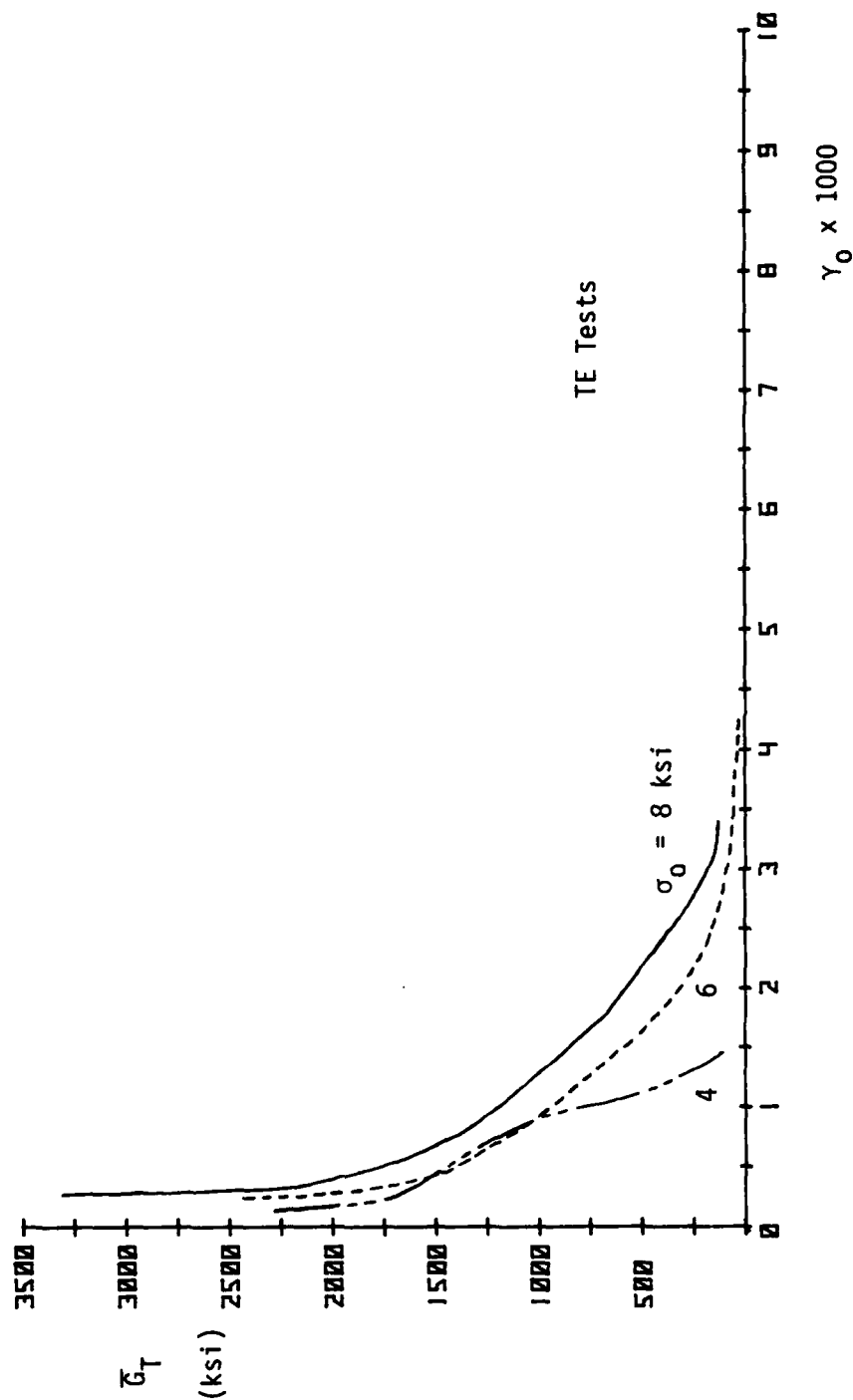


Fig. 4.100. Average Tangent Shear Modulus vs. Octahedral Shear Strain.

tests exhibit the slowest decreasing or flattest behavior, followed by the SS, then the TE tests where the steepest, fastest decreasing behavior exists. Notice also when comparing the $G_T-\tau_0$ and $G_T-\gamma_0$ results for the different stress paths, constant confining pressure, that for zero tangent shear modulus (i.e., peak of the $\tau_0-\gamma_0$ curve), the shear stresses (τ_0) and shear strains (γ_0) are largest for the TC tests and least for the TE tests, indicating higher shear strengths and more ductility in shear occur when tests are conducted along the TC stress path. Examination of these curves with their respective $\tau_0-\gamma_0$ average results makes this behavior very clear.

In Figs. 4.92-4.94 and 4.98-4.100, comparisons of $G_T-\tau_0$ and $G_T-\gamma_0$ results are made for varying confining pressures with identical stress paths. The shape of the curves in the initial stages is similar, as one would expect. Obviously, for zero tangent shear modulus, the shear stresses and shear strains are largest for the highest confining pressures, and smallest for the lowest confining pressures.

In summary, as in the $\tau_0-\gamma_0$ discussion of average results, the dependency on stress path and confining pressure appears again in the $G_T-\tau_0$ behavior and $G_T-\gamma_0$ behavior.

$\tau_0-\epsilon_0$

Individual and summary results of $\tau_0-\epsilon_0$ behavior are shown in Figs. 4.41-4.77. From these, average $\tau_0-\epsilon_0$ behavior was calculated and the comparative results are presented in:

- 1) Figs. 4.101-4.103 for different stress paths (TC, SS, TE); same confining pressure (σ_0).
- 2) Figs. 4.104-4.106 for the same stress path; different confining pressures ($\sigma_0 = 8, 6, 4$ ksi).

None of the τ_0 - ϵ_0 response curves shown in Figs. 4.69-4.77 have a common origin because of the scatter occurring in the volumetric response (σ_0 - ϵ_0) during HC, shown in the same figures and better seen in Fig. 4.78. Therefore, for discussion purposes, the average τ_0 - ϵ_0 results have been shifted to a common origin.

Notice the very linear behavior occurring in these curves until just prior to dilation (transition from volume contraction to expansion) when deviation from linearity occurs. Because of this nearly linear behavior, no plots of the τ_0 - ϵ_0 slope vs. shear stress (τ_0) or normal strain (ϵ_0) are shown as was done for the τ_0 - γ_0 results.

The slopes of these τ_0 - ϵ_0 curves are on the order of 5000 ksi and up, much higher than one sees for K or G, simply because of the small volumetric strains resulting from shear distortion. Even though the slopes are large and the coupling between τ_0 and ϵ_0 is secondary in comparison to that seen in the σ_0 - ϵ_0 behavior and the τ_0 - γ_0 behavior, the effect of volume change during shear distortion cannot and should not be neglected if one is to develop an accurate constitutive model to predict the behavior of this SFRC or any concrete for that matter because the τ_0 - ϵ_0 coupling is a phenomenon of behavior, i.e. volume change during shear distortion. In contrast, the secondary or tertiary coupling between σ_0 and γ_0 can safely be neglected because this behavior is due only to

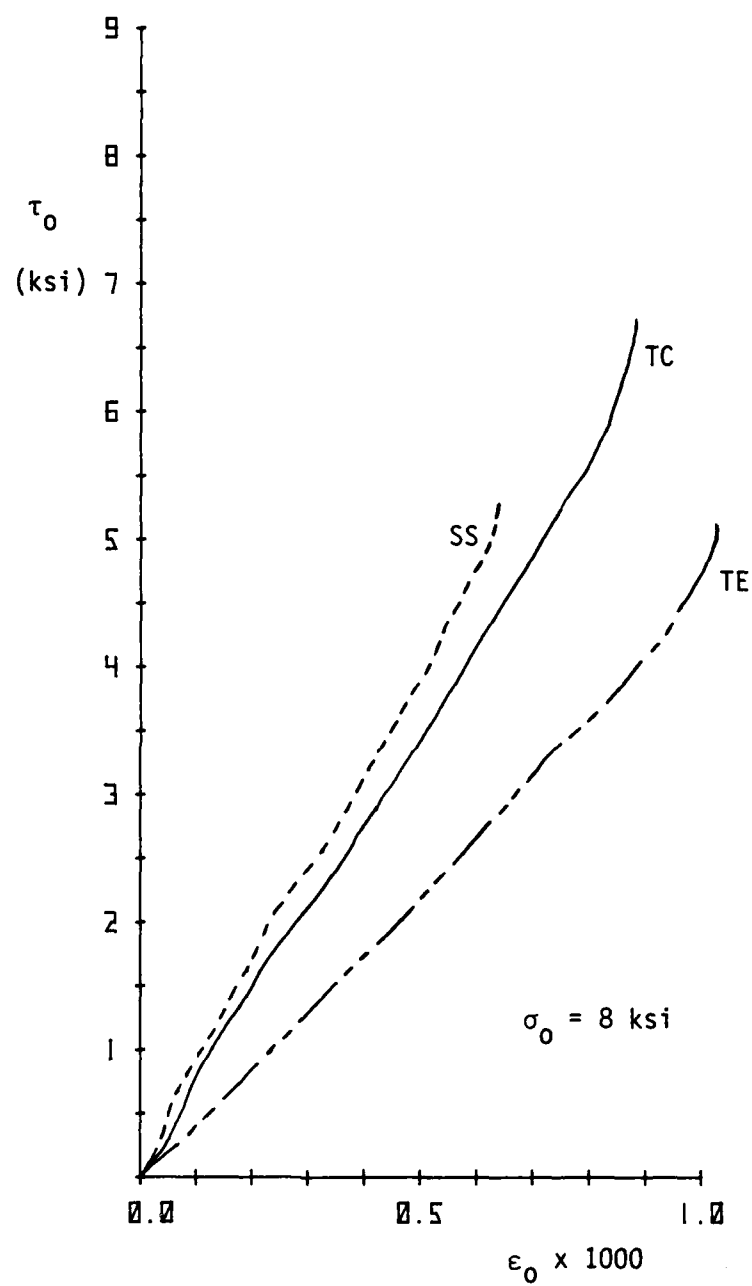


Fig. 4.101. Average Octahedral Shear Stress-Normal Strain Results.

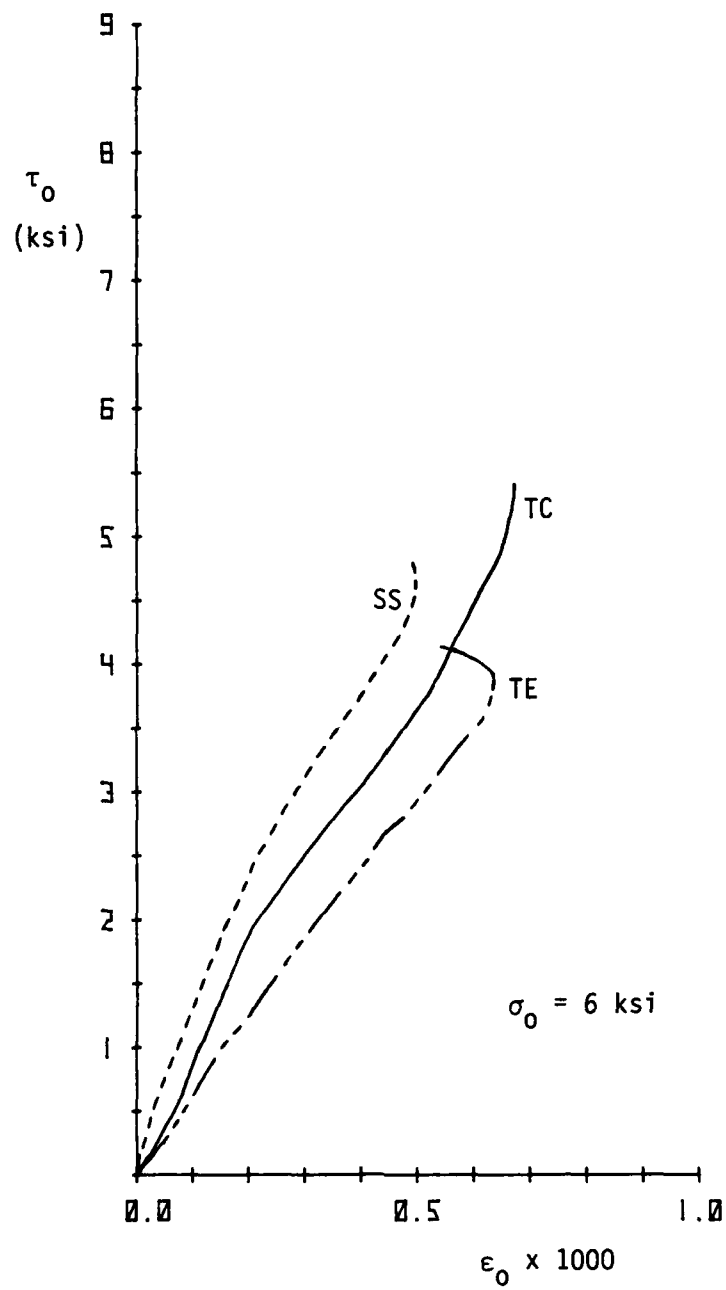


Fig. 4.102. Average Octahedral Shear Stress-Normal Strain Results.

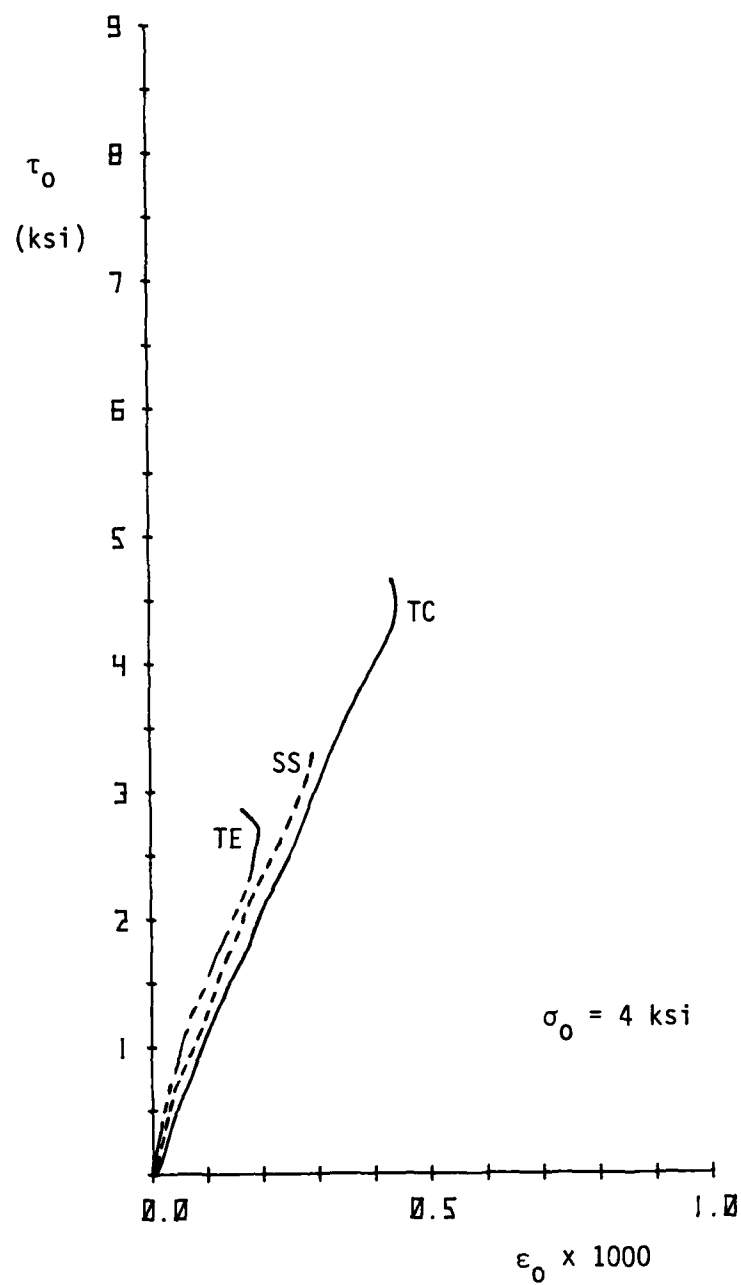


Fig. 4.103. Average Octahedral Shear Stress-Normal Strain Results.

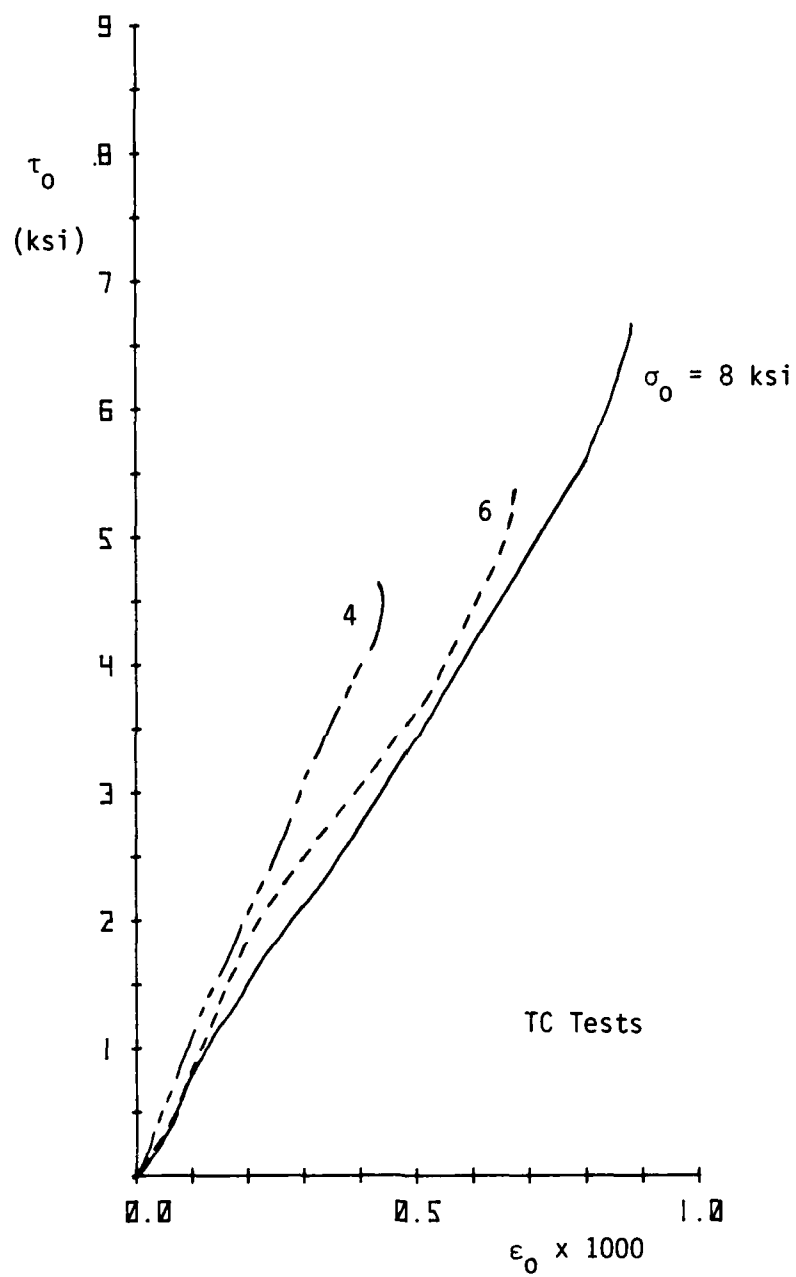


Fig. 4.104. Average Octahedral Shear Stress-Normal Strain Results.

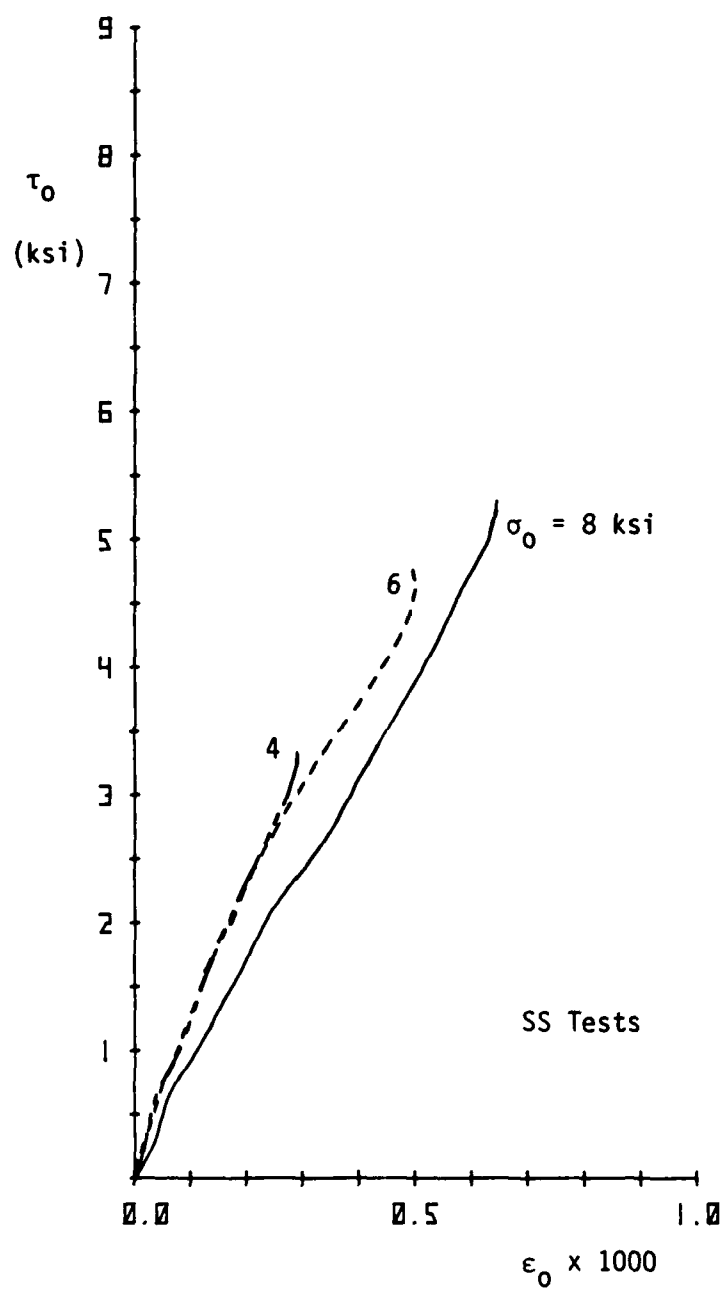


Fig. 4.105. Average Octahedral Shear Stress-Normal Strain Results.

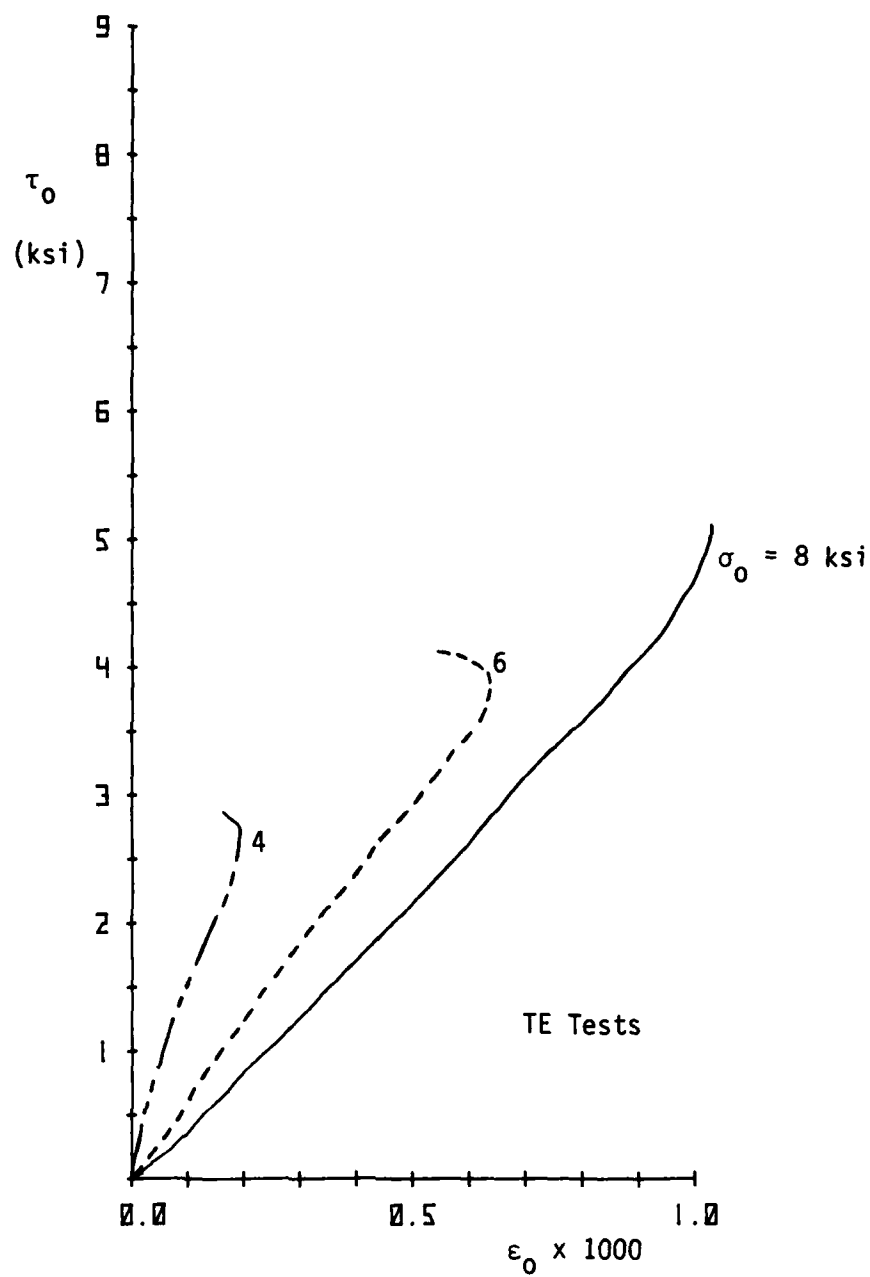


Fig. 4.106. Average Octahedral Shear Stress-Normal Strain Results.

slight anisotropy present in a material that was initially intended to be isotropic and was by no means cast to create anisotropy.

In Figs. 4.101-4.106 one can see that the τ_0 - ϵ_0 behavior is a function of the stress path and confining pressure. The stiffest to least stiff behavior occurs in the order of SS, TC and TE for the two highest confining pressures, i.e., $\sigma_0 = 8$, and 6 ksi (Figs. 4.101 and 4.102). The TE tests exhibit the most volumetric change from shear distortion, which makes sense considering that this type of test is an "extension" test from an initial hydrostatic stress state. Along the same line, one would expect the TC tests to possess the stiffest coupling behavior since it is a "compression" test. However, Figs. 4.101 and 4.102 show this not to be the case. The only conclusion for this SS, TC, TE stiff to soft behavior instead of TC, SS, TE is scatter in all the stress-strain results producing averages that appear in the order shown in the figures. It is interesting to note in Fig. 4.103 that for the lowest confining pressure tests where $\sigma_0 = 4$ ksi, the average behavior in the initial stages is nearly the same, regardless of the stress path, of course, until dilation occurs, indicating that the initial τ_0 - ϵ_0 behavior is stress path independent for low confining pressures. Dilation occurs at different levels of τ_0 in all the tests simply because the total behavior is not independent of the stress path or confining pressure.

Figs. 4.104-4.106 show that for the same stress path, the τ_0 - ϵ_0 behavior is a function of confining pressure, i.e. more volumetric change during shear distortion occurs at higher levels of

confinement. Note in Figs. 4.104 and 4.105, that the differences in this behavior for the TC and SS tests is not as great as for the TE tests (Fig. 4.106). In other words, the effect of confining pressure is felt the most for specimens sheared along the TE stress path.

Examination of all the figures showing the τ_0 - ϵ_0 behavior leads to the conclusion that in situations where confining pressures are small, say less than 4 ksi, the coupling between τ_0 and ϵ_0 is slight and could be neglected.

Mention has been made throughout the preceding discussions regarding dilation of the specimens. This is an important point in the stress-strain behavior because for this study, the stress state at which dilation occurred was defined as failure. Discussion of this is given in the section on strength, i.e. Section 4.3.4.

4.3.3 Method for Determination of Elastic Material Constants

Linear elastic constitutive models are used widely to approximate the behavior of many different engineering materials. In the form of Hooke's law, they state that there exists a linear relationship between strains (ϵ) and stresses (σ). The most general form of Hooke's law is

$$\epsilon_i = C_{ij} \sigma_j \quad (i, j = 1, 2, \dots, 6) \quad (4.2)$$

where the compliance matrix C_{ij} contains 36 independent terms for linear material behavior. Elastic behavior, creating symmetry of C_{ij} , reduces the number of independent constants to 21 for a general linear elastic, anisotropic material. Further reductions in the number of independent constants can occur when a material possesses certain planes or axes of symmetry. A material possessing symmetry about three orthogonal planes is termed orthotropic. A total of 9 constants remains in the compliance matrix C_{ij} .

Eq. 4.2 becomes:

$$\begin{Bmatrix} \epsilon_1 \\ \epsilon_2 \\ \epsilon_3 \\ \epsilon_4 \\ \epsilon_5 \\ \epsilon_6 \end{Bmatrix} = \begin{bmatrix} C_{11} & C_{12} & C_{13} & & & \\ C_{21} & C_{22} & C_{23} & & & \\ C_{31} & C_{32} & C_{33} & & & \\ \hline & & & C_{44} & 0 & 0 \\ & & & 0 & C_{55} & 0 \\ & & & 0 & 0 & C_{66} \end{bmatrix} \begin{Bmatrix} \sigma_1 \\ \sigma_2 \\ \sigma_3 \\ \sigma_4 \\ \sigma_5 \\ \sigma_6 \end{Bmatrix} \quad (4.3)$$

where

$$\begin{aligned} C_{12} &= C_{21} \\ C_{13} &= C_{31} \\ C_{23} &= C_{32} \end{aligned}$$

Rewriting Eqs. 4.3 in terms of the more familiar shear strains (γ) and shear stresses (τ) gives:

$$\begin{Bmatrix} \epsilon_1 \\ \epsilon_2 \\ \epsilon_3 \\ \gamma_{23} \\ \gamma_{13} \\ \gamma_{12} \end{Bmatrix} = \begin{bmatrix} C_{11} & C_{12} & C_{13} & & & \\ C_{12} & C_{22} & C_{23} & & & \\ C_{13} & C_{23} & C_{33} & & & \\ \hline & & & C_{44} & 0 & 0 \\ & & & 0 & C_{55} & 0 \\ & & & 0 & 0 & C_{66} \end{bmatrix} \begin{Bmatrix} \sigma_1 \\ \sigma_2 \\ \sigma_3 \\ \tau_{23} \\ \tau_{13} \\ \tau_{12} \end{Bmatrix} \quad (4.4)$$

The compliance matrix C_{ij} for orthotropic materials, when expressed in terms of Young's moduli E , Poisson's ratio ν , and the shear moduli G becomes:

$$C_{ij} = \begin{bmatrix} \frac{1}{E_1} & \frac{-\nu_{12}}{E_2} & \frac{-\nu_{13}}{E_3} & & & \\ \frac{-\nu_{21}}{E_1} & \frac{1}{E_2} & \frac{-\nu_{23}}{E_3} & & & \\ \frac{-\nu_{31}}{E_1} & \frac{-\nu_{32}}{E_2} & \frac{1}{E_3} & & & \\ \hline & & & \frac{1}{2G_{23}} & 0 & 0 \\ & & & 0 & \frac{1}{2G_{13}} & 0 \\ & & & 0 & 0 & \frac{1}{2G_{12}} \end{bmatrix} \quad (4.5)$$

where

E_i = Young's modulus in the i -direction.

ν_{ij} = Poisson's ratio for strain in the i -direction
(ϵ_i) divided by strain in the j -direction (ϵ_j)
when stressed in the j -direction (σ_j), i.e.,

$$\nu_{ij} = - \frac{\epsilon_i}{\epsilon_j} \text{ (for } \sigma = \sigma_j \text{)}$$

G_{ij} = shear modulus in the i - j plane.

Symmetry about the diagonal requires that:

$$\frac{\nu_{ij}}{E_j} = \frac{\nu_{ji}}{E_i} \quad (i, j = 1, 2, 3) .$$

A material may also have symmetry about an axis. Say for example, the material has equivalent properties in the 1-2 principal plane, i.e., the material is symmetric about the 3-axis. The resulting number of independent material constants required to represent this material is 5 and the material is termed transversely isotropic. The resulting compliance matrix is:

$$C_{ij} = \left[\begin{array}{ccc|ccc} C_{11} & C_{12} & C_{13} & & & \\ C_{12} & C_{11} & C_{13} & & 0 & \\ C_{13} & C_{13} & C_{33} & & & \\ \hline & & & C_{44} & 0 & 0 \\ & 0 & & 0 & C_{44} & 0 \\ & & & 0 & 0 & C_{66} \end{array} \right] \quad (4.6)$$

where $C_{66} = C_{11} - C_{12}$.

In terms of E , ν and G , the transversely isotropic compliance matrix becomes:

$$C_{ij} = \left[\begin{array}{ccc|ccc} \frac{1}{E_1} & \frac{-\nu_{12}}{E_1} & \frac{-\nu_{13}}{E_3} & & & \\ \frac{-\nu_{12}}{E_1} & \frac{1}{E_1} & \frac{-\nu_{13}}{E_3} & & & \\ \frac{-\nu_{31}}{E_1} & \frac{-\nu_{31}}{E_1} & \frac{1}{E_3} & & & \\ \hline & & & \frac{1}{2G_{13}} & 0 & 0 \\ & 0 & & 0 & \frac{1}{2G_{13}} & 0 \\ & & & 0 & 0 & \frac{1}{2G_{12}} \end{array} \right] \quad (4.7)$$

where $G_{12} = \frac{E_1}{2(1+\nu_{12})}$.

Again, symmetry about the diagonal requires that:

$$\frac{-\nu_{13}}{E_3} = \frac{-\nu_{31}}{E_1}.$$

A material is isotropic when it possesses symmetry about all axes and all planes. The material compliance matrix is then completely defined by only 2 independent constants, resulting in:

$$C_{ij} = \begin{bmatrix} C_{11} & C_{12} & C_{12} & 0 & 0 & 0 \\ C_{12} & C_{11} & C_{12} & 0 & 0 & 0 \\ C_{12} & C_{12} & C_{11} & 0 & 0 & 0 \\ 0 & 0 & 0 & C_{44} & 0 & 0 \\ 0 & 0 & 0 & 0 & C_{44} & 0 \\ 0 & 0 & 0 & 0 & 0 & C_{44} \end{bmatrix} \quad (4.8)$$

where $C_{44} = C_{11} - C_{12}$.

In terms of E , ν and G , Eq. 4.8 reduces to the very familiar form for a linearly elastic, isotropic material:

$$C_{ij} = \begin{bmatrix} \frac{1}{E} & \frac{-\nu}{E} & \frac{-\nu}{E} & 0 & 0 & 0 \\ \frac{-\nu}{E} & \frac{1}{E} & \frac{-\nu}{E} & 0 & 0 & 0 \\ \frac{-\nu}{E} & \frac{-\nu}{E} & \frac{1}{E} & 0 & 0 & 0 \\ 0 & 0 & 0 & \frac{1}{2G} & 0 & 0 \\ 0 & 0 & 0 & 0 & \frac{1}{2G} & 0 \\ 0 & 0 & 0 & 0 & 0 & \frac{1}{2G} \end{bmatrix} \quad (4.9)$$

where $G = \frac{E}{2(1+\nu)}$

The cubical test cell described in Chapter 2 has the capability of applying three independent principal stresses to 4 in. cubical specimens. No shear stresses can be applied. Also, the principal directions (1,2 and 3) for hydrostatic loading are synonymous with the material axes (x,y and z). Therefore, the stress-strain

relations from Eqs. 4.3, written in x, y and z terms and represented in incremental form become:

$$\begin{aligned}\Delta\epsilon_x &= C_{xx} \Delta\sigma_x + C_{xy} \Delta\sigma_y + C_{xz} \Delta\sigma_z \\ \Delta\epsilon_y &= C_{yx} \Delta\sigma_x + C_{yy} \Delta\sigma_y + C_{yz} \Delta\sigma_z \\ \Delta\epsilon_z &= C_{zx} \Delta\sigma_x + C_{zy} \Delta\sigma_y + C_{zz} \Delta\sigma_z .\end{aligned}\quad (4.10)$$

It is clear from these equations that in the general case with nine unknown compliance terms, any simultaneous change in more than one of the applied stress increments would result in an indeterminate system of equations. However, by superimposing only a uniaxial compressive stress increment on an existing stress state, and measuring the resulting strain increments, each equation in Eqs. 4.10 will contain only one unknown compliance value on the right hand side. For $\Delta\sigma_x \neq 0$ and $\Delta\sigma_y = \Delta\sigma_z = 0$, the result is:

$$\begin{aligned}\Delta\epsilon_x &= C_{xx} \Delta\sigma_x & C_{xx} &= \Delta\epsilon_x / \Delta\sigma_x \\ \Delta\epsilon_y &= C_{yx} \Delta\sigma_x & \text{or } C_{yx} &= \Delta\epsilon_y / \Delta\sigma_x \\ \Delta\epsilon_z &= C_{zx} \Delta\sigma_x & C_{zx} &= \Delta\epsilon_z / \Delta\sigma_x .\end{aligned}\quad (4.11)$$

For $\Delta\sigma_y \neq 0$ and $\Delta\sigma_x = \Delta\sigma_z = 0$:

$$\begin{aligned}\Delta\epsilon_x &= C_{xy} \Delta\sigma_y & C_{xy} &= \Delta\epsilon_x / \Delta\sigma_y \\ \Delta\epsilon_y &= C_{yy} \Delta\sigma_y & \text{or } C_{yy} &= \Delta\epsilon_y / \Delta\sigma_y \\ \Delta\epsilon_z &= C_{zy} \Delta\sigma_y & C_{zy} &= \Delta\epsilon_z / \Delta\sigma_y .\end{aligned}\quad (4.12)$$

And for $\Delta\sigma_z \neq 0$; $\Delta\sigma_x = \Delta\sigma_y = 0$:

$$\begin{aligned}\Delta\epsilon_x &= C_{xz} \Delta\sigma_z & C_{xz} &= \Delta\epsilon_x / \Delta\sigma_z \\ \Delta\epsilon_y &= C_{yz} \Delta\sigma_z & \text{or } C_{yz} &= \Delta\epsilon_y / \Delta\sigma_z \\ \Delta\epsilon_z &= C_{zz} \Delta\sigma_z & C_{zz} &= \Delta\epsilon_z / \Delta\sigma_z .\end{aligned}\quad (4.13)$$

Thus all nine principal compliances can be determined.

In seven of the final series' tests, the stress path shown in Fig. 4.107 was employed to determine the elastic constants of the CU-SFRC. The uniaxial compressive stress increments, first $\Delta\sigma_x$, then $\Delta\sigma_y$ followed by $\Delta\sigma_z$ were superimposed on an initial hydrostatic stress state. One cycle ($\Delta\sigma_x$, $\Delta\sigma_y$, $\Delta\sigma_z$) returned the stress state back to the hydrostatic axis. The $\Delta\sigma_x$ increment allowed determination of the first column of the compliance matrix for that cycle. The $\Delta\sigma_y$ increment made possible calculation of the second column and the $\Delta\sigma_z$, the third column. See Eqs. 4.11-4.13. In all seven of the tests, at least three of these cycles were performed, consequently at least three compliance matrices were determined for each specimen. After all the cycles had been completed, the specimen was then loaded, as all others were, to the prescribed level of hydrostatic stress followed by monotonic shear deviation in an octahedral plane. The shear stresses induced during this stepped-hydrostatic loading were sufficiently small to remain in the elastic range of the SFRC, therefore no material degradation existed and the same specimens were used with confidence for the remainder of the test.

From the three or more compliance matrices determined for each specimen, average values were calculated and are listed in TABLE 4.2 along with the corresponding specimen numbers. Before the averages were calculated, the compliance values were examined and any values of opposite sign to that expected were eliminated from the sample. The mean was then calculated from the remainder of the values. Notice that no C_{yz} (i.e. C_{23}) values are given for the

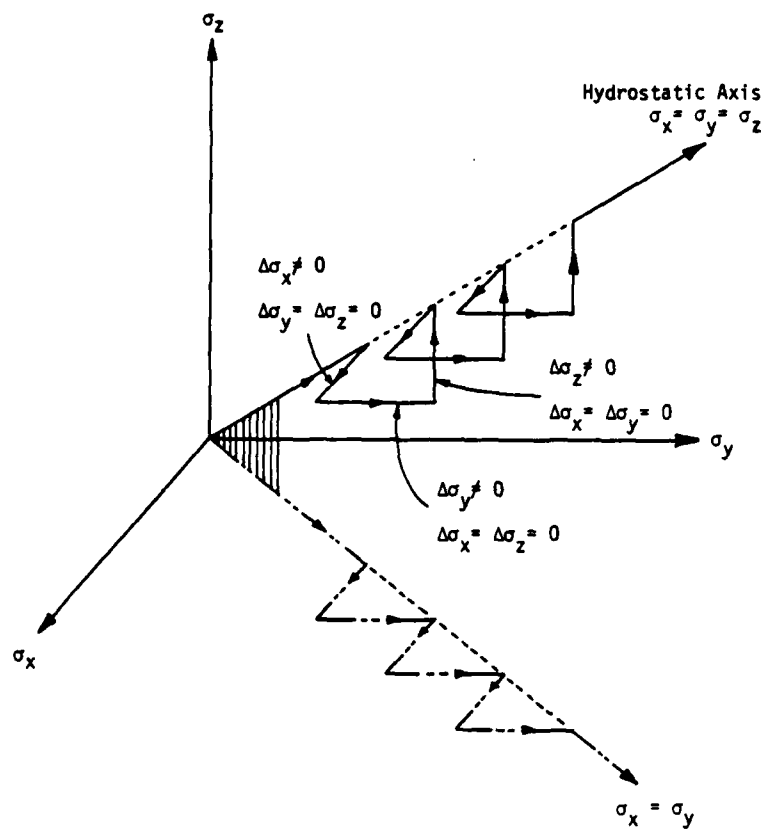


Fig. 4.107. Stress Path Along Hydrostatic Axis Used to Determine the Elastic Constants.

TABLE 4.2

SUMMARY OF AVERAGE* COMPLIANCE VALUES FOR
EACH OF SEVEN SPECIMENS.

* VALUES OF OPPOSITE SIGN TO THAT EXPECTED
WERE EXCLUDED FROM AVERAGE.

Specimen No.	Compliance Values $C_{ij} (i,j = x,y,z) \times 10^{-7} \text{ psi}^{-1}$		
	C_{xx} C_{yx} C_{zx}	C_{xy} C_{yy} C_{zy}	C_{xz} C_{yz} C_{zz}
F1C4	4.2749 -0.2119 -0.1139	-0.0840 3.8813 -0.1642	-0.0728 -0.0180 3.8204
F1C5	5.2978 -0.2056 -0.0608	-0.2668 6.2001 -0.1680	-0.2505 ----- 4.7103
F1B1	3.7333 -0.2000 -0.2800	-0.1500 3.8333 -0.2667	-0.3000 -0.2400 3.3333
F1D2	4.5707 -0.2382 -0.1942	-0.3442 4.1542 -0.2214	-0.0700 -0.1325 3.9797
F1C1	3.8353 -0.1715 -0.0300	-0.0008 3.7854 -0.2058	-0.2119 ----- 3.8216
F1C2	4.1909 -0.2626 -0.2750	-0.1727 3.7634 -0.4078	-0.2512 -0.3379 3.6944
F1A6	3.3373 -0.2673 -0.3753	-0.2884 3.8399 -0.3719	-0.3109 -0.3846 3.5283

specimens F1C5 or F1C1. In these two, all values were positive and therefore eliminated. Listed in TABLE 4.3 is the overall average compliance matrix calculated by taking the weighted average of the compliance values for all seven specimens. Notice it is nearly symmetric. Since the specimens were cast into the molds and vibrated under gravity forces acting in the z-direction, one might expect transverse isotropy about the z-axis to exist in the test specimens. In other words, the x-y plane is the plane of isotropy. By forcing the compliance matrix to take the form shown in Eq. 4.6, where there is symmetry about the diagonal and in the x-y plane, and calculating the compliances from the weighted mean of all values in the sample, the following compliance matrix is obtained if the SFRC is assumed to be transversely isotropic about the z-axis:

Transverse Isotropy

$$[C] = \begin{bmatrix} 4.1414 & -0.2080 & -0.2375 \\ -0.2080 & 4.1414 & -0.2375 \\ -0.2375 & -0.2375 & 3.7777 \end{bmatrix} * 10^{-7} \text{ psi}^{-1} .$$

From Eq. 4.7, the elastic constants are:

$$E_x = E_y = 2415 \text{ ksi}$$

$$E_z = 2647 \text{ ksi}$$

$$\nu_{xy} = \nu_{yx} = 0.0502$$

$$\nu_{zx} = \nu_{zy} = 0.0573$$

$$\nu_{xz} = \nu_{yz} = 0.0629 .$$

If one assumes complete isotropy, the compliance matrix takes the form shown in Eq. 4.8 where complete symmetry about the diagonal

TABLE 4.3
OVERALL AVERAGE COMPLIANCE MATRIX FOR
ALL SPECIMENS LISTED IN TABLE 4.2.

Compliance Values $C_{ij} (i,j = x,y,z) \times 10^{-7} \text{ psi}^{-1}$		
C_{xx}	C_{xy}	C_{xz}
C_{yx}	C_{yy}	C_{yz}
C_{zx}	C_{zy}	C_{zz}
4.1217	-0.1855	-0.2200
-0.2241	4.1611	-0.2379
-0.2228	-0.2675	3.7777

exists. Forcing the numerical compliances in the sample to take this form by calculating the mean values based on that assumption, the following compliance matrix is obtained if isotropy is assumed:

Isotropic

$$[C] = \begin{bmatrix} 4.0202 & -0.2285 & -0.2285 \\ -0.2285 & 4.0202 & -0.2285 \\ -0.2285 & -0.2285 & 4.0202 \end{bmatrix} * 10^{-7} \text{ psi}^{-1}.$$

From Eq. 4.9, the elastic constants become:

$$E = 2487 \text{ ksi}$$

$$\nu = 0.0568$$

$$\text{Bulk Modulus } K = \frac{E}{3(1-2\nu)} = 936 \text{ ksi}$$

$$\text{Shear Modulus } G = \frac{E}{2(1+\nu)} = 1177 \text{ ksi.}$$

Notice the large differences between Young's Modulus E obtained in this manner and the average E measured from the stress-strain curves of 3x6 in. cylinders tested in unconfined compression (3720 ksi; TABLE 4.1). (Poisson's Ratio ν was not measured for the cylinders). Some of the difference can be attributed to different specimen types, boundary effects and test conditions. Another reason is that the E calculated from tests conducted in the cubical device is an average E over the range of tests employing the stepped-loading, resulting perhaps in a slightly lower than actual modulus simply because the stress-strain response during HC is not perfectly linear. In addition to that, some error could have arisen from the inability to keep the change in the intermediate and minor

principal stresses during the stepped-loading exactly equal to zero since the high pressure gauges are only calibrated every 25 psi. Also, since the step sizes in this loading method were small (at most 1000 psi), only small strain changes would develop. Therefore when taking the difference in strains between two successive steps, any error in the deformation measuring system, perhaps due to electronic drift or pressure sensitivity, would induce large errors in the calculated stiffnesses or compliances resulting in values different than one might expect, for instance, positive compliances when negative ones should occur. But what are the expected values? One can only say that the values of E and ν and consequently K and G , calculated from the stepped-loading on cubical specimens, assuming isotropy, are low in comparison to the initial average values of K and G seen in the K_T vs. σ_0 and G_T vs. τ_0 curves shown in Figs. 4.79 and 4.87 which result from cubical tests as well. Aside from any error in the system, only the loading conditions of the two different types of tests can be blamed for the differences seen in K and G (or E and ν) since the specimen types and boundary conditions are identical. Keep in mind that the initial shear modulus G determined from the slope of the τ_0 - γ_0 curves and shown in Fig. 4.87 is not calculated until the HC part of the test is complete and shearing begins. However in the stepped-loading, K and G are calculated directly from E and ν by assuming the material is linearly elastic. It is felt that the initial values of K and G obtained from Figs. 4.79 and 4.87 are more reliable or more accurate of the true initial bulk and shear moduli

of the material than are the values of K and G calculated from E and ν obtained from the stepped-loading tests.

Making the assumption that the SFRC is isotropic is a good one considering the fact that not much shear strain (γ_0) is developed during HC and also that the differences between the calculated E 's and ν 's for transverse isotropic and isotropic assumptions are small.

If isotropy is not assumed, then any formulation used to predict stress-strain and/or strength behavior based on octahedral or invariant quantities cannot be used.

4.3.4 Strength

The stress state at which dilation occurs is an important point in the stress-strain behavior because different investigations might define failure differently, resulting in inconsistent failure envelopes. Therefore, the definition of failure must be clear before proceeding with the presentation of failure or strength results.

The points of dilation are shown on some of the τ_0 - ϵ_0 curves in Figs. 4.41-4.77 and also on the σ_1 - ϵ_V curves in Figs. 4.4-4.40, as the point of direction reversal in the τ_0 - ϵ_0 and/or σ_1 - ϵ_V curves where the volumetric strain (ϵ_V or $3\epsilon_0$) begins to decrease (compression positive). Point A in Figs 4.5 and 4.42 are examples for when dilation occurs. Bieniawski (23) studied the mechanism of brittle fracture of rocks in multiaxial compression and defines the stress state at dilation as the point of critical energy release where the onset of unstable fracture propagation begins.

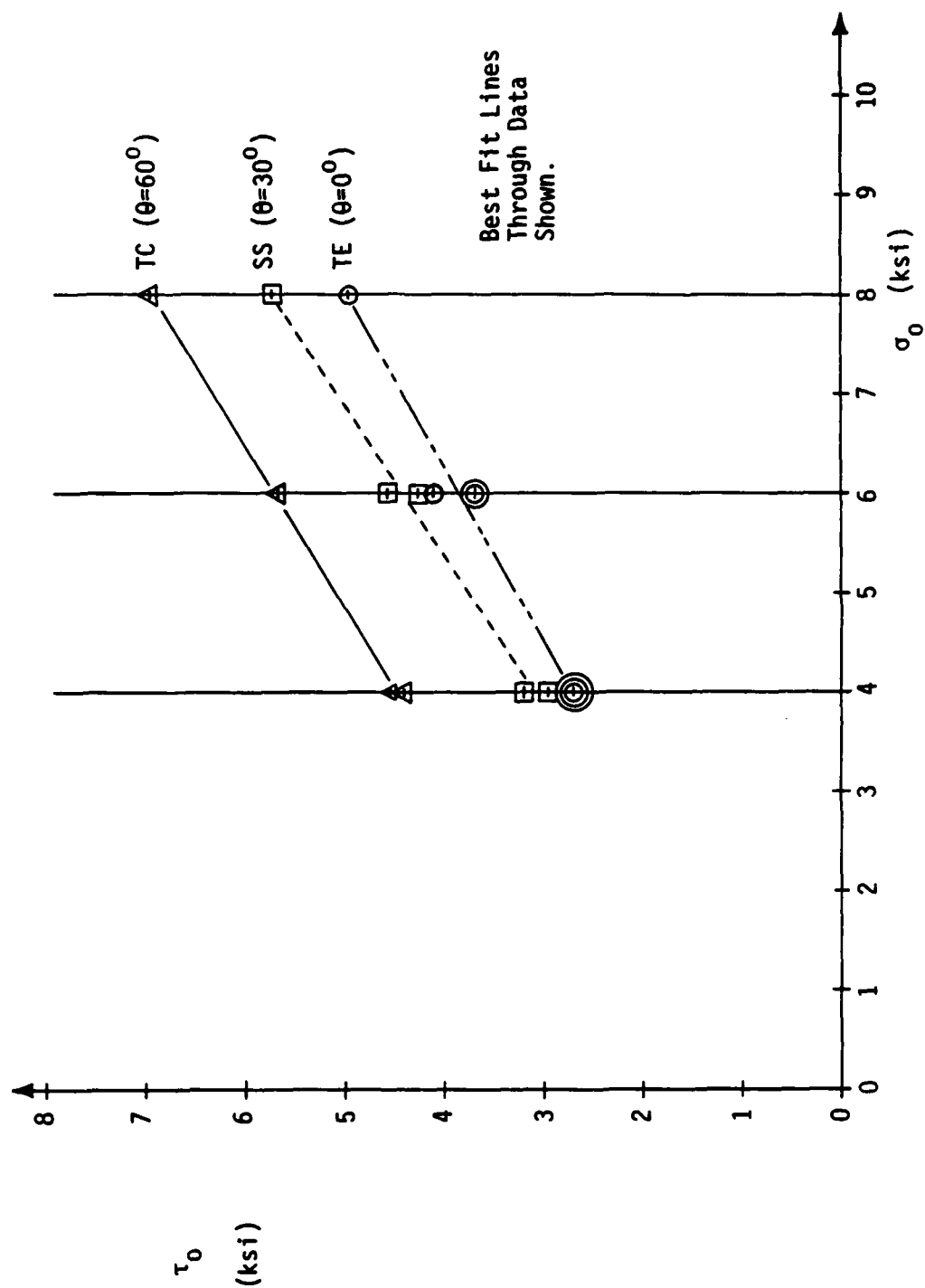
Since the cubical testing apparatus is a stress-controlled device, not being as stiff as one would like, some of the specimens did not dilate because of brittle failures occurring (usually a corner or edge failure). Therefore no failure stresses were recorded for these specimens. However, in some of the tests, slight increases in shear stress (τ_0) were applied beyond the point of dilation, seen for example in Figs. 4.5 and 4.42, but the percent increase was small. Therefore to be consistent in defining failure, the dilation point was conservatively chosen to be synonymous with failure. Based on this, strengths were found and are presented below. Of the 28 specimens tested, 16 reached failure. TABLE 4.4 lists the failure data for these specimens and the following figures show the data in:

- 1) τ_0 - σ_0 plane ; Fig. 4.108
- 2) Octahedral or Deviatoric Plane ; Fig. 4.109
- 3) Rendulic or Triaxial Plane ; Fig. 4.110.

Notice in TABLE 4.4 (also shown in Fig. 2.32) that the x,y,z directions of the specimens do not always correspond to the 1,2,3 principal directions. For the TC and SS tests, σ_z , σ_x and σ_y correspond to σ_1 , σ_2 , and σ_3 respectively. The reason for the differences is to be consistent with the sign convention employed in the conventional cylindrical triaxial test for the TC and TE paths. The SS path is not possible in conventional triaxial tests, therefore the SS sign convention was arbitrarily chosen to be the same as the TC's. For the above reasons, the data presented in the Rendulic or Triaxial plane, shown in Fig. 4.110, is plotted as σ_z

TABLE 4.4
FAILURE DATA FOR CU-SFRC
(COMPRESSIVE STRESSES POSITIVE)

Load Path (Fig. 2.31)	Spec. No.	σ_1 (psi)	σ_2 (psi)	σ_3 (psi)	σ_o (psi)	τ_o (psi)
Triaxial Compression (TC) ($\theta=60^\circ$)		σ_z	σ_x	σ_y		
	F1A1	10400	800	800	4000	4525.48
	F2B2	10200	900	900	4000	4384.06
	F1B3	14000	2000	2000	6000	5656.85
	F1D6	17800	3100	3100	8000	6929.64
Simple Shear (SS) ($\theta=30^\circ$)		σ_z	σ_x	σ_y		
	F2B3	7900	4000	100	4000	3184.33
	F1A6	7600	4000	400	4000	2939.38
	F2D3	11600	6000	400	6000	4572.38
	F1A5	11200	6000	800	6000	4245.78
	F1B2	15000	8000	1000	8000	5715.47
Triaxial Extension (TE) ($\theta=0^\circ$)		σ_x	σ_y	σ_z		
	F2C2	5900	5900	200	4000	2687.00
	F2C1	5900	5900	200	4000	2687.00
	F1B1	5900	5900	200	4000	2687.00
	F2D4	8900	8900	200	6000	4101.21
	F2C5	8600	8600	800	6000	3676.95
	F1C5	8600	8600	800	6000	3676.95
	F1A2	11500	11500	1000	8000	4949.74

Fig. 4.108. Failure Data in τ_0 - σ_0 Plane.

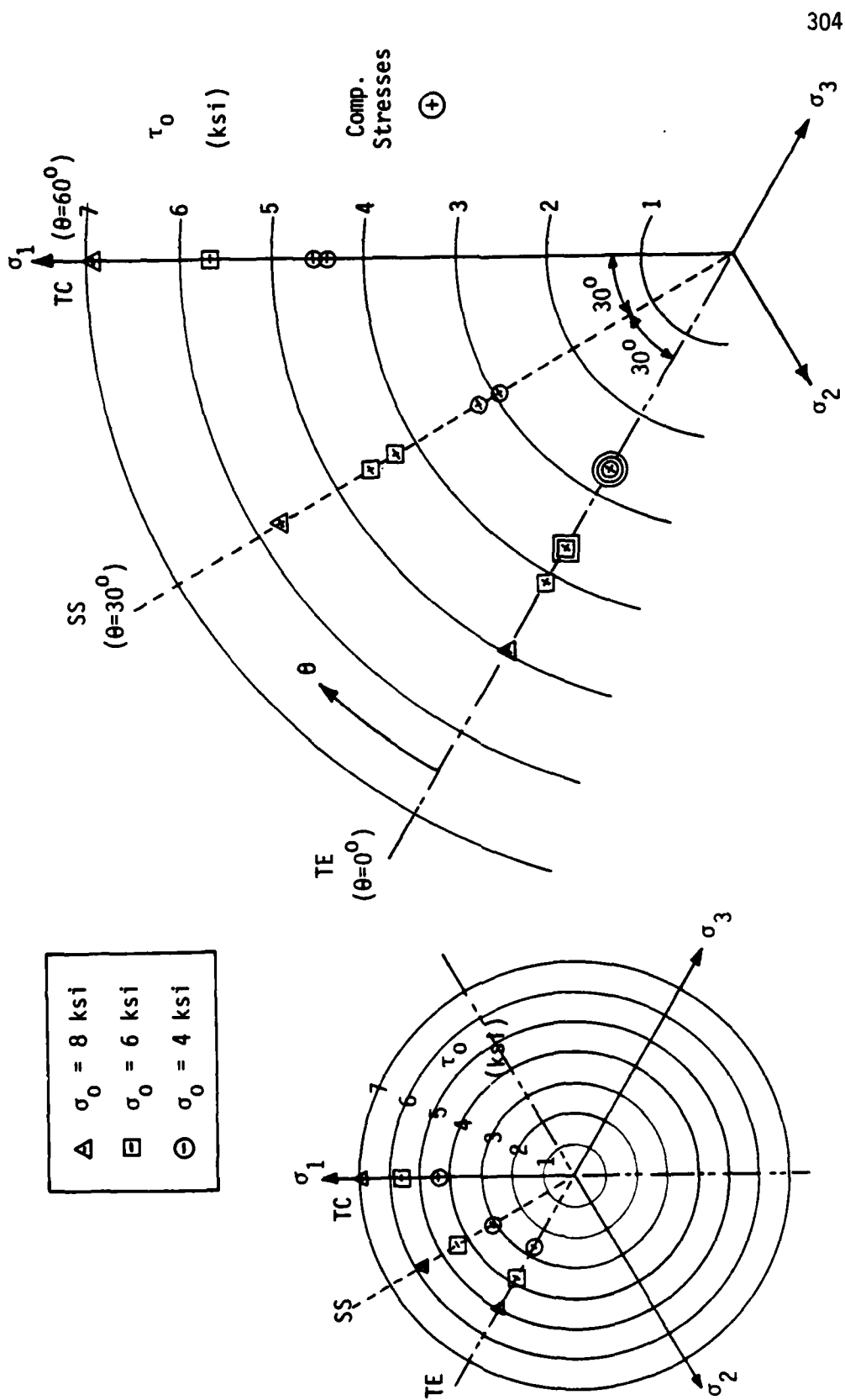


Fig. 4.109. Failure Data in Octahedral Planes.

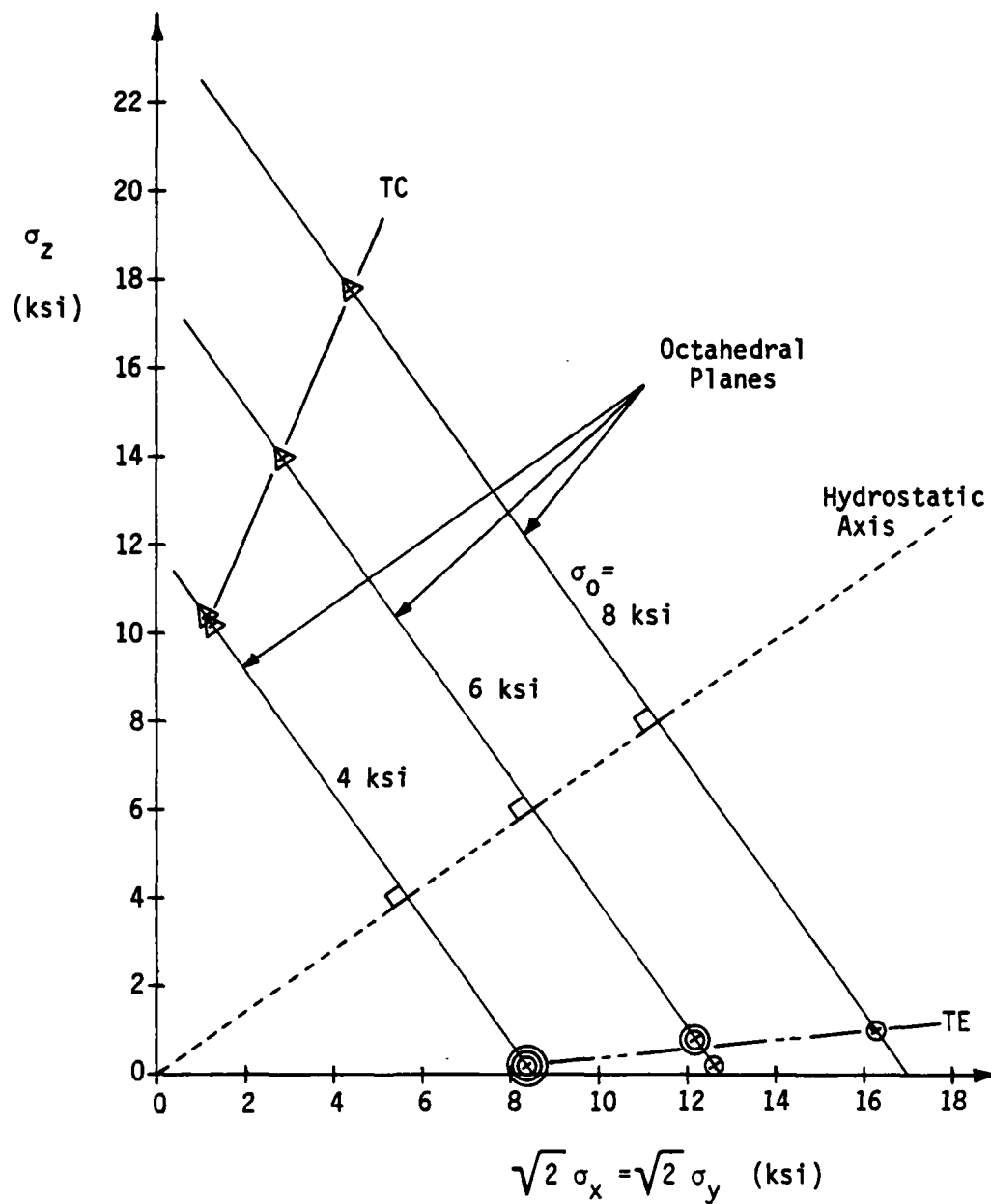


Fig. 4.110. Failure Data in Rendulic Plane With Best Fit Lines Through Data.

vs. $\sqrt{2} \sigma_x$, $\sqrt{2} \sigma_y$ and not as σ_1 vs. $\sqrt{2} \sigma_2$, $\sqrt{2} \sigma_3$. The SS data is not plotted in this figure simply because the SS stress path does not lie in the Rendulic plane.

Several conclusions can be drawn from examination of the strength results shown in Figs. 4.108-4.110:

- 1) The octahedral shear strength of the SFRC specimens is strongly dependent upon the stress path (θ or J_3).
In the tests with constant hydrostatic or confining pressure (σ_0), the order of strength from largest to smallest is TC, SS, TE. Had the strengths proven to be independent of the stress path, the three lines through the strength data in Fig. 4.108 would lie atop each other and a Drucker-Prager shaped envelope would have resulted.
- 2) There is a direct relationship between strength and confining pressure. Examining Fig. 4.108 shows that in the range of confining pressures employed in this study, the relationship between strength and confining pressure is linear for constant σ_0 stress paths. Had the strengths been independent of confining pressure, the lines through the data in Fig. 4.108 would be horizontal. Note that the slope of the best fit line through the SS data is the greatest, followed by the TC then the TE slopes.
- 3) The failure envelopes in the octahedral planes (Fig. 4.109) are non-circular, i.e. they depend on the

stress path (θ). Many researchers, including Gerstle, et al. (51), have observed similar results for plain concrete. See Fig. 1.13. Had the SFRC results proven to be independent of the stress path, the failure data would plot as circles in the octahedral planes. If the results had been independent of hydrostatic pressure, the failure envelopes would be identical for varying hydrostatic pressure. With some thought and imagination, one can see that the SFRC failure surface that will develop is basically cone-shaped, having a non-circular cross-section, similar to the one shown in Fig. 1.8. Any failure criteria used to predict the strength behavior of the SFRC must include the effects of stress path (θ) and hydrostatic pressure (σ_0).

- 4) Finally, through examination of the data in the Rendulic Plane (Fig. 4.110) and in TABLE 4.4, one can see that if tests had been conducted along the TE stress path at confining pressures lower than 4 ksi, they would have ended before the specimens failed because tensile stresses would have been required, which was impossible at the time this research was conducted.

CHAPTER 5

ANALYTICAL PREDICTIONS OF STRENGTH AND BEHAVIOR

5.1 Introduction

In this chapter, the constitutive models for predicting the strength and behavior of the CU-SFRC are presented. Section 5.2 discusses two strength models including the Willam-Warnke five-parameter and Lade three-parameter failure criteria. Each model is calibrated from the experimental data and used to predict the failure envelope of this material. Comparisons are made with the experimentally determined results. In Section 5.2.3, a parametric study is presented between the two failure criteria where they are compared with one another when calibrated from identical input strength data, some of which is from tests where the specimen type and boundary conditions differ from test to test. Then in Section 5.2.4, by showing the past-failure plastic strain increment vectors superimposed on the failure envelope, the normality of the data is discussed.

Section 5.3 deals with Gerstle's "Simple formulation", which is the model employed for predicting the stress-strain behavior of the material. It is based on octahedral quantities with varying material moduli functions. The model is calibrated from the experimental data and comparisons are made with the predicted and experimentally determined results.

5.2 Failure Criteria

A commonly used constitutive model for the compressive postfailure condition of concrete is to assume that plastic yielding occurs when the compressive failure criterion is satisfied by the stress state.

In general, the yield function may be written as:

$$F = F(\sigma_{ij}, d\epsilon_{ij}^P) \leq 0 \quad (5.1)$$

with equality during yielding and negative during unloading, where

σ_{ij} = state of stress

$d\epsilon_{ij}^P$ = plastic strain increment.

With the assumption of the normality principle and associated flow rule, the increment of plastic strain must be normal to the yield surface; hence

$$d\epsilon_{ij}^P = d\lambda \frac{\partial F}{\partial \sigma_{ij}} \quad (5.2)$$

where $d\lambda$ is the unknown hardening parameter giving the magnitude of the plastic strain increments, with the direction governed by the normality rule. Following classical plasticity and solving for this hardening parameter $d\lambda$, leads to the derivation of the

elastic-plastic constitutive tensor C_{ijkl}^{e-p} used in a stress analysis. Hence

$$d\sigma_{ij} = C_{ijkl}^{e-p} d\epsilon_{kl} \quad (5.3)$$

The elastic-plastic constitutive tensor changes form with respect to the yield function (F) and hardening parameter ($d\lambda$) selected.

The Von Mises yield criterion could be chosen with the yield function F defined as

$$F = \sqrt{J_{2D}} - k = 0 \quad (5.4)$$

where

$$\begin{aligned} J_{2D} &= \frac{1}{6} [(\sigma_1 - \sigma_2)^2 + (\sigma_2 - \sigma_3)^2 + (\sigma_3 - \sigma_1)^2] \\ &= \frac{3}{2} \tau_0^2 \end{aligned} \quad (5.5)$$

and k is the strain hardening parameter. In principal stress space, this yield criterion plots as a right circular cylinder centered on the hydrostatic axis as shown in Fig. 5.1. For hardening behavior, the radius of the yield surface will increase when the stress state is such that the yield surface is reached as deformation occurs. Thus the dependence on the parameter k . This criterion is seen to be independent of hydrostatic pressure as well as shear stress distribution. The yielding of metals is described fairly well by the Von Mises criterion. However, for a material such as concrete, the yield or failure strength shows a dependence on J_1 and J_3 (or σ_0 and θ ; Section 4.3.4) implying that the Von Mises criterion would not be valid for representing the strength of concrete materials.

A better approximation to the yielding of concrete would be the Drucker-Prager or extended Von Mises yield criterion which forms a right circular cone in principal stress space, centered on the hydrostatic axis as shown in Fig. 5.2. The Drucker-Prager yield function F may be expressed as

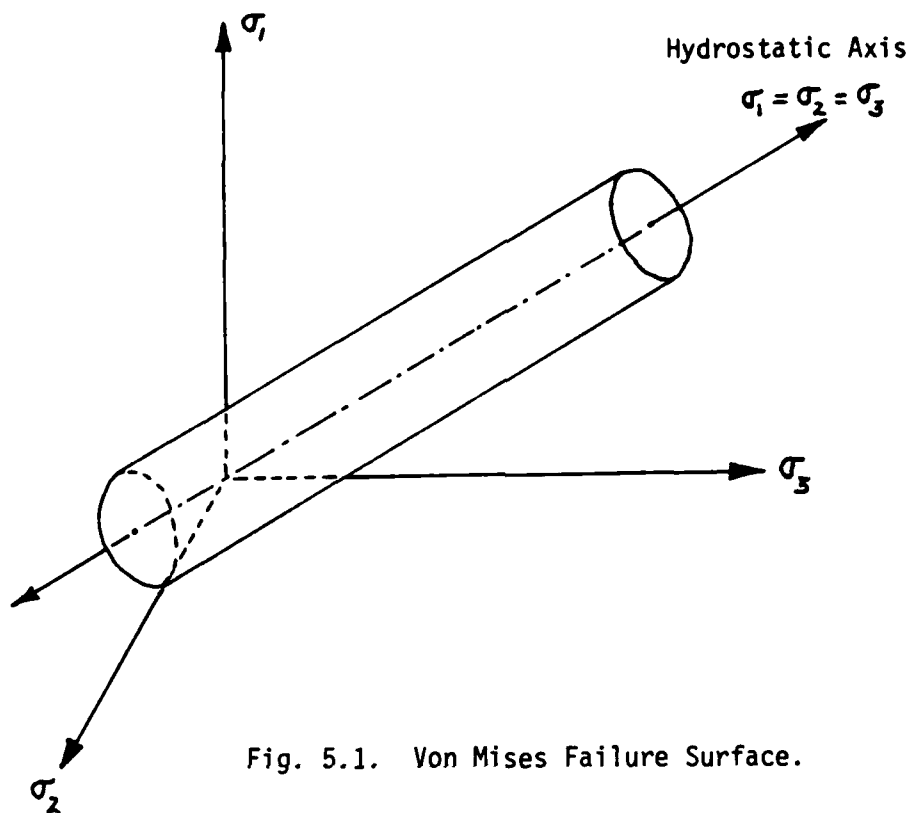


Fig. 5.1. Von Mises Failure Surface.

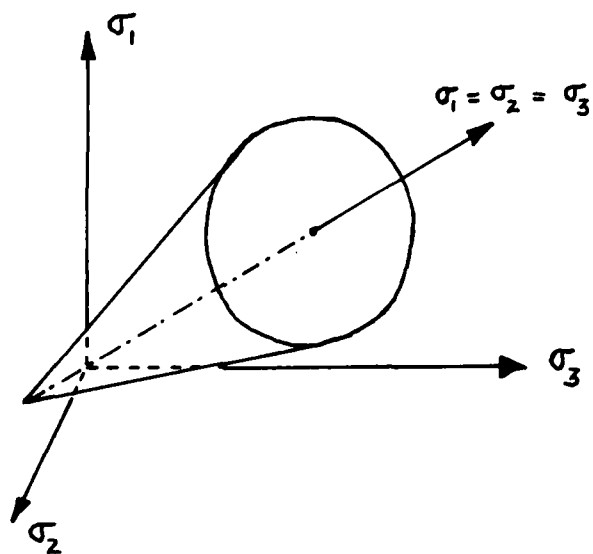


Fig. 5.2. Drucker-Prager Failure Surface.

$$F = \sqrt{J_{2D}} - \alpha J_1 - k = 0 \quad (5.6)$$

where

$$\begin{aligned} J_1 &= \sigma_1 + \sigma_2 + \sigma_3 \\ &= 3\sigma_0 \end{aligned} \quad (5.7)$$

with J_{2D} given by Eq. 5.5. Note that this yield function reduces to the Von Mises cylinder for $\alpha = 0$ (purely cohesive materials).

As shown on the failure surface, the Drucker-Prager criterion does include the effect of hydrostatic pressure. However, as in the Von Mises criterion, the dependence on J_3 (or θ) is not incorporated. This can be seen in the octahedral plane because the Drucker-Prager surface plots as a circle.

The Drucker-Prager failure criterion is more realistic than the Von Mises criterion for describing the failure of plain concrete and SFRC. However, it is still deficient in many facets. As shown in Section 4.3.4, the SFRC exhibits a strong stress path as well as confining pressure dependency governing failure. In the octahedral plane for instance, the failure envelope is definitely non-circular (Fig. 4.109). Therefore any criterion used to predict the failure of this material cannot neglect the dependence on J_1 and J_3 (σ_0 and θ) as is done in the Von Mises criterion or simply J_3 as in the Drucker-Prager criterion.

Other failure criteria have been developed for concrete-type materials that do incorporate stress path and confining pressure dependency; two of which are of particular interest in fitting the experimental data obtained. They are:

1) Willam-Warnke failure criterion discussed in Section 5.2.1.

2) Lade failure criterion discussed in Section 5.2.2.

Note here that the terms yield and failure have been used interchangeably up to this point. If a material is assumed to behave or does behave as an ideally plastic material, i.e., associated flow and the normality principle hold, then yield and failure describe the same state. For hardening materials however, failure represents the ultimate strength state whereas yield describes irreversible deformation.

The point of the previous discussion was to show that even if the SFRC were to behave as an ideally plastic material, simple yield or failure functions like those employed in the Von Mises and Drucker-Prager criteria are insufficient for describing the true shape of the SFRC failure surface obtained experimentally.

The validity of the normality flow rule for the post failure condition in the compressive regime of the SFRC is tested in Section 5.2.4. There the plastic strain increment vectors at failure are calculated and shown on various failure envelope sections.

5.2.1 Willam-Warnke Five-Parameter Failure Criterion.

The following is a mathematical model developed by Willam and Warnke (134) for the triaxial failure surface of concrete type materials. The failure envelope is fully described in principal stress space, assuming isotropic material behavior. It is basically a cone with curved meridians and a non-circular section as shown in Fig. 1.8. Since isotropic material behavior is assumed, only a

sextant of the principal stress space need be considered for the mathematical model; the rest will be symmetric. The surface is represented by hydrostatic and deviatoric sections. The hydrostatic section forms a meridional plane, containing the hydrostatic axis as an axis of revolution. It can be represented in $\tau_0 - \sigma_0$ stress space as shown in Fig. 5.3 where the hydrostatic axis lies along the abscissa. The deviatoric section lies in a plane perpendicular to the hydrostatic axis, described by the polar coordinates r and θ as shown in Fig. 5.4.

The Willam-Warnke five-parameter model differs from their previous three-parameter model (134) in that it employs curved meridians in the hydrostatic section to accommodate low as well as high compression regimes, i.e., for hydrostatic stress states high in comparison to the uniaxial strength of the material ($\sigma_0/f_{cu} = \xi > 1$). The three parameter model (not discussed here) uses straight meridians to represent failure results in the $\tau_0 - \sigma_0$ plane.

The failure surface function $F(\sigma)$ for the five-parameter model is defined as:

$$F(\sigma) = F(\sigma_a, \tau_a, \theta) = \frac{1}{r(\sigma_a, \theta)} \frac{\tau_a}{|f_{cu}|} - 1 \quad (5.8)$$

= 0 for material failure

where

$$\begin{aligned} \sigma_a &= \text{average normal stress} \\ &= \frac{1}{3} (\sigma_1 + \sigma_2 + \sigma_3) \\ &= \sigma_0, \end{aligned} \quad (5.9)$$

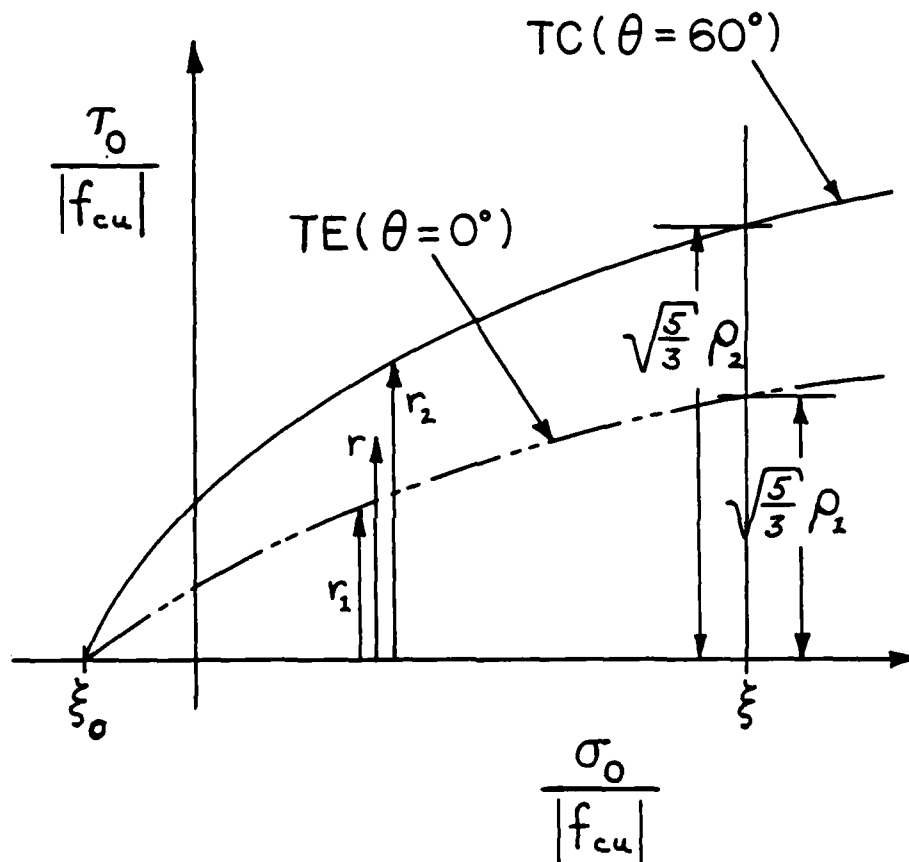


Fig. 5.3. $\tau_0 - \sigma_0$ or Hydrostatic Section of Proposed Willam-Warnke Failure Surface.

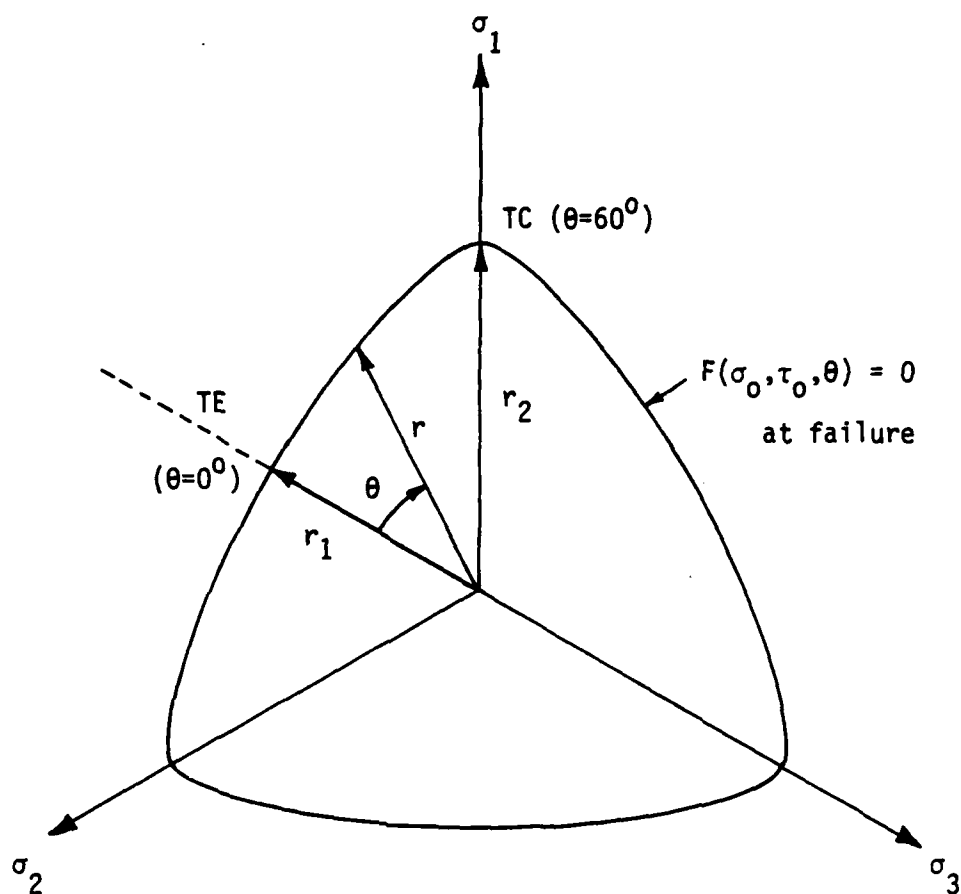


Fig. 5.4. Deviatoric or Octahedral Section of Proposed Willam-Warnke Failure Surface.

τ_a = average shear stress

$$= \frac{1}{\sqrt{15}} [(\sigma_1 - \sigma_2)^2 + (\sigma_2 - \sigma_3)^2 + (\sigma_3 - \sigma_1)^2]^{1/2} \quad (5.10)$$

$$= \sqrt{\frac{3}{5}} \tau_o$$

and

f_{cu} = uniaxial compressive strength
(used for normalizing).

Note at this time that Willam and Warnke assumed tension positive when formulating their failure criterion. Since compression is assumed positive in this report and octahedral normal and shear stresses rather than average normal and shear stresses are used in this study, the Willam-Warnke failure criterion has been altered slightly to accommodate these two features; i.e., compression positive and octahedral rather than average stresses. If one prefers to assume tension positive, refer to their report (134) for a detailed discussion. Rewriting $F(\sigma)$ to account for these

$$F(\sigma) = F(\sigma_o, \tau_o, \theta) = \frac{1}{r(\sigma_o, \theta)} \frac{\tau_o}{|f_{cu}|} - 1 = 0 \quad (5.11)$$

The failure surface is constructed by approximating the meridians in the τ_o - σ_o section at $\theta = 0^\circ$ (TE) and $\theta = 60^\circ$ (TC), shown in Fig. 5.3, by two second order parabolas r_1 and r_2 , connected by an ellipse in the deviatoric plane as shown in Fig. 5.5. The failure surface r is then defined as a function of the angular measure θ , bounded within the position vectors r_1 and r_2 :

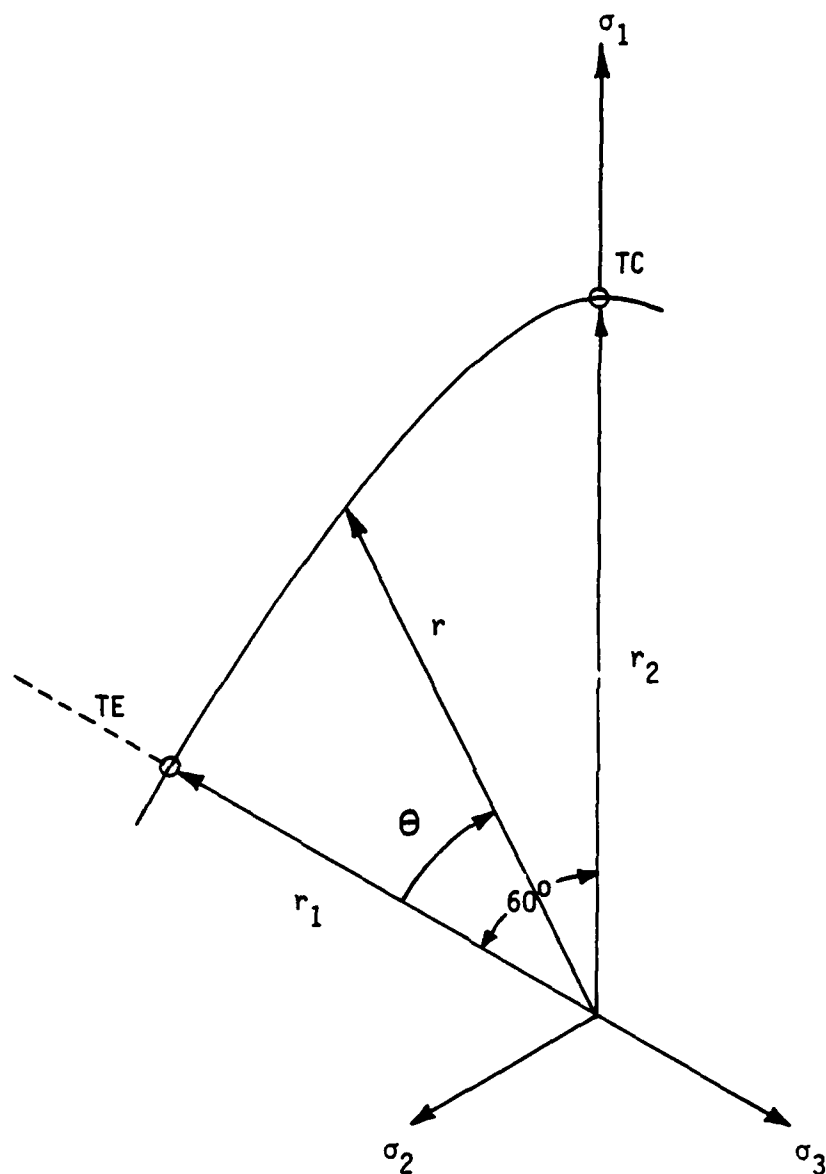


Fig. 5.5. Willam-Warnke Failure Surface Showing One Sextant of Ellipse in Deviatoric Plane. The Rest is Symmetrical.

$$\begin{aligned}
 r(\sigma_0, \theta) = & \{ 2r_2(r_2^2 - r_1^2)\cos\theta \\
 & + r_2(2r_1 - r_2) \sqrt{4(r_2^2 - r_1^2)\cos^2\theta + 5r_1^2 - 4r_1r_2} \} \\
 & \cdot \frac{1}{\{4(r_2^2 - r_1^2)\cos^2\theta + (r_2 - 2r_1)^2\}}
 \end{aligned} \quad (5.12)$$

where

$$\begin{aligned}
 \cos\theta &= \frac{\sigma_1 + \sigma_2 - 2\sigma_3}{\sqrt{2} [(\sigma_1 - \sigma_2)^2 + (\sigma_2 - \sigma_3)^2 + (\sigma_3 - \sigma_1)^2]^{1/2}} \\
 &= \frac{\sigma_0 - \sigma_3}{\sqrt{2} \tau_0} .
 \end{aligned} \quad (5.13)$$

The vectors r_1 ($\theta=0^\circ$, TE) and r_2 ($\theta=60^\circ$, TC) are second order, functions of the octahedral normal stress σ_0 and are written as:

$$r_1 \left(\frac{\sigma_0}{|f_{cu}|} \right) = a_0 + a_1 \left(\frac{\sigma_0}{|f_{cu}|} \right) + a_2 \left(\frac{\sigma_0}{|f_{cu}|} \right)^2 ; \text{ TE } (\theta = 0^\circ) \quad (5.15)$$

$$r_2 \left(\frac{\sigma_0}{|f_{cu}|} \right) = b_0 + b_1 \left(\frac{\sigma_0}{|f_{cu}|} \right) + b_2 \left(\frac{\sigma_0}{|f_{cu}|} \right)^2 ; \text{ TC } (\theta = 60^\circ) \quad (5.16)$$

To determine the constants a_0, a_1, a_2 from the TE meridian and b_0, b_1, b_2 from the TC meridian, thereby defining r_1 and r_2 , the following six values must be known:

- 1) f_{cu} (uniaxial compressive strength)
- 2) f_{cb} (equi-biaxial compressive strength)
- 3) f_t (uniaxial tensile strength)
- 4) σ_0 in the high compression regime
- 5) τ_0 at $\theta=0^\circ$ (TE) for the above σ_0
- 6) τ_0 at $\theta=60^\circ$ (TC) for the above σ_0 .

With these six values, five parameters are obtained. They are:

$$\text{for a given } \xi = \frac{\sigma_0}{|f_{cu}|} ; \quad (5.17)$$

$$\rho_1 = \sqrt{\frac{3}{5}} \frac{\tau_0}{|f_{cu}|} \quad \text{at } \theta = 0^\circ \text{ (TE)} \quad (5.18)$$

$$\rho_2 = \sqrt{\frac{3}{5}} \frac{\tau_0}{|f_{cu}|} \quad \text{at } \theta = 60^\circ \text{ (TC)} \quad (5.19)$$

and the strength parameters

$$\alpha_z = \left| \frac{f_t}{f_{cu}} \right| \quad (5.20)$$

$$\alpha_u = \left| \frac{f_{cb}}{f_{cu}} \right| \quad (5.21)$$

Note that it is required that all five of these parameters be positive and if the compression positive sign convention is followed, they will be. From these five parameters, the unknown constants in Eqs. 5.15 and 5.16 can be determined. For the TE ($\theta=0^\circ$) meridian:

$$a_2 = \frac{\sqrt{2} \xi (\alpha_z - \alpha_u) - \sqrt{2} \alpha_z \alpha_u + \sqrt{\frac{5}{3}} \rho_1 (2\alpha_u + \alpha_z)}{(2\alpha_u + \alpha_z) (\xi^2 - \frac{2}{3} \alpha_u \xi + \frac{1}{3} \alpha_z \xi - \frac{2}{9} \alpha_z \alpha_u)} \quad (5.22)$$

$$a_1 = \frac{1}{3} (\alpha_z - 2\alpha_u) a_2 + \frac{\sqrt{2} (\alpha_u - \alpha_z)}{2\alpha_u + \alpha_z} \quad (5.23)$$

$$a_0 = \frac{\sqrt{2}}{3} \alpha_u - \frac{2}{3} a_1 \alpha_u - \frac{4}{9} a_2 \alpha_u^2 \quad (5.24)$$

It is required that the TE and TC meridians intersect at a common point on the hydrostatic axis in the tensile regime (because concrete has tensile strength) such that $r_1 = r_2 = 0$. If the value

of $\frac{\sigma_0}{|f_{cu}|} = -\xi_0$ (implying a tensile stress) where ξ_0 is positive, to

to give $r_1 = r_2 = 0$, it follows from Eq. 5.15 that:

$$a_2 \xi_0^2 - a_1 \xi_0 + a_0 = 0 \quad (5.25)$$

or

$$\xi_0 = \frac{a_1 - \sqrt{a_1^2 - 4a_0a_2}}{2a_2} \quad (5.26)$$

where ξ_0 must be positive.

For the TC ($\theta=60^\circ$) meridian:

$$b_2 = \frac{\sqrt{\frac{5}{3}} \rho_2 (\xi_0 + \frac{1}{3}) - \frac{2}{3} (\xi_0 + \xi)}{(\xi + \xi_0)(\xi - \frac{1}{3})(\xi_0 + \frac{1}{3})} \quad (5.27)$$

$$b_1 = \frac{\sqrt{15} \rho_2 - \sqrt{2}}{3\xi - 1} - (\xi + \frac{1}{3}) b_2 \quad (5.28)$$

$$b_0 = \xi_0 b_1 - \xi_0^2 b_2 \quad (5.29)$$

The surface will be convex, as it should be, if the above determined constants satisfy the following constraints:

$$a_0 > 0 \quad b_0 > 0$$

$$a_1 \geq 0 \quad \text{and} \quad b_1 \geq 0$$

$$a_2 \leq 0 \quad b_2 \leq 0$$

and

$$\frac{r_1(\sigma_0)}{r_2(\sigma_0)} > \frac{1}{2} \quad (5.31)$$

The five-parameter model is illustrated in Fig. 1.7 comparing it with experimental data reported by Launay, et al. (83). Very good strength predictions are made based on experimental results.

From this five-parameter model, other failure criteria can be derived:

The Von Mises model is obtained if

$$a_0 = b_0 \text{ and } a_1 = b_1 = a_2 = b_2 = 0 . \quad (5.32)$$

The Drucker-Prager model is obtained if

$$\begin{aligned} a_0 &= b_0 \\ a_1 &= b_1 \end{aligned} \quad \text{and} \quad a_2 = b_2 = 0 . \quad (5.33)$$

The three-parameter, straight meridian model (previously mentioned) is obtained if

$$\frac{a_0}{b_0} = \frac{a_1}{b_1} \text{ and } a_2 = b_2 = 0 . \quad (5.34)$$

This is a nice feature of the Willam-Warnke five-parameter model in that it does degenerate to other simpler failure criteria.

5.2.1.1 Fitting of CU-SFRC Strength Results to the Willam-Warnke Model

In using the Willam-Warnke failure criterion, the authors suggest the use of six strength measurements obtained from various types of tests as discussed in the previous section. The five parameters (Eqs. 5.17-5.21) are then determined from these six values, followed by the constants defining the meridians (Eqs. 5.22-5.29) that are needed for the formulation. However, the ability to obtain (without estimating) all these parameters was not possible in this test series. At the time this research on SFRC was conducted, the ability to determine the uniaxial tensile strength of a cubical specimen was not possible because the cubical device used to perform the tests employ fluid cushion compressive type loading

only. The addition of brushes to apply tensile stresses to a cubical specimen is now in the design stages. Also, the uniaxial and equi-biaxial compressive strengths of cubical specimens were not obtained either. But according to the Willam-Warnke formulation, one does not necessarily need these parameters to determine the required constants used to calibrate the model. Examining Eqs. 5.15 and 5.16 shows that since these meridian equations are second order, the constants in the equations can be just as easily determined by fitting first Eq. 5.15 to three failure data points on the TE path, and secondly Eq. 5.16 to three points on the TC path. Once the meridians r_1 and r_2 are determined, the strength envelope defined by Eq. 5.12 can readily be determined.

Note here that when calibrating a model such as this one, one should not use strength values obtained from tests where the boundary conditions are different. For instance, using the uniaxial compressive strength of a cylinder tested in an apparatus employing rigid end platens and multiaxial compressive strengths obtained from a device employing fluid cushions. The boundary conditions are completely different. Consequently, a strength envelope based on mixed boundary conditions cannot be representative of true strengths. If one needs strength values such as f_{cu} , f_{cb} and so on, as those in the Willam-Warnke model, they should be obtained in the same apparatus. Gerstle, et al. (51) showed what effect boundary conditions have on observed strengths of identical concrete specimens. In later sections of this chapter, parametric studies are presented showing the effects of using strengths from mixed

boundary conditions to calibrate failure criteria on the predicted strength envelope compared to the observed SFRC cubical specimen strengths.

In TABLE 4.4 all the failure data obtained for the CU-SFRC cubical specimens tested in the final series is listed. In all, sixteen of twenty-eight specimens were taken to failure, i.e., volume dilation. This failure data is shown plotted in the τ_0 - σ_0 plane (Fig. 4.108), the octahedral or deviatoric plane (Fig. 4.109) and the Rendulic or triaxial plane (Fig. 4.110).

Eqs. 5.15 and 5.16 defining the meridians r_1 and r_2 use the uniaxial compressive strength f_{cu} for nondimensionalizing. Since this value of f_{cu} for a specimen tested in the cubical apparatus was not determined, the two meridian equations are rewritten by eliminating the normalizing parameter f_{cu} . They become:

$$r_1 = A_0 + A_1 \sigma_0 + A_2 \sigma_0^2 ; \text{TE } (\theta=0^\circ) \quad (5.35)$$

$$r_2 = B_0 + B_1 \sigma_0 + B_2 \sigma_0^2 ; \text{TC } (\theta=60^\circ) \quad (5.36)$$

Notice the use of capital letters for the coefficients in the above expressions so as not to confuse them with the coefficients given in Eqs. 5.15 and 5.16 and defined by Eqs. 5.22-5.29. Also note that eliminating f_{cu} as the nondimensionalizing parameter in Eqs. 5.15 and 5.16 does not affect the equation of the failure surface, r , defined by Eq. 5.12. However, the failure function $F(\sigma)$ given in Eq. 5.11 must be rewritten to account for the lack of f_{cu} .

It becomes

$$F(\sigma) = \frac{\tau_0}{r(\sigma_0, \theta)} - 1 = 0 \quad (5.37)$$

A least-squares fit through the $\tau_0 - \sigma_0$ strength data (Fig. 4.108) was conducted in order to determine the coefficients in Eqs. 5.35 and 5.36. A straight rather than parabolic fit was used for two reasons:

- 1) The failure data plotted in the $\tau_0 - \sigma_0$ plane plots nearly as a straight line, for all three stress paths, between the range of hydrostatic stresses employed in the tests, i.e. $\sigma_0 = 4000$ to 8000 psi.
- 2) A least squares parabolic fit through the TE data again plotted as a straight line. But more importantly, a least-squares parabolic fit through the TC data plotted as a parabola which was slightly concave upward. That is to say, if one extended this parabola for higher hydrostatic stresses than used in the tests, the predicted rate of strength increase of the specimen would accelerate. This trend is clearly unacceptable. Therefore, the straight line fits were used to calibrate the Willam-Warnke model.

The six coefficients in Eqs. 5.35 and 5.36, determined from the least squares straight line fits through the failure data in the $\tau_0 - \sigma_0$ plane between $\sigma_0 = 4000$ and 8000 psi were found to be:

$$\begin{array}{ll} A_0 = 424 \text{ psi} & B_0 = 1980 \text{ psi} \\ A_1 = 0.566 & B_1 = 0.617 \\ A_2 = 0 & B_2 = 0 \end{array} \quad (5.38)$$

Eqs. 5.35 and 5.36 then become:

$$r_1 = 424 + 0.566 \sigma_0 ; \text{ TE}(\theta=0^\circ) \quad (5.39)$$

$$r_2 = 1980 + 0.617 \sigma_0 ; \text{ TC}(\theta=60^\circ) \quad (5.40)$$

where σ_0 , r_1 and r_2 are in psi. Even though straight line meridians are employed here ($A_2 = B_2 = 0$), the Willam-Warnke five-parameter failure criterion, calibrated for the CU-SFRC, does not degenerate to their original three parameter criterion previously mentioned because not all the conditions of Eq. 5.34 are met; i.e., $A_0/B_0 \neq A_1/B_1$.

With the equations for r_1 and r_2 , the radius vector $r(\sigma_0, \theta)$ given by Eq. 5.12 and representing the analytical expression for τ_0 at failure is now fully defined with σ_0 and θ as the independent variables. The predicted failure envelope can now be compared with experimentally determined strength values. Figs. 5.6, 5.7 and 5.8 show the experimental strength results in the $\tau_0 - \sigma_0$, deviatoric and Rendulic planes respectively, for the CU-SFRC, with the Willam-Warnke predicted failure curves also shown. Eq. 5.12 defines r with Eqs. 5.39 and 5.40 used for r_1 and r_2 . In all the figures, the average TE and TC experimental failure data matches the predicted Willam-Warnke strengths exactly because these were the paths used to calibrate the model. The SS ($\theta=30^\circ$) path was not used in determining the model parameters, therefore, the strengths obtained experimentally along this path allow one to compare predicted with actual strengths of specimens tested and observe the effectiveness of the model in predicting strengths on a path other than those used to calibrate the model. Along the SS path, there is close agreement between the observed and predicted strengths for the lowest hydrostatic stress, i.e. $\sigma_0 = 4$ ksi. For higher levels of σ_0 , the

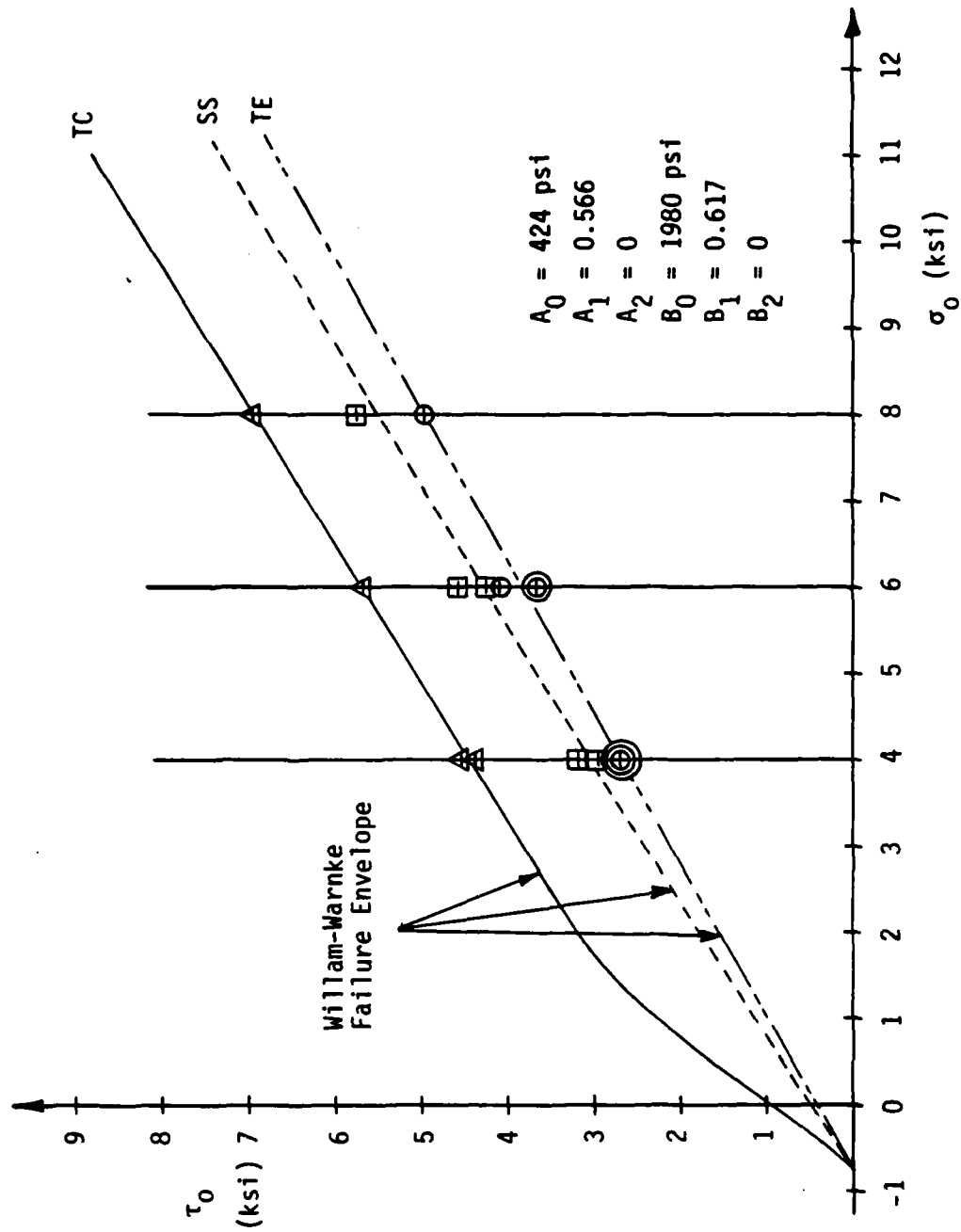


Fig. 5.6. Failure Data in τ_0 - σ_0 Plane with Willam-Warnke Prediction.

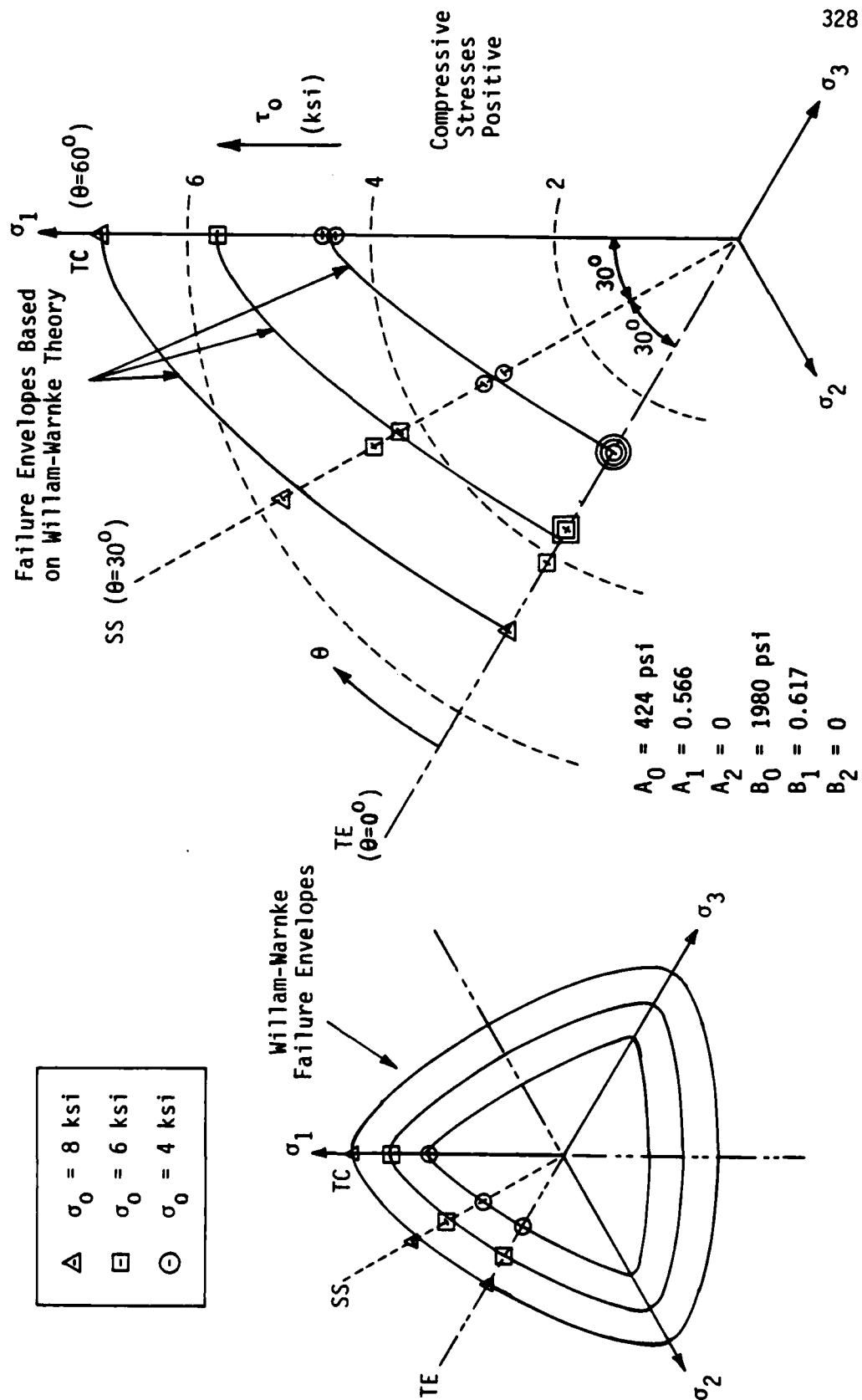


Fig. 5.7. Failure Data in Octahedral Planes with William-Warke Predictions.

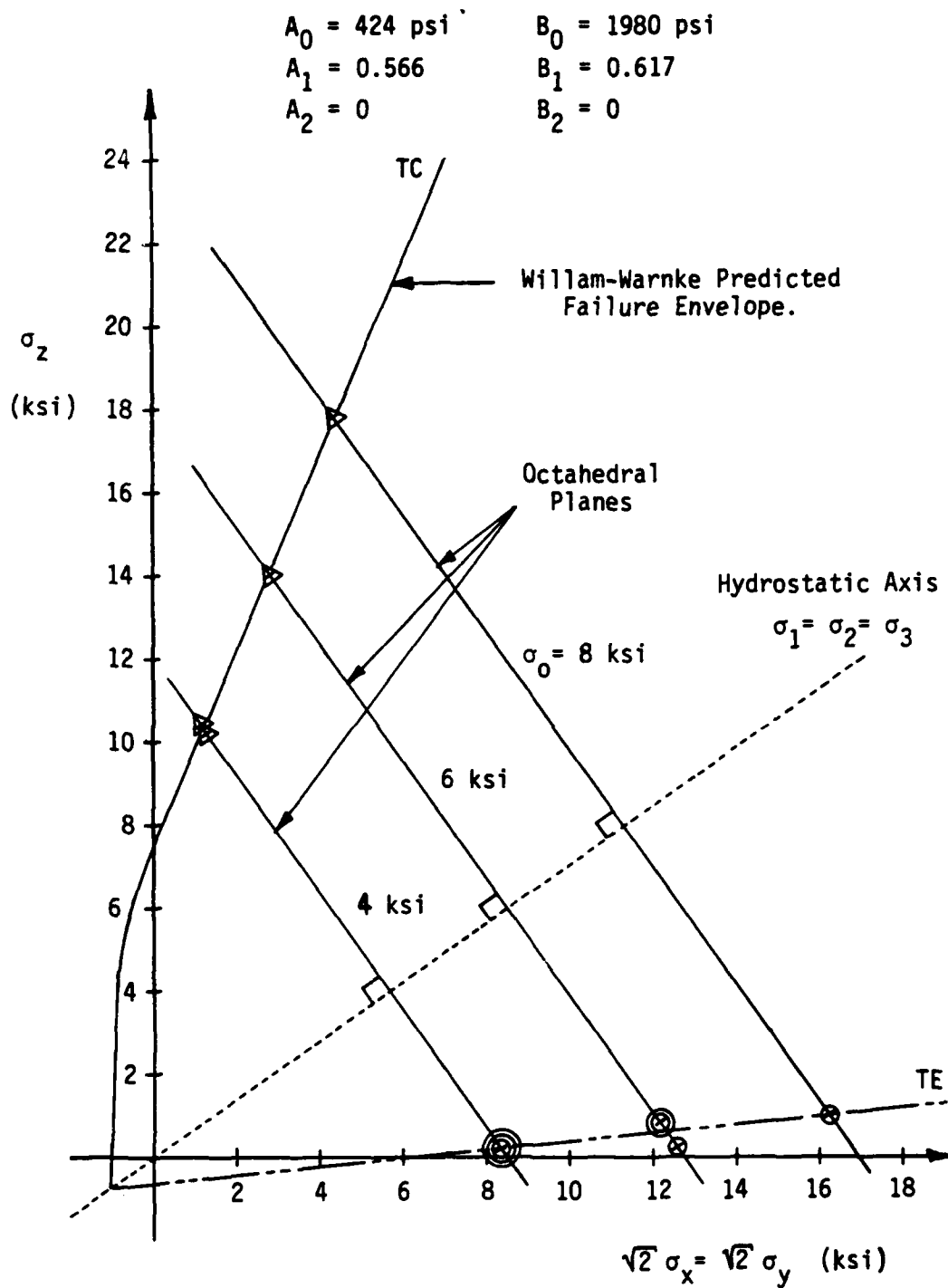


Fig. 5.8. Failure Data in Rendulic Plane with Willam-Warnke Prediction.

model is slightly conservative in predicting strengths. This may not be the fault of the model. Notice in Figs. 5.6 and 5.7 that only one failure point was obtained experimentally for the SS path at $\sigma_0 = 8$ ksi. Perhaps this specimen had an abnormally higher strength than others. Assuming all specimens to be identical, one could say the Willam-Warnke criterion predicts slightly conservative results for this stress path. Notice also that the failure surfaces in Fig. 5.7 become more convex with increasing hydrostatic stress. The surface for $\sigma_0 = 4$ ksi nearly plots as a triangle with the tendency toward circular failure surfaces with increasing hydrostatic stress. Perhaps with even greater hydrostatic stress, the failure envelope would take the Drucker-Prager shape and eventually the Von Mises shape.

In Figs. 5.6 and 5.8, notice that the predicted TC meridian in the low compression regime is curved, when a straight line was fitted through the TC strength data between $\sigma_0 = 4$ and 8 ksi to determine r_2 . The reason is that the failure surface, regardless of the stress path, must start at a point in the tensile regime along the hydrostatic axis, called the apex where $\tau_0 = 0$ for some value of σ_0 negative. This apex is near the τ_0, σ_0 point for uniaxial tension, which lies on the TE path. The predicted failure envelope is calculated from r . Therefore, with the condition of the common origin or apex of the failure envelope, the TC and SS strength curves must be curved in the tension through the low compression regime of hydrostatic stress before becoming linear and passing through the experimental failure data. Unfortunately, no experimental strength data in the tension and/or low compression

regime is available for calibration and comparison purposes.

Based on the predicted strength envelope, values of f_{cu} , f_t and f_{cb} can be derived very easily. The uniaxial compressive strength f_{cu} lies on the TC meridian whereas the uniaxial tensile and equi-biaxial compressive strengths both lie on the TE meridian.

These predicted strengths are:

$$\begin{aligned} f_{cu} &= 7450 \text{ psi} && \text{(Compression} \\ f_t &= -643 \text{ psi} && \text{positive)} \\ f_{cb} &= 4500 \text{ psi} \end{aligned} \quad (5.41)$$

The predicted biaxial failure envelope for compression only, calculated from Eq. 5.37, is shown in Fig. 5.9 for reference. No experimental biaxial strength data was obtained. Therefore no comparisons can be made regarding the validity of the predicted biaxial strengths. However, it should be noted that calibrating the five-parameter model as was done for the CU-SFRC gives a different biaxial failure envelope shape than one might expect, based on the envelopes previously obtained experimentally for plain concrete (Figs. 1.6 and 1.10) and fiber reinforced mortar (Fig. 1.5). The derived value of f_{cb} seems somewhat low, when for plain concrete, this value is at least as large as f_{cu} . This could indicate that perhaps the Willam-Warnke failure criterion should have been calibrated by including a biaxial strength, even if it had to be assumed.

The other two predicted strengths, f_{cu} and f_t , given in Eq. 5.41, can be compared to the observed unconfined compressive strength (f'_c) and the split cylinder tensile strength (T), both of 3 x 6 in. cylinders, as reported in Chapter 3. These values were:

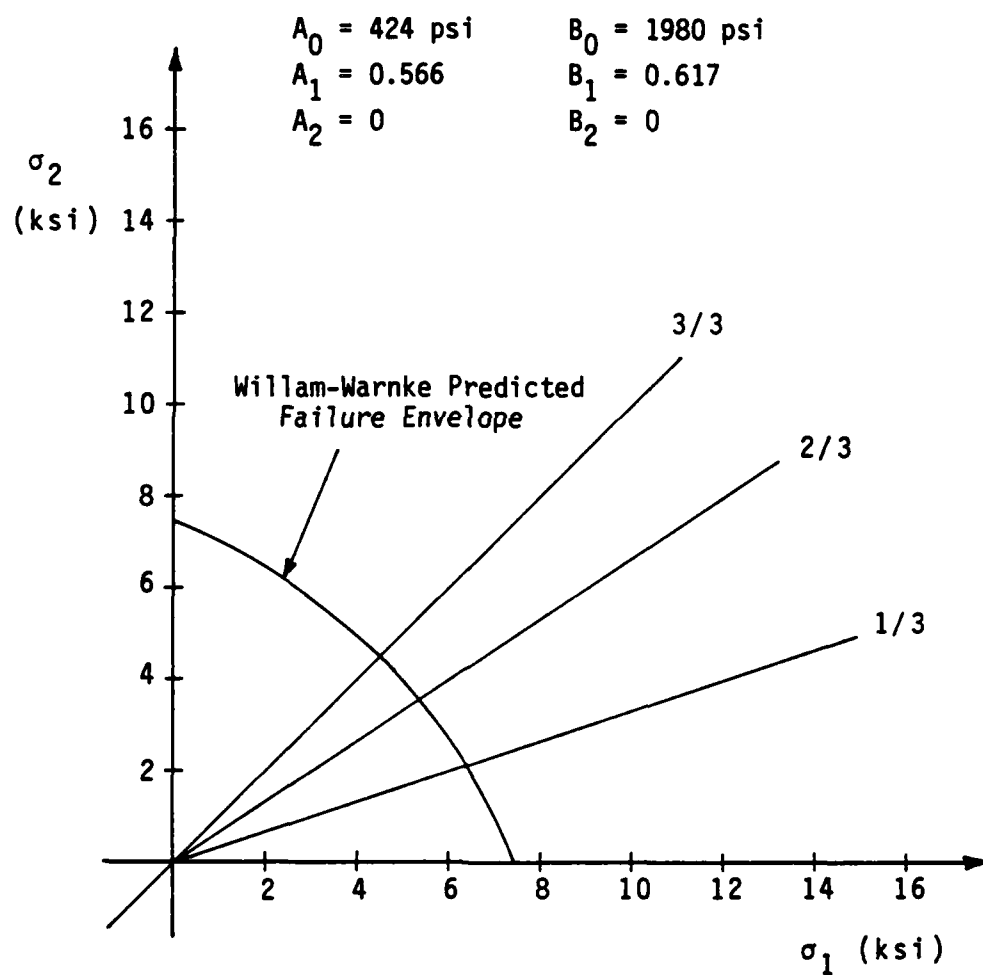


Fig. 5.9. Predicted Biaxial Failure Envelope
Based on Willam-Warnke Failure Criterion.

$$\begin{array}{lll} f_c' = 9200 \text{ psi} & \text{(Compression)} & (5.42) \\ T = -953 \text{ psi} & \text{positive)} & \end{array}$$

The differences between these predicted and observed strengths can be attributed primarily to specimen types and boundary conditions because the predicted values were derived from the failure envelope calibrated from the strengths of cubical specimens with fluid cushion boundaries and the observed strengths were from 3 x 6 in. cylinders with rigid boundaries.

It should be emphasized that the range of validity of the Willam-Warnke model in predicting strengths of SFRC should not exceed the maximum hydrostatic stress levels for which the model was calibrated. However, predicted strengths for higher hydrostatic stresses could be extrapolated from the results if one uses good judgement in deciding upon the limits of extrapolation. For the model was calibrated for the CU-SFRC in such a way that it predicts linearly increasing shear strengths (τ_o) for increasing hydrostatic stress (σ_o). That is, the trend for the predicted strength of the SFRC does not level off according to the Willam-Warnke model calibrated as it was. Launay, et. al. (83) showed that the strength of concrete type materials does level off for increasing confining pressure as demonstrated in Fig. 1.7. Therefore, the range of validity of any numerical formulation for failure criterion should conservatively remain between the levels of hydrostatic stress for which the experiments were conducted and the formulation calibrated.

All in all, the Willam-Warnke failure criterion is a good, fairly simple formulation to work with and proved to predict very closely the strengths obtained experimentally for the CU-SFRC.

5.2.2 Lade Three-Parameter Failure Criterion for Concrete

The following three-parameter failure criterion for concrete proposed by Lade (79) stems from a general, three dimensional failure criterion previously developed by Lade (77) for cohesionless soils. The criterion is expressed in terms of stress invariants and involves three material parameters describing the three independent characteristics for a concrete failure surface: (1) the opening angle of the failure surface or the friction angle, (2) the curvature of the failure surface in planes containing the hydrostatic axis, i.e., curved meridians, and (3) the tensile strength. These three parameters can be easily determined from any type of strength tests, conventional or not, as described below.

The failure surface function $F(\sigma)$ for this three-parameter criterion is expressed in terms of the first and third stress invariants as follows:

$$F(\sigma) = \left(\frac{J_1^3}{J_3} - 27 \right) \cdot \left(\frac{J_1}{p_a} \right)^m - \eta_1 \quad (5.43)$$

$$= 0 \text{ for material failure}$$

where

$$J_1 = \bar{\sigma}_1 + \bar{\sigma}_2 + \bar{\sigma}_3 = \bar{\sigma}_x + \bar{\sigma}_y + \bar{\sigma}_z \quad (5.44)$$

$$J_3 = \bar{\sigma}_1 \cdot \bar{\sigma}_2 \cdot \bar{\sigma}_3$$

$$\begin{aligned} &= \bar{\sigma}_x \cdot \bar{\sigma}_y \cdot \bar{\sigma}_z + \tau_{xy} \cdot \tau_{yz} \cdot \tau_{zx} + \tau_{yx} \cdot \tau_{zy} \cdot \tau_{xz} \\ &\quad - (\bar{\sigma}_x \cdot \tau_{yz} \cdot \tau_{zy} + \bar{\sigma}_y \cdot \tau_{zx} \cdot \tau_{xz} + \bar{\sigma}_z \cdot \tau_{xy} \cdot \tau_{yx}) \end{aligned} \quad (5.45)$$

$$p_a = \text{atmospheric pressure (positive) in the same units as the stresses} \quad (5.46)$$

(Compression Positive)

The meaning of the a 's will be clarified next. In order for the failure criterion given by Eq. 5.43, originally formulated for cohesionless soils (77), to be applicable to concrete, the cohesion and tensile strength sustained by concrete must be included. This is done by translating the principal stress space along the hydrostatic axis as shown in Fig. 5.10 by the addition of a constant stress $a \cdot p_a$ added to the normal stresses. As shown in the figure, the value of $a \cdot p_a$ reflects the effect of the tensile strength of the concrete, where " a " is a dimensionless parameter (positive) and p_a is the atmospheric pressure described by Eq. 5.46. The value of $a \cdot p_a$ must be slightly larger than the absolute value of the uniaxial tensile strength. The resulting normal failure stresses $\bar{\sigma}_x, \bar{\sigma}_y, \bar{\sigma}_z$ or the resulting principal failure stresses $\bar{\sigma}_1, \bar{\sigma}_2, \bar{\sigma}_3$ used in Eqs. 5.44 and 5.45 are then expressed as:

$$\begin{aligned} \bar{\sigma}_x &= \sigma_x + a \cdot p_a \\ \bar{\sigma}_y &= \sigma_y + a \cdot p_a \\ \bar{\sigma}_z &= \sigma_z + a \cdot p_a \end{aligned} \quad (5.47)$$

or

$$\begin{aligned} \bar{\sigma}_1 &= \sigma_1 + a \cdot p_a \\ \bar{\sigma}_2 &= \sigma_2 + a \cdot p_a \\ \bar{\sigma}_3 &= \sigma_3 + a \cdot p_a \end{aligned} \quad (5.48)$$

where $\sigma_x, \sigma_y, \sigma_z, \tau_{xy}$, etc. or $\sigma_1, \sigma_2, \sigma_3$ are the actual stresses at failure. Note that for a cohesionless soil, $a=0$, the normal and translated coordinates in Fig. 5.10 coincide, and the resulting failure function in Eq. 5.43 reduces to that given by Lade for cohesionless soils (77).

The determination of the three parameters, a, η_1 and m is very simple. As previously mentioned, the value of $a \cdot p_a$ is slightly greater than f_t as indicated on Fig. 5.10. If the uniaxial tensile strength f_t is not determined experimentally, Lade (79) gives an approximate formula relating f_t to the unconfined compressive strength f_{cu} through the following power function:

$$f_t = T \cdot p_a \cdot \left(\frac{f_{cu}}{p_a} \right)^t \quad \begin{array}{l} \text{(compression} \\ \text{positive)} \end{array} \quad (5.49)$$

where T and t are dimensionless numbers, found for plain concrete to be $T = -0.61$ and $t = 2/3$. Once f_t is known, the value of " a " (>0) can be estimated. From studies conducted by Lade (79), $a \cdot p_a$ was found to be 0.3% to 1.4% greater than f_t . In other words:

$$1.003 \cdot f_t \leq a \cdot p_a \leq 1.014 \cdot f_t \quad (5.50)$$

With the estimated value of " a ", the resulting stresses in Eqs. 5.47 or 5.48 are calculated, then substituted into the expressions for the stress invariants given by Eqs. 5.44 and 5.45. The parameters η_1 and m are then determined by plotting $(J_1^3/J_3 - 27)$ vs. (p_a/J_1) at failure on log-log paper and determining from a regression analysis the best fitting straight line through the data. The intercept of this line with $(p_a/J_1) = 1$ is the value of η_1 , and m is the slope of the line.

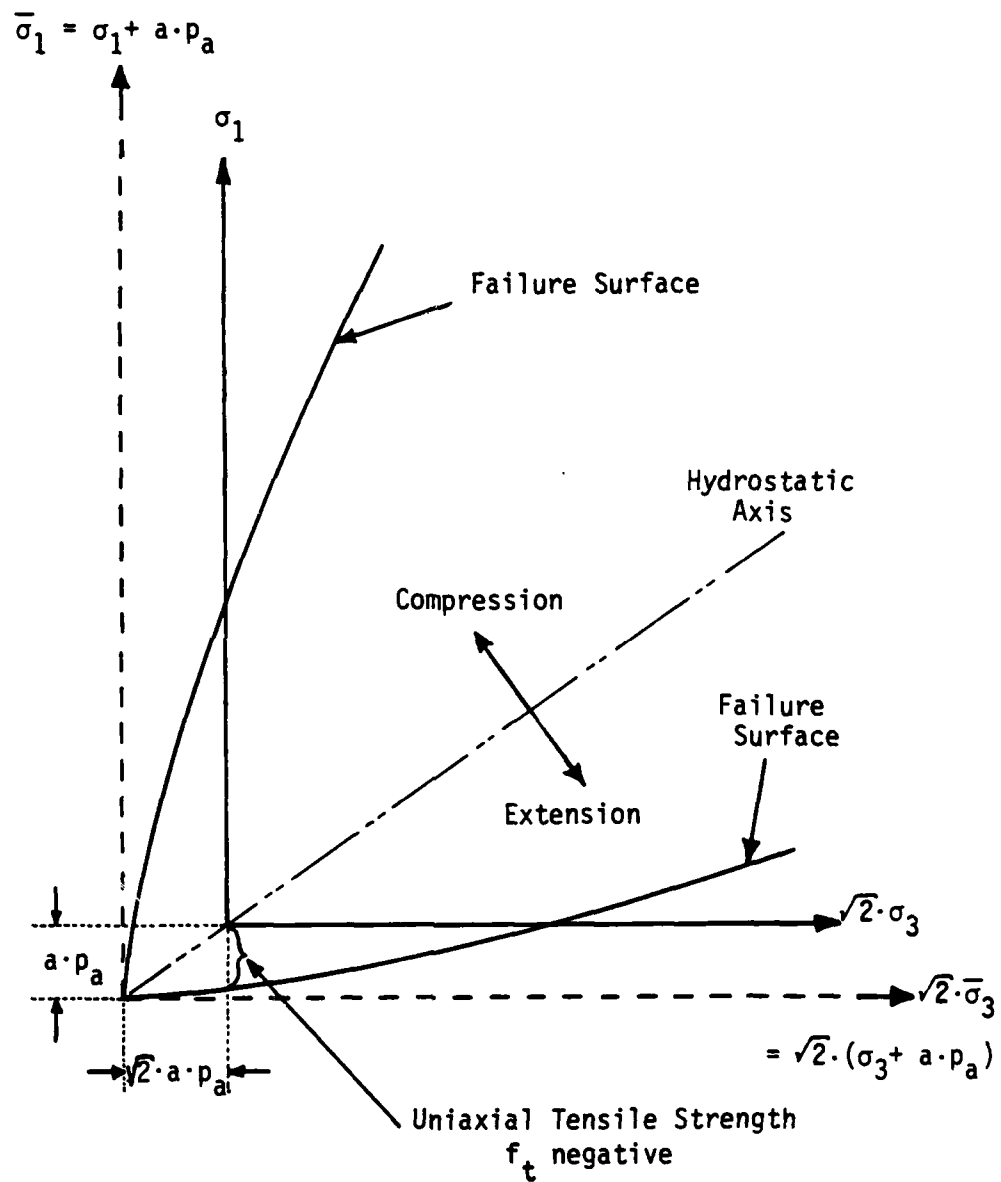


Fig. 5.10. Translation of Principal Stress Space Along Hydrostatic Axis to Include Effect of Tensile Strength in Lade's Failure Criterion. {Lade(79)}.

Fig. 5.11 shows an example of finding these parameters and the effect of varying the estimated parameter "a" on the values of η_1 , m and the coefficient of determination r^2 for tests on plain concrete by Mills and Zimmerman (79). By varying the value of "a", all failure points in Fig. 5.11 move since the stress invariants incorporate "a" in their calculations. However, the uniaxial tensile strength point is the only one that shows this movement because the others are very slight. Note that the value of "a" is estimated from the uniaxial tensile strength but this tensile strength does not necessarily need to be incorporated into the determination of the other material parameters as demonstrated in Fig. 5.11. Lade points out that without it, i.e., if only compressive strengths were used, the resulting parameters would describe the failure surface in the region of compressive stresses with reasonable accuracy. However the tensile strength, even if just an estimate, should be included because it tends to influence the location of the best fit straight line. Consequently, the parameters found would then better describe the failure surface for regions of compressive as well as tensile stresses.

Figs. 5.12-5.14 show the comparisons between the experimental results of Mills and Zimmerman and the predictions made by the three parameter model, with material parameters of "a" = 23.20, η_1 = 119,339 and m = 1.127 as shown in Fig. 5.11. There is some scatter present, but the three-parameter model is seen to represent the data very well.

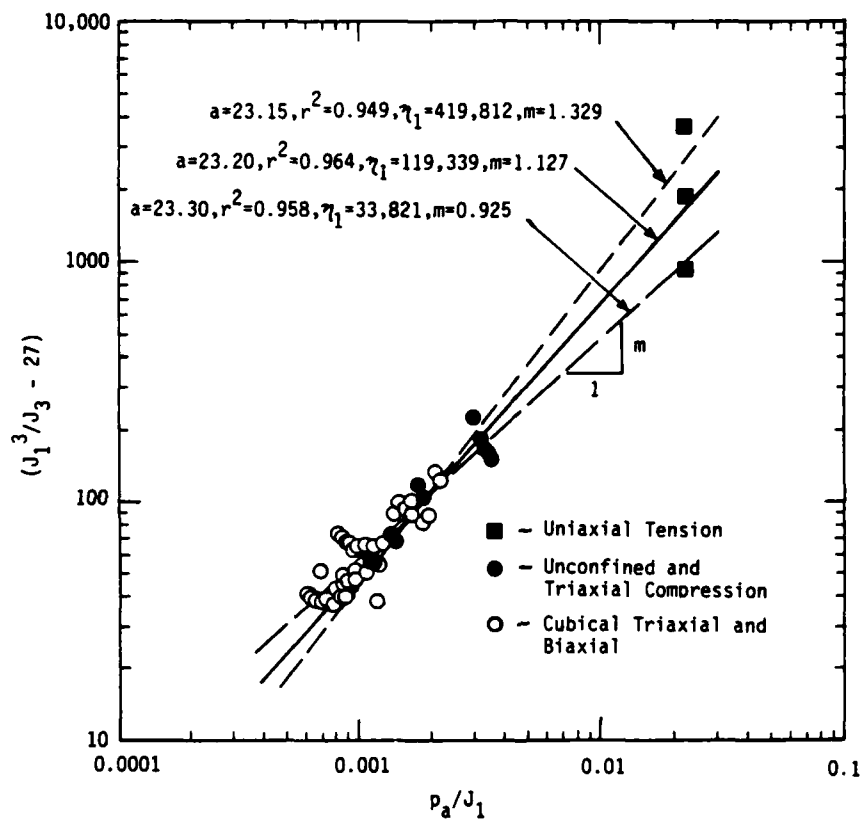


Fig. 5.11. Example of Determination of Material Parameters Involved in Lade's Failure Criterion for Concrete Tested by Mills and Zimmerman. { Lade(79) } .

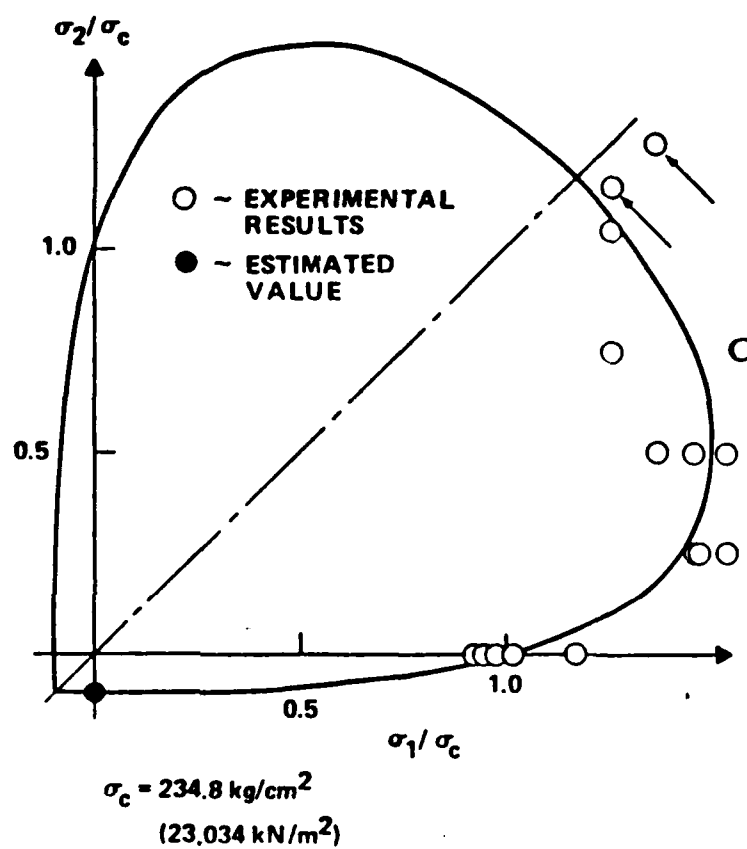


Fig. 5.12. Comparison of Lade Failure Criterion in Biaxial Planes with Results of Biaxial Tests Performed by Mills and Zimmerman [Lade (79)].

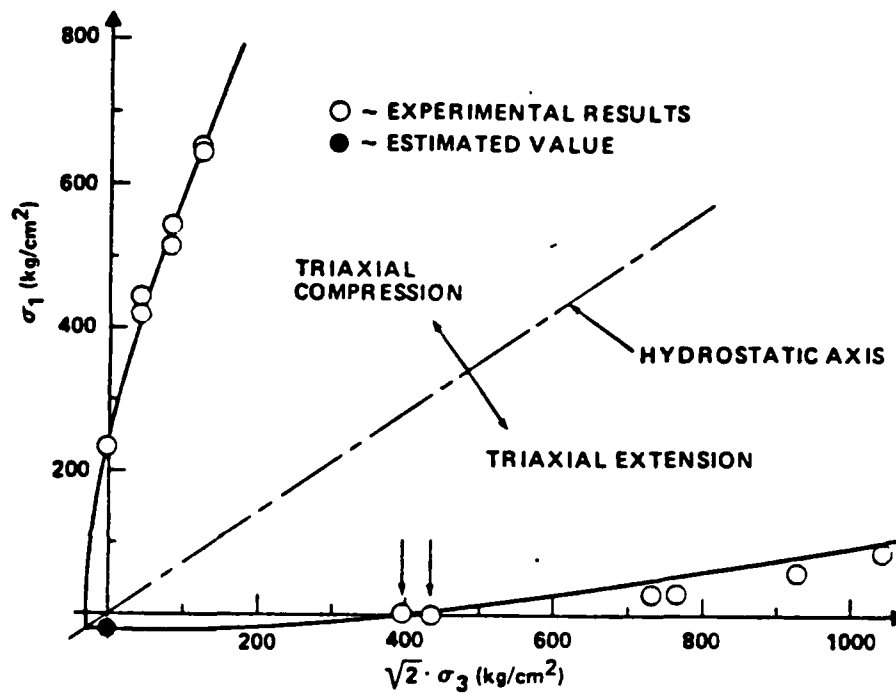


Fig. 5.13. Comparison of Lade Failure Criterion in Triaxial Plane with Results of Triaxial Compression and Extension Tests Performed by Mills and Zimmerman [Lade (79)].

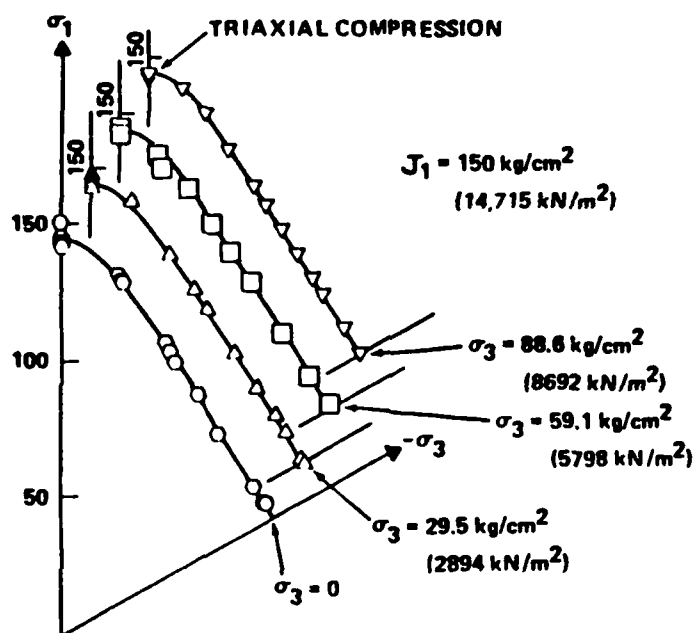


Fig. 5.14. Comparison of Lade Failure Criterion in Octahedral Planes with Results of Tests on Concrete Performed by Mills and Zimmerman [Lade (79)].

5.2.2.1 Fitting of the CU-SFRC Strength Results to the Lade Three-Parameter Model

Lade's three-parameter model requires some value of tensile strength from which the parameter "a" can be estimated. No tensile strength data for cubical specimens of the CU-SFRC was obtainable. Therefore f_t was estimated using Eq. 5.49 with values of $T = -0.61$, $t = 2/3$ (the same numbers found for plain concrete) and $f_{cu} = 7500$ psi. The value of the unconfined compressive strength f_{cu} , was extrapolated from the failure data shown in Fig. 4.110 along the TC meridian, rather than mixing boundary conditions and using the unconfined compressive strength of 3 x 6 in. cylinders ($f'_c = 9200$ psi). With these values, f_t was calculated as -573 psi. Then using Eq. 5.50 as a guideline, $a \cdot p_a$ was estimated to be 581 psi, resulting in "a" = 39.52. Note that this is the upper limit on "a" suggested in Eq. 5.50, i.e., $a \cdot p_a = 1.014 \cdot \sigma_t$.

The data used to calibrate Lade's model for the CU-SFRC was the failure data obtained for the cubical specimens listed in TABLE 4.4 and the assumed uniaxial tensile strength. With the value of $a \cdot p_a$ found above, the resulting principal stresses and stress invariants (Eqs. 5.48, 5.44 and 5.45) for all the strength data were calculated incorporating the required parameter "a". The data was plotted as $(J_1^3/J_3 - 27)$ vs. (p_a/J_1) , and shown in Fig. 5.15. With "a" = 39.52, the two other parameters were determined from the figure as: $\eta_1 = 17030$ and $m = 0.807$. The best fit line produced an r^2 coefficient equal to 0.812. These three parameters now fully define the failure envelope for the CU-SFRC using Lade's failure criterion. From Eq. 5.43, the predicted failure envelope was calculated and compared

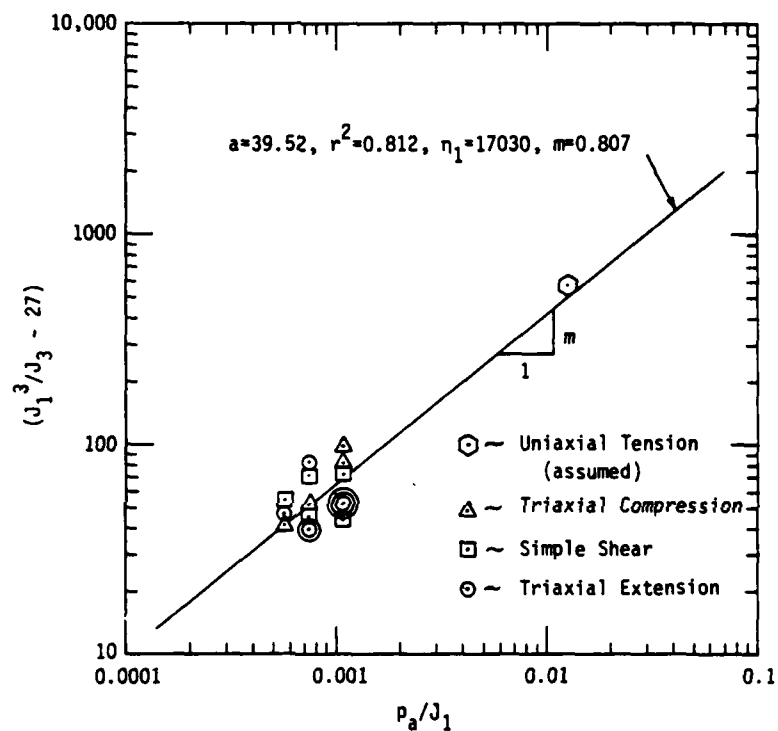


Fig. 5.15. Determination of Material Parameters Involved in Lade's Failure Criterion for the CU-SFRC.

with the experimentally determined strength values. These comparisons are shown in Figs. 5.16, 5.17 and 5.18 for the τ_0 - σ_0 , octahedral or deviatoric and triaxial or Rendulic planes respectively. Good correlation between predicted and experimental results is made.

The predicted failure envelope has the required shape, i.e., curved meridians in the τ_0 - σ_0 and triaxial planes and a triangular section with rounded corners in the octahedral plane. The meridians in the τ_0 - σ_0 plane (Fig. 5.16) show that shear strength predictions (τ_0) do not increase linearly for increasing high hydrostatic stress (σ_0) as did the Willam-Warnke predictions described in Section 5.2.1.1 and shown in Fig. 5.6. Rather, the meridians show, as they should, a tendency towards a horizontal for increasing σ_0 . For hydrostatic stresses $\sigma_0 \leq 8$ ksi, the predictions using Lade's model and Willam-Warnke's model are nearly the same for the TE and SS meridians. However, the TC meridians are quite different for $\sigma_0 \leq 4$ ksi. The TC meridian predicted using Lade's model is more smoothly curved to the apex than the Willam-Warnke prediction, where a sharp change in predicted strength occurs at $\sigma_0 \approx 2$ ksi. The reason the Willam-Warnke TC prediction does this is due to the way it was calibrated. In the triaxial plane (Fig. 5.18 for Lade and Fig. 5.8 for Willam-Warnke), one can again see that the TE meridians predicted using both models are nearly the same for $\sigma_0 \leq 8$ ksi. Beyond that, the Lade prediction continues to be curved as one would expect, whereas the Willam-Warnke prediction is linear. The TC meridians are different, as discussed above. Examination of Fig. 5.17 for Lade and 5.7 for Willam-Warnke shows that the

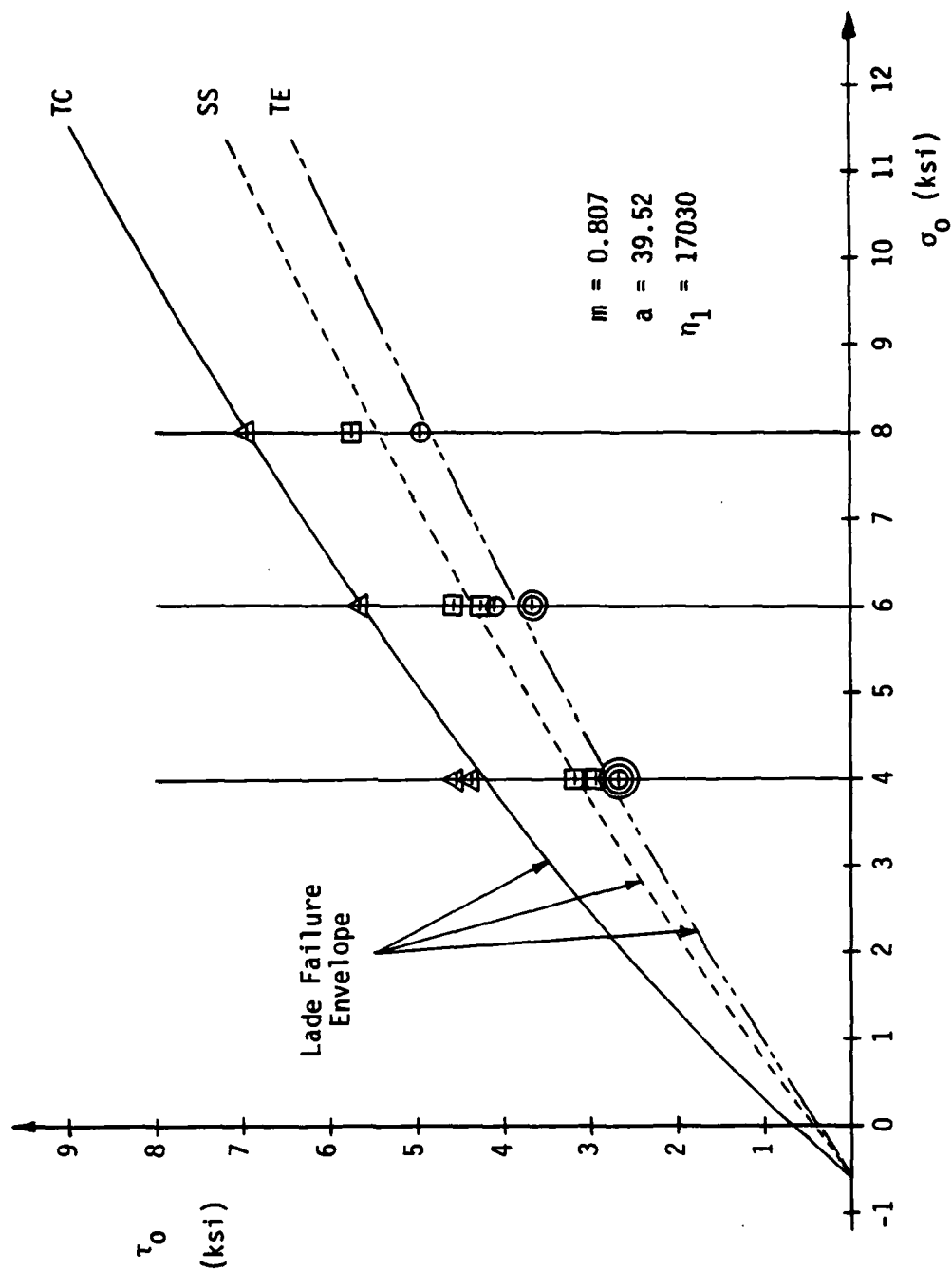


Fig. 5.16. Failure Data in τ_0 - σ_0 Plane with Lade Prediction.

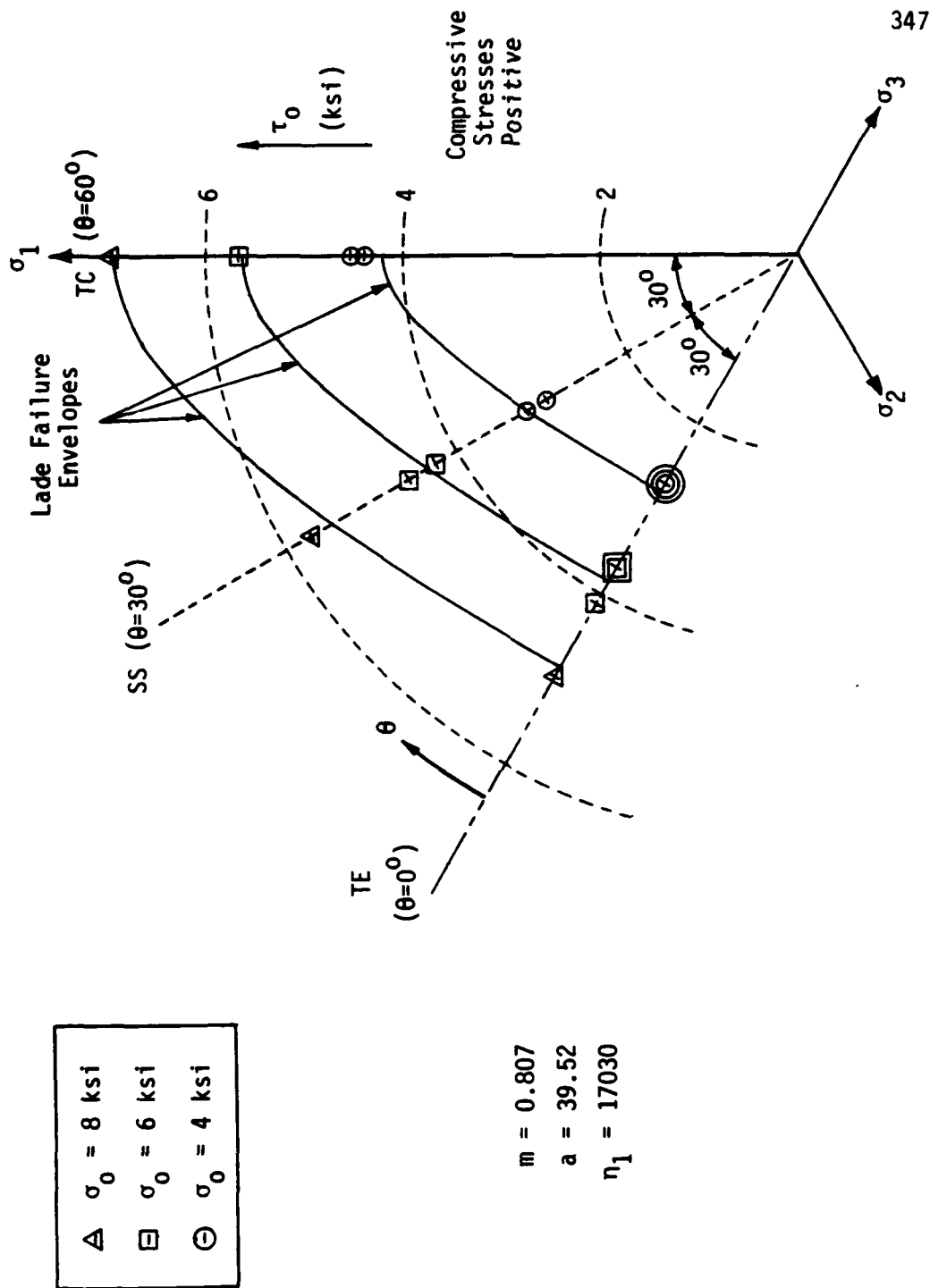


Fig. 5.17. Failure Data in Octahedral Planes with Lade Predictions.

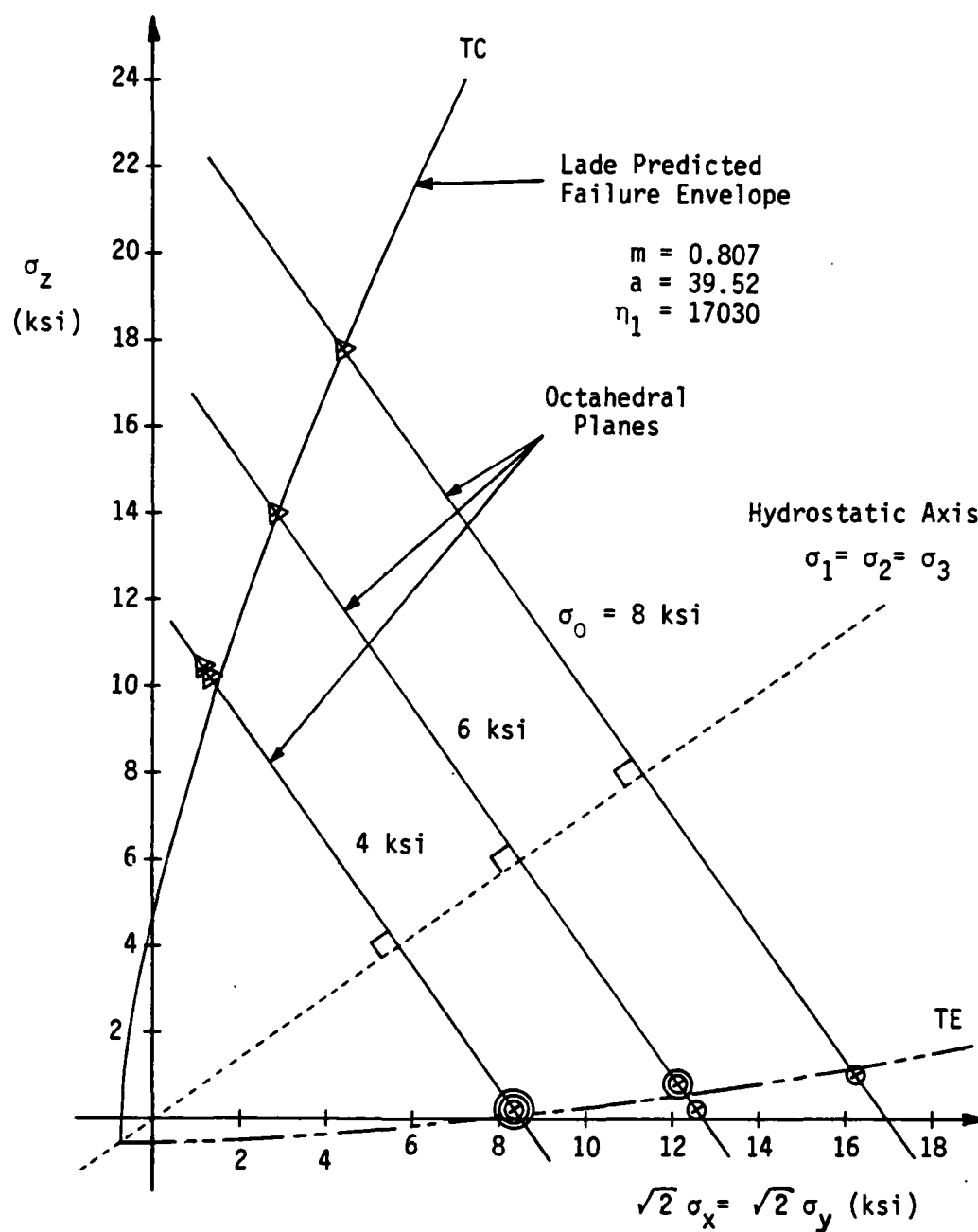


Fig. 5.18. Failure Data in Triaxial Plane With Lade Prediction.

predicted failure envelopes in the octahedral planes are nearly the same for both models.

Fig. 5.19 shows the biaxial failure envelope predicted using Lade's model. It is for reference only since no experimental biaxial strength data was obtained. When comparing with biaxial failure envelopes obtained for plain concrete (Figs. 1.6 and 1.10) and fiber reinforced mortar (Fig. 1.5), the shape of the predicted CU-SFRC failure envelope using Lade's model is more reasonable than that obtained using the Willam-Warnke model (Fig. 5.9). Again, these shapes are a result of how each model was calibrated.

Based on the Lade failure envelope, predicted values of the uniaxial compressive strength f_{cu} , equi-biaxial compressive strength f_{cb} and uniaxial tensile strength f_t can be calculated. These predicted strengths are:

$$\begin{aligned} f_{cu} &= 4750 \text{ psi} \\ f_{cb} &= 5650 \text{ psi} \\ f_t &= -573 \text{ psi} . \end{aligned} \tag{5.51}$$

Note that an assumed value of $f_{cu} = 7500$ psi was used to calculate f_t required for Lade's model. However, this value of f_{cu} was not in itself used as a strength value in calibrating the model simply to keep the number of assumed strengths to a minimum. The predicted uniaxial compressive strength seems somewhat low when examining the failure data shown in Fig. 4.110, from which the assumed value was taken. This difference could also be due to the regression analysis through the log-log failure data that was conducted in order to

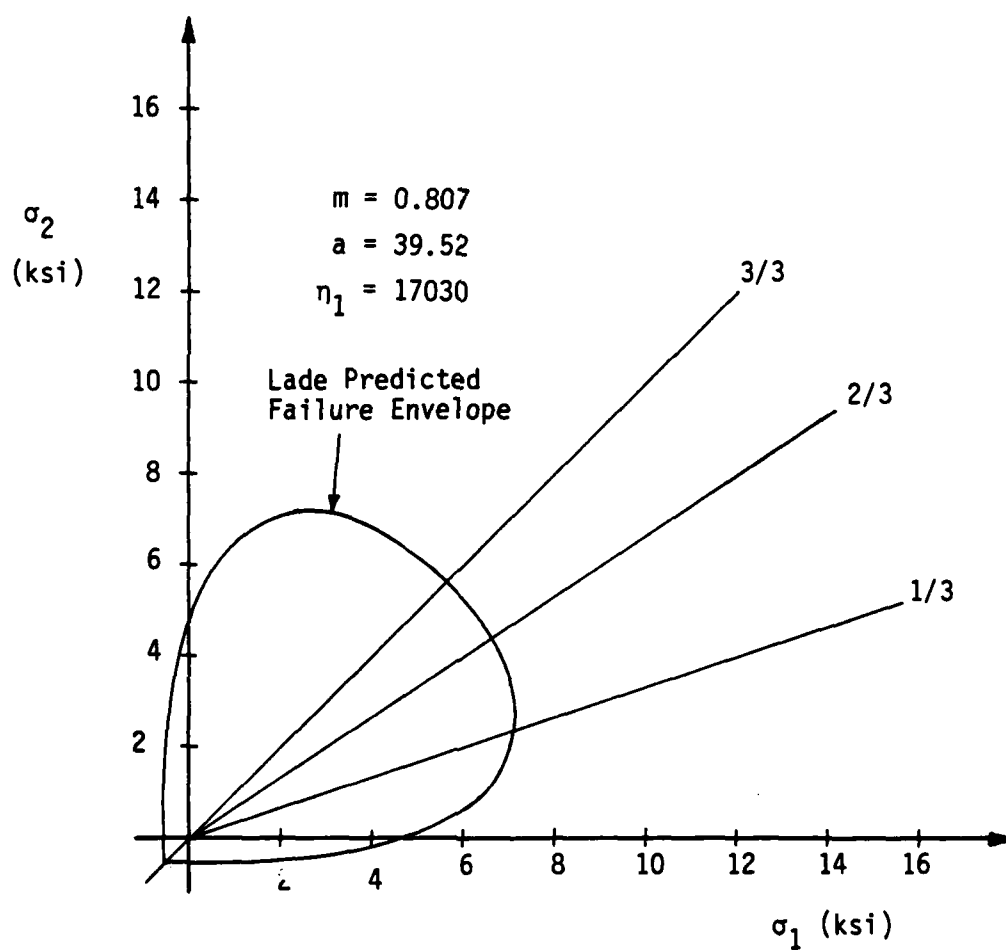


Fig. 5.19. Predicted Biaxial Failure Envelope Based on Lade Failure Criterion.

determine the necessary parameters. The predicted tensile strength does match the assumed value, as one would expect, because the best fit line nearly intersects this failure point as shown in Fig.

5.15. If one calculated the uniaxial tensile strength by doing a linear regression through the TE failure data shown in Fig. 4.110, a value of -643 psi would result. This is the same as that predicted using the Willam-Warnke failure criterion discussed in Section 5.2.1.1 because a linear regression was performed through the TC and TE failure data to calibrate that model for the CU-SFRC. The two predicted values of tensile strength are quite similar. In fact, this value of tensile strength, as well as others calculated from Eq. 5.49 using different f_{cu} 's, were used in estimating the "a" parameter to calibrate Lade's model, in conjunction with the failure data of the cubical specimens. The value of $f_t = -573$ psi (based on Eq. 5.49 with $f_{cu} = 7500$ psi) gave the highest r^2 value from regression analyses. Therefore this was the tensile strength used in calibrating Lade's model as shown in Fig. 5.15 in order to predict the strengths shown in Figs. 5.16-5.19.

In the next section, some parametric studies of the Willam-Warnke and Lade failure criteria are presented to show how the models compare when using identical input data to calibrate them and their effectiveness in predicting strengths by comparing them with the CU-SFRC experimental results.

In conclusion, the Lade three-parameter failure criterion is a very simple model to use and is seen to predict the strength of the CU-SFRC very well. It is interesting to note that this model was

originally developed for soils and with a slight improvement or modification is seen to also work well for concrete.

5.2.3 Comparison of the Willam-Warnke and Lade Failure Criteria Using Various Input Strength Data

TABLE 5.1 summarizes the contents of this section, whose purpose is fourfold:

- 1) To recap the discussions in Sections 5.2.1.1 and 5.2.2.1 regarding the Willam-Warnke and Lade failure criteria: Cases I, IV.
- 2) To observe the differences between the Willam-Warnke and Lade predicted failure envelopes when the same strength data is used to calibrate the respective formulations: Cases II, III, VI, VII.
- 3) To show the effect of calibrating each failure criteria with the same strength data, obtained from tests where specimen type and boundary conditions are different: Cases III, VII.
- 4) To show the effect of calibrating the Lade failure criterion with the minimum number of required input strengths, obtained from conventional cylinder tests, and the predicted failure envelope that results: Case V.

TABLE 5.1 is self-explanatory, listing the failure criteria, the strength data used to calibrate the respective failure criteria, the resulting strength parameters calculated from the theory described in previous sections and the figure numbers showing the respective predicted failure envelopes along with the CU-SFRC observed strengths. The results of the different cases are discussed below.

TABLE 5.1
SUMMARY OF STRENGTHS USED FOR CALIBRATING WILLIAM-WARNKE AND LADE
FAILURE CRITERIA AND PARAMETERS OBTAINED FOR PARAMETRIC STUDY.
(Compression Positive)

Case	Failure Criterion	Inputted Strength Data	Calculated Strength Parameters	Figure Nos. of Predicted Strength Envelopes
I	William-Warnke	1) Linear Regression Through all Cubical Strengths Listed in TABLE 4.4	$A_0 = 424 \text{ psi}$ $A_1 = 0.566$ $A_2 = 0$ $B_0 = 1980 \text{ psi}$ $B_1 = 0.617$ $B_2 = 0$	5.6 $\tau_0 - \sigma_0$ Octahedral 5.7 Octahedral 5.8 Triaxial 5.9 Biaxial
II	William-Warnke	1) $f_{cu} = 7500 \text{ psi}$ (Extrapolated from Fig. 4.110) 2) $f_t = -573 \text{ psi}$ (Using Eq. 5.49) 3) $f_{cb} = 1.3 f_{cu} = 9750 \text{ psi}$ (Assumed) 4) $\tau_0 = 4949.74 \text{ psi}$ ($\theta=0^\circ, \sigma_0=8000 \text{ psi}$) FIA2 (TABLE 4.4) 5) $\tau_0 = 6929.64 \text{ psi}$ ($\theta=60^\circ, \sigma_0=8000 \text{ psi}$) FID6 (TABLE 4.4)	$a_0 = 0.0608$ $a_1 = 0.963$ $a_2 = -0.376$ $b_0 = 0.0841$ $b_1 = 1.332$ $b_2 = -0.511$	5.20 $\tau_0 - \sigma_0$ Octahedral 5.21 Octahedral 5.22 Triaxial 5.23 Biaxial

TABLE 5.1 (Continued)

SUMMARY OF STRENGTHS USED FOR CALIBRATING WILLAM-WARNKE AND LADE FAILURE CRITERIA AND PARAMETERS OBTAINED FOR PARAMETRIC STUDY.

Case	Failure Criterion	Inputted Strength Data	Calculated Strength Parameters	Figure Nos. of Predicted Strength Envelope
III	Willam-Warnke	1) $f_{cu} = f'_c = 9200$ psi (Unconfined Compression of 3x6 in. cyls.) 2) $f_t = T = -953$ psi (Split cyl.) 3) $f_{cb} = 1.3 f_{cu} = 11960$ psi (Assumed) 4) $\tau_o = 4949.74$ psi ($\theta=0^\circ, \sigma_o=8000$ psi) FIA2 (TABLE 4.4) 5) $\tau_o = 6929.64$ psi ($\theta=60^\circ, \sigma_o=8000$ psi) FID6 (TABLE 4.4)	$a_0 = 0.945$ $a_1 = 24.94$ $a_2 = -29.21$ $b_0 = 0.0564$ $b_1 = 1.521$ $b_2 = -0.828$	5.24 $\tau_o - \sigma_o$ Octahedral 5.25 Octahedral 5.26 Triaxial No Biaxial
IV	Lade	1) All Cubical Strengths (TABLE 4.4) 2) $f_t = -573$ psi (Eq. 5.49 with $f_{cu} = 7500$ psi)	$m = 0.807$ $a = 39.52$ $\eta_1 = 17030$	5.16 $\tau_o - \sigma_o$ Octahedral 5.17 Octahedral 5.18 Triaxial 5.19 Biaxial

TABLE 5.1 (Continued)

SUMMARY OF STRENGTHS USED FOR CALIBRATING WILLAM-WARKE AND LADE FAILURE CRITERIA AND PARAMETERS OBTAINED FOR PARAMETRIC STUDY.

Case	Failure Criterion	Inputted Strength Data	Calculated Strength Parameters	Figure Nos. of Predicted Strengths Envelopes
V	Lade	1) $f_{cu} = f'_c = 9200$ psi (Unconfined Compression of 3x6 in. cyls.) 2) $f_t = T = -953$ psi (Split cyl.)	$m = 0.666$ $a = 65.78$ $\eta_1 = 13910$	5.27 $\tau_o - \sigma_o$ Octahedral 5.28 $\tau_o - \sigma_o$ Octahedral 5.29 $\tau_o - \sigma_o$ Triaxial 5.30 $\tau_o - \sigma_o$ Biaxial
VI	Lade (to Compare with II. Same Input Data)	1) $f_{cu} = 7500$ psi (Extrapolated from Fig. 4.110) 2) $f_t = -573$ psi (Using Eq. 5.49) 3) $f_{cb} = 1.3 f_{cu}$ (Assumed) = 9750 psi 4) F1A2 (TABLE 4.4) 5) F1D6 (TABLE 4.4)	$m = 0.760$ $a = 39.52$ $\eta_1 = 19710$	5.31 $\tau_o - \sigma_o$ Octahedral 5.32 $\tau_o - \sigma_o$ Octahedral 5.33 $\tau_o - \sigma_o$ Triaxial 5.34 $\tau_o - \sigma_o$ Biaxial

TABLE 5.1 (Continued)

SUMMARY OF STRENGTHS USED FOR CALIBRATING WILLAM-WARNKE AND LADE
FAILURE CRITERIA AND PARAMETERS OBTAINED FOR PARAMETRIC STUDY.

Case	Failure Criterion	Inputted Strength Data	Calculated Strength Parameters	Figure Nos. of Predicted Strengths Envelopes
VII	Lade (to Compare with III. Same Input Data)	1) $f_{cu} = f'_c = 9200$ psi (Unconfined Compression of 3x6 in. cyls.) 2) $f_t = T = -953$ psi (Split cyl.) 3) $f_{cb} = 1.3 f_{cu} = 11960$ psi (Assumed) 4) F1A2 (TABLE 4.4) 5) F1D6 (TABLE 4.4)	$m = 0.919$ $a = 65.78$ $\eta_1 = 53520$	5.35 $\tau_0 - \sigma_0$ 5.36 Octahedral 5.37 Triaxial 5.38 Biaxial

Case I

The Willam-Warnke failure criterion calibrated as done for the CU-SFRC by doing a linear regression through the TC and TE cubical strength data to find the model parameters. The constants A_0 through B_2 are defined in Eqs. 5.35 and 5.36. A complete discussion of results is given in Section 5.2.1.1.

Case II

The Willam-Warnke criterion, calibrated as the authors suggest, described in Section 5.2.1. The six model parameters are defined in Eqs. 5.15 and 5.16 and calculated from Eqs. 5.22-5.29. The unconfined compressive strength f_{cu} was extrapolated from the strength data shown in Fig. 4.110. The tensile strength f_t was calculated from Eq. 5.49 (Lade's equation for tensile strength). This value is seen to be a reasonable estimate when examining Fig. 4.110. The biaxial strength f_{cb} was assumed, based on a range given by Willam-Warnke (134). The two required shear strength values (τ_0) at high confining pressure (σ_0) were from the CU-SFRC experimental results.

The resulting τ_0 - σ_0 failure envelope shown in Fig. 5.20 predicts decreasing shear strengths for increasing confining pressure beyond σ_0 of 9 to 10 ksi. This is a phenomenon that should not occur and is a drawback inherent in the Willam-Warnke formulation. That is, the meridian equations employed by their model, being second-order functions of σ_0 , will at some point intersect the hydrostatic axis ($\tau_0=0$).

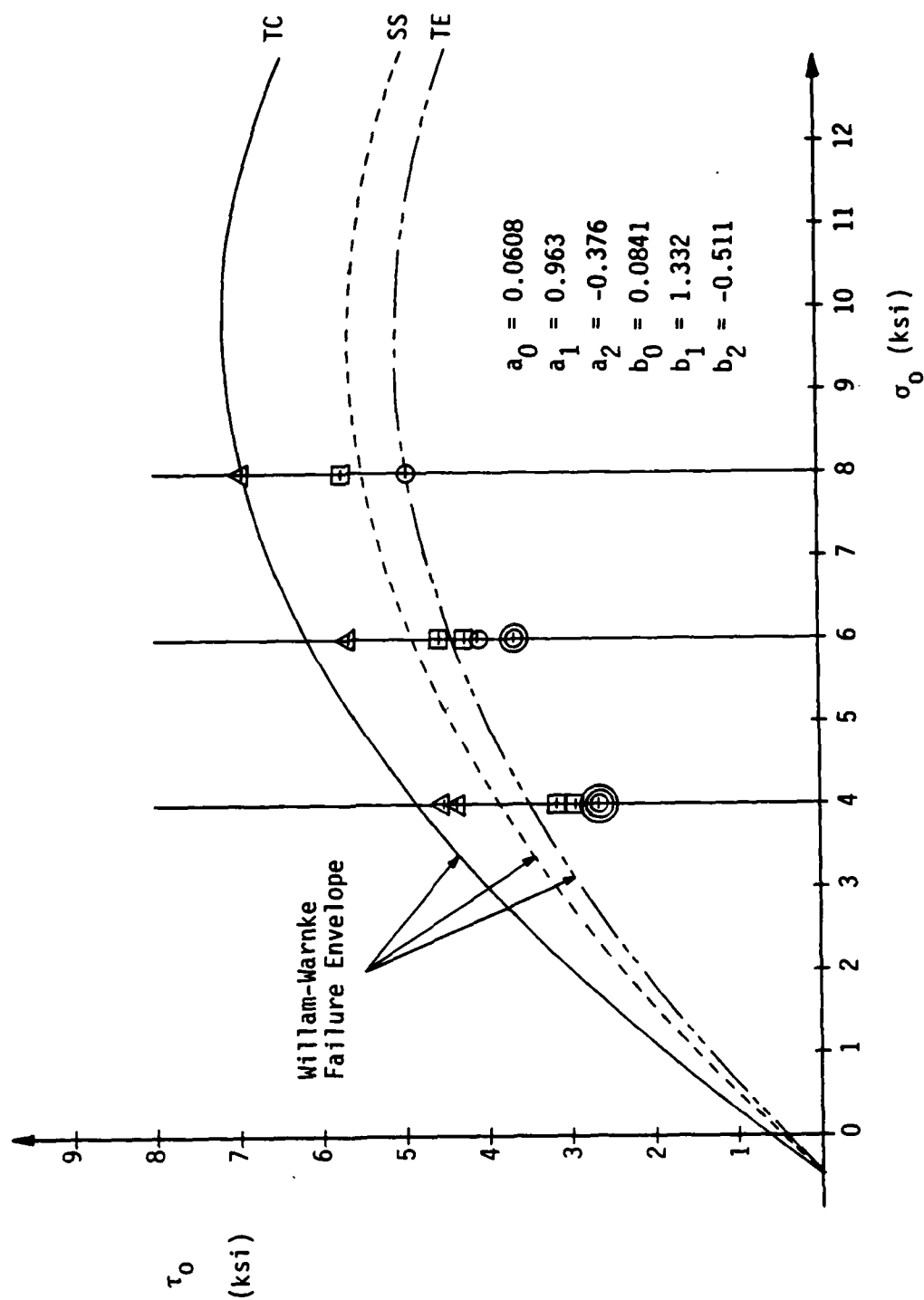


Fig. 5.20. Failure Data in τ_0 - σ_0 Plane with Willam-Warnke Prediction.

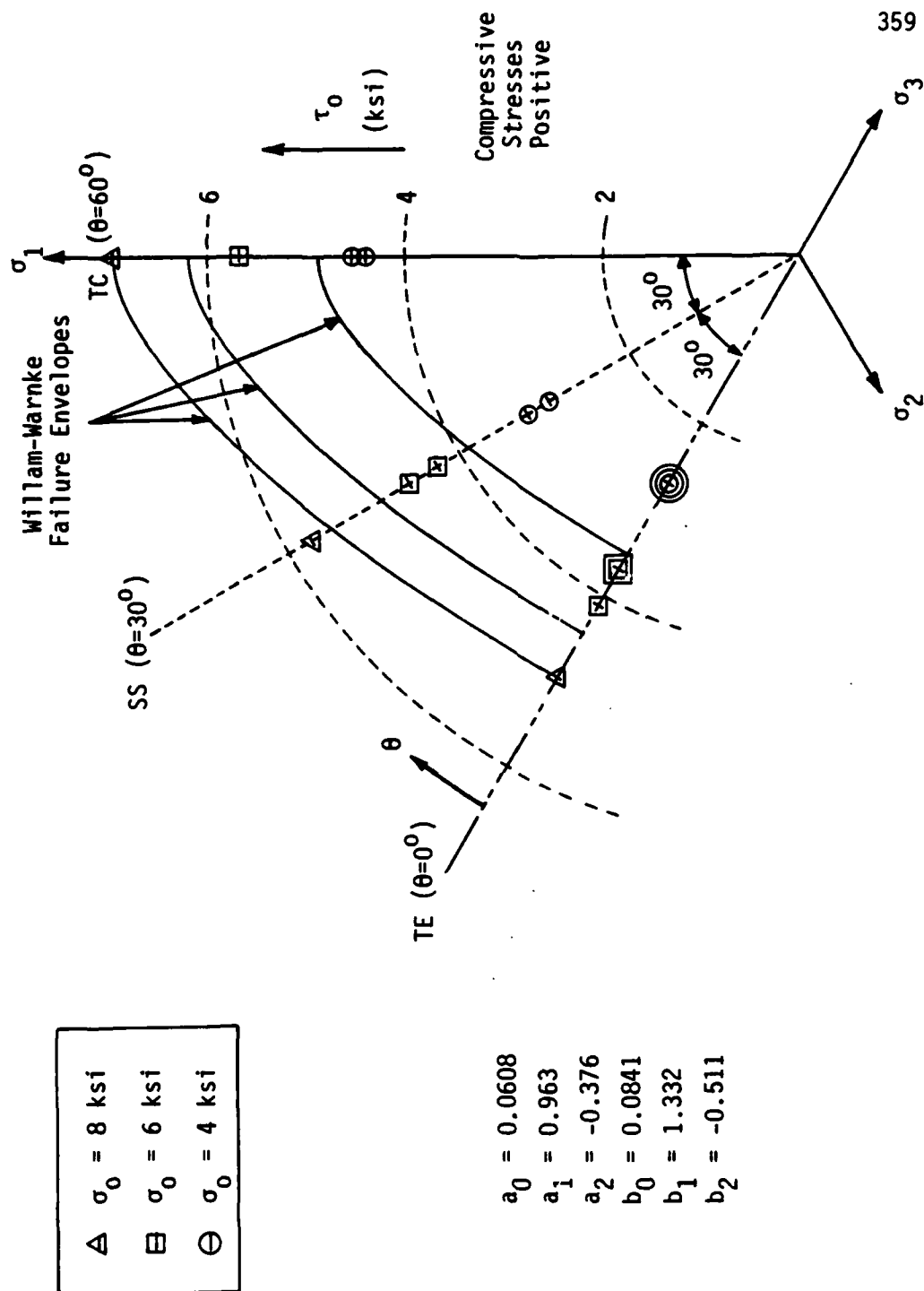


Fig. 5.21. Failure Data in Octahedral Planes with Willam-Warneke Predictions.

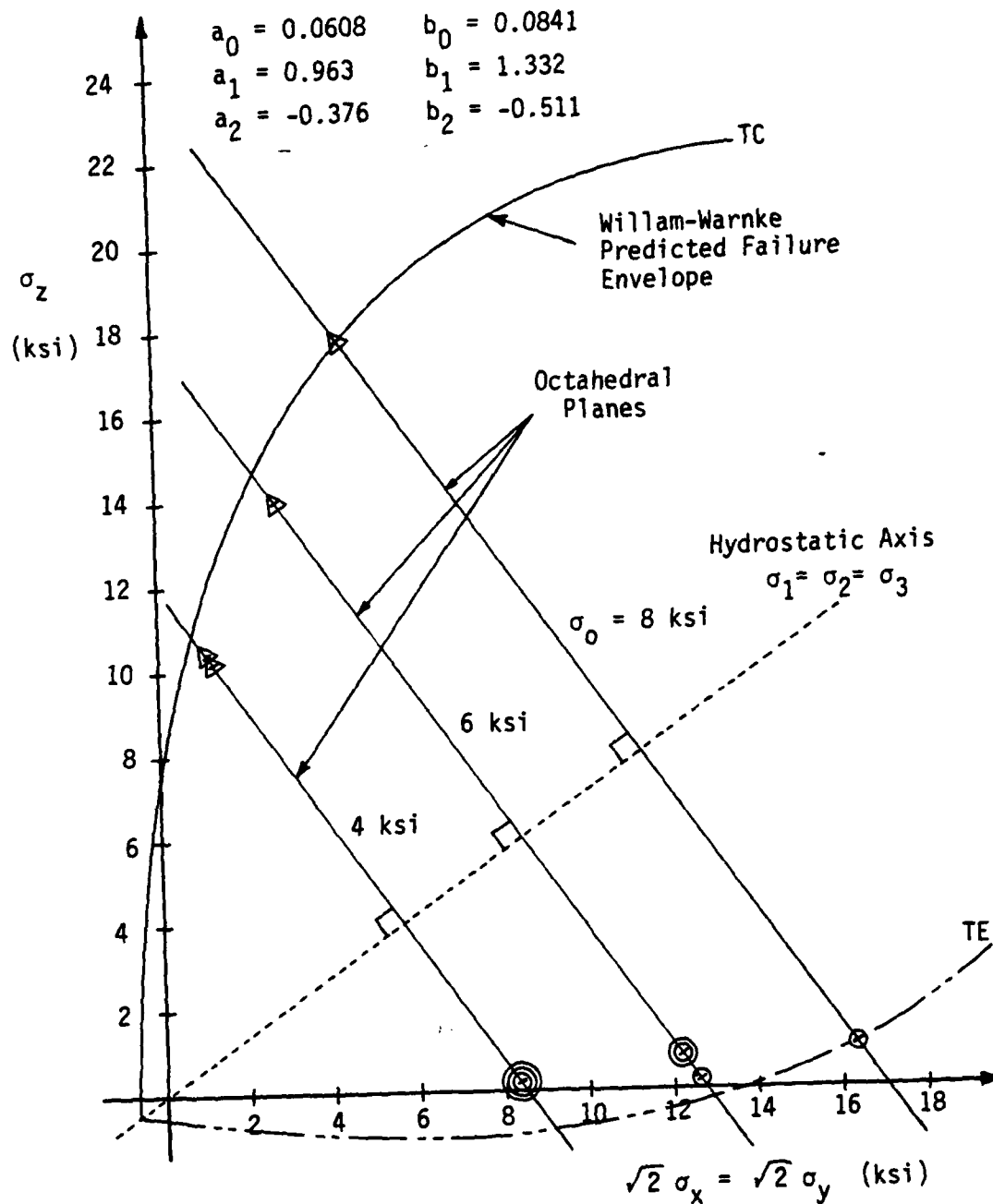


Fig. 5.22. Failure Data in Triaxial Plane with Willam-Warnke Prediction.

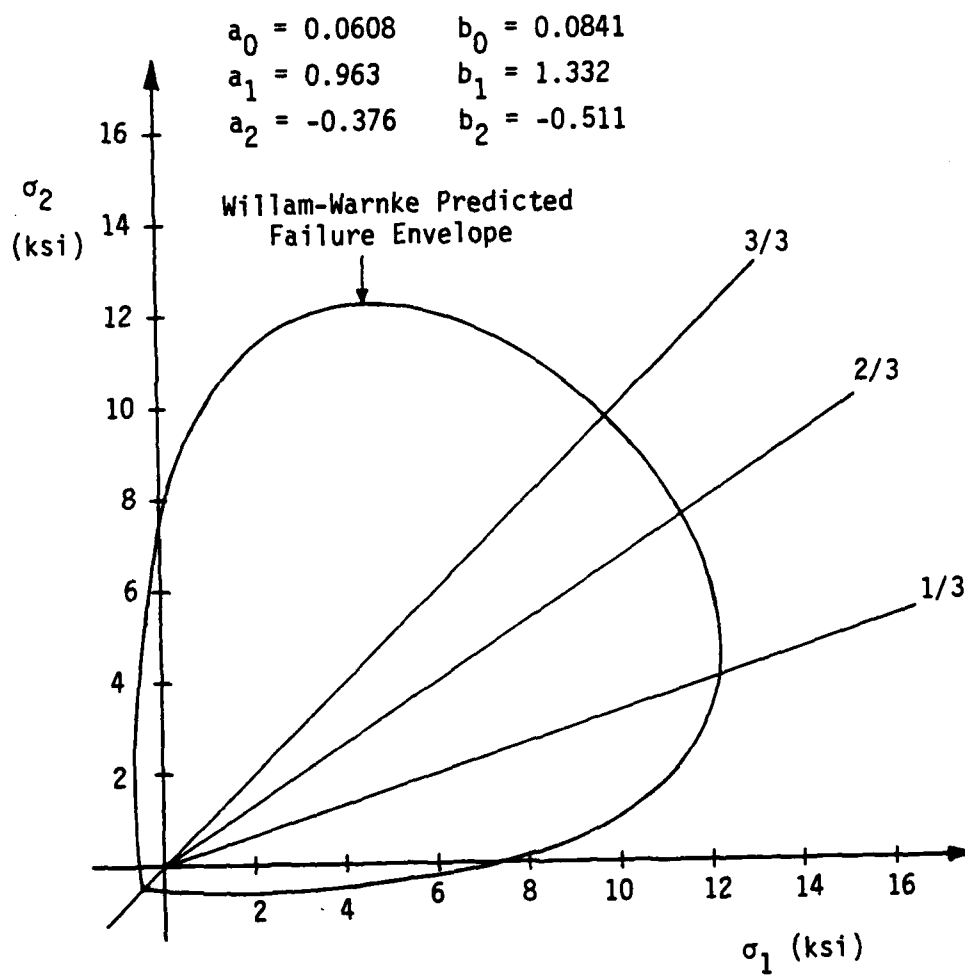


Fig. 5.23. Predicted Biaxial Failure Envelope
Based on Willam-Warnke Failure Criterion.

Case III

The Willam-Warnke criterion also calibrated as the authors suggest. However, the input strength data came from tests in which the boundary conditions and specimen types varied. The compressive and tensile strengths came from 3x6 in. cylinder tests with rigid boundary conditions. But the two shear strengths (τ_0) were from the CU-SFRC cubical tests in which fluid cushion boundary conditions were employed. The biaxial strength f_{cb} was again assumed. The model parameters were calculated from Eqs. 5.22-5.29.

The point is to show what happens to this failure criterion when mixed boundary condition and specimen type test results are used to calibrate it. The resulting shape of the predicted failure envelopes shown in Figs. 5.24-5.26 are incorrect. Notice the failure meridians in Fig. 5.24 are in a reverse order, contrary to what they should be, because of the large values of f_{cu} and f_{cb} used. The TC meridian has the correct shape; however, it overestimates the strengths compared with experimental results. Beyond $\sigma_0 \approx 8$ ksi, all the meridians predict negative octahedral shear strengths which is impossible! Notice also that in the octahedral planes, Fig. 5.25, the failure envelope for $\sigma_0 = 8$ ksi is fine but those for $\sigma_0 = 4$ and 6 ksi are not. Also, Fig. 5.26 shows the erroneous TE meridian and what happens to the failure envelope for values of σ_0 at or near 8 ksi. All these spurious results are an outcome of calibrating this formulation with strength data obtained from tests in which the specimen type and boundary conditions vary considerably. The point is that for any model, the

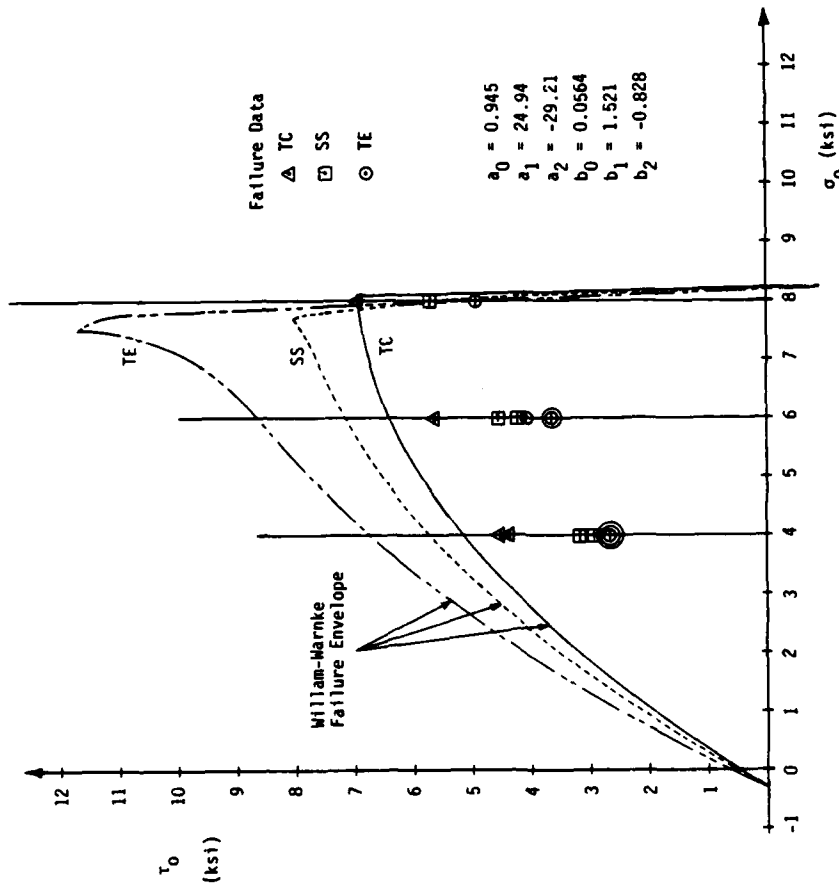


Fig. 5.24. Failure Data in τ_0 - σ_0 Plane with Willam-Warnke Prediction.

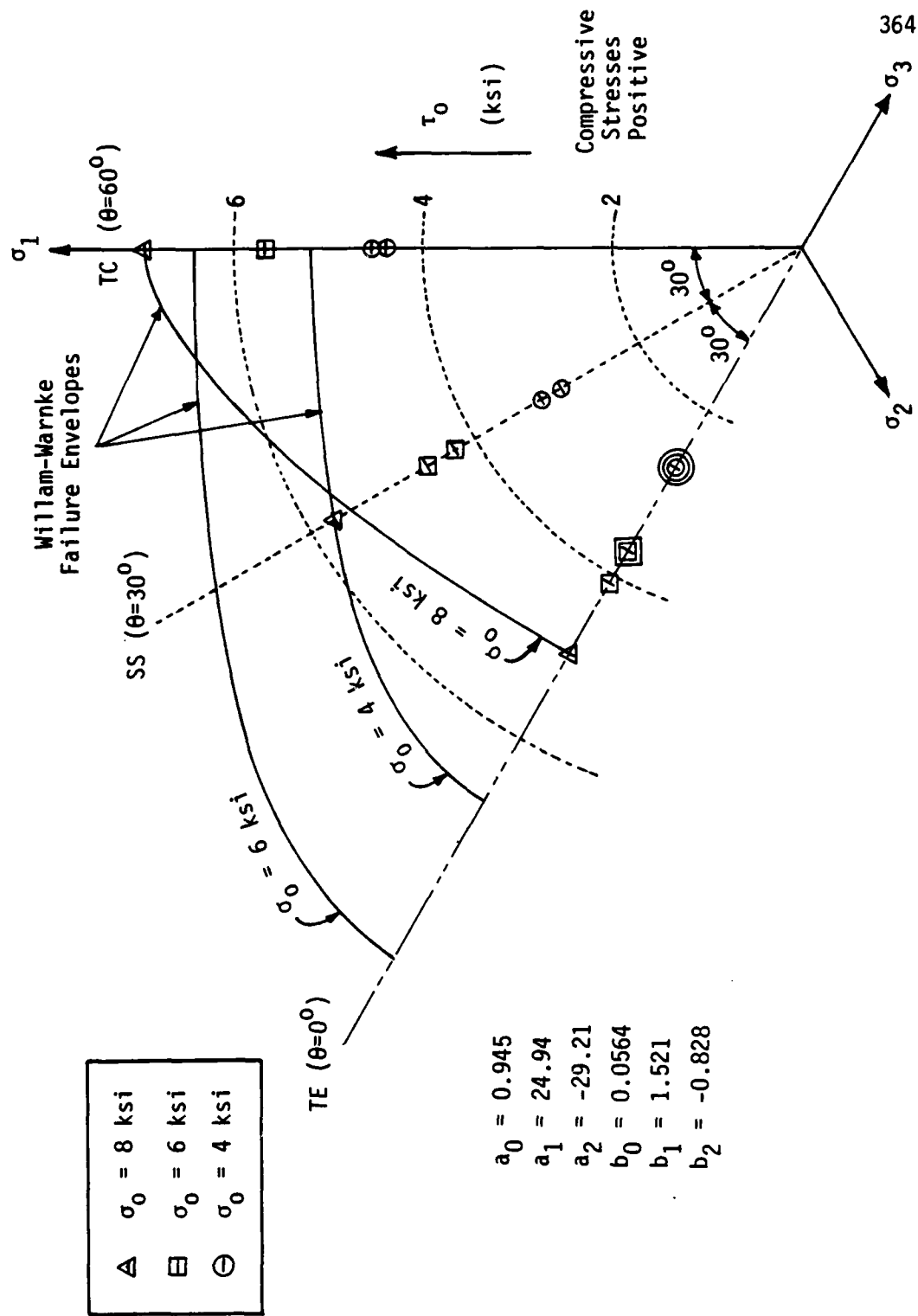


Fig. 5.25. Failure Data in Octahedral Planes with Willam-Warnke Predictions.

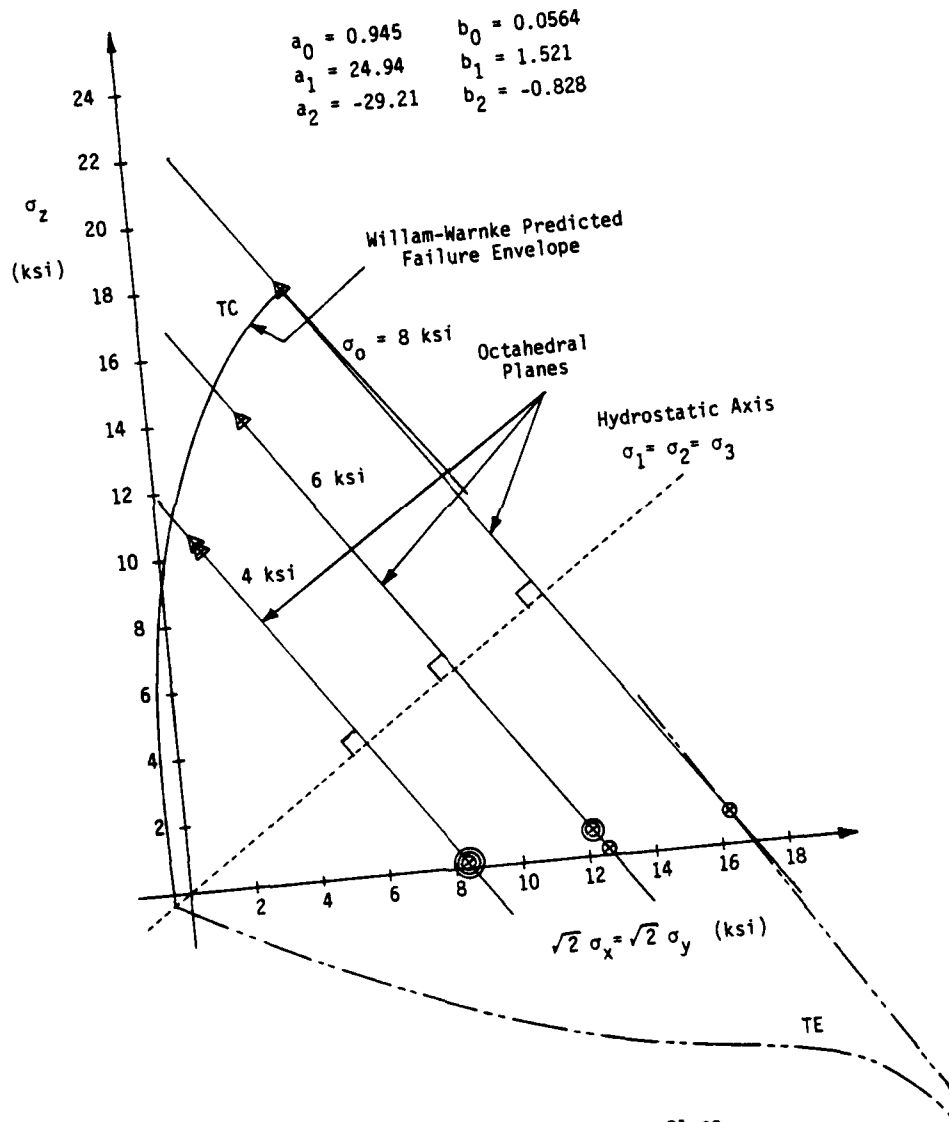


Fig. 5.26. Failure Data in Triaxial Plane with Willam-Warnke Prediction.

input data should be obtained from tests where these varying conditions do not occur, or gross inaccuracies may result.

Case IV

Lade's failure criterion calibrated as the author suggests, for the CU-SFRC. The tensile strength f_t was the only assumption made. A complete discussion of results is given in Section 5.2.2.1.

Case V

Lade's criterion calibrated with only two strength values which represent the minimum required. Both are from 3 x 6 in. cylinder tests where rigid boundary conditions existed: unconfined compression and split cylinder. The point of the predicted results is to show that rigid boundary condition tests cannot be used to calibrate this model (or any other for that matter) and be accurate in trying to predict the strengths of specimens subjected to fluid cushion boundary conditions. The shape of the predicted failure envelope is acceptable but the strengths are considerably overestimated.

Case VI

Lade's criterion calibrated as suggested, with the same input strength data as was used to calibrate the Willam-Warnke failure criterion for Case II. The point is to compare the predicted strengths using different failure criteria, each calibrated with identical input data. There exists a definite difference between the two. The strengths predicted by Lade are unconservative but the meridians shown in Fig. 5.31 do not have the same characteristics as do those shown in Fig. 5.20 for the Willam-Warnke criterion. That

AD-A114 168

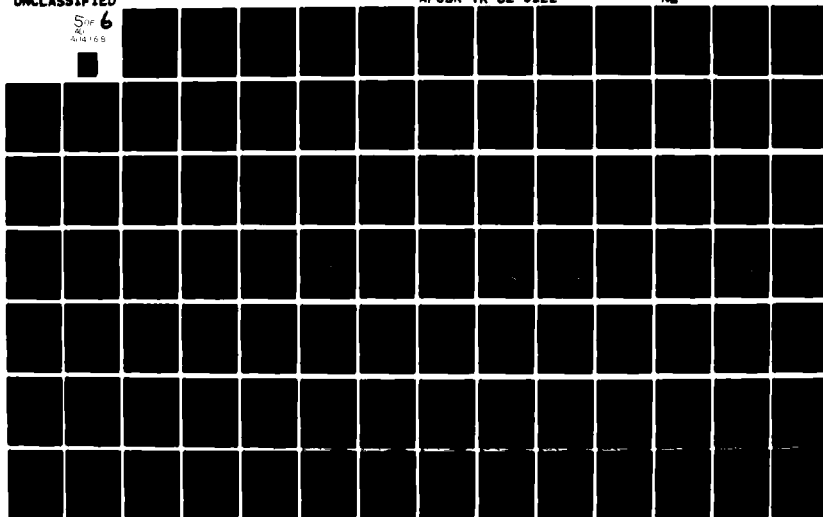
COLORADO UNIV AT BOULDER DEPT OF CIVIL ENVIRONMENTAL --ETC F/6 20/11
CONSTITUTIVE RELATIONS OF RANDOMLY ORIENTED STEEL FIBER REINFOR--ETC(U)
DEC 81 D E EGGING, H KO AFOSR-79-0045

UNCLASSIFIED

AFOSR-TR-82-0122

NL

5 of 6
AD-A114 168



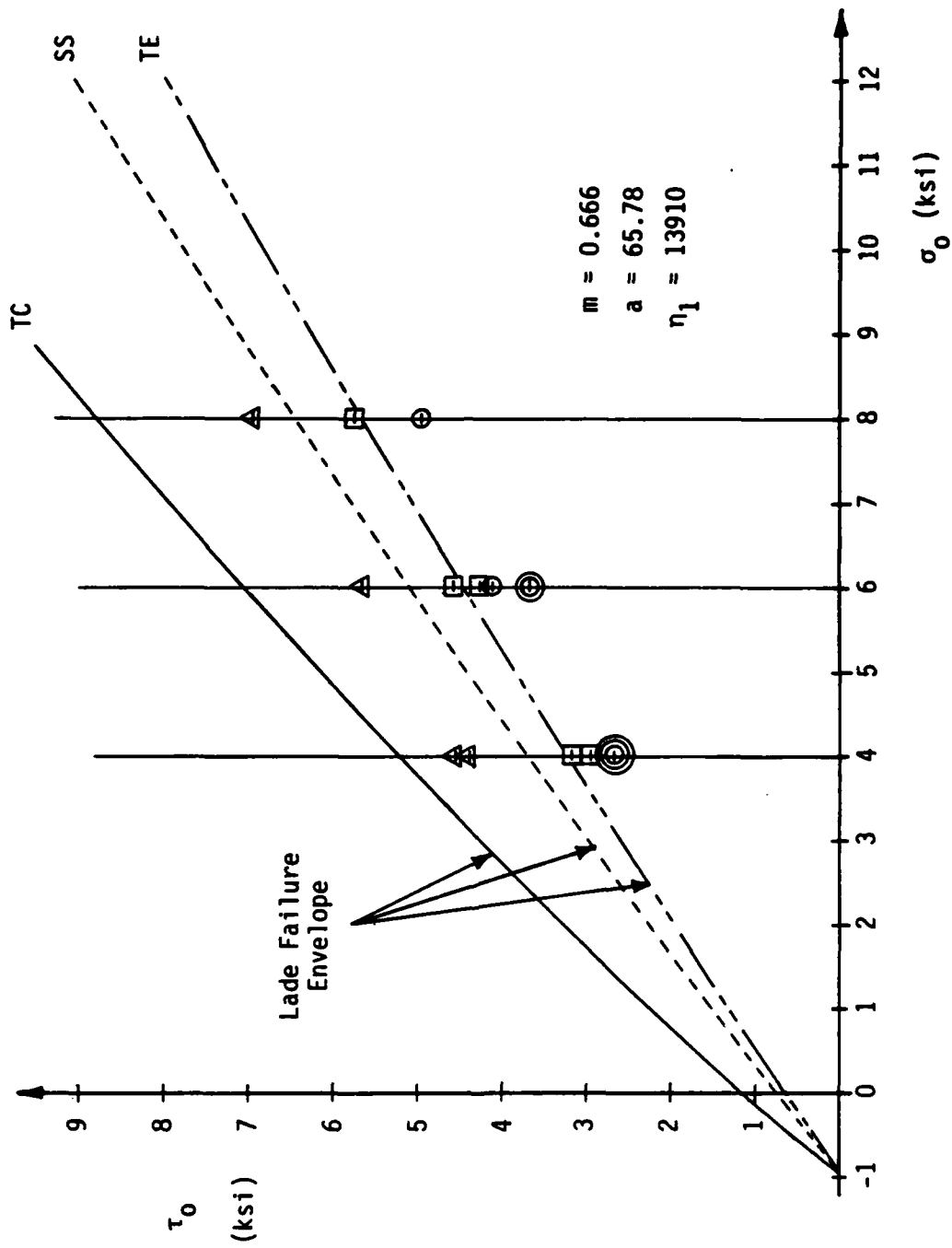


Fig. 5.27. Failure Data in $\tau_0 - \sigma_0$ Plane with Lade Prediction.

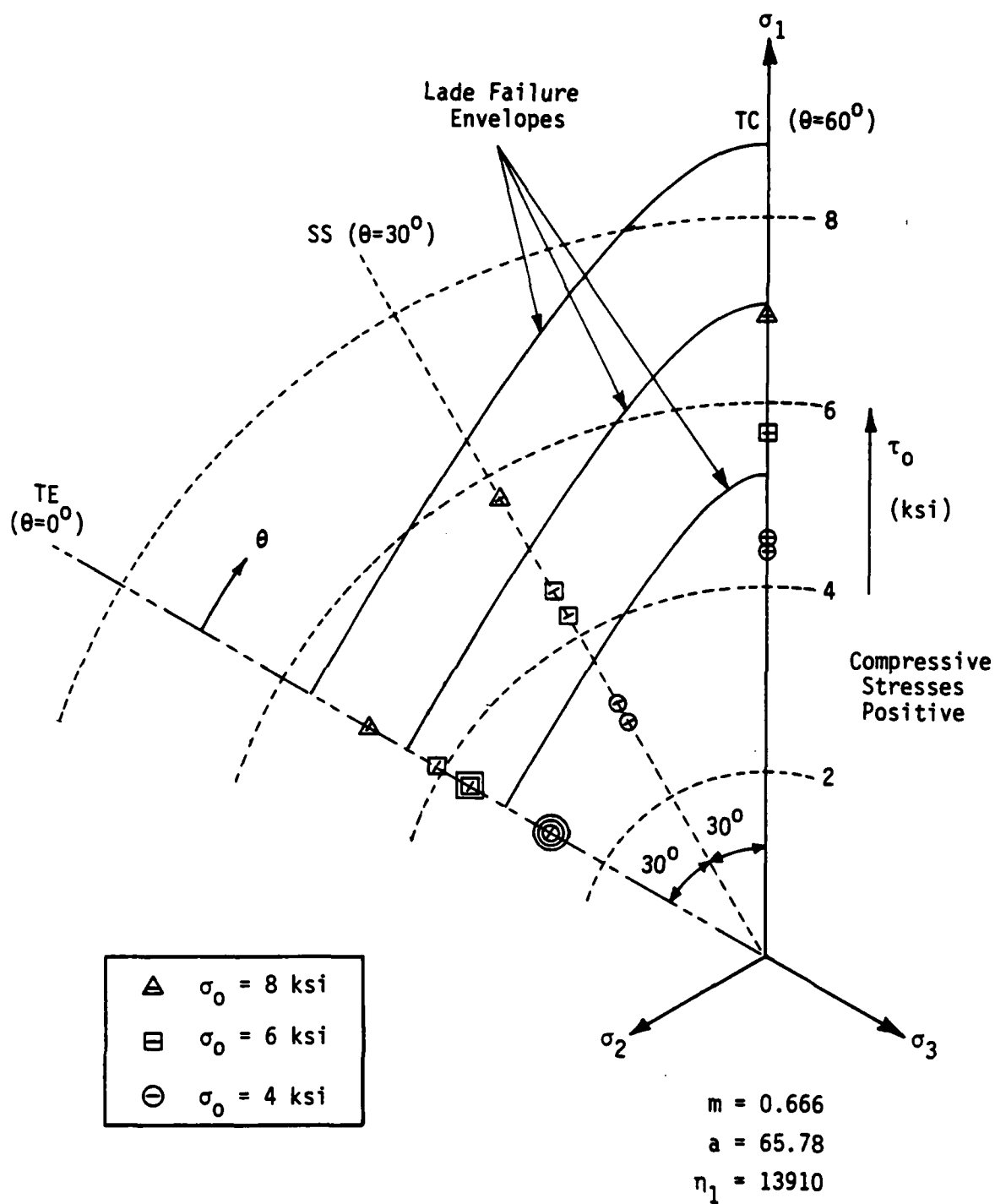


Fig. 5.28. Failure Data in Octahedral Planes with Lade Predictions.

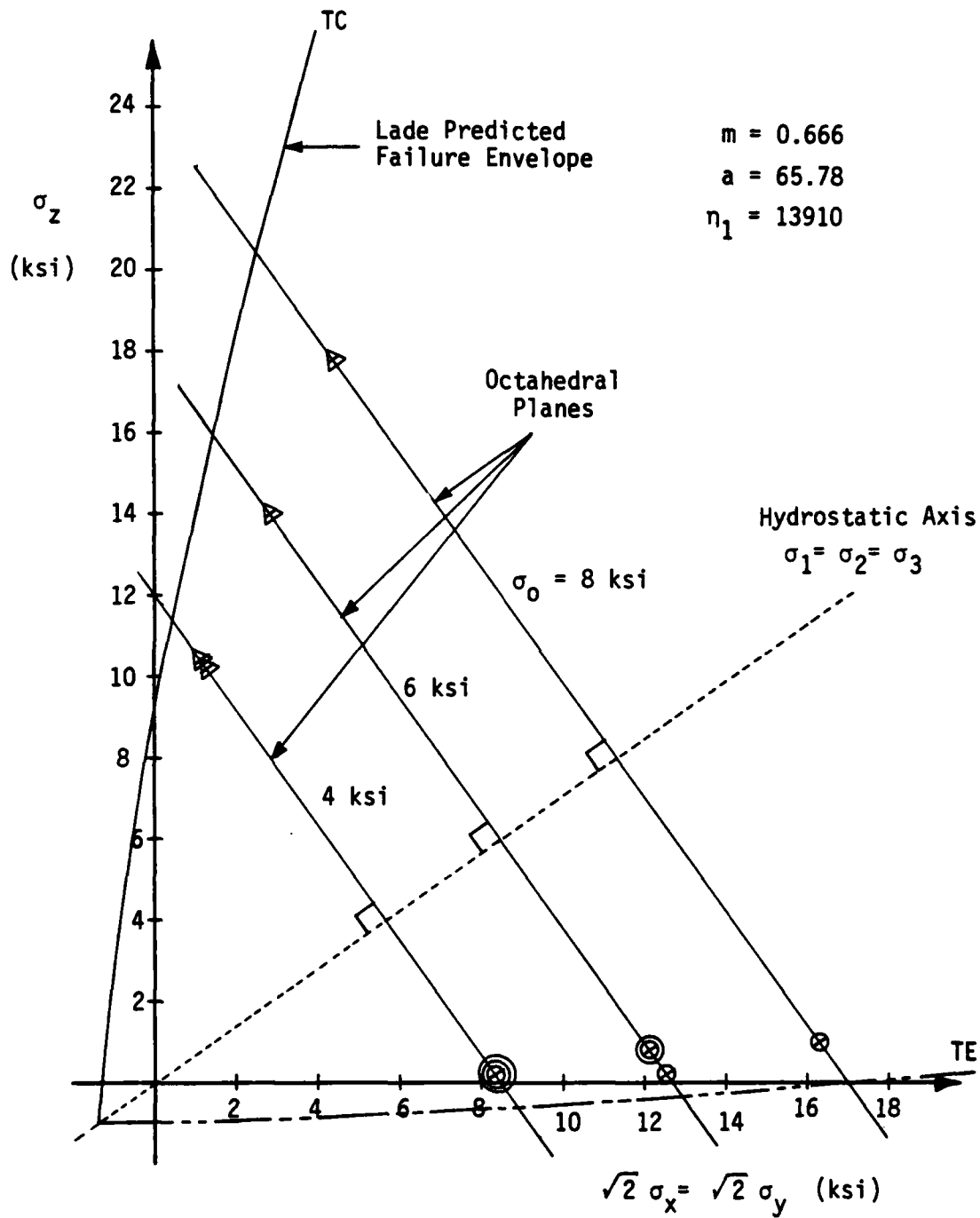


Fig. 5.29. Failure Data in Triaxial Plane with Lade Prediction.

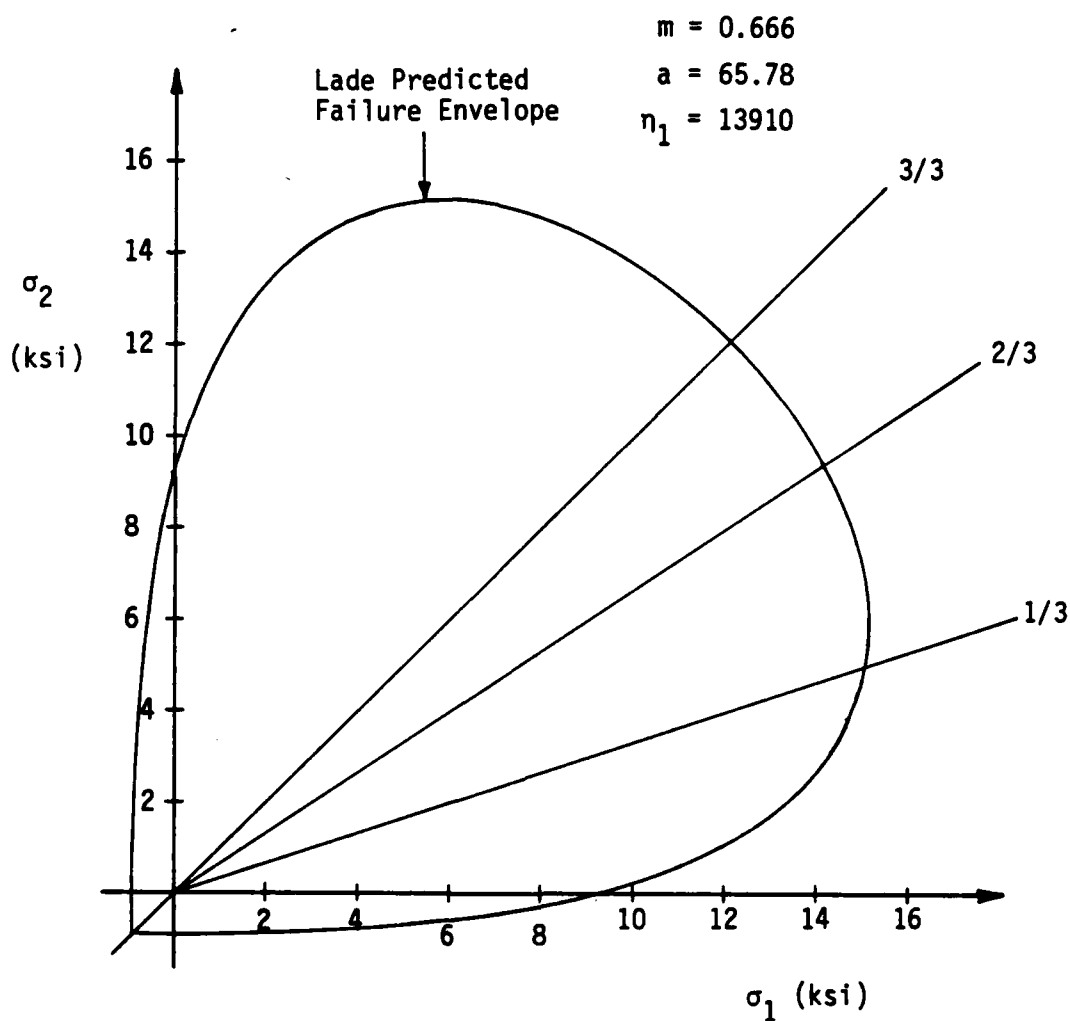


Fig. 5.30. Predicted Biaxial Failure Envelope
Based on Lade Failure Criterion.

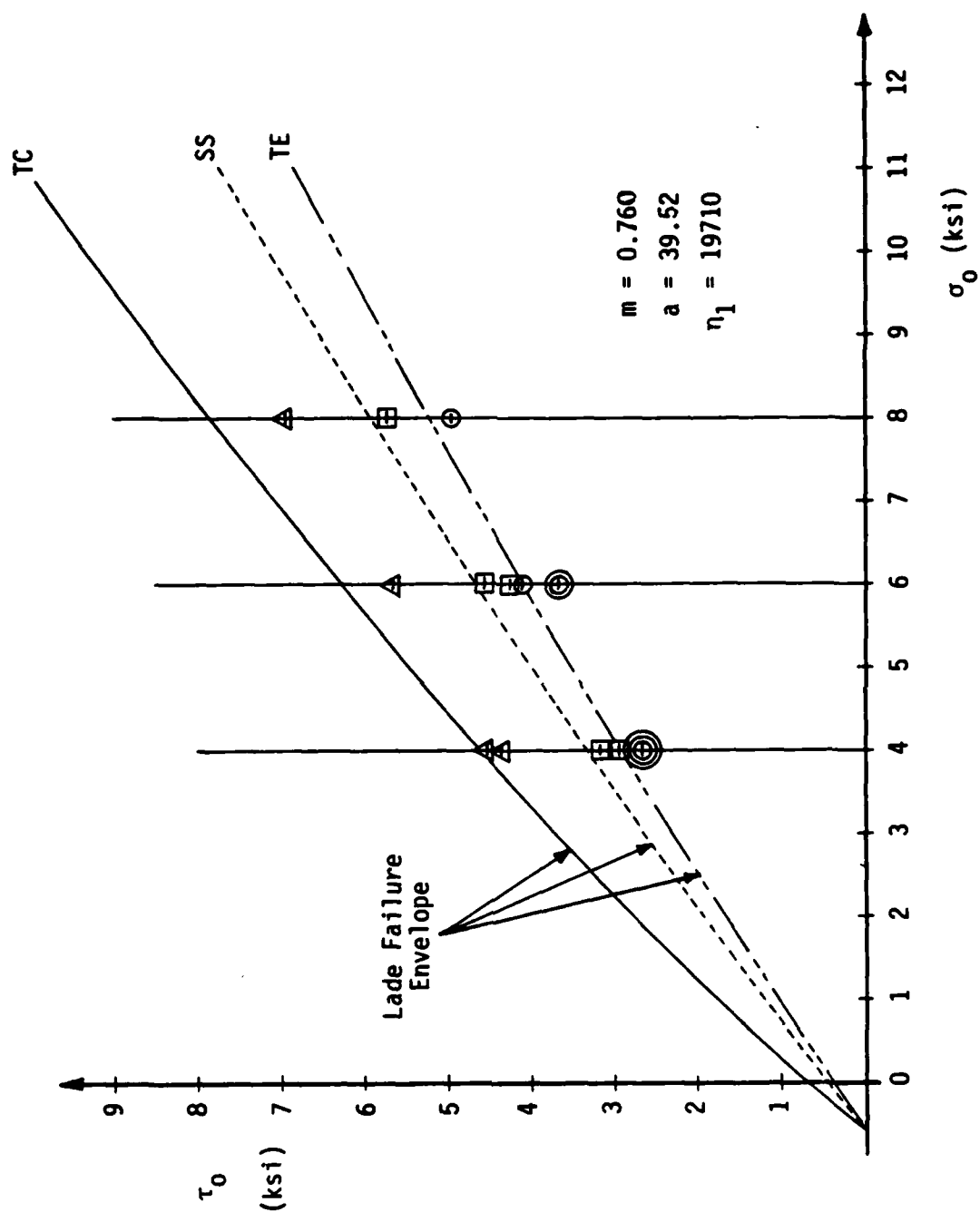


Fig. 5.31. Failure Data in τ_0 - σ_0 Plane with Lade Prediction.

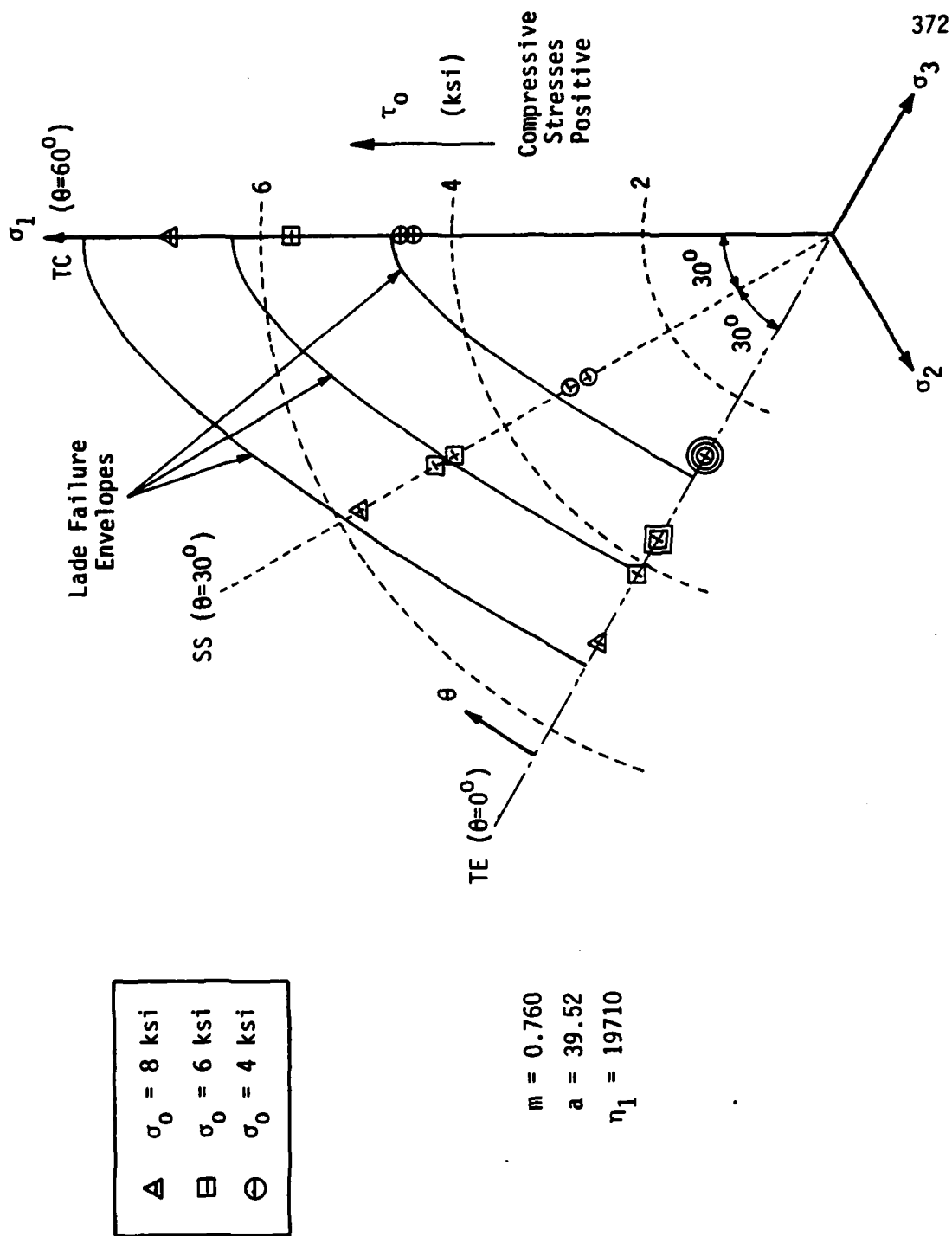


Fig. 5.32. Failure Data in Octahedral Planes with Lade Predictions.

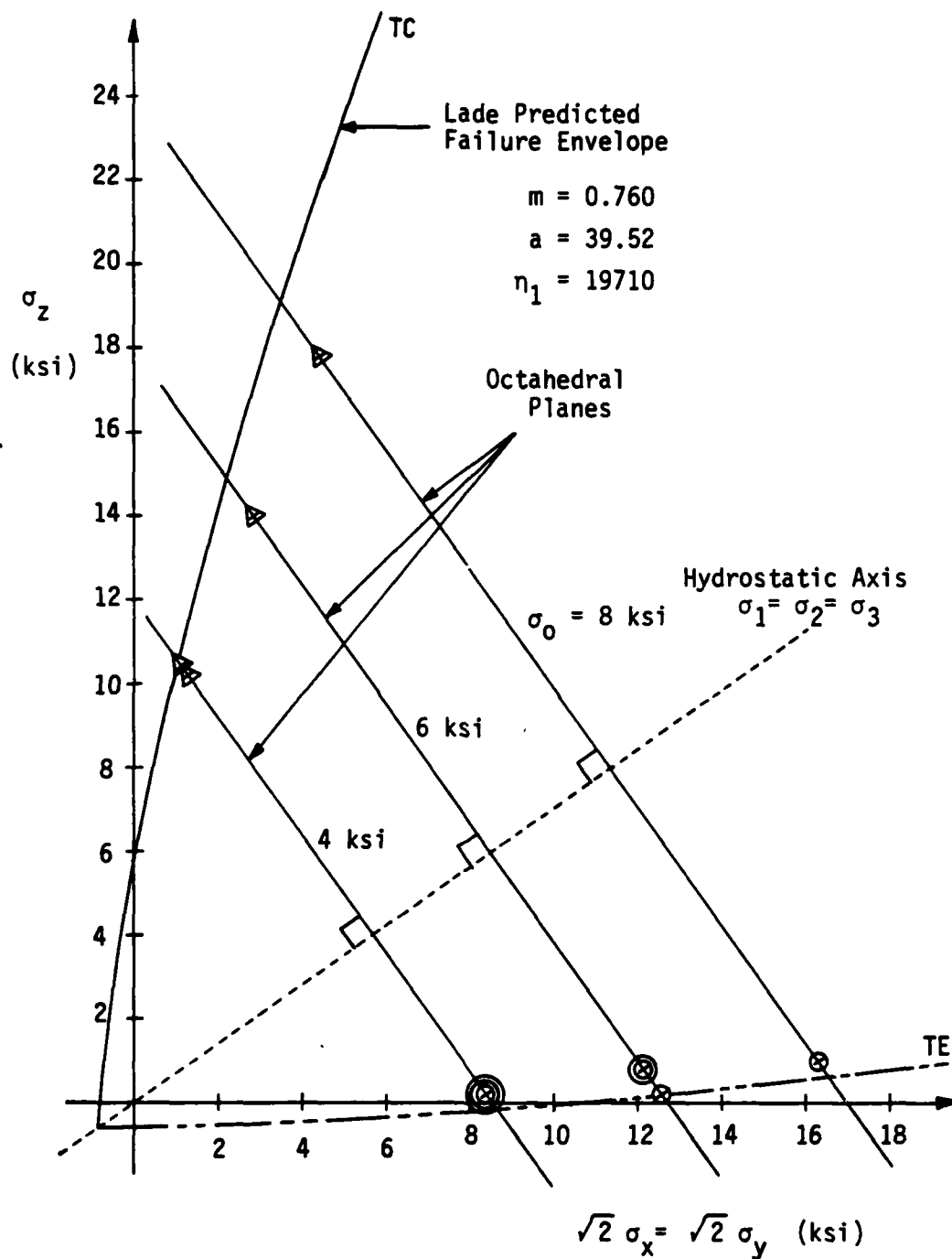


Fig. 5.33. Failure Data in Triaxial Plane with Lade Prediction.

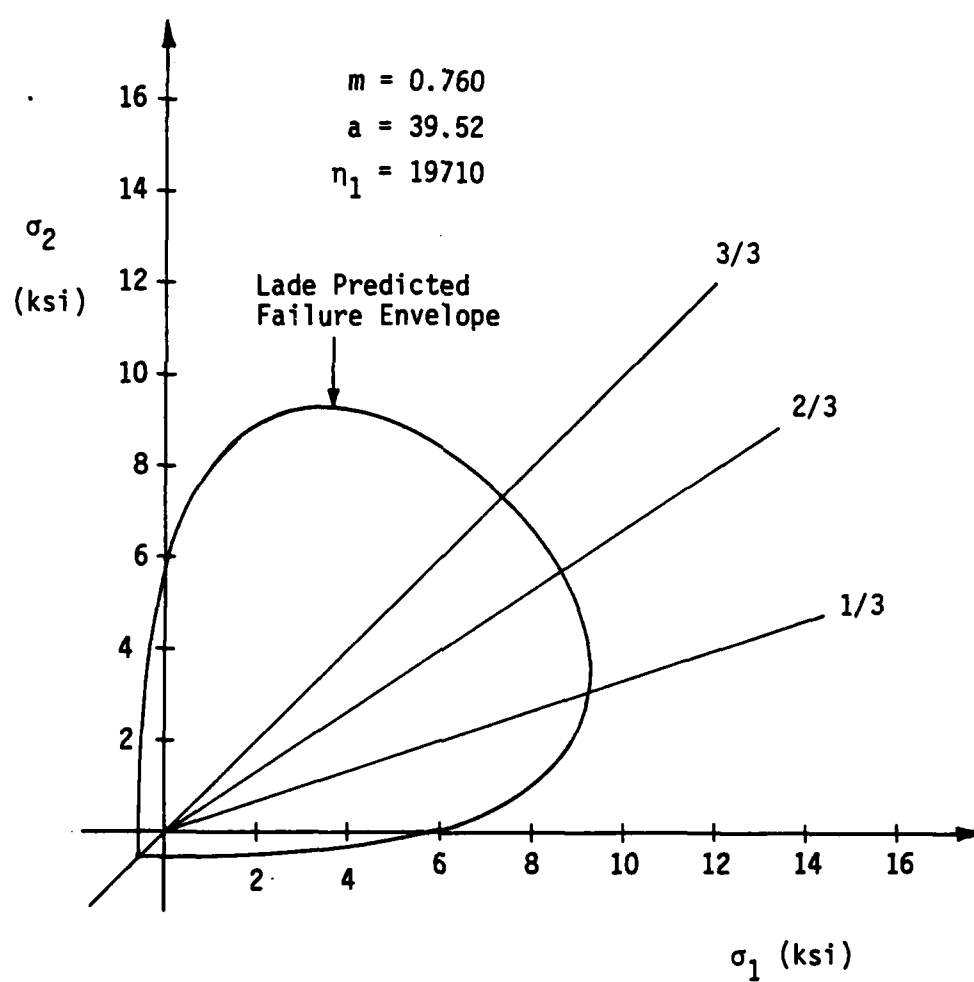


Fig. 5.34. Predicted Biaxial Failure Envelope Based on Lade Failure Criterion.

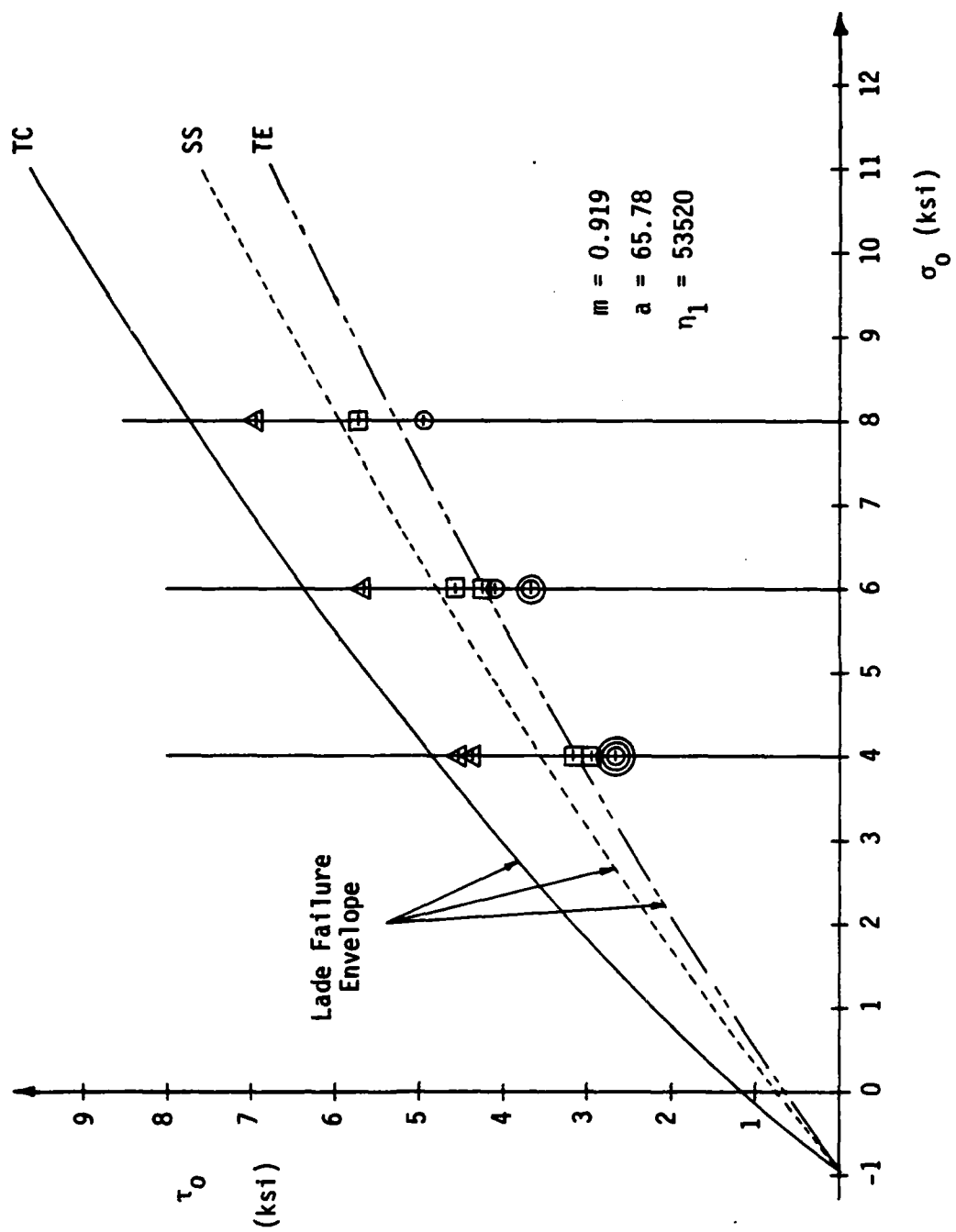
is, the shear strengths do not decrease with increasing confining pressure σ_0 , simply because Lade does not employ parabolic meridian equations in his formulation. The meridians do, however, predict an increasing rate of shear strength (τ_0) with respect to σ_0 faster than they should.

Case VII

Lade's criterion also calibrated as suggested with the same input strength data as used for the Willam-Warnke criterion in Case III. Again, the point is to compare the predicted strength envelope by Lade with that obtained using the Willam-Warnke criterion, each calibrated with identical input data, and to observe the effects on Lade's criterion when using input data of mixed boundary conditions and specimen types. Since the Lade criterion employs a regression analysis to determine the model parameters, it appears to be less sensitive than the Willam-Warnke failure criterion to differences in input data. Even with this data coming from tests where boundary conditions and specimen types differ, for this case the Lade formulation predicts the strengths better by far than the Willam-Warnke criterion. Even though the predicted strength envelope is very unconservative in comparison to the experimental strength results, at least the resulting shape is correct.

5.2.4 Normality of CU-SFRC With Respect to the Willam-Warnke Failure Criterion

Some constitutive models developed for concrete have utilized the elastic-perfectly plastic model for the post-failure condition in the compressive regime. In these models, the failure surface is taken as the yield surface with the assumption that the normality



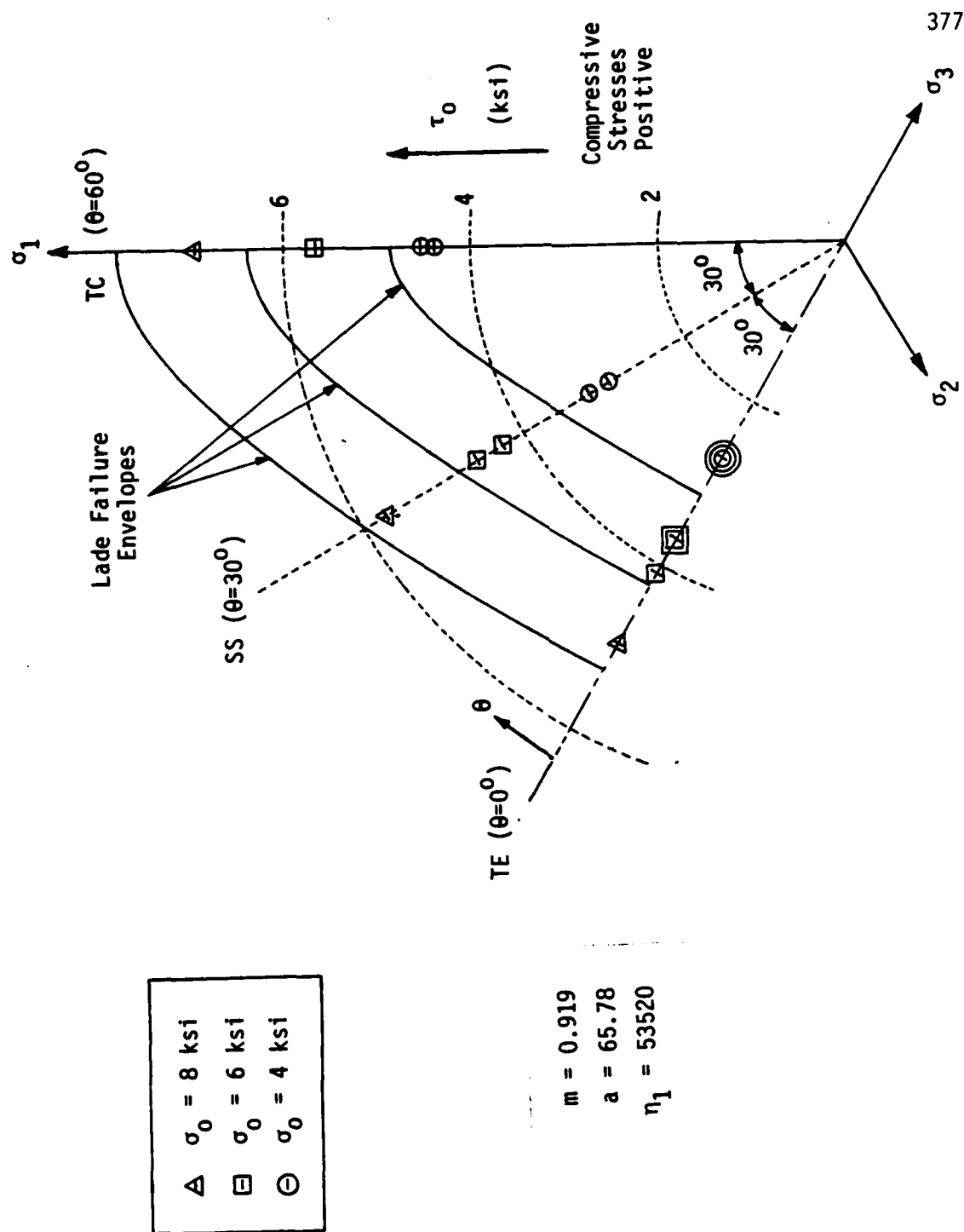


Fig. 5.36. Failure Data in Octahedral Planes with Lade Predictions.

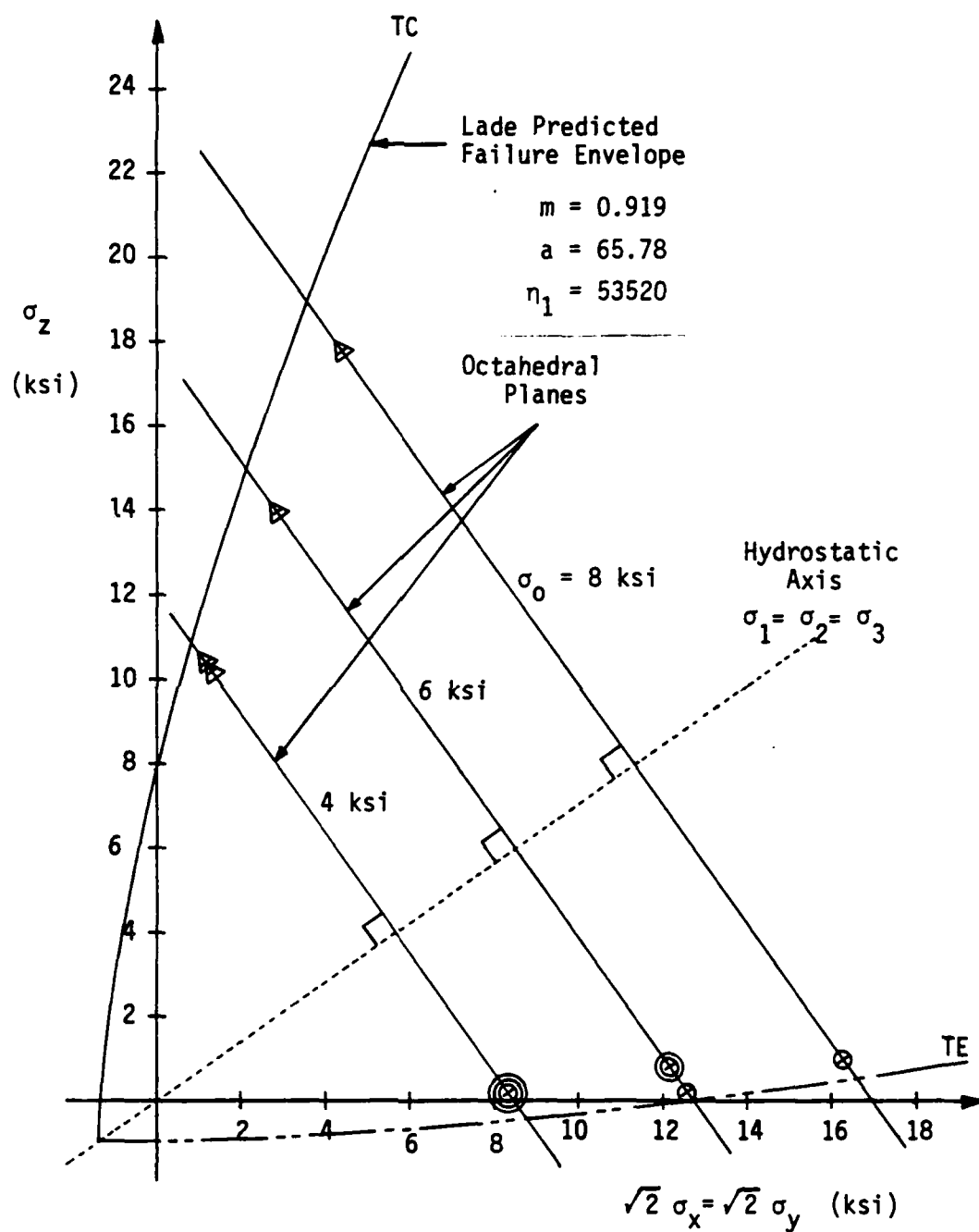


Fig. 5.37. Failure Data in Triaxial Plane with Lade Prediction.

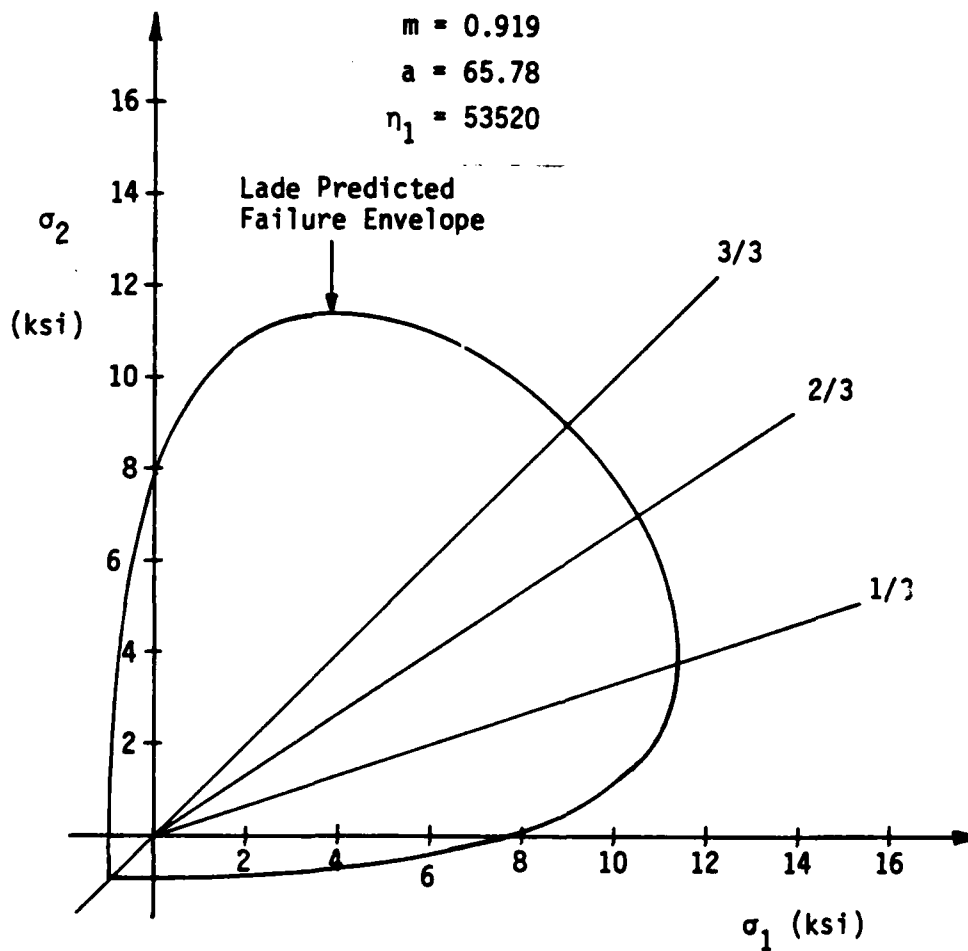


Fig. 5.38. Predicted Biaxial Failure Envelope Based on Lade Failure Criterion.

condition and associated flow rule is valid. One objection to the use of these models is that the normality condition of Eq. 5.2 implies a volume expansion exceeding that which occurs in actual concrete type materials.

In order to test the validity of the normality flow rule of classical plasticity for any material, the plastic strain increment vectors at failure need to be calculated. This can be accomplished by simply subtracting the elastic component from the total strain increment for all three principal directions, thus determining the plastic strain contribution. This method is demonstrated in Fig. 5.39 for the one-dimensional case of a strain hardening material. C^e and C^{e-p} are the elastic and elastic-plastic stiffnesses respectively. The total elastic and total plastic strains are ϵ^e and ϵ^p , the increments of elastic and plastic strains are $d\epsilon^e$ and $d\epsilon^p$, and $d\sigma$ is the increment of stress over which the strains are determined. Once again, failure for the CU-SFRC was defined as the point at which volume expansion (dilation) occurred along the shearing stress path after the initial contraction of the specimen during hydrostatic compression.

Andenes (8) measured these plastic strain increment vectors from biaxial compression tests on mortar to ascertain the validity of the normality principle on that material. The tests were conducted in the University of Colorado cubical cell, the same apparatus used for this research. These vectors are shown in Fig. 5.40. No claim to normality can be made on the basis of these results.

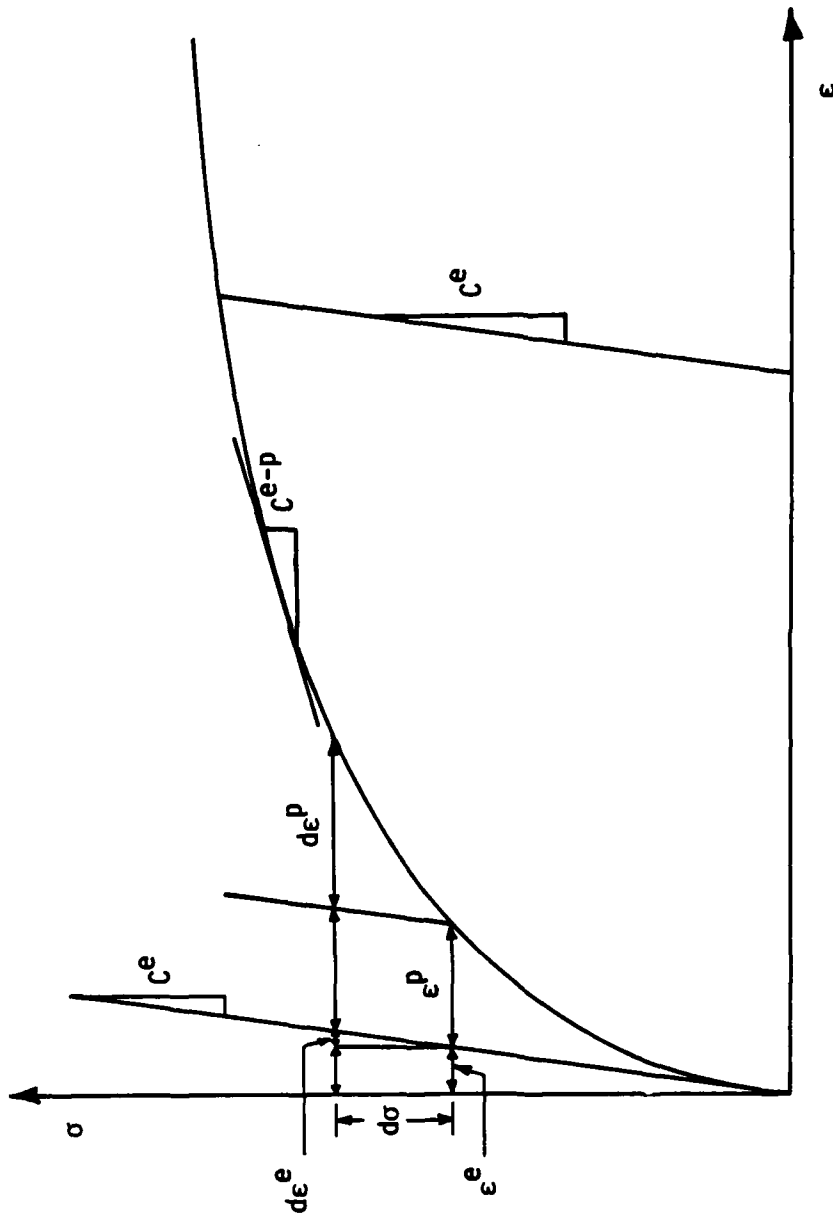


Fig. 5.39. Stress-Strain Response Curve for an Elasto-Plastic Hardening Material. [Mould (89)].

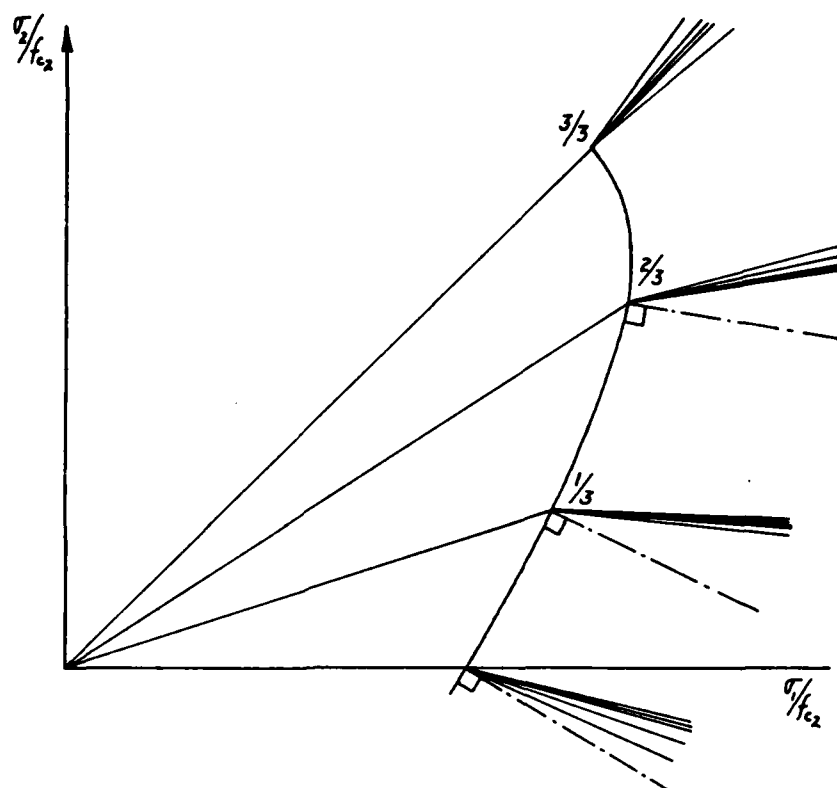


Fig. 5.40. Post-Failure Strain Rate Vectors of Mortar from Steel Plate Series [Andenes (8)].

The plastic strain increment vectors for the CU-SFRC were calculated in the manner described above. If they are to be plotted on a failure surface, other than an experimentally estimated one, then a failure criterion must be chosen that accurately describes the failure of this material. Both the Willam-Warnke and Lade failure criteria predict the strengths of the CU-SFRC quite well, when calibrated for this material as discussed in Sections 5.2.1.1 and 5.2.2.1 respectively. Therefore the Willam-Warnke failure criterion was arbitrarily chosen to represent the failure surface upon which the plastic strain increment vectors are superimposed. The following figures show these results:

- 1) Fig. 5.41 Invariant Plane

$$\sqrt{J_{2D}} \text{ vs. } J_1$$

$$[2\sqrt{6}I_2^P] \text{ vs. } [\frac{1}{3}\delta I_1^P]$$

- 2) Fig. 5.42 Deviatoric (Octahedral) Plane

- 3) Fig. 5.43 Rendulic (Triaxial) Plane

$$\sigma_z \text{ vs. } \sqrt{2} \sigma_x$$

$$[d\epsilon_z^P] \text{ vs. } [\sqrt{2} d\epsilon_x^P]$$

- 4) Fig. 5.44 Exploded View of Fig. 5.43

- 5) Fig. 5.45 Rendulic (Triaxial) Plane

$$\sigma_z \text{ vs. } \sqrt{2} \sigma_y$$

$$[d\epsilon_z^P] \text{ vs. } [\sqrt{2} d\epsilon_y^P]$$

- 6) Fig. 5.46 Exploded View of Fig. 5.45

J_{2D} and J_1 are defined by Eqns. 5.5 and 5.7 respectively. The

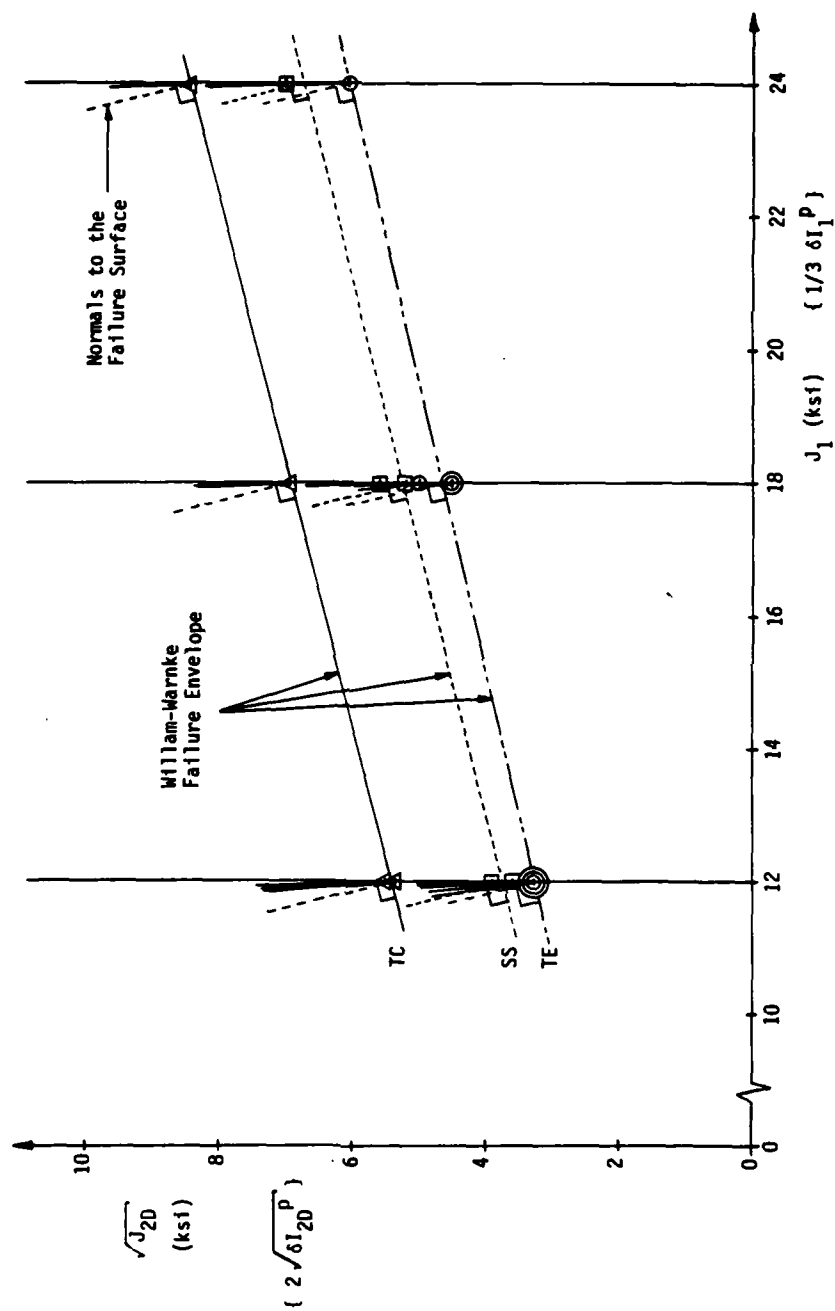


Fig. 5.41. Post-Failure Plastic Strain Increment Vectors Superimposed Upon Failure Envelope in Invariant Plane.

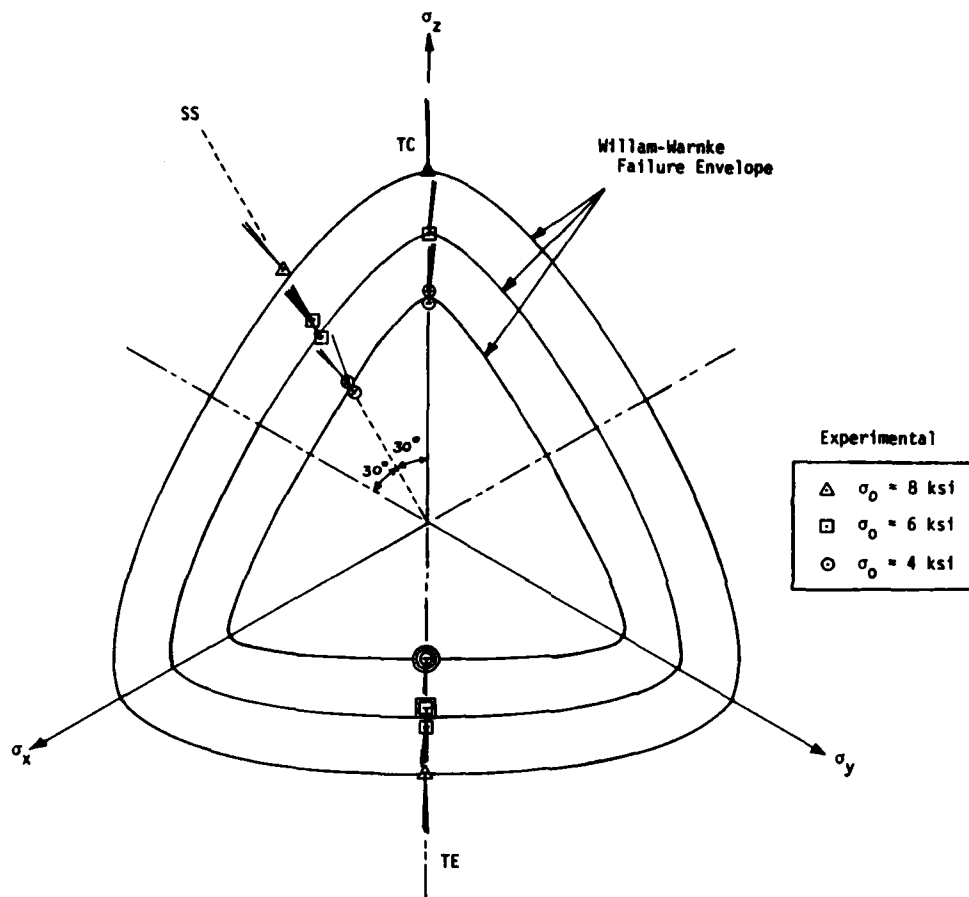


Fig. 5.42. Post-Failure Plastic Strain Increment Vectors Superimposed Upon Failure Envelopes in Deviatoric Planes.

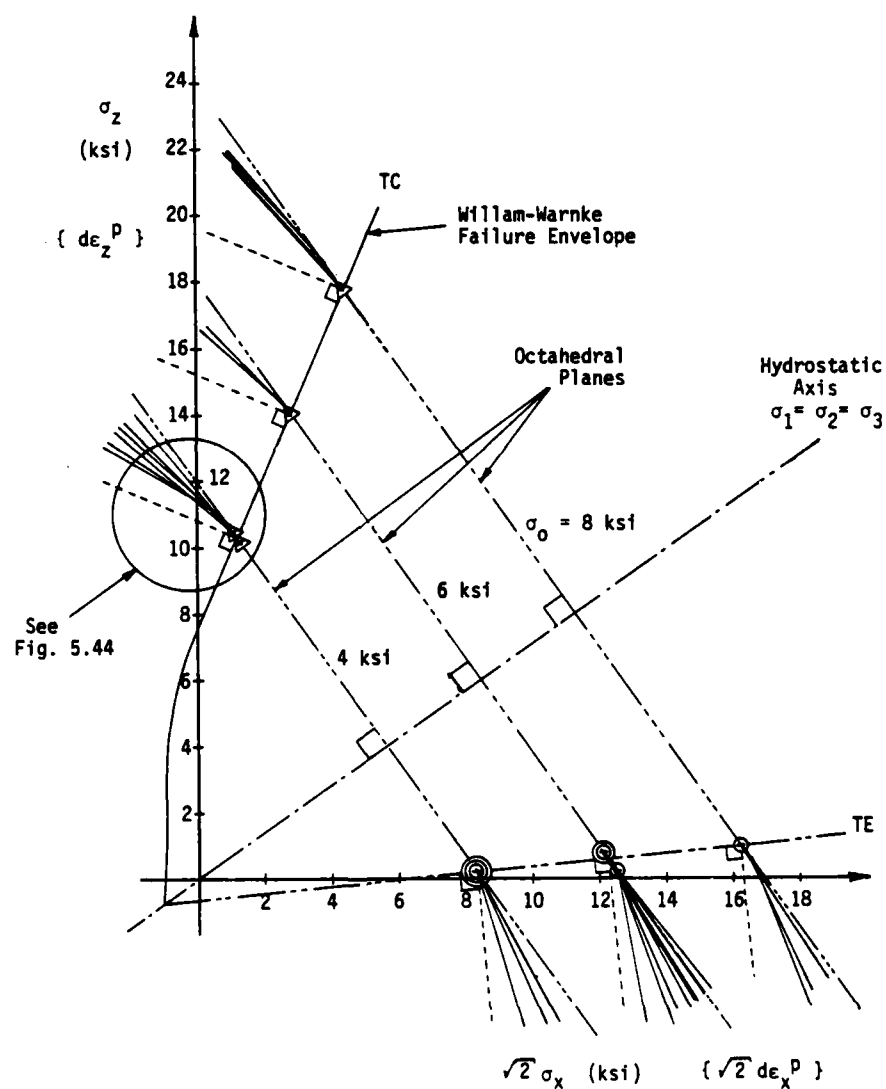


Fig. 5.43. Post-Failure Plastic Strain Increment Vectors Superimposed Upon Failure Envelope in Triaxial Plane.

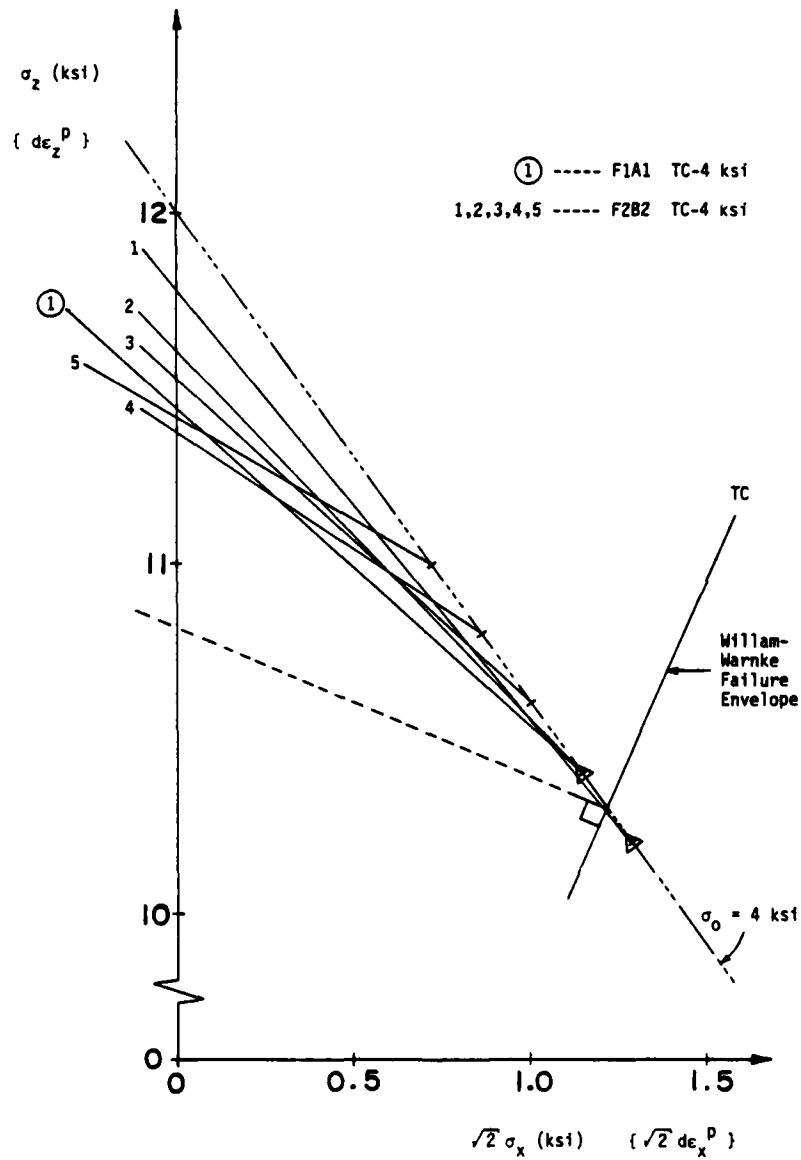


Fig. 5.44. Exploded View for Part of Fig. 5.43.

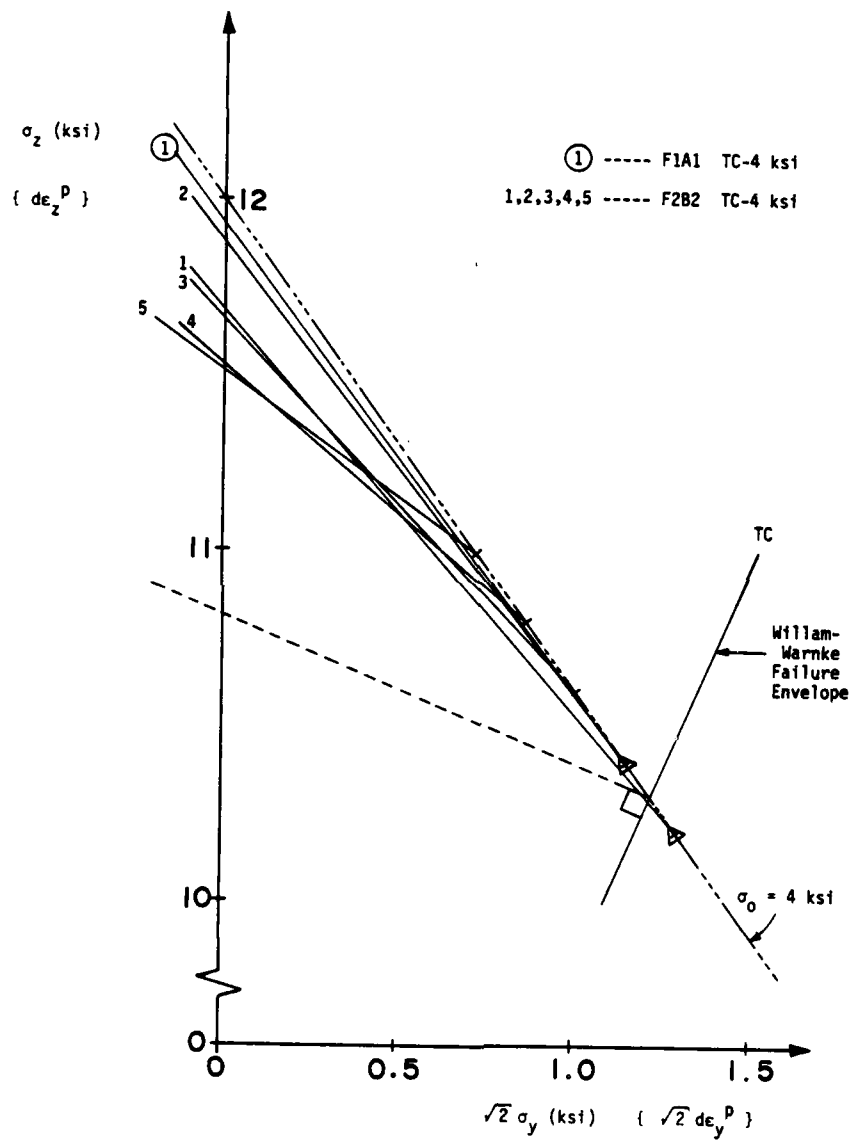


Fig. 5.46. Exploded View for Part of Fig. 5.45.

first strain invariant I_1 and the second deviatoric strain invariant I_{2D} are defined as follows:

$$\begin{aligned} I_1 &= \epsilon_1 + \epsilon_2 + \epsilon_3 \\ &= 3\epsilon_0 \end{aligned} \quad (5.52)$$

$$\begin{aligned} I_{2D} &= \frac{1}{6} [(\epsilon_1 - \epsilon_2)^2 + (\epsilon_2 - \epsilon_3)^2 + (\epsilon_3 - \epsilon_1)^2] \\ &= \frac{3}{2} \gamma_0^2 \end{aligned} \quad (5.53)$$

The variation in the invariants for the plastic strain increments then become:

$$\delta I_1^P = d\epsilon_1^P + d\epsilon_2^P + d\epsilon_3^P \quad (5.54)$$

$$\delta I_{2D}^P = \frac{1}{6} [(d\epsilon_1^P - d\epsilon_2^P)^2 + (d\epsilon_2^P - d\epsilon_3^P)^2 + (d\epsilon_3^P - d\epsilon_1^P)^2] \quad (5.55)$$

Note that in Fig. 5.41 that $\frac{1}{3} I_1^P$ and $2\sqrt{\delta I_{2D}^P}$ are the plastic strain increment invariant components corresponding to J_1 and $\sqrt{J_{2D}}$, as determined by Sture (121).

Since the point of all these graphs is to verify the normality condition for the CU-SFRC, it was felt unnecessary to plot the plastic strain increment vectors for each test on separate figures. Therefore the increments for all the specimens that failed are superimposed on the same graphs. In some cases, only one vector was obtained because equipment breakdown occurred at the same time the specimen failed. These are plotted at the failure stress state for that particular specimen.

For others tested, a higher deviator stress (resulting in increased shear strains) was applied before the system failed and after dilation of the specimen began. For these, more than one plastic strain increment vector was calculated; the first at the

onset of failure; the remaining at higher stress levels. They are therefore plotted at the corresponding state of stress at which they were obtained; whether it be failure or higher. These are shown in all figures but are best seen in the Rendulic plane, i.e. Figs. 5.43 and 5.45. For instance examine the exploded sections of these two figures, shown in Figs. 5.44 and 5.46 for the TC stress path at the confining pressure σ_0 of 4 ksi. The line labeled ① is the plastic strain increment vector for specimen F1A1. Only one vector was obtained for this specimen for reasons just described. The lines 1,2,3,4 and 5 are the vectors for specimen F2B2. As seen in Figs. 5.44 and 5.46 the vectors are plotted starting with the first, at failure, then increasing to the fifth for corresponding states of stress post-failure. Shown in all the figures, the CU-SFRC exhibits little volume dilatancy at failure but then tends to dilate more, the farther beyond failure the stress state goes. That is, with increasing deviator stress beyond the failure state, the plastic strain increment vectors rotate and approach the normal to the failure surface. In an elastic-perfectly plastic plasticity model, the normality condition is assumed. This would give rise to a volume dilatancy during plastic straining exceeding that which occurs in the CU-SFRC tested here, if this plasticity model were used to predict the behavior of this material.

In conclusion, for plasticity, the plastic strain increment vectors are always perpendicular to the potential surface. For associated flow, the potential and yield surfaces coincide. If one assumes the yield and failure surfaces are the same for concrete and that concrete follows the associated flow rule, then for an

elastic-perfectly plastic model, the plastic strain increment vectors must be normal to the failure surface for the concrete to flow as a perfectly plastic material. The CU-SFRC does not behave in this fashion as previously explained and shown in figure form. Therefore, no claim to normality can be made for this material.

Although there are theoretical objections to the use of the plasticity model for plain concrete, reasonable results have been obtained for practical problems such as those involving prestressed concrete reactor vessels (11,13). Since the steel fiber reinforced concrete has been proven to be a more ductile material than plain concrete, perhaps even better results would be obtained if one uses the plasticity model for this material.

5.3 Simple Formulation of Multiaxial Concrete Behavior¹

Predicting the stress-strain behavior of concrete structures by the finite element method requires as key input some constitutive relations for the concrete that can model its nonlinear response when subjected to multiaxial states of stress. Many formulations have been developed which attempt to model this behavior, with various degrees of success. The CU-SFRC has exhibited behavior when subjected to triaxial stresses similar to that observed for plain concrete. Therefore a formulation that predicts the behavior of plain concrete should also work well for the CU-SFRC. In this

¹ Parts of this section are a rewritten summary taken from Gerstle (48), Gerstle and Cornelius (49) and personal communication with both Gerstle and Cornelius.

section a description is given of a "Simple Formulation" developed by Gerstle (48) and improved upon by Gerstle and Cornelius (49) to predict the behavior of concrete under multiaxial stresses. It will be tested here on the CU-SFRC.

The simple formulation is intended to predict the principal strains due to monotonically, but not necessarily proportionally, increasing compressive stresses. The theory cannot handle tensile stresses nor is it capable of predicting behavior under cyclic loads when stiffness degradation occurs. In addition, inherent material anisotropy and induced by previous stress-histories are not considered in this formulation.

The theory stems from experimentally observed octahedral stress-strain and strength results. It incorporates the use of three variable material moduli which in conjunction with the octahedral stresses calculated from given principal stress increments are used to predict the octahedral strains and consequently the principal strains.

The problem may in general be stated as follows:

Given: existing principal stress state $\sigma_1, \sigma_2, \sigma_3$, and
principal stress increments $d\sigma_1, d\sigma_2, d\sigma_3$.

Find: corresponding principal strain increments $d\epsilon_1$,
 $d\epsilon_2, d\epsilon_3$.

The octahedral normal and shear stresses (σ_o, τ_o) and strains (ϵ_o, γ_o) are defined by the relations

$$\sigma_o = \frac{1}{3} (\sigma_1 + \sigma_2 + \sigma_3) \quad (5.56)$$

$$\tau_0 = \frac{1}{3} \sqrt{(\sigma_1 - \sigma_2)^2 + (\sigma_2 - \sigma_3)^2 + (\sigma_3 - \sigma_1)^2} \quad (5.57a)$$

$$= \sqrt{\frac{1}{3} [(\sigma_1 - \sigma_0)^2 + (\sigma_2 - \sigma_0)^2 + (\sigma_3 - \sigma_0)^2]} \quad (5.57b)$$

$$= \sqrt{\frac{1}{3} s_{ij} s_{ij}} \quad (5.57c)$$

where s_{ij} is the stress deviator tensor defined as

$$s_{ij} = \sigma_{ij} - \sigma_0 \delta_{ij} \quad (5.58)$$

$$\epsilon_0 = \frac{1}{3} (\epsilon_1 + \epsilon_2 + \epsilon_3) \quad (5.59)$$

$$\gamma_0 = \frac{1}{3} \sqrt{(\epsilon_1 - \epsilon_2)^2 + (\epsilon_2 - \epsilon_3)^2 + (\epsilon_3 - \epsilon_1)^2} \quad (5.60a)$$

$$= \sqrt{\frac{1}{3} [(\epsilon_1 - \epsilon_0)^2 + (\epsilon_2 - \epsilon_0)^2 + (\epsilon_3 - \epsilon_0)^2]} \quad (5.60b)$$

$$= \sqrt{\frac{1}{3} e_{ij} e_{ij}} \quad (5.60c)$$

where e_{ij} is the strain deviator tensor

defined as

$$e_{ij} = \epsilon_{ij} - \epsilon_0 \delta_{ij} \quad (5.61)$$

The incremental octahedral normal and shear stresses ($\Delta\sigma_0, \Delta\tau_0$) and strains ($\Delta\epsilon_0, \Delta\gamma_0$) defined by Gerstle (48) are valid only for proportional loading. Therefore in order to be valid for non-proportional loading, the incremental octahedral normal and shear stresses ($d\sigma_0, d\tau_0$) and strains ($d\epsilon_0, d\gamma_0$) need to be redefined as follows.

$$d\sigma_0 = \frac{1}{3} (d\sigma_1 + d\sigma_2 + d\sigma_3) \quad (5.62a)$$

$$= \frac{1}{3} d\sigma_{ii} \quad (5.62b)$$

$$d\epsilon_0 = \frac{1}{3} (d\epsilon_1 + d\epsilon_2 + d\epsilon_3) \quad (5.63a)$$

$$= \frac{1}{3} d\epsilon_{ii} . \quad (5.63b)$$

Differentiating Eq. 5.57c with respect to the stress deviator tensor s_{ij} results in:

$$\frac{d\tau_0}{ds_{ij}} = \frac{1}{\sqrt{3}} \frac{s_{ij}}{\sqrt{s_{ij} s_{ij}}} \quad (5.64a)$$

$$= \frac{1}{3} \frac{s_{ij}}{\tau_0} \quad (5.64b)$$

It follows therefore that

$$d\tau_0 = \frac{1}{3\tau_0} s_{ij} ds_{ij} , \quad (5.65a)$$

and in terms of principal components only

$$d\tau_0 = \frac{1}{3\tau_0} (s_{11} ds_{11} + s_{22} ds_{22} + s_{33} ds_{33}) . \quad (5.65b)$$

In terms of principal stresses, one obtains

$$d\tau_0 = \frac{\sigma_1(2d\sigma_1 - d\sigma_2 - d\sigma_3) + \sigma_2(2d\sigma_2 - d\sigma_3 - d\sigma_1) + \sigma_3(2d\sigma_3 - d\sigma_1 - d\sigma_2)}{3 \sqrt{(\sigma_1 - \sigma_2)^2 + (\sigma_2 - \sigma_3)^2 + (\sigma_3 - \sigma_1)^2}} \quad (5.65c)$$

Analogous to $d\tau_0$, $d\gamma_0$ is obtained by differentiating Eq. 5.60c with respect to the strain deviator tensor e_{ij} .

$$d\gamma_0 = \frac{1}{3\gamma_0} e_{ij} de_{ij} , \quad (5.66a)$$

$$= \frac{1}{3\gamma_0} [e_{11} de_{11} + e_{22} de_{22} + e_{33} de_{33}] \quad (5.66b)$$

or in terms of principal strains

$$d\gamma_0 = \frac{\epsilon_1(2d\epsilon_1 - d\epsilon_2 - d\epsilon_3) + \epsilon_2(2d\epsilon_2 - d\epsilon_3 - d\epsilon_1) + \epsilon_3(2d\epsilon_3 - d\epsilon_1 - d\epsilon_2)}{3 \sqrt{(\epsilon_1 - \epsilon_2)^2 + (\epsilon_2 - \epsilon_3)^2 + (\epsilon_3 - \epsilon_1)^2}} \quad (5.66c)$$

The octahedral stress increments defined by Eqs. 5.62 and 5.65 are now valid for any loading condition, proportional or non-proportional, as long as the increments in principal stresses, i.e. the step size chosen, remain small. These octahedral stress increments are related to the octahedral strain increments of Eqs. 5.63 and 5.66 through three variable material moduli by the following constitutive relations:

$$d\epsilon_o = \frac{d\sigma_o}{3K_T(\sigma_o)} + \frac{d\tau_o}{H_T(\sigma_o)} \quad (5.67a)$$

$$d\gamma_o = \frac{d\tau_o}{2G_T(\tau_o)} \quad (5.67b)$$

The three moduli K_T , G_T and H_T are tangent values depending on the current stress state. K_T is the bulk modulus, relating volumetric stresses with strains and G_T is the shear modulus relating deviatoric stresses with strains. The coupling modulus H_T accounts for the volume change of the material caused by stress deviation, which has been observed to occur in the CU-SFRC as shown in Figs. 4.101-4.106. The expressions developed for these moduli with respect to the CU-SFRC will be discussed later.

The octahedral normal and shear strain increments are determined from the constitutive relations in Eq. 5.67, from given stress increments. These octahedral strain increments must now be transformed to principal strain increments $d\epsilon_1$, $d\epsilon_2$ and $d\epsilon_3$. With three unknowns, three equations are needed, two of which are provided by Eqs. 5.63 and 5.66. The third stems from the assumed

coaxiality of the principal deviator stress and strain increment vectors ds and de . That is:

$$\frac{ds_2}{ds_1} = \frac{de_2}{de_1}$$

or

$$\frac{d\sigma_2 - d\sigma_0}{d\sigma_1 - d\sigma_0} = \frac{d\epsilon_2 - d\epsilon_0}{d\epsilon_1 - d\epsilon_0} \equiv B \quad (5.68)$$

where B is a constant. Solving Eqs. 5.63, 5.66 and 5.68 simultaneously for the principal strain increments results in

$$d\epsilon_1 = d\epsilon_0 + de_1 \quad (5.69)$$

$$d\epsilon_2 = d\epsilon_0 + de_2 \quad (5.70a)$$

$$= d\epsilon_0 + B \cdot de_1 \quad (5.70b)$$

$$d\epsilon_3 = d\epsilon_0 + de_3 \quad (5.71a)$$

$$= d\epsilon_0 - (B+1) \cdot de_1 \quad (5.71b)$$

Defining

$$C_1 = \frac{3\gamma_0}{\epsilon_1 + B \cdot \epsilon_2 - (B+1) \cdot \epsilon_3} \quad , \quad (5.72)$$

the principal strain increments can be rewritten in terms of the desired octahedral strain increments as

$$d\epsilon_1 = d\epsilon_0 + C_1 \cdot d\gamma_0 \quad (5.73)$$

$$d\epsilon_2 = d\epsilon_0 + B \cdot C_1 \cdot d\gamma_0 \quad (5.74)$$

$$d\epsilon_3 = d\epsilon_0 - (B+1) \cdot C_1 \cdot d\gamma_0 \quad (5.75)$$

For the first load step (initial values of stress equal to zero), the parameter C_1 is undefined. Since the total principal strains and increments of principal strains are the same for the first load step, the value of C_1 reduces to

$$C = \sqrt{\frac{3}{2} \cdot \frac{1}{1 + B + B^2}} \quad (5.76)$$

which is the same as the definition given by Gerstle (48) for proportional loading. Note also that for proportional loading, the increments of stresses and strains defined above in Eqs. 5.62-5.66 reduce to those given by Gerstle (48).

5.3.1 Representation of Moduli Deviatoric Stress-Strain Relations

As a result of the work conducted by Gerstle, et. al. (50), deviatoric ($\tau_0 - \gamma_0$) stress-strain curves were obtained for concrete under monotonically increasing biaxial and triaxial loads. Gerstle (47,48) later observed that these curves can be expressed by an exponential form, analogous to creep curves for a Kelvin element as:

$$\tau_0 = \tau_{ou} \left(1 - e^{\frac{-2G_0}{\tau_{ou}} \gamma_0} \right) . \quad (5.77)$$

Differentiating this with respect to γ_0 to find the tangent shear modulus G_T , i.e. $\frac{d\tau_0}{d\gamma_0} = 2G_T$ and solving for G_T results in a linearly decreasing relationship as

$$G_T = G_0 \left(1 - \frac{\tau_0}{\tau_{ou}} \right) . \quad (5.78)$$

G_0 is the initial shear modulus and τ_{ou} is the octahedral shear strength. Gerstle (47,48) suggests that τ_{ou} is to be selected as the shear strength obtained from tests leading to ductile failure. According to plasticity theory, ductile failure occurs when the shear modulus $G_T = 0$. This value of τ_{ou} could then be measured directly from experiment or predicted by a suitable failure

criterion (134,79) that has been calibrated from the experimental results. It remains to determine the initial shear modulus G_0 . It could be calculated through the elastic relation as

$$G_0 = \frac{E}{2(1+\nu)} \quad (5.79)$$

where the modulus of elasticity E and Poisson's ratio ν can be measured from a uniaxial compression test. G_0 , for the CU-SFRC, was not determined in this manner for several reasons. First, although the modulus E from uniaxial compression tests on 3 x 6 in. cylinders was measured as 3720 ksi, Poisson's ratio ν was not determined. Secondly, E and ν measured from the stepped-loading sequence on cubical specimens, described in Section 4.3.3 (assuming isotropy), were 2487 ksi and 0.057 respectively, which are quite different results. Thirdly, in an unconfined compression test, the specimen's stress state is comprised of both normal and shear stresses simultaneously. However, in the stress paths employed in the cubical tests, aside from the stepped loading, shearing did not begin until the hydrostatic compression part of the test was completed. Therefore G_0 calculated from elasticity using E and ν measured from an unconfined compression test may inaccurately represent the shear modulus which could be determined from the τ_0 - γ_0 curves during pure shearing of the cubical specimens. Finally, trying to estimate a value of G_0 from the G_T - τ_0 summary curves (when $\tau_0=0$) shown in Fig. 4.87 would be very difficult because of the large amount of scatter present. For these reasons, G_0 was determined for the CU-SFRC in the following manner.

First of all, the τ_o - γ_o experimental curves were assumed to have the exponential form proposed by Gerstle (47,48) and given in Eq. 5.77. Rewriting this equation to the form

$$e^{\frac{-2G_0}{\tau_{ou}} \gamma_o} = 1 - \frac{\tau_o}{\tau_{ou}} \quad (5.80)$$

and taking the natural log of both sides gives

$$\frac{-2G_0}{\tau_{ou}} \gamma_o = \ln \left(1 - \frac{\tau_o}{\tau_{ou}} \right) . \quad (5.81)$$

Solving for γ_o :

$$\gamma_o = - \frac{\tau_{ou}}{2G_0} \ln \left(1 - \frac{\tau_o}{\tau_{ou}} \right) \quad (5.82)$$

or terms of the common log

$$\gamma_o = \frac{- \ln(10) \tau_{ou}}{2G_0} \log \left(1 - \frac{\tau_o}{\tau_{ou}} \right) . \quad (5.83)$$

Plotting γ_o vs. $\log \left(1 - \frac{\tau_o}{\tau_{ou}} \right)$ should give a straight line with a slope of $\frac{-\ln(10)\tau_{ou}}{2G_0}$ if the τ_o - γ_o experimental curves do behave

according to the exponential relationship given by Eq. 5.77. In Eq. 5.83, τ_o and γ_o are from experiment and τ_{ou} is the shear strength which for the CU-SFRC was calculated from the Willam-Warneke failure criterion (134) described in Section 5.2.1.1. G_0 is the unknown in this equation. With the slope obtained from the figure, and τ_{ou} known, G_0 can easily be calculated.

Two examples of this method are shown in Fig. 5.47 for specimens F1D6 and F1C4. These curves originate from the right-hand side, when $\tau_0 = 0$. Notice that the γ_0 vs. $\log (1 - \frac{\tau_0}{\tau_{ou}})$ results are not entirely linear for either specimen. This is because the experimental τ_0 - γ_0 curves do not exactly possess the exponential form prescribed by Eq. 5.77. However, between steps 1 and 11 for F1D6 and steps 4 and 13 for F1C4, the exponential form is a good approximation. These ranges are also shown on the respective τ_0 - γ_0 curves in Figs. 4.42 and 4.48. Therefore within these ranges, a linear regression was performed to determine the best fit line and to calculate its slope and subsequently G_0 . If this linear range did not include points near the origin of the τ_0 - γ_0 curves, then those specimens were not used as part of the sample. The results of this procedure are shown in Fig. 5.48 where the initial shear moduli for all the tests are plotted as a function of the confining pressure σ_0 and stress path. The reason is to see if there are any confining pressure and/or stress path dependencies related to G_0 . Considerable scatter is present in this figure but on the average it appears the G_0 goes from the greatest to the least in the TE, SS, TC stress path order. This is consistent with the τ_0 - γ_0 behavior observed and discussed in Chapter 4. However, any conclusions about G_0 being dependent on the confining pressure σ_0 are difficult to make except that on the average for the TC tests G_0 decreases as σ_0 increases. It seems that more tests would have to be conducted before any substantial conclusions can be made.

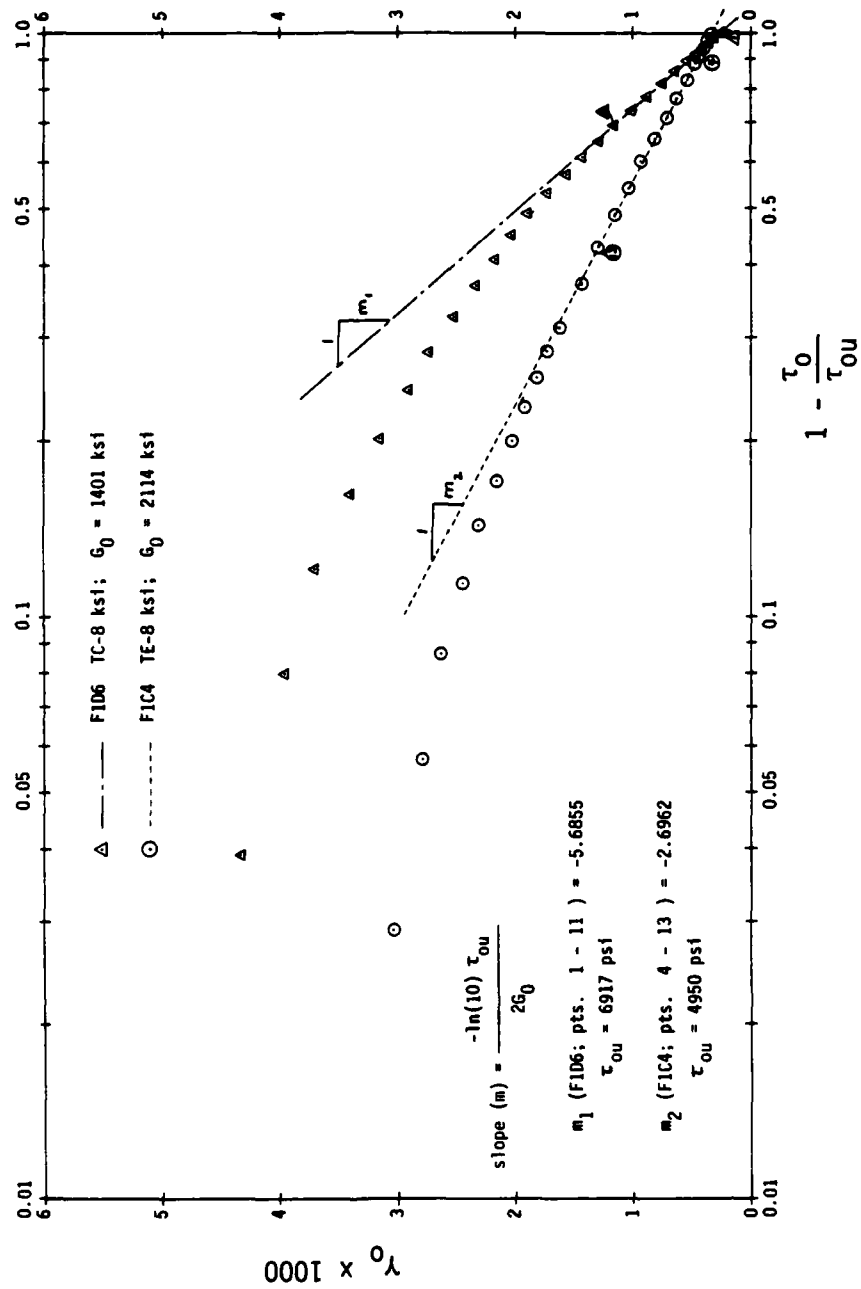


Fig. 5.47. γ_0 vs. $\log(1 - \tau_0/\tau_{ou})$ Examples for Determining G_0 .

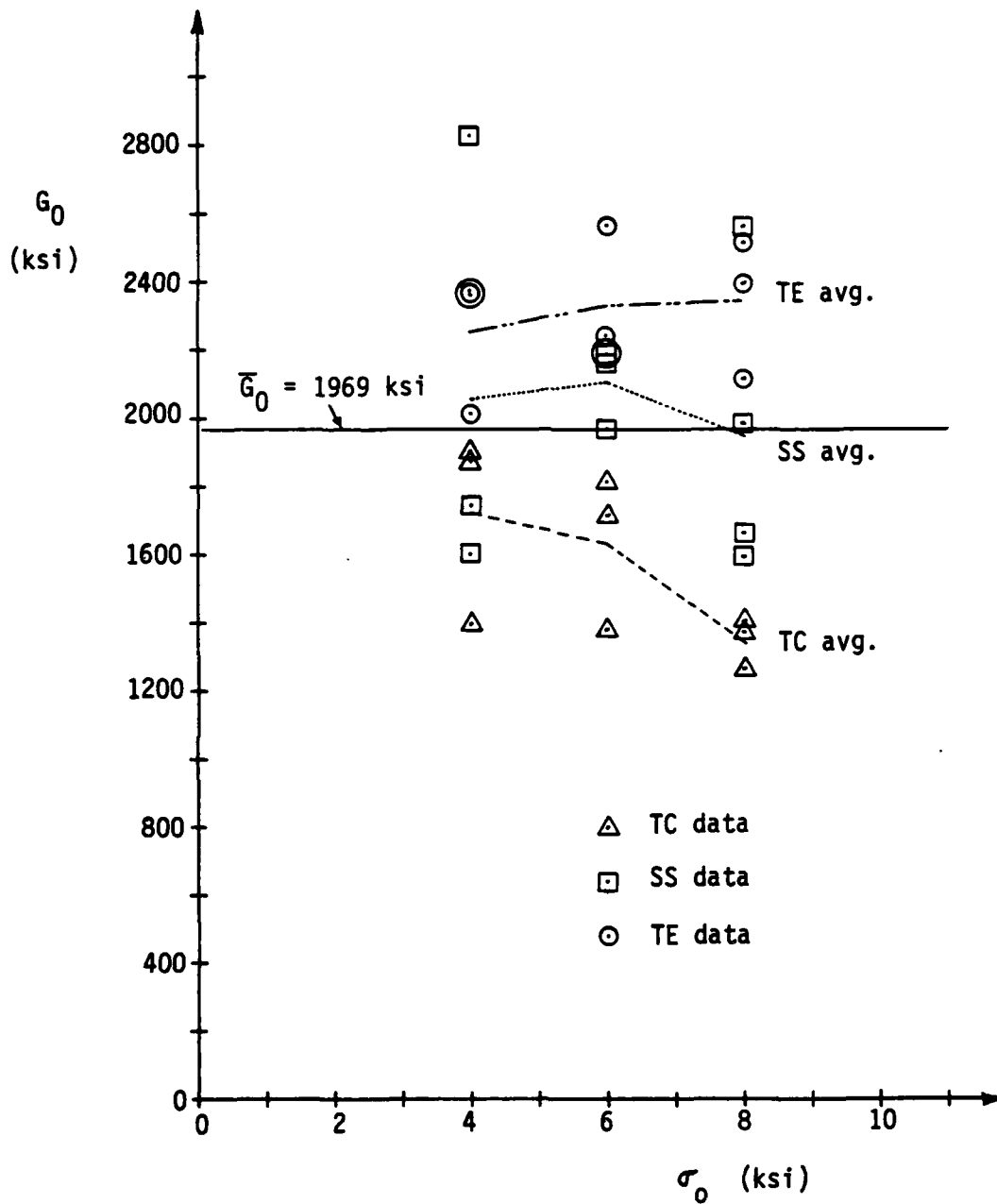


Fig. 5.48. Initial Shear Modulus G_0 vs. Confining Pressure σ_0 .

It still remains to determine one value of G_0 to use in the simple formulation. From the method just described, an overall average value of the initial shear modulus was determined to be $G_0=1969$ ksi. This is the value that will be used in the simple formulation for the behavior predictions of the experimental results. Fig. 5.49 shows the normalized G_T/G_0 vs. τ_0/τ_{ou} curves where $G_0=1969$ ksi and τ_{ou} is calculated from the Willam-Warnke failure criterion (134) described in Section 5.2.1.1. The straight, solid line is defined by Eq. 5.78, the basis for part of the simple formulation. The straight, dashed line will be discussed later.

Volumetric Stress-Strain Relations

In addition to the deviatoric stress-strain curves obtained by Gerstle, et. al. (50), volumetric stress-strain curves ($\sigma_0-\epsilon_0$) were also obtained. Gerstle (47,48) suggests that the bulk modulus K_T

describing this volumetric behavior, i.e. $\frac{d\sigma_0}{d\epsilon_0} = 3 K_T$, can be represented by a linearly decreasing relationship as

$$K_T = K_0 \left(1 - \alpha \frac{\sigma_0}{\sigma_{ou}} \right) . \quad (5.84)$$

K_0 is the initial bulk modulus and α is an experimentally obtained constant. σ_{ou} is not the normal stress at failure due to hydrostatic compression alone. Rather it is the normal stress which exists when failure due to shear takes place. The α term stems from the fact that during a pure hydrostatic compression test, the tangent bulk modulus K_T does not decrease to zero with increasing confining pressure. If it did, failure under hydrostatic compression would occur, a phenomenon that is not possible. The

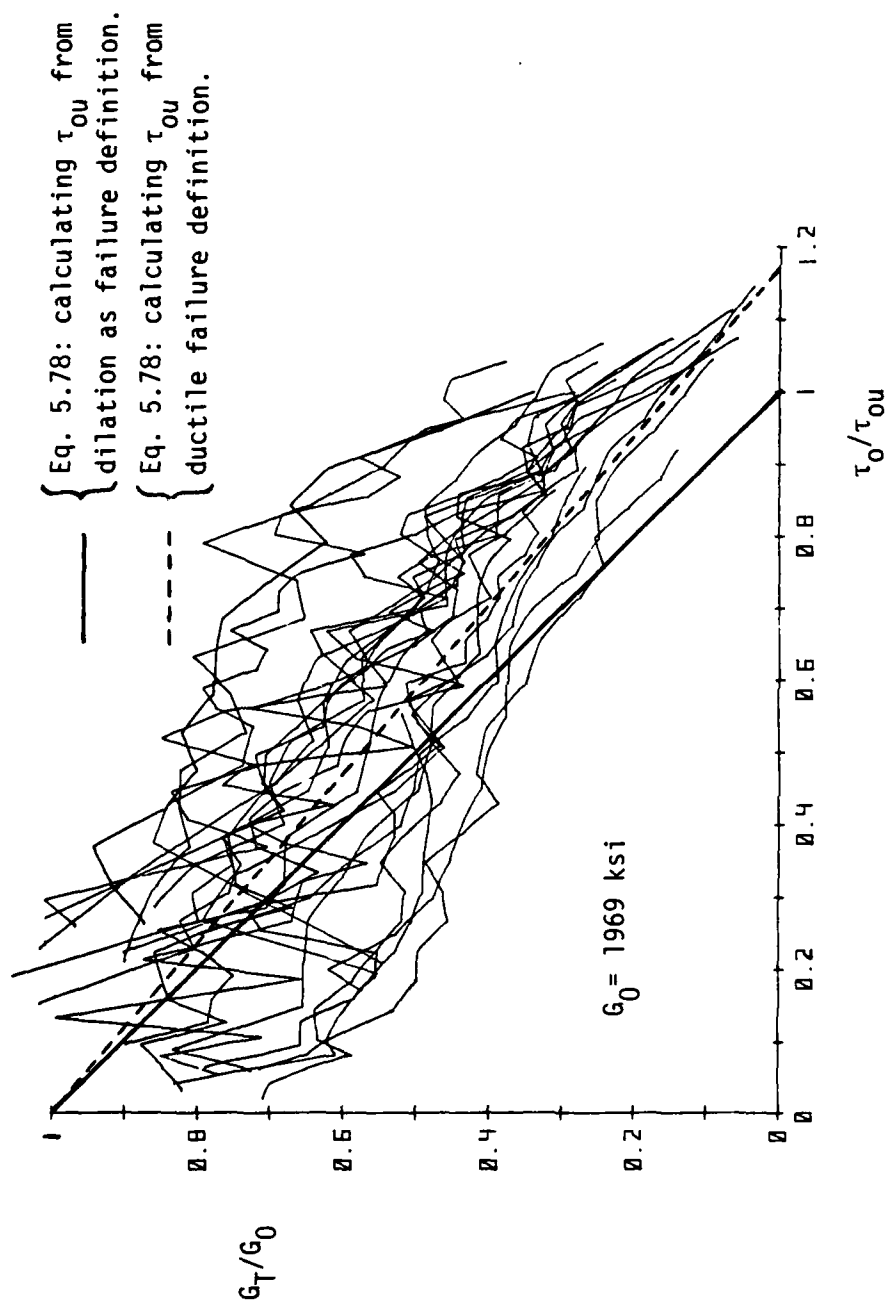


Fig. 5.49. Normalized G_T/G_0 vs. τ_o/τ_{ou} Results.

determination of this constant will be discussed later. K_0 could be determined from an unconfined compression test through the elastic relation

$$K_0 = \frac{E}{3(1-2\nu)} . \quad (5.85)$$

Analogous to G_0 , K_0 for the CU-SFRC was not determined in this manner. Another way would be to estimate a value for K_0 from the K_T - σ_0 summary curves shown on Fig. 4.79. However, so much scatter is present here that similar to G_0 , a more systematic and consistent approach was taken to find K_0 . The following discussion describes this procedure.

Based on the linearly varying tangent bulk modulus relation proposed by Eq. 5.84, a volumetric stress-strain relation (σ_0 - ϵ_0) can be derived having an exponential form similar to that given for the deviatoric curves in Eq. 5.77. Integrating Eq. 5.84 and evaluating the constants results in

$$\sigma_0 = \frac{\sigma_{ou}}{\alpha} \left(1 - e^{\frac{-3\alpha K_0}{\sigma_{ou}} \epsilon_0} \right) . \quad (5.86)$$

The σ_0 - ϵ_0 experimental results were then assumed to take this form. Following the same procedure given in Eqs. 5.80-5.83, and solving for ϵ_0 gives

$$\epsilon_0 = \frac{-\ln(10) \sigma_{ou}}{3\alpha K_0} \log \left(1 - \alpha \frac{\sigma_0}{\sigma_{ou}} \right) . \quad (5.87)$$

Plotting ϵ_0 vs. $\log \left(1 - \alpha \frac{\sigma_0}{\sigma_{ou}} \right)$ should give a straight line with a

slope of $\frac{-\ln(10) \sigma_{ou}}{3\alpha K_0}$ if the σ_0 - ϵ_0 experimental curves have the exponential form given by Eq. 5.86. In these relations, σ_0 and ϵ_0 are from experiment and σ_{ou} is calculated on the basis of the known stress path. For pure hydrostatic loading followed by monotonic shear deviation to failure at a constant confining pressure, σ_{ou} is the value of the confining pressure at which shear failure occurs. Two unknowns remain in Eq. 5.87: α and K_0 . There is no unique solution, therefore α was estimated from Fig. 4.79 as 0.52. With the slope obtained from this procedure, K_0 can be calculated.

The same two examples used to demonstrate the determination of G_0 are used here to find K_0 : F1D6 and F1C4. Fig. 5.50 shows the results. Again, complete linearity does not exist because the exponential form proposed by Eq. 5.86 does not predict the experimental σ_0 - ϵ_0 results exactly. Therefore a linear regression was conducted between steps 4 and 11 for F1D6 and 7 and 16 for F1C4 because between these points, the relation is valid. From the slopes of the best fit lines, K_0 was easily calculated. Figs. 4.42 and 4.48 show these ranges on respective σ_0 - ϵ_0 curves. This same procedure was followed for all the specimens and an overall average value of the initial bulk modulus was found to be $K_0 = 1622$ ksi. Fig. 5.51 shows the normalized K_T/K_0 vs. σ_0/σ_{ou} experimental curves with the straight, solid line representing the linearly varying bulk modulus formulation given by Eq. 5.84 with $\alpha = 0.52$ that will be used in the simple formulation to predict the behavior of the experimental results.

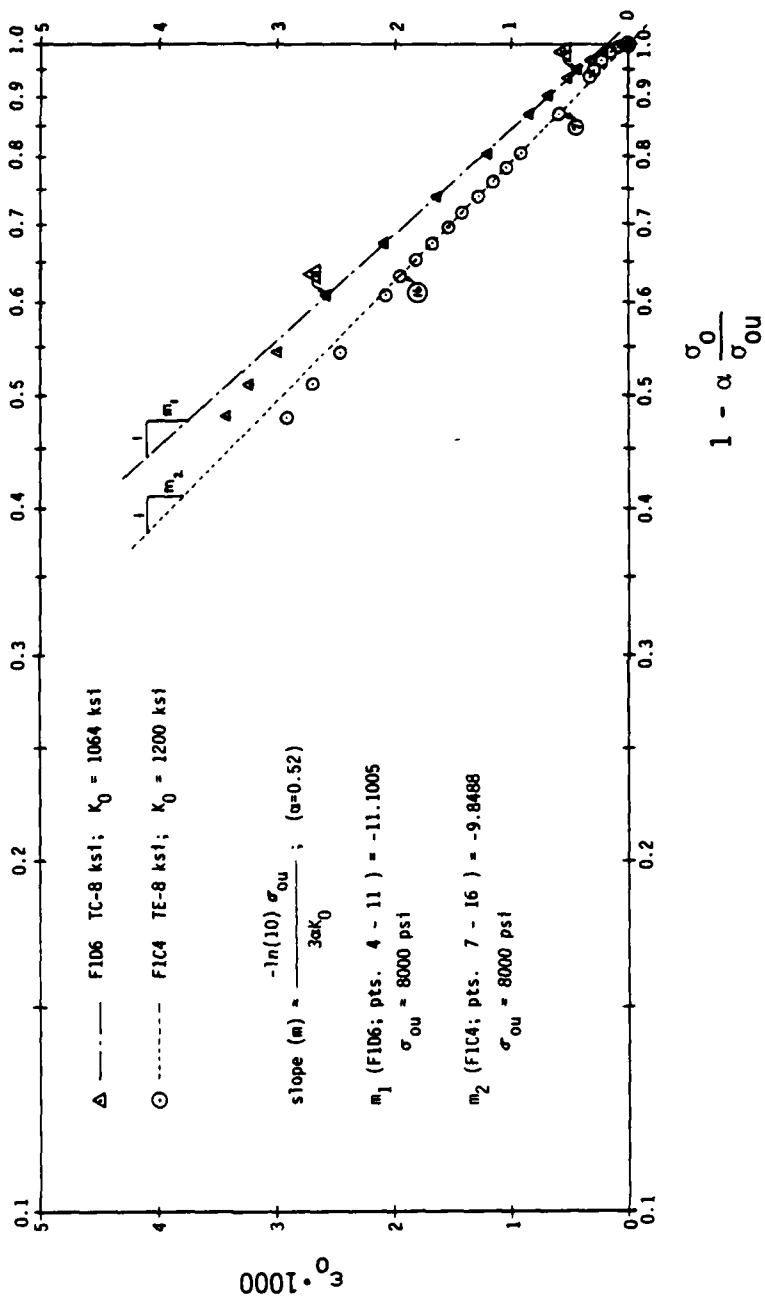


Fig. 5.50. ϵ_0 vs. $\log(1 - \alpha \cdot \sigma_0 / \sigma_{ou})$ Examples for Determining K_0 ($\alpha=0.52$).

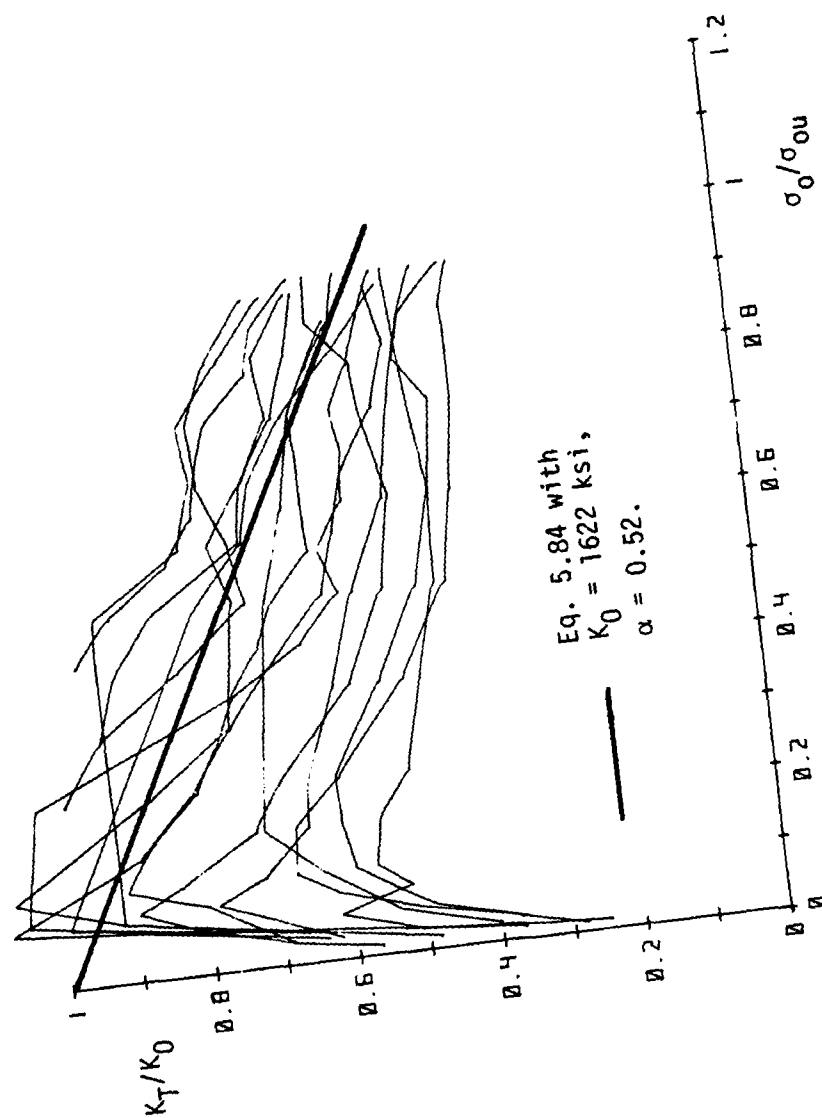


Fig. 5.51. Normalized K_T/K_0 vs. σ_0/σ_{ou} Results.

Coupling Relations

Gerstle, et. al. (50) observed that plain concrete exhibits a volume change due to stress deviation as shown in Fig. 1.16. This phenomenon is expressed by the coupling modulus H_T according to Eq. 5.67a where H_T is the slope of the τ_0 - ϵ_0 curves, i.e.

$$H_T = \frac{d\tau_0}{d\epsilon_0} . \text{ This observed volume change during deviatoric loading}$$

was found to be essentially linear, possessing a constant slope at constant confining pressure σ_0 . However, it was observed that the coupling modulus decreased radically with increasing confining pressure σ_0 as shown in Fig. 1.18. Gerstle (48) developed an analytical function relating the coupling modulus H_T with σ_0 by a hyperbola of the following form:

$$H_T = a + \frac{b}{\sigma_0 - c} ; \sigma_0 > c \quad (5.88)$$

where a and c are the horizontal and vertical asymptotes of the hyperbolic relation, respectively, and b governs the shape. Notice that for $\sigma_0 \leq c$, no coupling between volume change and shear deviation occurs, as observed by Gerstle, et. al. (50).

The same phenomenon of volume change under shear deviation was seen to occur in the CU-SFRC as demonstrated in Figs. 4.41-4.68 for individual specimens with average results shown in Figs.

4.101-4.106. The coupling is essentially linear until volume dilation (failure as defined in this report) takes place and was found to be a function of the confining pressure σ_0 . Therefore the same relation given by Eq. 5.88 is used relating H_T with σ_0 . It remains to determine the three constants a , b and c since those

given by Gerstle (48) are not valid for the CU-SFRC because this material has exhibited stiffer behavior than plain concrete. The procedure is described below.

Since the coupling between τ_0 and ϵ_0 shown in Figs. 4.41-4.68 is essentially linear, a linear regression through the τ_0 - ϵ_0 data below the dilation point was performed on all the results to determine the best fit lines and consequently the slopes H_T . These values are plotted vs. the confining pressure σ_0 and shown in Fig. 5.52. Since three levels of hydrostatic stress were employed in this research, average H_T values at those pressures were calculated in order to determine the three constants a, b and c given in Eq. 5.88. These values are:

σ_0 (ksi)	H_T (ksi)
4	13,390
6	8,000
8	6,140

Substituting these three average data points into Eq. 5.88 results in three equations which when solved simultaneously for the unknowns a, b and c result in:

$$\begin{aligned}
 a &= 2,300 \text{ ksi (horizontal asymptote)} \\
 b &= 23,450 \text{ ksi}^2 \\
 c &= 1.885 \text{ ksi (vertical asymptote)}
 \end{aligned}
 \tag{5.89}$$

Eq. 5.88 becomes:

$$H_T = 2,300 + \frac{23,450}{\sigma_0 - 1.885} \quad (\text{ksi})
 \tag{5.90}$$

with $\sigma_0 > 1.885$ ksi. This hyperbolic curve is also shown on Fig.

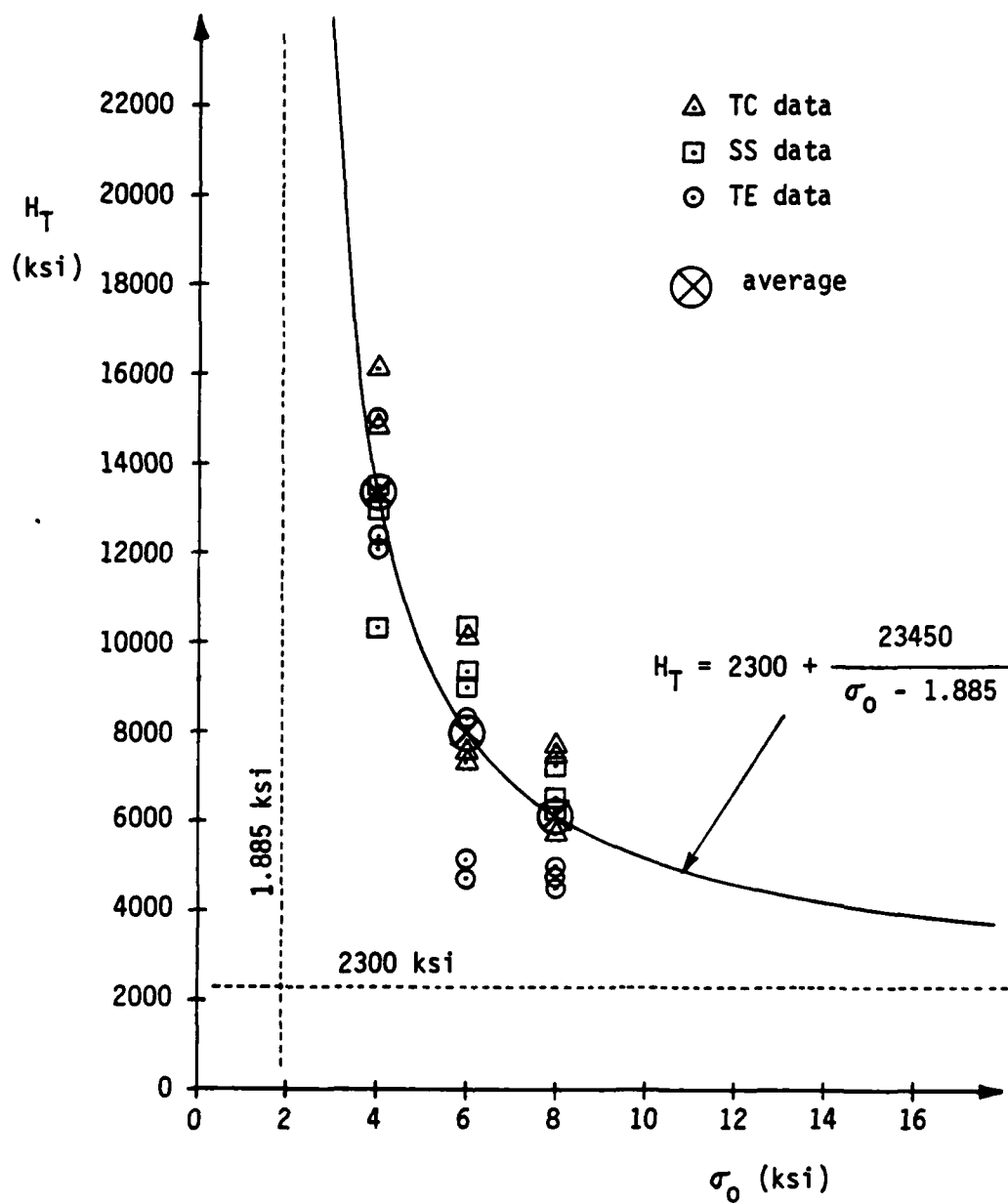


Fig. 5.52. Variation in Coupling Modulus H_T with Confining Pressure σ_0 .

5.52. As Gerstle (48) suggests, the data base for determining the coupling relation H_T must be considered as very preliminary.

5.3.2 Experimental Verification of the "Simple Formulation" with the CU-SFRC

The CU-SFRC triaxial test program is described in Section 2.8, where the specimens were loaded hydrostatically to a predefined level of hydrostatic stress, followed subsequently by monotonic shear deviation at constant confining pressure to failure along either the TC, SS or TE stress path as shown in Figs. 2.31 and 2.32.

The incremental octahedral stresses and strains defined by Eqs. 5.62-5.66 are general and valid for non-proportional loading as long as the step sizes remain small. But for the CU-SFRC research, proportional loading was employed, therefore, these relations reduce to those given by Gerstle (47,48). No non-proportional loading tests were conducted, therefore verification of Eqs. 5.62-5.66 is not possible.

Some sort of failure data determined experimentally or analytically is required in the simple formulation to define the tangent shear modulus relation given by Eq. 5.78. The CU-SFRC tests were carried to failure, thus permitting the determination of the failure envelope. The Willam-Warnke failure criterion (134) calibrated for this material as described in Section 5.2.1.1 was the analytical model used to predict the strengths required for the simple formulation.

The relations for the moduli G_T , K_T and H_T given by Eqs. 5.78, 5.84 and 5.90 with $G_0 = 1969$ ksi, $K_0 = 1622$ ksi and $\alpha = 0.52$, in conjunction with the constitutive relations given in Eqs. 5.67

permit the prediction of the principal strain increments (Eqs. 5.73-5.75) and subsequently principal strains from given principal stress increments.

Figs. 5.53-5.61 show the principal stress-strain summary curves for all the experimental results. The stress path (TC, SS or TE) and level of hydrostatic stress at which shear deviation occurred ($\sigma_{om} = 4, 6$ or 8 ksi) are given in the figures. Note that the major principal stress σ_1 is normalized with respect to σ_{om} . Superimposed on these curves, by dashed lines, are the predictions employing the simple theory where the variations in the bulk and shear moduli are shown by solid lines on Figs. 5.51 and 5.49 respectively. The dashed-dot lines shown were obtained by using a different shear modulus relation, given by the dashed line on Fig. 5.49, but employ the same bulk modulus relation. These will be discussed later.

The purpose of the simple formulation is to predict the principal strains from given principal stresses. Therefore octahedral stress-strain results showing the comparisons between experiment and the predictions by the simple formulation are not presented.

On the average, the simple formulation predicts the response during hydrostatic compression as well as can be expected in light of the amount of scatter present. After hydrostatic compression, the predictions are good for the lower levels of shear deviation but then become more compliant than what is seen experimentally in all cases. This can be explained by the shear modulus G_T variation used, as shown by the solid line in Fig. 5.49 where for a given

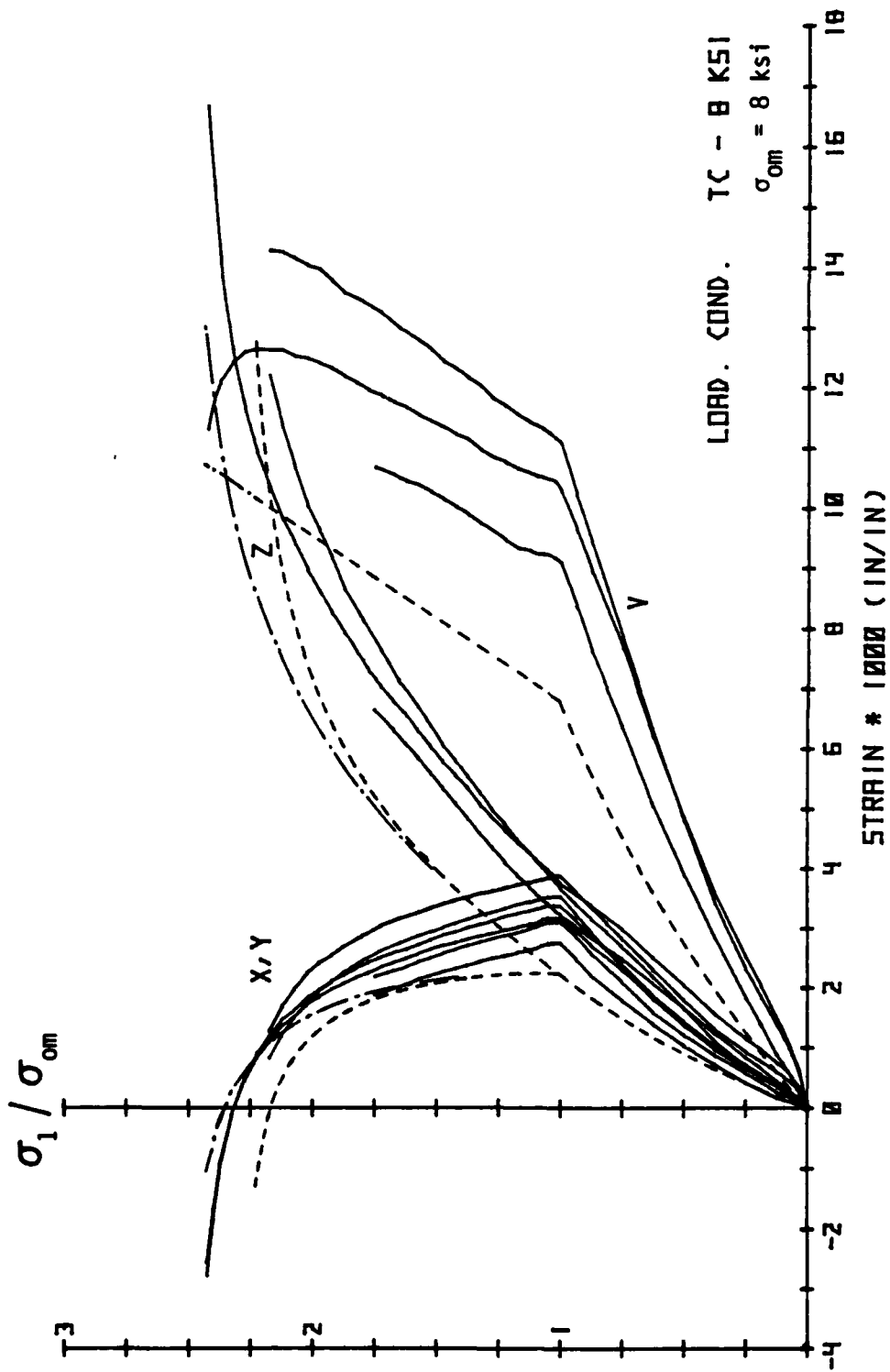


Fig. 5.53. Principal Stress-Strain Summary Results with Predictions from the "Simple Formulation".

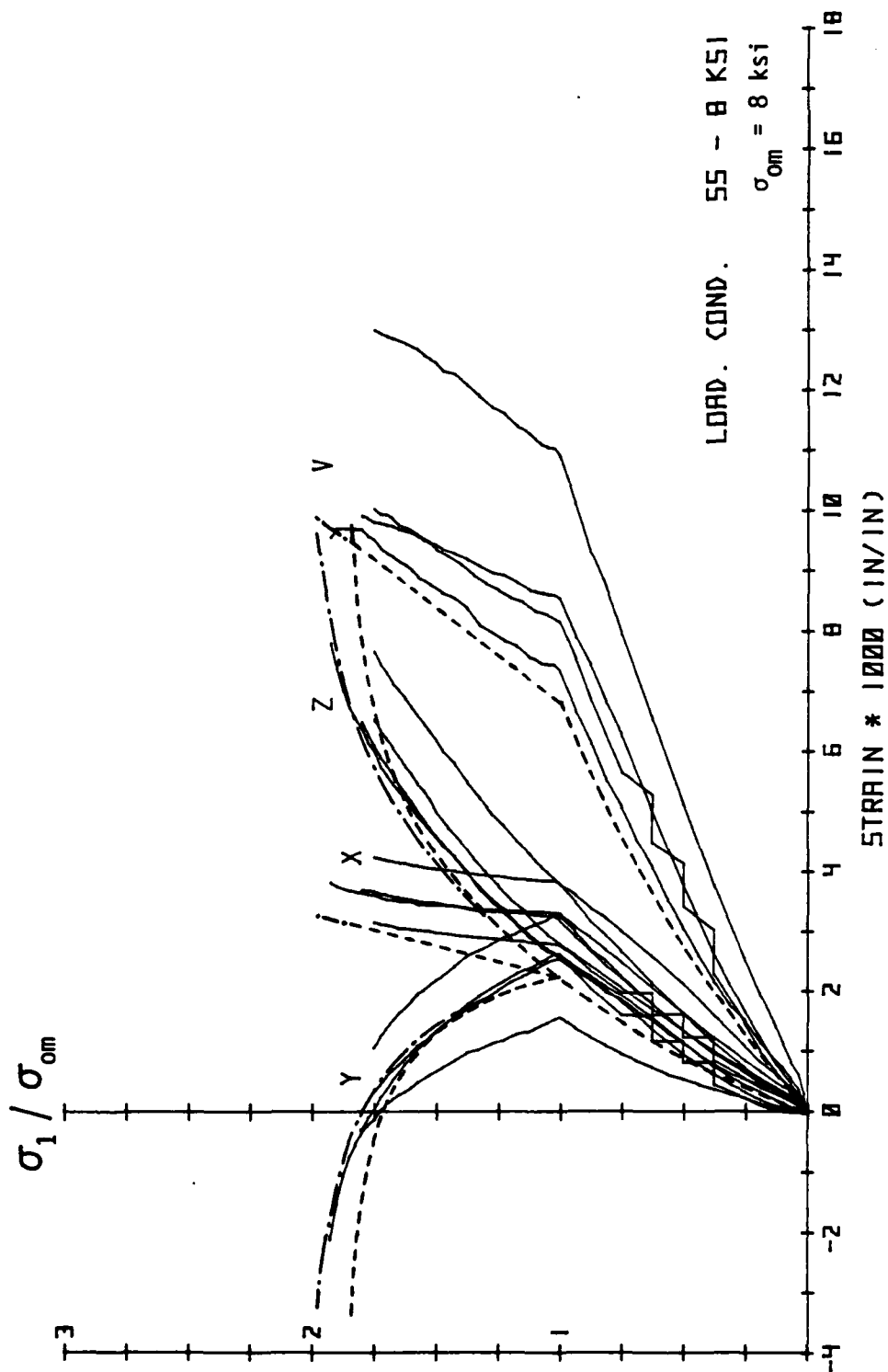


Fig. 5.54. Principal Stress-Strain Summary Results with Predictions from the "Simple Formulation".

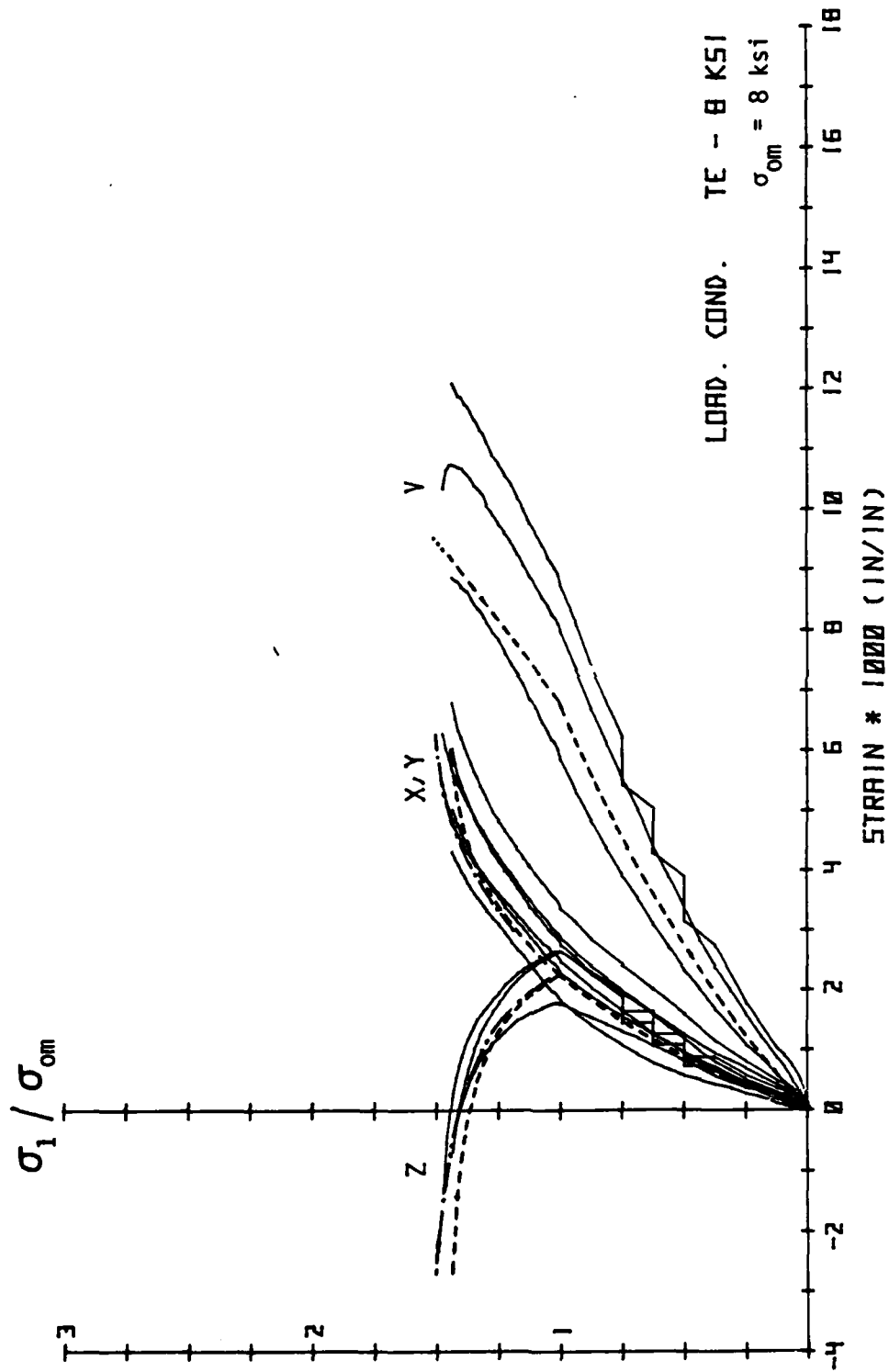


Fig. 5.55. Principal Stress-Strain Summary Results with Predictions from the "Simple Formulation".

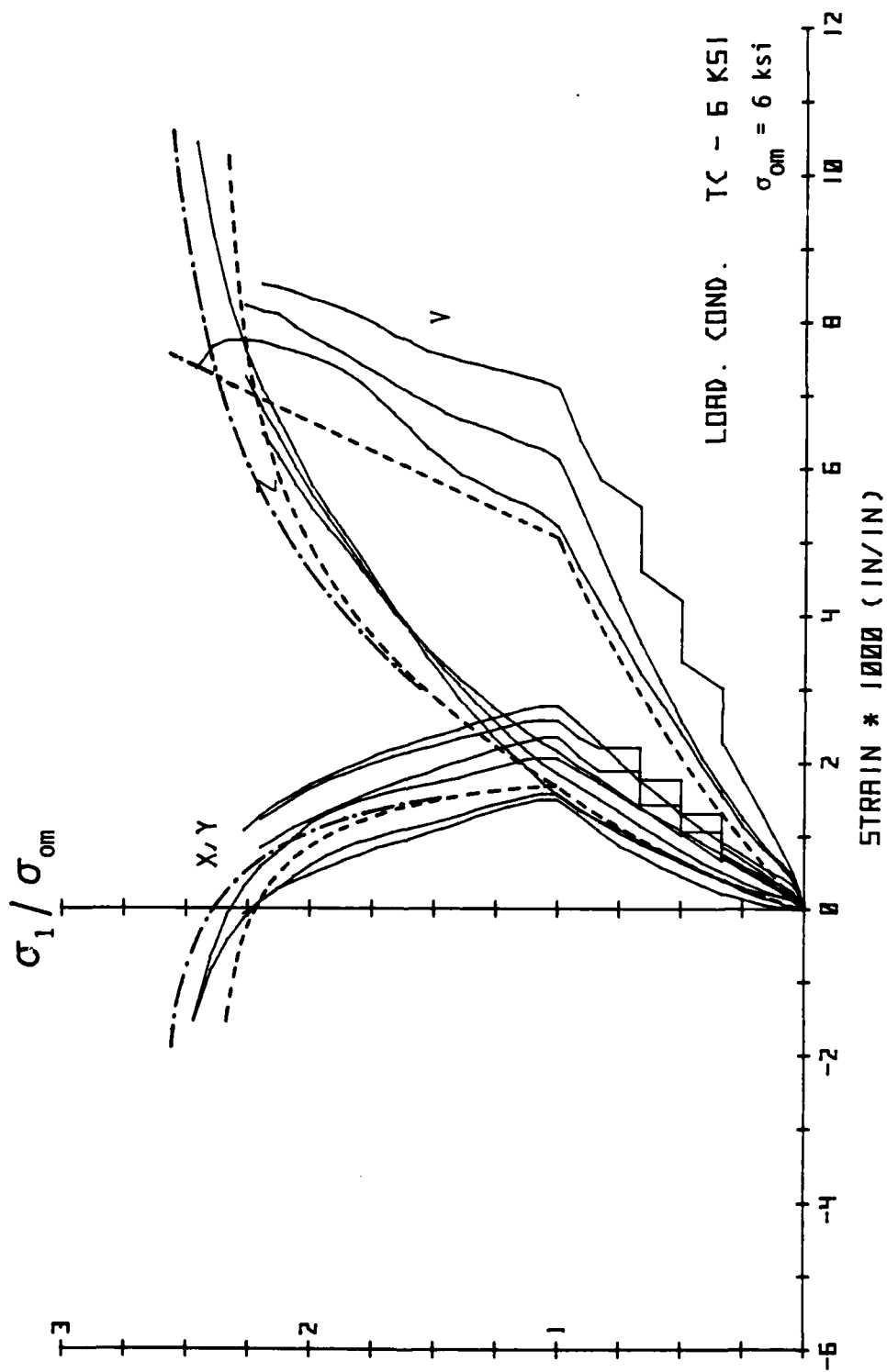


Fig. 5.56. Principal Stress-Strain Summary Results with Predictions from the "Simple Formulation".

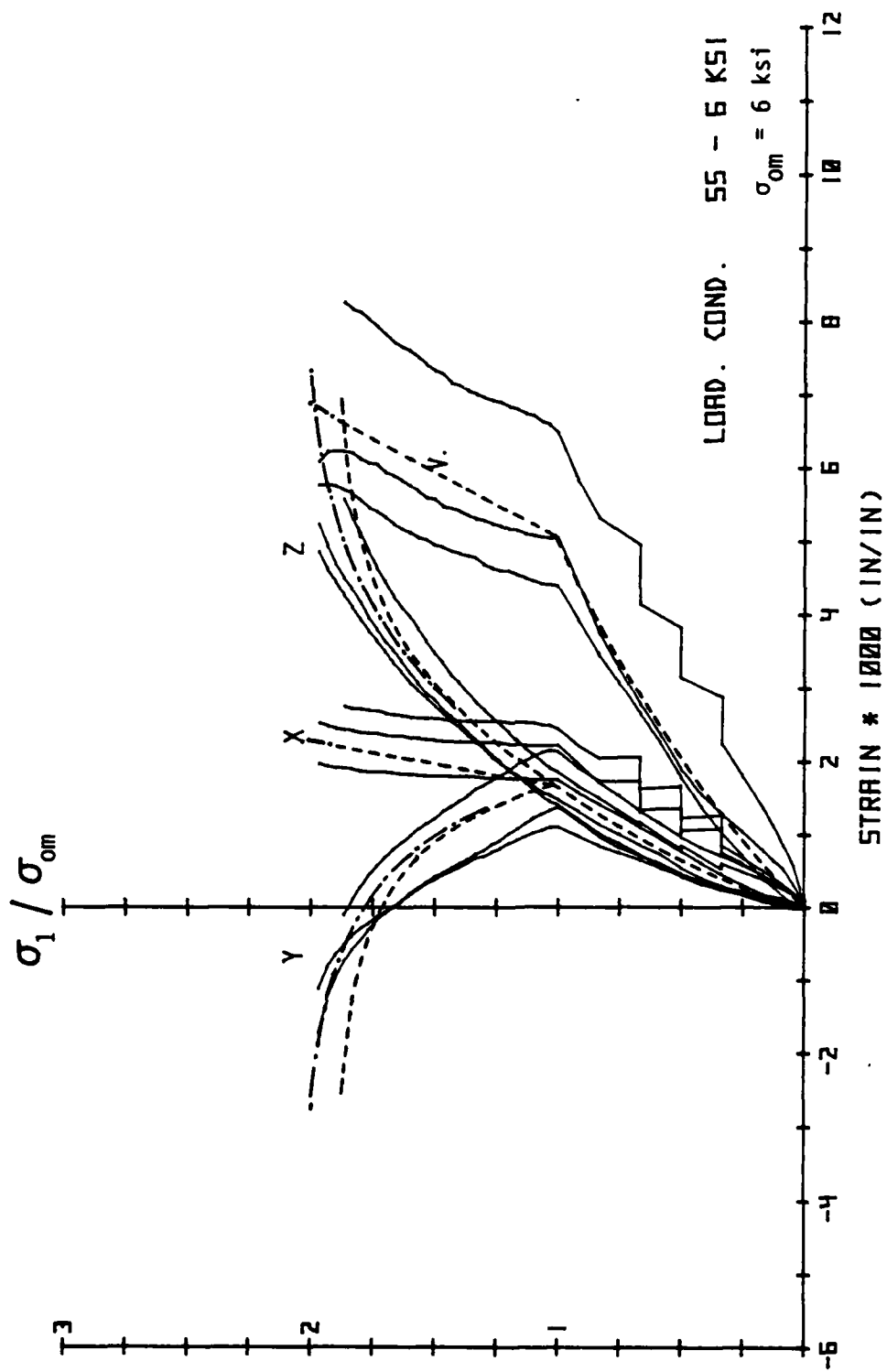


Fig. 5.57. Principal Stress-Strain Summary Results with Predictions from the "Simple Formula".

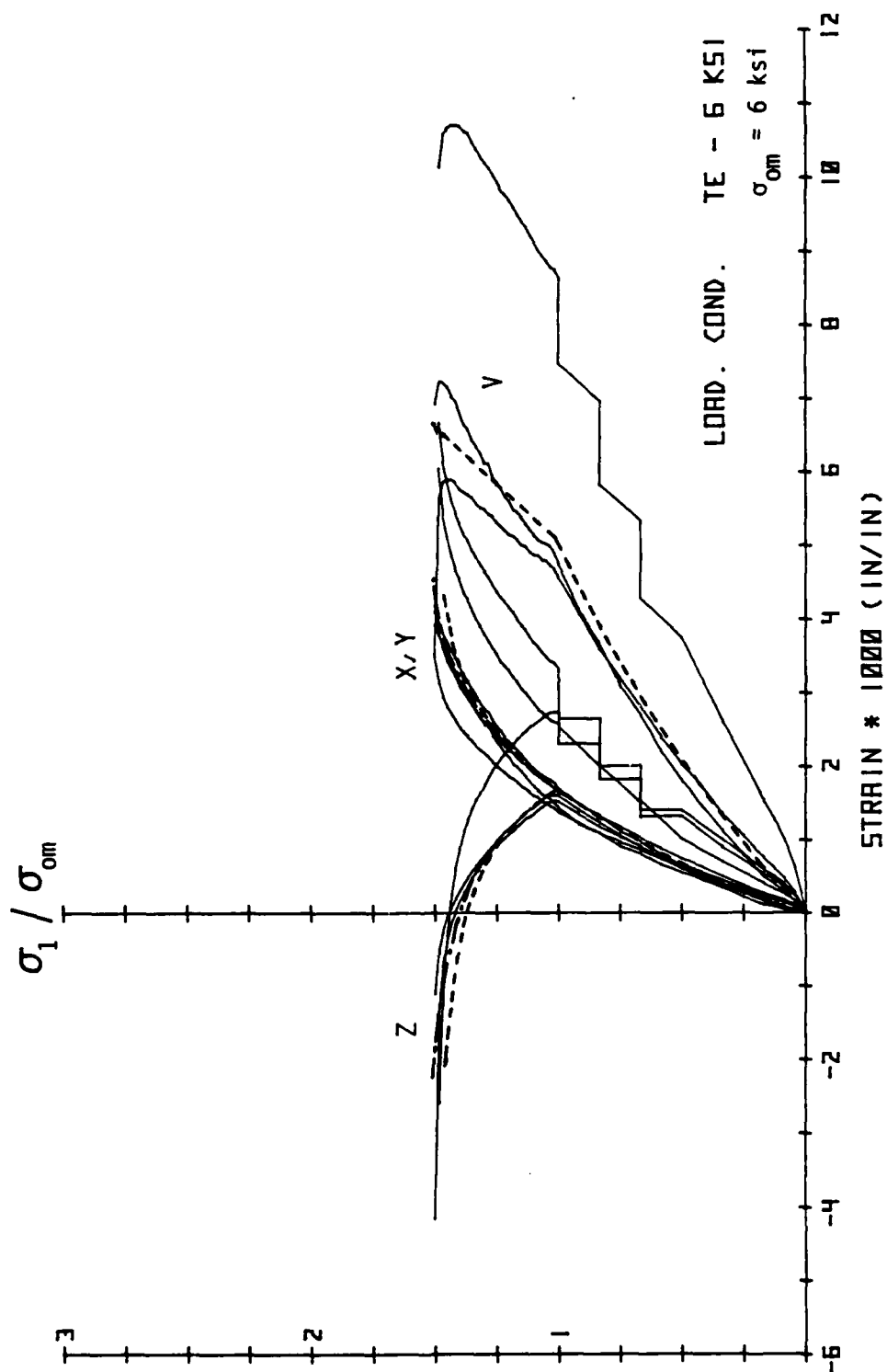


Fig. 5.58. Principal Stress-Strain Summary Results with Predictions from the "Simple Formulation".

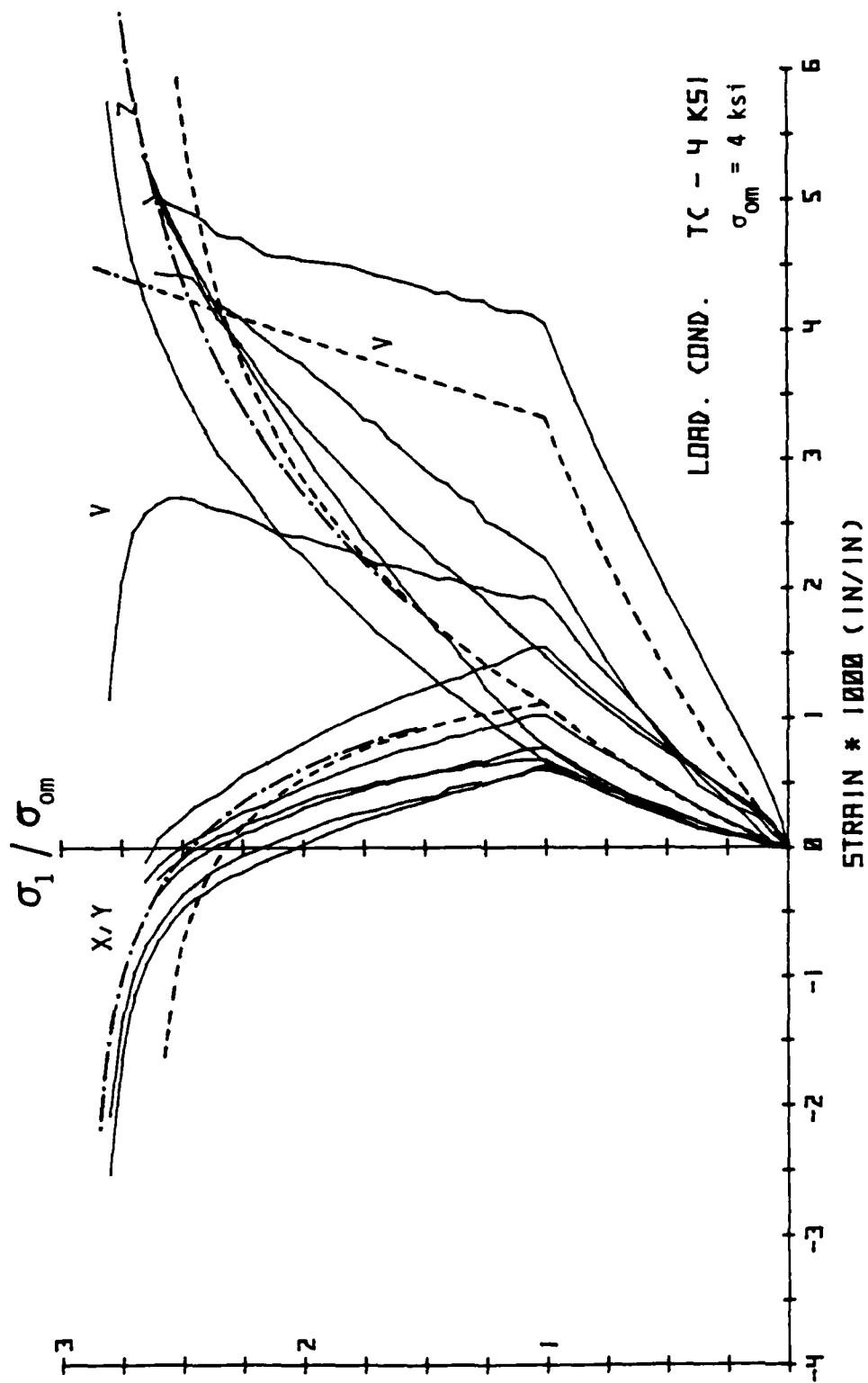


Fig. 5.59. Principal Stress-Strain Summary Results with Predictions from the "Simple Formulation".

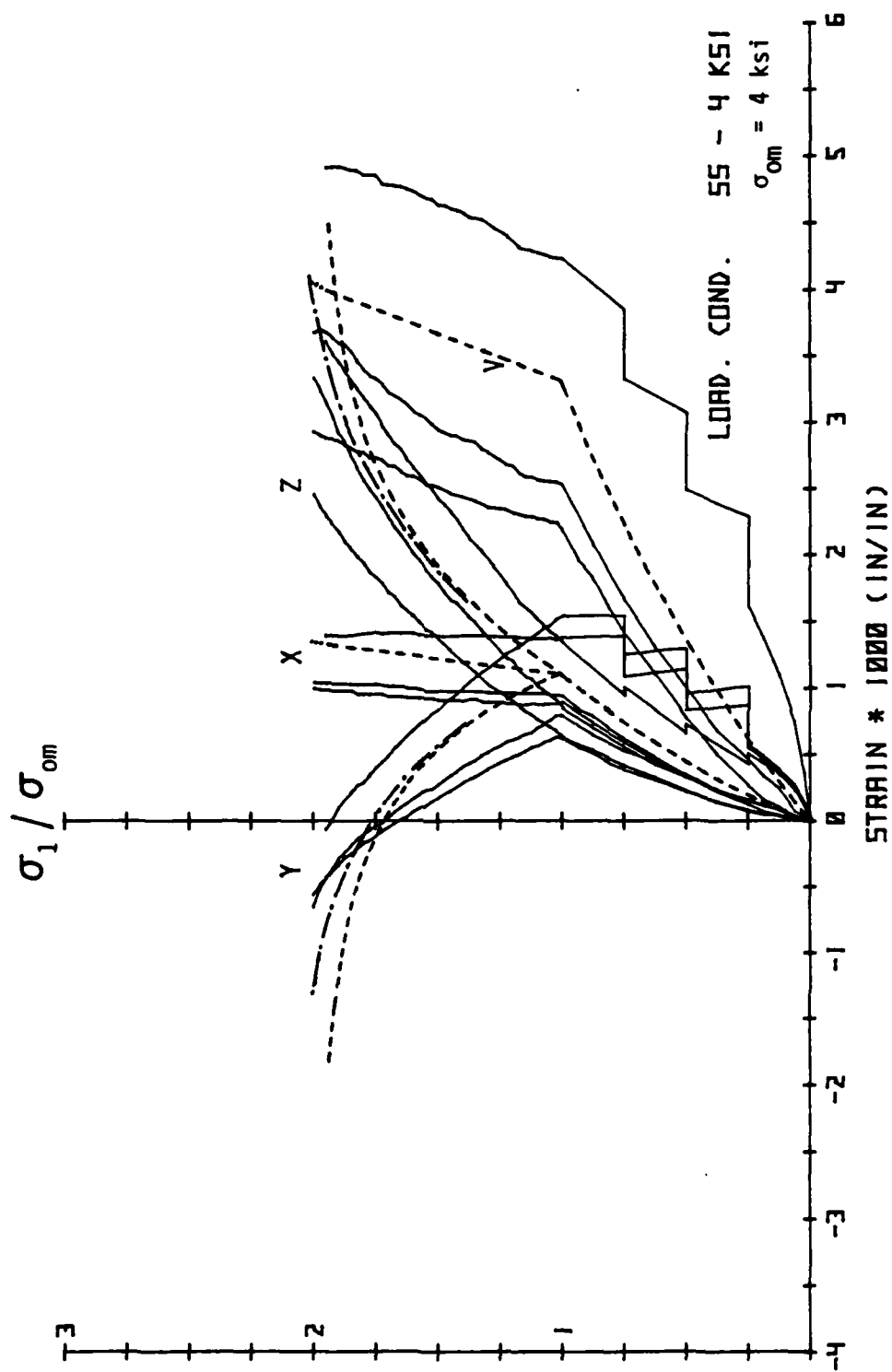
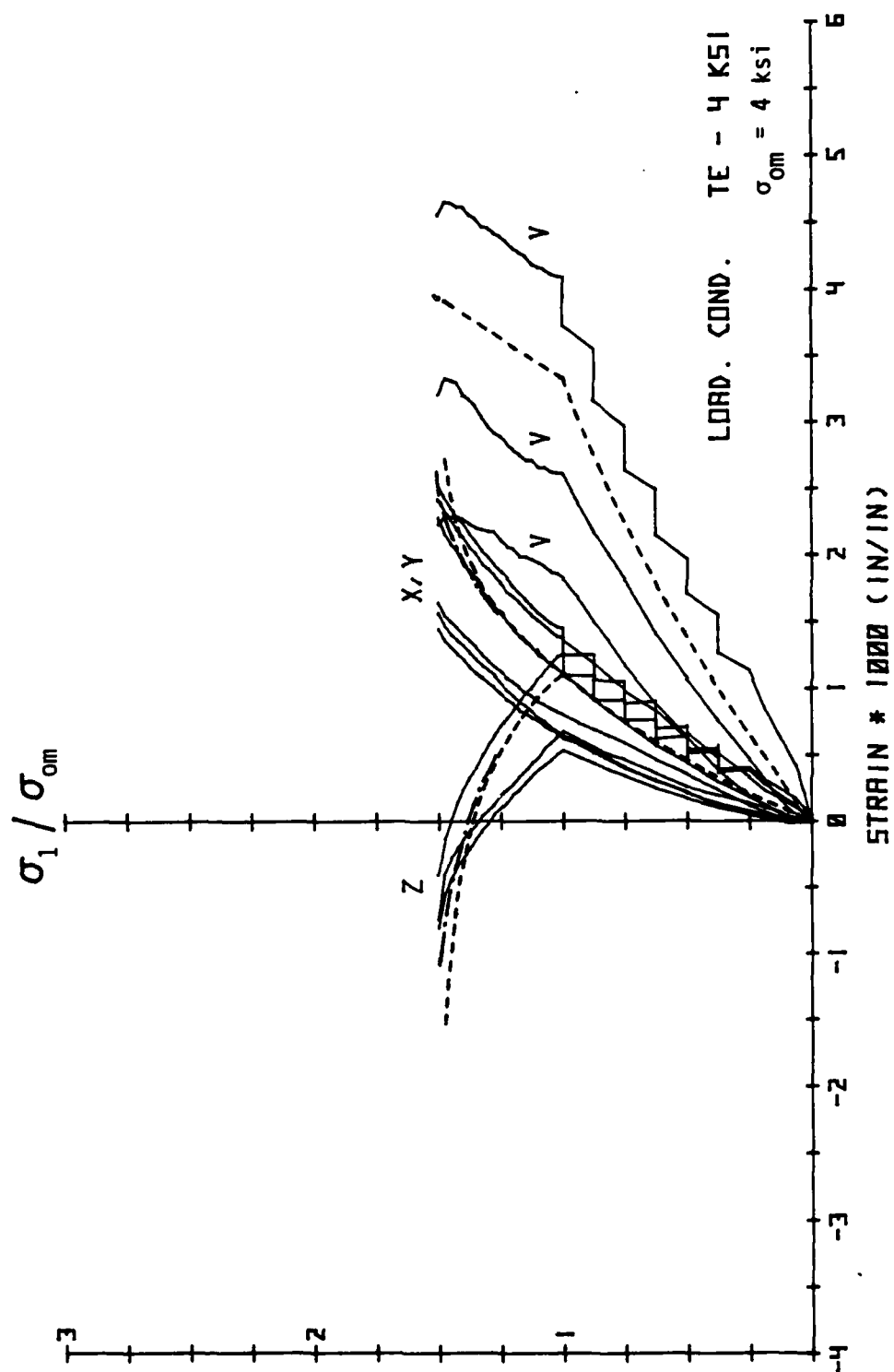


Fig. 5.60. Principal Stress-Strain Summary Results with Predictions from the "Simple Formulation".



shear stress τ_0 , at the higher levels, the modulus G_T calculated from the relation is lower than what is, on the average, seen experimentally. This stems from the calculation of the failure strengths τ_{ou} , in which dilation was chosen as failure resulting in lower strengths than would be obtained had a ductile failure definition been used. Examining the average tangent shear modulus vs. octahedral shear stress curves ($G_T - \tau_0$) shown in Figs. 4.89-4.91, one can determine the ductile failure strengths by extrapolating these curves to find the value of τ_0 at which the tangent shear modulus G_T becomes zero. Doing this for all the results, one finds that on the average, the strengths predicted employing the ductile failure definition are about 15% higher than those determined from the failure as dilation criterion.

If the ductile failure strength envelope is employed in a new shear modulus variation as shown by the dashed line in Fig. 5.49 is obtained. Then for a given shear stress τ_0 , the shear modulus G_T predicted is shown to better match the experimental results. Employing this relation in the simple formulation results in stiffer, better predicted response on the average during shear deviation, especially at the higher levels, as shown by the dashed-dot lines in Figs. 5.53-5.61.

Notice also in the figures that the volumetric stress-strain curves during shear deviation, regardless of which shear modulus variation is used, are linear to failure. This is because the coupling modulus H_T calculated from Eq. 5.90 is constant for constant confining pressure. Therefore the coupling between shear

deviation τ_0 and volumetric response ϵ_v must be linear. Consequently, with the coupling relation as it stands, the simple formulation cannot predict the behavior after failure.

The question arises as to the definition of failure. Should it be defined as the point at which dilation of the specimen occurs, or should it be determined from the ductile failure definition according to plasticity theory when $G_T = 0$ as suggested by Gerstle (47,48)? One could argue both points. Certainly, failure defined by dilation is conservative in comparison with ductile strengths. Problems arise in using the latter when a fluid cushion testing apparatus is employed, simply because one never gets a ductile failure in such a device, whereas specimen dilation can be obtained quite consistently. If one desires to determine the ductile strengths, then the G_T - τ_0 results must be plotted, allowing through extrapolation, the estimation of the strengths τ_{ou} where $G_T = 0$. This procedure is much easier than trying to "guess" the value of τ_{ou} at which $G_T=0$ from a deviatoric stress-strain (τ_0 - γ_0) curve.

All in all, the overall correlation between the experimental results and the predictions by the simple formulation, using both shear modulus relations, is satisfactory. The formulation appears to capture some of the essential characteristics of the response for the type of stress paths employed here.

Some of the drawbacks of the simple formulation were given in the first part of this section. In short, the theory is incapable of predicting the behavior under tensile or cyclic loads. Material anisotropy is not incorporated into the formulation because the assumption of isotropy is made in order to be able to assume the

coaxiality of the incremental deviatoric stress and strain vectors,

namely $\frac{ds_2}{ds_1} = \frac{de_2}{de_1}$ as given by Eq. 5.68. Stress induced anisotropy from previous stress histories are not considered either. Some additional drawbacks are given below.

With the proposed exponential deviatoric stress-strain ($\tau_o - \gamma_o$) relation given by Eq. 5.77, the simple formulation cannot predict post-peak behavior, i.e., the descending branch of the stress-strain curve, because this relation has an asymptote at $\tau_o = \tau_{ou}$, and has no descending branch. Dilatation cannot be predicted either because the proposed coupling modulus relation is a function of confining pressure only.

At this time, the simple formulation does not take into account the dependency on the stress path, i.e. the effect of the third stress invariant is not included except in the calculations of the shear strength τ_{ou} . These latter calculations for shear strength are based on the Willam-Warnke failure criterion which does include the third stress invariant in calculating the failure envelope. Any other criterion that incorporated this would be suitable as well. In this way, the shear stiffness relation proposed for the material becomes dependent on the stress path because it incorporates τ_{ou} in its calculation. However if the Drucker-Prager failure criterion had been employed, a circular failure envelope in the deviatoric plane would result, making the simple formulation totally independent of the stress path.

CHAPTER 6

SUMMARY, CONCLUSIONS AND RECOMMENDATIONS FOR FUTURE WORK

6.1 Summary

In this investigation, two sets of tests were conducted. The first consisted of basic tests on five concretes with different randomly oriented steel fibers. The purpose was to aid in the determination of one steel fiber reinforced concrete for the second set of tests where the strength and deformational response of the material subjected to multiaxial compressive stresses along three different monotonic stress paths was studied. In both sets, all tests were conducted in triplicate, and the results of the second set of compression tests were used to calibrate several constitutive models for predicting the strength and behavior of the steel fiber reinforced concrete under multiaxial compressive loads.

6.2 Conclusions

The addition of steel fibers to the plain concrete mix definitely decreases the workability of the mixture but by no means were any of the mixes unworkable because the volume percentage employed remained well below the critical volume percentage. It was observed that the workability decreased as the fiber aspect ratio (or length) increased, primarily in the placing and vibrating the concrete into the molds. However, all fibers performed well during

mixing and good workability was achieved for all the mixes at the 0.6% fiber volume percentage.

It is concluded from the preliminary test series that the addition of steel fibers to concrete increases the ductility, toughness, stiffness and strength of the material. It was found that the fiber aspect ratio should not be singled out as the only parameter that affects the material properties. Other fiber properties should be considered as well. For instance, the compressive strength was found to increase proportionally with the number of fibers per cubic inch of concrete. At the same time, an inverse relationship was found between the fiber length and aspect ratio with compressive strength whereas the material's tensile strength increased proportionally with increasing fiber length. It was also noticed that the deformed ends on the "Dramix" fibers added to the fiber development length in comparison with the straight "Fibercon" fibers.

Quantitative values of the strengths with percentage improvements over the same plain concrete mix properties are given in TABLE 3.2 for all the mixes in the preliminary test series.

From the preliminary test results, it was necessary to make a decision as to which fiber to use for the final test series. Based on those results the ZP 30/.40 "Dramix" deformed fiber was chosen because first of all, for the same volume percentage, the deformed fibers proved to be superior to the straight fiber in load carrying capacity in tension due simply to the bent ends increasing the development length. Since one purpose of the study was to investigate the effect of varying aspect ratio and/or length on the

different material properties, the "Fibercon" fiber which was available in only one size was never intended to be used in the final test series. The mix employing the ZP 30/.40 deformed fiber produced experimental results that were intermediate with all other mixes tested in the preliminary series. The consistency of this mix was good and the reproducibility of the test results was very good. Above all, from a workability standpoint, this mix was the easiest to work with and specimens could be the most easily prepared using this mix.

Many conclusions are drawn from the final test series. First of all, under multiaxial compression, the material's deformational and strength response is strongly stress path and confining pressure dependent resulting in a bullet-shaped failure envelope. These observations are nothing new to plain concrete behavior and should be been anticipated for the SFRC as well.

The coupling between stress deviation τ_0 and volumetric response ϵ_0 (the dilatancy effect) was observed to be also stress path dependent for higher confining pressures but independent of the stress path for the lowest confining pressure employed in the tests. From this coupling response came the decision to use the point of dilation (transition from volume contraction to expansion) as failure, as past researchers have done for plain concrete, because it was an easily quantifiable value from the response rather than guessing at a value at which ductile failure might occur, i.e.,

the value of τ_0 at which $G_T = 0$. The point of dilation has been described as the onset of unstable fracture propagation or the point of critical energy release in the material.

Several constitutive models were investigated for predicting the strength and behavior of the SFRC. They were the Willam-Warnke and Lade failure criteria and Gerstle's "Simple Formulation" for the stress-strain behavior. Both of the investigated failure criteria predicted the strength of the SFRC very well when calibrated for that material. The Willam-Warnke failure criterion proved to be very sensitive to the input data and gave very spurious results when calibrated from strength data obtained from tests where the specimen type and boundary conditions were different. The Lade failure criterion proved to be less sensitive to the input data because it employs a regression analysis to determine the model parameters, whereas the Willam-Warnke criterion does not. Based on these results, it was deduced that no model should be calibrated from tests where the boundary conditions and specimen types differ.

The normality of the SFRC was examined by plotting the post-peak plastic strain increment vectors and superimposing them on the failure surface. With failure defined as dilation, no claim to normality can be made for this material, as one would expect, since concrete is not an elastic-perfectly plastic material.

Gerstle's "Simple Formulation" proved to work quite well in predicting the stress-strain behavior. The formulation appears to capture the essential characteristics of the material's response but certain shortcomings are foreseen in the model that did not affect

the behavior predictions of the SFRC. At this point the formulation is incapable of predicting material behavior under tensile or cyclic loads. Stress-induced anisotropy is not possible either. In addition, the only way the formulation incorporates the stress path is via the arbitrary failure criterion employed by it. If a failure criterion that does not include the third stress invariant had been used, the formulation would be totally stress path independent.

All in all, the bottom line conclusions from the multiaxial tests are that the SFRC appears to possess many of the same characteristics under multiaxial compression as plain concrete. Even constitutive models formulated for plain concrete work well for the SFRC in the range of stresses investigated in this research. For higher confining pressures, it remains to be seen how much more ductile this material is than plain concrete. But more importantly, the improvements in this material over plain concrete under combined compression-tension loads are needed.

6.3 Recommendations for Future Work

As just mentioned, tests in the low compression and combined tension compression regimes are needed in order to elucidate the response of the material under this type of loading and see what improvements the SFRC offers over plain concrete, since the fibers are supposed to greatly improve the tensile capabilities of the material.

It is also necessary to conduct some multiaxial compression tests on the same plain concrete mix as used in the SFRC, but of course without the fibers, to see what improvements overall are

provided by the addition of steel fibers to a plain concrete mix. This is necessary because one cannot simply take behavior results from any plain concrete, normalize them, and apply them to this plain concrete used for the SFRC simply because the materials are completely different.

It would be interesting to have test results where the fiber volume percentage were, say, twice as much as what was used in this research, to observe the effect of increasing fiber concentration on the material properties. With a fiber concentration of 160 lbs/yd³, the mix would still be workable, but approaching the limit of workability, as discussed in Chapter 2.

BIBLIOGRAPHY

1. Aleszka, J.C. and P.W.R. Beaumont, "The Fracture Behavior of Plain, Polymer-Impregnated, and Fiber-Reinforced Concrete," UCLA-ENG-7396, December, 1973.
2. Ali, M.A., A.J. Majumdar and B. Singh, "Properties of Glass Fibre Cement--The Effect of Fibre Length and Content," Journal of Materials Science, Vol. 10, 1975, pp. 1732-1740.
3. ACI Committee 544, "State-of-the-Art Report on Fiber Reinforced Concrete," Journal of the American Concrete Institute, Proceedings, Vol. 70, No. 11, Nov. 1973, pp. 729-744.
4. ACI Committee 544, "State-of-the-Art Report on Fiber Reinforced Concrete," Fiber Reinforced Concrete; an International Symposium, Publ. by ACI., Publication SP-44, © 1974, pp. 535-550.
5. ACI Journal, "Concrete--Year 2000," Journal of the American Concrete Institute, N8, 1971, pp. 581-589.
6. American Concrete Institute (ACI SP-34), Concrete for Nuclear Reactors, American Concrete Institute, Special Publication SP-34, Vol. 1, © 1972.
7. American Society for Testing and Materials (ASTM), Annual Book of ASTM Standards, Part 14, Published by ASTM, © 1975.
8. Andenes, E., "Response of Mortar to Biaxial Compression," M.S. Thesis, University of Colorado, Dept. of Civil, Environmental and Architectural Engineering, 1974.
9. Andenes, E., K. Gerstle, and H.Y. Ko, "Response of Mortar and Concrete to Biaxial Compression," Journal of the Engineering Mechanics Division, ASCE, Vol. 103, No. EM4, Proc. Paper 13115, Aug. 1977, pp. 515-526.
10. Argyris, J.H., K.E. Buck, D.W. Scharpf and K.J. Willam, "Non-Linear Methods of Structural Analysis," Nuclear Engineering and Design, Vol. 19 (1972), No. 1, pp. 169-197.
11. Argyris, J.H., G. Faust, J. Szimmat, E.P. Warnke and K.J. Willam, "Recent Developments in the Finite Element Analysis of Prestressed Concrete Reactor Vessels," Nuclear Engineering and Design, Vol. 28 (1974), No. 1, pp. 42-75.

12. Argyris, J.H., G. Faust and K.J. Willam, "A Unified Stress-Strain Law for Triaxial Concrete Failure," 3rd Post Conference on Computational Aspects of the Finite Element Method, Sept. 8-9, 1975, pp. 359-402. © Imperial College, London, United Kingdom.
13. Argyris, J.H., G. Faust and K.J. Willam, "Limit Load Analysis of Thick-Walled Concrete Structures- A Finite Element Approach to Fracture," Computer Methods in Applied Mechanics and Engineering, Vol. 8, (1976), pp. 215-243, © North-Holland Publishing Company.
14. Argyris, J.H., L.E. Vaz and K.J. Willam, "Improved Solution Methods for Inelastic Rate Problems," Computer Methods in Applied Mechanics and Engineering, Vol. 16, (1978), pp. 231-277, © North-Holland Publishing Company.
15. Atkinson, R. H., "A Cubical Test Cell for Multiaxial Testing of Materials," Report Submitted to Bureau of Mines, U.S. Dept. of the Interior, Under Grant No. G0110894, "Constitutive Relations of Coal," Dept. of Civil and Environmental Engineering, University of Colorado, Boulder, Colorado, July 1972.
16. Atkinson, R.H., and H.Y. Ko, "A Fluid Cushion, Multiaxial Cell for Testing of Cubical Rock Specimens," Int. J. Rock Mech. Min. Science, Vol. 10, 1973, pp. 351-361.
17. Aveston, J., G.A. Cooper and A. Kelly, "Single and Multiple Fracture," The Properties of Fiber Composites, IPC Science and Technology Press, 1971, pp. 15-26.
18. Aveston, J. and A. Kelly, "Theory of Multiple Fracture of Fibrous Composites," Journal of Materials Science, Vol. 8, 1973, pp. 352-362.
19. Aveston, J., R.A. Mercer and J.M. Sillwood, "Fiber Reinforced Cements--Scientific Foundations for Specifications," Composites--Standards, Testing and Design, IPC Science and Technology Press, 1974, pp. 93-102.
20. Balmer, G.G., "Shearing Strength of Concrete Under High Triaxial Stress--Computation of Mohrs Envelope as a Curve," Structural Research Laboratory Report No. SP-23, United States Dept. of the Interior, Bureau of Reclamation, Washington, D.C., 1949.
21. Bazant, Z. P. and T. Tsubaki, "Total Strain Theory and Path-Dependence of Concrete," Journal of the Engineering Mechanics Division, ASCE, Vol. 106, No. EM6, Proc. Paper 15911, Dec. 1980, pp. 1151-1173.

22. Beckett, R.E., "Handling and Placing of Fibrous Concrete," Fiber Reinforced Concrete, An International Symposium, Publ. by ACI, Publication SP-44, © 1974, pp. 337-350, SP 44-19.
23. Bieniawski, Z.T., "Mechanism of Brittle Fracture of Rock," International Journal of Rock Mechanics and Mining Sciences, Vol. 4, No. 4, October 1967, pp. 395-406.
24. Biryukovich, K.L. i dr. Steklocement, "Budivelnik," Kiev, 1964.
25. Blume, J.A., "Structural Dynamics in Earthquake Resistant Design," Transactions, ASCE, 125, 1088-1139 (1960).
26. Boresi, A.P., O.M. Sidebottom, F.B. Seely and J.O. Smith, Advanced Mechanics of Materials, Third Edition, Published by John Wiley and Sons, © 1978.
27. Brandshaug, T., V. Ramakrishnan, W.V. Coyle and E.K. Schrader, "A Comparative Evaluation of Concrete Reinforced with Straight Steel Fibers and Collated Fibers with Deformed Ends," prepared for: BEKAERT STEEL WIRE CORPORATION by South Dakota School of Mines and Technology, Report SDSM&T--CBS 7801, May 1978.
28. Bresler, B., and K.S. Pister, "Failure of Plain concrete Under Combined Stresses," Proceedings,--Separate No. 674, Transactions, April, 1955.
29. Bresler, B. and K.S. Pister, "Strength of Concrete Under Combined Stresses," ACI Journal, V. 30, No. 3, September 1958 (Proceedings V.55), p. 321.
30. Brown, Lt. Col. D., "Steel Fiber-Reinforced Concrete, a Second Generation Version," The Military Engineer, Vol. 71, No. 462, July-Aug. 1979, pp. 246-248.
31. Buckley, G.L. and N.J. Everard, "Prediction of the Modulus of Rupture of Fiber Reinforced Portland Cement Mortar and Concrete," Fiber Reinforced Concrete, an International Symposium, Publ. by ACI, Publication SP-44, © 1974, pp. 163-175, SP 44-9.
32. Cedolin, L., Y.R.J. Crutzen and S. Dei Poli, "Triaxial Stress-Strain Relationship for Concrete," Journal of the Engineering Mechanics Division, ASCE, Vol. 103, No. EM3, Proc. Paper 12969, June 1977, pp. 423-439.
33. Chen, A.C.T. and W.F. Chen, "Constitutive Relations for Concrete," Journal of the Engineering Mechanics Division, ASCE, Vol. 101, No. EM4, Proc. Paper 11529, August 1975, pp. 465-481.
34. Chen, A.C.T. and W.F. Chen, "Constitutive Equations and Punch-Indentation of Concrete," Journal of the Engineering

Mechanics Division, ASCE, Vol. 101, No. EM6, Proc. Paper 11809, Dec. 1975, pp. 889-906.

35. Chen, W.F., Limit Analysis and Soil Plasticity, Elsevier Scientific Publishing Co., Inc., Amsterdam, the Netherlands, 1975.
36. Chen, W.F. and J.L. Carson, "Stress-Strain Properties of Random Wire Reinforced Concrete," Journal of the American Concrete Institute, Proceedings Vol. 68, No. 12, Dec. 1971, pp. 933-936.
37. Chen, W.F. and J.L. Carson, "Bearing Capacity of Fiber Reinforced Concrete," Fiber Reinforced Concrete, an International Symposium, ACI Publication SP-44, 1974, pp. 209-220, SP 44-12.
38. Chironis, N.P., "Sprayed Fibrous Concrete for Mines," Coal Age, Vol. 20, December 1974, pp. 56-59.
39. Commission II - Structural Analysis, CEB - Task Group, "Concrete Under Multiaxial States of Stresses," "Strength of Concrete Subjected to Multiaxial Stresses."
40. Davis, E.H., "Theories of Plasticity and the Failure of Soil Masses," Ch.6 of Soil Mechanics Selected Topics, Ed. I.K. Lee, Butterworth, London, 1969.
41. Dieter, G.E., Jr., Mechanical Metallurgy, Published by McGraw-Hill Book Company, © 1961.
42. Dodge, W.G., Z.P. Bazant and R.H. Gallagher, "A Review of Analysis Methods for Prestressed Concrete Reactor Vessels," Prepared by the Oak Ridge National Laboratory, Oak Ridge, Tennessee 37830, ORNL-5173, Dist. Category UC-77, Gas Cooled Reactor Technology, Contract No. W-7405-eng-26, Engineering Technology Division, HTGR Base Technology Program, Prestressed Concrete Nuclear Pressure Vessel Development (189a OH003), PCRV Analytical Studies--Milestone 1b, Feb. 1977.
43. Drucker, D.C., "A Definition of Stable Inelastic Material," Journal of Applied Mechanics, Transactions of the ASME, March 1959, pp. 101-106.
44. Duncan, J.M. and C.Y. Chang, "Nonlinear Analysis of Stress and Strain in Soils," Journal of the Soil Mechanics and Foundations Division, ASCE, Vol. 96, No. SM5, Proc. Paper 7513, Sept. 1970, pp. 1629-1653.
45. Edgington, J., D.J. Hannant and R.I.T. Williams, "Steel Fiber Reinforced Concrete," Building Research Establishment, Building Research Station, Dept. of the Environment, Garston, Watford, WD27JR.

46. Endebrock, E.G. and L.A. Traina, "Static Concrete Constitutive Relations Based on Cubical Specimens," Air Force Weapons Laboratory, AFWL-TR-72-59, Vol. 1, December, 1972.
47. Gerstle, K.H., "Simple Formulation of Biaxial Concrete Behavior," Journal of the American Concrete Institute, Proc. Vol. 78, No. 1, Jan-Feb. 1981, pp. 62-68.
48. Gerstle, K.H., "Simple Formulation of Triaxial Concrete Behavior," Journal of the American Concrete Institute, Proc. Vol. 78, No. 5, Sept.-Oct. 1981, pp. 382-387.
49. Gerstle, K.H. and H.V. Cornelius, "Simple Formulation of Multiaxial Concrete Behavior," presented at ASCE Meeting June 1981 in Boulder, Colo.
50. Gerstle, K.H., H. Aschl, R. Bellotti, P. Bertacchi, M.D. Kotsovos, H.Y. Ko, D.H. Linse, J.B. Newman, P. Rossi, G. Schickert, M.A. Taylor, L.A. Traina, H. Winkler and R.M. Zimmerman, "Behavior of Concrete Under Multiaxial Stress States," Journal of the Engineering Mechanics Division, ASCE, Vol. 106, No. EM6, Proc. Paper 15945, Dec. 1980, pp.1383-1403.
51. Gerstle, K.H., D.L. Linse, P. Bertacchi, M.D. Kotsovos, H.Y. Ko, J.B. Newman, P. Rossi, G. Schickert, M.A. Taylor, L.A. Traina and R.M. Zimmerman, "Strength of Concrete Under Multiaxial Stress States," Douglas McHenry International Symposium on Concrete and Concrete Structures, American Concrete Institute, Publication SP-55, pp. 103-131, SP 55-5.
52. Gray, B.H., "Fiber Reinforced Concrete--A General Discussion of Field Problems and Applications," New Materials in Concrete Construction, Proceedings of the Conference University of Illinois at Chicago Circle, Dec. 15-17, 1972, pp. 1-V to 14-V.
53. Halvorsen, G.T., "Concrete Reinforced With Plain and Deformed Steel Fibers," Prepared for Federal Railroad Adm., Dept. of Transportation, Report No. DOT-TST-76T-20, prepared by Dept. of Civil Eng., University of Illinois at Urbana-Champaign, Report No. UILU-ENG-76-2011, August 1976.
54. Halvorsen, G.T., W.G. Keske, J.A. Stout and C.E. Kesler, "Concrete For Tunnel Liners--Behavior of Fiber Reinforced Quick Setting Cement Concrete," Prepared for Federal Railroad Adm., Dept. of Transportation, Report No. FRA OR&D75-87, Prepared by Univ. of Illinois @ Urbana-Champaign, Dept. of Civil Eng., Report No. UILU-ENG-75-0008., August 1975.
55. Halvorsen, G.T., C.E. Kesler, A.R. Robinson and J.A. Stout, "Durability and Physical Properties of Steel Fiber Reinforced Concrete," prepared for the Federal Railroad Adm., U.S. Dept. of Transportation, Report No. DOT-TST-76T-21, prepared by

Dept. of Civil Eng., Univ. of Illinois at Urbana-Champaign,
Report No. UILU-ENG-76-2013, August 1976.

56. Harris, B., J. Varlow and C.D. Ellis, "The Fracture Behavior of Fibre Reinforced Concrete," Cement and Concrete Research, Vol. 2, No. 4, 1972, pp. 447-461.
57. Hawk, D.J., "A Study of the Orthotropy of Coal and Other Rock Materials," M.S. Thesis, University of Colorado, Dept. of Civil, Environmental and Architectural Engineering, 1979.
58. Hegemier, G.A., "Evaluation of Material Models for MX Siting, Volume II: Reinforced Concrete Models," Final Report, Nov. 1979, SSS-R-80-4155, by Systems, Science, and Software, P.O. Box 1620, La Jolla, CA. 92038.
59. Henager, C.H., "Steel Fibrous, Ductile Concrete Joint for Seismic-Resistant Structures," American Concrete Institute, SP 53-14.
60. Henager, C.H. and T.J. Doherty, "Analysis of Reinforced Fibrous Concrete Beams," Journal of the Structural Division, ASCE, Vol. 102, No. ST1, Proc. Paper 11847, Jan. 1976, pp. 177-188.
61. Herring, K.S. and C.E. Kesler, "Concrete For Tunnel Liners: Behavior of Steel Fiber Reinforced Concrete Under Combined Loads," Department of Civil Engineering, University of Illinois, Urbana, IL, Report No. FRA-ORDD 75-7 (UILU-ENG-74-2025), August 1974, p. 76.
62. Jackson, J.G., Jr., "Analysis of Laboratory Test Data to Derive Soil Constitutive Properties," Miscellaneous Paper S-69-16, U.S. Engineer Waterways Experiment Station, Corps of engineers, Vicksburg, MS, April 1969.
63. Johnston, C.D., "Steel Fiber Reinforced Mortar and Concrete--A Review of Mechanical Properties," Fiber Reinforced Concrete, an International Symposium, Publ. by ACI, Publication SP-44, © 1974, pp. 127-142, SP 44-7.
64. Juvinall, R.C., Stress, Strain, and Strength, Published by McGraw-Hill Book Company, © 1967.
65. Kar, J.N. and A.K. Pal, "Strength of Fiber-Reinforced Concrete," Journal of the Structural Division, ASCE, Vol. 98, No. ST5, Proc. Paper 8909, May 1972, pp. 1053-1068.
66. Kesler, C.E., "Concrete For the Future," New Materials in Concrete Construction, Proceedings of the Conference University of Illinois at Chicago Circle, Dec. 15-17, 1972, pp. 1-I to 19-I.

67. Kesler, C.E. and G.T. Halvorsen, "Fiber-Reinforced Concrete--Workable and Economical," The Military Engineer, Vol. 71, No. 462, July-Aug. 1979, pp. 234-347.
68. Khrometz, Yu N, i dr. Mechanicheskie Svoistva Gipsovykh Izdelij Armirovannykh Steklovoloknom, "Stroitelnye Materialy," N2, 1973, pp. 21-22.
69. Ko, H.Y., and R.F. Scott, "A New Soil Testing Apparatus," Geotechnique, Vol. 17, 1967, pp. 40-57.
70. Ko, H.Y. and S. Sture, "Three-Dimensional Mechanical Characterization of Anisotropic Composites," Journal Composite Materials, Vol. 8, 1974, pp. 178-190.
71. Kotsovos, M.D. and J.B. Newman, "Generalized Stress-Strain Relations for Concrete," Journal of the Engineering Mechanics Division, ASCE, Vol. 104, No. EM4, Proc. Paper 13922, August 1978, pp. 845-856.
72. Krenchel, H., "Fiber Reinforced Brittle Matrix Materials," Fiber Reinforced Concrete, An International Symposium, Publ. by ACI, Publication SP-44, © 1974, pp. 45-77, SP 44-3.
73. Kupfer, H.B. and K.H. Gerstle, "Behavior of Concrete Under Biaxial Stresses," Journal of the Engineering Mechanics Division, ASCE, Vol. 99, No. EM4, Proc. Paper 9917, Aug. 1973, pp. 853-866.
74. Kupfer, H., H.K. Hilsdorf and H. Rusch, "Behavior of Concrete Under Biaxial Stresses," Journal of the American Concrete Institute, Proceedings V. 66, No. 8, Aug. 1969, pp. 656-666.
75. Kurbatov, L.G., i. dr. Mnogoslojnie sfericheskie obolochki dlia peredvizhnykh domov, "Benton i Zhelezobeton," N7, 1973, pp. 19-20.
76. Lade, P.V., "Elastoplastic Stress-Strain Theory for Cohesionless Soil," Errata, Journal of the Geotechnical Engineering Division, ASCE, Vol. 102, No. G13, Mar. 1976, p. 270.
77. Lade, P.V., "Elasto-Plastic Stress-Strain Theory for Cohesionless Soil with Curved Yield Surfaces," Int. J. Solids Structures, 1977, Vol. 13, pp. 1019-1035, Pergamon Press.
78. Lade, P.V., "Prediction of Undrained Behavior of Sand," Journal of the Geotechnical Engineering Division, ASCE, Vol. 104, No. G16, Proc. Paper 13834, June 1978, pp. 721-735.
79. Lade, P.V., "Three-Parameter Failure Criterion for Concrete," Paper Presented at Joint ASME/ASCE Mechanics Conference, Boulder, CO, June 22-24, 1981.

80. Lade, P.V. and J.M. Duncan, "Elastoplastic Stress-Strain Theory for Cohesionless Soil," Journal of the Geotechnical Engineering Division, ASCE, Vol. 101, No. GT10, Proc. Paper 11670, Oct. 1975, pp. 1037-1053.
81. Lade, P.V. and H.M. Musante, "Three-Dimensional Behavior of Remolded Clay," Journal of the Geotechnical Engineering Division, ASCE, Vol. 104, No. GT2, Proc. Paper 13551, Feb. 1978, pp. 193-209.
82. Lankard, D.R., "Fiber Concrete Applicatons," RILEM Symposium, 1975, pp. 3-19.
83. Launay, P. and H. Gachon, "Strain and Ultimate Strength of Concrete Under Triaxial Stress," ACI Special Publication SP-34, Paper SP-34-13, 1972, pp. 269-282.
84. Liu, T.C.Y., A.H. Nilson and F.O. Slate, "Biaxial Stress-Strain Relations for Concrete," Journal of the Structural Division, ASCE, Vol. 98, No. ST5, Proc. Paper 8905, May 1972, pp. 1025-1034.
85. Luke, C.E., B.L. Waterhouse and J.F. Wooldridge, "Steel Fiber Reinforced Concrete Optimization and Applications," Fiber Reinforced Concrete, An International Symposium, Publ. by ACI., Publication SP-44, © 1974, pp. 393-413, SP44-23.
86. Majumdar, A.J., "Fibre Cement and Concrete--a Review," Composites, Vol. 6, No. 1, Jan. 1975, pp. 7-16.
87. Mendelson, A., Plasticity: Theory and Application, Published by the MacMillan Company, MacMillan Series in Applied Mechanics, © 1968.
88. Moens, J.E.C., "Steel Fiber Concrete Mix Proportioning," Paper Presented at the American Concrete Institute Annual Convention, Philadelphia, Pennsylvania, March 1976.
89. Mould, J.C., Jr., "Multiaxial Testing and Analytical Constitutive Characterization of Granular Materials," M.S. Thesis, Virginia Polytechnic Institute and State University, 1979.
90. Naaman, A.E., F. Moavenzadeh and F.J. McGarry, "Probabilistic Analysis of Fiber-Reinforced Concrete," Journal of the Engineering Mechanics Division, ASCE, Vol. 100, No. EM2, Proc. Paper 10491, April 1974, pp. 397-413.
91. Nair, N.G., "Mechanics of Glass Fiber Reinforced Cement," RILEM Symposium, 1975, pp. 81-103.
92. Nelson, I. and M.L. Baron, "Application of Variable Moduli Models to Soil Behavior," International Journal of Solids and Structures, April 1971, Vol. 7, No. 4, pp. 399-417.

93. Nielsen, L.E. and P.E. Chen, "Young's Modulus of Composites Filled with Randomly Oriented Fibers," Journal of Materials, ASTM, Vol. 3, No. 2, June 1968, pp. 352-358.
94. NIWA, Y., S. Kobayashi and W. Koyanagi, "Failure Criterion of Lightweight Aggregate Concrete Subjected to Triaxial Compression," Memoirs, Faculty of Engineering, Kyoto University, V. 29, Part 2, April, 1967.
95. Oakley, D.R. and B.A. Proctor, "Tensile Stress-Strain Behavior of Glass Fiber Reinforced Cement Composites," RILEM Symposium, 1975, pp. 347-359.
96. Opoczky, L. and L. Pentek, Jr., "Investigation of the "Corrosion" of Asbestos Fibers in Asbestos Cement and Sheets Weathered for Long Times," RILEM Symposium, 1975, pp. 269-276.
97. Ottosen, N.S., "A Failure Criterion for Concrete," Journal of the Engineering Mechanics Division, ASCE, Vol. 103, No. EM4, Proc. Paper 13111, Aug. 1977, pp. 527-535.
98. Pakotiprapha, B., R. P. Pama and S.L. Lee, "Mechanical Properties of Cement Mortar with Randomly Oriented Short Steel Wires," Magazine of Concrete Research, Vol. 26, No. 86, March 1974, pp. 3-15.
99. Palaniswamy, R. and S.P. Shah, "Fracture and Stress-Strain Relationship of Concrete Under Triaxial Compression," Journal of the Structural Division, ASCE, Vol. 100, No. ST5, Proc. Paper 10547, May 1974, pp. 901-916.
100. Parmi, S.R. and J.K. Sridhar Rao, "On the Fracture Toughness of Fiber Reinforced Concrete," Fiber Reinforced Concrete; An International Symposium, Publ. by ACI, Publication SP-44, © 1974, pp. 79-92, SP 44-4.
101. Petersson, H. and E.P. Popov, "Constitutive Relations for Generalized Loadings," Journal of the Engineering Mechanics Division, ASCE, Vol. 103, No. EM4, Proc. Paper 13144, Aug. 1977, pp. 611-627.
102. Poad, M.E. and M.O. Servousek, "Engineering Properties of Shotcrete," U.S. Bureau of Mines, Spokane Mining Research Center, Spokane, WA, presented at the 1972 North American Rapid Excavation and Tunneling Conference, Chicago, IL, (Sponsored by ASCE and AIME), 1972, p. 19.
103. Popovics, S., "A Review of Stress-Strain Relationships for Concrete," A State-of-the-Art Report, Journal of the American Concrete Institute, Proceedings V. 67, No. 3, March 1970, pp. 243-248.

104. Portland Cement Association, "Design and Control of Concrete Mixtures," Eleventh Edition, Published by Portland Cement Association, © 1968, July.
105. Ramakrishnan, V., W.V. Coyle, L.J. Fowler and E.K. Schrader, "A Comparative Evaluation of Fiber Shotcretes," prepared for: BEKAERT STEEL WIRE CORPORATION, by South Dakota School of Mines and Technology, Civil Engineering Dept., Report SDSM&T-CBS 7902, August 1979.
106. Richart, F.E., A. Brandtzaeg and R. L. Brown, "A Study of the Failure of Concrete Under Combined Compressive Stresses," Bulletin No. 185, Univ. of Illinois, Engineering Experimental Station, Urbana, Ill, 1928.
107. RILEM International Symposium, "The Deformation and the Rupture of Solids Subjected to Multiaxial Stresses," RILEM International Symposium, Vols. I-IV, Cannes, France, October, 1972.
108. Ritche, A.G.B. and T.A. Rahman, "Effect of Fiber Reinforcement on the Rheological Properties of Concrete Mixes," Fiber Reinforced Concrete; An International Symposium, Publ. by ACI, Publication SP-44, © 1974, pp. 29-44, SP 44-2.
109. Romualdi, J.P. and G.B. Batson, "Behavior of Reinforced Concrete Beams with Closely Spaced Reinforcement," Journal of the American Concrete Institute, Proceedings Vol. 60, No. 6, June 1963, pp. 775-789.
110. Romualdi, J.R. and J.A. Mandel, "Tensile Strength of Concrete Affected by Uniformly Distributed and Closely Spaced Lengths of Wire Reinforcement," ACI Journal, Vol. 61, 1964, pp. 657-670.
111. Ryan, T.F., "Continuous Sprayed Concrete Tunnel Lining," Tunnels and Tunneling, (England), November 1973, pp. 539-543.
112. Schnütgen, B., "Some Results of Investigations on Steel Fiber Reinforced Concrete," Proceedings, RILEM Symposium, Construction Press, 1975, pp. 105-116.
113. Schrader, E.K. and A.V. Munch, "Deck Slabs Repaired by Fibrous Concrete Overlay," Journal of the Construction Division, ASCE, Vol. 102, No. C01, Proc. Paper 11976, March 1976, pp. 179-196.
114. Schrader, E.K. and A.V. Munch, "Fibrous Concrete Repair of Cavitation Damage," Journal of the Construction Division, ASCE, June 1976, pp. 385-399.
115. Shah, S.P., "Mineral, Organic or Metallic Fiber Reinforced Concrete," New Materials in Concrete Construction, Proceedings

of the Conference University of Illinois at Chicago Circle, Dec. 15-17, 1972, pp. 1-IV to 23-IV.

116. Shah, S.P. and A.E. Naaman, "Mechanical Properties of Glass and Steel Fiber Reinforced Mortar," Journal of the American Concrete Institute, Proceedings Vol. 73, No.1, Jan. 1973, pp. 50-53.
117. Shah, S.P. and B. V. Rangan, "Fiber Reinforced Concrete Properties," Journal of the American Concrete Institute, Proceedings Vol. 68, No. 2, Feb. 1971, pp. 126-135.
118. Sokolnikoff, I.S., Mathematical Theory of Elasticity, McGraw-Hill, New York, 1956.
119. Starovisky, P., "Response of Concrete to Multiaxial Compression," M.S. Thesis, University of Colorado, 1976.
120. Sture, S., "An Improved Multiaxial Cubical Cell and Its Application to the Testing of Anisotropic Materials," M.S. Thesis, University of Colorado, 1973.
121. Sture, S., "Development of a Multiaxial Cubical Test Device with Pore Water Pressure Monitoring Facilities," Report To The National Science Foundation, Report No. VPI-E-79.18, Grant No. NSF ENG 7717047, Specialized Research Equipment Grant, May 1979, Dept. of Civil Engineering, Virginia Polytechnic Institute and State University, Appendices A-D, pp. 98-123.
122. Sundara Raja Iyengar, K.T. and C. S. Viswanatha, "Stress-Strain Properties of Random Wire Reinforced Concrete," Discussion of above paper Wai-Fah Chen and J.L. Carson, Journal of the American Concrete Institute, Proceedings, Vol. 69, No. 6, June 1972, DISC 68-77, pp. 346-349.
123. Swamy, R.N., "Fibre-Reinforced Concrete: Mechanics, Properties, and Applications," The Indian Concrete Journal, Vol. 48, No. 1, Jan. 1974, pp. 7-29.
124. Swamy, R.N., "Fibre Reinforcement of Cement and Concrete," RILEM Matériaux et Constructions, Materials and Structures, Vol. 8, No. 45, May-June 1975, pp. 235-254.
125. Swamy, R.N. and B. Kent, "Some Practical Structural Applications of Steel Fiber Reinforced Concrete," Fiber Reinforced Concrete; An International Symposium, Publ. by ACI, Publication SP-44, © 1974, pp. 319-336, SP 44-18.
126. Swamy, R.N. and P.S. Mangat, "The Onset of Cracking and Ductility of Steel Fiber Concrete," Cement and Concrete Research, Vol. 5, No. 1, 1975, pp. 37-53.
127. Swamy, R.N., P.S. Mangat and C.V.S.K. Rao, "The Mechanics of Fiber Reinforcement of Cement Matrices," Fiber Reinforced

Concrete; An International Symposium, Publ. by American Concrete Institute, Publication SP-44, © 1974, pp. 1-28; SP 44-1.

128. Taylor, M.A., A.K. Jain and M.R. Ramey, "Path Dependent Biaxial Compressive Testing of an All Lightweight Aggregate Concrete," ACI Journal, Proceedings V. 69, No. 12, Dec. 1972, pp. 758-764.
129. Taylor, M.A. and M.R. Ramey, "Triaxial Properties of Fiber Reinforced Concrete," March 1972, University of California, Berkeley, California.
130. Taylor, M.A., M.K. Tai and M.R. Ramey, "Biaxial Compressive Behavior of Fiber Reinforced Mortar," Journal of the American Concrete Institute, Proceedings V. 72, No. 9, Sept. 1975, pp. 496-501.
131. Theocaris, P.S. and J.N. Prassianakis, "The Mohr Envelope of Failure for Concrete: A Study of its Tension-Compression Part," Magazine of Concrete Research, Vol. 26, No. 87, June 1974, pp. 73-82.
132. Trambovetsky, V.P., Benton, Armirovaniy Disperswoj Armaturoj, "Benton i Zhelezobeton," N. 12, 1974, pp. 40-42.
133. Vile, G.W.D., "The Strength of Concrete Under Short-Term Static Biaxial Stress," The Structure of Concrete, Cement and Concrete Association, London, England, 1968, pp. 275-288.
134. Willam, K.J. and E. P. Warnke, "Constitutive Model for the Triaxial Behavior of Concrete," International Association for Bridge and Structural Engineers, (IABSE), Reports 19-21, 1974-1975, Seminar, "Concrete Structures Subjected to Triaxial Stresses," ISMES-Bergamo-1974, Proceedings, Organized by the Italian Group of IABSE & ISMES (Istituto Sperimentale Modeli E Strutture), Session III, Reports on General Subject, pp. III-1 to III-30.
135. Williamson, G.R., "Effect of Steel Fibers on the Compressive Strength of Concrete," Fiber Reinforced Concrete, An International Symposium, Publ. by ACI, Publication SP-44, © 1974, pp. 195-207, SP 44-11.
136. Zienkiewicz, O.C., The Finite Element Method, Third Edition, Published by McGraw-Hill Book Company, © 1977.
137. Zonsveld, J.J., "Properties and Testing of Concrete Containing Fibers Other Than Steel," RILEM Symposium, 1975, pp. 217-226.

APPENDIX A

PRINCIPAL AND OCTAHEDRAL STRESS-STRAIN
CURVES FOR INDIVIDUAL PRELIMINARY TESTS

and

TABULATED PRINCIPAL STRESS-STRAIN
DATA FOR INDIVIDUAL FINAL TESTS

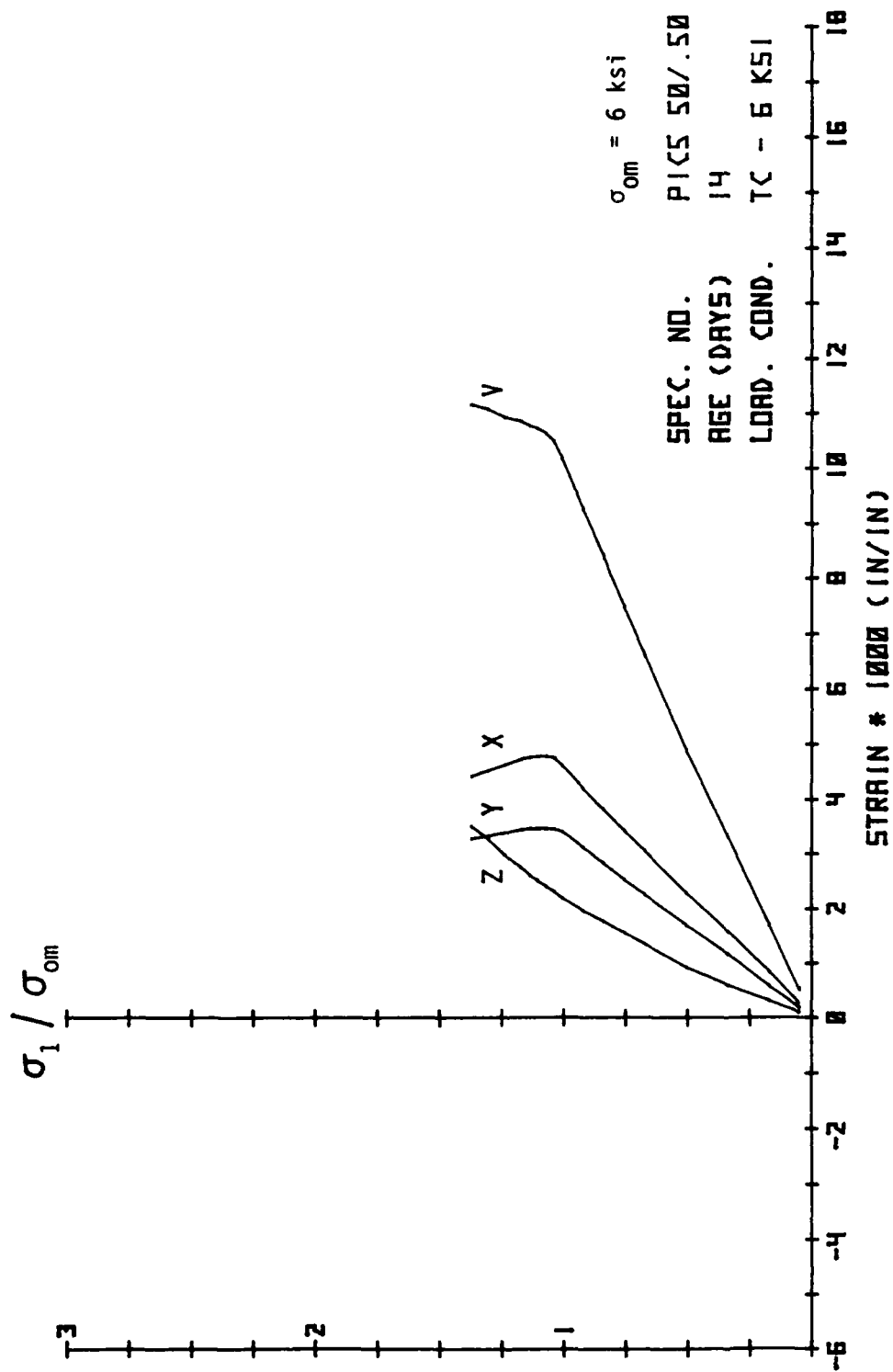


Fig. A.1. Principal Stress-Strain Results from Preliminary Tests.

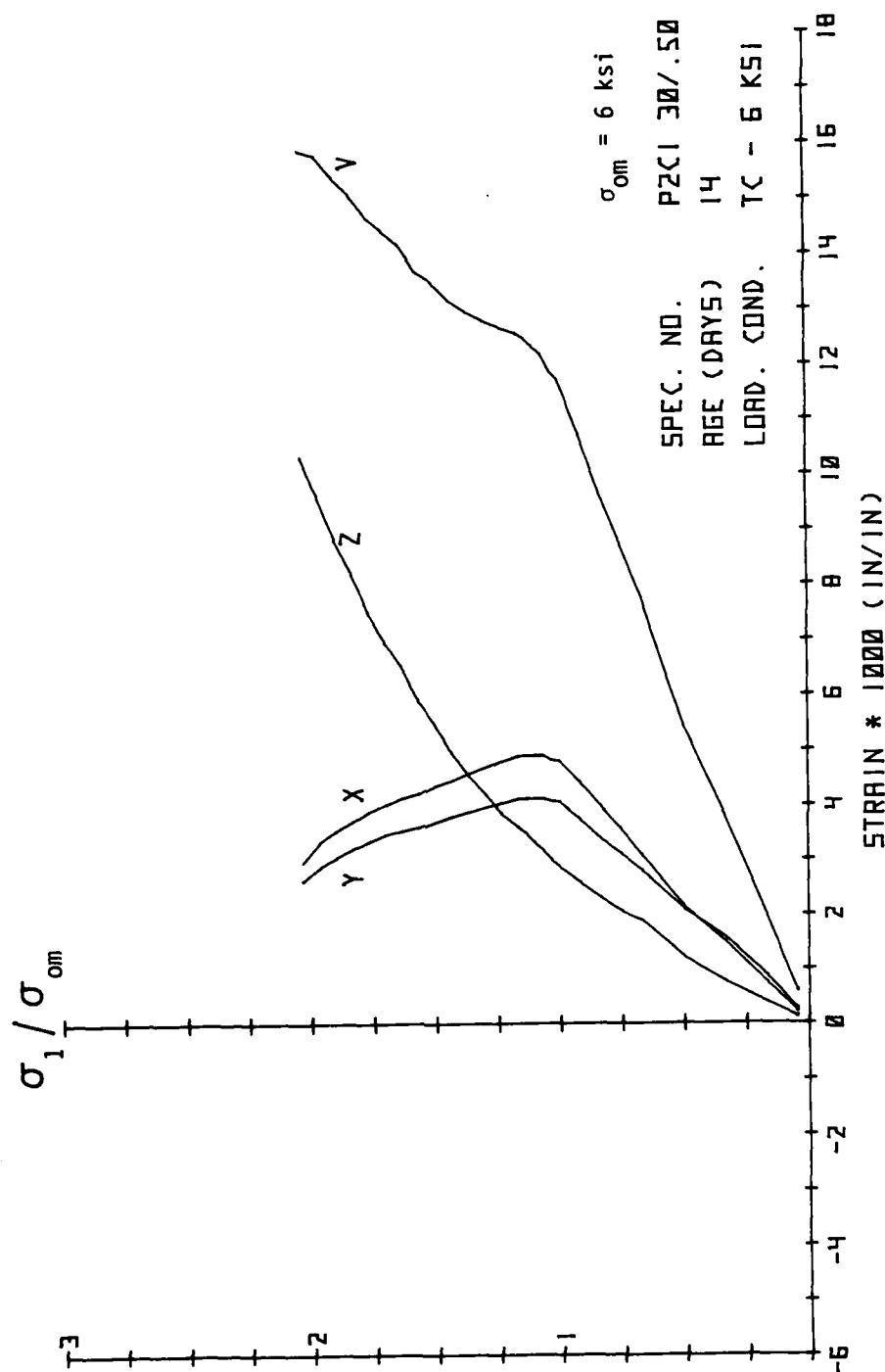


Fig. A.2. Principal Stress-Strain Results from Preliminary Tests.

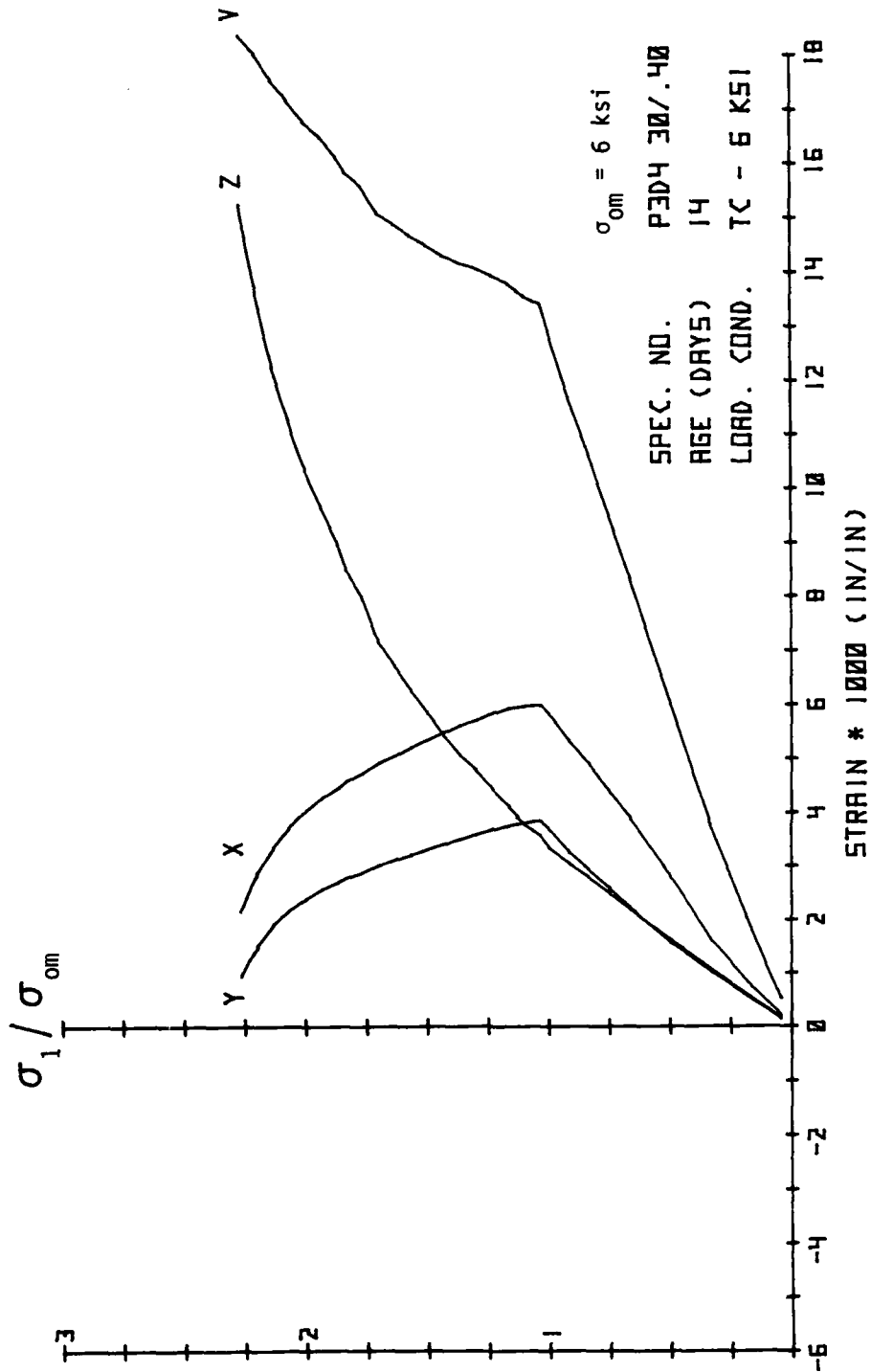


Fig. A.3. Principal Stress-Strain Results from Preliminary Tests.

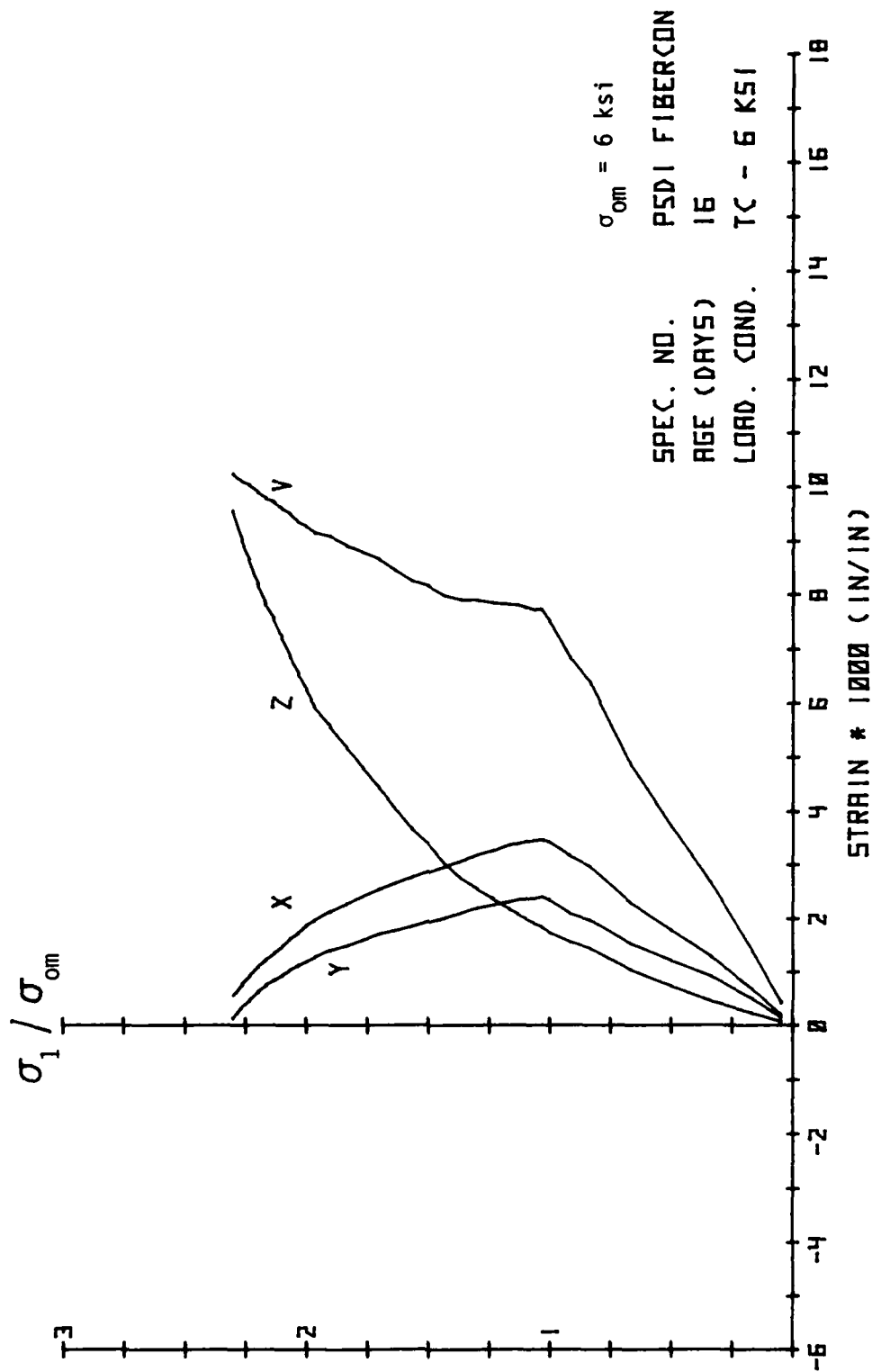


Fig. A.4. Principal Stress-Strain Results from Preliminary Tests.

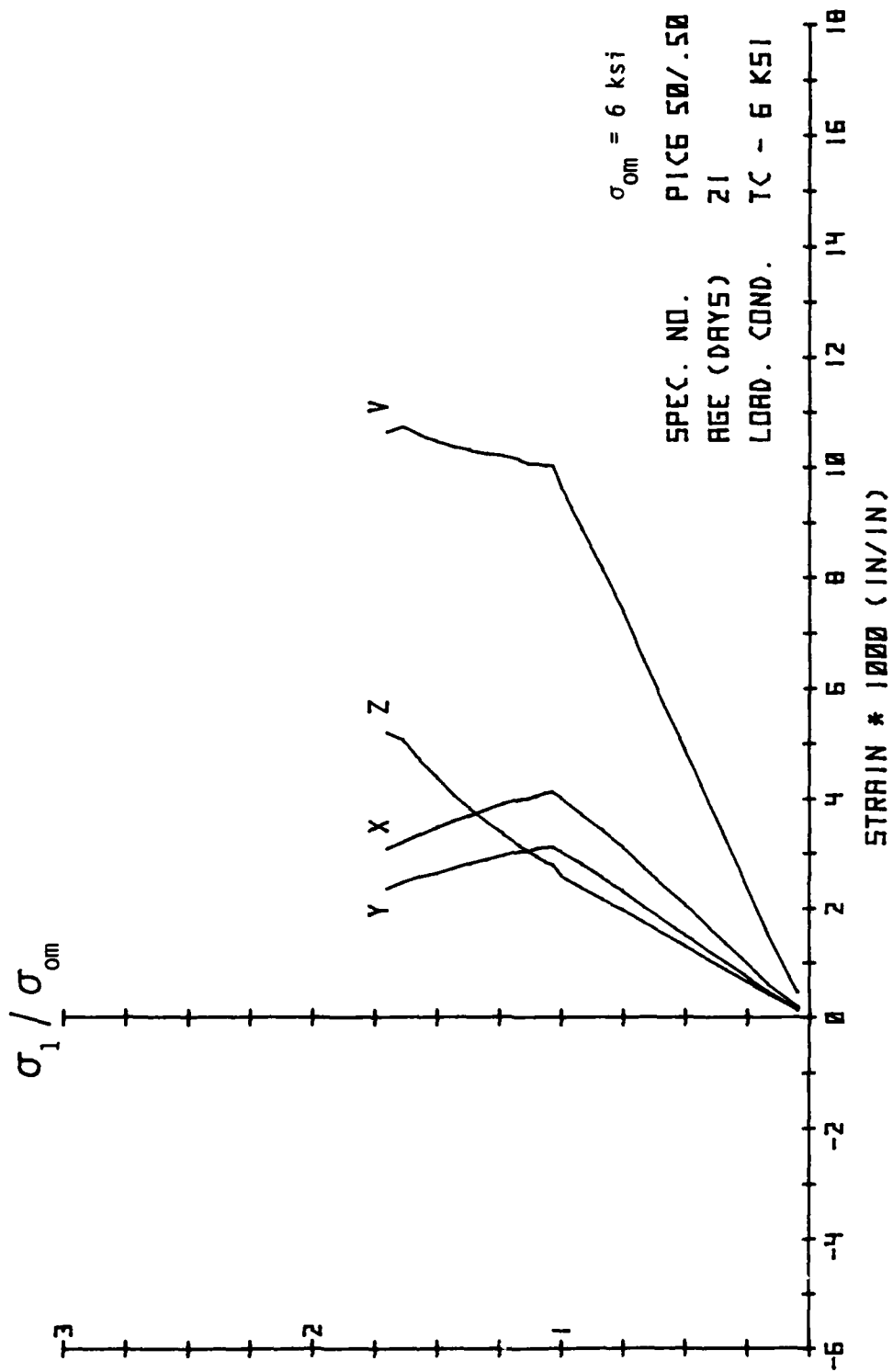


Fig. A.5. Principal Stress-Strain Results from Preliminary Tests.

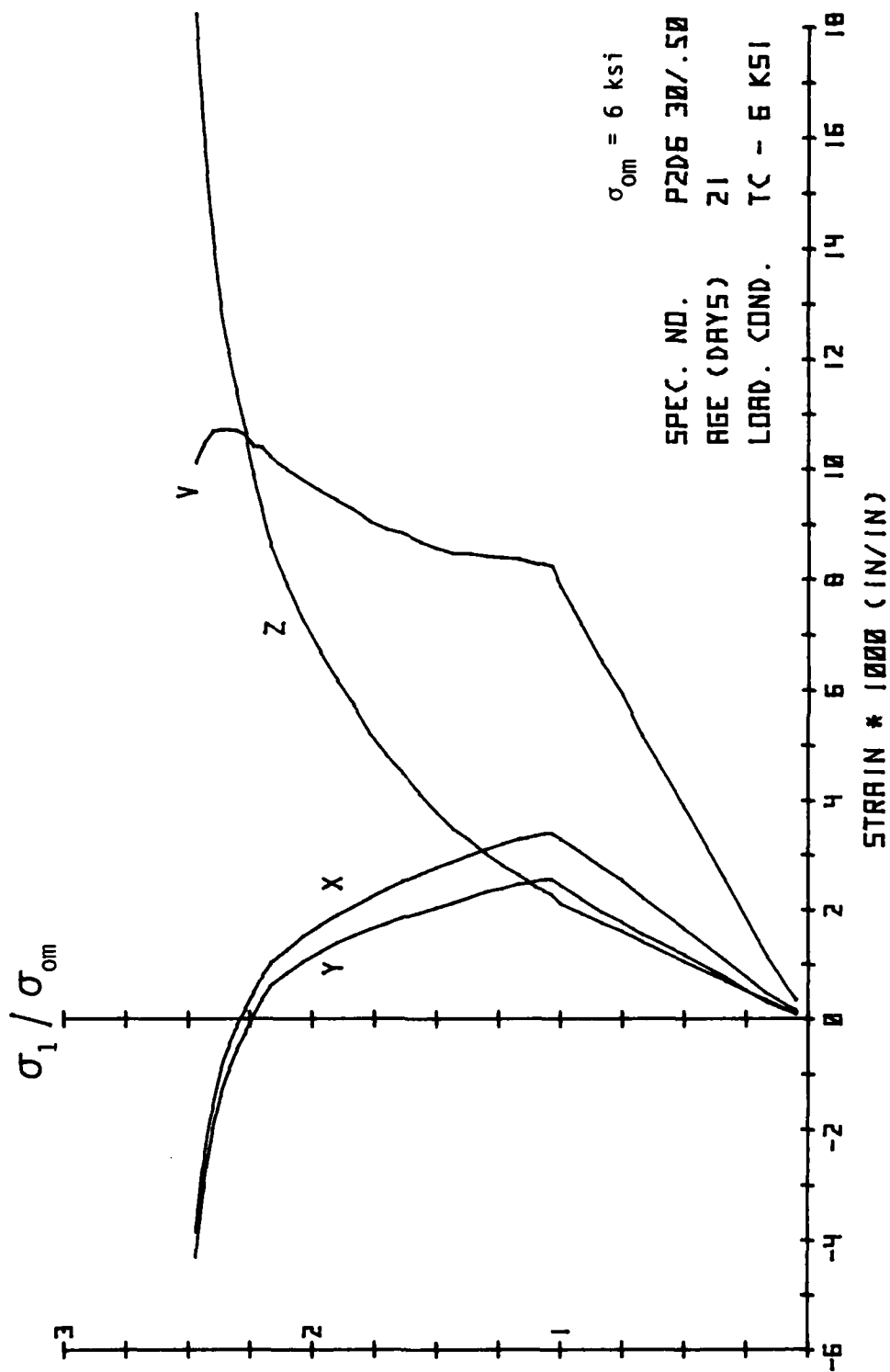


Fig. A.6. Principal Stress-Strain Results from Preliminary Tests.

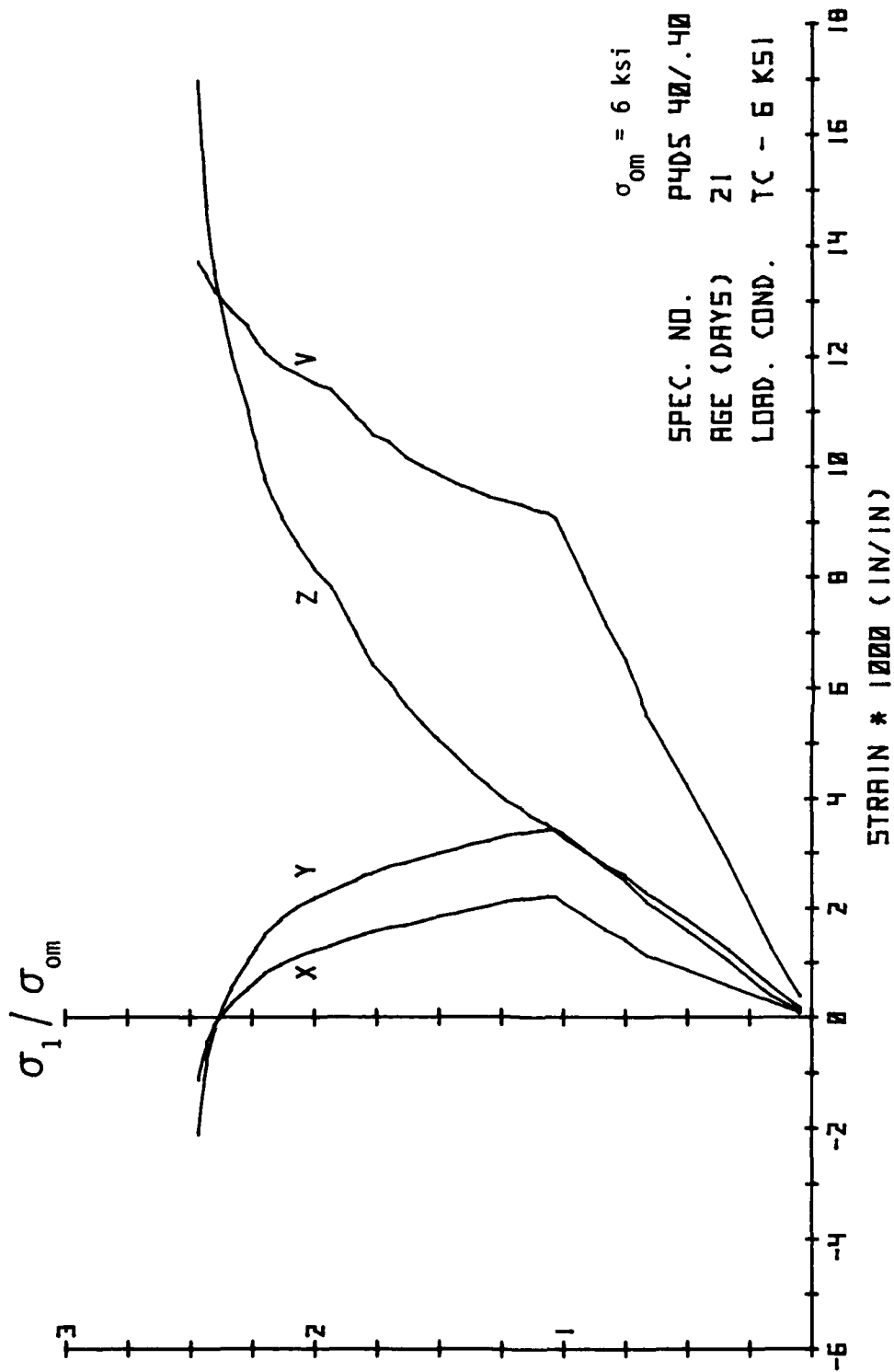


Fig. A.7. Principal Stress-Strain Results from Preliminary Tests.

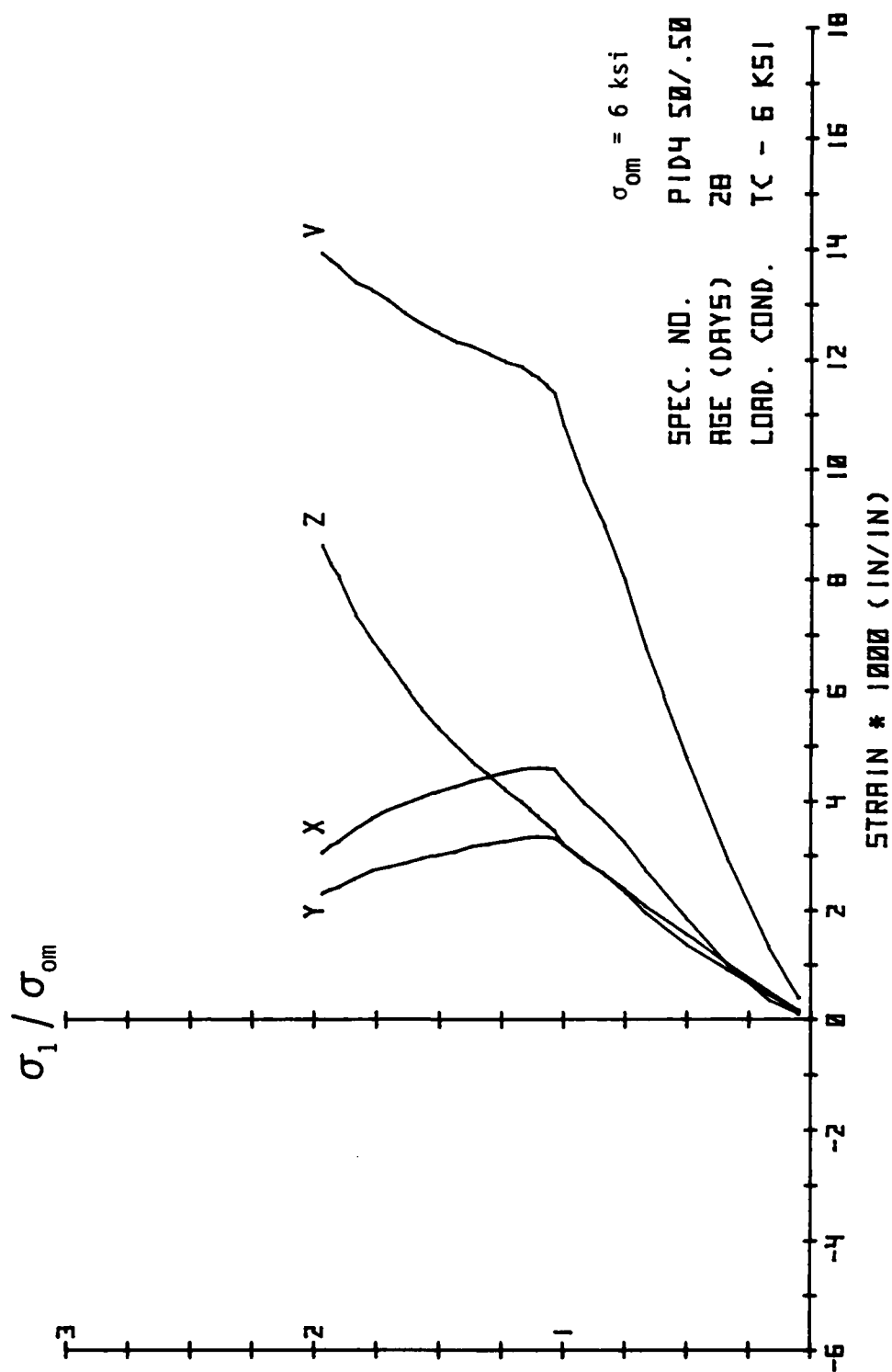


Fig. A.8. Principal Stress-Strain Results from Preliminary Tests.

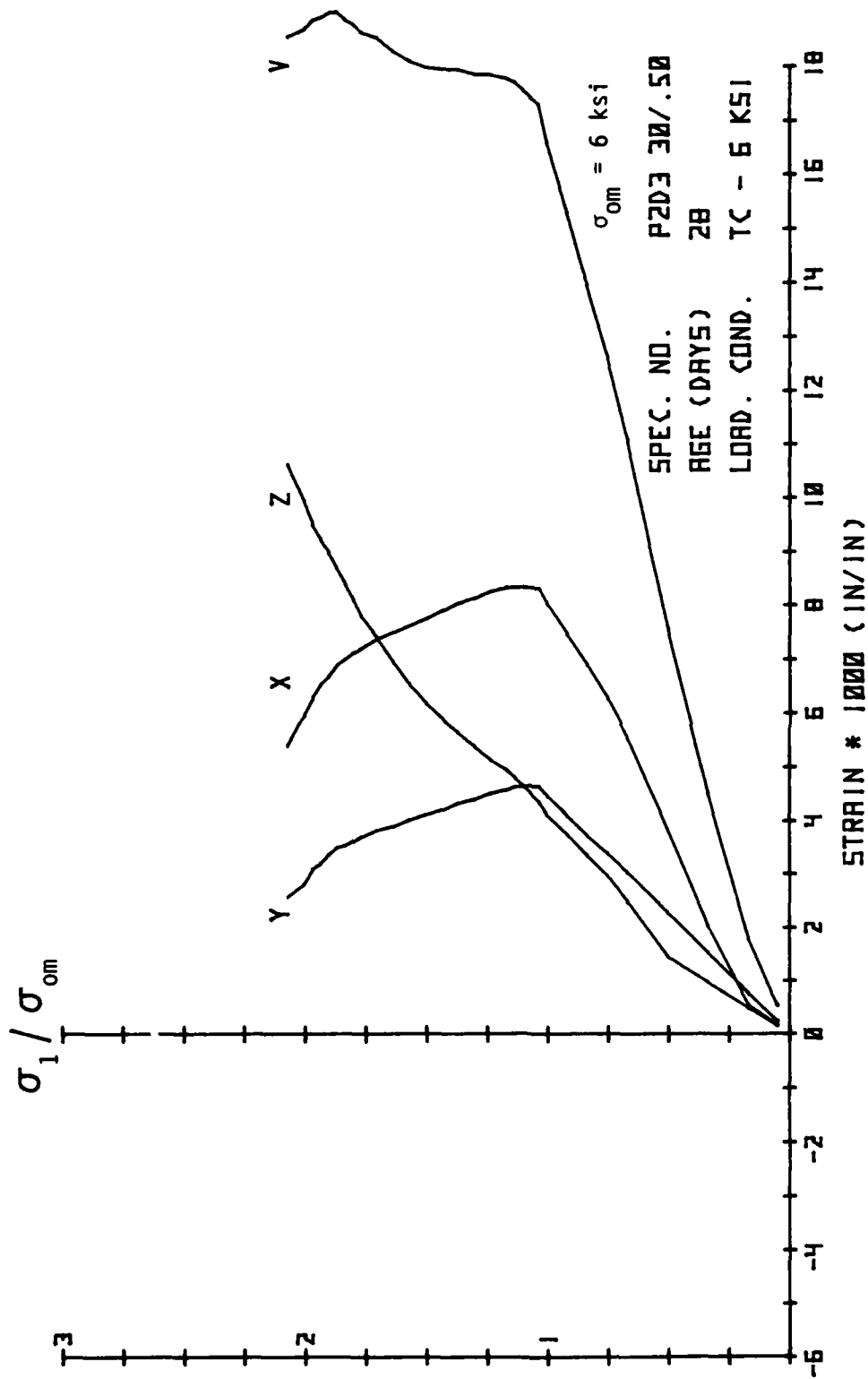


Fig. A.9. Principal Stress-Strain Results from Preliminary Tests.

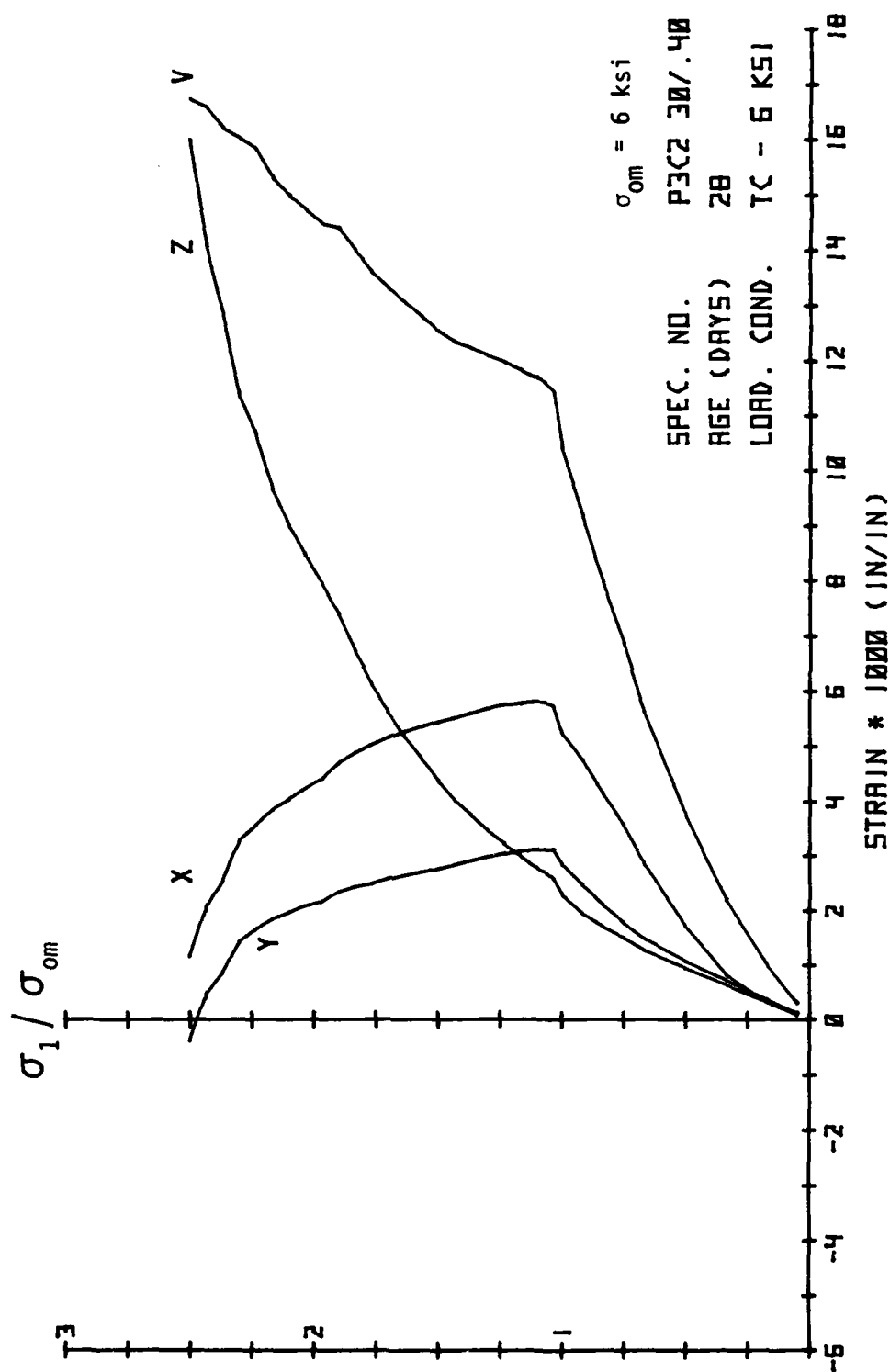


Fig. A.10. Principal Stress-Strain Results from Preliminary Tests.

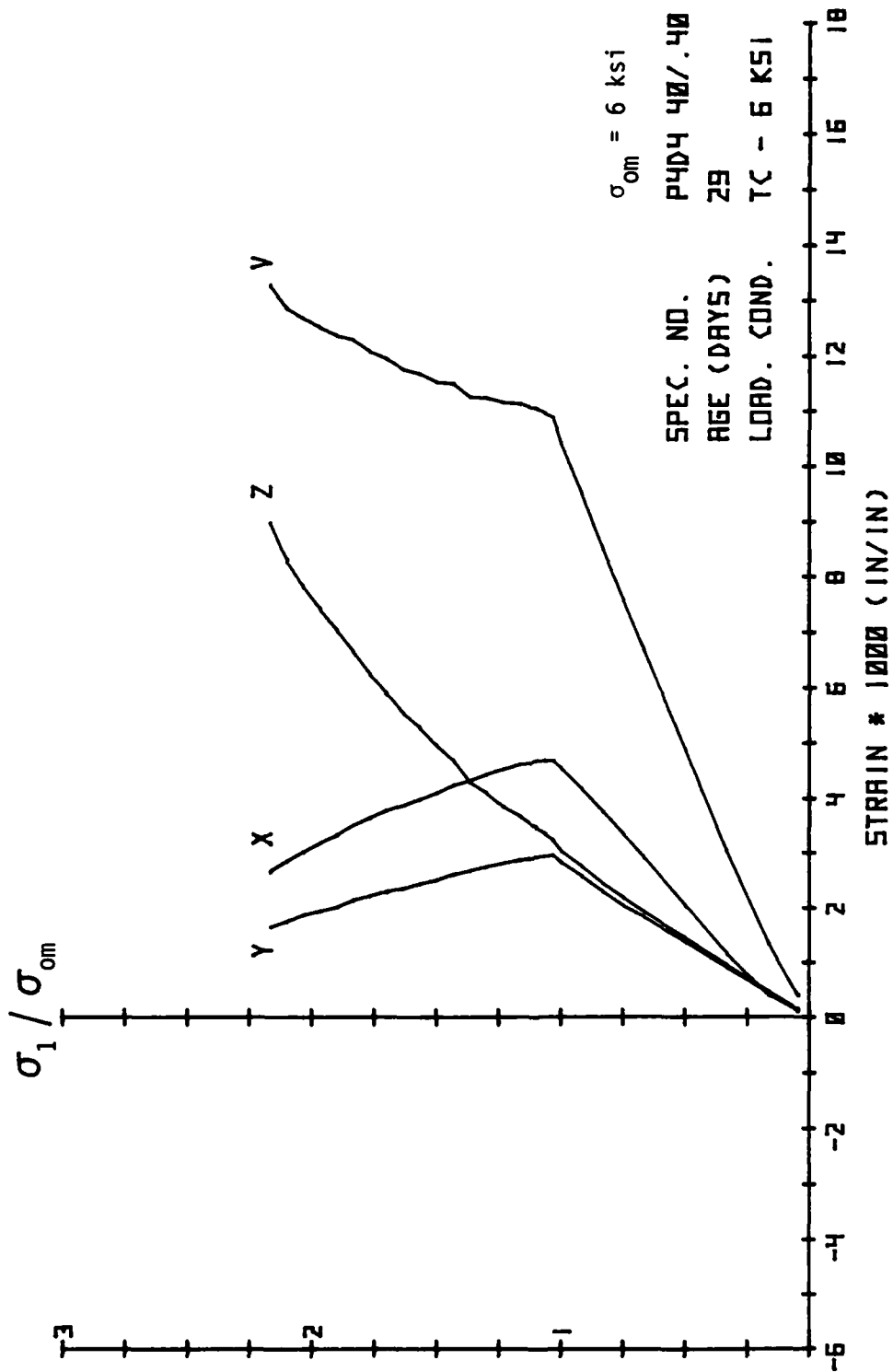


Fig. A.11. Principal Stress-Strain Results from Preliminary Tests.

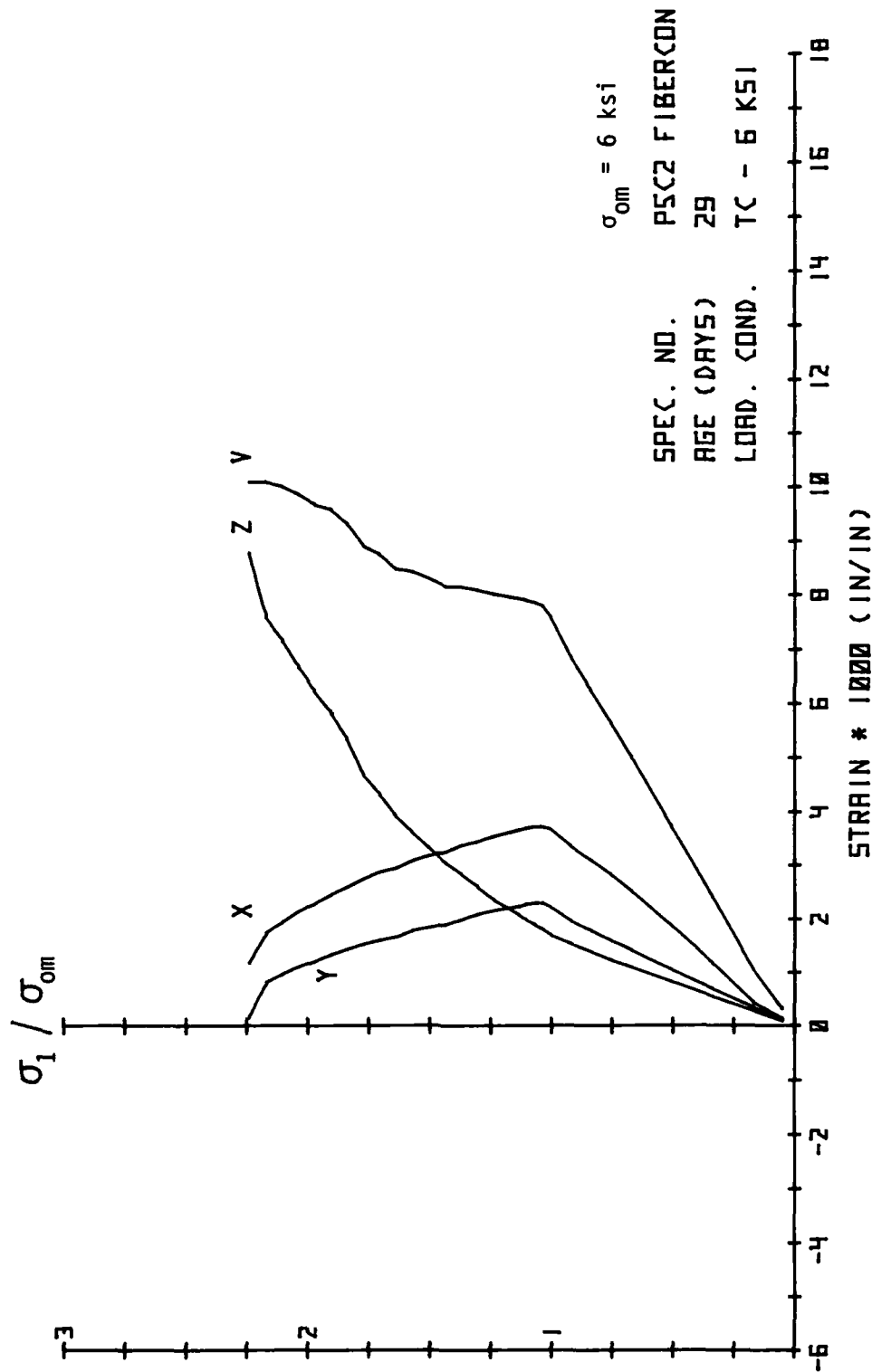


Fig. A.12. Principal Stress-Strain Results from Preliminary Tests.

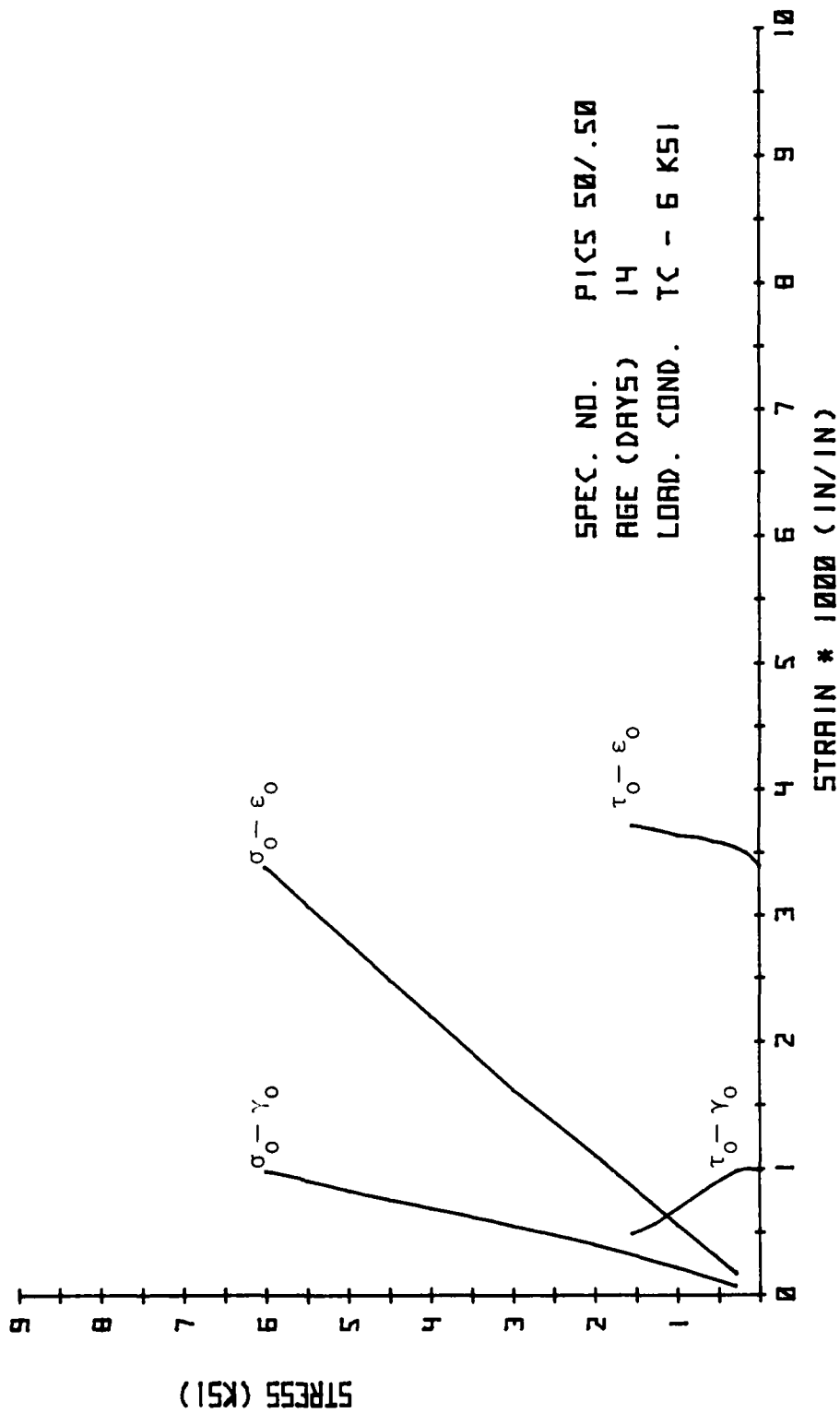


Fig. A.13. Octahedral Stress-Strain Results from Preliminary Tests.

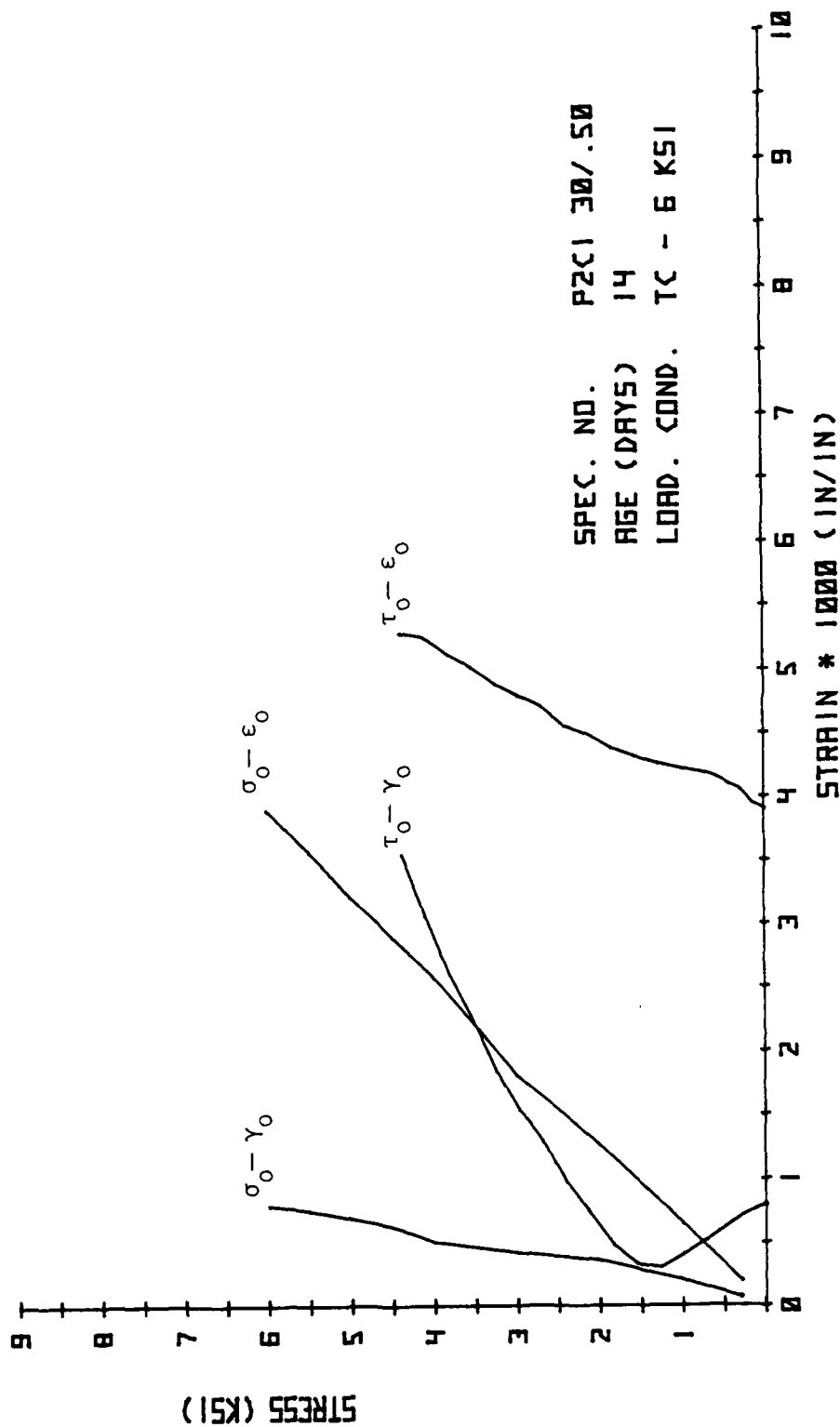


Fig. A.14. Octahedral Stress-Strain Results from Preliminary Tests.

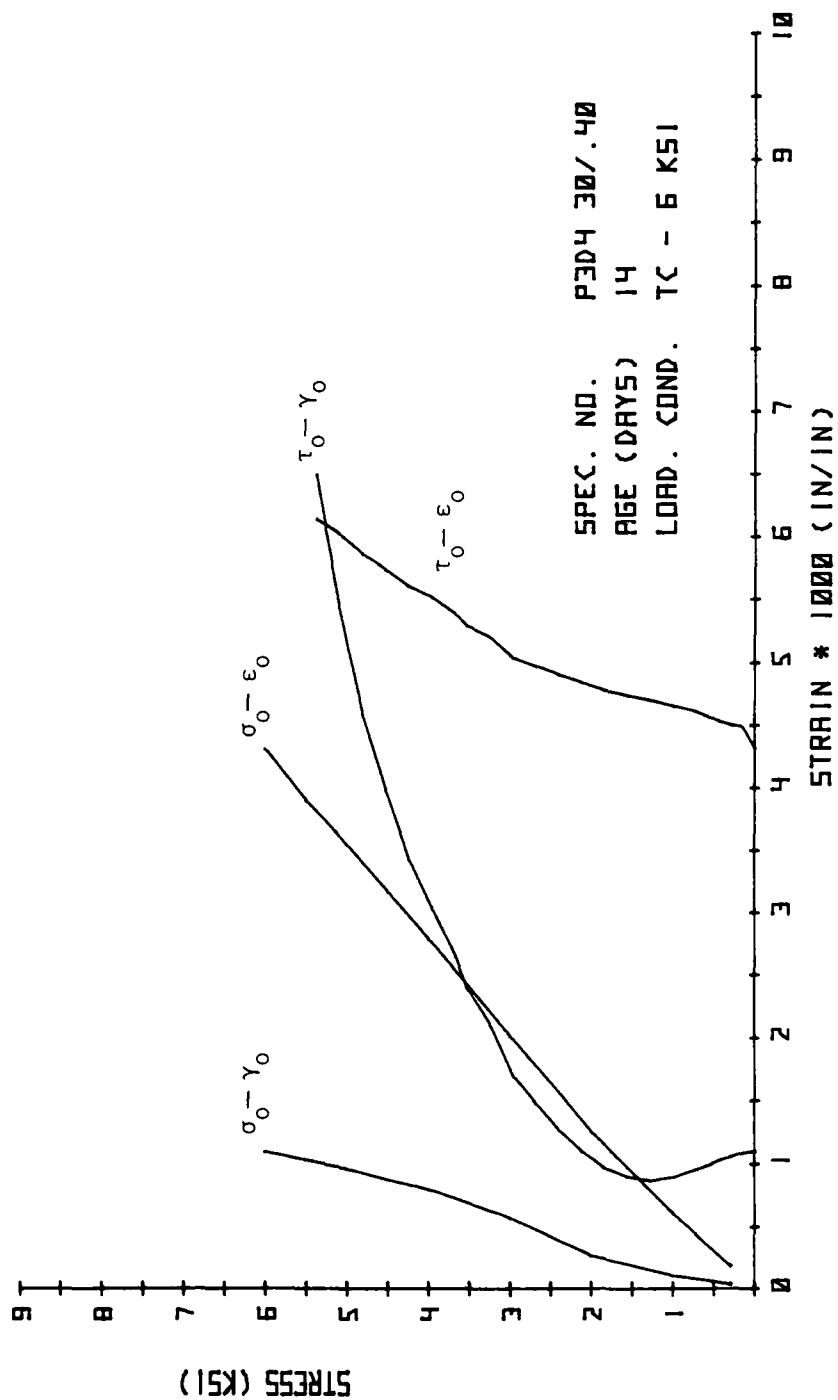


Fig. A.15. Octahedral Stress-Strain Results from Preliminary Tests.

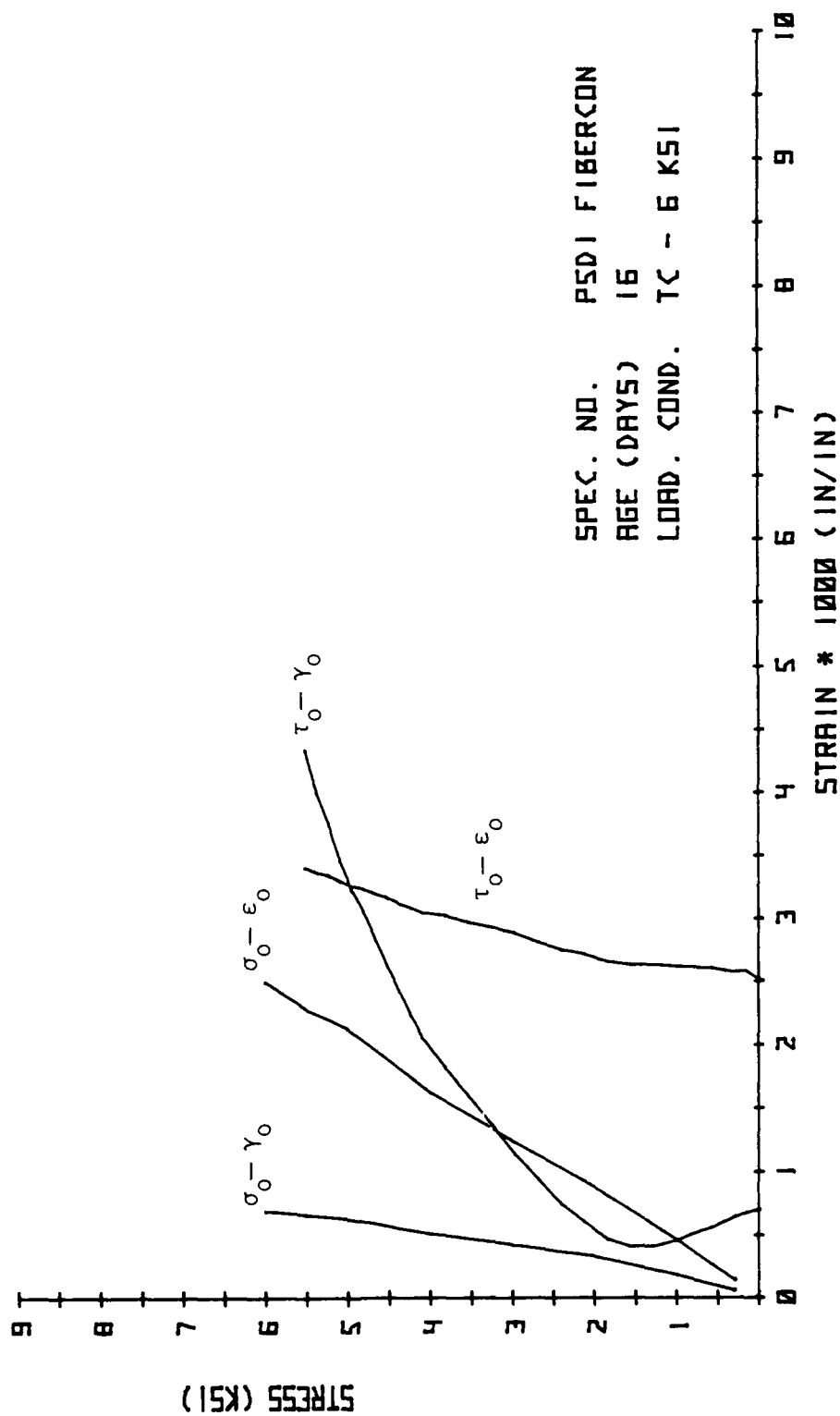


Fig. A.16. Octahedral Stress-Strain Results from Preliminary Tests.

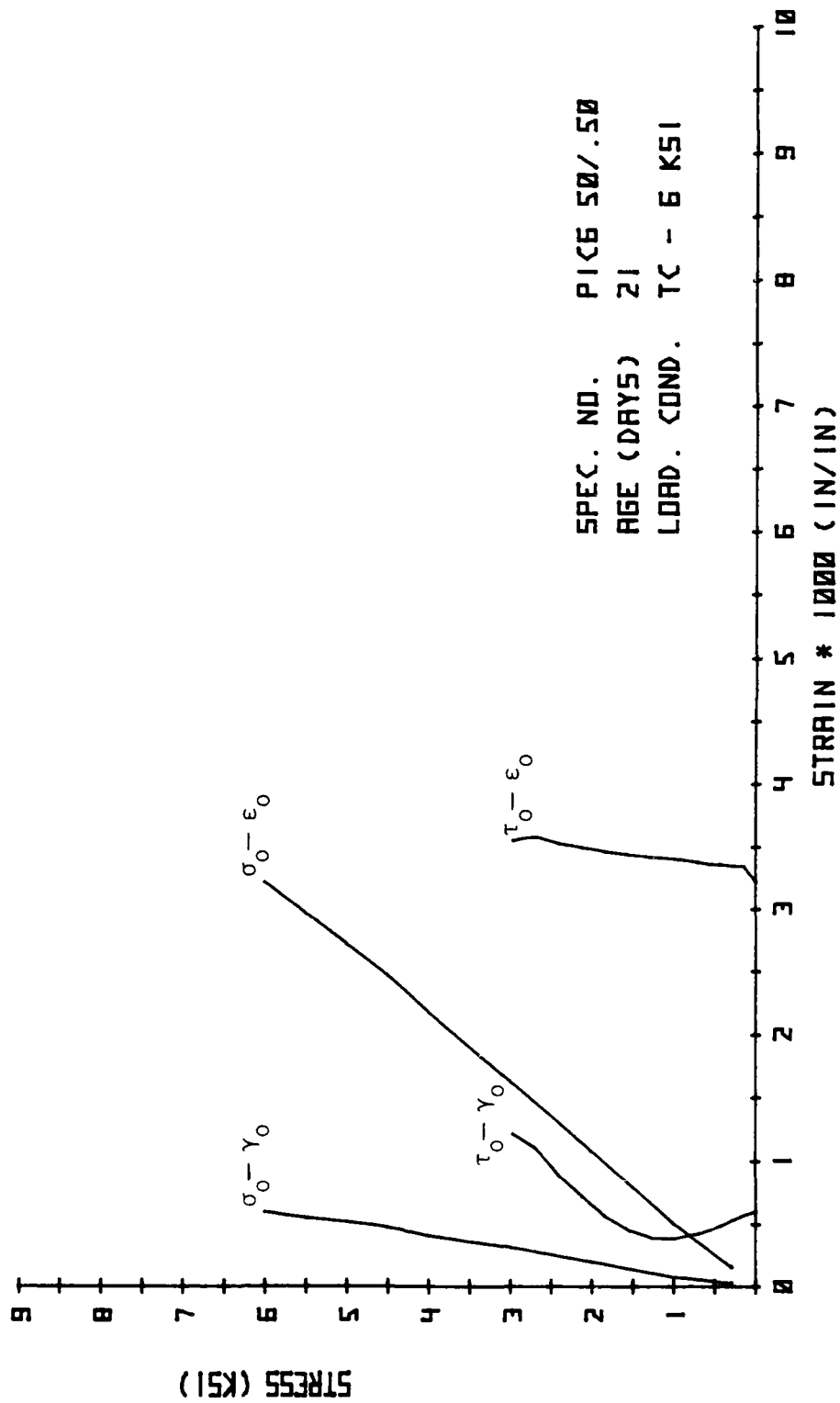


Fig. A.17. Octahedral Stress-Strain Results from Preliminary Tests.

AD-A114 168

COLORADO UNIV AT BOULDER DEPT OF CIVIL ENVIRONMENTAL --ETC F/O 20/11
CONSTITUTIVE RELATIONS OF RANDOMLY ORIENTED STEEL FIBER REINFOR--ETC(U)
DEC 81 D E EGGING, H KO AFOSR-79-0065

UNCLASSIFIED

AFOSR-TR-82-0122

NL

6 OF 6
PAGE 10/10



END
DATE
FILMED
9-82
NTIC

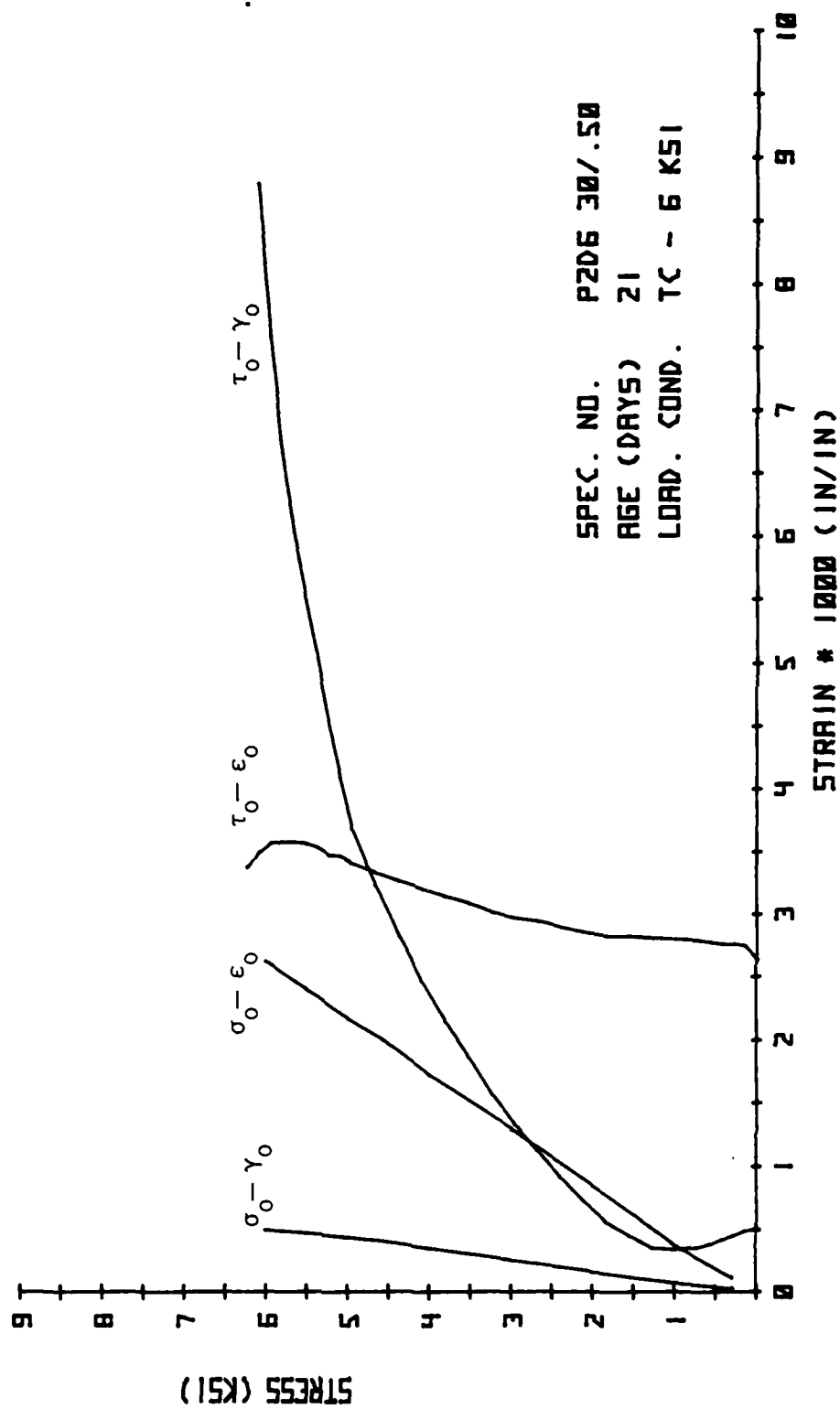


Fig. A.18. Octahedral Stress-Strain Results from Preliminary Tests.

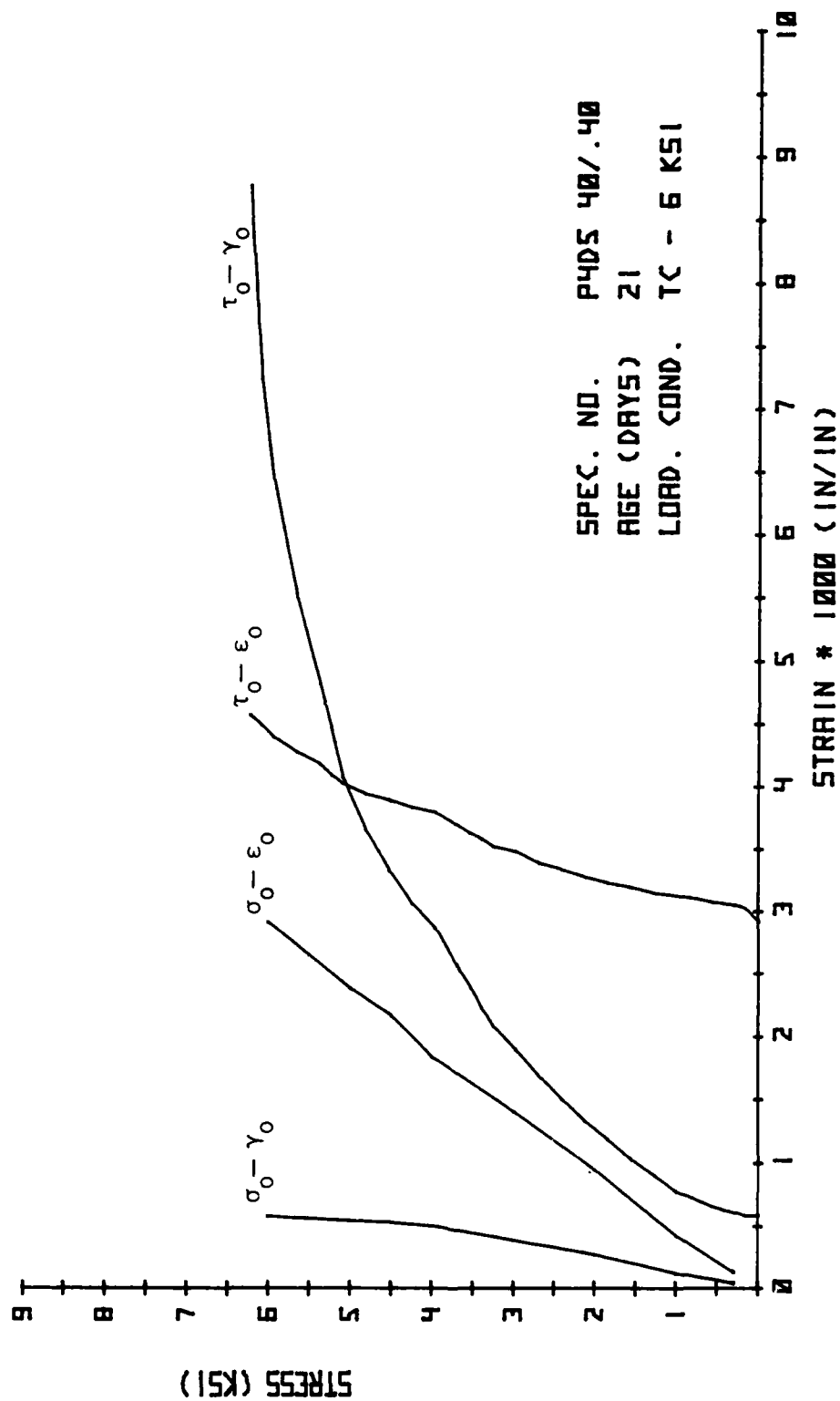


Fig. A.19. Octahedral Stress-Strain Results from Preliminary Tests.

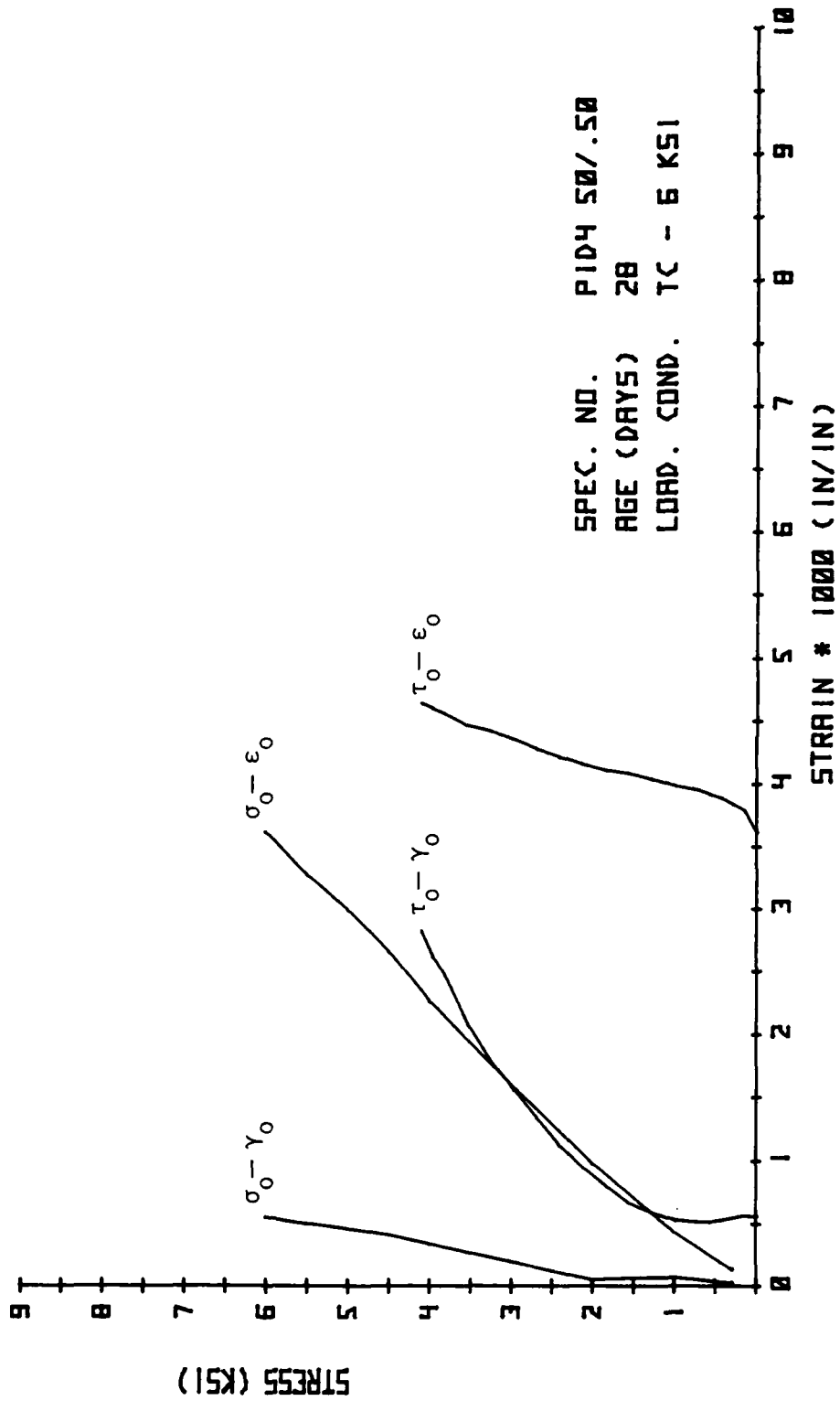


Fig. A.20. Octahedral Stress-Strain Results from Preliminary Tests.

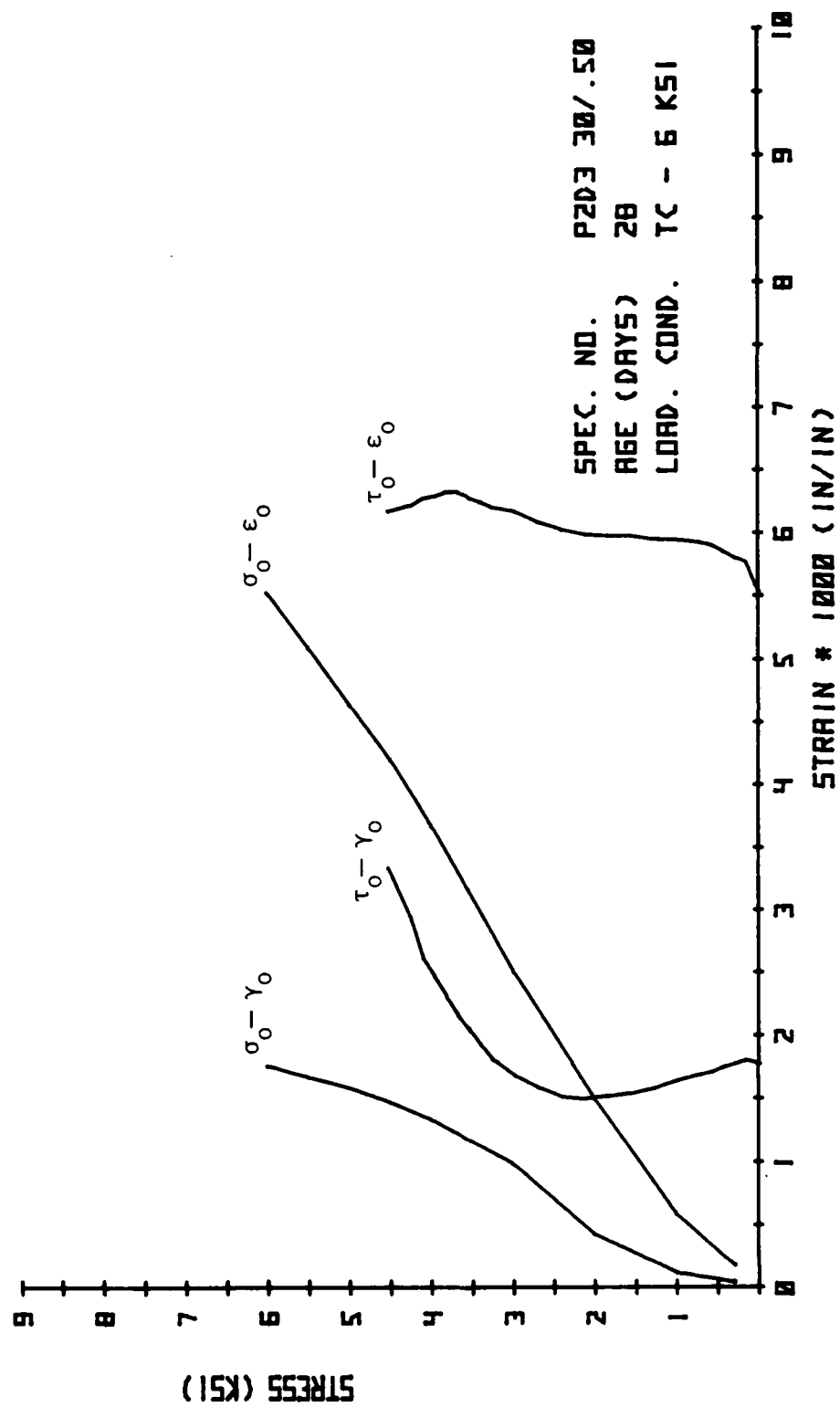


Fig. A.21. Octahedral Stress-Strain Results from Preliminary Tests.

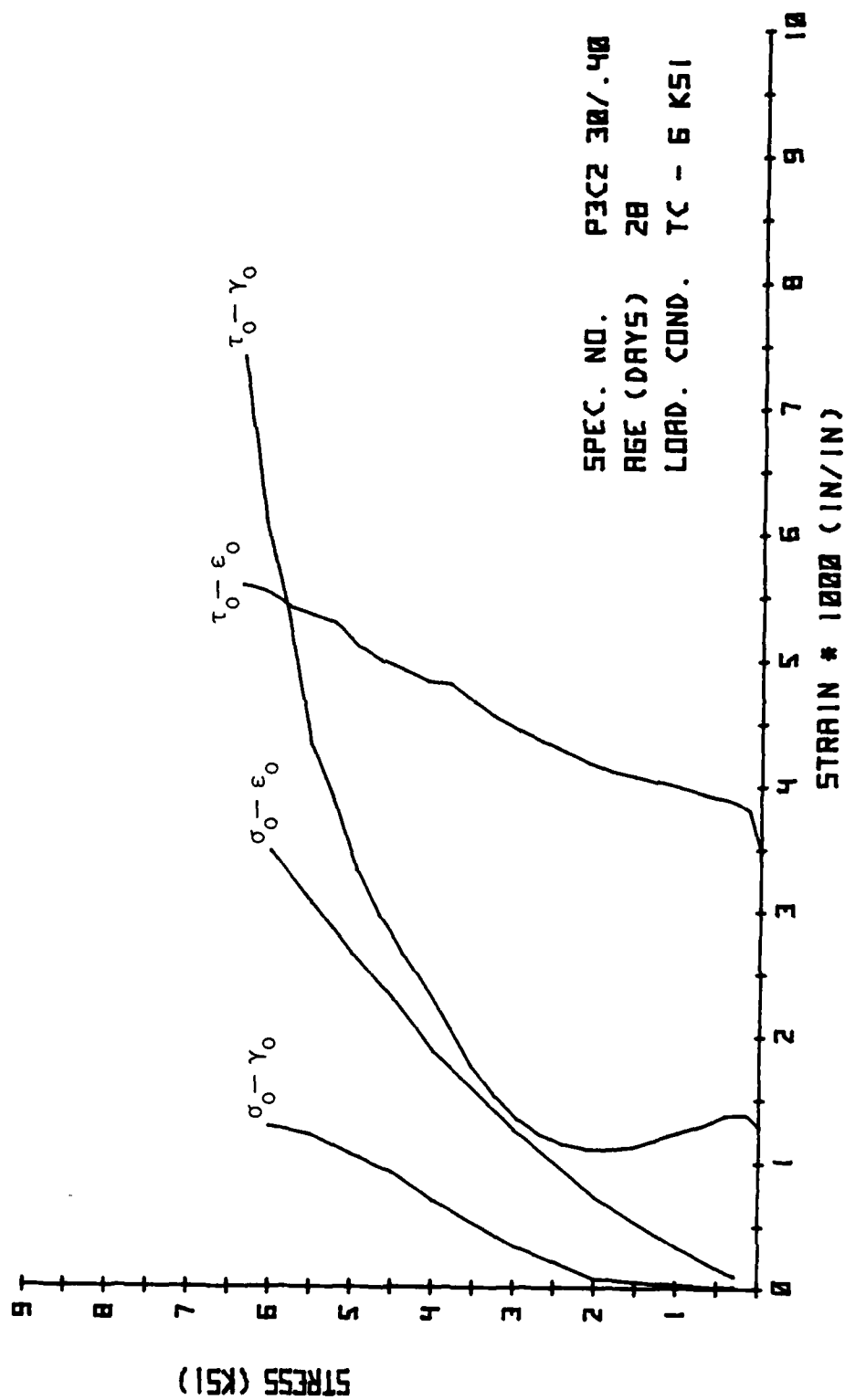


Fig. A.22. Octahedral Stress-Strain Results from Preliminary Tests.

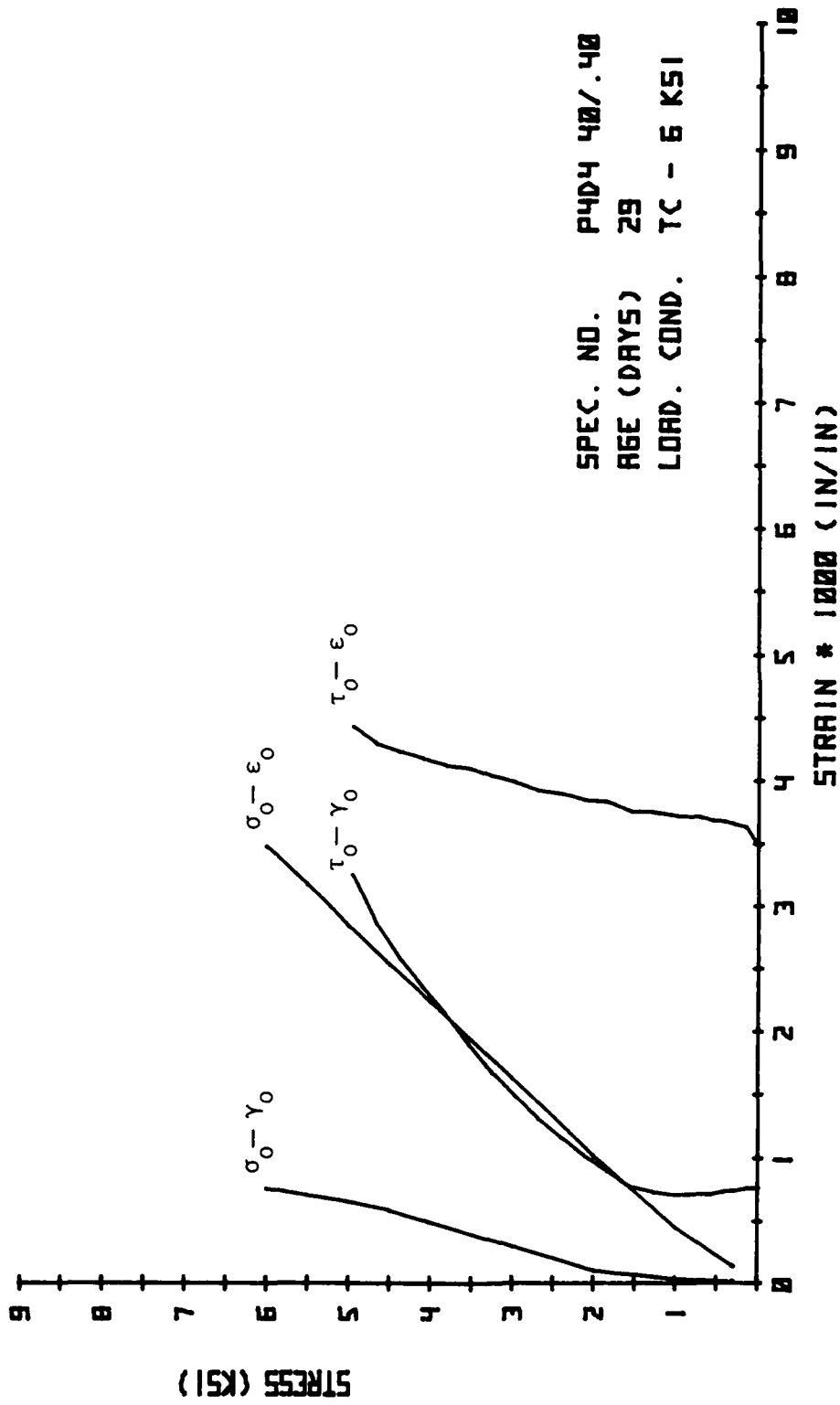


Fig. A.23. Octahedral Stress-Strain Results from Preliminary Tests.

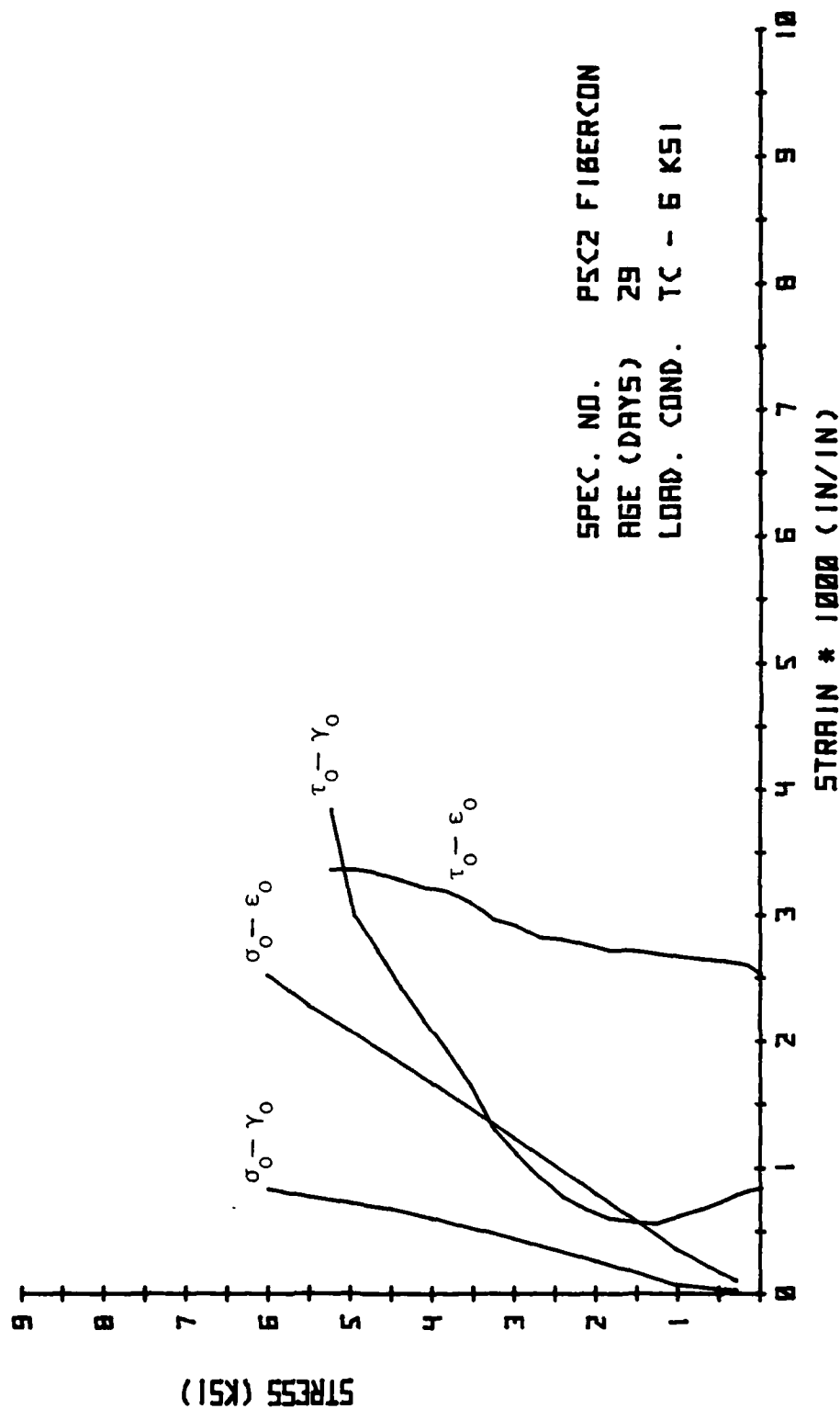


Fig. A.24. Octahedral Stress-Strain Results from Preliminary Tests.

TABLE A.1

SPECIMEN NO.: FID3
LOAD CONDITION: TRIAXIAL COMPRESSION (TC) --- 8000 PSI

σ_x (psi)	σ_y (psi)	σ_z (psi)	$\epsilon_x \cdot 1000$	$\epsilon_y \cdot 1000$	$\epsilon_z \cdot 1000$
0	0	0	0.000	0.000	0.000
250	250	250	0.028	0.083	0.143
500	500	500	0.087	0.160	0.248
750	750	750	0.128	0.220	0.358
1000	1000	1000	0.172	0.273	0.444
1500	1500	1500	0.298	0.428	0.655
2000	2000	2000	0.416	0.578	0.843
3000	3000	3000	0.720	0.892	1.244
4000	4000	4000	1.036	1.213	1.656
5000	5000	5000	1.398	1.592	2.072
6000	6000	6000	1.793	2.097	2.485
7000	7000	7000	2.208	2.580	2.840
7500	7500	7500	2.483	2.863	3.033
8000	8000	8000	2.752	3.103	3.220
7000	7000	8200	2.742	3.108	3.302
7800	7800	8400	2.722	3.080	3.403
7600	7600	8600	2.698	3.049	3.478
7500	7500	8800	2.652	3.009	3.576
7500	7500	9000	2.625	2.983	3.677
7300	7300	9400	2.561	2.900	3.872
7100	7100	9800	2.516	2.854	4.030
6900	6900	10200	2.476	2.803	4.335
6700	6700	10600	2.420	2.752	4.576
6500	6500	11000	2.365	2.695	4.833
6300	6300	11400	2.311	2.625	5.085
6100	6100	11800	2.257	2.556	5.338
5900	5900	12200	2.186	2.490	5.587
5700	5700	12600	2.123	2.417	5.842
5500	5500	13000	2.046	2.333	6.069
5300	5300	13400	1.977	2.274	6.302
5000	5000	14000	1.874	2.173	6.635

TABLE A.2

SPECIMEN NO.: FID6
LOAD CONDITION: TRIAXIAL COMPRESSION (TC) --- 8000 PSI

σ_x (psi)	σ_y (psi)	σ_z (psi)	$\epsilon_x \cdot 1000$	$\epsilon_y \cdot 1000$	$\epsilon_z \cdot 1000$
0	0	0	0.000	0.000	0.000
250	250	250	0.147	0.000	0.334
500	500	500	0.211	0.215	0.503
750	750	750	0.282	0.305	0.662
1000	1000	1000	0.362	0.385	0.756
1500	1500	1500	0.506	0.558	0.972
2000	2000	2000	0.653	0.717	1.154
3000	3000	3000	0.976	1.035	1.570
4000	4000	4000	1.380	1.432	2.049
5000	5000	5000	1.836	1.874	2.569
6000	6000	6000	2.299	2.394	2.990
7000	7000	7000	2.789	2.865	3.380
7500	7500	7500	2.956	3.128	3.567
8000	8000	8000	3.151	3.373	3.751
7900	7900	8200	3.173	3.385	3.876
7800	7800	8400	3.145	3.356	3.969
7700	7700	8600	3.122	3.333	4.052
7600	7600	8800	3.071	3.310	4.149
7500	7500	9000	3.049	3.275	4.248
7300	7300	9400	2.994	3.220	4.431
7100	7100	9800	2.949	3.177	4.630
6900	6900	10200	2.892	3.104	4.849
6700	6700	10600	2.848	3.045	5.069
6500	6500	11000	2.799	2.996	5.343
6300	6300	11400	2.744	2.926	5.555
6100	6100	11800	2.694	2.868	5.784
5900	5900	12200	2.631	2.791	6.028
5700	5700	12600	2.551	2.712	6.290
5500	5500	13000	2.478	2.627	6.561
5300	5300	13400	2.403	2.567	6.788
5100	5100	13800	2.338	2.499	7.031
4900	4900	14200	2.241	2.418	7.295
4700	4700	14600	2.155	2.317	7.607
4500	4500	15000	2.059	2.204	7.926
4300	4300	15400	1.963	2.101	8.253
4100	4100	15800	1.839	1.959	8.607
3900	3900	16200	1.709	1.818	8.963
3700	3700	16600	1.498	1.611	9.413
3500	3500	17000	1.352	1.453	9.817
3300	3300	17400	1.098	1.187	10.340
3100	3100	17800	0.841	0.893	10.905
2900	2900	18200	0.451	0.484	11.635
2700	2700	18600	-0.100	-0.115	12.623
2500	2500	19000	-0.947	-1.047	14.080
2400	2400	19200	-1.697	-1.824	15.328
2300	2300	19400	-2.571	-2.769	16.646

TABLE A.3

SPECIMEN NO.: F105
LOAD CONDITION: TRIAXIAL COMPRESSION (TC) -- 8000 PSI

σ_x (psi)	σ_y (psi)	σ_z (psi)	$\epsilon_x \cdot 1000$	$\epsilon_y \cdot 1000$	$\epsilon_z \cdot 1000$	σ_x (psi)	σ_y (psi)	σ_z (psi)	$\epsilon_x \cdot 1000$	$\epsilon_y \cdot 1000$	$\epsilon_z \cdot 1000$
0	0	0	0.000	0.000	0.000	0	0	0	0.000	0.000	0.000
100	100	100	0.097	0.049	0.066	100	100	100	0.047	-0.004	0.048
250	250	250	0.259	0.138	0.149	250	250	250	0.096	-0.015	0.107
500	500	500	0.402	0.240	0.252	500	500	500	0.178	-0.009	0.188
750	750	750	0.505	0.321	0.335	1000	1000	1000	0.306	0.020	0.354
1000	1000	1000	0.599	0.398	0.398	1500	1500	1500	0.411	0.112	0.492
1500	1500	1500	0.775	0.535	0.534	2000	2000	2000	0.570	0.242	0.665
2000	2000	2000	0.933	0.692	0.692	3000	3000	3000	0.864	0.464	0.985
3000	3000	3000	1.306	1.011	1.108	4000	4000	4000	1.245	0.487	0.982
4000	4000	4000	1.789	1.371	1.658	5000	5000	5000	1.251	0.833	0.956
5000	5000	5000	2.308	1.815	2.189	6000	6000	6000	1.237	0.836	1.365
6000	6000	6000	2.823	2.347	2.683	7000	7000	7000	1.630	0.810	1.370
6500	6500	6500	3.086	2.643	2.929	8000	8000	8000	1.630	1.173	1.351
7000	7000	7000	3.352	2.926	3.154	9000	9000	9000	1.601	1.185	1.251
7500	7500	7500	3.598	3.225	3.399	10000	10000	10000	1.978	1.176	1.222
8000	8000	8000	3.879	3.530	3.667	11000	11000	11000	1.990	1.603	1.706
8500	8500	8500	3.855	3.513	3.788	12000	12000	12000	1.992	1.613	2.073
9000	9000	9000	3.870	3.495	3.905	13000	13000	13000	2.374	2.066	2.451
9500	9500	9500	3.805	3.478	4.023	14000	14000	14000	2.602	2.344	2.627
10000	10000	10000	3.777	3.456	4.141	15000	15000	15000	2.791	2.562	2.815
11000	11000	11000	3.749	3.427	4.240	16000	16000	16000	2.825	2.594	2.972
12000	12000	12000	3.705	3.376	4.468	17000	17000	17000	2.824	2.375	3.160
13000	13000	13000	3.651	3.308	4.734	18000	18000	18000	2.860	2.261	3.375
14000	14000	14000	3.593	3.246	4.974	19000	19000	19000	2.870	2.155	3.549
15000	15000	15000	3.563	3.202	5.259	20000	20000	20000	2.892	2.023	3.781
16000	16000	16000	3.495	3.130	5.538	21000	21000	21000	2.916	1.881	4.005
17000	17000	17000	3.434	3.065	5.799	22000	22000	22000	2.928	1.775	4.241
18000	18000	18000	3.396	2.994	6.048	23000	23000	23000	2.950	1.643	4.519
19000	19000	19000	3.328	2.927	6.382	24000	24000	24000	2.992	1.511	4.751
20000	20000	20000	3.246	2.850	6.692	25000	25000	25000	3.005	1.341	5.024
21000	21000	21000	3.151	2.734	7.105	26000	26000	26000	3.029	1.247	5.210
22000	22000	22000	3.032	2.608	7.608	27000	27000	27000	3.034	1.156	5.358
23000	23000	23000	2.861	2.445	8.126	28000	28000	28000	3.049	1.097	5.481
24000	24000	24000	2.684	2.252	8.647	29000	29000	29000	3.059	0.990	5.639
25000	25000	25000	2.536	2.082	9.160	30000	30000	30000	3.080	0.891	5.767
26000	26000	26000	2.410	1.937	9.611	31000	31000	31000	3.076	0.778	5.929
27000	27000	27000	2.273	1.751	10.046	32000	32000	32000	3.112	0.695	6.081
28000	28000	28000	1.973	1.491	10.685	33000	33000	33000	3.136	0.588	6.226
29000	29000	29000	1.681	1.212	11.359	34000	34000	34000	3.149	0.455	6.358
30000	30000	30000	1.273	0.817	12.194	35000	35000	35000	3.173	0.333	6.546

TABLE A.4

SPECIMEN NO.: F101
LOAD CONDITION: SIMPLE SHEAR (SS) -- 8000 PSI

σ_x (psi)	σ_y (psi)	σ_z (psi)	$\epsilon_x \cdot 1000$	$\epsilon_y \cdot 1000$	$\epsilon_z \cdot 1000$
0	0	0	0.000	0.000	0.000
100	100	100	0.047	-0.004	0.048
250	250	250	0.096	-0.015	0.107
500	500	500	0.178	-0.009	0.188
750	750	750	0.306	0.020	0.354
1000	1000	1000	0.411	0.112	0.492
1500	1500	1500	0.570	0.242	0.665
2000	2000	2000	0.864	0.464	0.985
3000	3000	3000	1.245	0.487	0.982
4000	4000	4000	1.251	0.833	0.956
5000	5000	5000	1.237	0.836	1.365
6000	6000	6000	1.630	0.810	1.370
7000	7000	7000	1.630	1.173	1.351
8000	8000	8000	1.601	1.185	1.251
9000	9000	9000	1.978	1.176	1.222
10000	10000	10000	1.990	1.603	1.706
11000	11000	11000	1.992	1.613	2.073
12000	12000	12000	2.374	2.066	2.451
13000	13000	13000	2.602	2.344	2.627
14000	14000	14000	2.791	2.562	2.815
15000	15000	15000	2.825	2.594	2.972
16000	16000	16000	2.824	2.375	3.160
17000	17000	17000	2.860	2.261	3.375
18000	18000	18000	2.870	2.155	3.549
19000	19000	19000	2.892	2.023	3.781
20000	20000	20000	2.916	1.881	4.005
21000	21000	21000	2.928	1.775	4.241
22000	22000	22000	2.950	1.643	4.519
23000	23000	23000	2.992	1.511	4.751
24000	24000	24000	3.005	1.341	5.024
25000	25000	25000	3.029	1.247	5.210
26000	26000	26000	3.034	1.156	5.358
27000	27000	27000	3.049	1.097	5.481
28000	28000	28000	3.059	0.990	5.639
29000	29000	29000	3.080	0.891	5.767
30000	30000	30000	3.076	0.778	5.929
31000	31000	31000	3.112	0.695	6.081
32000	32000	32000	3.136	0.588	6.226
33000	33000	33000	3.149	0.455	6.358
34000	34000	34000	3.173	0.333	6.546

TABLE A.5

SPECIMEN NO.: F1D1
LOAD CONDITION: SIMPLE SHEAR (SS) -- 8000 PSI

σ_x (psi)	σ_y (psi)	σ_z (psi)	$\epsilon_x \cdot 1000$	$\epsilon_y \cdot 1000$	$\epsilon_z \cdot 1000$
0	0	0	0.000	0.000	0.000
100	100	100	0.056	0.075	0.164
250	250	250	0.127	0.168	0.321
500	500	500	0.188	0.236	0.402
750	750	750	0.286	0.324	0.522
1000	1000	1000	0.370	0.411	0.641
1500	1500	1500	0.544	0.560	0.840
2000	2000	2000	0.743	0.705	1.098
3000	3000	3000	1.155	1.018	1.610
4000	4000	4000	1.642	1.359	2.145
5000	5000	5000	2.153	1.799	2.607
6000	6000	6000	2.686	2.264	3.024
6500	6500	6500	2.953	2.529	3.248
7000	7000	7000	3.188	2.721	3.411
7500	7500	7500	3.497	3.015	3.624
8000	8000	8000	3.814	3.282	3.809
8000	7800	8200	3.865	3.285	3.900
8000	7600	8400	3.870	3.201	4.000
8000	7400	8600	3.861	3.155	4.094
8000	7200	8800	3.880	3.124	4.195
8000	7000	9000	3.887	3.083	4.318
8000	6800	9400	3.902	2.977	4.536
8000	6200	9800	3.933	2.905	4.778
8000	5800	10200	3.947	2.791	4.986
8000	5400	10600	3.974	2.693	5.247
8000	5000	11000	3.999	2.595	5.500
8000	4600	11400	4.036	2.427	5.810
8000	4200	11800	4.042	2.262	6.029
8000	4000	12000	4.063	2.191	6.198
8000	3800	12200	4.077	2.112	6.335
8000	3600	12400	4.088	2.029	6.475
8000	3400	12600	4.114	1.963	6.611
8000	3200	12800	4.125	1.850	6.752
8000	3000	13000	4.157	1.737	6.894
8000	2800	13200	4.163	1.640	7.032
8000	2600	13400	4.194	1.525	7.157
8000	2400	13600	4.209	1.382	7.322
8000	2200	13800	4.234	1.246	7.473
8000	2000	14000	4.263	1.070	7.678

TABLE A.6

SPECIMEN NO.: F1L3
LOAD CONDITION: SIMPLE SHEAR (SS) -- 8000 PSI

σ_x (psi)	σ_y (psi)	σ_z (psi)	$\epsilon_x \cdot 1000$	$\epsilon_y \cdot 1000$	$\epsilon_z \cdot 1000$
0	0	0	0.000	0.000	0.000
100	100	100	0.147	0.013	-0.044
250	250	250	0.262	0.007	-0.001
500	500	500	0.353	0.040	0.077
750	750	750	0.425	0.075	0.149
1000	1000	1000	0.504	0.101	0.210
1500	1500	1500	0.583	0.210	0.343
2000	2000	2000	0.868	0.340	0.457
2500	2500	2500	1.062	0.476	0.589
3000	3000	3000	1.243	0.635	0.767
4000	4000	4000	1.648	0.969	1.167
5000	5000	5000	2.080	1.385	1.576
6000	6000	6000	2.505	1.830	1.952
6500	6500	6500	2.707	2.046	2.046
7000	7000	7000	2.916	2.270	2.274
7500	7500	7500	3.096	2.429	2.406
8000	8000	8000	3.325	2.644	2.587
8000	7800	8200	3.327	2.623	2.672
8000	7600	8400	3.342	2.563	2.729
8000	7400	8600	3.354	2.504	2.788
8000	7200	8800	3.354	2.439	2.888
8000	7000	9000	3.339	2.392	2.977
8000	6600	9400	3.365	2.303	3.155
8000	6200	9800	3.381	2.178	3.379
8000	5800	10200	3.378	2.053	3.550
8000	5400	10600	3.392	1.934	3.760
8000	5000	11000	3.418	1.794	3.993
8000	4600	11400	3.451	1.604	4.242
8000	4200	11800	3.480	1.399	4.499
8000	4000	12000	3.501	1.330	4.612
8000	3800	12200	3.504	1.231	4.742
8000	3600	12400	3.505	1.127	4.893
8000	3400	12600	3.528	1.037	5.028
8000	3200	12800	3.553	0.908	5.189
8000	3000	13000	3.571	0.794	5.316
8000	2800	13200	3.590	0.654	5.461
8000	2600	13400	3.604	0.528	5.633
8000	2400	13600	3.633	0.367	5.787
8000	2200	13800	3.647	0.240	5.922
8000	2000	14000	3.685	0.030	6.104
8000	1800	14200	3.703	-0.109	6.303
8000	1600	14400	3.720	-0.296	6.503

TABLE A.7

SPECIMEN NO.: F1B2
LOAD CONDITION: SIMPLE SHEAR (SS) -- 8000 PSI

σ_x (psi)	σ_y (psi)	σ_z (psi)	$\epsilon_x \cdot 1000$	$\epsilon_y \cdot 1000$	$\epsilon_z \cdot 1000$
0	0	0	0.000	0.000	0.000
250	250	250	0.184	-0.009	0.193
500	500	500	0.262	0.012	0.273
750	750	750	0.340	0.053	0.337
1000	1000	1000	0.408	0.067	0.378
1500	1500	1500	0.556	0.144	0.457
2000	2000	2000	0.712	0.251	0.560
2500	2500	2500	0.826	0.304	0.649
3000	3000	3000	0.995	0.390	0.802
3500	3500	3500	1.178	0.469	0.967
4000	4000	4000	1.365	0.554	1.156
4500	4500	4500	1.567	0.635	1.336
5000	5000	5000	1.804	0.752	1.534
5500	5500	5500	2.003	0.862	1.686
6000	6000	6000	2.243	0.978	1.881
6500	6500	6500	2.444	1.108	2.094
7000	7000	7000	2.701	1.263	2.213
7500	7500	7500	2.929	1.402	2.360
8000	8000	8000	3.204	1.583	2.564
8500	8500	8500	3.572	1.830	2.657
9000	9000	9000	3.783	1.478	2.690
9500	9500	9500	3.279	1.438	2.759
10000	10000	10000	3.305	1.383	2.862
10500	10500	10500	3.320	1.335	2.934
11000	11000	11000	3.342	1.288	3.133
11500	11500	11500	3.343	1.189	3.359
12000	12000	12000	3.362	1.131	3.507
12500	12500	12500	3.363	1.032	3.720
13000	13000	13000	3.406	0.982	4.009
13500	13500	13500	3.446	0.855	4.255
14000	14000	14000	3.459	0.730	4.459
14500	14500	14500	3.462	0.612	4.710
15000	15000	15000	3.469	0.490	4.947
15500	15500	15500	3.514	0.406	5.057
16000	16000	16000	3.523	0.333	5.245
16500	16500	16500	3.523	0.283	5.356
17000	17000	17000	3.551	0.210	5.481
17500	17500	17500	3.544	0.136	5.628
18000	18000	18000	3.586	0.028	5.773
18500	18500	18500	3.627	-0.122	6.022
19000	19000	19000	3.629	-0.211	6.169
19500	19500	19500	3.654	-0.360	6.400
20000	20000	20000	3.680	-0.530	6.559
20500	20500	20500	3.705	-0.740	6.751
21000	21000	21000	3.740	-1.051	7.037
21500	21500	21500	3.784	-1.478	7.388
22000	22000	22000	3.840	-2.106	7.811

TABLE A.8

SPECIMEN NO.: F1C4
LOAD CONDITION: TRIAXIAL EXTENSION (TE) -- 8000 PSI

σ_x (psi)	σ_y (psi)	σ_z (psi)	$\epsilon_x \cdot 1000$	$\epsilon_y \cdot 1000$	$\epsilon_z \cdot 1000$
0	0	0	0.000	0.000	0.000
100	100	100	0.126	0.012	0.102
200	200	200	0.242	0.056	0.195
300	300	300	0.337	0.116	0.260
400	400	400	0.419	0.165	0.308
500	500	500	0.475	0.186	0.349
600	600	600	0.793	0.416	0.568
700	700	700	1.145	0.713	0.870
800	800	800	1.574	0.713	0.853
900	900	900	1.569	1.070	0.840
1000	1000	1000	1.567	1.067	1.245
1100	1100	1100	2.000	1.041	1.236
1200	1200	1200	1.988	1.408	1.215
1300	1300	1300	1.980	1.429	1.620
1400	1400	1400	2.401	1.413	1.612
1500	1500	1500	2.418	1.853	1.616
1600	1600	1600	2.406	1.853	1.953
1700	1700	1700	2.833	2.248	2.287
1800	1800	1800	3.113	2.519	2.455
1900	1900	1900	3.349	2.744	2.635
2000	2000	2000	3.470	2.838	2.614
2100	2100	2100	3.531	2.900	2.585
2200	2200	2200	3.588	2.948	2.566
2300	2300	2300	3.659	3.003	2.527
2400	2400	2400	3.788	3.141	2.483
2500	2500	2500	3.921	3.262	2.486
2600	2600	2600	4.049	3.373	2.327
2700	2700	2700	4.193	3.533	2.351
2800	2800	2800	4.342	3.692	2.146
2900	2900	2900	4.502	3.858	2.044
3000	3000	3000	4.649	3.984	1.917
3100	3100	3100	4.814	4.145	1.776
3200	3200	3200	4.965	4.297	1.614
3300	3300	3300	5.180	4.487	1.436
3400	3400	3400	5.305	4.587	1.344
3500	3500	3500	5.401	4.670	1.245
3600	3600	3600	5.539	4.774	1.116
3700	3700	3700	5.631	4.863	0.998
3800	3800	3800	5.777	5.000	0.817
3900	3900	3900	5.906	5.131	0.650
4000	4000	4000	6.031	5.249	0.467
4100	4100	4100	6.191	5.400	0.255
4200	4200	4200	6.311	5.534	0.033
4300	4300	4300	6.521	5.741	-0.283
4400	4400	4400	6.774	6.005	-0.698

TABLE A.9

SPECIMEN NO.: F182
LOAD CONDITION: TRIAXIAL EXTENSION (TE) -- 8000 PSI

σ_x (psi)	σ_y (psi)	σ_z (psi)	$\epsilon_x \cdot 1000$	$\epsilon_y \cdot 1000$	$\epsilon_z \cdot 1000$
0	0	0	0.000	0.000	0.000
250	250	250	0.137	0.022	0.117
500	500	500	0.341	0.056	0.167
750	750	750	0.541	0.120	0.231
1000	1000	1000	0.742	0.171	0.282
1500	1500	1500	1.006	0.282	0.386
2000	2000	2000	1.338	0.396	0.498
2500	2500	2500	1.679	0.513	0.550
3000	3000	3000	2.016	0.645	0.794
3500	3500	3500	2.340	0.769	0.970
4000	4000	4000	2.658	0.935	1.176
4500	4500	4500	2.968	1.096	1.372
5000	5000	5000	3.268	1.245	1.563
5500	5500	5500	3.555	1.454	1.764
6000	6000	6000	3.826	1.628	1.925
6500	6500	6500	4.086	1.833	2.102
7000	7000	7000	4.334	2.023	2.271
7500	7500	7500	4.568	2.255	2.461
8000	8000	8000	4.788	2.462	2.641
8500	8500	8500	4.991	2.544	2.823
9000	9000	9000	5.177	2.599	2.955
9500	9500	9500	5.346	2.635	3.071
10000	10000	10000	5.498	2.700	3.172
10500	10500	10500	5.635	2.772	3.265
11000	11000	11000	5.758	2.895	3.355
11500	11500	11500	5.868	2.995	3.486
12000	12000	12000	5.966	3.122	3.615
12500	12500	12500	6.054	3.224	3.722
13000	13000	13000	6.132	3.360	3.844
13500	13500	13500	6.200	3.472	3.935
14000	14000	14000	6.258	3.593	4.008
14500	14500	14500	6.306	3.723	4.063
15000	15000	15000	6.346	3.844	4.133
15500	15500	15500	6.378	3.935	4.225
16000	16000	16000	6.403	4.008	4.294
16500	16500	16500	6.422	4.063	4.375
17000	17000	17000	6.437	4.133	4.474
17500	17500	17500	6.448	4.188	4.574
18000	18000	18000	6.456	4.225	4.683
18500	18500	18500	6.461	4.294	4.788
19000	19000	19000	6.464	4.375	4.886
19500	19500	19500	6.466	4.474	4.984
20000	20000	20000	6.466	4.574	5.086
20500	20500	20500	6.464	4.683	5.188
21000	21000	21000	6.461	4.788	5.291
21500	21500	21500	6.456	4.886	5.394
22000	22000	22000	6.448	4.984	5.498
22500	22500	22500	6.437	5.086	5.598
23000	23000	23000	6.422	5.188	5.696
23500	23500	23500	6.403	5.291	5.791
24000	24000	24000	6.378	5.394	5.886
24500	24500	24500	6.346	5.498	5.984
25000	25000	25000	6.306	5.598	6.086
25500	25500	25500	6.258	5.696	6.188
26000	26000	26000	6.200	5.791	6.291
26500	26500	26500	6.132	5.886	6.394
27000	27000	27000	6.054	5.984	6.498
27500	27500	27500	5.966	6.086	6.598
28000	28000	28000	5.868	6.188	6.696
28500	28500	28500	5.758	6.291	6.791
29000	29000	29000	5.635	6.394	6.886
29500	29500	29500	5.498	6.498	6.984
30000	30000	30000	5.346	6.598	7.086
30500	30500	30500	5.177	6.696	7.188
31000	31000	31000	5.000	6.791	7.291
31500	31500	31500	4.818	6.886	7.394
32000	32000	32000	4.635	6.984	7.498
32500	32500	32500	4.448	7.086	7.598
33000	33000	33000	4.258	7.188	7.696
33500	33500	33500	4.063	7.291	7.791
34000	34000	34000	3.868	7.394	7.886
34500	34500	34500	3.668	7.498	7.984
35000	35000	35000	3.464	7.598	8.086
35500	35500	35500	3.258	7.696	8.188
36000	36000	36000	3.046	7.791	8.291
36500	36500	36500	2.826	7.886	8.394
37000	37000	37000	2.600	7.984	8.498
37500	37500	37500	2.368	8.086	8.598
38000	38000	38000	2.132	8.188	8.696
38500	38500	38500	1.891	8.291	8.791
39000	39000	39000	1.646	8.394	8.886
39500	39500	39500	1.398	8.498	8.984
40000	40000	40000	1.146	8.598	9.086
40500	40500	40500	0.891	8.696	9.188
41000	41000	41000	0.635	8.791	9.291
41500	41500	41500	0.378	8.886	9.394
42000	42000	42000	0.117	8.984	9.498
42500	42500	42500	-0.146	9.086	9.598
43000	43000	43000	-0.400	9.188	9.696
43500	43500	43500	-0.646	9.291	9.791
44000	44000	44000	-0.886	9.394	9.886
44500	44500	44500	-1.117	9.498	9.984
45000	45000	45000	-1.338	9.598	10.086
45500	45500	45500	-1.546	9.696	10.188
46000	46000	46000	-1.746	9.791	10.291
46500	46500	46500	-1.937	9.886	10.394
47000	47000	47000	-2.117	9.984	10.498
47500	47500	47500	-2.286	10.086	10.598
48000	48000	48000	-2.446	10.188	10.696
48500	48500	48500	-2.598	10.291	10.791
49000	49000	49000	-2.741	10.394	10.886
49500	49500	49500	-2.876	10.498	10.984
50000	50000	50000	-3.000	10.598	11.086
50500	50500	50500	-3.117	10.696	11.188
51000	51000	51000	-3.226	10.791	11.291
51500	51500	51500	-3.326	10.886	11.394
52000	52000	52000	-3.417	10.984	11.498
52500	52500	52500	-3.500	11.086	11.598
53000	53000	53000	-3.576	11.188	11.696
53500	53500	53500	-3.646	11.291	11.791
54000	54000	54000	-3.709	11.394	11.886
54500	54500	54500	-3.764	11.498	11.984
55000	55000	55000	-3.811	11.598	12.086
55500	55500	55500	-3.850	11.696	12.188
56000	56000	56000	-3.881	11.791	12.291
56500	56500	56500	-3.904	11.886	12.394
57000	57000	57000	-3.919	11.984	12.498
57500	57500	57500	-3.926	12.086	12.598
58000	58000	58000	-3.926	12.188	12.696
58500	58500	58500	-3.917	12.291	12.791
59000	59000	59000	-3.900	12.394	12.886
59500	59500	59500	-3.876	12.498	12.984
60000	60000	60000	-3.846	12.598	13.086
60500	60500	60500	-3.809	12.696	13.188
61000	61000	61000	-3.764	12.791	13.291
61500	61500	61500	-3.711	12.886	13.394
62000	62000	62000	-3.650	12.984	13.498
62500	62500	62500	-3.581	13.086	13.598
63000	63000	63000	-3.506	13.188	13.696
63500	63500	63500	-3.426	13.291	13.791
64000	64000	64000	-3.341	13.394	13.886
64500	64500	64500	-3.250	13.498	13.984
65000	65000	65000	-3.154	13.598	14.086
65500	65500	65500	-3.054	13.696	14.188
66000	66000	66000	-2.949	13.791	14.291
66500	66500	66500	-2.839	13.886	14.394
67000	67000	67000	-2.726	13.984	14.498
67500	67500	67500	-2.609	14.086	14.598
68000	68000	68000	-2.486	14.188	14.696
68500	68500	68500	-2.358	14.291	14.791
69000	69000	69000	-2.226	14.394	14.886
69500	69500	69500	-2.091	14.498	14.984
70000	70000	70000	-1.946	14.598	15.086
70500	70500	70500	-1.791	14.696	15.188
71000	71000	71000	-1.626	14.791	15.291
71500	71500	71500	-1.454	14.886	15.394
72000	72000	72000	-1.276	14.984	15.498
72500	72500	72500	-1.091	15.086	15.598
73000	73000	73000	-0.898	15.188	15.696
73500	73500	73500	-0.698	15.291	15.791
74000	74000	74000	-0.491	15.394	15.886
74500	74500	74500	-0.276	15.498	15.984
75000	75000	75000	-0.054	15.598	16.086
75500	75500	75500	0.176	15.696	16.188
76000	76000	76000	0.400	15.791	16.291
76500	76500	76500	0.617	15.886	16.394
77000	77000	77000	0.826	15.984	16.498
77500	77500	77500	1.026	16.086	16.598
78000	78000	78000	1.217	16.188	16.696
78500	78500	78500	1.400	16.291	16.791
79000	79000	79000	1.576	16.394	16.886
79500	79500	79500	1.746	16.498	16.984
80000	80000	80000	1.909	16.598	17.086
80500	80500	80500	2.064	16.696	17.188
81000	81000	81000	2.211	16.791	17.291
81500	81500	81500	2.350	16.886	17.394
82000	82000	82000	2.481	16.984	17.498
82500	82500	82500	2.604	17.086	17.598
83000	83000	83000	2.720	17.188	17.696
83500	83500	83500	2.829	17.291	17.791
84000	84000	84000	2.931	17.394	17.886
84500	84500	84500	3.026	17.498	17.984
85000	85000	85000	3.114	17.598	18.086
85500	85500	85500	3.196	17.696	18.188
86000	86000	86000	3.272	17.791	18.291
86500	86500	86500	3.341	17.886	18.394
87000	87000	87000	3.403	17.984	18.498
87500	87500	87500	3.458	18.086	18.598
88000	88000	88000	3.506	18.188	18.696
88500	88500	88500	3.546	18.291	18.791
89000	89000	89000	3.579	18.394	18.886
89500	89500	89500	3.606	18.498	18.984
90000	90000	90000	3.626	18.598	19.086
90500	90500	90500	3.639	18.696	19.188
91000	91000	91000	3.646	18.791	19.291

TABLE A.11

SPECIMEN NO.: F102
LOAD CONDITION: TRIAXIAL COMPRESSION (TC) -- 6000 PSI

σ_x (psi)	σ_y (psi)	σ_z (psi)	$\epsilon_x \cdot 1000$	$\epsilon_y \cdot 1000$	$\epsilon_z \cdot 1000$
0	0	0	0.000	0.000	0.000
100	100	100	0.106	0.049	0.074
250	250	250	0.195	0.127	0.149
500	500	500	0.298	0.214	0.242
750	750	750	0.389	0.301	0.331
1000	1000	1000	0.497	0.382	0.409
1500	1500	1500	0.678	0.542	0.556
2000	2000	2000	0.862	0.718	0.702
3000	3000	3000	1.335	0.683	0.681
4000	4000	4000	1.300	1.061	1.045
5000	5000	5000	1.298	1.041	1.027
6000	6000	6000	1.773	1.027	1.007
7000	7000	7000	1.775	1.421	1.410
8000	8000	8000	1.768	1.437	1.389
9000	9000	9000	2.191	1.414	1.389
10000	10000	10000	2.205	1.888	1.955
11000	11000	11000	2.193	2.096	2.155
12000	12000	12000	2.577	2.354	2.279
13000	13000	13000	2.579	2.331	2.431
14000	14000	14000	2.542	2.279	2.600
15000	15000	15000	2.489	2.224	2.769
16000	16000	16000	2.433	2.158	2.968
17000	17000	17000	2.376	2.082	3.141
18000	18000	18000	2.325	2.010	3.351
19000	19000	19000	2.252	1.937	3.563
20000	20000	20000	2.193	1.844	3.802
21000	21000	21000	2.132	1.779	4.036
22000	22000	22000	2.075	1.696	4.339
23000	23000	23000	1.994	1.613	4.625
24000	24000	24000	1.915	1.521	4.917
25000	25000	25000	1.829	1.415	5.183
26000	26000	26000	1.743	1.315	5.461
27000	27000	27000	1.635	1.207	5.788
28000	28000	28000	1.500	1.106	6.153
29000	29000	29000	1.352	0.958	6.467
30000	30000	30000	1.216	0.824	

TABLE A.12

SPECIMEN NO.: F1B4
LOAD CONDITION: TRIAXIAL COMPRESSION (TC) -- 6000 PSI

σ_x (psi)	σ_y (psi)	σ_z (psi)	$\epsilon_x \cdot 1000$	$\epsilon_y \cdot 1000$	$\epsilon_z \cdot 1000$
0	0	0	0.000	0.000	0.000
100	100	100	0.158	-0.009	0.033
250	250	250	0.311	-0.007	0.112
500	500	500	0.422	0.011	0.171
750	750	750	0.485	0.029	0.207
1000	1000	1000	0.571	0.059	0.256
1500	1500	1500	0.743	0.136	0.373
2000	2000	2000	0.924	0.218	0.512
2500	2500	2500	1.104	0.332	0.645
3000	3000	3000	1.310	0.456	0.805
3500	3500	3500	1.546	0.581	0.985
4000	4000	4000	1.762	0.734	1.148
4500	4500	4500	2.018	0.871	1.340
5000	5000	5000	2.279	1.078	1.517
5500	5500	5500	2.537	1.259	1.686
6000	6000	6000	2.771	1.498	1.854
6500	6500	6500	2.763	1.497	2.000
7000	7000	7000	2.714	1.440	2.181
7500	7500	7500	2.657	1.390	2.381
8000	8000	8000	2.597	1.324	2.602
8500	8500	8500	2.530	1.256	2.815
9000	9000	9000	2.448	1.167	3.058
9500	9500	9500	2.383	1.092	3.286
10000	10000	10000	2.322	1.020	3.549
10500	10500	10500	2.238	0.945	3.821
11000	11000	11000	2.171	0.881	4.089
11500	11500	11500	2.100	0.820	4.367
12000	12000	12000	1.989	0.721	4.655
12500	12500	12500	1.899	0.644	4.913
13000	13000	13000	1.795	0.548	5.327
13500	13500	13500	1.690	0.449	5.649
14000	14000	14000	1.555	0.359	6.011
14500	14500	14500	1.430	0.244	6.422
15000	15000	15000	1.284	0.093	6.784
15500	15500	15500	1.062	-0.085	7.242

TABLE A.13

SPECIMEN NO. 1, F1E3
LOAD CONDITION: TRIAXIAL COMPRESSION (TC) -- 6000 PSI

σ_x (psi)	σ_y (psi)	σ_z (psi)	$\epsilon_x \cdot 1000$	$\epsilon_y \cdot 1000$	$\epsilon_z \cdot 1000$
0	0	0	0.000	0.000	0.000
250	250	250	0.220	0.119	0.119
500	500	500	0.306	0.072	0.163
750	750	750	0.390	0.122	0.202
1000	1000	1000	0.457	0.154	0.223
1500	1500	1500	0.590	0.263	0.292
2000	2000	2000	0.757	0.402	0.407
2500	2500	2500	0.917	0.518	0.536
3000	3000	3000	1.083	0.645	0.578
3500	3500	3500	1.240	0.773	0.809
4000	4000	4000	1.388	0.904	0.937
4500	4500	4500	1.567	1.051	1.103
5000	5000	5000	1.742	1.212	1.226
5500	5500	5500	1.901	1.386	1.368
6000	6000	6000	2.061	1.580	1.561
5800	5800	6400	2.065	1.568	1.746
5600	5600	6800	2.031	1.522	1.962
5400	5400	7200	1.972	1.467	2.154
5200	5200	7600	1.913	1.412	2.374
5000	5000	8000	1.855	1.348	2.628
4800	4800	8400	1.787	1.269	2.865
4600	4600	8800	1.736	1.206	3.173
4400	4400	9200	1.691	1.147	3.448
4200	4200	9600	1.643	1.089	3.784
4000	4000	10000	1.592	1.037	4.097
3800	3800	10400	1.533	0.965	4.438
3600	3600	10800	1.470	0.903	4.787
3400	3400	11200	1.383	0.816	5.109
3200	3200	11600	1.287	0.713	5.427
3000	3000	12000	1.162	0.577	5.779
2800	2800	12400	0.954	0.418	6.216
2600	2600	12800	0.750	0.249	6.644
2400	2400	13200	0.563	0.087	7.068
2200	2200	13600	0.284	-0.146	7.602
2000	2000	14000	-0.087	-0.443	8.272
1800	1800	14400	-0.669	-0.856	9.171
1600	1600	14800	-1.528	-1.545	10.417

TABLE A.14

SPECIMEN NO. 1, F1E2
LOAD CONDITION: SIMPLE SHEAR (SS) -- 6000 PSI

σ_x (psi)	σ_y (psi)	σ_z (psi)	$\epsilon_x \cdot 1000$	$\epsilon_y \cdot 1000$	$\epsilon_z \cdot 1000$
0	0	0	0.000	0.000	0.000
100	100	100	0.116	0.086	0.072
250	250	250	0.163	0.176	0.190
500	500	500	0.215	0.272	0.269
750	750	750	0.319	0.371	0.330
1000	1000	1000	0.432	0.453	0.406
1500	1500	1500	0.695	0.622	0.509
2000	2000	2000	0.867	0.763	0.623
2500	2500	2500	1.282	0.740	0.577
3000	3000	3000	1.271	1.090	0.533
3500	3500	3500	1.239	1.059	0.873
4000	4000	4000	1.681	1.025	0.845
4500	4500	4500	1.657	1.373	0.803
5000	5000	5000	1.634	1.337	1.190
5500	5500	5500	2.034	1.315	1.182
6000	6000	6000	2.074	1.746	1.146
5800	5800	6400	2.054	1.762	1.527
5600	5600	6800	2.054	1.762	1.527
5400	5400	7200	2.230	1.935	1.685
5200	5200	7600	2.230	2.156	1.877
5000	5000	8000	2.464	2.156	1.932
4800	4800	8400	2.509	2.168	1.932
4600	4600	8800	2.510	2.127	2.019
4400	4400	9200	2.544	2.081	2.109
4200	4200	9600	2.547	2.017	2.193
4000	4000	10000	2.545	1.968	2.303
3800	3800	10400	2.548	1.892	2.419
3600	3600	10800	2.570	1.822	2.525
3400	3400	11200	2.571	1.758	2.620
3200	3200	11600	2.574	1.695	2.722
3000	3000	12000	2.570	1.635	2.831
2800	2800	12400	2.569	1.546	2.965
2600	2600	12800	2.573	1.479	3.097
2400	2400	13200	2.579	1.401	3.206
2200	2200	13600	2.600	1.330	3.373
2000	2000	14000	2.615	1.237	3.497
1800	1800	14400	2.615	1.165	3.651
1600	1600	14800	2.621	1.088	3.822
1400	1400	15200	2.634	0.991	3.991
1200	1200	15600	2.652	0.902	4.118
1000	1000	16000	2.669	0.812	4.261
800	800	16400	2.683	0.696	4.470
600	600	16800	2.717	0.580	4.650
400	400	17200	2.727	0.450	4.877
200	200	17600	2.742	0.291	5.114
0	0	18000	2.743	0.112	5.333
0	0	18400	2.770	-0.092	5.590

TABLE A.15

SPECIMEN NO.: F1R5
LOAD CONDITION: SIMPLE SHEAR (SS) -- 6000 PSI

σ_x (psi)	σ_y (psi)	σ_z (psi)	$\epsilon_x \cdot 1000$	$\epsilon_y \cdot 1000$	$\epsilon_z \cdot 1000$	σ_x (psi)	σ_y (psi)	σ_z (psi)	$\epsilon_x \cdot 1000$	$\epsilon_y \cdot 1000$	$\epsilon_z \cdot 1000$
0	0	0	0.000	0.000	0.000	0	0	0	0.000	0.000	0.000
100	100	100	0.117	0.013	0.034	250	250	250	0.039	0.010	-0.001
250	250	250	0.200	0.030	0.050	500	500	500	0.093	0.038	0.032
500	500	500	0.320	0.050	0.070	750	750	750	0.151	0.080	0.070
750	750	750	0.380	0.080	0.140	1000	1000	1000	0.197	0.097	0.121
1000	1000	1000	0.460	0.110	0.170	1500	1500	1500	0.329	0.186	0.210
1500	1500	1500	0.600	0.140	0.200	2000	2000	2000	0.471	0.258	0.313
2000	2000	2000	0.720	0.230	0.240	2500	2500	2500	0.628	0.342	0.425
2500	2500	2500	0.730	0.330	0.250	3000	3000	3000	0.788	0.454	0.567
3000	3000	3000	0.840	0.380	0.350	3500	3500	3500	0.962	0.554	0.744
3500	3500	3500	0.990	0.480	0.450	4000	4000	4000	1.120	0.671	0.877
4000	4000	4000	1.170	0.620	0.590	4500	4500	4500	1.292	0.768	1.028
4500	4500	4500	1.340	0.720	0.740	5000	5000	5000	1.440	0.872	1.168
5000	5000	5000	1.550	0.840	0.900	5500	5500	5500	1.600	1.005	1.340
5500	5500	5500	1.740	1.000	1.040	6000	6000	6000	1.774	1.133	1.502
6000	6000	6000	1.990	1.210	1.240	6500	6500	6500	1.763	1.107	1.562
6500	6500	6500	2.240	1.400	1.430	7000	7000	7000	1.758	1.068	1.603
7000	7000	7000	2.420	1.340	1.480	7500	7500	7500	1.761	1.029	1.687
7500	7500	7500	2.230	1.290	1.550	8000	8000	8000	1.782	0.982	1.757
8000	8000	8000	2.220	1.240	1.640	8500	8500	8500	1.784	0.939	1.835
8500	8500	8500	2.230	1.160	1.730	9000	9000	9000	1.799	0.892	1.923
9000	9000	9000	2.250	1.090	1.830	9500	9500	9500	1.798	0.822	1.999
9500	9500	9500	2.260	0.940	2.020	10000	10000	10000	1.799	0.776	2.082
10000	10000	10000	2.280	0.880	2.110	10500	10500	10500	1.807	0.711	2.192
10500	10500	10500	2.290	0.800	2.220	11000	11000	11000	1.824	0.682	2.291
11000	11000	11000	2.280	0.740	2.320	11500	11500	11500	1.824	0.616	2.383
11500	11500	11500	2.290	0.670	2.420	12000	12000	12000	1.813	0.559	2.483
12000	12000	12000	2.300	0.610	2.540	12500	12500	12500	1.818	0.502	2.570
12500	12500	12500	2.300	0.550	2.630	13000	13000	13000	1.822	0.451	2.672
13000	13000	13000	2.300	0.480	2.720	13500	13500	13500	1.814	0.388	2.772
13500	13500	13500	2.320	0.420	2.800	14000	14000	14000	1.824	0.330	2.885
14000	14000	14000	2.320	0.350	2.950	14500	14500	14500	1.832	0.250	2.993
14500	14500	14500	2.340	0.270	3.090	15000	15000	15000	1.855	0.182	3.106
15000	15000	15000	2.350	0.200	3.230	15500	15500	15500	1.852	0.100	3.246
15500	15500	15500	2.380	0.090	3.390	16000	16000	16000	1.867	0.025	3.373
16000	16000	16000	2.360	0.030	3.540	16500	16500	16500	1.886	-0.058	3.525
16500	16500	16500	2.380	-0.070	3.660	17000	17000	17000	1.886	-0.116	3.659
17000	17000	17000	2.410	-0.160	3.820	17500	17500	17500	1.887	-0.203	3.803
17500	17500	17500	2.400	-0.250	3.980	18000	18000	18000	1.898	-0.276	3.957
18000	18000	18000	2.410	-0.440	4.180	18500	18500	18500	1.923	-0.376	4.122
18500	18500	18500	2.440	-0.570	4.360	19000	19000	19000	1.944	-0.503	4.287
19000	19000	19000	2.460	-0.730	4.520	19500	19500	19500	1.944	-0.633	4.471
19500	19500	19500	2.430	-0.930	4.710	20000	20000	20000	1.967	-0.803	4.634
20000	20000	20000	2.510	-1.240	4.950	20500	20500	20500	1.993	-1.104	4.876
20500	20500	20500	2.550	-1.710	5.250						

TABLE A.16

SPECIMEN NO.: F2D3
LOAD CONDITION: SIMPLE SHEAR (SS) -- 6000 PSI

σ_x (psi)	σ_y (psi)	σ_z (psi)	$\epsilon_x \cdot 1000$	$\epsilon_y \cdot 1000$	$\epsilon_z \cdot 1000$
0	0	0	0.000	0.000	0.000
250	250	250	0.039	0.010	-0.001
500	500	500	0.093	0.038	0.032
750	750	750	0.151	0.080	0.070
1000	1000	1000	0.197	0.097	0.121
1500	1500	1500	0.329	0.186	0.210
2000	2000	2000	0.471	0.258	0.313
2500	2500	2500	0.628	0.342	0.425
3000	3000	3000	0.788	0.454	0.567
3500	3500	3500	0.962	0.554	0.744
4000	4000	4000	1.120	0.671	0.877
4500	4500	4500	1.292	0.768	1.028
5000	5000	5000	1.440	0.872	1.168
5500	5500	5500	1.600	1.005	1.340
6000	6000	6000	1.774	1.133	1.502
6500	6500	6500	1.763	1.107	1.562
7000	7000	7000	1.758	1.068	1.603
7500	7500	7500	1.761	1.029	1.687
8000	8000	8000	1.782	0.982	1.757
8500	8500	8500	1.784	0.939	1.835
9000	9000	9000	1.799	0.892	1.923
9500	9500	9500	1.798	0.822	1.999
10000	10000	10000	1.799	0.776	2.082
10500	10500	10500	1.807	0.711	2.192
11000	11000	11000	1.824	0.682	2.291
11500	11500	11500	1.824	0.616	2.383
12000	12000	12000	1.813	0.559	2.483
12500	12500	12500	1.818	0.502	2.570
13000	13000	13000	1.822	0.451	2.672
13500	13500	13500	1.814	0.388	2.772
14000	14000	14000	1.824	0.330	2.885
14500	14500	14500	1.832	0.250	2.993
15000	15000	15000	1.855	0.182	3.106
15500	15500	15500	1.852	0.100	3.246
16000	16000	16000	1.867	0.025	3.373
16500	16500	16500	1.886	-0.058	3.525
17000	17000	17000	1.886	-0.116	3.659
17500	17500	17500	1.887	-0.203	3.803
18000	18000	18000	1.898	-0.276	3.957
18500	18500	18500	1.923	-0.376	4.122
19000	19000	19000	1.944	-0.503	4.287
19500	19500	19500	1.944	-0.633	4.471
20000	20000	20000	1.967	-0.803	4.634
20500	20500	20500	1.993	-1.104	4.876

TABLE A.17

SPECIMEN NO.: F1C5
LOAD CONDITION: TRIAXIAL EXTENSION (TE) -- 6000 PSI

σ_x (psi)	σ_y (psi)	σ_z (psi)	$\epsilon_x \cdot 1000$	$\epsilon_y \cdot 1000$	$\epsilon_z \cdot 1000$
0	0	0	0.000	0.000	0.000
100	100	100	0.053	0.098	0.106
250	250	250	0.134	0.233	0.229
500	500	500	0.258	0.390	0.429
750	750	750	0.330	0.502	0.544
1000	1000	1000	0.409	0.593	0.634
2000	2000	2000	0.702	1.006	0.899
3000	3000	3000	1.016	1.409	1.328
4000	4000	4000	1.519	1.982	1.924
5000	5000	5000	2.013	2.609	2.525
6000	6000	6000	2.511	3.236	3.134
7000	7000	7000	3.007	3.863	3.630
8000	8000	8000	3.503	4.490	4.126
9000	9000	9000	4.000	5.117	4.622
10000	10000	10000	4.497	5.744	5.118
11000	11000	11000	4.994	6.371	5.614
12000	12000	12000	5.491	6.998	6.110
13000	13000	13000	5.988	7.625	6.606
14000	14000	14000	6.485	8.252	7.102
15000	15000	15000	6.982	8.879	7.598
16000	16000	16000	7.479	9.506	8.094
17000	17000	17000	7.976	10.133	8.590
18000	18000	18000	8.473	10.760	9.086
19000	19000	19000	8.970	11.387	9.582
20000	20000	20000	9.467	12.014	10.078
21000	21000	21000	9.964	12.641	10.574
22000	22000	22000	10.461	13.268	11.070
23000	23000	23000	10.958	13.895	11.566
24000	24000	24000	11.455	14.522	12.062
25000	25000	25000	11.952	15.149	12.558
26000	26000	26000	12.449	15.776	13.054
27000	27000	27000	12.946	16.403	13.550
28000	28000	28000	13.443	17.030	14.046
29000	29000	29000	13.940	17.657	14.542
30000	30000	30000	14.437	18.284	15.038
31000	31000	31000	14.934	18.911	15.534
32000	32000	32000	15.431	19.538	16.030
33000	33000	33000	15.928	20.165	16.526
34000	34000	34000	16.425	20.792	17.022
35000	35000	35000	16.922	21.419	17.518
36000	36000	36000	17.419	22.046	18.014
37000	37000	37000	17.916	22.673	18.510
38000	38000	38000	18.413	23.300	19.006
39000	39000	39000	18.910	23.927	19.502
40000	40000	40000	19.407	24.554	19.998
41000	41000	41000	19.904	25.181	20.494
42000	42000	42000	20.401	25.808	20.990
43000	43000	43000	20.898	26.435	21.486
44000	44000	44000	21.395	27.062	21.982
45000	45000	45000	21.892	27.689	22.478
46000	46000	46000	22.389	28.316	22.974
47000	47000	47000	22.886	28.943	23.470
48000	48000	48000	23.383	29.570	23.966
49000	49000	49000	23.880	30.197	24.462
50000	50000	50000	24.377	30.824	24.958
51000	51000	51000	24.874	31.451	25.454
52000	52000	52000	25.371	32.078	25.950
53000	53000	53000	25.868	32.705	26.446
54000	54000	54000	26.365	33.332	26.942
55000	55000	55000	26.862	33.959	27.438
56000	56000	56000	27.359	34.586	27.934
57000	57000	57000	27.856	35.213	28.430
58000	58000	58000	28.353	35.840	28.926
59000	59000	59000	28.850	36.467	29.422
60000	60000	60000	29.347	37.094	29.918
61000	61000	61000	29.844	37.721	30.414
62000	62000	62000	30.341	38.348	30.910
63000	63000	63000	30.838	38.975	31.406
64000	64000	64000	31.335	39.602	31.902
65000	65000	65000	31.832	40.229	32.398
66000	66000	66000	32.329	40.856	32.894
67000	67000	67000	32.826	41.483	33.390
68000	68000	68000	33.323	42.110	33.886
69000	69000	69000	33.820	42.737	34.382
70000	70000	70000	34.317	43.364	34.878
71000	71000	71000	34.814	43.991	35.374
72000	72000	72000	35.311	44.618	35.870
73000	73000	73000	35.808	45.245	36.366
74000	74000	74000	36.305	45.872	36.862
75000	75000	75000	36.802	46.499	37.358
76000	76000	76000	37.299	47.126	37.854
77000	77000	77000	37.796	47.753	38.350
78000	78000	78000	38.293	48.380	38.846
79000	79000	79000	38.790	49.007	39.342
80000	80000	80000	39.287	49.634	39.838
81000	81000	81000	39.784	50.261	40.334
82000	82000	82000	40.281	50.888	40.830
83000	83000	83000	40.778	51.515	41.326
84000	84000	84000	41.275	52.142	41.822
85000	85000	85000	41.772	52.769	42.318
86000	86000	86000	42.269	53.396	42.814
87000	87000	87000	42.766	54.023	43.310
88000	88000	88000	43.263	54.650	43.806
89000	89000	89000	43.760	55.277	44.302
90000	90000	90000	44.257	55.904	44.798

TABLE A.18

SPECIMEN NO.: F2C5
LOAD CONDITION: TRIAXIAL EXTENSION (TE) -- 6000 PSI

σ_x (psi)	σ_y (psi)	σ_z (psi)	$\epsilon_x \cdot 1000$	$\epsilon_y \cdot 1000$	$\epsilon_z \cdot 1000$
0	0	0	0.000	0.000	0.000
250	250	250	0.103	0.085	0.080
500	500	500	0.169	0.142	0.160
750	750	750	0.220	0.195	0.200
1000	1000	1000	0.272	0.244	0.237
1500	1500	1500	0.382	0.352	0.322
2000	2000	2000	0.504	0.449	0.404
2500	2500	2500	0.633	0.562	0.527
3000	3000	3000	0.744	0.652	0.635
3500	3500	3500	0.889	0.745	0.766
4000	4000	4000	1.031	0.869	0.914
4500	4500	4500	1.185	0.976	1.046
5000	5000	5000	1.329	1.097	1.185
5500	5500	5500	1.498	1.235	1.349
6000	6000	6000	1.657	1.388	1.531
6500	6500	6500	1.701	1.436	1.531
7000	7000	7000	1.749	1.470	1.510
7500	7500	7500	1.792	1.514	1.489
8000	8000	8000	1.826	1.534	1.441
8500	8500	8500	1.879	1.589	1.404
9000	9000	9000	1.915	1.609	1.353
9500	9500	9500	1.959	1.651	1.305
10000	10000	10000	2.021	1.691	1.279
10500	10500	10500	2.052	1.725	1.229
11000	11000	11000	2.113	1.788	1.183
11500	11500	11500	2.176	1.834	1.118
12000	12000	12000	2.216	1.863	1.073
12500	12500	12500	2.279	1.920	1.019
13000	13000	13000	2.337	1.963	0.968
13500	13500	13500	2.382	2.009	0.930
14000	14000	14000	2.462	2.067	0.868
14500	14500	14500	2.529	2.128	0.777
15000	15000	15000	2.600	2.181	0.720
15500	15500	15500	2.664	2.226	0.636
16000	16000	16000	2.736	2.282	0.553
16500	16500	16500	2.835	2.348	0.462
17000	17000	17000	2.919	2.405	0.359
17500	17500	17500	3.004	2.461	0.259
18000	18000	18000	3.088	2.527	0.152
18500	18500	18500	3.230	2.624	0.003
19000	19000	19000	3.328	2.711	-0.142
19500	19500	19500	3.444	2.809	-0.364
20000	20000	20000	3.621	2.954	-0.729
20500	20500	20500	3.821	3.148	-1.344
21000	21000	21000	4.189	3.493	-4.160

TABLE A.19

SPECIMEN NO.: F204
LOAD CONDITION: TRIAXIAL EXTENSION (TE) -- 5000 PSI

σ_x (psi)	σ_y (psi)	σ_z (psi)	$\epsilon_x \cdot 1000$	$\epsilon_y \cdot 1000$	$\epsilon_z \cdot 1000$
0	0	0	0.000	0.000	0.000
250	250	250	0.026	0.020	0.107
500	500	500	0.083	0.044	0.150
750	750	750	0.124	0.092	0.182
1000	1000	1000	0.168	0.114	0.214
1500	1500	1500	0.271	0.218	0.305
2000	2000	2000	0.386	0.350	0.385
2500	2500	2500	0.512	0.458	0.491
3000	3000	3000	0.643	0.555	0.610
3500	3500	3500	0.800	0.663	0.741
4000	4000	4000	0.975	0.810	0.905
4500	4500	4500	1.120	0.917	1.062
5000	5000	5000	1.338	1.094	1.247
5500	5500	5500	1.493	1.218	1.412
6000	6000	6000	1.692	1.447	1.610
6100	6100	5800	1.771	1.503	1.613
6200	6200	5600	1.820	1.522	1.689
6300	6300	5400	1.846	1.600	1.581
6400	6400	5200	1.884	1.625	1.543
6500	6500	5000	1.918	1.676	1.495
6600	6600	4800	1.980	1.737	1.440
6700	6700	4600	2.023	1.792	1.404
6800	6800	4400	2.083	1.854	1.361
6900	6900	4200	2.152	1.923	1.303
7000	7000	4000	2.219	1.990	1.248
7100	7100	3800	2.267	2.025	1.194
7200	7200	3600	2.332	2.120	1.151
7300	7300	3400	2.396	2.172	1.102
7400	7400	3200	2.481	2.264	1.058
7500	7500	3000	2.535	2.336	0.987
7600	7600	2800	2.617	2.421	0.899
7700	7700	2600	2.734	2.548	0.838
7800	7800	2400	2.772	2.568	0.766
7900	7900	2200	2.868	2.668	0.711
8000	8000	2000	2.963	2.762	0.622
8100	8100	1800	3.051	2.829	0.550
8200	8200	1600	3.154	2.946	0.473
8300	8300	1400	3.228	3.027	0.386
8400	8400	1200	3.358	3.151	0.289
8500	8500	1000	3.484	3.289	0.181
8600	8600	800	3.575	3.379	0.068
8700	8700	600	3.694	3.514	-0.057
8800	8800	400	3.821	3.652	-0.252
8900	8900	200	3.949	3.795	-0.507
9000	9000	0	4.103	3.928	-1.112

TABLE A.20

SPECIMEN NO.: F1H1
LOAD CONDITION: TRIAXIAL COMPRESSION (TC) -- 4000 PSI

σ_x (psi)	σ_y (psi)	σ_z (psi)	$\epsilon_x \cdot 1000$	$\epsilon_y \cdot 1000$	$\epsilon_z \cdot 1000$
0	0	0	0.000	0.000	0.000
100	100	100	0.000	0.015	0.085
250	250	250	0.167	0.025	0.192
500	500	500	0.259	0.086	0.296
750	750	750	0.345	0.152	0.373
1000	1000	1000	0.427	0.204	0.444
1500	1500	1500	0.616	0.325	0.601
2000	2000	2000	0.773	0.456	0.740
2500	2500	2500	0.952	0.603	0.900
3000	3000	3000	1.127	0.728	1.075
3500	3500	3500	1.328	0.866	1.260
4000	4000	4000	1.546	1.022	1.475
4200	3900	4200	1.535	1.019	1.556
4400	3800	4400	1.507	0.996	1.640
4600	3700	4600	1.460	0.961	1.717
4800	3600	4800	1.410	0.937	1.815
5000	3500	5000	1.387	0.920	1.913
5200	3400	5200	1.352	0.885	1.985
5400	3300	5400	1.307	0.859	2.073
5600	3200	5600	1.289	0.848	2.155
5800	3100	5800	1.255	0.808	2.212
6000	3000	6000	1.220	0.784	2.323
6200	2800	6400	1.157	0.745	2.478
6400	2600	6800	1.075	0.674	2.676
6600	2400	7200	1.001	0.617	2.875
6800	2200	7600	0.904	0.536	3.076
7000	2000	8000	0.806	0.468	3.267
7200	1900	8200	0.755	0.424	3.383
7400	1800	8400	0.701	0.378	3.487
7600	1700	8600	0.653	0.333	3.597
7800	1600	8800	0.603	0.299	3.746
8000	1500	9000	0.560	0.275	3.876
8200	1400	9200	0.486	0.223	3.995
8400	1300	9400	0.415	0.158	4.158
8600	1200	9600	0.367	0.118	4.355
8800	1100	9800	0.317	0.063	4.512
9000	1000	10000	0.221	0.006	4.706
9200	900	10200	0.149	-0.060	4.888
9400	800	10400	0.065	-0.143	5.109
9600	700	10600	-0.108	-0.258	5.342

TABLE A.22

SPECIMEN NO.: F3B2
LOAD CONDITION: TRIAXIAL COMPRESSION (TC) -- 4000 PSI

σ_x (psi)	σ_y (psi)	σ_z (psi)	$\epsilon_x \cdot 1000$	$\epsilon_y \cdot 1000$	$\epsilon_z \cdot 1000$
0	0	0	0.000	0.000	0.000
300	300	300	0.016	0.007	0.016
500	500	500	0.044	0.052	0.044
750	750	750	0.085	0.092	0.085
1000	1000	1000	0.129	0.121	0.105
1500	1500	1500	0.203	0.212	0.159
2000	2000	2000	0.289	0.308	0.237
2500	2500	2500	0.377	0.392	0.328
3000	3000	3000	0.450	0.469	0.423
3250	3250	3250	0.481	0.498	0.484
3500	3500	3500	0.540	0.529	0.537
3750	3750	3750	0.593	0.577	0.596
4000	4000	4000	0.634	0.605	0.657
3900	3900	4200	0.605	0.597	0.735
3800	3800	4400	0.565	0.556	0.791
3700	3700	4600	0.541	0.543	0.857
3600	3600	4800	0.517	0.518	0.923
3500	3500	5000	0.489	0.495	1.011
3400	3400	5200	0.455	0.490	1.065
3300	3300	5400	0.434	0.473	1.150
3200	3200	5600	0.415	0.458	1.210
3100	3100	5800	0.380	0.392	1.289
3000	3000	6000	0.354	0.383	1.373
2800	2800	6400	0.298	0.345	1.530
2600	2600	6800	0.237	0.287	1.688
2400	2400	7200	0.179	0.256	1.859
2200	2200	7600	0.105	0.197	2.040
2000	2000	8000	0.023	0.124	2.266
1900	1900	8200	-0.020	0.090	2.338
1800	1800	8400	-0.057	0.053	2.434
1700	1700	8600	-0.098	0.015	2.560
1600	1600	8800	-0.141	-0.025	2.692
1500	1500	9000	-0.195	-0.060	2.833
1400	1400	9200	-0.227	-0.111	2.937
1300	1300	9400	-0.276	-0.156	3.048
1200	1200	9600	-0.347	-0.217	3.213
1100	1100	9800	-0.399	-0.391	3.380
1000	1000	10000	-0.481	-0.373	3.561
900	900	10200	-0.595	-0.482	3.786
800	800	10400	-0.726	-0.615	3.991
700	700	10600	-0.908	-0.762	4.244
600	600	10800	-1.150	-0.971	4.550
500	500	11000	-1.643	-1.361	5.016
400	400	11200	-2.528	-2.071	5.751

TABLE A.21

SPECIMEN NO.: F3B6
LOAD CONDITION: TRIAXIAL COMPRESSION (TC) -- 4000 PSI

σ_x (psi)	σ_y (psi)	σ_z (psi)	$\epsilon_x \cdot 1000$	$\epsilon_y \cdot 1000$	$\epsilon_z \cdot 1000$
0	0	0	0.000	0.000	0.000
250	250	250	0.035	0.034	0.035
500	500	500	0.078	0.079	0.078
750	750	750	0.095	0.099	0.095
1000	1000	1000	0.116	0.111	0.116
1500	1500	1500	0.164	0.165	0.164
2000	2000	2000	0.258	0.272	0.273
2500	2500	2500	0.347	0.369	0.391
3000	3000	3000	0.472	0.473	0.507
3500	3500	3500	0.618	0.569	0.643
4000	4000	4000	0.771	0.678	0.780
3900	3900	4200	0.756	0.679	0.861
3800	3800	4400	0.747	0.672	0.943
3700	3700	4600	0.720	0.663	1.044
3600	3600	4800	0.694	0.646	1.141
3500	3500	5000	0.659	0.633	1.233
3400	3400	5200	0.654	0.627	1.328
3300	3300	5400	0.627	0.601	1.478
3200	3200	5600	0.601	0.590	1.611
3100	3100	5800	0.582	0.588	1.683
3000	3000	6000	0.562	0.566	1.801
2800	2800	6400	0.525	0.536	2.039
2700	2700	6600	0.495	0.508	2.163
2600	2600	6800	0.483	0.503	2.291
2500	2500	7000	0.446	0.458	2.394
2400	2400	7200	0.423	0.455	2.539
2300	2300	7400	0.391	0.434	2.675
2200	2200	7600	0.370	0.410	2.797
2100	2100	7800	0.335	0.389	2.925
2000	2000	8000	0.305	0.353	3.084
1900	1900	8200	0.255	0.318	3.218
1800	1800	8400	0.217	0.272	3.365
1700	1700	8600	0.181	0.237	3.506
1600	1600	8800	0.133	0.204	3.658
1500	1500	9000	0.104	0.171	3.814
1400	1400	9200	0.051	0.117	3.987
1300	1300	9400	0.025	0.089	4.098
1200	1200	9600	-0.032	0.035	4.273
1100	1100	9800	-0.087	-0.007	4.485
1000	1000	10000	-0.163	-0.087	4.673
900	900	10200	-0.251	-0.159	4.834
800	800	10400	-0.362	-0.244	5.051

TABLE A.24

SPECIMEN NO. 1 F2B3
LOAD CONDITION: SIMPLE SHEAR (SS) -- 4000 PSI

σ_x (psi)	σ_y (psi)	σ_z (psi)	$\epsilon_x \cdot 1000$	$\epsilon_y \cdot 1000$	$\epsilon_z \cdot 1000$
0	0	0	0.000	0.000	0.000
250	250	250	0.028	0.008	0.028
500	500	500	0.079	0.079	0.079
750	750	750	0.110	0.108	0.110
1000	1000	1000	0.155	0.147	0.155
1500	1500	1500	0.218	0.229	0.225
2000	2000	2000	0.322	0.342	0.325
2500	2500	2500	0.445	0.437	0.418
3000	3000	3000	0.586	0.523	0.553
3500	3500	3500	0.732	0.642	0.697
4000	4000	4000	0.888	0.787	0.843
4000	3900	4100	0.866	0.777	0.898
4000	3800	4200	0.867	0.742	0.940
4000	3700	4300	0.862	0.714	0.972
4000	3600	4400	0.864	0.688	1.007
4000	3500	4500	0.872	0.654	1.059
4000	3400	4600	0.857	0.639	1.081
4000	3300	4700	0.865	0.618	1.126
4000	3200	4800	0.870	0.595	1.194
4000	3100	4900	0.870	0.580	1.221
4000	3000	5000	0.884	0.551	1.272
4000	2800	5200	0.888	0.507	1.372
4000	2700	5300	0.883	0.481	1.428
4000	2600	5400	0.911	0.445	1.489
4000	2500	5500	0.906	0.422	1.527
4000	2400	5600	0.887	0.396	1.579
4000	2300	5700	0.898	0.363	1.631
4000	2200	5800	0.901	0.335	1.658
4000	2100	5900	0.903	0.297	1.715
4000	2000	6000	0.896	0.261	1.783
4000	1900	6100	0.917	0.231	1.859
4000	1800	6200	0.912	0.222	1.883
4000	1700	6300	0.913	0.185	1.947
4000	1600	6400	0.914	0.157	1.998
4000	1500	6500	0.922	0.119	2.073
4000	1400	6600	0.932	0.086	2.140
4000	1300	6700	0.933	0.056	2.198
4000	1200	6800	0.926	0.011	2.275
4000	1100	6900	0.949	-0.027	2.349
4000	1000	7000	0.943	-0.049	2.423
4000	900	7100	0.937	-0.082	2.483
4000	800	7200	0.946	-0.115	2.554
4000	700	7300	0.948	-0.147	2.647
4000	600	7400	0.979	-0.194	2.739
4000	500	7500	0.971	-0.252	2.847
4000	400	7600	0.975	-0.297	2.910
4000	300	7700	0.975	-0.374	3.017
4000	200	7800	0.983	-0.443	3.126
4000	100	7900	0.981	-0.518	3.238
4000	0	8000	0.997	-0.661	3.323

TABLE A.23

SPECIMEN NO. 1 F1A6
LOAD CONDITION: SIMPLE SHEAR (SS) -- 4000 PSI

σ_x (psi)	σ_y (psi)	σ_z (psi)	$\epsilon_x \cdot 1000$	$\epsilon_y \cdot 1000$	$\epsilon_z \cdot 1000$
0	0	0	0.000	0.000	0.000
100	100	100	0.108	0.127	0.115
250	250	250	0.222	0.248	0.264
500	500	500	0.340	0.378	0.368
750	750	750	0.459	0.479	0.426
1000	1000	1000	0.543	0.566	0.501
2000	2000	2000	0.902	0.555	0.456
2000	2000	2000	0.857	1.004	0.418
3000	3000	3000	1.134	0.946	0.718
3000	3000	3000	1.125	0.920	0.688
4000	4000	4000	1.078	1.284	0.647
4000	3900	4100	1.078	1.241	1.003
4000	3800	4200	1.078	1.197	1.063
4000	3700	4300	1.078	1.153	1.136
4000	3600	4400	1.078	1.109	1.210
4000	3500	4500	1.078	1.065	1.284
4000	3400	4600	1.078	1.021	1.358
4000	3300	4700	1.078	0.977	1.432
4000	3200	4800	1.078	0.933	1.506
4000	3100	4900	1.078	0.889	1.580
4000	3000	5000	1.078	0.845	1.654
4000	2900	5100	1.078	0.801	1.728
4000	2800	5200	1.078	0.757	1.802
4000	2700	5300	1.078	0.713	1.876
4000	2600	5400	1.078	0.669	1.950
4000	2500	5500	1.078	0.625	2.024
4000	2400	5600	1.078	0.581	2.098
4000	2300	5700	1.078	0.537	2.172
4000	2200	5800	1.078	0.493	2.246
4000	2100	5900	1.078	0.449	2.320
4000	2000	6000	1.078	0.405	2.394
4000	1900	6100	1.078	0.361	2.468
4000	1800	6200	1.078	0.317	2.542
4000	1700	6300	1.078	0.273	2.616
4000	1600	6400	1.078	0.229	2.690
4000	1500	6500	1.078	0.185	2.764
4000	1400	6600	1.078	0.141	2.838
4000	1300	6700	1.078	0.097	2.912
4000	1200	6800	1.078	0.053	2.986
4000	1100	6900	1.078	0.009	3.060
4000	1000	7000	1.078	-0.035	3.134
4000	900	7100	1.078	-0.081	3.208
4000	800	7200	1.078	-0.127	3.282
4000	700	7300	1.078	-0.173	3.356
4000	600	7400	1.078	-0.219	3.430
4000	500	7500	1.078	-0.265	3.504
4000	400	7600	1.078	-0.311	3.578
4000	300	7700	1.078	-0.357	3.652
4000	200	7800	1.078	-0.403	3.726
4000	100	7900	1.078	-0.449	3.800
4000	0	8000	1.078	-0.495	3.874

TABLE A.25

SPECIMEN NO.: F313
LOAD CONDITION: SIMPLE SHEAR (SS) -- 4000 PSI

σ_x (psi)	σ_y (psi)	σ_z (psi)	$\epsilon_x \cdot 1000$	$\epsilon_y \cdot 1000$	$\epsilon_z \cdot 1000$
0	0	0	0.000	0.000	0.000
300	300	300	0.002	0.002	0.002
500	500	500	0.032	0.032	0.032
750	750	750	0.062	0.062	0.062
1000	1000	1000	0.119	0.119	0.119
1500	1500	1500	0.217	0.214	0.144
2000	2000	2000	0.332	0.314	0.222
2500	2500	2500	0.473	0.433	0.321
3000	3000	3000	0.615	0.582	0.413
3250	3250	3250	0.695	0.643	0.470
3500	3500	3500	0.783	0.704	0.527
3750	3750	3750	0.836	0.750	0.570
4000	4000	4000	0.934	0.817	0.629
4000	3900	4100	0.941	0.826	0.671
4000	3800	4200	0.943	0.854	0.702
4000	3700	4300	0.957	0.871	0.731
4000	3600	4400	0.957	0.889	0.759
4000	3500	4500	0.950	0.912	0.796
4000	3400	4600	0.949	0.912	0.823
4000	3300	4700	0.952	0.911	0.858
4000	3200	4800	0.952	0.911	0.889
4000	3100	4900	0.956	0.911	0.930
4000	3000	5000	0.961	0.911	0.961
4000	2800	5200	0.960	0.911	1.020
4000	2600	5400	0.973	0.922	1.110
4000	2400	5600	0.971	0.928	1.186
4000	2200	5800	0.967	0.927	1.276
4000	2000	6000	0.975	0.925	1.365
4000	1900	6100	0.975	0.925	1.413
4000	1800	6200	0.977	0.925	1.437
4000	1700	6300	0.986	0.986	1.489
4000	1600	6400	0.995	0.986	1.537
4000	1500	6500	0.995	0.986	1.573
4000	1400	6600	1.011	0.983	1.612
4000	1300	6700	1.013	0.983	1.676
4000	1200	6800	1.010	0.980	1.711
4000	1100	6900	1.018	0.981	1.780
4000	1000	7000	1.027	0.981	1.827
4000	900	7100	1.013	0.981	1.863
4000	800	7200	1.018	0.981	1.926
4000	700	7300	1.017	0.981	1.979
4000	600	7400	1.025	0.981	2.038
4000	500	7500	1.026	0.981	2.091
4000	400	7600	1.030	0.981	2.170
4000	300	7700	1.034	0.981	2.226
4000	200	7800	1.035	0.981	2.287
4000	100	7900	1.032	0.981	2.355
4000	0	8000	1.041	0.981	2.450

TABLE A.26

SPECIMEN NO.: F1B1
LOAD CONDITION: TRIAXIAL EXTENSION (TE) -- 4000 PSI

σ_x (psi)	σ_y (psi)	σ_z (psi)	$\epsilon_x \cdot 1000$	$\epsilon_y \cdot 1000$	$\epsilon_z \cdot 1000$
0	0	0	0.000	0.000	0.000
100	100	100	0.050	0.050	0.050
250	250	250	0.110	0.110	0.110
500	500	500	0.180	0.180	0.180
750	750	750	0.240	0.240	0.240
1000	1000	1000	0.340	0.340	0.340
1500	1500	1500	0.520	0.520	0.370
1500	1500	1500	0.510	0.510	0.370
1500	1500	1500	0.480	0.480	0.350
1500	1500	1500	0.670	0.670	0.510
2000	2000	2000	0.660	0.660	0.720
2000	2000	2000	0.620	0.620	0.640
2000	2000	2000	0.840	0.840	0.740
2000	2000	2000	0.830	0.830	0.910
2500	2500	2500	0.830	0.830	0.900
2500	2500	2500	0.990	0.990	0.890
2500	2500	2500	1.010	1.010	0.750
3000	3000	3000	1.000	1.000	0.920
3000	3000	3000	1.190	1.190	0.910
3500	3500	3500	1.190	1.190	0.910
3500	3500	3500	1.370	1.370	1.100
3500	3500	3500	1.390	1.390	1.100
4000	4000	4000	1.380	1.380	1.270
4000	4000	4000	1.400	1.400	1.240
4000	4000	4000	1.440	1.440	1.190
4000	4000	4000	1.480	1.480	1.140
4000	4000	4000	1.520	1.520	1.080
4000	4000	4000	1.560	1.560	1.010
4000	4000	4000	1.610	1.610	0.970
4000	4000	4000	1.660	1.660	0.900
4000	4000	4000	1.700	1.700	0.840
4000	4000	4000	1.740	1.740	0.780
4000	4000	4000	1.800	1.800	0.720
4000	4000	4000	1.850	1.850	0.650
4000	4000	4000	1.900	1.900	0.580
4000	4000	4000	1.940	1.940	0.500
4000	4000	4000	2.020	2.020	0.410
4000	4000	4000	2.070	2.070	0.330
4000	4000	4000	2.140	2.140	0.240
4000	4000	4000	2.200	2.200	0.140
4000	4000	4000	2.280	2.280	0.010
4000	4000	4000	2.350	2.350	-0.130
4000	4000	4000	2.430	2.430	-0.400

TABLE A.27

SPECIMEN NO. 1, F201
LOAD CONDITION: TRIAXIAL EXTENSION (TE) -- 4000 PSI

σ_x (psi)	σ_y (psi)	σ_z (psi)	$\epsilon_x \cdot 1000$	$\epsilon_y \cdot 1000$	$\epsilon_z \cdot 1000$
0	0	0	0.000	0.000	0.000
300	300	300	-0.014	0.003	0.003
500	500	500	0.006	0.030	0.025
750	750	750	0.027	0.060	0.044
1000	1000	1000	0.057	0.085	0.059
1500	1500	1500	0.129	0.149	0.117
2000	2000	2000	0.229	0.223	0.184
2500	2500	2500	0.313	0.320	0.259
3000	3000	3000	0.417	0.409	0.356
3250	3250	3250	0.488	0.473	0.398
3500	3500	3500	0.541	0.521	0.444
3750	3750	3750	0.606	0.588	0.492
4000	4000	4000	0.656	0.635	0.543
4100	4100	4100	0.686	0.672	0.510
4200	4200	4200	0.718	0.697	0.465
4300	4300	4300	0.763	0.728	0.431
4400	4400	4400	0.790	0.769	0.394
4500	4500	4500	0.839	0.794	0.344
4600	4600	4600	0.880	0.825	0.295
4700	4700	4700	0.910	0.847	0.241
4800	4800	4800	0.956	0.896	0.206
4900	4900	4900	1.001	0.931	0.145
5000	5000	5000	1.050	0.969	0.100
5100	5100	5100	1.108	1.020	0.058
5200	5200	5200	1.142	1.053	-0.008
5300	5300	5300	1.181	1.090	-0.067
5400	5400	5400	1.225	1.124	-0.130
5500	5500	5500	1.279	1.167	-0.197
5600	5600	5600	1.327	1.226	-0.273
5700	5700	5700	1.368	1.266	-0.334
5800	5800	5800	1.418	1.317	-0.442
5900	5900	5900	1.482	1.368	-0.552
6000	6000	6000	1.577	1.456	-0.798

TABLE A.28

SPECIMEN NO. 1, F202
LOAD CONDITION: TRIAXIAL EXTENSION (TE) -- 4000 PSI

σ_x (psi)	σ_y (psi)	σ_z (psi)	$\epsilon_x \cdot 1000$	$\epsilon_y \cdot 1000$	$\epsilon_z \cdot 1000$
0	0	0	0.000	0.000	0.000
300	300	300	0.034	0.000	0.000
500	500	500	0.070	0.030	0.070
750	750	750	0.131	0.078	0.112
1000	1000	1000	0.194	0.130	0.148
1500	1500	1500	0.310	0.249	0.210
2000	2000	2000	0.445	0.360	0.268
2500	2500	2500	0.576	0.471	0.371
3000	3000	3000	0.751	0.599	0.474
3250	3250	3250	0.839	0.656	0.513
3500	3500	3500	0.919	0.697	0.560
3750	3750	3750	1.025	0.748	0.626
4000	4000	4000	1.119	0.813	0.689
4100	4100	4100	1.154	0.835	0.638
4200	4200	4200	1.186	0.860	0.594
4300	4300	4300	1.231	0.888	0.554
4400	4400	4400	1.258	0.913	0.487
4500	4500	4500	1.316	0.957	0.448
4600	4600	4600	1.357	0.977	0.392
4700	4700	4700	1.404	1.023	0.340
4800	4800	4800	1.455	1.061	0.286
4900	4900	4900	1.514	1.089	0.245
5000	5000	5000	1.569	1.134	0.196
5100	5100	5100	1.625	1.172	0.130
5200	5200	5200	1.680	1.211	0.086
5300	5300	5300	1.742	1.261	0.043
5400	5400	5400	1.833	1.318	-0.025
5500	5500	5500	1.886	1.367	-0.071
5600	5600	5600	1.933	1.408	-0.126
5700	5700	5700	2.033	1.465	-0.194
5800	5800	5800	2.091	1.509	-0.273
5900	5900	5900	2.176	1.562	-0.397
6000	6000	6000	2.292	1.650	-0.730

